Mohd Fadzli Bin Abdollah
Hilmi Amiruddin
Amrik Singh Phuman Singh
Fudhail Abdul Munir
Asriana Ibrahim *Editors*

Proceedings of the 7th International Conference and Exhibition on Sustainable Energy and Advanced Materials (ICE-SEAM 2021), Melaka, Malaysia

Springer

Lecture Notes in Mechanical Engineering

Mohd Fadzli Bin Abdollah ·
Hilmi Amiruddin · Amrik Singh Phuman Singh ·
Fudhail Abdul Munir · Asriana Ibrahim
Editors

Proceedings of the 7th International Conference and Exhibition on Sustainable Energy and Advanced Materials (ICE-SEAM 2021), Melaka, Malaysia

Springer

Editors
Mohd Fadzli Bin Abdollah
Fakulti Kejuruteraan Mekanikal
Universiti Teknikal Malaysia Melaka
Malacca, Malaysia

Amrik Singh Phuman Singh
Fakulti Kejuruteraan Mekanikal
Universiti Teknikal Malaysia Melaka
Malacca, Malaysia

Asriana Ibrahim
Fakulti Kejuruteraan Mekanikal
Universiti Teknikal Malaysia Melaka
Malacca, Malaysia

Hilmi Amiruddin
Fakulti Kejuruteraan Mekanikal
Universiti Teknikal Malaysia Melaka
Malacca, Malaysia

Fudhail Abdul Munir
Fakulti Kejuruteraan Mekanikal
Universiti Teknikal Malaysia Melaka
Malacca, Malaysia

Editorial Preface

The 7th International Conference and Exhibition on Sustainable Energy and Advanced Material (ICE-SEAM 2021) was organized by Universiti Teknikal Malaysia Melaka (UTeM), Malaysia, in association with the Universitas Sebelas Maret (UNS), Indonesia, on 23 November 2021. The theme for ICE-SEAM 2021 is Energy Efficient and Advanced Material for Sustainable Development.

The main objective of ICE-SEAM 2021 is to create a platform for scientists, scholars, researchers, engineers, and students from higher educational institutions, research institutions, and industries to present their findings of ongoing/completed original research activities, hence fostering research collaborations between the universities and industries.

The first ICE-SEAM conference was organized by UNS in 2009. The later ICE-SEAM conferences were jointly organized by UNS and UTeM. In the years 2011, 2015, and 2019, ICE-SEAM was held in Solo, Indonesia, and in 2013 and 2017, it was held in Melaka, Malaysia. ICE-SEAM 2021 was held virtually due to the COVID-19 pandemic.

During the conference, 114 contributions were presented virtually. A total of 130 papers was submitted to the conference. After the paper selection was done through a peer-review process involving both local and international reviewers, 109 papers were published in the Springer Book Series: Lecture Notes in Mechanical Engineering. Areas of interest of the conference include but are not limited to the following topics: additive manufacturing, advanced materials and processes, design and optimization, energy efficiency, energy engineering and management, modelling and simulation, surface engineering and tribology, and thermal and fluids.

Finally, as the editors of this proceeding, we would like to thank the organizing committee, sponsors, reviewers, and participants for making this conference a success.

<div style="text-align: right">

Mohd Fadzli Bin Abdollah
Hilmi Amiruddin
Amrik Singh Phuman Singh
Fudhail Abd Munir
Asriana Ibrahim

</div>

Contents

Contents

Modeling and Simulation

Surface Engineering and Tribology

Additive Manufacturing

Design and Development of Filament Extruder for 3D Printing Machine

Lim Huat Ng[1], Shafizal Mat[1,3(✉)], Syahibudil Ikhwan Abdul Kudus[2,3],
Faiz Redza Ramli[1,3], Abd Rahman Dullah[1,3], and Mohd Rizal Alkahari[1,3]

[1] Fakulti Kejuruteraan Mekanikal, Universiti Teknikal Malaysia Melaka, Hang Tuah Jaya, 76100 Durian Tunggal, Melaka, Malaysia
shafizal@utem.edu.my

[2] Fakulti Teknologi Kejuruteraan Mekanikal dan Pembuatan, Universiti Teknikal Malaysia Melaka, Hang Tuah Jaya, 76100 Durian Tunggal, Melaka, Malaysia

[3] Centre for Advanced Research on Energy, Universiti Teknikal Malaysia Melaka, Hang Tuah Jaya, 76100 Durian Tunggal, Melaka, Malaysia

Abstract. This project intends to design and develop an extruder that can recycle the 3D printing wastes into a functional filament. The study aims to form the recycled filaments by using the product wastes from Acrylonitrile butadiene styrene (ABS) and Polylactic acid (PLA) types. Concept generation using a morphological chart and weighted matrix decision are utilised to build a 3D printer filament extruder. The process parameters for the extrusion process are determined using the Taguchi method to get the finest output of the recycled filament. The recycled filament is then used to fabricate the specimen with an open-source 3D printer. The relationship between the extrusion temperature and the filament thickness has been studied where the thickness is decreased as the temperature increased. The extruded from the recycled filament showed a low percentage of error in terms of filament's thickness when compared with the thickness from commercial filament which is 1.75 mm. The observation and evaluation are done by comparing the output of filament and specimen between the recycled and virgin material. The result also shows some well-printed specimens printed with the recycled filaments that qualified in thickness when compared with virgin materials.

Keywords: Filament extruder · Recycled filament · 3D printing

1 Introduction

In modern era, additive manufacturing has increased its popularity due to its low-cost production and good rate of efficiency. The 3D printers like Fuse Deposition Modelling (FDM) and Stereolithography (SLA) provide the opportunity for a user to create their desktop 3D printers due to the simplicity of conducting and cost-effectiveness. The primary principle of FDM is the "additive" principle by placing down material onto each other in layers [1]. The most commonly material used as a printing filament when it comes to FDM are Acrylonitrile butadiene styrene (ABS) and Polylactide acid (PLA) as they have shown magnificent results against several stresses [2].

However, there are many discarded or waste of 3D products generated before the successful print due to human or technical error. With the significant increase in the number of users, the plastic waste from 3D printing products will become a great factor that leads to heavy pollution. Furthermore, the bio-degradation process of some type of plastic especially PLA can also resulting release toxic agents that are harmful to living things [3]. Hence, a technique of recycling 3D printed parts is feasible since it can provides to an environmental benefits, such as decreasing the volume of landfills, CO2 pollution from waste transport, and the production cost for 3D printing [4]. This project aims is to design and develop a low-cost filament extruder machine that could particularly produce the recycled ABS and PLA filament from the shredded waste 3D printed products and to discover the optimized parameter for extruding the desired filament for ABS and PLA. The recycled filament must be qualified and adapted to an open-source 3D printer for reprocessing the 3D printing.

2   Methodology

2.1   Concept Design and Selection

In the initial stage, the filament extruder is distinguished in many parts where some parts like extrusion components, heating elements and electronic devices are fixed. The designable parts include the structure material, coupling mechanism, hopper mount and housing design are listed as different options in the morphological chart for concept generation and concept evaluation.

Table 1. Weighted matrix decision.

Criterion	Concept		1		2		3
	Weight	Rating	Score	Rating	Score	Rating	Score
Cost	0.25	3	0.75	2	0.50	4	1.00
Safety	0.20	5	1.00	4	0.80	4	0.80
Manufacturability	0.20	4	0.80	3	0.60	3	0.60
Installation	0.10	4	0.40	5	0.50	3	0.30
Size	0.10	4	0.40	3	0.30	5	0.50
Automation	0.15	3	0.45	4	0.60	3	0.45
Total	1.00		3.80		3.30		3.65
Ranking			**1**		**3**		**2**

Based on the past studies of filament extruder, there are some critical factors that must be determined to build a valuable extruder compared to the available products in the market. The cost rating is related to the material selection and the manufacturing process for the extruder and must be low cost. The safety of the extruder is also important where the strength of the material and stability will be considered. Manufacturability means the complexity when fabricating the machine which considers the number of equipment used, procedures, repairable, fabrication time consumed and any special skills

or techniques required. The mentioned criterions are very important when building the extruder hence the higher weights are given. The installation relates to the ease of use and the shape of the housing and extruder mounting. As for the size, it was a major criterion that relates to many criteria such as cost, safety and manufacturability since the size of the filament extruder is aimed to be fabricated in a desktop-size. Lastly, the rating of automation is only scored by judging the hopper attachment and hopper size. Because a larger volume of hopper means a longer time for the production of filament [5]. The rating of 1 to 5 is given to each concept based on the criterion. The rating is ascending as the status from poor to good.

From Table 1, concept 1 is chosen with the highest score of 3.8. This concept has an excellent score in cost, manufacturability, and installation due to its wooden design. It offers a low start-up cost and involves the only process of measuring, cutting and joint with nails and screws which make concept 1 scored better since the complexity is quite low. The box-shaped design with compact size provides sufficient protection to hold all components tightly while the use of a jaw coupler provides natural kickback protection for the auger bit during the extrusion process. This concept shows an inferior score in automation due to its design of a non-fixed hopper on a T-pipe. But the T-pipe also makes easier installation and low complexity.

2.2 Modelling and Fabrication

After choosing the concept, all of the components are prepared before model the detailed dimension. 3D modelling of the mounting and housing for the extruder is drawn by using CATIA V5 software and then proceed to the fabrication stage. The fabrication involves the motor mount, coupling, auger bit, barrel mount, heating elements with temperature probe, nozzle and the electrical circuit for extrusion and heating process. Lastly, all components are assembled as shown in Fig. 1.
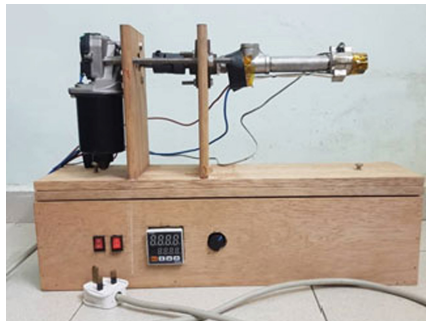
Fig. 1. Assembled filament extruder.

Next, the Taguchi method and ANOVA are utilized to determine that extrusion temperature which is the most significant factor that affect to the filament thickness. An experiment of filament extrusion is conducted separately by increasing the extrusion temperature using a fixed rotating speed to identify the optimal temperature to extrude

the ABS and PLA filament from the shredded product waste. After that, the recycled filaments are then proceeded to print out the tensile specimen and then compared the visualization with the virgin specimen to validate this project [6].

3   Results and Discussion

3.1   Filament Thickness

Figure 2 shows that the filament thickness is decreased as the extrusion temperature increased. The recycled filament has a close thickness to the virgin filament with 1.75 mm when being extruded in 220 °C and 180 °C for ABS and PLA respectively. Hence, the optimal process parameters for extrusion are determined. To print out five specimens, a filament with 7500 mm long is extruded for both materials as the estimation made from slicer software, Repetier-Host that one specimen will consume about 1500 mm. After that, the filament thickness is measured by using Vernier Caliper for every 150 mm and obtained an averaged of 1.70 mm ± 0.10 mm for both ABS and PLA.
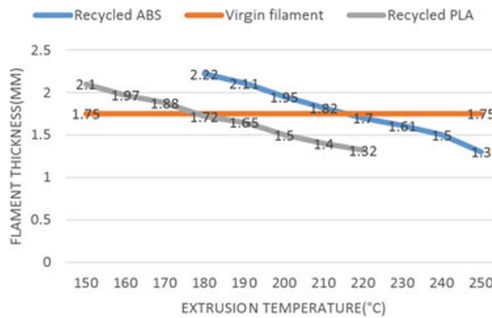
Fig. 2. Extrusion temperature against filament thickness (ABS and PLA).

3.2   Comparison for Visualization

As expected, the specimens printed with the virgin filament of ABS and PLA showed a smooth surface with exact dimensions as the specimen's modelling. The recycled specimens also showed an exact dimension as the virgin specimen with an error of ±0.10 mm. However, there are some visible but small defects found on several specimens especially for top and bottom surfaces such as micro holes, cracks and missing layers (Fig. 3).

This can be explained since the specimen is printed with a filament consist of inconstant thickness. Missing layers occurred on the large surface of the specimen randomly because that certain section is printed with the filament with smaller thickness where material volume is insufficient to print a perfect layer. An air gap may occur among the microstructure of the filament during the extrusion process of turning the flakes form into liquid form and then solidified again. The imperfect microstructure of filament may weaken the layer bonding between the layers of the specimen which causing micro holes or cracks in a certain area.

Fig. 3. Defects on specimens.

4   Conclusion

A filament extruder is designed and fabricated. The optimal process parameters for the extrusion process are determined as well using DOE and experiments. The recycled filament for both ABS and PLA show a qualified thickness of 1.70 mm $\pm$ 0.10 mm. The recycled specimen did show little defects in a certain area but these defects did not affect much on its dimension or shape. Hence, it can be concluded that this recycling method of using a filament extruder is acceptable where the pollution from 3D product waste can be reduced.

References

1. Wojtyła, S., Klama, P., Baran, T.: Is 3D printing safe? Analysis of the thermal treatment of thermoplastics: ABS, PLA, PET, and nylon. J. Occup. Environ. Hyg. **14**(6), D80–D85 (2017)
2. Dhinesh, S.K., Arun, P.S., Senthil, K.K.L., Megalingam, A.: Study on flexural and tensile behavior of PLA, ABS and PLA-ABS materials. Mater. Today Proc. **45**, 1175–1180 (2020)
3. Ramli, F.R., et al.: Parameter optimization in 3D printer recycle machine. ARPN J. Eng. Appl. Sci. **15**(21), 2385–2392 (2020)
4. Zhong, S., Rakhe, P., Pearce, J.M.: Energy payback time of a solar photovoltaic powered waste plastic recyclebot system. Recycling **2**(2), 1–16 (2017)
5. Baechler, C., Devuono, M., Pearce, J.M.: Distributed recycling of waste polymer into RepRap feedstock. Rapid Prototyp. J. **19**(2), 118–125 (2013)
6. Aris, M.A.I.Z., Mat, S., Sam, M.S., Ramli, F.R., Alkahari, M.R., Kudus, S.I.A.: Design and development of 3D printer filament extruder. In: Proceedings of Mechanical Engineering Research Day, pp. 293–294 (2020)

Product Redesign by Topology Optimization for Additive Manufacturing Process

Wongani Salima[1], Faiz Redza Ramli[2(✉)], and Shafizal Mat[2]

[1] Faculty of Engineering, University of Malawi, The Polytechnic, P/Bag 303, Blantyre 3, Malawi

[2] Fakulti Kejuruteraan Mekanikal, Universiti Teknikal Malaysia Melaka, Hang Tuah Jaya, 76100 Durian Tunggal, Melaka, Malaysia

`faiz@utem.edu.my`

Abstract. Using Topology Optimization (TO), this study analyses an existing Alcoa bearing bracket typically used on aircraft control surfaces, by redesigning the bracket to reduce weight while staying within the same target design envelope and meeting technical criteria. The methodology started with pre-analysis and topology optimization, where 15-5PH Steel, Ti6Al4V ELI-0406, and Ti-6Al-2Sn-4Zr-6Mo were compared, and one material was selected for the design process based on physical properties then TO process was performed to obtain a design with excellent strength to weight ratio, von Mises stress, displacement, mass, and factor of safety. Then build orientation optimization in Fusion 360 was conducted to obtain the minimum amount of support structure during AM. An Artificial Neural Network tool (ANN) was implemented to make the required geometric compensations on the bracket to control deformation arising due to the AM heating process. Then a conformity check was conducted to validate and to show the improvements achieved on the bracket after the ANN tool was implemented. Then the methodology finalizes with 3D printing of the bracket just to visualize the outcome of the TO process since the study's focus was entirely on computer simulations and not experiments. The results selected a 40% volume retention using Ti-6Al-2Sn-4Zr-6Mo, also selected Rank 1 build orientation, and the ANN achieved 59.75% and 61.784% reduction in conformity error for Cartesian and Layered tetrahedral mesh respectively. Therefore, TO and AM have the potential to revolutionize industries, similarly, ANN proved to supplement the existing deformation prediction models.

Keywords: Topology optimization (TO) · Weight reduction · Additive manufacturing (AM)

1 Introduction

Improvements in aircraft fuel economy are critical in lowering carbon emissions, which have a negative impact on the environment [1]. As rules tighten, lighter, non-traditional components are becoming a more appealing option for fulfilling requirements. In aircraft, lighter components not only improve fuel economy but also allows it to carry more load.

But these components must comply with safety regulations. There are several ways of achieving these compliant lighter components therefore, this study focuses on topology optimization (TO) and AM processes. TO is a type of structural optimization technique that aims to find the best shape possible given a set of constraints [1].

Product development through advanced finite element analysis and structural optimization is a growing concern and focus in the aerospace industry. In an attempt to optimize various aircraft components for minimum weight, Alcoa fastening systems engaged in various case studies, Fig. 1 below shows one of the case studies with a challenge to redesign the bracket to minimize the weight from the total weight of 868 g [2] by TO. Even though TO has the capability of creating compliant optimal structures for a given constraint and design domain, it does not take manufacturability into account because the structures it creates are often impossible to manufacture using traditional processes, hence, one way of avoiding these impossibilities is by using AM. Therefore, this paper seek to redesign the same Alcoa bearing bracket by TO for excellent strength to weight ratio, von Mises stress, displacement, mass, and factor of safety while fitting in the same target design envelope and meeting the technical requirements.

2 Methodology

Using solidThinking Inspire three materials namely 15-5PH stainless steel, Ti6Al4V ELI-0406, and Ti-6Al-2Sn-4Zr-6Mo were applied on the bracket and compared, then one material was selected based on excellent strength to weight ratio, von Mises stress, displacement, and factor of safety under three load cases on each material such as in Fig. 1. This FEA Pre-Analysis section was carried out to identify one material that could outperform and replace the existing material 15-5PH steel.

Integrated Bearing

Load case 1: 5560.277 N   Load case 2: 8340.416 N   Load case 3: 11120.550 N
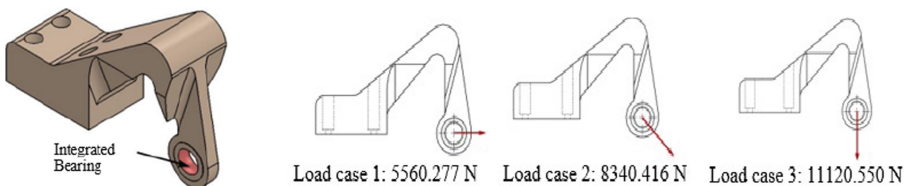
Fig. 1. Alcoa bearing bracket and the load cases.

Using the material selected in the Pre-analysis method, seven weight retentions were varied; 10%, 20%, 30%, 40%, 50%, 60%, and 70% in solidThinking Inspire to obtain the best design. The bulk removal of material usually leaves the models rough, therefore, SolidWorks and solidThinking Inspire were used in redesigning and smoothening of the selected TO design.

To minimize the amount of support structure, a build orientation process was laid out with the help of Fusion 360 software then since during AM process thermal deformations usually occur on the part, ANN tool in MATLAB was used to train the deformed and the original coordinates of the TO model to learn from the data and make the required STL geometric compensation in an attempt to produce a more accurate component by

counteracting thermal deformations arising from AM process and finally the bracket was 3D printed to visualize the outcome of the TO process.

3 Results and Discussion

3.1 FEA Pre-analysis Results and Discussion

The results of the FEA Pre-analysis simulations were analyzed based on strength to weight ratio, von Mises stress, factor of safety, and displacement. Ti-6Al-2Sn-4Zr-6Mo was selected as the material to use in the design because it had a superior stress-to-weight ratio of 2.098 MPa/g against 1.790 MPa/g and 1.031 MPa/g for 15-5PH steel and Ti6Al4V ELI-0406 respectively. For TO simulation, 8340.416 N force was selected to be used because it was the second greater force to meet design requirements.

3.2 Topology Optimization Results and Discussion

Using an evaluation matrix based on mass, max. von Mises stress, max. displacement, and factor of safety, 40%, 50%, 60%, and 70% volume retentions emerged as favorable design models, then, 40% model was selected amongst the favorites for its lower mass, and it went through further analysis and development in the study. The max. allowable displacement is 0.02–0.07 in. representing 0.508–1.778 mm [3]. The optimized Ti-6Al-2Sn-4Zr-6Mo re-designed model had a weight reduction of 189.3 g against 868 g of the existing bracket, representing 78.19% weight saving than the original 15-5PH steel bracket. The optimized re-designed model had an improved increase in strength to weight ratio of 3.622 MPa/g against 1.031 MPa/g of the existing bracket, see Fig. 2 and Fig. 3 showing part of the results. The re-designed model also had a significant von Mises stress reduction of 38%. There was an increase in displacement of 0.574 mm representing a 63% increase, from 0.910 mm of the existing bracket to 1.484 mm of the optimized re-designed model. But 1.484 mm is within the maximum allowable displacement range of 0.508 mm–1.778 mm. Therefore, these results of the optimized re-designed model were very satisfactory.
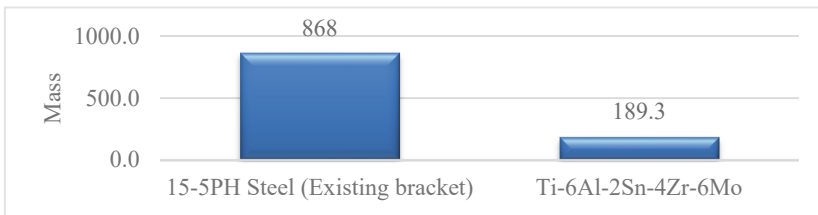
Fig. 2. Comparison of mass between existing model and re-designed model.
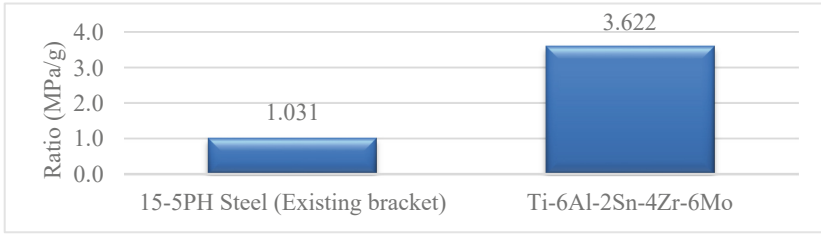
Fig. 3. Comparison of strength to weight ratio between existing model and re-designed model.

3.3 Build Orientation, Artificial-Neural-Network (ANN), and 3D Print Results and Discussion

Build orientation results were automatically ranked by the software in order of the best result to least that is from 1, 2, 3 up to 13, with Rank 1 showing best results and Rank 13 showing poor results. A conformity check was conducted to validate and show the improvements achieved after the ANN tool was implemented. It was found that before compensation, the conformity score of the deformed nodes after AM simulation was 76.312 for bracket with Cartesian mesh and 85.196 for bracket with Layered tetrahedral mesh while the conformity score after the AM simulation of the compensated bracket the conformity was 89.726 on Cartesian mesh bracket and 94.342 on Layered tetrahedral mesh bracket showing that there was an increase in conformity after the compensation. These conformity scores showed that there was a 59.75% and 61.784% reduction in conformity error for Cartesian mesh and layered tetrahedral mesh respectively.

The dimensional accuracy of the printed part and the CAD model were similar; 120.560 mm × 30.311 mm × 82.210 mm in length, width (thickness), and height.

4 Conclusions

In this paper a 40% weight retention was selected as the best TO model for further development in the study. The bracket was intended to be additively manufactured, therefore, the best build orientation was simulated for minimum support volume where Rank 1 was selected as the best build orientation, and after the implementation of the ANN tool the conformity scores showed that there was a 59.75% and 61.784% reduction in conformity error for Cartesian mesh and Layered tetrahedral mesh respectively. Finally, the bracket was additively printed to visualize the outcome of the TO process since the study's focus was entirely on computer simulations and not experiments. Therefore, TO together with AM serves as powerful tools to revolutionize industries in productivity similarly the ANN tool proves to be very useful in supplementing the already existing AM thermo-mechanical deformation prediction models.

References

1. Jankovics, D., Barari, A.: Customization of automotive structural components using additive manufacturing and topology optimization. IFAC-PapersOnLine **52**(10), 212–217 (2019)

2. Krishna, A., et al.: Optimization of engine truss mounting bracket. Int. J. Eng. Appl. Sci. Technol. **5**(2), 258–263 (2020)
3. Sammut-Bonnici, T., McGee, J.: Structural Optimisation and Finite Element Analysis to support weight reduction of an aerospace component for Additive Manufacture, pp. 68–69 (2002). https://evotechcae.com/wp-content/uploads/2018/09/Evotech-Case-Study-Alcoa-Fastening-Systems.pdf. Accessed 1 Apr 2021
4. Autodesk: The ALCOA Bracket (2018). https://knowledge.autodesk.com/search-result/caas/CloudHelp/cloudhelp/ENU/AGD-Tutorials/files/GUID-2032B925-FFBD-4448-953E-AE4B6997664A-htm.html. Accessed 26 July 2021

Production of Open-Cell Foam Using Additive Manufacturing Method and Porous Morphology Effects

K. A. Mustapha[1], F. Shikh Anuar[2(✉)], F. A. Z. Mohd Sa'at[1], N. H. M. Zini[1], E. Mat Tokit[1], N. Satishwara Rao[1], Kamel Hooman[3], and Iman Ashtiani Abdi[4]

[1] Fakulti Kejuruteraan Mekanikal, Universiti Teknikal Malaysia Melaka, Hang Tuah Jaya, 76100 Durian Tunggal, Melaka, Malaysia

[2] Fakulti Teknologi Kejuruteraan Mekanikal dan Pembuatan, Universiti Teknikal Malaysia Melaka, Hang Tuah Jaya, 76100 Durian Tunggal, Melaka, Malaysia
fadhilah@utem.edu.my

[3] Process and Energy Department, Delft University of Technology, Leeghwaterstraat 39, 2628, CB Delft, The Netherlands

[4] PCM Group Australia Pty Ltd., Brisbane, Australia

Abstract. In this study, 3D printed open-cell foam were produced and reconstructed from open-cell metal foam structure using a tomography scanning method and two different additive manufacturing technologies. The materials used in the 3D printing were nylon powder and plastic acid. The porous morphology and surface finish of the 3D printed foams were investigated using a microscope. The results showed that the surface finish and structure strength depend on the printing process, used material and foam size. This study found that laser-sintering technology would have smoother pores with lesser residue than stereolithographic. However, the ligaments of the small-size 3D printed foam were fragile and could be easily broken.

Keywords: 3D printing · Porous media · Morphology

1 Introduction

An open-cell metal foam was a structure made of a solid matrix from metallic material with interconnected pores. Normally, the pore size was determined in terms of PPI (pores per inches) where the greater the PPI, the smaller the pore size.

Its unique porous structure provides advantageous properties such as lightweight, high surface area, and good thermal conductivity, thus it was possible for diverse industries such as medical, aerospace, and automotive [1]. However, since the cost of metal foam is quite high, a lot of numerical studies have been preferable to understand the metal foams under different conditions. Alternatively, another cheaper solution such as additive manufacturing method (3D printing) can be proposed for more experimental studies. Unfortunately, the complicated structure of the metal foam with random pore-ligament construction could not be easily drawn using CAD software. Thus, it is challenging to

produce open-cell foam using the additive manufacturing method without a detail image of an open-cell metal foam. However, thanks to Computed Tomography (CT) scanner and additive manufacturing technologies [2], a prototype sample with the exact design parameters of a real object can be produced. The tomographic image is collected by the scanner from the translated X-ray beam on the object [3]. For the additive manufacturing method, there are many different technologies available in the market, such as selective laser melting, fused deposition modeling, and electron-beam melting [4]. In this study, the open-cell foams were produced using the CT-scan and two different 3D printing technologies. This study produced the exact same porous structure of metallic foam to enable further experimental investigations for diverse applications, e.g., thermoacoustic system, heat exchanger and sound absorber. Note that, further modifications on the 3D printed foam and experimental conditions must be applied to suit the nature of those applications. As a first step, this study focused on morphology of the printed foams obtained using different 3D printer technologies and materials.

2   Methodology

The production process includes 3D scanning of a 5 PPI metal foam using a CT scanner and reconstruct the 3D model in Blender and SOLIDWORKS software. The detail properties of the 5 PPI aluminium metal foam could be found in [4]. In the present study, three different sizes of 3D printed foams were produced, with the first one is 7.5 mm long, and the other two foams were enlarged with a scale of 4 and 8 from the first one. Figure 1(a) shows the CAD image of the open-cell foam constructed using Blender software and Fig. 1(b) shows the 3D printing process using the stereolithography (SLA) method. Note that this study used two different additive manufacturing technologies: the SLA and Selective Laser Sintering (SLS). The SLA method used Flashforge CreatorPro and Polylactic Acid (PLA) type filament, printing at a temperature range from 190 °C–200 °C. Meanwhile, the SLS technology used nylon powder (FS 3300 PA) with a bulk density of 0.48 g/cm^3 and melting point at 183 °C. The 3D printed form and its porous structure was examined using a RS Pro USB Wi-Fi microscope with 1280 × 1024 pixels, and up to 200× magnification.
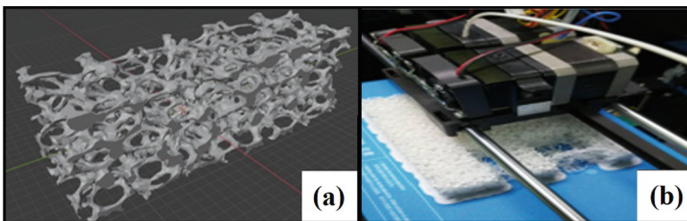
Fig. 1.   (a) CAD drawing and (b) printing process (stereolithography).

3   Result and Discussion

Figure 2 shows the 3D printed foams produced using different 3D printing technologies and materials. The yellowish 3D sample in Fig. 2(a) shows the smallest sample of the 3D printed foams in this study, with some damaged structures in red circles. The smallest foam means it also has the thinnest and most fragile ligament construction. For a hollow or porous structure, the shape can be easily deformed. Thus, producing 3D printed open-cell foam as small as the original metallic foam using the abovementioned techniques with the proposed material was impractical. In this case, the foam ligament should be more than size 2.0 mm to maintain those complicated porous structures. Meanwhile, Fig. 2(b) shows the other foam sizes (scale factors; 4 and 8). The yellowish and larger foam was produced from nylon while the pure white foam was from PLA. Regardless of the used material, the larger 3D printed foam was stronger, and the interconnected region (lump) was nicely connected (Fig. 2(c)). However, close observation showed that the Flashforge printer with PLA would cause more residues (thin strings within the porous structure) as shown in Fig. 2(d), unlike the foam produced from SLS with a smoother surface as shown in Fig. 2(e). Under a microscope with 100× magnification, the layering effects from the SLS process could be seen as expected in Fig. 2(f). Hence, the surface roughness of these 3D printed foams should be expected to be higher than the original metallic open-cell metal foam. From [5], the average roughness of the nylon parts is 34.0 ± 7.6 µm. Note that, the surface roughness would be important parameters for certain applications with a major concern of pumping power or contact surface. However, by manipulating the pore size and external shape, this lightweight 3D printed foam would be promising for aerospace (e.g., cabin interior, tray table and arm rests) and automotive industries (e.g., door sill and internal parts of door panel).
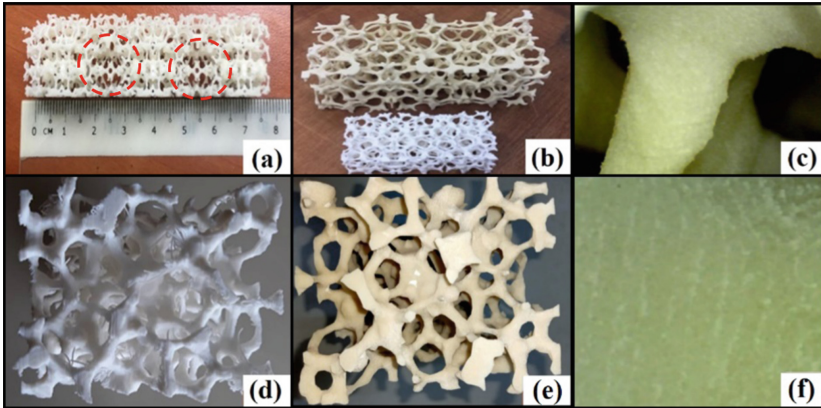
Fig. 2. 3D printed foam (7.5 cm original sample), (b) Enlarged samples with scales of 4 and 8, (c) Interconnected pore-ligament region (d) Sample using Flashforge Creater Pro, (e) Sample using SLS and (f) Foam surface.

4   Conclusion

The original form of open-cell metal foam has been successfully produced using two different additive manufacturing methods; SLS and SLA. However, the ligament and pore sizes of 3D printed foams could not be as small as the metallic ones. The ligaments could be broken easily but was showing a stronger form in larger form sizes. The morphology of these foams depends on the printing process and material, where SLS with nylon powder produced a smoother finish surface than SLA with PLA material.

References

1. Tan, W.C., Saw, L.H., Thiam, H.S., et al.: Overview of porous media/metal foam application in fuel cells and solar power systems. Renew. Sustain. Energy Rev. **96**, 181–197 (2018). https://doi.org/10.1016/j.rser.2018.07.032
2. Matheson, K.E., Cross, K.K., Nowell, M.M., Spear, A.D.: A multiscale comparison of stochastic open-cell aluminum foam produced via conventional and additive-manufacturing routes. Mater. Sci. Eng. A **707**, 181–192 (2017). https://doi.org/10.1016/j.msea.2017.08.102
3. Fengshan, S., Lijun, L., Xianyue, G., et al.: Equivalent model of spatial random array vibration system on sound-absorbing computing for porous material. Appl. Acoust. **165**, 107299 (2020). https://doi.org/10.1016/j.apacoust.2020.107299
4. Adekanye, S.A., Mahamood, R.M., Akinlabi, E.T., Owolabi, M.G.: Additive manufacturing: the future of manufacturing: Dodajalna (3D) Tehnologija: Prihodnost Proizvajanja. Mater. Tehnol. **51**, 709–715 (2017). https://doi.org/10.17222/mit.2016.261
5. Kinstlinger, I.S., Bastian, A., Paulsen, S.J., et al.: Open-source selective laser sintering (OpenSLS) of nylon and biocompatible polycaprolactone. PLoS ONE **11**(2), e0147399 (2016). https://doi.org/10.1371/journal.pone.0147399

Development of 3D Printing Filament Material Using Recycled Polyethylene Terephthalate Reinforced with Sugar Palm Fiber

A. G. Muhammad Arief[1], M. Nuzaimah[1(✉)], R. Nadlene[2], and A. M. Radzi[3]

[1] Fakulti Teknologi Kejuruteraan Mekanikal dan Pembuatan, Universiti Teknikal Malaysia Melaka, Hang Tuah Jaya, 76100 Durian Tunggal, Melaka, Malaysia
nuzaimah@utem.edu.my

[2] Fakulti Kejuruteraan Mekanikal, Universiti Teknikal Malaysia Melaka, Hang Tuah Jaya, 76100 Durian Tunggal, Melaka, Malaysia

[3] Malaysia-Japan International Institute of Technology, University Teknologi Malaysia, Jalan Sultan Yahya Petra, Kampung Datuk Keramat, 54100 Kuala Lumpur, Kuala Lumpur, Malaysia

Abstract. Additive manufacturing is a cost-effective and widely used process that is currently being researched by numerous researchers to maximize its potential for producing better products, particularly in the manufacturing sector. Nowadays, many types of waste such as plastic waste that is derived from petroleum-based polymer such as PET become threat to the environment due to their non degradable property. Thus, to overcome this concern recycling of waste material is one of the promising solutions. Recycled Polyethylene Terephthalate (rPET) as matrix are combine with sugar palm fiber (SPF) to develop 3D printing filament material. Currently, SPF is not being used to its full potential, particularly in additive manufacturing. SPF's appealing qualities, such as high durability and ease of processing, would be extremely advantageous in the field of additive manufacturing. Thorough understanding of SPF qualities and behaviour is required in order to fully employ SPF in the development of 3D printing filament. SPF works as a reinforcing agent, which is a crucial feature in improving the composites that are being developed in combination with the rPET. This natural fibre and recycled polymer matrix are expected to improve the thermostability, lightweight, strength, and transparency of the filament material while also contributing to waste reduction in the environment.

Keywords: Sugar palm fiber · 3D printing filament · Recycled polyethylene terephthalate

1 Introduction

There are various types of filaments are available including bio composite filament. Due to it significant benefit such eco-friendly, availability in abundance, high strength, high elasticity modulus and most importantly low cost makes this type of filament to be used widely in manufacturing industries compared to synthetic filament. There are varies

of parameter to determine good criteria of filaments. In this case natural fiber filament depend on the type of plant fiber, the ratio of length and diameter of the filament, interface between filler and matrix. The most important factor that need to consider are method preparation of the composite [1]. To generate high-quality natural fiber filament, natural fiber must undergo a series of pre-treatments before being converted into composite. To begin, natural fiber must be extracted and prepared, which includes washing, cutting, grinding, sieving, and drying the fiber in an oven to completely remove all moisture. After that, the sugar palm fiber particle must be treated with a chemical agent. This procedure involves soaking sugar palm particles in a solution of concentrated sodium hydroxide. The fiber treatment procedure is vital for removing impurities and improving the adhesion of the filler and matrix, as well to improve the mechanical performance of the composite [2] (Fig. 1).
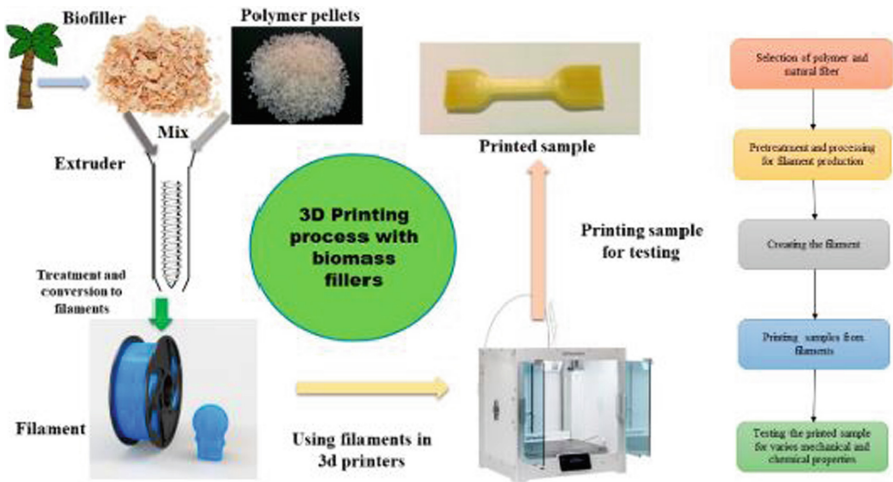
Fig. 1. Natural fiber filament process [2].

From the matrix point of view, thermoplastic is the best choice to be the material for printing filament as it gives advantages in term of environmental effect and recyclability. Amorphous type polymers are favored over those that are semicrystalline. Apart, from their lower solidification shrinkage their characteristics in the molten state are also better due to their liquid-like structure in the solid state. This is explained by the decrease in melt viscosity as the processing temperature approaches the polymer glass transition temperature [3].

2 Potential of Sugar Palm Fiber and Recycled Polyethylene Terephthalate as Filament Material

Sugar palm fibers are a type of natural fiber that exhibits a variety of characteristics and requires additional research to fully grasp its properties and maximize their potential.

There are numerous of study that have been done on sugar palm fiber to determine the properties of this fiber. For instance, study show the impacted properties of sugar palm fiber reinforced with epoxy polymer with chemical treatment. This study resulted on higher concentration with longer soaking time will enhance the impact strength of the fiber [4]. Modification treatment of fiber is important can be done through several chemical agent such as alkaline, silane and seawater. The optimum time (1 h, 4 h and 8 h) and concentration of sodium hydroxide solution (0.25M and 0.5M) must be carried out for a few times to obtain best result. The soaking time and concentration of solution of hydroxide are important parameter as improper treatment can lead to degradation of fiber. These recent years, sugar palm fiber reinforced thermoplastic composites have gained many interests from researcher due to its low cost and recyclable properties. In the previous study shows that effects of fiber size (160, 250 and 425 μm) on mechanical properties involved in impact strength and tensile flexural. The research findings reached out to find optimum temperature that used for extrusion was 190 °C, rotational velocity of 40 rpm and the best particle size μm with provide best result was 250 μm. Many researchers also focused on study the interface of sugar palm because interface adhesion between fiber and matrix play an important role in improving the composite. The interface will determine efficiency, load transfer and performance of the composite [5].

Polyethylene Terephthalate (PET) is the most widely used semi-crystalline and transparent thermoplastic in the polyester family, due to its great rigidity, mechanical strength, and chemical resistance. Intrinsic velocity is one of the most important properties that need to be understand when handling a PET. The length of the material's polymer chains determines its intrinsic viscosity. The longer the polymer chains, the more entanglements between them, hence the viscosity is higher [6]. In this research, rPET were used in form of thin films that were obtained from recycle factory, rPET later were then cut into small piece and grind to ease the mixing process between fiber and matrix. Furthermore, research conducted show that presence of polylactic acid causes decreased on tensile strength when mixing the polymers with polypropylene and polybutylene terephthalate [7]. This proves by utilizing recycled product such as rPET has a potential to improve the demand in 3D printing filament technologies. The performance of natural fiber reinforced with rPET depend on fiber types, fiber content and modification of fiber. Numerous natural fibers such as sugar bagasse, date palm leaf fiber, sawdust have been combined and studies into rPET via various of processing ways such as injection molding, compression molding, and so on. The lack of interfacial adhesion between hydrophilic natural fibers and hydrophobic polymers is a significant limitation of natural fibers used as reinforcement. The tendency of agglomeration tends to occur between filler and matrix it is because the hydrophilic polar natural fiber has a low water resistance and does not adhere well to nonpolar hydrophobic polymer matrices. Natural fibers that do not interlock well with impregnated polymer matrices result in composites with low quality mechanical characteristics [8]. Thus modification of fiber through chemical treatment are needed to reduce the hydrophilic nature of fiber and chemical agent that commonly used such as silane and sodium hydroxide, as well as a variety of other compatible substance that can be used to improve the adhesion between natural fibers and thermoplastic [9].

3 Characterization of Sugar Palm Fiber and Recycled Polyethylene Terephthalate Properties Used for Filament Material

One of the most important issues in study natural composite is to understand the degradation temperature of natural fiber it is because of one of the limitations of natural fiber is loss of strength and weakness while expose in high temperature. The degradation varies with different types of natural fiber because different types of fiber have different chemical composition and microstructures. The fire resistance can be improved by combine natural fiber with additives such as filler and coating that can improve fire resistance significantly. By adding the fillers to the natural fiber composite will increase the formation of heat barrier thus increase the fire resistance [10]. The TGA analyzer was used to determine the thermal stability of the fibers in terms of weight loss response to temperature increase. To investigate the thermal degradation of sugar palm fibers with varying fiber treatments, operating conditions were typically set at a temperature range of 25–600 °C, with the aid of a dynamic nitrogen atmosphere and a 10 °C heating rate, as well as conducting the analysis by depositing the fiber samples in an aluminum pan [11]. Research conducted on sugar palm fiber reinforced thermoplastic urethane showed that same thermal degradation occur as other natural fiber resulted which around 435 °C at decomposition stage [8].

Rheological properties are a study of interface that coexisted between filler and matrix. Rheological properties also can be influenced by type of filler, shape, size, and amount. In addition, understanding the filler effect on rheological properties of polymer is an important aspect in optimization, trouble shooting, and design equipment. Dynamic mechanical analysis is technique that commonly used where small deformation is applied to sample with different temperature to evaluate changes in viscosity and elastic [10]. Rheometers are a device use in determine the rheology properties of filler and matrix. Rheology can interpret the degree of dispersion, behavior, and fiber affinity. Ogah et al. (2017) evaluate effect of high fiber content on the rheological properties using corn, flax shive and wall nutshell flour which resulted high in viscosity [12]. Previous research shown that drawdown force of modified rPET increased with increased on chain extender concentration force at 0.9 wt% this is due to higher molar mass of the molecules [13].

4 Conclusion

In summary, natural fiber composites are an ideal alternative replace synthetic fiber composites as filament material due to their ease of access, low density, low cost, superior thermal and acoustic insulation, eco-friendliness, recyclability, and renewability, as well as satisfactory mechanical qualities. Previous research proved that recycled polyethylene terephthalate reinforced with sugar palm fiber can developed as material used for the filament which can overcome environmental issues and produce new promising sustainable material. Hence, study in understanding the rheological properties and thermal stability of the fibers and composite is required to achieve desirable and competitive material in order to be developed better printing filament quality. Also helps in ensuring the develop natural fiber composite filament using sugar palm fiber reinforced with recycled polyethylene terephthalate can be safely disposed.

References

1. Deb, D., Jafferson, J.M.: Natural fibers reinforced FDM 3D printing filaments. Mater. Today: Proc. **46**(2), 1308–1318 (2021)
2. Ahmed, W., Alnajjar, F., Zaneldin, E., Al-Marzouqi, A.H., Gochoo, M., Khalid, S.: Implementing FDM 3D printing strategies using natural fibers to produce biomass composite. Materials **13**(18), 4065 (2020)
3. Mazzanti, V., Malagutti, L., Mollica, F.: FDM 3D printing of polymers containing natural fillers: a review of their mechanical properties. Polymers **11**(7), 1094 (2019)
4. Rashid, B., Leman, Z., Jawaid, M., Ghazali, M.J., Ishak, M.R.: The mechanical performance of sugar palm fibres (ijuk) reinforced phenolic composites. Int. J. Precis. Eng. Manuf. **17**(8), 1001–1008 (2016). https://doi.org/10.1007/s12541-016-0122-9
5. Atiqah, A., Mastura, M.T., Jawaid, M., Sapuan, S.M., Ansari, M.N.M.: Interfaces in sugar palm fibres reinforced composites: a review. In: Interfaces in Particle and Fibre Reinforced Composites, pp. 199–217 (2020)
6. Ji, L.N.: Study on preparation process and properties of polyethylene terephthalate (PET). Appl. Mech. Mater. **312**, 406–410 (2013)
7. Oussai, A., Bártfai, Z., Kátai, L.: Development of 3D printing raw materials from plastic waste. A case study on recycled polyethylene terephthalate. Appl. Sci. **11**(16), 7338 (2021)
8. Atiqah, A., Jawaid, M., Sapuan, S.M., Ishak, M.R.: Mechanical and thermal properties of sugar palm fiber reinforced thermoplastic polyurethane composites: effect of silane treatment and fiber loading. J. Renew. Mater. **6**(5), 477–492 (2018)
9. Singh, A.K., Bedi, R., Kaith, B.S.: Composite materials based on recycled polyethylene terephthalate and their properties–a comprehensive review. Compos. B Eng. **219**, 108928 (2021)
10. Gholampour, A., Ozbakkaloglu, T.: A review of natural fiber composites: properties, modification and processing techniques, characterization, applications. J. Mater. Sci. **55**(3), 829–892 (2020)
11. Ilyas, R.A., et al.: Sugar palm (Arenga pinnata (Wurmb.) Merr) cellulosic fibre hierarchy: a comprehensive approach from macro to nano scale. J. Mater. Res. Technol. **8**(3), 2753–2766 (2019)
12. Ogah, O.A.: Rheological properties of natural fiber polymer composites. MOJ Polym. Sci. **1**(4), 1–3 (2017)
13. Makkam, S., Harnnarongchai, W.: Rheological and mechanical properties of recycled PET modified by reactive extrusion. Energy Procedia **56**, 547–553 (2014)

Effect of HIP on Porosity of Ti6Al4V Manufactured by Laser Powder Bed Fusion: A Brief Review

Fathin Iliana Jamhari [ID], Farhana Mohd Foudzi[(✉)] [ID],
and Minhalina Ahmad Buhairi [ID]

Universiti Kebangsaan Malaysia, 43600 Bangi, Selangor, Malaysia
farhana.foudzi@ukm.edu.my

Abstract. Laser Powder Bed Fusion (LPBF) uses rapid melting and solidification of Ti6Al4V powder layers to additively build the desired products. This has resulted in a steep temperature gradient and significant residual stress, which intensify the formation of porosity and flaws that deteriorate the mechanical performance. To overcome such issues, heat treatments such as hot isostatic pressing (HIP) are widely utilized. Although the use of HIP for LBPF parts is well applied, the significance of HIP in improving the components performance is under reported. Therefore, the purpose of this paper is to review the effect of HIP in improving the porosity and mechanical properties of LPBF-Ti6Al4V parts. HIP is found to be particularly effective in sealing pores and densifying Ti6Al4V components up to 99.6% which aids in resolving porosity concerns in LPBF products. This work suggests future research on the effects of HIP heating parameters on the mechanical and microstructure properties of LPBF-TI6Al4V components.

Keywords: Laser Powder Bed Fusion · Hot isostatic pressing · Porosity

1 Introduction

1.1 Laser Powder Bed Fusion

Laser Powder Bed Fusion (LPBF) uses a laser beam to melt and solidify powders in layers for materials like titanium alloy (Ti6Al4V). Additive manufacturing (AM) allows for mass customization, unique design, and reduced raw material use [1] LPBF encourages powder recycling, making it more cost effective and ecologically beneficial [2]. However, the main drawback of LPBF is the formation of residual stress that forms during the fast melting and cooling of powder layers. This resulted to weak performance of LPBF parts [2]. Heat treatment is frequently employed as a post-processing remedy to these problems, with hot isostatic pressing (HIP) is widely used to close pores [3–5]. HIP is a heat treatment that involves heating metal components at an elevated temperature under continuous isostatic pressure for a set duration. It is a common treatment applied to promote densification and pores shrinkage. This treatment will be further detailed in the subsequent section.

1.2   HIP Treatment

Promotion of densification [6], reduction of residual stress [7] and improvement of porosity [8] in LPBF products are all benefits of HIP treatment. The treatment has been shown to improve corrosion resistance [9], fatigue strength [10], and compressive strength [8]. The interest in utilizing HIP for LPBF products has also led to several studies on hybrid additive manufacturing of LPBF/HIP with promising results [11, 12]. HIP have a variety of heating parameters such as environment, cooling rate, and heating rate, but for the purposes of this paper, only three major parameters are considered in this review. The parameters are pressure (MPa), temperature ($^{\circ}$C), and holding duration (hours). Common HIP parameters setting for Ti6Al4V parts with heating temperature at 900 °C under 100 MPa for 2 h holding time were found to be adequate in improving the porosity and mechanical performance of Ti6Al4V parts [13].

Trend of HIP in LPBF

The use of HIP in LPBF has increased for the past five years. Figure 1 shows such trend that was collected from Web of Science™ search webpage in September 2021[14]. It was done by searching for the following keywords: "LPBF", "LPBF+Ti6Al4V" and "LPBF+Ti6Al4V+Hot Isostatic Pressing". Since, the term "LPBF" is commonly interchangeable with the term "Selective Laser Melting (SLM)", the keyword search has included the term "SLM". The trend indicates that the use of HIP in LPBF parts has gain great interest among researchers and it is expected that the number of publications in 2021 will surpass that of 2020 by end of year.
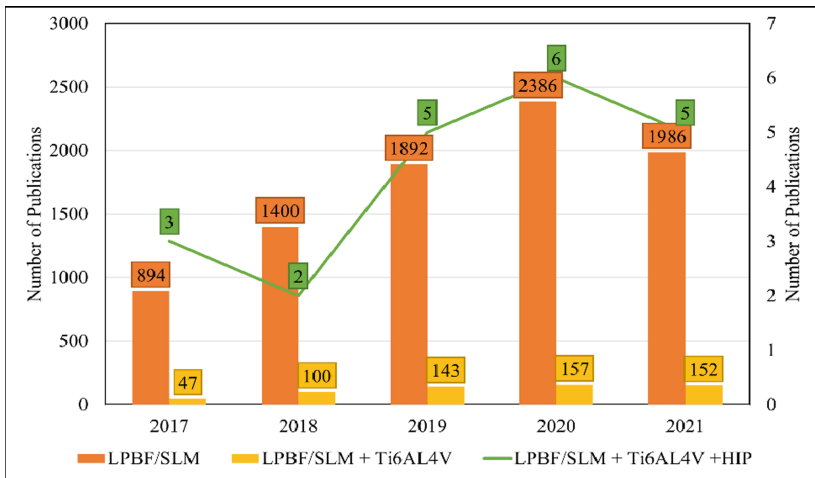
Fig. 1.   Trend for number of publications on HIP treatment in LPBF over the past five years.

Due to the increasing interest in HIP and novel heat treatment for LPBF, the effectiveness of HIP as a heat treatment needs to be reviewed. Past reviews on heat treatment have only focused on other heating treatments such as annealing and quenching, and the effects of heat treatment on residual stress and microstructure [2, 15, 16]. Therefore, this

paper aims to provide a brief overview on the influence of HIP treatment on the porosity and mechanical performance of Ti6Al4V produced via LPBF.

2   Effects of HIP on Ti6Al4V Porosity

HIP has been reported in past studies as to be very effective in improving the porosity issues of LPBF products. The application of isostatic pressure and heat encourages densification and closing of pores. Huang et al. claim that HIP can remove holes without affecting microstructure [17]. Masuo et al. showed improved fatigue performance with HIP for LPBF Ti6Al4V components [5]. Du Plessis and MacDonald investigated the different types of pores and the effectiveness of HIP in sealing them [18]. It was found that HIP could effectively remove contour pores, fusion pores, and keyhole holes up to 29.41%, 98.89%, and 99.77% respectively. Such improvement also enhances the mechanical properties of LPBF-Ti6Al4V parts, which will be discussed in full paper. It is concluded that HIP is an effective approach to address the porosity issues of LPBF.

3   Conclusion

This paper has discussed and reviewed the effectiveness of HIP in improving porosity in Ti6Al4V parts produced by LPBF. Past studies have shown that HIP is successful in controlling the porosity issues in LPBF products. This study suggests for further study in the influence of differing HIP parameters on the microstructure and mechanical properties of LPBF-Ti6Al4V products.

References

1. Harun, W.S.W., Kamariah, M.S.I.N., Muhammad, N., Ghani, S.A.C., Ahmad, F., Mo-hamed, Z.: A review of powder additive manufacturing processes for metallic biomaterials. Powder Technol. **327**, 128–151 (2018)
2. Zhang, J., Song, B., Wei, Q., Bourell, D., Shi, Y.: A review of selective laser melting of aluminum alloys: processing, microstructure, property and developing trends. J. Mater. Sci. Technol. **35**(2), 270–284 (2018)
3. Roudnicka, M., Mertova, K., Vojtech, D.: Influence of hot isostatic pressing on mechanical response of as-built SLM titanium alloy. IOP Conf. Ser. Mater. Sci. Eng. **629**, 1–8 (2019)
4. Yan, X., et al.: Effect of heat treatment on the phase transformation and mechanical properties of Ti6Al4V fabricated by selective laser melting. J. Alloy. Compd. **764**, 1056–1071 (2018)
5. Masuo, H., et al.: Effects of defects, surface roughness and HIP on fatigue strength of Ti-6Al-4V manufactured by additive manufacturing. Procedia Struct. Integr. **7**, 19–26 (2017)
6. Herzog, D., Bartsch, K., Bossen, B.: Productivity optimization of laser powder bed fusion by hot isostatic pressing. Addit. Manuf. **36**, 1–9 (2020)

7. Qin, S., Herzog, S., Kaletsch, A., Broeckmann, C.: Effects of pressure on microstructure and residual stresses during hot isostatic pressing post treatment of AISI M50 produced by laser powder-bed fusion. Metals **11**(4), 1–14 (2021)
8. Yan, X., et al.: Effect of hot isostatic pressing (HIP) treatment on the compressive properties of Ti6Al4V lattice structure fabricat-ed by selective laser melting. Mater. Lett. **255**, 1–4 (2019)
9. Yan, X., et al.: Effect of heat treatment on the corrosion resistance behavior of selective laser melted Ti6Al4V ELI. Surf. Coat. Technol. **396**, 1–10 (2020)
10. Benedetti, M., et al.: The effect of post-sintering treatments on the fatigue and biological behavior of Ti-6Al-4V ELI parts made by selective laser melting. J. Mech. Behav. Biomed. Mater. **71**, 295–306 (2017)
11. Hassanin, H., Essa, K., Qiu, C., Abdelhafeez, A.M., Adkins, N.J.E., Attallah, M.M.: Net-shape manufacturing using hybrid selective laser melting/hot isostatic pressing. Rapid Prototyp. J. **23**(4), 720–726 (2017)
12. Sebastian, R., Anke, K., Christoph, B.: Tailor-made net-shape composite components by combining additive manufacturing and hot isostatic pressing. Mater. Res. Proc. **10**, 203–209 (2019)
13. Su, C., Yu, H., Wang, Z., Yang, J., Zeng, X.: Controlling the tensile and fatigue properties of selective laser melted Ti–6Al–4V alloy by post treatment. J. Alloys Compd. **857**, 1–12 (2021)
14. Clarivate: Search in: Web of Science Core Collection. https://www-webofscience-com.ezp lib.ukm.my/wos/woscc/basic-search. Accessed 10 Sept 2021
15. Hamza, H.M., Deen, K.M., Khaliq, A., Asselin, E., Haider, W.: Microstructural, corrosion and mechanical properties of additively manufactured alloys: a review. Crit. Rev. Solid State Mater. Sci., 1–53 (2021)
16. Teixeira, Ó., Silva, F.J.G., Ferreira, P.: Quality and residual stresses of the Ti–6Al–4V parts produced by additive manufacturing. Metals **10**(8), 1–24 (2020)
17. Huang, X., Lang, L., Gong, S., Zhao, M.: Effect of post-treatment on the microstructure and mechanical properties of selective laser melted Ti6Al4V lattice structures. Rapid Prototyp. J. **26**(9), 1569–1577 (2020)
18. Du Plessis, A., Macdonald, E.: Hot isostatic pressing in metal additive manufacturing: X-ray tomography reveals details of pore closure. Addit. Manuf. **34**, 1–12 (2020)

Microstructure Comparison of SLM Ti6Al4V Using Manufacturer's Heat-Treatment Procedure

Rafidah Hasan[1,2(✉)] and Shafiqah Aini[1]

[1] Fakulti Kejuruteraan Mekanikal, Universiti Teknikal Malaysia Melaka, Durian Tunggal, Malaysia
rafidahhasan@utem.edu.my

[2] Centre for Advanced Research on Energy, Universiti Teknikal Malaysia Melaka, Durian Tunggal, Malaysia

Abstract. This study reports on the microstructure of SLM Ti6Al4V material after undergoing heat-treatment procedure as outlined by the SLM machine manufacturer. The heat-treatment follows a non-familiar route of single heating then associates with gradual cooling in steps, done in a fully controlled argon gas atmospheric environment. Comparison was done with microstructures obtained from previous studies using the well-known double heating and quenching treatment in producing a balance lamellar phase structure. Result of other's hot isostatic pressing was also referred. It is shown that the obtained microstructure in this study is sufficiently having the balance lamellar phase, and comparable to that of expensive and sophisticated hot isostatic pressing's result. This indicates that the SLM technology is at its mature level where the technology provider is preparing the process with a procedure that is reasonable to be applied, without the necessity to use the high-tech scientific procedure as being done for certain condition.

Keywords: Selective Laser Melting · Ti6Al4V · Microstructure

1 Introduction

One of the well-known additive manufacturing process is the Selective Laser Melting (SLM). The process starts with layer of metallic powder being spread onto a steel bed plate. A laser is then fired with controlled laser path and exposure time. The powder is selectively laser melted according to design instruction. A new layer of powder is then evenly spread over the area, and the laser is again operated. In this way, complex geometry is created layer by layer. The very high temperature gradient between a previous layer with the subsequent layer leads to fast cooling and heating. This produces some non-equilibrium acicular α' martensitic microstructures for titanium alloy material.

The SLM technology offers a complex metallic material forming strategy. An integrated approach is required, which comprises design, material, manufacturing process,

structural realization and application [1]. Due to this complexity, SLM produced materials are still being the subjects of research throughout the globe. Post-process heat-treatment has been the interest in SLM Ti6Al4V studies and being actively updated in recent literatures [2, 3].

Many heat-treatment processes have been introduced including as simple as stress-relieve annealing [4] to high technology hot isostatic pressing (HIP). All processes aim at producing a more balance microstructure of titanium alloy. The various heat-treatment procedures applied by researchers may lead to some confusion for SLM new users especially the industrial players. Therefore, this work aims to compare the microstructure of Ti6Al4V using heat-treatment procedure that is outlined by the SLM manufacturer, with few other results obtained from literatures. This comparison can eventually ensure the SLM users to confidently apply the procedures outlined by their respective technology provider.

2 Method

2.1 Material

Titanium alloy Ti6Al4V specimen was produced in simple cubic shape (10 mm $\times$ 10 mm $\times$ 10 mm) using SLM250 machine developed by the SLM Solutions GmbH. Previous SLM parameters were followed [5]. The metallic powder (Ti6Al4V ELI grade 23) comprised of standard chemical composition elements as can be found in other literature [6].

2.2 Procedure

Specimen consist of as-received SLM specimen and heat-treated specimen. The heat-treatment procedure follows the outlined post-process treatment as suggested by the SLM Solutions GmbH. The wording instruction from the manufacturer is as follow:

"For Ti-Alloy TIAL6V4 ELI (Grade 23): Heat Treatment Specimens were heated up in vacuum atmosphere at a rate of <450 °C/h up to 910 °C, then with <300 °C/h up to 940 °C. Subsequent holding at 940 $\pm$ 10 °C for 4 h −0/+30 min. Cooling down in vacuum at a rate of 40 $\pm$ 10 °C/h to 760 $\pm$ 15 °C, then in argon with 560 $\pm$ 100 °C/h to ≤480 °C, followed by gas fan quenching at any rate to ≤50 °C."

Figure 1 translates the manufacturer's wording into a schematic illustration. After heat-treatment, standard metallographic procedure and microstructure observation are followed, as described in previous works [6].
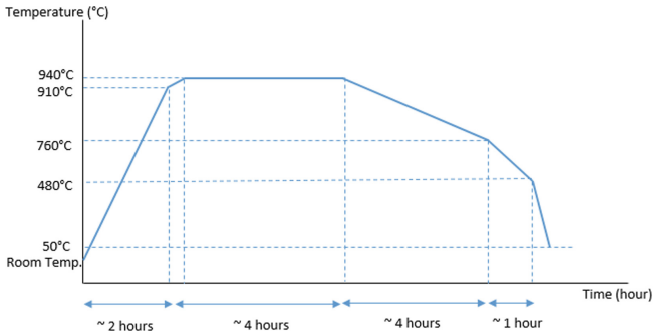
Fig. 1. Schematic of heat treatment procedure as instructed by the manufacturer's wording.

3   Result and Discussion

Microstructure of both as-received SLM and heat-treated SLM specimens are shown in Fig. 2. Acicular α' martensite can be clearly observed in SLM Ti6Al4V as-received specimen. Meanwhile, a balanced α/β phase can be observed in heat-treated specimen. This shows that the outcome from heat-treatment procedure as outlined in Fig. 1 is comparable to other procedure comprising quenching technique, double heat-treating [2, 6], as well as using the high-technology HIP [2]. The manufacturer has anticipated a good post treatment procedure for Ti6Al4V material produced from the SLM250 machine. Table 1 shows the microstructure comparison of several heat-treatment procedures from few literatures. Note that Route B, C and D are from reference [2], while Route A is not included for not being comparable.

(a)   **(b)**
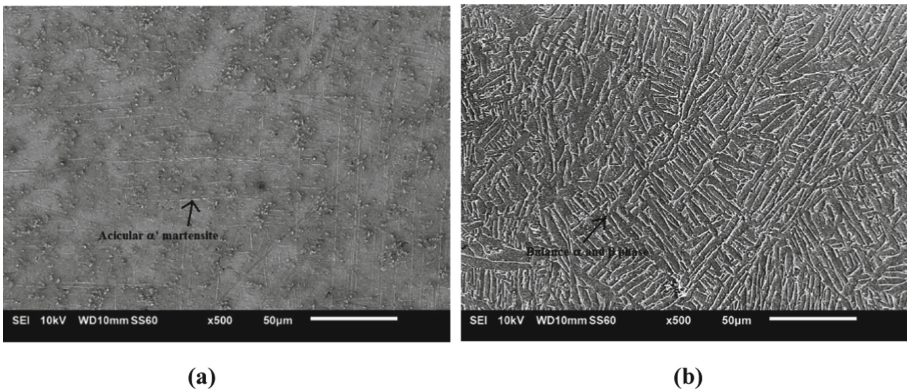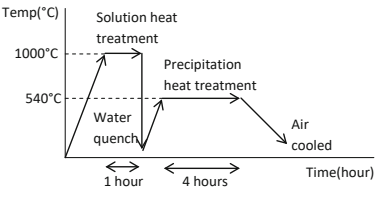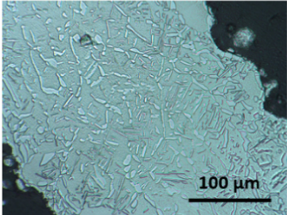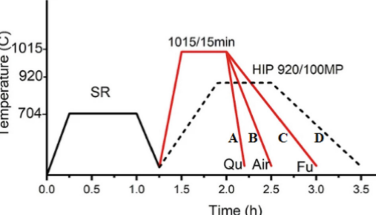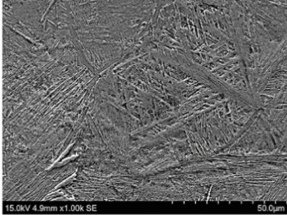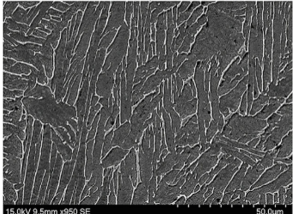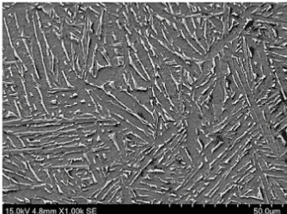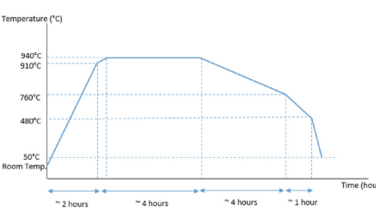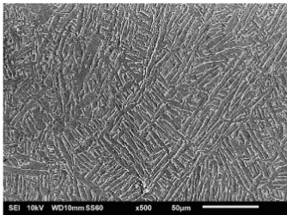
Fig. 2. Microstructure of SLM Ti6Al4V in this study; (a) as-received; (b) heat-treated.

Table 1. Comparison of SLM Ti6Al4V microstructure after several heat-treatments.

Schematic of Heat-Treatment	Microstructure	Ref.
		[6]
	Route B	[2]
Route C	Route D	[2]
		[This Study]

4   Conclusion

This study shows that similar microstructure of balance lamellar α and β phase can be obtained from heat-treatment procedure without double heating and cooling as been normally practiced in previous research study [6], due to gradual steps during heating and cooling of the single heat-treatment. The obtained microstructure is also comparable to that of HIP's treatment done by other study [2]. This confirms that the SLM technology has entered into its mature level, where the procedures outlined by the manufacturer is in-line with other current scientific findings.

References

1. Mines, R.: Metallic Microlattice Structures – Manufacture, Materials and Application. Springer, Cham (2019). https://doi.org/10.1007/978-3-030-15232-1
2. Eshawish, N., Malinov, S., Sha, W., Walls, P.: Microstructure and mechanical properties of Ti-6Al-4V manufactured by selective laser melting after stress relieving, hot isostatic pressing treatment, and post-heat treatment. J. Mater. Eng. Perform. **30**(7), 5290–5296 (2021). https://doi.org/10.1007/s11665-021-05753-w
3. Ge, J., et al.: A Detailed analysis on the microstructure and compressive properties of selected laser melted Ti6Al4V lattice structures. Mater. Des. **198**, 109292 (2021)
4. He, J., et al.: The martensitic transformation and mechanical properties of Ti6Al4V prepared via selective laser melting. Materials **12**, 321 (2019)
5. Hasan, R., Rosly, A.S.R.M., Harris, D.H.D.: Metallic parts realization using selective laser melting machine default parameters. J. Ind. Mod. Manuf. **1**(2), 1–11 (2020)
6. Hasan, R.: Progressive collapse of titanium alloy micro-lattice structures manufactured using selective laser melting. University of Liverpool, UK (2013)

Effects of Different Polyamide (PAa12) Composition on Dimensional Accuracy in Selective Laser Sintering

Mohammad Rafi Omar[1,2,4] , Muhammad Ilman Hakimi Chua Abdullah[1,4(✉)] ,
Mohd Rizal Alkahari[2,4] , Mohamed Saiful Firdaus Hussin[1,4] , Rohana Abdullah[1,3],
Mohd Fadzli Bin Abdollah[2,4], and Darrenveer Singh Gill[3]

[1] Fakulti Teknologi Kejuruteraan Mekanikal dan Pembuatan, Universiti Teknikal Malaysia Melaka, Hang Tuah Jaya, 76100 Durian Tunggal, Melaka, Malaysia
ilmanhakimi@utem.edu.my

[2] Fakulti Kejuruteraan Mekanikal, Universiti Teknikal Malaysia Melaka, Hang Tuah Jaya, 76100 Durian Tunggal, Melaka, Malaysia

[3] Fakulti Kejuruteraan Pembuatan, Universiti Teknikal Malaysia Melaka, Hang Tuah Jaya, 76100 Durian Tunggal, Melaka, Malaysia

[4] Centre for Advanced Research on Energy, Universiti Teknikal Malaysia Melaka, Hang Tuah Jaya, 76100 Durian Tunggal, Melaka, Malaysia

Abstract. One of the major issues for additive manufacturing technologies is dimensional accuracy. The selective laser sintering (SLS) is a 3D printing technology that is able to produce infinite types of precise 3D printed objects. This aim of the research is to determine the effects of different compositions of virgin, reheated, and recycled polyamide-12 (PA-12) materials on dimension accuracy. The samples were additively manufactured using a SLS Farsoon 402P machine with a 70-W laser beam. Next, a calibrated machine block was used to measure and analyze the samples' dimension accuracy in the X and Y axes using a ZEISS CONTURA G2 machine. Results showed that the recycled PA-12 material produced high accuracy with a mean value of 0.09% error in the X direction and 0.170% error in the Y direction.

Keywords: Additive manufacturing · 3D printing · Selective laser sintering · Polyamide 12

1 Introduction

Additive manufacturing (AM) is a technique for creating 3D objects by layering material, whether the material is plastic, metal, concrete, composite or human tissue [1]. Nowadays, the AM technique has improved in terms of speed, cost, complexity and resolution. AM has helped improve the efficiency of various industrial sectors and serve as a valuable resource for aerospace, automotive, and biomedical engineering [2].

There are various types of 3D printing technology. However, fused deposition machine, stereolithography (SLA) and selective laser sintering (SLS) are three of the

most employed techniques. SLS is an additive method that facilitates the manufacturing of 3D printed products by sintering/melting a powdered material layer by layer with a laser-powered heat source [3]. A thin layer of powder material is placed onto a heated build surface (usually warmed), and then different types of lasers may be used as a heat source to selectively sinter the powder. The capability of SLS in producing high quality printed parts without supports opens up practically limitless opportunities for complex design [4].

The primary parameter control in this study is the percentage of PA-12 in the material. This PA-12 powder is approximately 60–80 μ in particle size and has a melting point of 183 °C [5]. Among the material's characteristics include high toughness, good wear qualities, oil resistance, high dimensional stability, good wear properties, low density, and minimal moisture absorption [6]. The material recycling time is also critical in ensuring the finished product's dimensional accuracy and surface roughness. Other study has highlighted that an increase in material recycling periods may increase the amount of adhering powder, which results in an increase in the amount of powder with a high melting point [7].

This study investigates the factors that influence different PA-12 compositions on the dimension accuracy of SLS printed samples. The default configuration of the manufacturer Farsoon 402P machine was used as a constant parameter. Suitable percentage of PA-12 compositions were determined in order to produce samples with high accuracy.

2   Methodology

Prior to the experiment, the sample of SLS calibration block was prepared and the roughness test block was designed using CATIA V5 CAD software. Figure 1 shows the design size based on the calibration block SLS machine's specification.
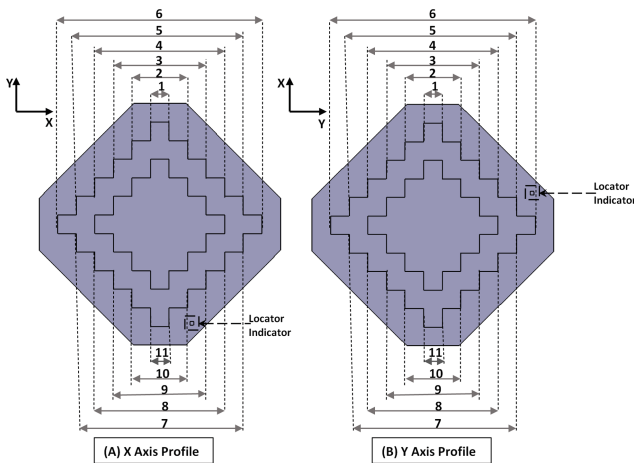
Fig. 1. Calibration block X axis (A) and Y axis (B).

As shown in Table 1, the specimens were prepared using three different classifications of PA-12 material with predetermined composition percentages (CP). The composition groups were identified as CP1, CP2 and CP3. The different composition group of PA-12 materials are made up of a homogeneous mixture of virgin, reheated and recycled powders. A powder machine was used to mix the CP1 and CP2 and then the powder was inserted into the SLS machine feeding chamber. The results showed that when scratched samples were sintered with virgin powder, the mixtures were looser and partially sintered producing fractured small powder instead of adhered powder samples [8].

Table 1. Composition Polyamide-12 percentage.

Composition (CP)	CP1	CP2	CP3
(%) Virgin	100	40	0
(%) Reheated	0	20	0
(%) Recycled	0	40	100

*Virgin: material refers to a new manufacturer's material that has not been used or exposed
*Reheated: heated material in the powder feeder chamber but never exposed to the laser beam (overflow powder)
*Recycled: un-sintered material and exposed to laser beam

The operation of SLS Farsoon 402P mainly has three main stages: pre-processing, printing and post-processing. During pre-processing, the translation of the digital solid model to printing instructions was done using BuildStar Version 1.4.2.22 software. Slicer software was also used to convert the CAD from stereolithography (STL) format to machine instructions, also known as G-Programming Language (G-Code). At the printing stage, the laser power was set at 70-W, the layer thickness at 0.006 mm, the hatching distance at 0.15 mm and the chamber temperature at 169.5 °C. In the the post-processing stage, the material block was collected from the SLS machine construction chamber and transported to the sieving machine for material block breakage procedure.

Later, three samples were prepared to measure the dimensional accuracy via SLS. A ZEISS CONTURA G2 coordinate measuring machine was used to take the dimensions. As indicated in Fig. 1, the calibration block required 11 points for X-axis measurement and 11 points for Y-axis measurement (A-B).

3   Results and Discussion

The most important key to obtain a high precision accuracy material is to understand the effects on the process parameters involved. Hence, the effects of the different material compositions on these process parameters were analyzed in this section. Based on Fig. 2, the results show CP3 has higher deviation compared to CP1 and CP2. Therefore, CP3 was found to have the most accurate composition material for X-axis printed direction, with an overall mean deviation error equivalence of 0.08%. CP3 composition also achieved a percentage score from an 11-point measurement of 7/11, indicating that CP3 has a lower error compared to other compositions. The second lower mean deviation error of 0.22% was found in the CP2 composition, while the highest mean deviation was found in CP1 with an overall mean deviation error of 0.32%.

Figure 3 depicts the Y-axis printed direction showing CP3 having the most accurate dimension measurement with an overall mean deviation error of only 0.134%. In addition, the X-axis printed direction for the CP3 indicated a higher accuracy compared to the Y-axis printed direction by approximately 0.09%. Consequently, it can be inferred that both the X-axis and Y-axis directions show only a small difference in error. Thus, this error had little effect on accuracy even with a large, printed part. In a previous study conducted by Zhi Zeng [10], the virgin polyamide 12 had an X-axis range accuracy of 1.23% to 1.5%, and a Y-axis accuracy of 1.14% to 3.35%
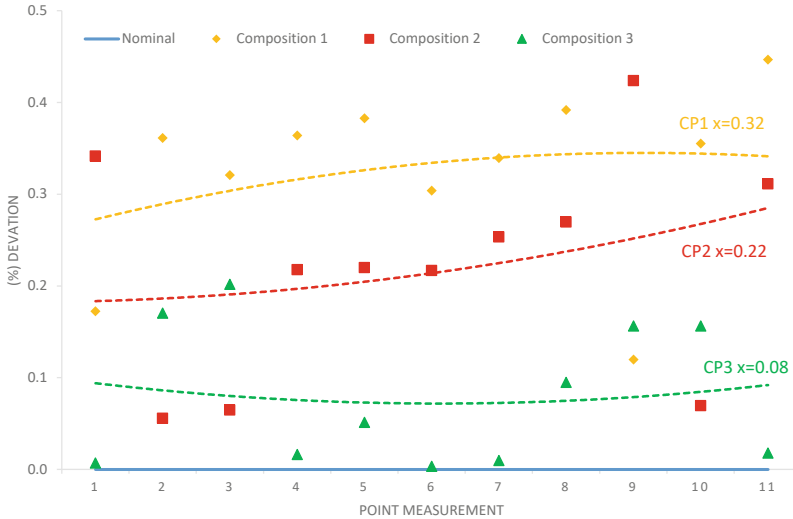
Fig. 2. X axis dimension accuracy SLS calibration block deviation graph.
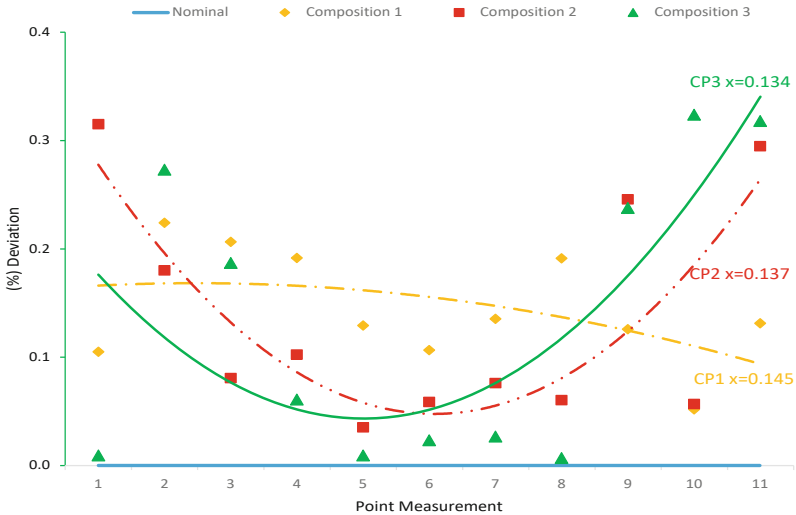
Fig. 3. Y axis dimension accuracy SLS calibration block deviation graph.

4 Conclusion

This study conclusively shows that the direction in which models are located, their geometrical characteristics and the material composition percentage have a significant effect on the accuracy. In comparison to the Y direction, the overall mean results demonstrate that the X direction has a higher accuracy. The composition 3 or CP3, which was made entirely of recycled materials, has the potential to be used in industrial printed precision products due to the better dimension accuracy results for the X-axis and Y-axis. This composition also is cheaper than composition 1 and composition 2 and is also recyclable multiple times. The composition 1 results showed a high deviation for X-axis and Y-axis compared to the Composition 2 and composition 3 results. Hence, the composition 3 with 100% recycled material obtained the highest dimensional accuracy (X direction of 0.09% error and Y direction of 0.170% error). For future work, the authors suggest increasing the melting point of the recycled material.

References

1. Bakar, N.S.A., Alkahari, M.R., Boejang, H.: Analysis on fused deposition modelling performance. J. Zhejiang Univ. Sci. A **11**(12), 972–977 (2010). https://doi.org/10.1631/jzus.A10 01365
2. Hussin, M.S.F., et al.: A bibliometric analysis of the global trend of using alginate, gelatine, and hydroxyapatite for bone tissue regeneration applications. Polymers **13**(647), 1–17 (2021)

3. Ali, M.H., Batai, S., Sarbassoy, D.: 3D printing: a critical review of current development and future prospects. Rapid Prototyp. J. **25**(6), 1108–1126 (2019)
4. Patel, A., Venoor, V., Yang, F., Chen, X., Sobkowicz, M.J.: Evaluating poly (ether ether ketone) powder recyclability for selective laser sintering applications. Polym. Degrad. Stab. **185**(109502), 1–11 (2021)
5. Liu, B., Fang, G., Lei, L.: An analytical model for rapid predicting molten pool geometry of selective laser melting (SLM). Appl. Math. Model. **92**, 505–524 (2021)
6. Wua, H., et al.: Recent developments in polymers/polymer nanocomposites for additive manufacturing. Prog. Mater. Sci. **111**(100638), 1–47 (2020)
7. Batistella, M., et al.: Selective laser sintering of polyamide 12/flame retardant compositions. Polym. Degrad. Stab. **181**(109318), 1–13 (2020)
8. Yao, B., Li, Z., Zhu, F.: Effect of powder recycling on anisotropic tensile properties of selective laser sintered PA2200 polyamide. Eur. Polym. J. **141**(110093), 1–10 (2020)
9. Petzold, S., Klett, J., Schauer, A., Osswald, T.A.: Surface roughness of polyamide 12 parts manufactured using selective laser sintering. Polym. Test. **80**(106094), 1–12 (2019)
10. Zeng, Z., Deng, X., Cui, J., Jiang, H., Yan, S., Peng, B.: Improvement on selective laser sintering and post-processing of polystyrene. Polym. (Basel). **11**(956), 1–15 (2019)

Flatwise and Edgewise Compression Properties of Composite PLA Core Fabricated via Additive Manufacturing Technique

Muhamad Shahirul Mat Jusoh[1(✉)], Muhammad Hazeem Salim[1],
Nuralis Batrisha Dzukieman[1], Mohd Yazid Yahya[2], Haris Ahmad Israr Ahmad[2],
and Abdul Halim Sulaiman[3]

[1] Department of Polymer Composite Processing Engineering Technology, Kolej Kemahiran
Tinggi MARA (KKTM), 78300 Masjid Tanah, Melaka, Malaysia
`shahirul.jusoh@mara.gov.my`
[2] School of Mechanical Engineering, Universiti Teknologi Malaysia (UTM),
81310 Johor Bahru, Johor, Malaysia
[3] CTRM Aero Composites Sdn. Bhd, Jalan Merdeka 33, Taman Merdeka,
75350 Batu Berendam, Melaka, Malaysia

Abstract. In the new era of industrial revolution of 4.0, additive manufacturing (AM) technique gains attention from academia, researchers and industries. Fabrication of Polylactic Acid (PLA) honeycomb core using 3D printing technique was employed in this study via fused deposition modelling (FDM). Two types of sandwich composites were fabricated between carbon fibre face sheet with printed PLA core (C/PLA) and Nomex honeycomb core (C/NMX) via hand lay-up and vacuum bagging processes. Compression tests were conducted in the flatwise and edgewise directions according to the ASTM C365 and ASTM C364, respectively. It was found that the C/PLA exhibited higher on the compression stresses both in the flatwise and edgewise directions as compared to C/NMX. Tested sample of C/PLA displayed the flatwise and edgewise compression stresses of 25.7 and 125.0 MPa, while the tested sample of C/NMX exhibited the value of 7.9 and 12.6 MPa, respectively. In terms of compression strain, it was observed that C/PLA exhibited 31.5% higher than C/NMX in the flatwise direction.

Keywords: Additive manufacturing · Compression · Polylactic acid

1 Introduction

Additive manufacturing (AM) method, also known as three-dimensional (3D) printing consists of many techniques. Some of these techniques are fused deposition modelling (FDM), electron beam melting (EBM), selective laser sintering (SLS), digital light projection (DLP) and laminated object manufacturing (LOM).

Composite printing is gaining attention of researchers in exploring new sandwich structure owing to its design flexibility offered [1, 2]. FDM is widely used nowadays due to its reliability, affordability, simplicity, minimal wastage and compatibility with

almost available material [3]. FDM techniques using PLA was used in the fabrication of lightweight composite structure [4], while Yuba Tao et al. use the combination of PLA with the wood flour (WF) as a hybrid filament during 3D printing process [3]. Polylactic acid (PLA) material widely used in composite application due to its advantages in terms of recyclability, chemical resistance, thermal resistance, sound insulation, water resistance and eco-friendly [5].

Flatwise compression test of Nomex honeycomb core was investigated by Longquan et al. [6] and it was found that debonding imperfections significantly affected on the mechanical behavior of the tested sandwich composite panel. Effect of printing layer thickness of PLA on the tensile and bending properties was studied and it was found that both mechanical properties significantly improved with decreasing layer thickness [7]. Present study is going to discover the behavior of printed PLA core compared with Nomex honeycomb core with carbon face sheet in resisting compression loading in the flatwise and edgewise directions.

2   Materials and Methods

2.1   Additive Manufacturing (AM) Technique

FDM methods was used in printing honeycomb core using polylactic acid (PLA) material. The honeycomb core was designed using Inventor software and exported to STL format file. Using 3D slicer software (Ultimaker Cura), the important parameters such as printing speed, temperature and layer thickness were set in generating G-code and transferred to the 3D printer using SD card.

During printing process, PLA filament was heated to the melting temperature up to $210 \pm 10\,°C$ and extruded through the extrusion nozzle. The liquefier head moves on the X-Y plane according to software-generated tool paths. The specimen was printed layer by layer with the movement of either print bed or extrusion nozzle to reserve allowable space for the next layer built-up. This process was continuously repeated until the desired dimensions completely printed using Ultimaker 3D printer as shown in Fig. 1.
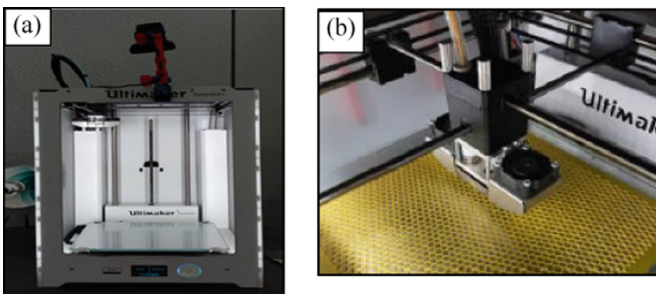
Fig. 1.   (a) Ultimaker 3D printer; (b) Printed honeycomb core using PLA.

2.2   Compression Test

The sandwich composite with PLA and Nomex honeycomb cores were fabricated using hand lay-up and vacuum bagging methods. Carbon fibre was used as face sheet for both samples. Flatwise and edgewise compression tests were conducted using universal testing machine (UTM), Instron 5969 according to the ASTM C365 (Standard Test Method for Flatwise Compressive Properties of Sandwich Cores) and ASTM C364 (Standard Test Method for Edgewise Compressive Strength of Sandwich Constructions), respectively.

Prior to test, samples were conditioning at temperature 23 ± 3 °C with relative humidity of $50 \pm 5\%$ using humidity chamber, Gotech GT-7005. Figure 2 below shows the position of the samples during flatwise and edgewise compression tests.
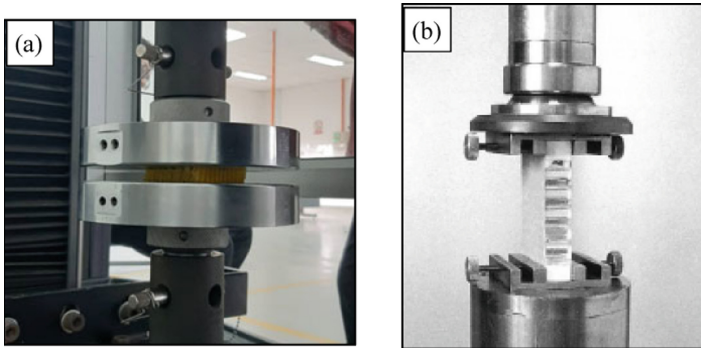
Fig. 2.   (a) Flatwise compression test; (b) Edgewise compression test.

3   Results and Discussion

Generally, compression tests are used to determine material's behavior by applying compressive pressure using platens or specialized fixtures and typically applied on brittle materials such as concrete, ceramics, plastics, and composites.

3.1   Flatwise Compression Properties

Figure 3 shows the result of flatwise compression properties between sandwich composite with PLA core (C/PLA) and Nomex core (C/NMX). Results showed that the C/PLA samples exhibited the maximum compressive stress of 25.7 MPa, which is 225.3% higher than C/NMX. In terms of compressive strain, there is not substantial different between both samples. C/NMX and C/PLA samples recorded the compressive strain value of 0.020 and 0.025 mm/mm, respectively.

In the flatwise compression, it is assumed the upper and lower face sheets are not deformed and affected the results as found in the previous study on the sandwich composite of basalt with Nomex honeycomb core. The strength of the compression specimen highly dependent on the core height and the maximum height allowable is 10 mm for the wall thickness of 0.05 mm to avoid premature yield [8].
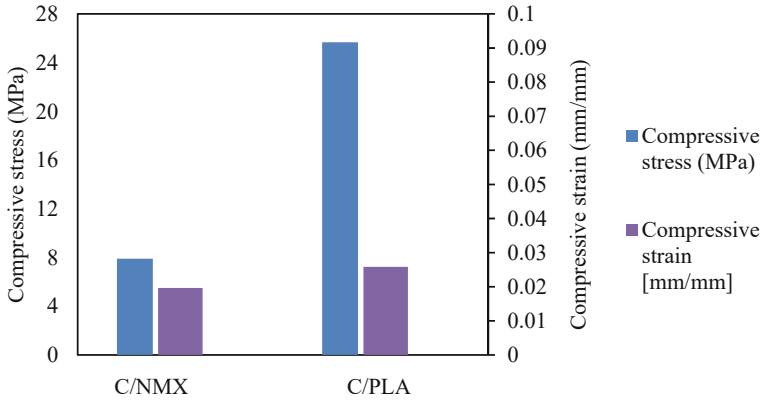
Fig. 3. Flatwise compressive stress and strain of C/NMX and C/PLA.

3.2 Edgewise Compression Properties

As shown in Fig. 4, the edgewise compression stress of C/PLA exhibited about 9 times higher than C/NMX with the compression stress value of C/NMX of 12.6 MPa. In terms of compressive strain, C/NMX displayed the value of 0.0073 mm/mm, while C/PLA exhibited about 15 times higher than C/NMX.

The edgewise compressive stress indicated that the sandwich composite constructed using PLA core able to resist higher of load-carrying capacity compared to C/NMX due to the higher capacity of the elongation offered. This finding agreed with the findings found by Mohamed et al. [9] upon investigation on the behavior of sandwich composite structure.
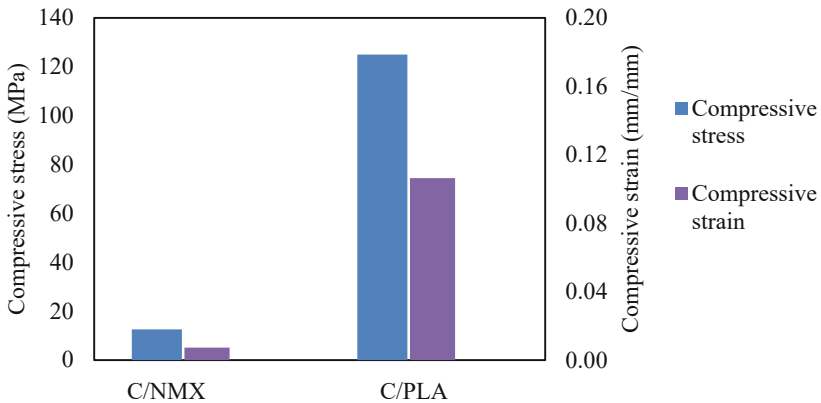
Fig. 4. Edgewise compressive stress and strain of C/NMX and C/PLA.

4   Conclusion

Compression stress of C/PLA and C/NMX in the edgewise direction exhibited 58.9 and 386% higher than flatwise direction, respectively. C/PLA recorded the flatwise and edgewise compression stresses of 25.7 and 125.0 MPa which is 225 and 892% higher than C/NMX. There is no substantial different on the compressive strain in the flatwise direction between C/NMX and C/PLA as compared to the edgewise direction. In the edgewise direction, it was observed that C/NMX recorded only 6.9% of the maximum compression strain as compared to C/PLA.

References

1. Yap, Y.L., Yeong, W.Y.: Additive manufacture of fashion and jewellery products: a mini review. Virtual Phys. Prototyp. **9**, 195–201 (2014)
2. Lee, J.M., Zhang, M., Yeong, W.Y.: Characterization and evaluation of 3D printed microfluidic chip for cell processing. Microfluid. Nanofluid. **20**(1), 1–15 (2015). https://doi.org/10.1007/s10404-015-1688-8
3. Yuba, T., Honglei, W., Zelong, L., Sheldon, Q.S.: Development and application of wood flour-filled polylactic acid composite filament for 3D printing. Materials **10**, 339 (2017)
4. Salvatore, B., Roberto, T.: Honeycomb sandwich specimens made of PLA and produced via 3D FDM printing process: an experiment study. J. Aircr. Spacecr. Technol. **4**(1), 54–69 (2020)
5. Jan, L., Marc, G., Warren, J.G., Andreas, K.: Understanding the development of interfacial bonding within PLA/wood-based thermoplastic sandwich composites. J. Ind. Crops Prod. **127**, 129–134 (2019)
6. Longquan, L., Peng, M., Hai, W., Zhongwei, G.: The flatwise compressive properties of Nomex honeycomb core with debonding imperfections in the double cell wall. Compos. Part B **89**, 233–246 (2014)
7. Ayrilmis, N., Kariz, M., Kwon, J.H., Kitek Kuzman, M.: Effect of printing layer thickness on water absorption and mechanical properties of 3D-printed wood/PLA composite materials. Int. J. Adv. Manuf. Technol. **102**(5–8), 2195–2200 (2019). https://doi.org/10.1007/s00170-019-03299-9
8. Zongwen, L., Jianxun, M.: Experimental study on mechanical properties of the sandwich composite structure reinforced by basalt fiber and nomex honeycomb. Materials **13**, 1–17 (2020)
9. Mohamed, M., Anandan, S., Huo, Z., Birman, V., Volz, J., Chandrashekhara, K.: Manufacturing and characterization of polyurethane-based sandwich composite structures. Compos. Struct. **123**, 169–179 (2015)

Parameters and Bead Geometry Relationship of Wire and Arc Additive Manufacturing for Aluminum Alloy ER5183

Nur Izan Syahriah Hussein[1(✉)], Amirul Nasriq Nasri[1], Suraya Laily[1], Mohamad Nizam Ayof[1,2], and Mohd Shahriman Adenan[2]

[1] Fakulti Kejuruteraan Pembuatan, Universiti Teknikal Malaysia Melaka, Hang Tuah Jaya, 76100 Durian Tunggal, Melaka, Malaysia
izan@utem.edu.my

[2] Faculty of Mechanical Engineering, Universiti Teknologi MARA, 40450 Shah Alam, Selangor, Malaysia

Abstract. Wire and arc additive manufacturing (WAAM) is one of the most suitable additive manufacturing (AM) technologies for producing large volume metallic components. However, one of the challenges for the WAAM process is poor part accuracy, which is emphasized by the bead geometry. In addition, deposition process parameters are the controlling factor for bead geometry. Aluminum Alloy ER5183 is chosen as a material due to its being lightweight and widely used in engineering structures for the transport sector. Therefore, the objective of this study is to investigate the effect of WAAM parameters on the bead width and height of three layers ER5183 deposits. WAAM process was conducted with a gas tungsten arc welding (GTAW) system. The deposition parameters were arc current (120–180 A), travel speed (25–30 cm/m), and wire feed rate (50–100 cm/m). Results show that welding current was the main controlling factor of the bead width and height. The high arc current (180 A) increases bead width, and the low arc current (120 A) increases the bead height. A set of optimization parameters for the bead width and height was then proposed.

Keywords: Wire and arc additive manufacturing · Gas tungsten arc welding · Aluminum Alloy ER5183 · Parameters · Bead dimension

1 Introduction

Additive Manufacturing (AM) is a technique that promises to minimize the cost of components by reducing resource waste and time to market [1]. AM also improves design freedom, potentially leading to weight savings and reducing complex assemblies previously made of several subcomponents. The review shows that major methods of AM are additive powder processing by selective laser sintering (SLS), selective laser melting (SLM), and liquid binding by three-dimensional printing (3DP) [2]. However, some of the disadvantages of powder-bed fusion, especially in aluminum alloy powders, are oxide film on the surface of the metal powder, and a relatively low melting point of

aluminum makes it challenging to find a suitable binder [3]. Thus, selecting wire-based deposition such as wire and arc additive manufacturing (WAAM) can eliminate these advantages. In addition, the wire has advantages over powder as a feedstock due to its lower cost, lower oxide content, and higher deposition rate [4]. A WAAM system consists of a moving welding torch attached to a robotic arm, static worktable, wire feeder, and computer numerical control (CNC) to make the motion device and the welder linked and work synchronously. WAAM by gas metal arc welding (GMAW) has been reported more than gas tungsten arc welding (GTAW), especially in regards to aluminum alloy deposition [5, 6].

Deposition process parameters are the controlling factor for bead geometry (bead width, height, and penetration [7]. According to Horgar et al. [5], wire feed rate, travel speed, arc current, and voltage are the varying parameters. In contrast, arc mode, shielding gas, nozzle diameter, and filler wire size are the constant parameters.

This study aims to investigate the effect of WAAM parameters on the bead width and height of three layers of ER5183 deposits on the ER5083 base plate and propose an optimization of parameters for WAAM of ER5183 wire on the AA5083 base plate.

2 Experimental Method

WAAM process was conducted using OTC-400 robotic GTAW. Based on AWS A5.10 ASME SFA 5.10, ER5183 and ER5083 were used as the feedstock and base plate, respectively. The wire diameter was 1.2 mm, and the base plate size was $25 \times 150 \times 5$ mm (width $\times$ length $\times$ thickness). A new jig was designed and fabricated to hold the base plate. A preliminary experiment with a one (1) layer deposit was performed to determine a range of suitable variables for the parameters of arc current, travel speed, and wire feed rate. Following the selection of the variables, a design matrix based on Full Factorial was generated using Minitab software. Three (3) layers were deposited for every sample, with all layers started at the same origin (unidirectional). The bead width and height were measured with a vernier caliper and welding gauge, respectively. Then, the Pareto chart and main effects plot from the Minitab software were used in the analysis. All results were discussed accordingly, and finally, a set of optimization parameters for the bead width and height was then proposed.

3 Results and Discussion

3.1 Selection of Parameters and Variables

Based on welding parameters and variables from the GTAW of ER5183, eight (8) samples were deposited in one (1) layer. Figure 1 shows an example of one (1) layer deposit built with 180 A arc current, 30 cm/m travel speed, and 100 cm/m wire feed rate. It has a poor start and weld crater at the end of the deposit. However, it can be considered as a good deposit from its straight and uniform bead with an oxide-free surface, no cracking, and no porosity on the bead's surface. Another good deposit from a lower level of arc current, travel speed, and wire feed rate was obtained from sample seven (7) built with 120 A, 25 cm/m travel speed, and 50 cm/m wire feed rate. Table 1 shows the selected parameters and their variables at low level and high level for the design of experiment (DOE).
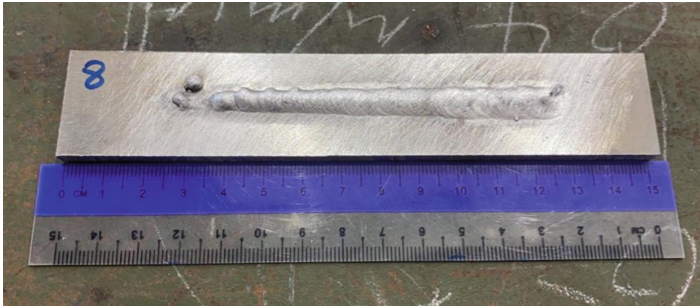
Fig. 1. Sample eight (8) of the preliminary experiment deposited with 180 A arc current, 30 cm/m travel speed, and 100 cm/m wire feed rate.

Table 1. Parameters and variables for WAAM process of ER5183 wire on AA5083 base plate using GTAW.

Parameter	Unit	Low level (−1)	High level (+1)
Arc current	A	120	180
Travel speed	cm/m	25	30
Wire feed rate	cm/m	50	100

3.2   Parameter and Bead Geometry Relationship

A design matrix was generated based on Table 1, and there were seven (7) sets of the experiment for the three (3) layer deposits. Bead width and height were measured and recorded for each sample. Pareto chart as in Fig. 2 suggested that welding current was the most significant factor affecting the bead width and height. Welding current is one of the factors in determining the total heat input besides voltage and travel speed [8]. Bead geometry plays a very important role in predicting the quality of weld as the cooling rate of the weld depends on the height and bead width.
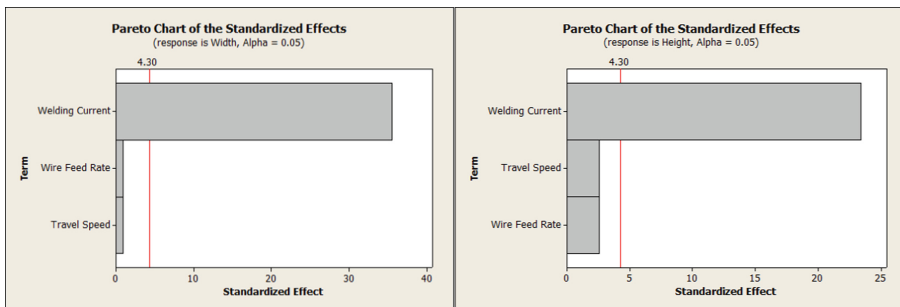
Fig. 2. Pareto charts of the standardized effects for bead width and height suggesting that welding current is the most significant factor.

3.3 Optimization of Parameter

Main effect plots were used to propose an optimization set of parameters for bead width and height. The optimization set of parameters proposed for bead width was when the three (3) layers deposit was built with 180 A, 30 cm/m travel, and 50 cm/m wire feed rate. The resulting bead width was 12.3 mm. On the other hand, to obtain a 3 mm bead height, the deposit was made with 120 A arc current, 30 cm/m travel speed, and 100 cm/m wire feed rate.

4 Conclusion

The preliminary experiment aided the parameters and their variables selection because the suitable set of parameters cannot be precisely determined from the literature review. The three (3) layers of deposition were a more accurate experiment to show the impact of WAAM deposition on the bead geometry (width and height). The arc current was the most significant factor affecting the bead width and height because arc current increases the total heat input during the WAAM process. In general, it can be concluded that high arc current (180 A) results in increased bead width, and low arc current (120 A) increases the bead height.

References

1. Williams, S.W., Martina, F., Addison, A.C., Ding, J., Pardal, G., Colegrove, P.: Wire and arc additive manufacturing. Mater. Sci. Technol. **32**(7), 641–647 (2016)
2. Dass, A., Moridi, A.: State of the art in directed energy deposition: from additive manufacturing to materials design. Coatings **9**(7), 1–26 (2019)
3. Leirmo, J.L., Baturynska, I.: Challenges and proposed solutions for aluminum in laser powder bed fusion. Procedia CIRP **93**, 114–119 (2020)
4. Hussein, N.I.S., Segal, J., McCartney, D.G., Pashby, I.R.: Microstructure formation in Waspaloy multilayer builds following direct metal deposition with laser and wire. Mater. Sci. Eng. A **497**, 260–269 (2008)
5. Horgar, A., Fostervoll, H., Nyhus, B., Ren, X., Eriksson, M., Akselsen, O.M.: Additive manufacturing using WAAM with AA5183 wire. J. Mater. Process. Tech. **259**, 68–74 (2018)
6. Tonelli, L., Laghi, V., Palermo, M., Trombetti, T., Ceschini, L.: AA5083 (Al-Mg) plates produced by wire-and-arc additive manufacturing: effect of specimen orientation on microstructure and tensile properties. Prog. Addit. Manuf. **6**, 479–494 (2021)
7. Gupta, S.K., Mehrotra, S., Raja, A.R., Vashista, M., Khan Yusufzai, M.Z.: Effect of welding speed on weld bead geometry and percentage dilution in gas metal arc welding of SS409L. Mater. Today Proc. **18**, 5032–5039 (2019)
8. Dinovitzer, M., Chen, X., Laliberte, J., Huang, X., Frei, H.: Effect of wire and arc additive manufacturing (WAAM) process parameters on bead geometry and microstructure. Addit. Manuf. **26**, 138–146 (2019)

Effect of SLM Processing Parameters and Energy Density on Physical and Mechanical Properties at Different Surfaces

Farhana Mohd Foudzi[(✉)] ⓘ, Minhalina Ahmad Buhairi ⓘ,
and Fathin Iliana Jamhari ⓘ

Universiti Kebangsaan Malaysia, 43600 Bangi, Malaysia
`farhana.foudzi@ukm.edu.my`

Abstract. Processing parameters and their energy density influence the performance of 3D parts manufactured by selective laser melting (SLM). Such performance covers the physical and mechanical properties such as surface roughness and microhardness. However, due to building direction, some 3D parts may have different surfaces or skins depending on their geometries. Although the processing parameters may have the dominant factor that influences the overall performance of a 3D part, each surface may have its own properties. It would be a practical approach to investigate the performance at different surfaces of a 3D part. In this work, the properties of surface roughness and microhardness at different skins of a Ti6Al4V cubic sample were investigated at various energy densities. Such sample was printed by different sets of parameters based on the Taguchi (L_9) method at a building direction of 30°. Based on such direction, a cubic sample has several skins such as up-skin, core-skin and down-skin. Surface roughness and microhardness tests were conducted on such skins. It was found that the surface roughness (R_a) is in range of 10–20 μm for all samples. For microhardness, the obtained range was 350 HV–480 HV. It can be concluded that the suitable range of energy density to obtain smoother R_a and higher microhardness is 60–90 J/mm^3, which does not differ much from the default setting of Ti6Al4V in SLM (69.44 J/mm^3).

Keywords: Processing parameters · Surface roughness · Microhardness

1 Introduction

1.1 Selective Laser Melting (SLM)

Additive manufacturing (AM) or also known as 3D printing, has gained great interest from many manufacturers and researchers due to its ability to build 3D parts having intricate features [1]. Such ability makes AM superior compared to other conventional methods such as casting and injection molding. AM is also applicable to most materials such as polymers, composites and metals. Metals are widely applied in AM due to its great mechanical properties such as high strength and suitable for high temperature applications. The most common process associated with metal is selective laser melting

(SLM). In SLM, the common metals are stainless steel (SS316L) and titanium alloy (Ti6Al4V).

Processing Parameters

In SLM, there are four main processing parameters such as laser power, scanning speed, hatching distance and layer height [2]. Laser power is defined by the total energy emitted by the laser per unit time. Scanning speed is the speed of laser spot and defined by point distance and exposure time. The space between two laser paths is known as hatching distance while layer height is the thickness of each layer of deposited powder bed. The interaction of these parameters gives the volumetric energy density formula.

$$Energy\ density \left(\frac{J}{mm^3}\right)$$
$$= \frac{Laser\ power(W)}{Scanning\ speed\left(\frac{mm}{s}\right) \times Layer\ height\ (mm) \times Hatching\ distance\ (mm)} \quad (1)$$

As the energy density increases, a large amount of energy (melting) is employed onto the powder bed which resulted to a fully dense part. Therefore, energy density is one of the important factors to take note during the selection of processing parameters [3]. However, many researchers only focused on few processing parameters such as laser power and scanning speed. It would be a more practical approach if energy density is used as an optimization metric in SLM where all processing parameters as mentioned in Eq. (1) are considered [4]. Some parts may require support structure according to their geometries and building directions. Building direction normally ranges from 0°–90° of angle, which can be obtained from the simulated 3D design (STL file) prior printing. A 3D part consists of several surfaces such as up-skin, down-skin and core skin, depending on building direction. Each of these surfaces may has its own performance in terms of physical and mechanical properties. Xu et al. (2019) reported that the building direction greatly influence the mechanical properties of SLM-ed Ti6Al4V tensile parts. It was found that edge oriented tensile bar gave the best tensile and ductility behavior [5]. In terms of appearance, down-skin has coarser surface roughness compared to up-skin, as reported by Covarrubias and Eshraghi (2017) [6]. However, the properties of core-skin are less reported. Therefore, the aim of this work is to investigate the properties of several surfaces of a SLM-ed Ti6Al4V cubic sample at different processing parameters and energy density.

2 Research Methodology

2.1 Sample Preparation

The titanium alloy (Ti6Al4V) powder used in this work is supplied by SLM Solution, Germany. The powder size ranges from 30 μm to 70 μm where the average size is 45 μm. The shape of the sample is cubic with the volume of 1 cm^3 (1 cm × 1 cm × 1 cm). The cubic design was drawn in Solidworks for the STL.file. The printing process was carried out using a SLM 280HL machine in Contraves Advanced Devices Sdn Bhd, Cyberjaya. The machine is equipped with 400 W continuous-wave Yb: YAG laser with

a beam diameter of 100 μm. The suitable building direction is 30° from the laser beam. Therefore, the cubic sample has different surfaces such as up-skin 1 (US1) up-skin 2 (US2), core-skin (CS) and down-skin (DS), as shown in Fig. 1. Take note that there are two sides of CS. However, based on the same orientation, CS is assumed to have the same properties regardless the side. In this work, the performance in terms of surface roughness and microhardness at different skins is investigated and compared. The cubic samples are printed at nine sets of parameters, denoted as P1–P9. These sets were varied based on Taguchi L$_9$ method, as shown by Table 1. Selection of the values in Table 1 was based on the default setting for Ti6Al4V parts by SLM. The default setting is denoted as Level 1 where the energy density is 69.44 J/mm^3. Table 2 shows the values of each processing parameters and energy density at all sets of parameters.
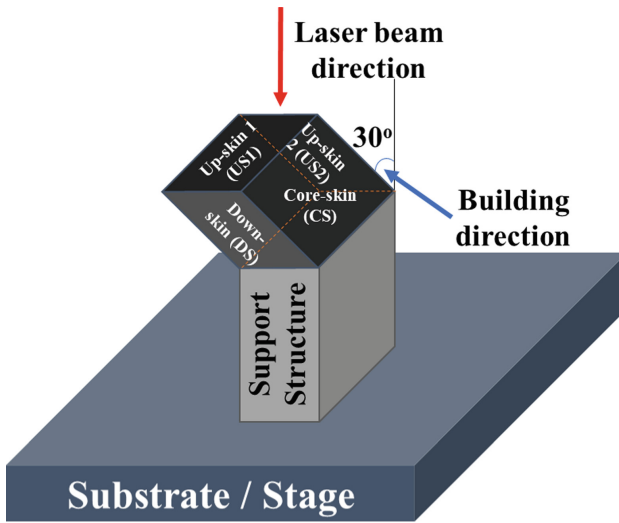
Fig. 1. Building orientation for the cubic sample.

Table 1. Factors (processing parameters) at different levels for Taguchi L$_9$ method.

Factors	Level		
	0	1	2
Layer height (mm)	–	0.03	–
Laser power (W)	225	275	325
Scanning speed (mm/s)	800	1100	1400
Hatching distance (mm)	0.10	0.12	0.14

Table 2. Processing parameters and energy density at all set of parameters (P1–P9).

Set of parameters	Layer height (mm)	Hatching distance (mm)	Scanning speed (mm/s)	Laser power (W)	Energy density (J/mm^3)
P1	0.03	0.10	800	225	93.75
P2	0.03	0.12	1100	275	69.44
P3	0.03	0.14	1400	325	55.27
P4	0.03	0.10	1100	325	98.50
P5	0.03	0.12	1400	225	44.64
P6	0.03	0.14	800	275	81.85
P7	0.03	0.10	1400	275	65.48
P8	0.03	0.12	800	325	112.85
P9	0.03	0.14	1100	225	48.70

3 Results and Discussion

3.1 Surface Roughness and Microhardness

Surface roughness (R_a) in the range of 10 μm–20 μm was measured for up-skin 1 (US1), core-skin (CS) and down-skin (DS) surfaces for all Ti6Al4V cubic samples, as shown by Fig. 2(a). Such range is acceptable in SLM with Ti6Al4V where the common reported value is less than 20 μm [7]. It was found that DS has the coarsest surface compared to US1 and CS, at all sets of parameters. This may be related to the condition of DS that overhangs due to the building direction. In addition, DS is opposite from the laser beam which means it is obstructed by other skins. This resulted to large volumes of partially melted powder particles adhered onto the DS surface due to the repeated heating and solidifying during printing [6]. Highest and lowest surface roughness is given by P1 and P5 cubic parts, respectively. This is due to lowest scanning speed of P1 compared to that of P5 (highest scanning speed). This resulted to splashing effect which normally occur at low scanning speed.

Since DS has the coarsest R_a, microhardness was conducted on US1 and CS, as shown in Fig. 2(b). It was found that the microhardness of all samples ranges from 350–477 HV. Such range is higher than the common reported range for Ti6Al4V manufactured by SLM, which is around 350–400 HV [8]. This may be due to the various processing parameters used in this work. In terms of comparison between US1 and CS, an average of 50 HV difference is observed for all cubic samples. This may be due to the position of CS that is not directly to the laser beam. This may result to less amount of melting (energy density) that was employed to CS compared to US1. This leads to incomplete fusion that may deteriorates the hardness value. Both of US1 and CS of P6 has the highest microhardness compared to P9 which gives the lowest. This is due to the energy density that is slightly higher than the default setting (P2; 69.44 J/mm^3). However, as the energy density increased above 90 J/mm^3, the microhardness decreased compared

to P6. It was reported that high energy density may form incomplete bonds which leads to severe voids and reduces hardness [9].
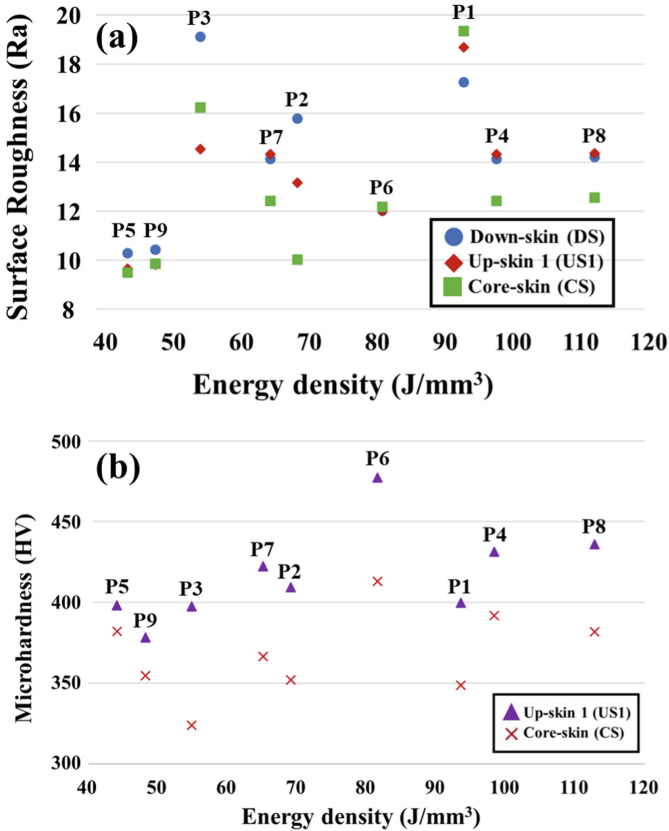
Fig. 2. (a) Surface roughness (R_a) and (b) microhardness for Ti6Al4V cubic samples at different skins and different energy density for all set of parameters (P1–P9).

Overall, it can be concluded that the preferred range of energy density that takes account both on smoother surface roughness (R_a) and higher microhardness should be in between 60–90 J/mm^3, as shown by cubic samples P7, P2 and P6 in Fig. 2. In addition, all cubic samples showed a great performance based on the surface roughness and microhardness evaluation although each cubic sample was printed at different processing parameters and energy densities. In addition, some findings were found to be better than that of reported works by other researchers. Meanwhile, in terms of application, although the cubic samples were varied based on their processing parameters and energy densities, it is believed that there will be no significant effect that may affect the performance. This is because the geometry is simple (cubic) and was built at only one building direction (30°). However, performance may vary when the geometry of printed parts is intricate with internal structures and different building orientations are applied.

4 Conclusion

Influence of processing parameters and energy density on the surface roughness (R_a) and microhardness at different surfaces of Ti6Al4V cubic samples was successfully evaluated. It was found that the suitable range of energy density that promises smoother surface roughness and higher microhardness is between 60–90 J/mm^3. In addition, the condition of each skin due to building orientation may also influence the microhardness where up-skin 1 (US1) was found to be better compared to other skins, regardless the energy density.

References

1. Triantaphyllou, A., et al.: Surface texture measurement for additive manufacturing. Surf. Topogr. Metrol. Prop. **3**(2), 024002 (2015)
2. Victor, A.M.: Analysis of the optimal parameters for 3D printing aluminum parts with a SLM 280 machine. Master's thesis, Universitat Politècnica de Catalunya, pp. 17–22 (2017)
3. Wang, Y., Kamath, C., Voisin, T., Li, Z.: A processing diagram for high-density Ti-6Al-4V by selective laser melting. Rapid Prototyp. J. **24**(9), 1469–1478 (2018)
4. Palousek, D., et al.: SLM process parameters development of Cu-alloy Cu7. 2Ni1. 8Si1Cr. Rapid Prototyp. J. **25**(2), 266–276 (2019)
5. Xu, Z.W., Liu, A., Wang, X.S.: The influence of building direction on the fatigue crack propagation behavior of Ti6Al4V alloy produced by selective laser melting. Mater. Sci. Eng. A **767**, 138409 (2019)
6. Covarrubias, E., Eshraghi, M.: Effect of build angle on surface properties of nickel superalloys processed by selective laser melting. JOM **70**(3), 336–342 (2018)
7. Longhitano, G.A., Larosa, M.A., Munhoz, A.L.J., Zavaglia, C.A.C., Ierardi, M.C.F.: Surface finishes for Ti-6Al-4V alloy produced by direct metal laser sintering. Mater. Res. **18**(4), 838–842 (2015)
8. Zuback, J.S., DebRoy, T.: The hardness of additively manufactured alloys. Materials **11**(11), 2070 (2018)
9. Qian, M., Xu, W., Brandt, M., Tang, H.P.: Additive manufacturing and postprocessing of Ti-6Al-4V for superior mechanical properties. MRS Bull. **41**(10), 775–784 (2016)

The Effects of Varying Oxygen Concentrations on Tensile Strength and Surface Roughness of 3D Printer

M. A. Che Mat[1], F. R. Ramli[1,2]([✉]), M. N. Sudin[1], S. G. Herawan[3], M. S. Mat[1,2], and M. R. Alkahari[1,2]

[1] Fakulti Kejuruteraan Mekanikal, Universiti Teknikal Malaysia Melaka, Hang Tuah Jaya, 76100 Durian Tunggal, Melaka, Malaysia
`faiz@utem.edu.my`
[2] Centre for Advanced Research on Energy, Universiti Teknikal Malaysia Melaka, Hang Tuah Jaya, 76100 Durian Tunggal, Melaka, Malaysia
[3] Faculty of Engineering, Bina Nusantara University, 11480 Jakarta, Indonesia

Abstract. The part produced by the fused filament fabrication 3D printer in terms of tensile strength and surface roughness depends mainly on the printing parameters and the environmental printing conditions. In this paper, nitrogen gas had been allowed to flow inside the 3D printer chamber to exclude oxygen in the printing environment. Tensile and surface roughness tests were performed on samples of three different layer thicknesses (0.1 mm, 0.2 mm, and 0.3 mm) of ABS in FFF. The scanning electron microscope observed a strong bonding of microstructure for 0% oxygen, compared to 10% and 20%. A significant increase in tensile strength and surface roughness was found, possibly partially due to the prevention of oxidation processes. Reduced polymer surface degradation at relatively high printing temperatures demonstrates these effects. Printing in 3D under exclusion oxygen can be generated reasonably quickly by filling the printing chamber with nitrogen in potential applications to manufacturing FFF-printed parts with improved mechanical properties.

Keywords: Fused filament fabrication · 3D printer · Additive manufacturing

1 Introduction

Additive Manufacturing (AM), or the commonly used term 3D printer, is a layer-by-layer fabrication of geometric three-dimensional (3D) shapes based on design CAD data. One of the 3D printing technology that widely used in the market is fused filament fabrication (FFF) because of its performance, FFF parts become primary consideration to the manufacturer and users, and the mechanical characteristics of the FFF part, such as tensile strength and surface roughness are often being discussed [1]. One of the drawbacks of FFF is that the printed part's surface roughness is excessively rough due to layer-by-layer deposition [2]. Several studies have been conducted on improving both the strength and the surface by controlling the environment conditions such as reducing

oxygen content from the environment [3]. However, in [3], the content of oxygen during experiments is not stated so in this paper the aim is to study the variation percentage of oxygen concentrations during 3D printing towards the mechanical characteristics of tensile strength and surface roughness.

2 Methodology

The 3D printer machine used for this experiment is an open-source fused filament fabrication Anet A8 (do-it-yourself kit), which is commonly available in the market. In order to avoid oxygen from being environmentally safe, the 3D printer system was located within an enclosed chamber of $(550 \times 550 \times 450)$ mm^3. Nitrogen gas was setup to flow through an inlet pipeline and fill the gas into the chamber. The chamber was operated under nitrogen with a pressure of $+$ 5 bar (vs. atmospheric pressure) and a flow rate of 12 m^3 h^{-1}. An oxygen detector (Uyigao UA6070B) was used to ensure the percentage concentration of oxygen within the chamber while the gas was flowing out by nitrogen. This process takes several minutes to flow out at the specific level of oxygen content inside the chamber. Therefore, both inlet and the outlet of the chambers were closed after the oxygen was removed. This experiment was repeated using different nitrogen gas levels, 0%, 10%, and 20% oxygen, in the chamber.

The tensile test samples were fabricate using FFF based on ASTM D638-14 standard. While for surface roughness test, a simple geometry block with measurements of 10 mm (L) $\times$ 10 mm (W) $\times$ 10 mm (H) square was fabricated using the 3D printer machine. The block measured the surface roughness using a 3D non-contact profilometer with a 90º traverse direction (perpendicular to building direction) to all four faces of the block i.e. Face 1-4. Table 1 below shows all of the samples were printed by the FFF setup processing parameters.

Table 1. Summary of the operating setup of the 3D printer.

Processing parameter	Value
Material used	ABS filament
Temperature (°C)	240
Infill pattern linear	Rectilinear, honeycomb
Level of oxygen in the chamber (%)	0, 10, 20
Layer thickness (mm)	0.1, 0.2, 0.3
Infill design %	0
Raster angle	90º

3   Results and Discussion

3.1   Tensile Strength

Figure 1 shows the tensile strength of the dog bone samples with different layer thickness and oxygen level. Low percentage of oxygen gives a higher tensile strength value compare to high percentage concentration. While high layer thickness for all 3D printer for all samples, gives the highest tensile strength for all oxygen concentration.
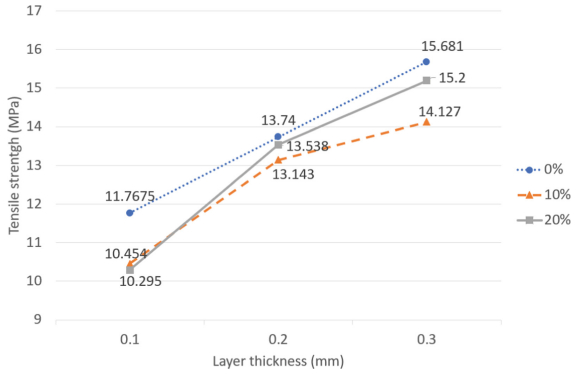
Fig. 1.   The effect of layer thickness on tensile strength with different levels of oxygen.

3.2   Surface Roughness

Figure 2 shows the surface roughness when printing conditions are absent in oxygen during printing. The surface roughness was slightly better, more stable, and relevant when there is no oxygen was in the chamber. Comparison between 0% with 20% of oxygen shows the same graph trend of surface roughness. However, the value of R_a for 0% are lower for all faces compared to those with oxygen. This shows that when the filaments deposited inside the chamber, oxygen may inhibit on the surface layer of the samples. Thus, removing oxygen provides better quality to 3D printed parts.

3.3   The Surface Morphology of FFF Part

Figure 3 shows the 0%, 10%, and 20% of oxygen levels with 0.1mm layer thickness. The 0% sample which has the highest tensile strength of 11.767 (MPa) compared to (b) and (c) with 10.454 (MPa) and 10.295 (MPa) respectively. Small voids area appears in (a) compares to (b) and (c), with larger voids area. This incident happens because of the reduction of oxygen in the samples and thus, the oxidation also decreases.
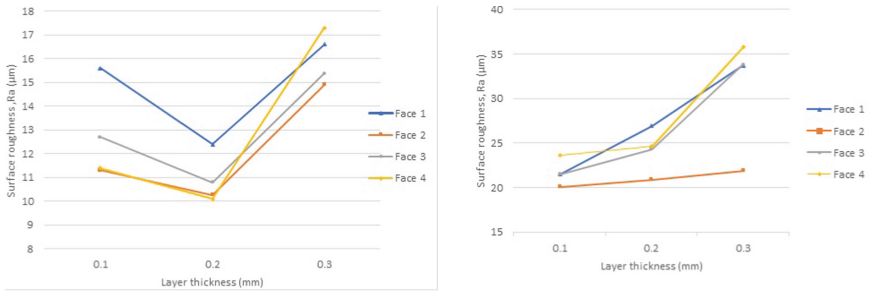
Fig. 2. The effect of layer thickness on surface roughness with different levels of oxygen concentration (0% - left, 20% - right).
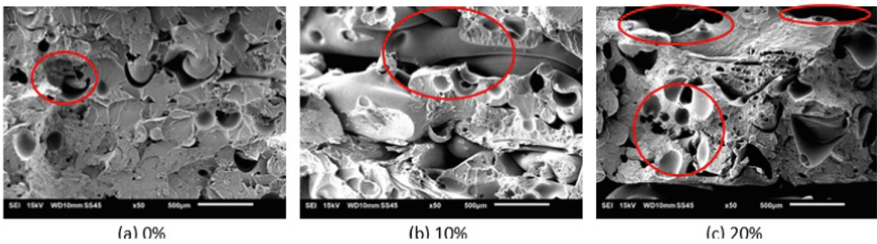
Fig. 3. SEM micrographs of the fracture surfaces of FDM specimens with layer thickness 0.1 mm and increasing the concentration level of oxygen.

4   Conclusions

In this paper the tensile strength of the 3D printed part and the specimen's surface roughness shown changes in different printing conditions. In addition, the inert gas (nitrogen) assisted the printing process, by removing oxygen content from the surrounding chamber. This is consistent with the result obtained in [3] where both tensile test and surface roughness improved with different 3D printing setup. Low content of oxygen in printing surrounding improve both the tensile strength and the surface quality of the 3D printed part.

References

1. Buj-Corral, I., Domínguez-Fernández, A., Durán-Llucià, R.: Influence of print orientation on surface roughness in fused deposition modeling (FDM) processes. Materials **12**(23), 3834 (2019). https://doi.org/10.3390/ma122333834

2. Alsoufi, M.S., Elsayed, A.E.: How surface roughness performance of printed parts manufactured by desktop FDM 3D printer with PLA+ is influenced by measuring direction. Am. J. Mech. Eng. **5**(5), 211–222 (2017). https://doi.org/10.12691/ajme-5-5-4
3. Nur, S., Mazlan, H., Alkahari, M.R., Maidin, N.A., Ramli, F.R., Sudin, M.N.: Influence of inert gas assisted 3D printing machine on the surface roughness and strength of printed component, no. May, pp. 154–155 (2018)

The Effects of Lightweight Design on Additive Manufacturing: A Thermal-Stress Case Study on Lattice Structure Parts

Pierre Chou Fang Cheng[1] and Abdul Hadi Azman[1,2(✉)] [ID]

[1] Department of Mechanical and Manufacturing Engineering, Faculty of Engineering and Built Environment, Universiti Kebangsaan Malaysia, Bangi, Malaysia
`hadi.azman@ukm.edu.my`
[2] Centre for Automotive Research (CAR), Faculty of Engineering and Built Environment, Universiti Kebangsaan Malaysia, Bangi, Malaysia

Abstract. The focus of this research is to produce and design a lightweight brake caliper that would be produced using additive manufacturing. The use of additive manufacturing in producing brake calipers are not yet common. To design a lightweight brake caliper, lattice structures are integrated in the parts of the brake caliper models. Body Centered Cubic with z-strut and Face Centered Cubic with z-strut as they are both the most used strut-based lattice structures in the industries. Strut-based lattice structure does also possess the characteristics of higher yield strength and provides lower mass. The lattice structures were divided into 5 different solid fractions 10%, 15%, 20%, 25% and 30% with 11 sample models of the brake caliper including the solid-state model designed. Structural and thermal stress simulation were conducted, and the results data were analyzed and compared to choose the optimum model at the end of the research. Lattice structure Face Centered Cubic with z-strut with 25% of solid fraction has been chosen to be the optimum model after comparing the result data and fulfills all the requirements. In conclusion, the brake caliper's mass decreased by 30% from 7.17 kg to 4.78 kg. In conclusion, the technology of integrating lattice structure inside a solid model for weight reduction in the field of additive manufacturing is the future for the automotive industry.

Keywords: Additive manufacturing · Lattice structure · Topology optimization

1 Introduction

Additive manufacturing which is also known as Three-dimensional printing is a manufacturing technology to produce a 3D solid product from a CAD drawing. The most common materials are polymer and metal, and the process of 3D printing is a layer-by-layer process [1]. The technology of additive manufacturing has been introduced for decades and is now applied in various industries including aerospace, oil and gas, marine as well as the automotive industry. Additive manufacturing provides the freedom to design and produce parts that have very high complexity [2]. The weight of the

product formed can also be optimized to be lighter to improves the performance as well as to reduce the production cost [3].

A brake caliper is one of the essential parts in a braking system functioning to stop or to reduce the speed of the vehicle. Inside a braking system, the tire is connected with a piece of brake disc and the rotor that keep the tires turning. The function of this brake caliper in this system would be to squeeze the brake disc using the brake pad when the driver intends to stop the vehicle. The friction between the brake pad and the brake disc would produce high temperature, thus it is important to take in consideration that the brake caliper produced in this study shall possess the ability to work under the conditions with high temperatures.

2   Methodology

Brake caliper is chosen as the component to be produced and designed in this study. The CAD model of brake caliper is designed using Autodesk Inventor 2021 software. Finite Element Analysis (FEA) is first conducted to identify the design space for optimization. The objective is to reduce the material used and weight reduction. The types of lattice structures are identified based on their mechanical properties. Body Centered Cubic with z-strut and Face centered Cubic with z-strut are chosen in this study. Strut-based lattice structures contain more struts than other surface-based lattice structure, which would help to distribute the force exerted on the model product. BCCz and FCCz lattice structures have higher strength, and are lightweight, making it suitable to be integrated in the brake caliper designs. Five different CAD models with solid fractions ranging from 10%, 15%, 20%, 25% and 30% were created, as shown in Fig. 1. The shape of the model of the brake caliper in this study is referred to the Brembo caliper.

(a)   (b)   (c)   (d)   (e)

(f)   (g)   (h)   (i)   (j)
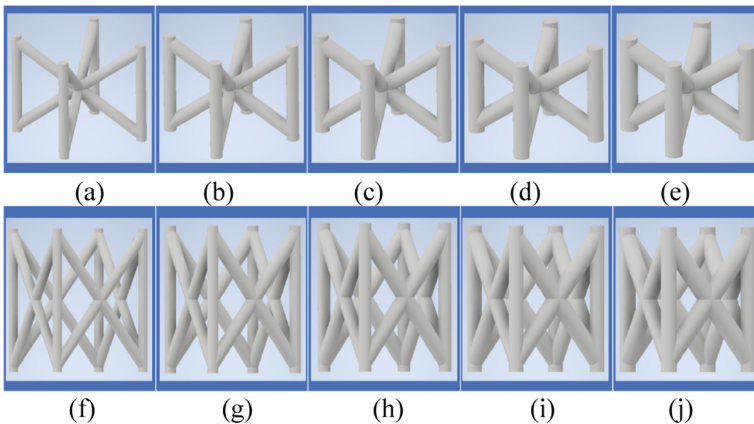
Fig. 1. Lattice structure model of Body Centered Cubic with z-strut (a) 10%, (b) 15%, (c) 20%, (d) 25% (d) 30%, and Face Centered Cubic with z-strut (a) 10%, (b) 15%, (c) 20%, (d) 25%, and (e) 30%.

3   Results and Discussion

The forces acted on brake calipers of a vehicle usually ranges from 1300 N to 1500 N, thus, the structural stress simulation is conducted a 1500 N force applied to imitate a normal working condition. As shown in the Fig. 2 shows the result data for the total displacement and Von-Mises Stress for both types of lattice structure BCCZ and FCCZ with different percentage of solid fractions. It can be observed that FCCZ and BCCZ with a solid fraction of 25% showed a better result. For the lattice structure of FCCZ with the solid fraction of 25%, it has a total displacement of 0.7518 mm, thermal gradient of 1.80E−7 °C/mm and the heat flux of 3.012E−8 W/mm^2 as shown in Fig. 3.
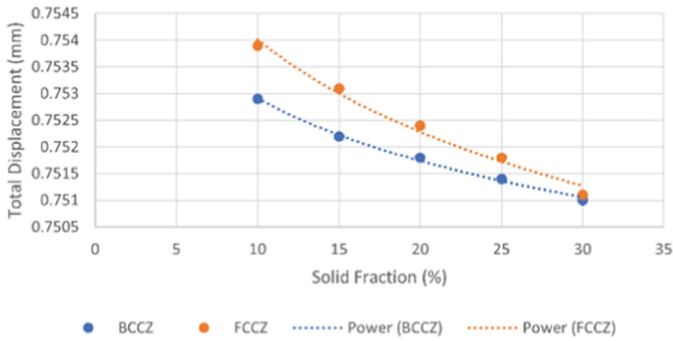
Fig. 2.   Total displacement in function of solid fraction.
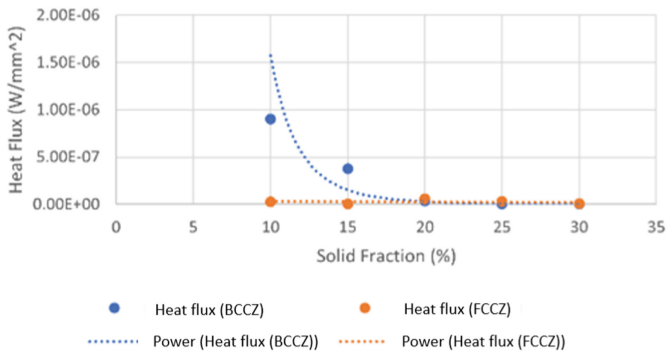
Fig. 3.   Heat flux in function of solid fraction.

As for the lattice structure of BCCZ with the solid fraction of 25%, it has a total displacement of 0.7514 mm, thermal gradient of 2.36E−8 °C/mm and the heat flux of 3.948E−9 W/mm^2. The result data is then compared again with the solid brake caliper as shown in Fig. 4.
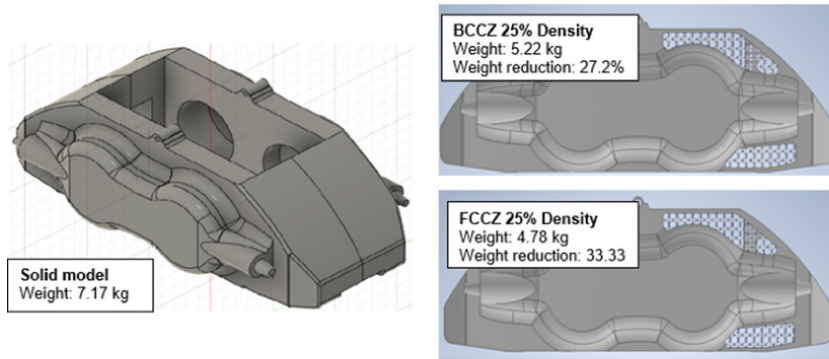
Fig. 4. Comparison of weight reduction with the solid brake caliper model.

4   Conclusion

In conclusion, the lattice structure Face centered Cubic with z-strut with 25% solid fraction has been chosen as the most suitable combination of lattice structure to be integrated inside the brake caliper model to lighten its weight while not affecting its usual functions. The total weight of the solid brake caliper has successfully been reduced as much of 30% from 7.17 kg to 4.78 kg. The results of the model with lattice structure FCCZ 25% from the analysis was verified and that the model still meets the part's requirements when exerted with 1500 N force and 150 °C. Through this research study, integrating lattice structure inside a model holds many potentials in the additive manufacturing for its lightweight characteristics and energy distribution. Further research must be conducted with more variety of sample models and different types of lattice structure to obtain a more detailed result.

References

1. Abdulhameed, O., Al-Ahmari, A., Ameen, W., Mian, S.H.: Additive manufacturing: challenges, trends, and applications. Adv. Mech. Eng. **11**(2), 1–27 (2016)
2. Azman, A.H., Vignat, F., Villeneuve, F., Nguyen, D.S.: Creation of lattice structures with skeleton model for additive manufacturing. Int. J. Interact. Des. Manuf. (IJIDeM) **15**(4), 381–396 (2021). https://doi.org/10.1007/s12008-021-00767-z
3. Seharing, A., Azman, A.H., Abdullah, S.: Finite element analysis of gradient lattice structure patterns for bone implant design. Int. J. Struct. Integr. **4**(11), 535–545 (2020)

Advanced Materials and Processes

Extraction of Silica from Sugarcane Bagasse via Acid Leaching Treatment

Mohamad Haiqal Amin Mohamad Azhar, Mimi Azlina Abu Bakar[(✉)], and Shahrul Azam Abdullah Ab Azam

School of Mechanical, College of Engineering, UiTM, 40450 Shah Alam, Selangor, Malaysia
mimi_azlina@uitm.edu.my

Abstract. Agriculture waste were produced for more than 1 million tons annually in our country. The disposal of the waste by open burning tend to bring environmental pollution such as air pollution. Thus it is essential to identify an alternative usage of the agriculture waste. Agricultural waste can be considered as good source of silica and have potential for the large scale production and acid leaching is one of the proper route to extract silica. In this project, sugarcane bagasse which is one of the agriculture waste is use to extract silica via acid leaching method. The purpose of this research is to study the effect of the leaching parameters such as leaching time and acid concentration on the extraction of the silica. Hydrochloric acid (HCL) with concentration of 1.0M and 2.0M were used as extraction solvent of silica from sugarcane bagasse. Leaching time was varied at 30 min, 60 min and 90 min. Various samples were prepared and characterized using Scanning Electron microscopy (SEM), X-ray diffraction (XRD) and energy dispersed x-ray (EDX) analysis. Based on the result of the analysis, it was proven that sugarcane bagasse can be considered as one of the alternative source in producing silica. The result indicates that the percentage of silica was increased from 57.10% to 99.0% when the leaching time increased from 30 to 90 min. Result of XRD analysis indicates that the extracted silica has an amorphous phase structure whilst the peak angle and intensity of the highest silica's percentage were recorded at Bragg angle of 21.54° and intensity of 188.33 cps respectively.

Keywords: Sugarcane bagasse · Acid leaching · Hydrochloric acid · Silica · Agriculture waste

1 Introduction

The agricultural wastes, which include sugarcane bagasse have a considerably high amount of silicate materials and regarded as cheapest source for silica production. Silica is one of the valuable inorganic multipurpose chemical compounds that can be used in the industry. From the previous researches, rice husk ash is used to extract silica because it serves as one of the way to solve the disposal problem in rice milling industry due to the disposal of the rice husk that contribute to the environmental pollution [1, 2, 4].

According to previous research, Rahman, et al. (1997) found 70 to 80% silica in rice husk ash prior to extraction process. With proper route of extraction method, high

concentration of silica can be extracted from the waste [5]. Other than that, according to research by C.P. Faizul., C. Abdullah and Md. Fazlul (2016) palm ash contain about 46% silicon element and when extracted, about 90% pure silica were produced [2]. Other than that, a research conducted by Sun, (2004) found that sugarcane bagasse which is the fiber of the sugarcane stalks has potentially studied as the large biomass products [3].

Currently, sugarcane which is also one of the agriculture waste might have the same problem due to the main product gained from processing sugar cane is sugar and it applied to most of the Asian country. Silica can be extracted from sugarcane bagasse via acid leaching treatment method. This can be applied by stirring some amount of the sugarcane bagasse powder into acid solution such as hydrochloric acid (HCl) or nitric acid for a certain time at a certain temperature. The parameter such as type of acid and the time taken for the leaching duration can affect the process of extracting silica from the bagasse.

2   Material and Methodology

Raw Materials and Reagents
The sugarcane bagasse was obtained from seller around Section 2 and 7, Shah Alam, Selangor. The bagasse was cut into small pieces and dried in drying oven Model T3D-YT for 24 h at 70 °C. The pieces were grounded by using Planetary Mono Mill Fritsch Pulverisette 6 to become fine powder for 3 h at rotational speed of 350 rpm. Sugarcane bagasse powder were sieved by using vibratory sieve shaker with 50 mesh chambers. The solvent used is 1.0M and 2.0M of hydrochloric acid (HCl).

Leaching Process
About 10 g of sugarcane bagasse powder were stirred together with 500 ml of hydrochloric acid (HCL) solution in a beaker. Different samples were prepared at different acid concentration which is 1.0M and 2.0M. The beaker was placed on the hot plate magnetic stirrer at temperature of 60 °C and the reaction time set was at 30 min, 60 min and 90 min. The mixture was filtered by using filter paper when the leaching reaction is finished. Then, the mixture will be rinsed with distilled water to remove HCL solution.

The process was considered completed when the filtered and rinsed solution turn colorless. Then, the samples were dried at 80 °C for 2 h in the oven.

Characterization of Samples
The characterization of the extracted sample was carried out using Rigaku Ultima IV XRD/EDX to determine the phases and chemical composition whilst DSM 982 Scanning Electron Microscopy (SEM) was used to study the morphological structure.

3   Results and Discussion

Characterization of Sugarcane Bagasse Powder
The chemical composition was analyzed using Energy Dispersed X-Ray (EDX) as shown in Table 1.

Table 1. Chemical composition of untreated sugarcane bagasse powder.

Element	Atomic percentage (%)
O	52.50
C	34.90
Al	2.40
Si	4.60
Zr	5.60

It can be seen in the Table 1, the percentage of silica in the untreated sugarcane bagasse was about 4.6%. Although the percentage is low, it was confirmed the existence of silica in the sugarcane bagasse sample collected.

Morphological Surface and Phase Analysis of Untreated Bagasse Powder
Figure 1 shown the morphological structure of the untreated sugarcane bagasse with 5000× magnification of the image. It was observed that the bagasse sample have a flaky and crushed surface.
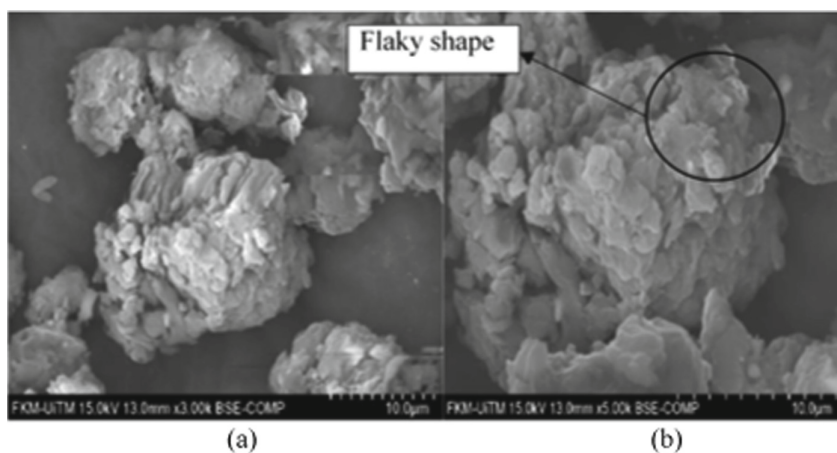
Fig. 1. SEM micrograph at (a) 3000× magnification (b) 5000× magnification.

Phase analysis was done by using XRD machine with the parameters setup at 2θ for the diffraction of Cu and Kα with range between 10° to 60° and the step scan was set at 5°/min. Figure 2 shows a pattern of amorphous structure of the untreated sugarcane bagasse powder.
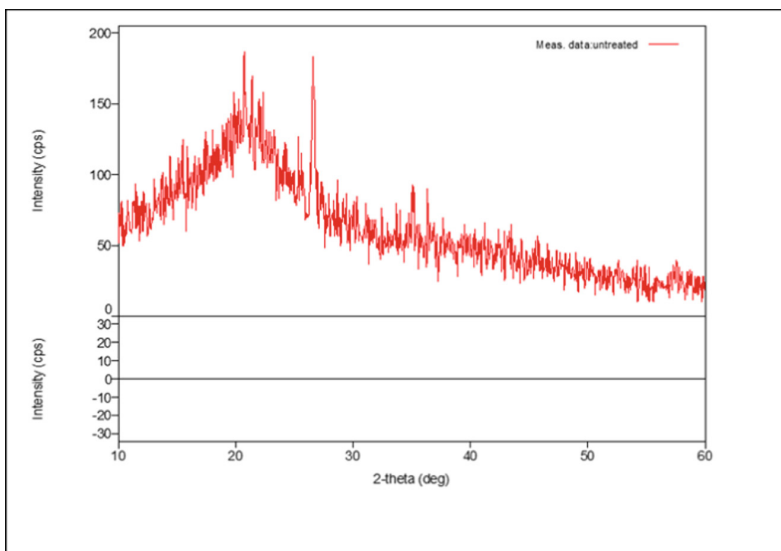
Fig. 2. XRD pattern for untreated sugarcane bagasse.

The major reflection or peaks of SiO_2 were observed at Bragg 28 angles of 21.99° whilst the peak intensity was recorded at l82 cps. This analysis proved the presence of silica in the raw or untreated sugarcane bagasse.

Chemical Composition of Treated Sugarcane Bagasse
The extraction process was done under different concentration of hydrochloric acid (HCl) with different time of the leaching process as depicted in Table 2. The time for the leaching process was varied from 30, 60 and 90 min while the concentration of the hydrochloric acid used were 1.0M and 2.0M.

Table 2. Chemical composition of treated sugarcane bagasse.

Concentration of acid	Leaching time (min)	SiO_2 (wt%)
Untreated	–	57.1
1.0M	30	91.4
	60	94.0
	90	99.0
2.0M	30	90.8
	60	97.6
	90	58.5

As shown in Table 2, the percentage of silica in the sugarcane bagasse increase from 57.1% to maximum of 99.0% when using 1.0M of HCI for 90 min. The highest percentage of silica obtained using 2.0M of HCL for 60 min of leaching time i.e. 97.6% of silica existence. This proved that the time for the stirring and leaching process affect the extraction of silica from the sugarcane bagasse. It can be assumed that the optimum parameter for the extraction process, based on the result obtained is at 90 min leaching time by using 1.0M HCI solution. It is supported by previous researchers that leaching solution and time affected the silica content [6–8].

4 Conclusions

From the result obtained, it is proven that highest percentage of silica increased from 57.1% to 99.0% using 1.0M of HCI at stirring time of 90 min and 57.1 to 97.6% by 2.0 M of HCI at stirring time 60 min. The morphological study of the extracted silica was carried out using SEM analysis shows that the untreated one has a flaky shape. The surface for silica sample of 1.0M HCI shows the surface is a bit rough and porous with irregular shape whilst silica sample of 2.0 M of HCI showed the surface is flaky and more compact shape in surface. The acid leaching treatment is significantly useful and effective to remove the impurities from the sugarcane bagasse and increased the purity of silica.

References

1. Kalapathy, U., Proctor, A., Shultz, J.: A simple method for production of pure silica from rice hull ash. Bioresour. Technol. **73**, 257–262 (2000)
2. Faizul, C.P., Abdullah, C., Fazlul, B.: Extraction of silica from palm ash using citric acid leaching treatment: preliminary result. Adv. Mater. Res. **795**, 701–706 (2016)
3. Sun, J.X.: Fractional extraction and structural characterization of sugarcane bagasse hemicelluloses. Carbohydr. Polym. **56**, 195–204 (2004)
4. Umeda, J., Kondoh, K.: High-purity amorphous silica originated in rice husks via carboxylic acid leaching process. J. Mater. Sci. **43**(22), 7084–7090 (2008)
5. Rahman, I.A., Ismail, J., Osman, H.: Effect of nitric acid digestion on organic materials and silica in rice husk. J. Mater. Chem. **7**(8), 1505–1509 (1997)
6. Azat, S., Sartova, Z., Bekseitova, K., Askaruly, K.: Extraction of high-purity silica from rice husk via hydrochloric acid leaching treatment. Turk. J. Chem. **43**(5), 1258–1269 (2019)
7. Music, S., Filipovic-Vincekovic, N., Sekovanic, L.: Precipitation of amorphous SiO2 particles and their properties. Braz. J. Chem. Eng. **28**(1), 89–94 (2011)
8. Falk, G., Shinhe, G.P., Teixeira, L.B., Moraes, E.G., de Oliveira, A.P.N.: Synthesis of silica nanoparticles from sugarcane bagasse ash and nano-silicon via magnesiothermic reactions. Ceram. Int. **45**(17), 1618–1624 (2019)

Effect of Heating Temperature on Mechanical Properties and Biodegradation Rate of Magnesium/HA/Shellac as Bone Screw Material

Alfa Rizcha Nurfaizi[1], Wijang Wisnu Raharjo[2], and Joko Triyono[2(✉)]

[1] Graduate School of Mechanical Engineering, Sebelas Maret University, Surakarta, Indonesia
[2] Department of Mechanical Engineering, Sebelas Maret University, Surakarta, Indonesia
`jokotriyono@staff.uns.ac.id`

Abstract. This study aims to determine the effect of heating temperature on the hardness, compressive strength, and biodegradation rate of magnesium/Hydroxyapatite (HA)/Shellac. This research used Magnesium/HA/Shellac material which was mixed using a magnetic stirrer for 15 min. Materials mixed with a ratio of Magnesium/HA/shellac was 70/30 (% wt). The material was then compacted with a pressure of 20 bar for 15 min and then sintered at a temperature variation of 100, 150, 200, and 250 °C. The testing phase for Magnesium/HA/Shellac includes hardness test, compressive strength test, degradation rate test and SEM-EDS observation. In the hardness test, the highest hardness was obtained at a temperature variation of 250 °C (62.44 HVN). The highest compressive strength was obtained at a temperature of 250 °C (47,06 MPa). Composites of Magnesium/HA/Shellac specimens with temperature variation of 250 °C had the lowest biodegradation rate of 0.57 cm/year. Observation of Scanning Electron Microscopy (SEM) show different crack sizes at each temperature variation. This biocomposite has the potential to be developed as a bone screw material.

Keywords: Mechanical properties · Magnesium · Hydroxyapatite · Shellac · Bone screw material

1 Introduction

Traffic accidents are the biggest cause of fractures in Indonesia and will continue to increase. It was recorded that traffic accidents that caused fractures were 62.6%, and most were men at 63.8% [1]. Since 10 years in 2007, there were 49,553 accidents, and in 2015 there were 98,970 accidents that resulted in bone fractures. In such cases, medical treatment that can repair the fractured bone is needed [2]. The bone screw is a very appropriate medical treatment for bone injury problems. The screws in the bone cortex are generally made of stainless steel because this material has seven times the mechanical properties of ordinary bone so that it can be used as a support bone. Stainless steel has the disadvantage of being toxic to the body, making it unsuitable for body tissues [3].

World researchers are currently developing new biomaterials specifically for a bone screw with metal-based materials, namely magnesium, zinc, and iron [4]. Magnesium is one material that has good mechanical properties close to the mechanical properties of human bones. Magnesium can be combined with other elements to improve its mechanical properties. One of magnesium's advantages that it has a modulus of elasticity of 40–50 GPa, where the modulus of elasticity is close to human bone, which is 10–40 GPa [4].

To tighten the process of the Magnesium-Hydroxyapatite mixture, new materials are needed to bind. Shellac is a material for binding because it can improve mechanical properties such as its compressive strength [5]. Shellac is a natural polymer that is derived from the secretions of fleas. Shellac is the right choice because it can be degraded by the body and has good adhesion properties, and this material is widely available in nature [6]. The research on the effect of sintering temperature on the mechanical properties of W-Cu shows that at 900 °C, it gets the best mechanical properties and density [7].

Research on the effect of heating temperature from a mixture of magnesium with hydroxyapatite-shellac alloys on mechanical properties and degradation rates needs to be done from this description. The heating temperature variations used in this study were 100, 150, 200, and 250 °C and the volume fractions used were 70% Magnesium and 30% Hydroxyapatite Shellac.

2 Material and Methods

2.1 Material

The process of making shellac solution is carried out by smoothing the secretions of lak lice until the size of 200 mesh powder is obtained. Then the powder is mixed with 96% ethanol solution in a ratio of 1:10. The mixing process was carried out by stirring the magnetic stirrer for 4 h, so that it was evenly mixed. Then, the solution is precipitated and then filtered, so that the shellac solution is obtained. Magnesium and hydroxyapatite used ready-made materials.

2.2 Methods

HA/shellac mixing was carried out with a magnetic stirrer with a temperature of 100 ºC and a magnetic rotating speed of 200 rpm for 2 h. The Magnesium/HA/Shellac mixing process was carried out with a magnetic stirrer at a room temperature and a rotating speed 200 rpm for 15 min. This process was carried out, in order to make each material is evenly mixed. Then, the material was printed by a compacting process with 362,43 MPa for 10 min, the speciment was in the tablet-form with a size of 13×5 (mm). After the specimen was formed, the sintering process was carried out with temperature variations, namely 100, 150, 200, 250 °C.

3   Result and Discussion

3.1   Hardness Value

Figure 1a shows the hardness value of the material. Hardness values at temperatures of 100, 150, 200 and 250 °C are 51.71, 55.57, 58.34, 62.44 HVN, respectively. These values are lower than the hardness of POC-HA (90.24 HVN) and stainless steel (249 HVN). Hardness of bone is 48 HVN [5].
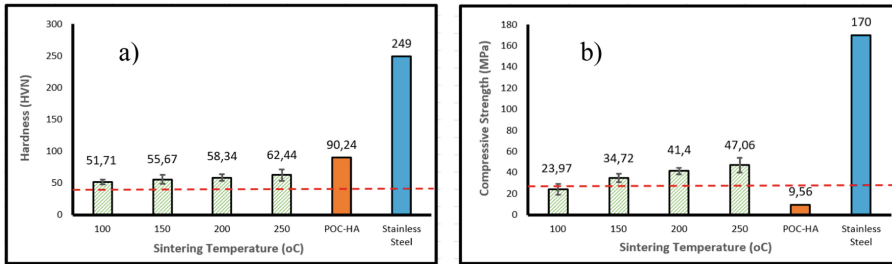
Fig. 1. Resulted of hardness and compression.

3.2   Diametral Compression Test

Figure 1b shows the compressive strength of the material. Hardness values at temperatures of 100, 150, 200 and 250 °C are 23.97, 34.72, 41.4, 47.06 MPa respectively. These values are higher than POC-HA hardness (9.56 MPa) and lower than stainless steel (170 MPa). Compressive strength of bone is 28 MPa [5].

As the temperature increases, the compressive strength value will increase because the necking process has occurred perfectly to minimize the occurrence of cracks in the material. Surface morphology also greatly affects the compressive strength value. If there is a lot of porosity or voids and cracking in the material, the compressive strength value will decrease. It is reinforced by research of Jhony and Widyastuti (2014) that more porosity will result in the crack which will decrease the value of the compressive strength of the material [8].

3.3   Biodegradation Rate

Figure 2 shows the rate of biodegradation of the material. Its values at temperatures of 100, 150, 200 and 250 °C are 0.8, 0.72, 0.64, 0.57 cm/year, respectively. These values are higher than POC-HA hardness values (9.56 cm/year) and lower than stainless steel (170 cm/year). Biodegradation rate of bone scaffold is 0,05 cm/year [5].

3.4   Scanning Electron Microscopy (SEM)

Figure 3 shows about SEM observation of materials. There were cracks and voids in all materials. Voids can be formed due to the imperfect necking process, while cracks are
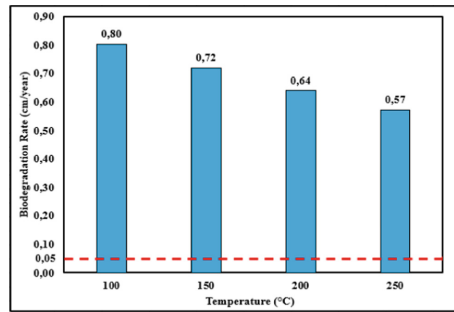
Fig. 2. Biodegradation rate of materials.

caused by gas trapped during compacting. During the sintering process, the gas trapped in the specimen tries to escape as it increases temperature, but the specimen was already necking. At 100 °C, low bonding in the specimen can cause cracks because the trapped gas will push in all directions, and there will be bloating so that the pressure in the porosity is higher than the pressure outside. Another factor in cracks in the cooling process is too fast, causing the material's sudden shrinkage. As the temperature increases, the cracks only occur in hydroxyapatite agglomeration. This area does not experience necking but is only bound by shellac not to hold the gas trapped in it. It is reinforced by research by Xiong, et al. (2016) that agglomeration is very dangerous mechanical properties of the material such as hardness and compressive strength of the material [9].
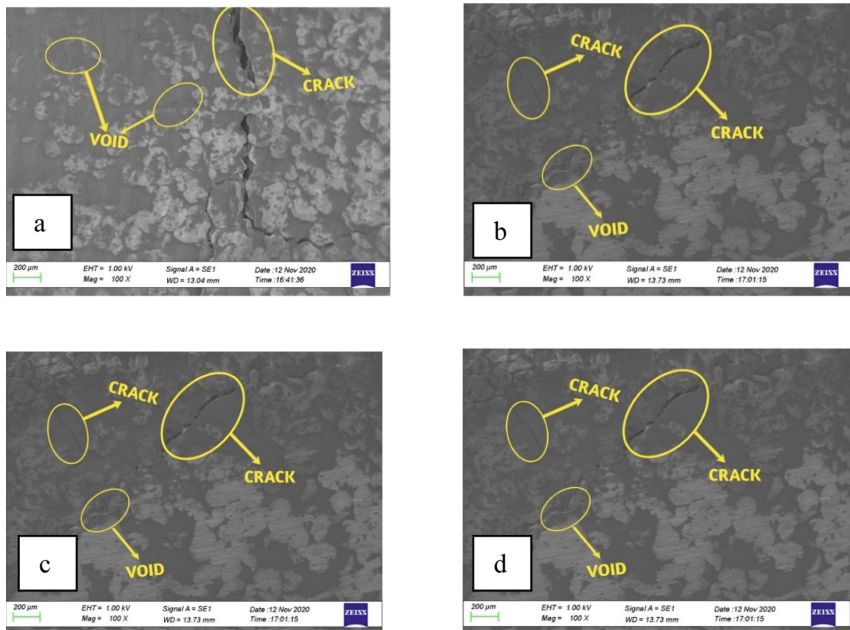
Fig. 3. Scanning electron microscopy (a = 100 °C, b = 150 °C, c = 200 °C, d = 250 °C).

4   Conclusion

The development of bone screw materials from magnesium/HA/shellac composites is a preliminary study. Based on the results of mechanical testing, biodegradation rate and microstructure observations, this biocomposite has the potential to be further developed as a biomaterial.

References

1. Desiartama, A., Aryana, I.W.: Characteristics of femoral fracture patients due to traffic accidents in adults at sanglah general hospital denpasar in 2013. E-J. Med. **6**(5), 1–4 (2017)
2. Lembaga Ilmu Pengetahuan Indonesia, "Metal Alloys Replace Bones", pp. 2018–2020 (2018). http://lipi.go.id/lipimedia/Padukan-Logam-Gantikan-Tulang/19869
3. Sezer, N., Evis, Z., Kayhan, S.M., Tahmasebifar, A., Koç, M.: Review of magnesium-based biomaterials and their applications. J. Magnes. Alloy. **6**(1), 23–43 (2018)
4. Hermanto, A., Burhanudin, Y., Sukmana, I.: Opportunities and challenges of application magnesium metal-based degradable bone bolts. Din. Tek. Mesin **6**(2), 93–98 (2016)
5. Triyono, J., Susmartini, S., Susilowati, E., Murdiyantara, S.A.: Shellac coated hydroxyapatite (HA) scaffold for increasing compression strength. Adv. Mater. Res. **1123**, 378–382 (2015)
6. Wang, X., Li, J., Fan, Y., Jin, X.: Present research on the composition and application of lac. For. Stud. China **8**(1), 65–69 (2006)
7. Safrudin, M., Widyastuti: Effect of variation of sintering temperature and sintering resistant time on density and hardness of MMC W-Cu by powder metallurgy process. J. Tek. Pomits **3**(1), 44–49 (2014)
8. Jhony, P., Widyastuti: Analysis of the Effect Sintering Temperature and Holding Time on Interface Bonding for Metal Matrix Composites (MMCs) (2014)
9. Xiong, G., et al.: Characterization of biomedical hydroxyapatite/magnesium composites prepared by powder metallurgy assisted by microwave sintering. Curr. Appl. Phys. **16**(8), 830–836 (2016)

Temperature Quenching Effect on Tensile Strength of DGEBA Cured Cycloaliphatic Hardener

Heru Sukanto[✉], Wijang Wisnu Raharjo, Dody Ariawan, and Joko Triyono

Universitas Sebelas Maret, Surakarta, Indonesia
herusukanto@staff.uns.ac.id

Abstract. Sudden changes in working temperature or thermal shock, such as quenching treatment, are very likely to be experienced by thermosetting epoxy resins when applied during their service life, which can degrade their performance. This article reports the change in tensile strength of thermoset epoxies subjected to quenching treatment. The material used is DGEBA resin which is cured with cycloaliphatic hardener with a ratio of resin and hardener of 2:1. The quenching treatment was carried out at the target temperature of 75 °C, 100 °C, 125 °C, and 150 °C and the cooling medium of pure water at ambient temperature. The tensile test was performed on the specimens referring to the ASTM D638-14 standard. The result reveals that the tensile strength of epoxy resin has decreased significantly at the quenching temperature of 75 °C, 100 °C, and 125 °C. The quenching target temperature of 150 °C produces tensile and elongation strengths commensurate with the properties of epoxy resins without quenching.

Keywords: Cycloaliphatic amine · Quenching · Mild thermal shock · Epoxy elongation

1 Introduction

Thermosetting epoxy resins are widely used as a coating, adhesive, or matrix of a composite. The availability of the material is also very abundant in the market, allowing material experts or practitioners to choose an epoxy resin that strictly conforms to a requirement of loading characteristics. Epoxy diglycidyl ether bisphenol-A (DGEBA) and amines hardener are among the most widely used ingredients of thermosetting resin in engineering applications. Its mechanical and chemical toughness properties and its affordable price make this epoxy a favorite choice for materials engineers [1].

However, exposure to an open environment that creates mechanical, thermal, and chemical loading of the epoxy resin during its economic life reduces its performance [2, 3]. For instance, rapid changes in temperature or thermal shock impact the worsening of mechanical properties of epoxy resin [4, 5]. Therefore, a thermal shock has been developed for epoxy resin crack testing by elevating temperature at a certain level then immediately quenched or flashed with water [6].

This article reports the effects of quenching treatment as a representation of thermal shock on the tension stress and strain of the epoxy resin DGEBA cured isophorone diamines (IPDA).

2   Method

The materials used were DGEBA by Eposchon and curing agent or hardener of modified cycloaliphatic amine, namely isophorone diamine (IPDA) with trademark Eposchon EP-555. The main content of DGEBA is 3-aminomethyl-3,5,5-trimethylcyclohexylamine [7]. DGEBA and IPDA with the weight ratio of 1:2 were mixed securely and homogenously as recommended by the manufacturer. The mixture was poured into the mold and allowed to cure for 48 h. The post-curing treatment was conducted in the oven dryer for 6 h at a temperature of 60 °C. The cured epoxy was then cut using a laser to conform to the shape and size requirements of the test specimen.

Furthermore, the specimens were quenched from the target temperatures of 75 °C, 100 °C, 125 °C, and 150 °C. The specimens were heated in a programmable electric oven with an average heating rate of 25 °C/min and allowed to stand for 2 min. Pure water is used as the cooling medium with a volume of at least sixty times the volume of the specimen to ensure that there is no increase in water temperature during quenching.

The universal testing machine was used to apply axial tensile loads to the specimens at an average speed of 5 mm/min until they broke according to the ASTM D638-14 standard [8]. The grip of specimens must be ensured that they do not slip during displacement because the surface of specimens was generally hard and smooth. Macroscopic images were taken as pieces of evidence and to explain changes in specimen properties that may occur after quenching.

3   Result and Analysis

The unquenched epoxy resin exhibits a tensile strength of 27.36 MPa and an elongation of 0.08 or 8%, as shown Fig. 1a. This strength is common to most of the epoxy resins used as a composite matrix, such as phenolic resins (34 MPa) [9] or polyester resins (42 MPa) [10]. The tensile strength of the epoxy resin is dominated by the presence of cross-links connecting between the polymer chains. Cross-links are formed from C – N bonds resulting from the reaction between epoxy and hardener. These bonding atoms create an amorphous phased epoxy resin. The form of this un-crystalline phase decreases the epoxy's elasticity so that it becomes brittle with a very low elongation value [11]. Figure 1b shows the fracture model of the specimens depicting the brittle nature of these epoxies.

Referring to Fig. 1a, the quenching treatment at temperatures below 150 °C resulted in a decrease in the tensile strength and elongation of the epoxy resin. Heating at a temperature of 75 °C and 100 °C does not produce enough heat energy to form tertiary polymer bonds but instead only keeps the distance between the polymer atoms far apart. The addition of atomic spacing during heating allows oxygen atoms to oxidize atoms in the polymer to form hydrogen, carbon monoxide, carbon dioxide, or nitrogen. Figure 2 shows the possible gases formed in the oxidation reaction of the epoxy resin. Heating to
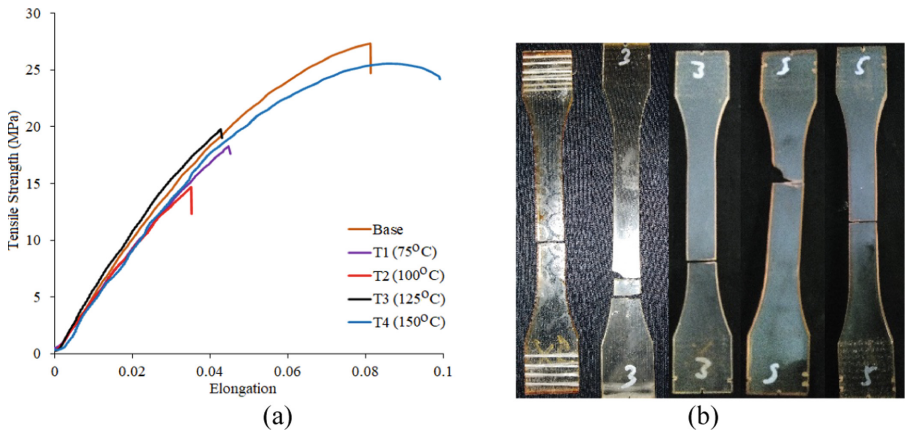
Fig. 1. (a) The tensile strength versus elongation graph of DGEBA-IPDA hardener epoxy resin under quenching with temperature varies. (b) The shape of epoxy resin fractures under tensile load, indicating a brittle material.

the temperature of 125 °C creates enough energy to start a tertiary reaction between the epoxide groups so that the cross-linking process can begin to shift the oxidation reaction. The mixing ratio of 2:1 or 1:0.5 between epoxy resin and hardener is a slight mismatch to stoichiometry equilibrium condition, which should be 1:0.557 [12]. This condition results in an epoxy system rich in epoxide groups; thus, it will become easier for the tertiary curing process to occur when there is sufficient additional energy to drive it, as illustrated in Fig. 3. Furthermore, heating at a temperature of 150 °C causes the polymer atoms to move more easily and quickly. As a result, more epoxides are bonded to each other, increasing the tensile strength and elongation of the epoxy resin.
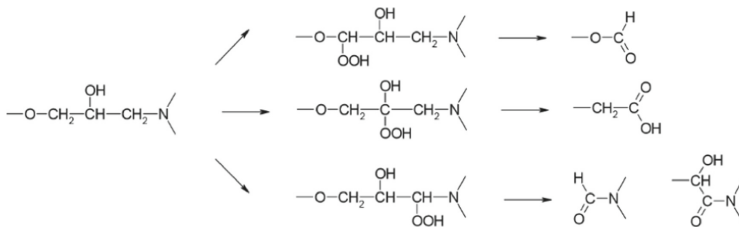
Fig. 2. Possibility of oxidation product in thermosetting polymer system of epoxy-amines [13].
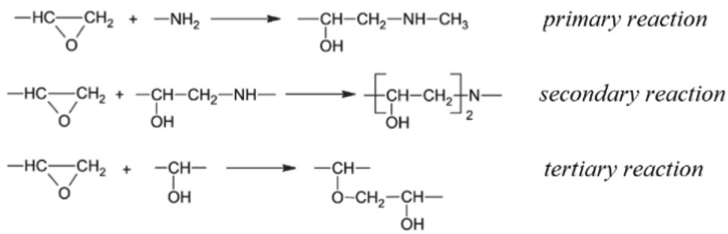
Fig. 3. The curing reaction stages of epoxides with diamine [13].

4   Conclusion

The quenching treatment at temperatures below 125 °C causes the dominance of the oxidation reaction in the epoxy resin, resulting in a decrease in the tensile strength and elongation of the resin. The tertiary cross-link network formed during the heating process at a temperature of 150 °C causes an increase in the bond between the epoxides to compensate for the oxidation reaction. Therefore, quenching at a target temperature of 150 °C does not change the tensile strength and elongation significantly.

References

1. Sukanto, H., Raharjo, W.W., Ariawan, D., Triyono, J., Kaavesina, M.: Epoxy resins thermosetting for mechanical engineering. Open Eng. **11**, 797–814 (2021)
2. Drummond, J.L.: Degradation, fatigue and failure of resin dental composite materials. J. Dent Res. **87**, 710–719 (2008)
3. Bockenheimer, C., Fata, D., Possart, W.: New aspects of aging in epoxy networks: thermal aging. J. Appl. Polym. Sci. **91**, 361–368 (2004)
4. Chakraverty, A.P., Mohanty, U.K., Alsubari, S., Ali, J.S.M., Mahapatra, T.R., Panda, S.K., et al.: Thermal shock effect on mechanical and physical properties of pre-moisture treated GRE composite thermal shock effect on mechanical and physical properties of pre-moisture treated GRE composite. In: Conference Series: Materials Science and Engineering, pp. 1–6. IOP Publishing (2017)
5. Kubouchi, M., Tsuda, K., Hojo, H.: Thermal shock behavior and evaluation of epoxy resins toughened with hard particulates. In: Riew, C.K., Kinloch, A.J. (eds.) Nov Approaches Science Engineering, 2nd edn, pp. 119–132 (1996)
6. Wang, S., Li, Q., Zhang, W., Zhou, H.: Crack resistance test of epoxy resins under thermal shock. Polym. Test. **21**, 195–199 (2002)
7. Suryanto, H., Marsyahyo, E., Surya Irawan, Y., Soenoko, R., Aminudin: Improvement of interfacial shear strength of Mendong fiber (Fimbristylis globulosa) reinforced epoxy composite using the AC electric fields. Int. J. Polym. Sci. **2015**, 1–10 (2015)
8. ASTM D2344. Standard Test Method for Short-Beam Strength of Polymer Matrix Composite Materials and Their Laminates. Annu. B. ASTM Stand, pp. 136–140 (2003)
9. Pizzi, A., Ibeh, C.: Phenol formaldehydes. In: Dodiuk, H. (eds.) Handbook of Thermoset Plastics, 3rd edn, pp. 25–44. Elsevier Inc. (2014)

10. Ratna, D.: Handbook of Thermoset Resins, 1st edn. Shropshire: iSmithers (2009)
11. Zhao, J., Yu, P., Dong, S.: The influence of crosslink density on the failure behavior in amorphous polymers by molecular dynamics simulations. Materials **9**, 1–10 (2016)
12. Mirmohseni, A., Nikafshar, S., Mirmohseni, F.: RSC Advances epoxy – diamine system using an inorganic ultra-accelerator. RSC Adv. **5**, 53025–53035 (2015)
13. Ernault, E., Richaud, E., Fayolle, B.: Thermal oxidation of epoxies: influence of diamine hardener. Polym. Degrad. Stab. **134**, 76–86 (2016)

A Review on Polyacrylonitrile Electrospun Fibres and Their Applications in Membrane Distillation Technology

M. W. A. Arif[1], A. H. Nurfaizey[2(✉)], M. A. M. Rosli[2], M. R. Mansor[2], M. A. Salim[2], and N. A. Masripan[2]

[1] Fakulti Kejuruteraan Mekanikal, Universiti Teknikal Malaysia Melaka, Hang Tuah Jaya, 76100 Durian Tunggal, Melaka, Malaysia
[2] Centre for Advanced Research on Energy, Universiti Teknikal Malaysia Melaka, Hang Tuah Jaya, 76100 Durian Tunggal, Melaka, Malaysia
`nurfaizey@utem.edu.my`

Abstract. Water scarcity is a major issue in some part of the world today. In some countries, seawater desalination through membrane distillation (MD) technology has been used to overcome the issue. However, there are two major issues impeding the efficiency of MD process, namely vapour flux declination and membrane wetting. Recently, electrospun fibres have been proposed as an alternative approach in developing new membrane modules for MD process. In this regard, polyacrylonitrile (PAN) in the form of electrospun fibres is a popular choice due to its relative superiority characteristics such as hydrophobic surface, nanoscale fibre diameter, low thermal conductivity, and possessed strong mechanical strength. However, it is dependent on the fabrication technique, which has a significant impact on the characteristics of the final products. Electrospinning is the most efficient technique in the production of polymeric electrospun fibres using electric charges. Although electrospinning can often be seen as a straightforward process, it consists of several complex processing parameters that need to be optimised in order to get high-quality fibre membranes. In this review, a brief overview is presented on the electrospinning of PAN electrospun fibres, as well as the range of optimum processing parameters. This review also focuses on the characteristics of PAN electrospun fibres and recent fabrication methods in developing high-performance membrane modules.

Keywords: Electrospinning · Polyacrylonitrile · Membrane distillation

1 Introduction

Water scarcity or lack of clean water resources is one of the main global challenges that require urgent attention. Nowadays, many parts of the world are categorised as water-stressed regions, such as in India, eastern China, Europe, US and parts of Australia [1]. It is estimated that by 2030, more than 40% of the world's population will be facing water scarcity and this percentage could be doubled due to climate change impact

[1, 2]. Thus, to cope with the demand for clean water, membrane distillation (MD) has become an alternative and prospective choice for water purification process, especially in near-sea countries [3]. Currently, MD is the most popular technology in treating saline and contaminated water. In some cases, the process treats high salinity in feedwater by utilising waste heat from the surroundings and operates at considerably low energy [4].

In a typical MD system, a hydrophobic membrane is used as a physical barrier between the hot-feed side and cold-permeate side (Fig. 1) [5, 6]. The membrane filters all non-volatile solutes and only water vapour (freshwater) to go through. Even though MD has a reputable high salt rejection efficiency, this technology has two major problems; i.e. vapour flux declination and membrane wetting [7]. Vapour flux declination occurs when particulate materials are accumulated onto a membrane surface or onto the membrane pores, also known as membrane fouling. Meanwhile, membrane wetting occurs when the membrane is unable to withstand hydraulic pressure, which means the operating pressure is greater than the liquid entry pressure (LEP) [8]. Hence, the saline solution tends to leak through the membrane pores and contaminate the permeate [9]. Apart from that, the changes of surface behaviour from hydrophobic to hydrophilic also could lead to fouling deposition and pore wetting [10].
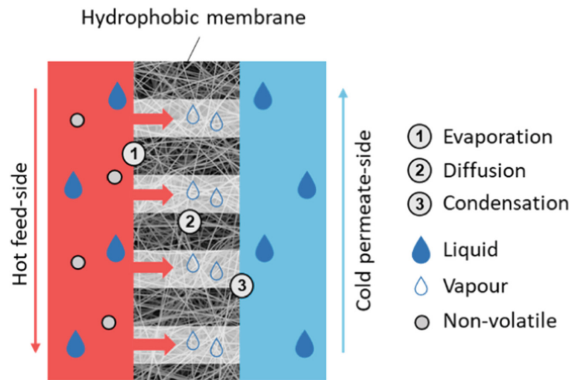
Fig. 1. Schematic diagram of membrane distillation process.

In order to resolve the above-mentioned issues, polymeric nanofibre coatings have been proposed as they have prodigious characteristics such as lightweight, small diameters, controllable pore structures, and high surface-area-to-volume ratios [11]. These features are very important in developing hydrophobic membrane module that will significantly affect the MD performance. To date, various polymers have been proposed to develop membrane module, such as polypropylene (PP), polyacrylonitrile (PAN), polyvinyl alcohol (PVA) and polyvinylidene fluoride (PVDF) [12]. In particular, polyacrylonitrile (PAN) is widely used in the fabrication of MD membranes due to its hydrophobic behaviour, thermal stability, good solvent resistance and possesses strong mechanical strength [13]. In recent years, numerous PAN-based membranes have been developed through various physical and chemical treatments. For instance, Wu et al. [14] modified PAN membrane with carbon tetrafluoride (CF_4) plasma treatment, followed by polydimethylsiloxane (PDMS) surface coating, where the modified PAN membrane

demonstrated good hydrophobic behaviour and capability to remove ethyl acetate (EtAc) from wastewater.

Furthermore, Seo et al. [15] also stated that membrane hydrophobisation is an effective method to overcome the wetting problem in the MD process. As an example, Fang et al. [16] managed to develop a superhydrophobic PAN nanofibres membrane by using silica nanoparticles as a coating solution in order to prevent membrane fouling. On the other hand, Liu et al. [17] discovered that the membrane morphology changed drastically when treating PAN membrane using 1H, 1H, 2H, 2H-perfluorodecyl methacrylate coating solution and plasma treatment. The modified membrane showed a stable vapour flux (59.42 kg/m^2/h) and higher salt rejection efficiency (99.93%). Additionally, when developing membrane module, researchers need to consider both the pros and cons of the selected approach. Ebrahimi et al. [18] modified the flat-sheet membrane using TiO$_2$ nanoparticles and 1H,1H,2H,2H-perfluoro-dodecyl trichlorosilane (FTCS) to increase the surface roughness and hydrophobic properties. Consequently, although the modified membrane exhibited high surface contact angle (174°), the vapour flux obtained only 2.3 kg/m^2/h due to blockage of the membrane pores. In addition, some studies also found that PAN fibres with large pore sizes and thick fibre diameter would result in a lower surface contact angle and poor mechanical strength [19, 20]. Hence, the search for effective ways to fabricate high-performance membranes has encouraged continuous research for new fabrication techniques and membrane designs.

Currently, there are several methods or techniques that have been introduced for the preparation of MD membrane, for example, self-assembly, template synthesis, melt blowing, electrospinning and phase separation [21]. However, electrospinning techniques provide better performance in terms of quality and quantity, where they have been regarded as one of the most simple, effective, and economical ways to produce fine polymeric fibrous materials [22]. According to Essalhi et al. [23] stated that electrospun nanofibres membranes produced via electrospinning possess a hydrophobic surface and strong physical structure. The technique has also been well adapted in industrial and academic research applications [24]. Electrospinning technique depends on five main processing parameters, namely solution concentration, applied voltage, distance between spinneret and grounded collector, flow rate of polymer solution, and ambient temperature. Extensive studies regarding electrospinning process parameters have been conducted previously. Although considerable amount of information on the effects of these parameters on fibre quality have been reported, contradictory findings were also reported especially when dealing with different solute and solvent systems [25]. Hence, optimising electrospinning parameters is crucial as it could significantly affect the behaviour of the nanofibre membranes.

The tremendous number of publications relating to MD and electrospun nanofibres published in scientific journals has accelerated the development of desalination technologies. However, to the best of the authors knowledge, very few of the published works focused specifically on electrospun MD membranes. This review takes a different approach by focusing on current research works on PAN-based electrospun nanofibres in the development of new MD membranes. This review is expected to provide insights

into electrospinning of PAN electrospun fibres, including the process parameters, characteristics of PAN electrospun fibres and their applications in membrane distillation technology.

2 The Electrospinning Process

Electrospinning is a fibre producing technique that uses very high electrical charges to create a stream of ultra-fine fibres. The technique was introduced in the early of 20th century, most notably through a series of inventions by Anton Formhals [26]. A basic electrospinning machine normally consists of four main components, namely a high-voltage power supply, a needle tip with a small orifice (also known as spinneret), a polymer solution supply, and a grounded collector electrode (Fig. 2) [27]. The electro-spinning process begins when a sufficient amount of electric voltage is applied at the tip of a spinneret. This will initiate a polymer jet stream at the vertex of the conical-shaped droplet, which is also known as the Taylor cone [28]. At this threshold voltage and beyond, strong electrostatic repulsive forces within the polymer overcome the surface tension of polymer droplet. Thus, the polymer solution will be ejected from the spin-neret and stretched longitudinally in the direction of the electric fields, travel towards the grounded collector electrode [29]. After a certain distance, the electrostatic repulsive forces become weaker and the motion of the charged jet polymer becomes unstable, creating a whipping instability formation [30]. Consequently, enormous mechanical stretching is formed, resulting in the thinning of the fibres. As the remaining solvent in the polymer jet continues to evaporate, the polymer finally landed on the grounded collector as dry fibre webs.
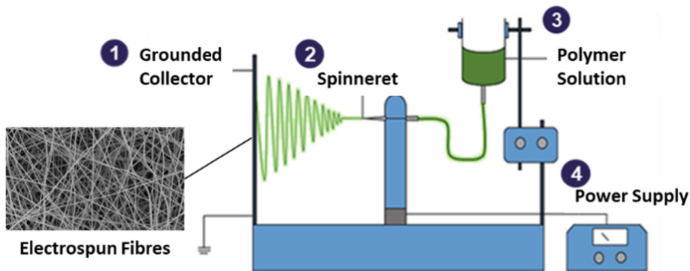
Fig. 2. Schematic diagram of a typical electrospinning machine.

In electrospinning process, solution concentration is one of the factors that allows the charged polymer solution to stretch and bend in a steady expanding loop motion [27]. Zhenyu and Wang [31] stated that at a very low solution concentration, the charged polymer solution does not have strong polymer entanglements required for fibre formation. Thus, this will cause instabilities during the electrospinning process and will create an 'electrospraying' phenomenon instead of electrospinning [32]. When electro-spraying happens, surface tension causes the stream of polymer to break up into smaller droplets as similarly described in Plateau–Rayleigh instability theory [33]. In contrast,

when the solution concentration is higher, the viscosity of the solution will increase thus, the amount of polymer chains entanglement also increases [34]. Strong chain entanglements will overcome the surface tensions prevent the polymer stream from breaking up producing smooth and continuous fibres.

Furthermore, fibre formation in electrospinning process only occurs when the applied voltage is higher than a threshold voltage (also called critical voltage) [35]. At a low applied voltage below the threshold, the generated electrostatic repulsive forces are insufficient to overcome the surface tension of the polymeric droplet, which result in no formation of fibres [36]. However, when the applied voltage exceeds the threshold voltage, polymer jet stream is ejected from the droplet. At an equilibrium, the polymer droplet transforms into a Taylor cone [37]. Nevertheless, if the applied voltage is too high beyond the optimum range (value of applied voltage at which defect-free fibres are formed), the motion of the whipping polymer jet becomes unstable, producing fibres with non-uniform diameters and with presence of beaded structures [38]. Therefore, optimising the applied voltage for creating a balanced electric fields is crucial in an electrospinning system.

On the other hand, electrospinning distance is the distance between the tip of the spinneret and the grounded collector. Previous studies showed that electrospinning distance greatly influences the production of electrospun fibres [39, 40]. For example, according to Nurfaizey and Munajat [41], when the electrospinning distance is too short, the area of fibre deposition decreases. Thus, the solvent does not have enough time to evaporate before reaching the grounded collector. This situation causes the deposition of wet fibres, tendency to produce beaded fibres, or abnormally thick fibres [42, 43]. On the contrary, if the electrospinning distance is sufficient, the duration of the electrospinning process also increases, hence resulting in the production of smooth and uniform electrospun fibres [44]. However, at a greater electrospinning distance, the electric field strength also reduced, hence causing the system to require a higher voltage to maintain the process [42]. Otherwise, as the momentum of flying fibres decreases, the fibres would wander aimlessly, causing significantly less fibre formation on the collector electrode [45].

Moreover, polymer solution feed rate also affects surface morphology and diameter of the electrospun fibres [46]. For example, an excessive feed rate will cause the motion of the polymer jet to become unstable, resulting in dripping of polymer droplets, producing large fibres with irregular structures [45]. In addition, the capillary tips tend to detach from the spinneret due to excessive forces [47]. Furthermore, the issue is more severe in a vertical electrospinning setup (polymer jet moves downward) as the feed amount of polymer solution also increases due to gravitational force [48]. Thus, this increases the tendency of forming fibres with beads and non-uniform diameters. Hence, most researchers currently perform electrospinning horizontally with a lower feed rate, where the polymer solution is ejected steadily and has enough time to evaporate before reaching the collector.

Ambient factors are also important in electrospinning process. It was reported that relative humidity (RH) and working temperature have a significant influence on diameter and morphology of the fibres [49]. Barua and Mrinal [50] stated that when the RH is beyond the optimum value, water molecules may permeate the fibres preventing fibre from drying out completely during electrospinning process. This result in porous and

Table 1. Summary of the effect of processing parameters on the morphology of the electrospun fibres.

Process parameter	Effects	Recommended range of value
Solution concentration	Too high: The charged polymer solution dries faster, producing non-continuous fibre, large fibre diameter and beaded structures [54]. Too low: Causing instabilities motion and create electrospraying phenomenon due to weak polymer chain entanglements [31].	6 to 12 wt% [27, 31, 32]
Applied voltage	Too high: Produced fibres with non-uniform diameters and with the presence of beaded structures [38]. Too low: No fibre formation due to insufficient electrostatic repulsive forces [36].	10 to 20 kV [36–38]
Electrospinning distance	Too long: Inconsistent fibre deposition due to weak electric field strength [42]. Too short: Produced wet fibres due to the solvent does not entirely evaporate [41].	10 to 20 cm [39, 40]
Flow rate	Too high: Produced large fibre diameter, increased fibre wetness and beaded structures [45]. Too low: Produced small fibre diameter and less fibre formation [45].	0.5 to 1.5 ml/h [45, 47]
Ambient temperature	Working temperature Too high: Produced poor fibre texture and large fibre diameter with beaded structures [55]. Too low: Produced wet fibre, wrinkles and rougher-surfaces fibres [55]. Humidity Too high: Produced porous and wrinkled fibre textures due to absorption of water molecules [50]. Too low: Produced non-continuous fibre and brittle structures [52].	25°C (room temp.) [19, 21] 40 - 60 % [50, 51]

wrinkled fibre textures [51]. On the other hand, when electrospinning is performed at a low RH, it produces smooth fibre textures and uniform orientations [52]. Apart from that, Yang et al. [53] investigated the effect of working temperature on the formation of PAN electrospun nanofibre. The authors discovered that increasing the temperature from 20 °C to 80 °C reduces the fibre diameter from 530 nm to 260 nm. In fact, with increasing temperature, the solvent evaporates much faster, thus resulting in solid and smooth fibres with smaller fibre diameters. Contrarily, lower working temperature causes a slower

evaporation process, thus resulting in wrinkles and rougher-surfaced fibres [53]. Hence, an understanding of electrospinning process parameters is required for the production of smooth electrospun fibres. To this end, various researchers have been investigated the effect of various processing parameters, including providing the common range of values for each parameter as indicated in Table 1.

3   Critical Characteristics of Polyacrylonitrile Electrospun Fibres for Membrane Distillation

A membrane module must meet certain requirements before it can be utilised in the desalination process, especially for MD system. According to Kusuma et al. [56], the membrane should be made of hydrophobic material with high porosity and optimum pore size. Thus, PAN electrospun fibres are thought to be a prospective choice as a foundation material or as a supporting layer in developing membrane modules. Based on literature, PAN electrospun fibres have a stable surface morphology, with an average fibre diameter of 100 to 800 nm, depending on processing parameters and experimental setups [57]. Fibre diameter in the nanoscale range is favourable because a smaller fibre diameter with smooth surfaces will increase filtration efficiency by forming a dense porous structure. On the contrary, a larger fibre diameter will create a more open structure, which allows more particles to pass through the membrane pores, resulting in lower filtration efficiency [58]. Membrane with a high porosity structure would result in a higher vapour flux due to increased evaporation surface area [6]. However, the high porosity will also cause a declination of salt rejection efficiency. Moreover, the pore size of PAN electrospun fibre is typically in the range of 0.3 to 0.8 μm [19, 59], where this range of values is highly recommended for MD process. Apart from that, electrospun membranes have a relatively narrow pore distribution, which will prevent water from easily penetrating the membrane pores.

In the MD process, only water vapour can be passed through the membrane pores. Water vapour goes through membrane pores from the hot feed-side into the cold permeate-side with a certain amount of pressure. This pressure is known as liquid entry pressure (LEP). Shahabadi et al. [60] mentioned that in order to obtain a long-lasting MD process, the value of membrane LEP should be as high as possible to avoid membrane wetting. There are several factors that influence the membrane LEP. For example, the membrane material must be hydrophobic, with a water contact angle (WCA) of more than 90° [61]. PAN nanofibres are categorised as hydrophobic membranes since the WCA is commonly in the range of 100° to 130° [62–64]. However, some studies found that a hydrophobic membrane may not be sufficient to prevent the declination of vapour flux and wetting problems [65]. Additionally, when the hydrophobicity increased, the membrane LEP also increased. Hence, in order to fabricate a superhydrophobic membrane (WCA more than 150°) with a high value of LEP, surface chemistry and surface morphology need to be tuned to obtain low surface energy and proper surface roughness [66, 67]. For instance, the addition of fluorinated materials and nanoparticles compounds are recommended approaches in developing superhydrophobic membranes [68].

Furthermore, since the MD was a non-isothermal process, the membrane material should have low thermal conductivity, which could increase both thermal efficiency and

the vapour flux drastically [61, 69]. Besides, a membrane module with excellent thermal stability and resistance to chemical corrosion is favourable since it can enhance the membrane lifespan for a longer period of time [70]. PAN membrane consists of a chain of carbon connected to one another, which makes them physically stronger than other polymeric materials [71]. PAN electrospun fibres have excellent thermal stability without obvious thermal distortion [72]. As an example, the glass transition temperature (T_g) and melting temperature (T_m) of PAN are commonly in the range of 110–130 °C and 335–360 °C, respectively [73–75]. In addition, the thermal conductivity of PAN fibres ranges from 0.02 to 0.04 W/mK, depending on the diameter of the fibre and the surface density of electrospun nanofibres [76]. The thermal conductivity of PAN electrospun fibres is much lower when compared to other hydrophobic polymers, which are typically in the range of 0.2 W/mK [77]. However, to achieve the desired fibre membrane, the membrane should undergo a stabilisation process that will enhance the molecular structure of the fibres.

On the other hand, membrane thickness also plays an important role in MD system. The effective membrane thickness was studied in the range of 10 to 60 µm [69]. As the membrane thickness decreased, the diffusion distance between the hot feed-side and cold permeate-side decreased, resulting in higher vapour flux. Apart from that, previous studies discovered that the average PAN thickness observed was 3 to 30 µm, depending on the duration of electrospinng process [78, 79]. In addition, PAN nanofibre membrane has strong mechanical properties, with tensile strength ranging from 10 to 50 MPa [78]. Hence, PAN electrospun fibres have a huge potential in developing high-performance membrane modules. The characteristics of PAN electrospun fibres are summarised in Table 2 as well as MD requirements.

Table 2. Characteristics of PAN electrospun fibres and MD requirements.

Characteristics	MD requirement	PAN electrospun fibres
Pore size	10 nm - 1 µm [6]	0.3 - 0.8 µm [19, 59]
Pore size distribution	Narrow [69]	Narrow [57]
Porosity	More than 80 % [56, 69]	80 - 90 % [57, 80]
Contact angle	More than 90° [56]	110 - 130° [62–64]
Thermal conductivity	Less than 0.2 W/mK [69]	0.02 - 0.04 W/mK [76]
Membrane thickness	10 - 60 µm [69]	3 - 30 µm [78, 79]

4 Current Application of Polyacrylonitrile Electrospun Fibres for Membrane Distillation

MD is known for its high salt rejection efficiency, lower energy consumption, and capability to operate at low temperatures [5, 81]. Although MD typically has an almost 100%

salt rejection efficiency, full industrial implementation of MD is still a challenge due to uncertainties related to long-term process efficiencies and operational costs [82, 83]. The two main issues of MD are low vapour flux and membrane wetting, especially when the membranes are utilised for a longer period of time. Hence, to overcome these issues, the developed membranes should fulfil all the MD requirements mentioned in Table 2. Currently, researchers have created a variety of membrane designs using PAN electrospun fibres as a precursor material. For instance, triple-layered structure, dual-layered structure, core-shell fibrous structure and surface coating and modification. In general, the properties of the membrane can be modified to a higher level by selecting the correct approach and optimum process conditions. A summarised list of the various membrane preparation techniques used in MD system is given in Table 3.

In an article journal, Cai et al. [84] fabricated dual-layered fibrous membranes by using polyvinylpyrrolidone (PVP) as a thin skin layer and PAN as a thick supporting layer and vice versa. The skin layer was electrospun on the surface of the supporting layer, which had an average thickness of 50 μm. Results showed that the composite fibrous membranes provided stable vapour flux with 19.2 ± 1.2 kg/m^2/h and 99.98% salt rejection efficiency. Surprisingly, the combination of skin layers with different pore sizes and porosity created a rougher surface and reduced surface energy, hence resulting in a higher contact angle (above 150°). It was reported that membranes with superhydrophobic surfaces could prevent membrane wetting and increase vapour flux [85]. Interestingly, this method can modify porous membranes with large pore sizes such that the modified membrane can be used in the MD system without compromising its performance.

On the other hand, Efome et al. [86] selected PAN electrospun nanofibres as one of the main materials in developing triple-layered structure membranes. The membranes were fabricated by using electrospun polyvinylidene fluoride (PVDF) mixed with hydrophobic silica nanoparticles as the top layer. The middle layer was made up of PAN nanofibres blended with metal-organic frameworks, while the bottom layer was made up of PVDF mixed with hydrophilic silica nanoparticles. The working concept of this approach is that the top hydrophobic layer will prevent feed water from entering the membrane, followed by a middle layer with a large pore size to reduce resistance during vapour transportation. The bottom hydrophilic layer is responsible for facilitating transmembrane vapour flux to the permeate-cold side. However, the drawback of this method is the obtained vapour flux was only 4.4 kg/m^2/h, which was due to the large membrane thickness (>600 μm).

Furthermore, Li et al. [87] used the coaxial electrospinning technique to fabricate core-shell polyacrylonitrile-polystyrene (PAN-PS) nanofibres membrane. Coaxial electrospinning technique operates by ejecting two polymer solutions simultaneously using a modified spinneret consisting of two coaxial capillaries with different orifice sizes. PAN core solution and PS shell solution were loaded into a syringe pump separately and electrospun at optimum electrospinning parameters. The obtained core-shell electrospun nanofibres were placed in a vacuum oven at 60 °C for 12 h before being cold-pressed at room temperature to achieve the desired thickness. The morphological analysis showed that the average diameter and WCA of fabricated nanofibres were 750 nm and 151.3°, respectively. The performance of PAN-PS core-shell nanofibres membrane provided significant and excellent results, where the obtained vapour flux and salt rejection efficiency

Table 3. A summarised list of the various PAN-based membrane preparation techniques.

Membrane design	Polymer	Membrane preparation technique	Vapor Flux (kg/m2/h)	Salt rejection efficiency (%)	Ref.
Dual-layered structure	PAN, & PVDF-HFP	Electrospun layer by layer, PVDF-HFP (skin layer) & PAN (support layer)	30.0	99.90	[20]
	PAN & PVP	Electrospun layer by layer, PVP (skin layer) & PAN (support layer)	19.2 ± 1.2	99.98	[84]
	PAN & PTFE	Electrospun PAN onto the surface of PTFE flat sheet membrane, EDA & NaOH hydrolysis	15.2	100.	[89]
Triple-layered structure	PAN & PVDF	Electrospun layer by layer, PVDF-hydrophobic / hydrophilic SiO_2 nanoparticles (top & bottom layer) & PAN nanofibres (middle layer)	4.4	99.99	[86]
Core-shell structure	PAN & PS	Electrospinning, PAN (core solution) & PS (shell solution)	60.1	99.99	[87]
Surface coating & modification	PAN, PVA	Electrospinning, PAN nanofibres immersed in HCL, NC surface coating & spray coated with PVA solution	238.7	99.80	[88]
	PAN & PFDA	Surface fluorination treatment, PFDA vapour permeated into the surface of PAN electrospun fibres	11.0	99.99	[90]

after a 36 h operating period were 60.1 kg/m^2/h and 99.99%, respectively. Nevertheless, the hindrance of this approach is that the membrane thickness (100 μm) exceeds the limit of effective thickness, which may degrade the MD performance.

In a recent study, Qin et al. [88] discovered an intriguing method for developing high-performance composite nanofibres by combining PAN nanofibres, nanofibre cellulose (NC) solution, and PVA-based film. PAN electrospun nanofibres were immersed in hydrochloric acid (HCL) for 120 s, followed by surface coating using 0.5 wt % of NC solution via the casting knife technique. PAN-NC nanofibres membrane was dried at room temperature (25 °C) for 120 min and placed in a vacuum oven for 4 h with a temperature of 60 °C. Lastly, the treated PAN nanofibres were spray-coated with PVA solution using airbrush equipment and dried at 100 °C for 15 min. The membrane thickness of PVA/NC-PAN observed was 3.78 μm with an average pore size of 150 nm.

The fabricated composite nanofibres membranes demonstrated extradentary pervapo-ration desalination properties, with a water flux of 238.7 kg/m^2/h and a salt rejection efficiency of 99.8%. To the best of the authors' knowledge, this method provides the highest vapour flux compared with other PAN-based membrane modules in desalina-tion technologies. This method also demonstrated that membrane thickness, pore size and surface hydrophobicity are crucial factors in increasing vapour flux while maintain-ing salt rejection efficiency. Therefore, before developing a new membrane module, it is important to consider the entire MD requirements in order to achieve optimal MD performances.

5   Conclusion

Polyacrylonitrile (PAN) is a promising precursor material for developing high-performance membrane modules for membrane distillation (MD) systems. PAN fibres produced via electrospinning technique possessed prodigious characteristics such as hydrophobic surface, nanoscale fibre diameter, porous structure and strong mechani-cal properties. In order to get desired membrane properties, the main electrospinning parameters (solution concentration, applied voltage, electrospinning distance, solution feed rate and ambient temperature) must be tuned until smooth fibres without beaded formation are formed. It is recommended to follow the range of values for each electro-spinning process parameter as given in Table 1. Besides that, there are several criteria that need to be highlighted while developing a new membrane module, such as pore size, pore size distribution, porosity, water contact angle, thermal conductivity and membrane thickness. PAN electrospun fibre is a polymeric material that fulfils all the MD require-ments and maybe even better than other hydrophobic materials (Table 2). Therefore, tremendous effort has been expended in developing PAN-based fibre membranes for MD systems. Various fabrication membrane preparation techniques have been reviewed, such as dual-layered structure, triple-layered structure, core-shell structure and surface coating and modification (Table 3). However, improvements in the declination of vapour flux and membrane wetting are still required in order to develop optimum membranes that provide positive output with cost-effective implementation. In summary, this review provides some useful guidance for future research activities relating to the optimum electrospinning process parameters, the characteristics of PAN electrospun fibre, and its potential application in MD systems.

References

1. Van Vliet, M.T.H., et al.: Global water scarcity including surface water quality and expansions of clean water technologies Environ. Res. Lett. **16**, 024020 (2021)

2. Kugarajah, V., et al.: Future applications of electrospun nanofibers in pressure driven water treatment: a brief review and research update. J. Environ. Chem. Eng. **9**, 105107 (2021)
3. Pistocchi, A., et al.: Can seawater desalination be a win-win fix to our water cycle? Water Res. **182**, 115906 (2020)
4. Roy, S., Humoud, M.S., Intrchom, W., Mitra, S.: Microwave-induced desalination via direct contact membrane distillation. ACS Sustain. Chem. Eng. **6**(1), 626–632 (2018)
5. Curto, D., Franzitta, V., Guercio, A.: A review of the water desalination technologies. Appl. Sci. **11**, 1–36 (2021)
6. Muhamad, N.A.S., Mokhtar, N.M., Naim, R., Lau, W.J., Ismail, A.F.: A review of membrane distillation process: - before, during and after testing. Int. J. Eng. Technol. Sci. **6**, 62–81 (2019)
7. Damtie, M.M., Kim, B., Woo, Y.C., Choi, J.S.: Membrane distillation for industrial wastewater treatment: studying the effects of membrane parameters on the wetting performance. Chemosphere **206**, 793–801 (2018)
8. Deshmukh, A., et al.: Membrane distillation at the water-energy nexus: limits, opportunities, and challenges. Energy Environ. Sci. **11**(5), 1177–1196 (2018)
9. Warsinger, D.M., et al.: Reversing membrane wetting in membrane distillation: comparing dryout to backwashing with pressurized air. Environ. Sci. Water Res. Technol. **3**, 930–939 (2017)
10. Rezaei, M., Warsinger, D.M., Duke, M.C., Matsuura, T., Samhaber, W.M.: Wetting phenomena in membrane distillation: mechanisms, reversal, and prevention. Water Res. **139**, 329–352 (2018)
11. Zhu, Z., et al.: Superhydrophobic-omniphobic membrane with anti-deformable pores for membrane distillation with excellent wetting resistance. J. Memb. Sci. **620**, 118768 (2021)
12. Zhang, R., Tang, W., Gao, H., Wu, C., Gray, S., Lu, X.: In-situ construction of superhydrophobic PVDF membrane via NaCl-H2O induced polymer incipient gelation for membrane distillation. Sep. Purif. Technol. **274**, 117762 (2021)
13. Ahmadi, Z., Ravandi, S.A.H., Haghighat, F., Dabirian, F.: Enhancement of the mechanical properties of PAN nanofiber/carbon nanotube composite mats produced via needleless electrospinning system. Fibers Polym. **21**(6), 1200–1211 (2020)
14. Wu, H., Shen, F., Su, Y., Chen, X., Wan, Y.: Modification of polyacrylonitrile membranes via plasma treatment followed by polydimethylsiloxane coating for recovery of ethyl acetate from aqueous solution through vacuum membrane distillation. Sep. Purif. Technol. **197**, 178–188 (2018)
15. Seo, D.H., et al.: Anti-fouling graphene-based membranes for effective water desalination. Nat. Commun. **9**(1), 1–12 (2018)
16. Fang, J., Wang, H., Wang, X., Lin, T.: Superhydrophobic nanofibre membranes: effects of particulate coating on hydrophobicity and surface properties. J. Text. Inst. **103**, 937–944 (2012)
17. Liu, L., et al.: A novel plasma-induced surface hydrophobization strategy for membrane distillation: etching, dipping and grafting. J. Memb. Sci. **499**, 544–554 (2016)
18. Ebrahimi, F., Orooji, Y., Razmjou, A.: Applying membrane distillation for the recovery of nitrate from saline water using pvdf membranes modified as superhydrophobic membranes. Polymers **12**(12), 2774 (2020)
19. Lee, J., Yoon, J., Kim, J.H., Lee, T., Byun, H.: Electrospun PAN–GO composite nanofibers as water purification membranes. J. Appl. Polym. Sci. **135**, 1–9 (2018)
20. Tijing, L.D., Woo, Y.C., Johir, M.A.H., Choi, J.S., Shon, H.K.: A novel dual-layer bicomponent electrospun nanofibrous membrane for desalination by direct contact membrane distillation. Chem. Eng. J. **256**, 155–159 (2014)
21. Bortolassi, A.C.C., et al.: Efficient nanoparticles removal and bactericidal action of electrospun nanofibers membranes for air filtration. Mater. Sci. Eng. C **102**, 718–729 (2019)

22. Meyva-Zeybek, Y., Kaynak, C.: Electrospinning of PLA and PLA/POSS nanofibers: use of Taguchi optimization for process parameters. J. Appl. Polym. Sci. **138**, 1–11 (2021)
23. Essalhi, M., Khayet, M., Tesfalidet, S., Alsultan, M., Tavajohi, N.: Desalination by direct contact membrane distillation using mixed matrix electrospun nanofibrous membranes with carbon-based nanofillers: a strategic improvement. Chem. Eng. J. **426**, 131316 (2021)
24. Roslan, N.S.A., Hamid, N.A., Mohamed Hafiz, M., Isa, N.M., Mansor, M.R., Munajat, N.A.: Nylon electrospun nanofibre water filtration media for wastewater treatment. Mater. Res. Exp. **5**(10), 105010 (2018)
25. Nonato, R.C., Morales, A.R., Rocha, M.C., Nista, S.V.G., Mei, L.H.I., Bonse, B.C.: Process parameters in the manufacture of ceramic ZnO nanofibers made by electrospinning. Appl. Phys. A Mater. Sci. Process. **123**, 1–8 (2017)
26. Su, Z., Ding, J., Wei, G.: Electrospinning: a facile technique for fabricating polymeric nanofibers doped with carbon nanotubes and metallic nanoparticles for sensor applications. RSC Adv. **4**, 52598–52610 (2014)
27. Haider, A., Haider, S., Kang, I.K.: A comprehensive review summarizing the effect of electrospinning parameters and potential applications of nanofibers in biomedical and biotechnology. Arab. J. Chem. **11**, 1165–1188 (2018)
28. Zhu, Z., et al.: Superhydrophobic-omniphobic membrane with anti-deformable pores for membrane distillation with excellent wetting resistance. J. Memb. Sci. **620**, 118768 (2020)
29. An, A.K., Lee, E.J., Guo, J., Jeong, S., Lee, J.G., Ghaffour, N.: Enhanced vapor transport in membrane distillation via functionalized carbon nanotubes anchored into electrospun nanofibres. Sci. Rep. **7**, 1–11 (2017)
30. Wang, T., Kumar, S.: Electrospinning of polyacrylonitrile nanofibers. J. Appl. Polym. Sci. **102**, 1023–1029 (2006)
31. Li, Z., Wang, C.: Effects of working parameters on electrospinning. In: Li, Z., Wang, C. (eds.) One-Dimensional Nanostructures, pp. 15–28. Springer, Heidelberg (2013). https://doi.org/10.1007/978-3-642-36427-3_2
32. Rivero, P.J., Redin, D.M., Rodríguez, R.J.: Electrospinning: a powerful tool to improve the corrosion resistance of metallic surfaces using nanofibrous coatings. Metals **10**(3), 350 (2020)
33. Stachewicz, U., Dijksman, J.F., Soudani, C., Tunnicliffe, L.B., Busfield, J.J.C., Barber, A.H.: Surface free energy analysis of electrospun fibers based on rayleigh-plateau/weber instabilities. Eur. Polym. J. **91**, 368–375 (2017)
34. Islam, M.S., Ang, B.C., Andriyana, A., Afifi, A.M.: A review on fabrication of nanofibers via electrospinning and their applications. SN Appl. Sci. **1**, 1–16 (2019)
35. Shi, X., et al.: Electrospinning of nanofibers and their applications for energy devices. J. Nanomater. (2015)
36. Can-Herrera, L.A., Oliva, A.I., Dzul-Cervantes, M.A.A., Pacheco-Salazar, O.F., Cervantes-Uc, J.M.: Morphological and mechanical properties of electrospun polycaprolactone scaffolds: effect of applied voltage. Polymers **13**, 1–16 (2021)
37. Aman, M.M., Hosseini, S.M., Yousefi, M.: Application of electrospinning technique in development of intelligent food packaging: a short review of recent trends. Food Sci. Nutr. **8**, 4656–4665 (2020)
38. Levitt, A.S., Vallett, R., Dion, G., Schauer, C.L.: Effect of electrospinning processing variables on polyacrylonitrile nanoyarns. J. Appl. Polym. Sci. **135**, 1–9 (2018)
39. Matabola, K.P., Moutloali, R.M.: The influence of electrospinning parameters on the morphology and diameter of poly (vinyledene fluoride) nanofibers-effect of sodium chloride. J. Mater. Sci. **48**, 5475–5482 (2013)
40. Hekmati, A.H., Rashidi, A., Ghazisaeidi, R., Drean, J.Y.: Effect of needle length, electrospinning distance, and solution concentration on morphological properties of polyamide-6 electrospun nanowebs. Text. Res. J. **83**, 1452–1466 (2013)

41. Nurfaizey, A.H., Munajat, N.A.: Effect of electrospinning distance and applied voltage on the production of polyacrylonitrile electrospun fibres, pp. 94–96 (2020)
42. Lamura, M.D.P., Pulungan, M.A., Jauhari, J., Sriyanti, I.: The influence of control parameter on the morphology polyethersulfone/polyacrylonitrile (PES/PAN) fiber using electrospinning technique. IOP Conf. Ser. Earth Environ. Sci. **1796**, 012084 (2021)
43. Long, F., Kamsom, R., Nurfaizey, A.H., Isa, M.H.M., Masripan, N.A.: The influence of electrospinning distances on fibre diameter of poly (vinyl alcohol) electrospun nanofibers. In: Proceedings of Mechanical Engineering Research Day, pp. 377–378. Centre for Advanced Research on Energy (2017)
44. Yuan, X.Y., Zhang, Y.Y., Dong, C., Sheng, J.: Morphology of ultrafine polysulfone fibers prepared by electrospinning. Polym. Int. **53**, 1704–1710 (2004)
45. Zargham, S., Bazgir, S., Tavakoli, A., Rashidi, A.S., Damerchely, R.: The effect of flow rate on morphology and deposition area of electrospun nylon 6 nanofiber. J. Eng. Fiber. Fabr. **7**, 42–49 (2012)
46. Tang, X.P., Si, N., Xu, L., Liu, H.Y.: Effect of flow rate on diameter of electrospun nanoporous fibers. Therm. Sci. **18**, 1447–1449 (2014)
47. Zhang, C., Yuan, X., Wu, L., Han, Y., Sheng, J.: Study on morphology of electrospun poly (vinyl alcohol) mats. Eur. Polym. J. **41**, 423–432 (2005)
48. Rafizadeh, M., Fallahi, D., Mohammadi, N., Vahidi, B.: Effects of feed rate and solution conductivity on jet current and fiber diameter in electrospinning of polyacrylonitrile solutions. E-Polymers (2009)
49. Veeramuthu, L., et al.: Conjugated copolymers through electrospinning synthetic strategies and their versatile applications in sensing environmental toxicants, pH, temperature, and humidity. Polymers **12**, 1–28 (2020)
50. Barua, B., Mrinal, C.S.: Influence of humidity, temperature, and annealing on microstructure and tensile properties of electrospun polyacrylonitrile nanofibers. Polym. Eng. Sci. 1–10 (2017)
51. Szewczyk, P.K., Stachewicz, U.: The impact of relative humidity on electrospun polymer fibers: from structural changes to fiber morphology. Adv. Colloid Interface Sci. **286**, 102315 (2020)
52. Nezarati, R.M., Eifert, M.B., Cosgriff-Hernandez, E.: Effects of humidity and solution viscosity on electrospun fiber morphology. Tissue Eng. Part C: Methods **19**(10), 810–819 (2013)
53. Yang, G.Z., Li, H.P., Yang, J.H., Wan, J., Yu, D.G.: Influence of working temperature on the formation of electrospun polymer nanofibers. Nanoscale Res. Lett. **12**(1), 1–10 (2017)
54. Ahire, J.J., Neveling, D.P., Dicks, L.M.T.: Polyacrylonitrile (PAN) nanofibres spun with copper nanoparticles: an anti-Escherichia coli membrane for water treatment. Appl. Microbiol. Biotechnol. **102**, 7171–7181 (2018)
55. Niu, Z., Bian, Y., Xia, T., Zhang, L., Chen, C.: An optimization approach for fabricating electrospun nanofiber air filters with minimized pressure drop for indoor PM2.5 control. Build. Environ. **188**, 107449 (2021)
56. Kusuma, N.C., et al.: Fabrication and characterization of modified PVDF hollow fiber membrane coated with hydrophobic surface modifying macromolecules for desalination application. J. Environ. Chem. Eng. **9**, 105582 (2021)
57. Jiang, S., Chen, Y., Duan, G., Mei, C., Greiner, A., Agarwal, S.: Electrospun nanofiber reinforced composites: a review. Polym. Chem. **9**, 2685–2720 (2018)
58. Ma, H., Hsiao, B.S.: Electrospun nanofibrous membranes for desalination. Elsevier Inc. (2018)
59. Roche, R., Yalcinkaya, F.: Electrospun polyacrylonitrile nanofibrous membranes for point-of-use water and air cleaning. ChemistryOpen **8**, 97–103 (2019)

60. Seyed Shahabadi, S.M., Rabiee, H., Seyedi, S.M., Mokhtare, A., Brant, J.A.: Super-hydrophobic dual layer functionalized titanium dioxide/polyvinylidene fluoride-co-hexafluoropropylene (TiO2/PH) nanofibrous membrane for high flux membrane distillation. J. Memb. Sci. **537**, 140–150 (2017)

61. Eykens, L., De Sitter, K., Dotremont, C., Pinoy, L., Van der Bruggen, B.: Membrane synthesis for membrane distillation: a review. Sep. Purif. Technol. **182**, 36–51 (2017)

62. Uddin, M.N., Desai, F.J., Rahman, M.M., Asmatulu, R.: A highly efficient fog harvester of electrospun permanent superhydrophobic-hydrophilic polymer nanocomposite fiber mats. Nanoscale Adv. **2**(10), 4627–4638 (2020)

63. Haider, M.K., et al.: Fabricating antibacterial and antioxidant electrospun hydrophilic poly-acrylonitrile nanofibers loaded with agnps by lignin-induced in-situ method. Polymers **13**, 1–20 (2021)

64. Yu, Y., et al.: Waterproof and breathable polyacrylonitrile/(polyurethane/fluorinated-silica) composite nanofiber membrane via side-by-side electrospinning. J. Mater. Res. **35**(9), 1173–1181 (2020)

65. Dong, S., et al.: Superhydrophobic alumina hollow ceramic membrane modified by TiO2 nanorod array for vacuum membrane distillation. J. Taiwan Inst. Chem. Eng. **117**, 2–8 (2020)

66. Szewczyk, P.K., et al.: Roughness and fiber fraction dominated wetting of electrospun fiber-based porous meshes. Polymers **11**, 34 (2018)

67. Heshmati, M.R., Amiri, S., Hosseini-Zori, M.: Synthesis and characterization of superhydrophobic-superoleophobic and anti-corrosion coatings via sol-gel process open. J. Org. Polym. Mater. **10**, 1–15 (2020)

68. Li, S., Huang, J., Chen, Z., Chen, G., Lai, Y.: A review on special wettability textiles: theo-retical models, fabrication technologies and multifunctional applications. J. Mater. Chem. A **5**, 31–55 (2017)

69. My, N.T.T., Nhi, V.T.Y., Thanh, B.X.: Factors affecting membrane distillation process for seawater desalination. J. Appl. Membr. Sci. Technol. **22**(1) (2018)

70. Gu, S., Cai, R., Yan, Y.: Self-crosslinking for dimensionally stable and solvent-resistant quaternary phosphonium based hydroxide exchange membranes. Chem. Commun. **47**, 2856–2858 (2011)

71. Khayyam, H., et al.: PAN precursor fabrication, applications and thermal stabilization process in carbon fiber production: experimental and mathematical modelling. Prog. Mater. Sci. **107**, 100575 (2020)

72. Li, W., Yang, Z., Meng, Q., Shen, C., Zhang, G.: Thermally stable and solvent resistant self-crosslinked TiO2/PAN hybrid hollow fiber membrane fabricated by mutual supporting method. J. Memb. Sci. **467**, 253–261 (2014)

73. Furushima, Y., Nakada, M., Takahashi, H., Ishikiriyama, K.: Study of melting and crystalliza-tion behavior of polyacrylonitrile using ultrafast differential scanning calorimetry. Polymer **55**, 3075–3081 (2014)

74. Szepcsik, B., Pukánszky, B.: The mechanism of thermal stabilization of polyacrylonitrile. Thermochim. Acta **671**, 200–208 (2019)

75. Munajat, N.A., Nurfaizey, A.H., Bahar, A.A.M., You, K.Y., Fadzullah, S.H.S.M., Omar, G.: High-frequency dielectric analysis of carbon nanofibers from pan precursor at different pyrolysis temperatures. Microw. Opt. Technol. Lett. **60**, 2198–2204 (2018)

76. Hamadneh, N.N., Khan, W.S., Khan, W.A.: Prediction of thermal conductivities of polyacry-lonitrile electrospun nanocomposite fibers using artificial neural network and prey predator algorithm. J. King Saud Univ. Sci. **31**, 618–627 (2019)

77. Luo, A., Lior, N.: Study of advancement to higher temperature membrane distillation. Desalination **419**, 88–100 (2017)

78. Arifeen, W.U., Kim, M., Choi, J., Yoo, K., Kurniawan, R., Ko, T.J.: Optimization of porosity and tensile strength of electrospun polyacrylonitrile nanofibrous membranes. Mater. Chem. Phys. **229**, 310–318 (2019)
79. Arif, M.W.A., Nurfaizey, A.H., Mustafa, Z., Nadlene, R., Jaafar, J., Tucker, N.: Investigation on fibre diameter, wettability and tensile behaviour of electrospun polyacrylonitrile nanofibres. Int. J. Nanoelectron. Mater. **14**, 213–224 (2021)
80. Liang, W., et al.: Hydrophobic polyacrylonitrile membrane preparation and its use in membrane contactor for CO2 absorption. J. Memb. Sci. **569**, 157–165 (2019)
81. Yalcinkaya, F.: A review on advanced nanofiber technology for membrane distillation. J. Eng. Fiber. Fabr. **14** (2019)
82. Liao, Y., Zheng, G., Huang, J.J., Tian, M., Wang, R.: Development of robust and superhydrophobic membranes to mitigate membrane scaling and fouling in membrane distillation. J. Memb. Sci. **601**, 117962 (2020)
83. Nthunya, L.N., et al.: A review of nanoparticle-enhanced membrane distillation membranes: membrane synthesis and applications in water treatment. J. Chem. Technol. Biotechnol. **94**, 2757–2771 (2019)
84. Cai, J., Liu, Z., Guo, F.: Transport analysis of anti-wetting composite fibrous membranes for membrane distillation. Membranes **11**, 1–14 (2021)
85. Chen, X.: Recent progress of membrane distillation technology applied in desalination. In: E3S Web Conference, vol. 131 (2019)
86. Efome, J.E., Rana, D., Matsuura, T., Yang, F., Cong, Y., Lan, C.Q.: Triple-layered nanofibrous metal-organic framework-based membranes for desalination by direct contact membrane distillation. ACS Sustain. Chem. Eng. **8**, 6601–6610 (2020)
87. Li, X., et al.: A novel profiled core-shell nanofibrous membrane for wastewater treatment by direct contact membrane distillation. J. Mater. Chem. A **4**, 14453–14463 (2016)
88. Qin, D., Zhang, R., Cao, B., Li, P.: Fabrication of high-performance composite membranes based on hierarchically structured electrospun nanofiber substrates for pervaporation desalination. J. Memb. Sci. **638**, 119672 (2021)
89. Tang, M., Hou, D., Ding, C., Wang, K., Wang, D., Wang, J.: Anti-oil-fouling hydrophobic-superoleophobic composite membranes for robust membrane distillation performance. Sci. Total Environ. **696**, 133883 (2019)
90. Cai, J., Liu, X., Zhao, Y., Guo, F.: Membrane desalination using surface fluorination treated electrospun polyacrylonitrile membranes with nonwoven structure and quasi-parallel fibrous structure. Desalination **429**, 70–75 (2018)

Characterization of Palm Trunk Under Different Heat Treatment

Noratiqah Syahirah Mohd Zarib[1(✉)], Shahrulazam Abdullah[1],
Siti Nabilla Abdul Ghani[2], and Che Muhd Ruzaidi Ghazali[2]

[1] Fakulti Kejuruteraan Mekanikal, Universiti Teknologi MARA (UiTM), 40450 Shah Alam,
Selangor, Malaysia
eiqasyahirah@gmail.com

[2] Fakulti Kejuruteraan Teknologi Mekanikal, Universiti Malaysia Perlis (UniMAP), Perlis,
Malaysia

Abstract. This study is to determine the properties and characterization of carbon that produce from material after it undergoes heat treatment in inert condition. In this study the raw material used were waste oil palm trunk from palm oil plantation. Besides that, parameter such as different temperature and different heating rate ware also compared. The sample were heat treated at different temperature which is 500 °C, 800 °C and 1000 °C and at different heating rate which is 5 °C/min, 10 °C/min and 20 °C/min for 2-h soaking time. Raw OPT morphology shows smooth surface compared to morphology of heat-treated sample. The holes and swollen surface shows the development of porosity in the heat-treated oil palm trunk while FTIR spectrum showed by raw OPT, spectra of palm trunk that's heat treated at 500 °C and 800 °C illustrate less absorption peak. This trend provides the evidence supporting that high temperature will produce better graphite carbon. It has the potential to reduce waste and improve environment quality.

Keywords: Palm trunk · Nitrogen gas · Heat treatment

1 Introduction

Malaysia is the world's second largest producer of crude palm oil while the palm oil industry is the 4th largest contributor to the country's gross national income (GNI) accounting for about 8% with almost RM 50 billion of gross national income for Malaysia. Malaysia had 5.08 million hectares of oil palm plantation and the biggest plantation are located at Sarawak and the second biggest plantation are located at Sabah. This large plantation area generated huge amount of lignocellulosic materials in the form of fronds and trunks [1]. The production of palm oil generates biomass residue from plantation and mill sites. Biomass is organic material available on renewable basis including forest and mill residue, wood waste, agricultural crops and waste, animal waste and municipal waste. Furthermore, organic materials are defined as materials containing carbon-based compound in which the carbon is attached to other carbon atoms, hydrogen, oxygen, or other elements in a chain, ring, or three-dimensional structures

[2]. This biomass residue can be classified into six types: oil palm fronds (OPF) and oil palm trunks (OPT) produced at plantation site, empty fruit bunches (EFB), palm kernel shells, monocarp fibre and palm oil mill effluent (POME) produced at mill sites. oil palm biomass residue as alternative raw material for biofuel production, paper-making pulp, wood production and bio-based chemicals [3] while earlier studies also found that Chips of oil palm trunks and oil palm shells have great potential as a raw material for activated carbon production [4] oil palm biomass residue as alternative raw material for biofuel production, paper-making pulp, wood production and bio based chemicals [5] while earlier studies also found that Chips of oil palm trunks and oil palm shells have great potential as a raw material for activated carbon production [6].

2   Materials and Methods

In this research, material that were used are palm trunk and nitrogen gas. Palm trunk is one of the residues in palm plantation that producing palm oil. They are usually removing by open burning. The anatomical of palm trunk is typical of monocot with xylem (water conducting tissue) and phloem (carbohydrate conducting tissue). Palm trunk also deposit lignin and cellulose. By cut it into small pieces sample and present it to a control heat treatment (600 °C to 900 °C) and in particular condition of heat treatment, palm trunk can be converting into beneficial carbon. Nitrogen (N2) gas is an inert gas, function of the nitrogen is to prevent the oxidation to occur during heat treatment in the tube furnace. Firstly, 5 g of palm trunk powder was used in thermal characterization by using he Hitachi SU3500 instrument. Sample specimens with a diameter of 15 mm each were coated with an aluminum sputter coater for 60 s at 15 mA current. The aluminum coating was required to ensure a conducting surface was obtained for electron bombardment and characterization. This step is crucial to do as the test specimens were nonconductive. To eliminate the electron charging effects the SEM was operated at 3 kV and a working distance of 15 mm. The functional group of the samples will be characterized by Fourier transform infrared spectroscopy (FTIR) test on the powder of raw and oil palm trunk that heat at different heating temperature.

3   Result and Discussion

3.1   Morphology of Analysis of Palm Trunk Undergo Heat Treatment

Figure 1 shows the morphology of a) raw oil palm trunk (OPT), heat treated palm trunk at temperature b) 500 °C, c) 800 °C and d) 1000 °C with the same heating rate which is 10 °C/min that were examined by field emission scanning electron microscope at magnification 3000X. Raw OPT morphology shows smooth surface compared to morphology of heat treated sample. The holes and swollen shows the development of porosity in the heat-treated oil palm trunk. It was suggested that the microspores, which has high contribution to the surface area, was mainly caused by the nitrogen which inhibits the contraction of the material during carbonization.
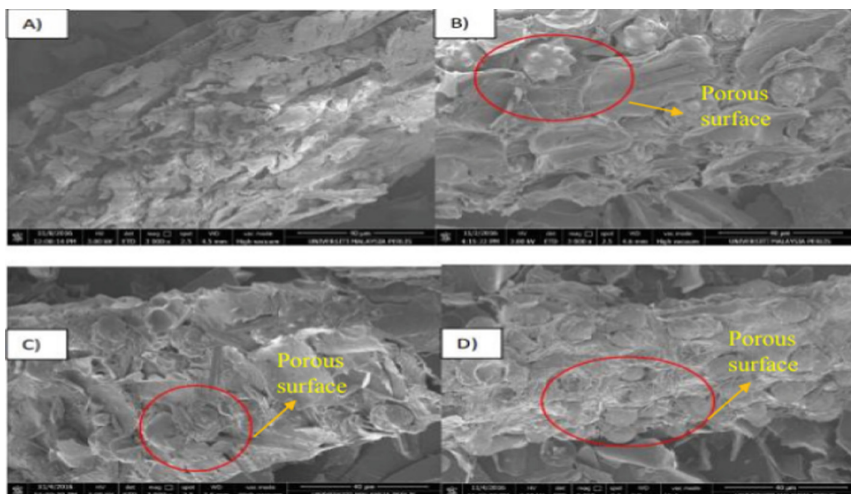
Fig. 1. The morphology of a) raw OPT, heat treated palm trunk at temperature of b) 500 °C, c) 800 °C and d) 1000 °C with the same heating rate which is 10 °C/min.

3.2 Functional Group Analysis

Figure 2 shows FTIR spectra of raw oil palm trunk powder and oil palm trunk powder that passed heat treatment at temperature 500 °C and 800 °C for 10 °C/min heating rate and 2-h soaking time. Based on this figure raw oil palm trunk (OPT) shows the most complicated and apparent spectrum. From the graph of raw OPT, the strong and broad adsorption peak was appeared at 3401.08 cm^{-1} corresponding to stretching O-H functional group thus it was indicating that existence of bonded hydroxide in this raw powder sample. There also has another peak observed at 2918.3 cm^{-1} corresponding to the C-H sp3 stretching. Besides that, a strong C = O peak also can be observed at 1734.6 cm^{-1}. Moreover, there are two important peaks which occurred at 1247.6 cm^{-1} and 1050.26 cm^{-1} which represent the stretching of C-O functional group.

Unlike the FTIR spectrum showed by raw OPT, spectra of palm trunk that's heat treated at 500 °C and 800 °C illustrate less absorption peak. FTIR spectra of 500 °C shows that the presence of different type of oxygen functionalities in that sample at 3436.01 cm^{-1} corresponding to O-H stretching vibration. Besides that, at 1566.3 cm^{-1} a peak occurs corresponding to skeletal vibration from unoxidized graphitic domain, at 1384.36 cm^{-1} also has a peak which corresponding to C-OH stretching vibration and lastly there is a peak at 871.85 cm^{-1} corresponding to C-O stretching vibrations. Based on the spectra obtained from this sample, it shows that the spectra trend of the sample is almost similar with the spectra trend of Graphene oxide [7].

In the spectrum of 800 °C, the absorption bands at 3432 cm^{-1} was known to be the O-H stretching vibrations; the peak located at 1469 cm^{-1} could be attributed to the skeletal vibration of C = C from unoxidized sp2 CC bonds. It is similar to spectra trend of graphite [8]. It is clearly showing that most of the absorption peaks of functional groups were diminished from the sample spectra obtained. During carbonization by heat treatment the functional group observed from raw oil palm trunk spectra were

Fig. 2. The FTIR spectra of raw oil palm trunk powder and oil palm trunk powder that passed heat treatment at temperature 500 °C and 800 °C for 10 °C/min heating rate and 2-h soaking time.

evaporated as volatile material when heat applied to the samples. This proved that the carbonization process has taken place successfully. Consequently, this also indicate that all the sample were successfully converted into carbon. The decreasing band suggest that heating temperature during heat treatment influence the formation of carbon.

4 Conclusion

The properties of carbon powder that produce from palm trunk via heat treatment process in nitrogen gas has been studied. Heat treatment were also done in varies heating rate and temperature which is 5 °C/min, 10 °C/min and 20 °C/min. and 500 °C, 800 °C and 1000 °C respectively. Besides, the microspores in oil pal trunk has high contribution to the surface area, was mainly caused by the nitrogen which inhibits the contraction of the material during carbonization. Moreover, for the characterization technique, raw palm trunk was analyzed, it shows the bonding of elements due to its functional groups on FTIR analysis.

References

1. Sharon, M., Sharon, M.: Carbon nano forms and applications. J. Introduction Nanoworld Carbon 11–20 (2010)
2. Bahari, M.A.M.B.: Oil Palm Trunk (Opt) As an Alternative Cellulosic Material for Brown Paper Production, Pahang Malaysia (2010)
3. Shrestha, R.M., Yadav, A.P., Pokharel, B.P., Pradhananga, R.R.: Preparation and characterization of activated carbon from Lapsi (Choerospondias axillaris) seed stone by chemical activation with phosphoric acid. Res. J. Chem. Sci. **2**, 80–86 (2012)
4. Arjmandi, R., Hassan, A., Mohamad Haafiz, M.K., Zakaria, Z.: Effects of micro- and nanocellulose on tensile and morphological properties of montmorillonite nanoclay reinforced polylactic acid nanocomposites. In: Jawaid, M., Qaiss, Ae.K., Bouhfid, R. (eds.) Nanoclay Reinforced Polymer Composites. EM, pp. 103–125. Springer, Singapore (2016). https://doi.org/10.1007/978-981-10-0950-1_5

5. Wang, D.Y., Gohs, U., Kang, N.J., Leuteritz, A.: Method for Simultaneously Improving the Thermal Stability and Mechanical Properties of Poly (lactic acid): Effect of High-Energy Electrons on the Morphological, Mechanical, and Thermal Properties of PLA/MMT Nanocomposites. ACS Publications, Chengdu (2012)
6. Zou, G.X., Zhang, X., Zhao, C.X., Li, J.: The Crystalline and Mechanical Properties of PLA/Layered Silicate Degradable Composites. Pleiades Publishing, Ltd., Jiangshu (2012)
7. Abdul Rahim, Z.R.S.D.: Comparison of various sources of high surface area carbon prepared by different type of activation. Malaysian J. Analytical Sci. **12**, 266–267 (2012)
8. Al-Qodah, R.S.Z.: Production and characterization of granular activated carbon from activated sludge. J. Chem. Eng. **26**, 127–136 (2009)

Effect of Dimple Size onto Wear Rate of Mild Steel AISI 1060 Surface

Mohd Rahimi Ramli[1(✉)], Norasiah Abd Razak[2], Izwan Ismail[1],
Ahmad Shahir Jamaludin[1], and Ahmad Rosli Abdul Manaf[1]

[1] Faculty of Manufacturing and Mechatronics Engineering Technology, Universiti Malaysia Pahang, 26600 Pekan, Pahang, Malaysia
mrahime@pmu.edu.my

[2] Automotive Engineering Centre, Universiti Malaysia Pahang, 26600 Pekan, Pahang, Malaysia

Abstract. This paper presents the effect of the dimple size and dimple density on the wear properties of mild steel AISI 1060 surface under constant loading. The dimple surface texture is produced using a ball-end-nose milling tool on a cross-sectioned surface of 32.5 mm cylindrical sample with a CNC milling method. The samples acted as the pin for pin-on-disk apparatus with constant loading setup. The dimples size is between 1 mm to 4 mm. The wear size on samples are analyzed using 3D laser confocal microscopy image analysis technique. The result shows that the highest wear rate occurred at the samples with the smallest dimple diameter of 1 mm, while no significant of wear observed on samples with the largest dimple size of 4 mm. It is expected that dimple size has a significant effect onto the contact between pin and surface, as the effect of friction reduced with the reduction of contact size.

Keywords: Surface texture · Dimple structure · Surface friction

1 Introduction

Surface friction control mechanisms are one of possible methods to reduced machine component failure due to vibration. The surface friction leads to an increase in the wear rate of the rubbing surface. Various approaches have been used to reduce surface friction, such as lubrication, coatings, and surface modifications. One of the promising approaches is the application of surface texturing [1]. Dimple structures on a metal surface can be produced through a variety of methods, such as 3-axis CNC micro drilling machine and a ball end nose tool. This method will produce dimples with higher accuracy [2]. There are three common types of dimple shapes, namely, elliptical, rectangular and rounds. The elliptical dimple shape shows the best performance in low compression load, while the rectangular shape showed the second-best, followed by the round shape. However, as the test load increases, the friction reduction effect of all shapes will increase due to ratio between the geometric shapes of the indentations becoming larger [3].

Surface texture is an appealing method for the application of a sliding contact element. Oval shaped dimple spread on a frictional surface are required to serve as fluid

reservoirs and help to facilitate the preservation of the thin lubricating layer between the mating components. In addition, in situations where there are repeated start/stop operations, it is assumed that the lubricant remaining in the pores can prevent an excessive increase in temperature due to dry running conditions [5]. At the actual sliding surface, the actual contact point (joint) is plastically deformed due contact and sliding motion during the tribological process. Thus, in the investigation of adhesive wear, it is important to establish the understanding of adhesion force between the real sliding surfaces rather than between ideal clean contact surfaces [6].

Among the dimple shapes, the round dimple is the simplest and most efficient to be manufactured. Therefore, preparing the best dimple size and distributions of rounded samples will benefit the friction reduction especially used under high compression loading. It is also found that friction on large textured surfaces area is significantly reduced [4]. Some studies also argue that increasing dimple patterns can reduce friction coefficients [7]. The purpose of the study is to investigate the effect of dimple size onto frictional behavior of textured surfaces, tested through pin-on-disk method. The textured sample is prepared into the shape of pin and tested on a galvanized surface plate.

2 Methodology

The process for producing the dimple on the surface of the sample was done by using CNC milling machine. The samples were initially in square shape 50 mm × 50 mm with the thickness of 10 mm (Fig. 1). Dimple textures are machined onto the sample surface with predetermined size and density (Table 1). The tool used to produce the dimple was ball-end-nose with the diameter of the twice value of the dimple depth. This method used to ensure the depth for each of the dimple was similar the radius of the cutting tools. This samples then cut into cylindrical shape with the diameter of 32.5 mm using a turning lathe. The wear behaviour for the mild steel AISI 1060 is measured using the pin-on-disk method. Pin-on-disk method is utilized to ensure uniform loading between pin and disk. The sample will act as the pin and a galvanized carbon steel plate will act as the disk (Figs. 1 and 2). The size of disk plate is 200 mm diameter with 2 mm thickness. The experiment was performed with a constant force exerted on the surface of the disk which is 10 N and the rotational speed of 60 rpm.

Table 1. Machining parameters for producing different dimple size.

Dimple diameter (mm)	1	2	3	4
Cutting tool diameter (mm)	1	2	3	4
Axial depth of cut (mm)	0.5	1.0	1.5	2.0
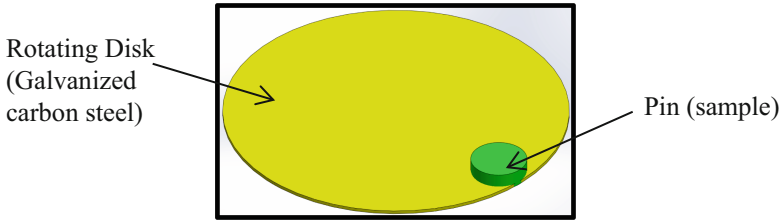
Fig. 1. Pin-on-disk schematic diagram.
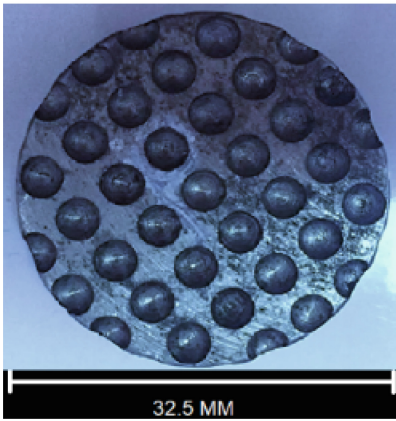
(a) Pin sample with ∅4 mm
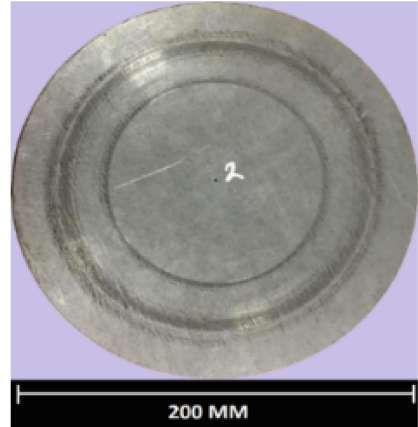
(b) Galvanized carbon steel plate as sliding surfaces 3mm

Fig. 2. The surface of pin and galvanized carbon steel plate used as sliding surface in the pin on disk test.

3   Result and Discussion

Table 2 shows the experimental result obtained from the pin-on-disk wear test between mild steel AISI 1060 dimple textured sample and galvanized carbon steel plate. From Table 2, it is observed that mass reduction of mild steel AISI 1060 for the dimple size of 1 mm shows the highest value, 0.09g, compared with 0.03g for 4 mm diameter, which is the lowest. It can be observed that the mass reduction rate decreases as the dimple diameter increases. It is assumed that contact size plays a major role in wear rate. As with larger dimple diameter, less contact between surfaces is possible while maintaining the contact loading properties. A larger dimple diameter will help in preparing lubricant/coolant pocket for future application purpose [7].

Table 2. Physical properties and wear rate of pin on disk for four variations of dimple size.

Dimple size (mm)	M_{pin}^1 (g)	M_{pin}^2 (g)	ΔM_{pin} (g)	%
1	65.99	65.90	0.09	0.14
2	64.21	64.14	0.07	0.11
3	61.22	61.18	0.04	0.07
4	58.06	58.03	0.03	0.05

M_{pin}^1: Mass before

M_{pin}^2: Mass after

ΔM_{pin}: Total mass reduction

4   Conclusion

The results obtained from the experiments shows that dimples have the potential to reduce friction. Wear rate shows gradual reduction with the increment of dimple size while maintaining similar loading condition. In the future, it is assumed that dimples texture is possible to be utilized as lubricant/coolant pockets for mechanical processes.

References

1. Bin Zaki, M.I., Saptaji, K., Ramdan, R.D., Kurniawan, T.: Fabrication of micro dimples pattern using ball end mill. IOP Conf. Ser.: Mater. Sci. Eng. **547**, 012009 (2019)
2. Cao, L., Chen, Y., Cui, J., Li, W., Lin, Z., Zhang, P.: Corrosion wear performance of pure Titanium Laser texturing surface by Nitrogen Ion Implantation. Metals **10**(8), 990 (2020)
3. Park, G.C., Ko, T.J., Kurniawan, R., Ali, S.: Characterization of elliptical dimple fabricated with dual frequency vibration assisted machining. Korean Soc. Manuf. Process Eng. **20**(2), 23–31 (2021)
4. Rosenkranz, A., Costa, H.L., Baykara, M.Z., Martini, A.: Synergetic effects of surface texturing and solid lubricants to tailor friction and wear – a review. Tribol. Int. **155**, 106792 (2021)
5. Roy, T., Choudhury, D., Ghosh, S., Bin Mamat, A., Pingguan-Murphy, B.: Improved friction and wear performance of micro dimpled ceramic-on-ceramic interface for hip joint arthroplasty. Ceram. Int. **41**(1), 681–690 (2015)
6. Zenebe Segu, D., Hwang, P.: Friction control by multi-shape textured surface under pin-on-disc test. Tribol. Int. **91**, 111–117 (2015)
7. Wang, X., Wang, J., Zhang, B., Huang, W.: Design principles for the area density of dimple patterns. Proc. Inst. Mech. Eng. Part J J. Eng. Tribol. **229**(4), 538–546 (2015)

Water Affinity Properties of Thermoplastic Cassava Starch/Wax Reinforced with Sugarcane Bagasse Fiber

Zatil Hafila Kamaruddin[1], Nurul' Ain Haniyun Mohamad Fodzi[2], and Ridhwan Jumaidin[2(✉)]

[1] Fakulti Kejuruteraan Mekanikal, Universiti Teknikal Malaysia Melaka, Hang Tuah Jaya, 76100 Durian Tunggal, Melaka, Malaysia

[2] Fakulti Teknologi Kejuruteraan Mekanikal dan Pembuatan, Universiti Teknikal Malaysia Melaka, Hang Tuah Jaya, 76100 Durian Tunggal, Melaka, Malaysia

ridhwan@utem.edu.my

Abstract. The aim of this study is to investigate the characteristics of thermoplastic cassava starch (TPCS) composites containing sugarcane bagasse fiber (SBF) in the range of 0% until 30%. TPCS was modified by incorporating the sugarcane bagasse fiber integrated with glycerol and beeswax. The mixture is mixed using a high-speed dry mixer at 1200 rpm for 2 min then undergoes hot compression molding to form a sample of the new material. The composites were characterized for their moisture content, water absorption, and thickness swelling. In terms of water transport, the water absorption of the TPCS/BW-Sugarcane bagasse fiber composites were clearly reduced by the addition of sugarcane fiber. Meanwhile, the dimensional stability of the composites for the thickness swelling, 30% fiber content swelling the most. Overall, incorporating the sugarcane bagasse fiber into the thermoplastic cassava starch has improved the functional properties of this green material.

Keywords: Thermoplastic starch · Sugarcane bagasse fiber · Starch

1 Introduction

Of late, non-biodegradable plastic has been causing many environmental issues worldwide, from water pollution to plastic degradation in landfills [1]. The problem has drawn attention to the new biodegradable material such as thermoplastic made from natural resources that will eventually degrade in the common environment condition. Together with the enforcement of environmental regulations, there is needed to develop product base from the biodegradable materials. Thus, in order to address environmental and ecological concerns, this century has focused on greater achievement in green technology product in the field of materials through development of bio-composite. Starch has been one of the most promising biopolymers and has been considered to suit many industrial needs owing to its low cost, abundant availability, biodegradability and renewability [2–4]. Starch is semi-crystalline granules and can be transformed into thermoplastic

material by addition of plasticizer, heat, and shear [5, 6]. However, starch is not widely used in industrial plastic manufacture due to the poor mechanical characteristics and high water sensitivity of starch-based plastics. Thus, starch must be modified to overcome the drawback when making strong rigid composite. The incorporation of natural reinforcing fibers such as hemp, jute, and ramie into a biopolymer matrix formed from starch has been a recent advancement in bio-composite production. Due to their superior biodegradability, non-toxicity, and perpetual renewable nature, the composites formed from this biodegradable polymer matrix and fibre have a promising potential for use as packaging material. Hence, the objective of this study is to investigate the effect of SBF on the physical properties of TPCS.

2   Materials and Methodology

2.1   Materials

Food grade cassava starch was purchased by Antik Sempurna Sdn. Bhd, (Selangor, Malaysia) and beeswax was purchased from Aldrich Chemistry Sdn. Bhd. Analytical grade glycerol (99.5% purity) as plasticiser was obtained from QRec Chemicals Sdn. Bhd., (Selangor, Malaysia).

2.2   Sample Preparation

Thermoplastic cassava starch (TPCS) was prepared by mixing cassava starch, glycerol and beeswax then followed by pre-mixing by using blender at 1200 rpm for 2 min. After the pre-liminary step, the mixtures were pressed with hot compression molding machine at temperature 145 °C for 1 h. The same process was used for the preparation of TPCS/BW-Sugarcane bagasse fiber composites. The modification of the matrix was carried out by inclusion of different percentage of fiber (0, 10, 20 and 30 wt%). The TPCS composites were kept immediately in the desiccator containing silica gel prior to the conditioning process in order to avoid unpredicted moisture absorption.

2.3   Moisture Content

Three specimens (10 × 10 × 3 mm) were prepared for each composition in order to determine the moisture content. The samples of TPCS/BW-Sugarcane bagasse fiber were heated in the oven at 105 °C for 24 h. The initial weight of the samples (M_i) before heating and the final weight (M_f) after heating was obtained in order to calculate the moisture content. The moisture content of TPCS/BW-Sugarcane bagasse fiber was determined using Eq. (1)

$$Moisture\ Content\ \% = \frac{M_i - M_f}{M_i} \times 100\% \tag{1}$$

2.4 Water Absorption

By using ASTM D570-98 as a reference with slight modification, for the water absorption test, three samples of each formulation with the size of $10 \times 10 \times 3$ mm. The samples of TPCS/BW-Sugarcane bagasse fiber were heated in the oven at 105 °C for 24 h. Then, the initial weight of samples (Wi) after heating was taken. The samples were then immersed in the distilled water for 0.5 h and 2 h. The amount of water absorbed by a sample was determined after enough immersion period and the final weight (W_f) was taken. The percentage of water absorption was calculated by using Eq. (2).

$$Water\ absorption\ \% = \frac{W_f - W_i}{W_i} \times 100\% \tag{2}$$

2.5 Thickness Swelling

With ASTM D570-98 as reference, three samples of each formulation with the size of $10 \times 10 \times 3$ mm was prepared. In an air circulating oven with the temperature of 105 °C $\pm$ 2, the samples were dried for 24 h to remove existing moisture from the samples. The samples were immersed in water at room temperature (23 ± 1 °C) for 0.5 h and 2 h. The thickness of the specimen was recorded before, (T_i) and after, (T_f) the testing and calculated using Eq. (3).

$$Thickness\ swelling\ \% = \frac{T_i - T_f}{T_i} \times 100\% \tag{3}$$

3 Result and Discussion

3.1 Moisture Content

Figure 1 shows the percentage of moisture content of TPCS/BW-Sugarcane bagasse fiber. Generally, when sugarcane bagasse fiber was incorporated in the TPCS/BW composites, the moisture content slightly decreased by the increased of fiber content. The moisture content decreased from 5.37% at 10% fiber content to 4.73% at 30% fiber content respectively. This might be associated to the formation of strong hydrogen bonds between sugarcane bagasse fiber and the starch matrix, resulting to the reduction in the available hydroxyl groups [7]. As a result, the moisture resistance of the TPCS/BW- sugarcane bagasse fiber composites increases. This finding is in good agreement with the results of other author who reported a decreasing moisture content of tapioca starch with the addition of jute and flax [8].
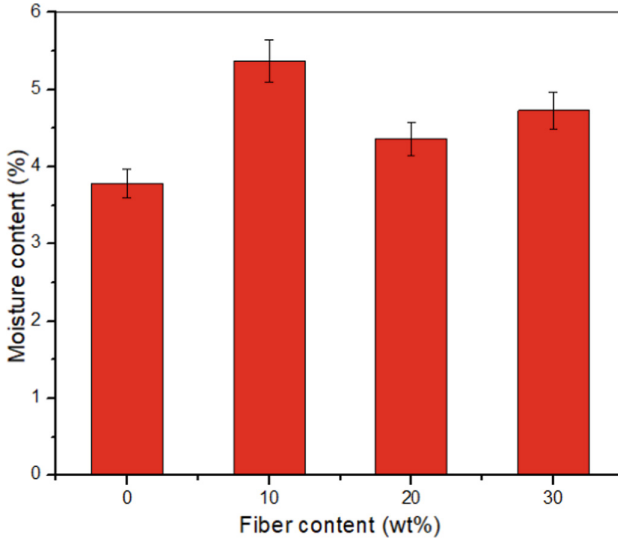
Fig. 1. Moisture content for TPCS/BW-sugarcane bagasse fiber composites.

3.2 Water Absorption

Figure 2 shows the percentage of water absorbed by TPCS/BW-Sugarcane bagasse with a different percentage of the fiber after immersion for 0.5 h and 2 h. Based on the graph, it was found that the water absorption TPCS/BW-Sugarcane bagasse fiber composites showed the decreasing trend as the fiber content increased. The sugarcane bagasse fiber could decrease the water absorption of the TPCS matrix due to the starch was more hydrophilic than cellulose fibers. Thus, the fibers' presence reduced the starch matrix's hydrophilicity [9]. Additionally, the high adhesion between the TPCS matrix and cellulosic fibers reduced the free volume of the starch molecular chains, resulting in difficulty in penetrating water. Besides, the least percentage of water absorbed is 30% fiber content which is 64.27% lower than 0% fiber content. This finding revealed that the composite has better water resistance than the TPCS matrix. This positive finding on the percentage of water absorbed by the TPCS/sugarcane fiber composite could also be explained by the chemical composition of lignin and wax on the fiber surface, which acts as a barrier to water absorption [10].
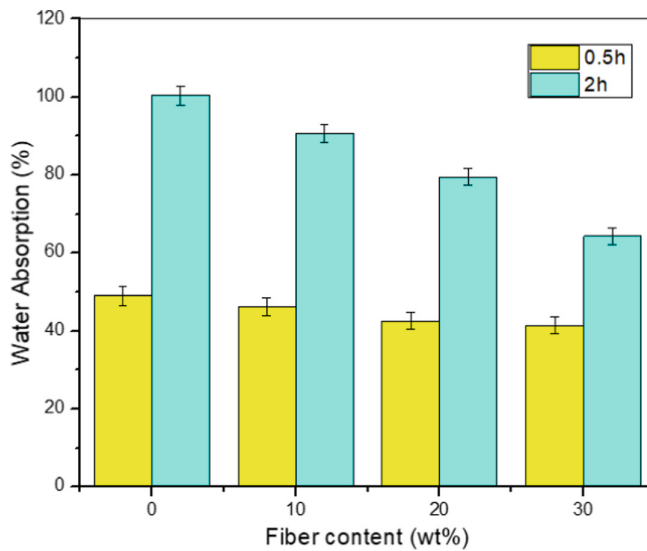
Fig. 2. Water absorption for TPCS/BW-sugarcane bagasse fiber composites.

3.3 Thickness Swelling

Thickness swelling is one of the testing done to study the dimensional stability of the specimen. Dimensional stability is crucial in the study of natural composite, as it indicates the material's capability to withstand a specific condition, such as indoor and outdoor uses, and to determine the shelf life of the material itself [11]. Figure 3 shows the swelling percentage of pure TPCS matrix and its composite with different amounts of fibers with 0.5-h and 2-h water immersion. The thickness of the matrix and the composites was affected by increasing of fiber content. The percentage of thickness swelling of the specimen with 0 wt% fiber content for 0.5 h and 2 h is 27.83% and 41.08%, respectively, and for a sample with 30 wt% fiber, it is 32.93% and 54.12%, respectively. It was found that the percentage of increment for 0.5 h is 5.10% and for 2 h is 13.04%. This pattern shows that the inclusion of fiber affected the thickness swelling behavior of the composites. The result might be due to the presence of void in the TPCS/BW-Sugarcane bagasse composite, leading to a higher thickness swelling rate. The result achieved is consistent with the findings from Saw et al. [12] on the void in the composite. When the void or porosity is present in the composite material, it will affect the dimensional stability of the materials.
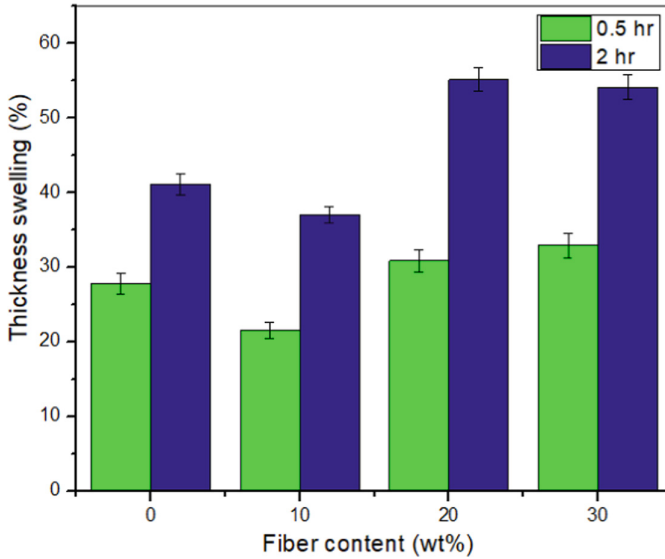
Fig. 3. Thickness swelling for TPCS/BW-sugarcane bagasse fiber composites.

4 Conclusion

This study successfully created a biodegradable composite made of TPCS and sugarcane bagasse fiber using a hot pressing machine. The water affinity qualities of TPCS were significantly improved when sugarcane bagasse was added. This was accompanied by a decrease in the composite's moisture content. Besides, it was found that the incorporation of 30 wt% sugarcane bagasse fiber to the cassava starch/beeswax composite reduces the water absorption of the specimen significantly. Hence, TPCS reinforced sugarcane bagasse fiber composites have shown potential as biodegradable materials.

References

1. Jumaidin, R., Sapuan Salit, M., Jawaid, M., Ridzwan Ishak, M., Sahari, J.: Seaweeds as renewable sources for biopolymers and its composites: a review. Curr. Anal. Chem. **13**, 249–267 (2017). https://doi.org/10.2174/1573411013666171009164355
2. Hazrati, K.Z., Sapuan, S.M., Zuhri, M.Y.M., Jumaidin, R.: Extraction and characterization of potential biodegradable materials based on dioscorea hispida tubers. Polymers **13**(4), 584 (2021). https://doi.org/10.3390/polym13040584
3. Ilyas, R.A., Sapuan, S.M., Ishak, M.R., Zainudin, E.S.: Development and characterization of sugar palm nanocrystalline cellulose reinforced sugar palm starch bionanocomposites. Carbohyd. Polym. **202**, 186–202 (2018). https://doi.org/10.1016/j.carbpol.2018.09.002

4. Sahari, J., Sapuan, S.M., Zainudin, E.S., Maleque, M.A.: Thermo-mechanical behaviors of thermoplastic starch derived from sugar palm tree (Arenga pinnata). Carbohyd. Polym. **92**(2), 1711–1716 (2013). https://doi.org/10.1016/j.carbpol.2012.11.031

5. Jumaidin, R., Sapuan, S.M., Jawaid, M., Ishak, M.R., Sahari, J.: Effect of seaweed on physical properties of thermoplastic sugar palm starch/agar composites. J. Mech. Eng. Sci. **10**(3), 2214–2225 (2016). https://doi.org/10.15282/jmes.10.3.2016.1.0207

6. Ibrahim, H., Farag, M., Megahed, H., Mehanny, S.: Characteristics of starch-based biodegradable composites reinforced with date palm and flax fibers. Carbohyd. Polym. **101**(1), 11–19 (2014). https://doi.org/10.1016/j.carbpol.2013.08.051

7. Edhirej, A., Sapuan, S.M., Jawaid, M., Zahari, N.I.: Cassava/sugar palm fiber reinforced cassava starch hybrid composites: physical, thermal and structural properties. Int. J. Biol. Macromol. **101**, 75–83 (2017). https://doi.org/10.1016/j.ijbiomac.2017.03.045

8. Soykeabkaew, N., Supaphol, P., Rujiravanit, R.: Preparation and characterization of jute-and flax-reinforced starch-based composite foams. Carbohyd. Polym. **58**(1), 53–63 (2004). https://doi.org/10.1016/j.carbpol.2004.06.037

9. Prachayawarakorn, J., Chaiwatyothin, S., Mueangta, S., Hanchana, A.: Effect of jute and kapok fibers on properties of thermoplastic cassava starch composites. Mater. Des. **47**, 309–315 (2013). https://doi.org/10.1016/j.matdes.2012.12.012

10. Sahari, J., Sapuan, S.M., Zainudin, E.S., Maleque, M.A.: Mechanical and thermal properties of environmentally friendly composites derived from sugar palm tree. Mater. Des. **49**, 285–289 (2013). https://doi.org/10.1016/j.matdes.2013.01.048

11. Lomelí Ramírez, M.G., Satyanarayana, K.G., Iwakiri, S., De Muniz, G.B., Tanobe, V., Flores-Sahagun, T.S.: Study of the properties of biocomposites. Part I. Cassava starch-green coir fibers from Brazil. Carbohydr. Polym. **86**(4), 1712–1722 (2011). https://doi.org/10.1016/j.carbpol.2011.07.002

12. Saw, S.K., Akhtar, K., Yadav, N., Singh, A.K.: Hybrid composites made from jute/coir fibers: water absorption, thickness swelling, density, morphology, and mechanical properties. J. Nat. Fibers **11**(1), 39–53 (2014). https://doi.org/10.1080/15440478.2013.825067

Analysis of Magnetorheological Elastomers Under Liquid Immersion

Wibowo, Novita Krismawati, Bhre Wangsa Lenggana, Ubaidillah[(✉)], Dody Ariawan, and Fitrian Imaduddin

Department of Mechanical Engineering, Faculty of Engineering, Universitas Sebelas Maret, Surakarta 57126, Indonesia
ubaidillah_ft@staff.uns.ac.id

Abstract. Magnetorheological elastomers (MRE) as intelligent materials are quite popularly used, both for indoor and outdoor applications that are often exposed to rain or sunlight depending on weather changes. In this case, the use of MRE material in outdoor use with exposure to freshwater and seawater needs further analysis. The analysis can then be used to evaluate the performance of the MRE. MRE specimens were molded in an isotropic state with vacuum treatment. Furthermore, the immersion treatment of the specimens was carried out for 6 weeks. In the 6-week immersion test, all specimens of material dissolution were dissolved, which was proven by a decrease in the percentage of absorption. The largest dissolution occurred in the 0%wt CIP heavy fraction specimen with seawater immersion treatment. In the hardness test of Durometer Shore A, both specimens of 0%wt CIP heavy fraction showed an increase in hardness, while in 70%wt CIP heavy fraction specimens, the opposite occurred. The greatest decrease occurred in specimens treated with freshwater immersion. The decrease in hardness can affect the stiffness of the material, resulting in a decrease in the damping function. The FTIR test showed that there were new peaks found in seawater immersion specimens.

Keywords: Magnetorheology · Absorption · Magnetorheological elastomers

1 Introduction

In this modern era, research in the field of materials is developing very rapidly. Mainly in the manufacture of new materials and the development of materials that are already available into materials that have more advantages than before. One of the advantages to be achieved is by creating materials that can be controlled according to needs or are often referred to as smart materials. For example, MRE is an intelligent material because its properties can be controlled using an external magnetic field [1].

MRE still has a wide range and scope to be developed and also more valuable product results. Some of the properties possessed and can be controlled by the magnetic field include stiffness, damping, and hysteresis [2]. These properties make MRE widely studied to be applied to vehicle shock absorbers [3], engine vibration dampers [4],

seismic vibration dampers in buildings [5], lateral vibration dampers on bridges [6] to its application in the marine field. In outdoor conditions, changes in temperature and humidity greatly influence the properties and durability of use [7]. As well as the use of MRE-based vibration dampers which are applied to bridges and in the marine sector. Exposure to high rain and seawater that contains salt are also factors in the durability of MRE materials.

Thus, the discussion related to the resistance of an MRE-based device to exposure to freshwater and seawater is a topic that needs further attention and evaluation. In fact, there are still not many MRE evaluations on the treatment of freshwater and seawater. Therefore, this paper will make a good contribution to the application of MRE-based devices in outdoor conditions.

2 Methodology

2.1 Sample Preparation

In general, the process of making MRE is by mixing the matrix with particles in the form of magnetic particles. For example, in the manufacture of silicon matrix MRE. The silicon matrix consisting of parts A and B is added with filler material and then mixed by stirring for a while. Then the mixture is poured into the prepared mold [8].

The curing process is divided into isotropic and anisotropic. Isotropic contains randomly distributed particles, while anisotropic particles make the particle content more organized [9]. The anisotropic process is proven to tighten the distance between magnetic particles compared to the isotropic process. In addition, it can strengthen the bonds between particles, which results in an increased sensitivity as the applied magnetic field increases.

2.2 Freshwater and Seawater Immersion

After the sample was finished fabricating, then the sample was given an immersion treatment before being tested hard and FTIR. MRE samples were soaked at room temperature for 6 weeks without any other treatment. This test followed the standard ASTM D-570 procedure. MRE samples were prepared in the form of chips with a diameter of 50.8 mm with a thickness of 3.2 mm.

2.3 Hardness Testing and FTIR

After the immersion treatment of freshwater and seawater is applied to the sample, then the sample is tested for hardness and FTIR to determine changes in the properties that occur in the sample. The hardness test was carried out by testing the shore A durometer. Meanwhile, the FTIR test was carried out using the Shimadzu tester with a wavelength of $4000 – 400$ cm^{-1}.

3   Result

3.1   Durometer Shore a Hardness Testing

Hard testing was carried out on the specimens before and after being given immersion treatment for 6 weeks. The hard test was carried out using the ASTM D2240 standard with the selection of shore A testing equipment.
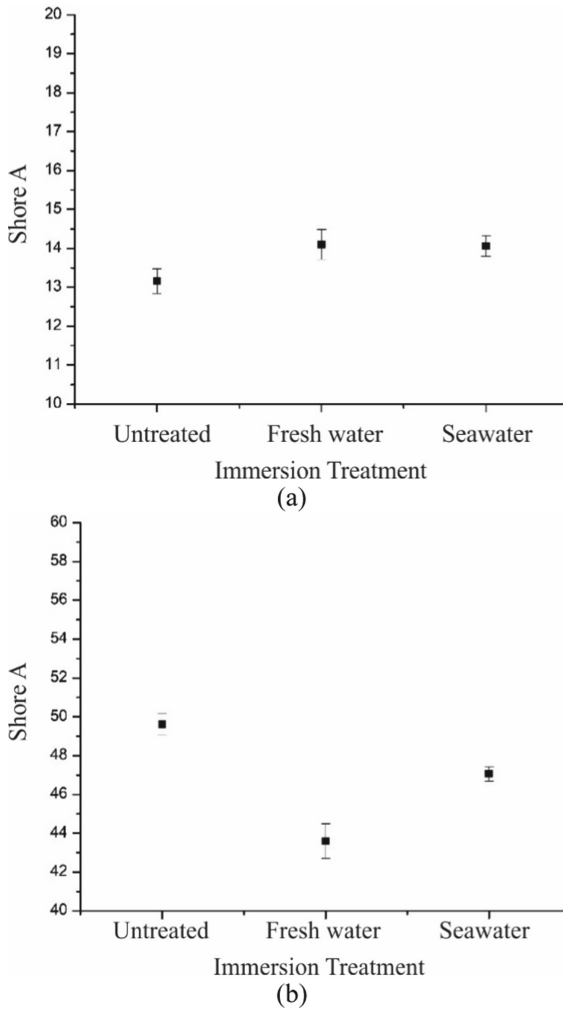
Fig. 1.   MRE sample hard test results; (a) 0%wt CIP; (b) 70%wt CIP.

The test was carried out at 5 different points then the results of the test were processed into a graph so that the differences between the test specimens could be seen.

In testing the hardness of the 0%wt CIP sample as shown in Fig. 1(a), the hardness of the sample before immersion is 13.1 A. After soaking for 6 weeks, the yield on the fresh water immersion sample was 14.1 A and the result of the seawater immersion was 14 A. From the two immersion samples, it was seen that there was an increase in the hardness of the silicon matrix material.

The 70%wt CIP sample, Fig. 1(b), result of hardness measurements in the sample before immersion was 47.6 A. After immersion within 6 weeks the result obtained on immersion specimens using freshwater was 43.6 A while in seawater immersion of 47 A. Based on the results obtained, it was seen that there was a decrease in the hardness of the 70%Wt CIP specimens in both freshwater and seawater immersion. This is inversely proportional to the results of immersion in the 0%Wt CIP sample.

3.2 Fourier Transform Infrared (FTIR) Testing

The FTIR test that has been carried out on the test samples produces data in the form of a graph of Wavelength (cm^{-1}) vs. %Transmission as shown in Fig. 2. The results of the interpretation will show the bonds formed on the test specimens as a result of immersion using fresh water and sea water. In the FTIR results, new absorption peaks were found, which were only found in specimens from seawater immersion. These peaks, among others, at 2853 are the absorption of the N-CH3 stretch bond and the 2921 peak which is a characteristic of the C-H stretch bond in the form of Methylene.
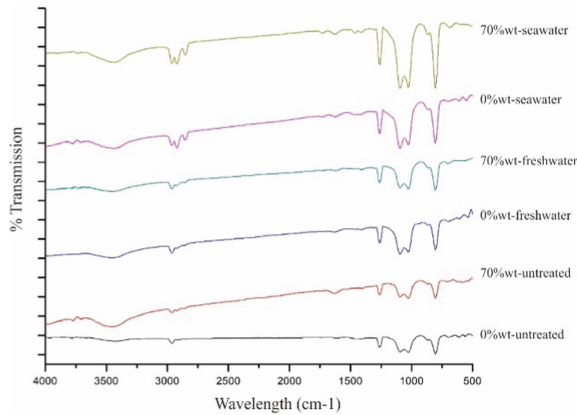
Fig. 2. FTIR result of MRE samples.

4   Conclusion

Durometer shore A tests and FTIR on MRE samples, both untreated and treated with freshwater and seawater immersion have been evaluated. The results show a fairly clear change. MRE samples immersed in seawater had the lowest resistance compared to other test samples. In addition, the content of 70%wt CIP affects the hardness of the material which tends to decrease compared to 0%wt CIP. The results of the FTIR test also found new peaks that were only owned by samples with seawater immersion.

References

1. Carlson, J.D., Jolly, M.R.: MR fluid, foam and elastomer devices. Mechatronics **10**, 555–569 (2000)
2. Cantera, M.A., Behrooz, M., Gibson, R.F.: Modeling of magneto-mechanical response of magnetorheological elastomers (MRE) and MRE-based systems: a review. Smart Mater. Struct. **26**, 023001 (2017)
3. Xin, F., Bai, X., Qian, L.: Principle, modeling, and control of a magnetorheological elastomer dynamic vibration absorber for powertrain mount systems of automobiles. J. Intell. Mater. Syst. Struct. **28**(16), 2239–2254 (2016)
4. Kavlicoglu, B., Wallis, B., Sahin, H., Liu, Y.: Magnetorheological elastomer mount for shock and vibration isolation, vol. 7977, no. 775, pp. 1–7 (2011)
5. Sun, S., Yang, J., Du, H., Zhang, S., Yan, T.: "Development of magnetorheological elastomers – based tuned mass damper for building protection from seismic events. J. Intel. Mater. Syst. Struct. **29**(8), 1777–1789 (2018)
6. Zhao, L., Yu, M., Fu, J., Zhu, M., Li, B.: A miniature MRE isolator for lateral vibration suppression of bridge monitoring equipment: design and verification. Smart Mater. Struct. **26**(4), 047001 (2017)
7. Lian, C., Lee, K.H., Lee, C.H.: Effect of temperature and relative humidity on friction and wear properties of silicone-based magnetorheological elastomer. Tribol. Trans. **61**(2), 238–246 (2018)
8. Khanouki, M.A., Sedaghati, R., Hemmatian, M.: Characterization of Magneto-Mechanical Properties and Quasi-Static Physical Modelling of MR Elastomers, no. January, pp. 1–9 (2019)
9. Ubaidillah, Sutrisno, J., Purwanto, A., Mazlan, S.A.: Recent Progress on Magnetorheological Solids: Materials, Fabrication, Testing, and Applications, pp. 1–35 (2014)

Feasibility Study on a Fabrication Resin Transfer Molding Machine for Aircraft Part (Hinge) Application

Ahmad Fitri Faizee bin Sulaiman[1(✉)], Fatimah binti Abdullah[1], Edynoor bin Osman[1], S. A. Rashidi[2], and Gunawan bin Mohd Jais[3]

[1] Kolej Kemahiran Tinggi MARA Masjid Tanah (KKTMMT), Melaka, Malaysia
fitrifaizee@mara.gov.my
[2] Aerospace Malaysia Innovation Center (AMIC), Kajang, Malaysia
[3] Composites Technology Research Malaysia (CTRM), Malacca, Malaysia

Abstract. The Resin Transfer Molding (RTM) process is one of the fundamental fabrication methods in composite material fields in aerospace and non-aerospace industries. It is a designation for a technology where, in general, a fiber preform is placed in a closed mold leaving a gap to allow the resin to be injected and impregnate the fibers. While, traditionally in aerospace manufacturing, autoclave which is known as an expensive process is utilized in the curing process of the parts. Thus, out-of-autoclave (OOA) manufacturing techniques is seeking to replace the autoclaving with a new process without compromising the quality parts. In this study, a newly developed RTM machine that has temperature and pressure controllers is used to produce hinge aircraft parts as a trial. This RTM machine has successfully injected a good quality of hinge part with a weight reduction of about 50% compares to the commercial. In conclusion, the RTM process has strong possibilities to develop and design for aircraft manufacturing parts to meet the future demand of less expensive aircraft part manufacturing.

Keywords: Resin Transfer Molding · Aircraft parts · Autoclave

1 Introduction

RTM is one of the best methods for mass production of composite parts. In just 20 years from 1970 to 1990, the RTM process become more mature and has been generally applied to manufacturing individual parts and even entire bodies [1]. RTM represent a closed-cavity molding technique that offers good dimensional precision and surface quality for the manufactured components. A good design by RTM leads to fabricate three-dimensional near-net-shape complex parts, offering production of cost-effective structural parts in medium-volume quantities using low cost tooling [2]. Consequently, this processing promotes wide application of RTM in aerospace engineering products. There are various studies on RTM that have been conducted by other researchers before. among them from Zeyu, who has studied the RTM process to produce parts for vehicle components [2], some studies have made experiments on products that have been

produced from this RTM process [3] dan [4]. However, research on the latest design
to facilitate the RTM process is less studied in this field. Various factors are taken into
account in developing a new model for this RTM machine (by taking into account the
time-consuming and cost-consuming aspects and using local parts as components in
the manufacture of this RTM machine). The previous process to produce aircraft parts
requires a long time (curing process for prepreg material using autoclave takes 6 to 8 h
to cure), but by using this new RM machine, curing hours takes only 2 to 3 h for curing
process.

In aerospace manufacturing, prepreg layers is stacked on a tool to form a laminate,
enclosed in a vacuum bag assembly, and placed in an autoclave (pressurized oven).
As reported, Autoclaves involve significant costs for acquisition, operation, and tool-
ing, particularly for large parts [3]. Thus, the curing process by autoclave processing
should be replaced with the other technique that can reduce the production cost without
compromising the properties of the product. In simply says, out-of-autoclave (OOA)
manufacturing techniques are now being considered for future demand especially in
aerospace manufacturing. Therefore, this study focused on producing aircraft parts by
the newly developed RTM machines that could reduce manufacturing steps dependent
on an autoclave curing process.

2   Experimental Work

2.1   Materials Used

In this study, the matrix used was a special low viscosity (RTM 6-2) bi-component epoxy
system for resin transfer molding technologies from Hexcel company. The mixing ratio
used for the epoxy resin (Part A) and hardener (Part B) is 100:68.1. The reinforcement
used was a non-crimp fabrics (NCFs) carbon fiber supplied by Saertex company.

2.2   Equipment Used

Newly developed RTM is used to fabricate hinge of aircraft part as shown in Fig. 1. There
are seven main parts of the RTM machines include frame body, mixer tank, vacuum
pump, weight balance, pressure release valve, stirrer, and control box. The design for
this RTM machine, as shown in Fig. 2, is adaptable for the requirement of this project
which using resin RTM 6-2. Three phases add the heater, band heater (to heat resin
while mixing), flex heater (to heat resin at the tube from tank to mold), and bottom
heater (to maintain the heat while mixing and inject the resin). This RTM machine is
using a smaller mixing tank (5 to 7 kg capacity resin). The size part can produce around
0.5 to 3 m^2. Hence, in this study, hinge of aircraft parts is considered for fabrication.

2.3   Fabrication of the Hinge of Aircraft Part

For fabrication hinge process, firstly, a mold releasing agent (Frekote 700NC) was
applied onto hinge mold, then place in the preform NCF carbon fiber with 12 con-
struction plies [45°/−45°, 90°/−0°, 45°/−45°, 90°/−0° 45°/−45°, 90°/−0°, 90°/−0°,
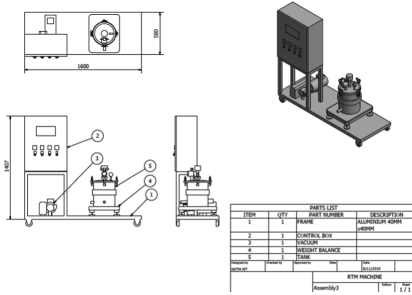
Fig. 1. CAD drawing for RTM machine.
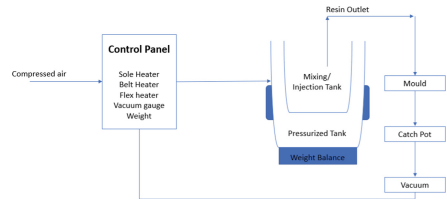
Fig. 2. Illustration of the injection machine workflow.

45°/−45°, 90°/−0°, 45°/−45°, 90°/−0°, 45°/−45°]. Closed the mold and applied vacuum. The vacuum test (leak test) was conducted to make sure all connectors fit properly and inside mold in vacuum condition and make sure the mold has no air leaking. Resin in mixing tank heated to 90 °C. Apply vacuum in the mixing tank to eliminate the bubble. This process is called degassing to ensure that the liquid injected from the mixing tank into the mold does not have bubbles. Meanwhile, the mold is heated to 120 °C to maintain the low viscosity as a requirement from the datasheet. When there is no leak, inject the resin into the mold 0.5 bar pressure. During the injection, slowly increase the pressure to 2 bar. When the cavity in the mold was fully filled, closed the outlet port from the mold and raised the pressure to 3 bar for the compacting process. After that, the temperature was increased to 180 °C for the curing process. The curing process will take 3 h. Finally, demold the product after it completely cured.

3 Result and Discussion

Before the fabrication process, RTM machine went through some testing to ensure that it has performed as desired. Therefore, blank mixing tank testing, liquid testing, and machine test are performed to ensure the effectiveness of this machine in producing the hinge of aircraft part.

As a results, the blank mixing tank test as shown in Table 1 show the condition of the booted mixing tank when it is in an empty state without any material in the tank. This test monitors the condition of vacuum, pressure, and heater part is functional as per requirement need. As for the liquid test, there is fluid in the mixing tank, and the liquid test is to ensure the absence of resin leaking, heat can be set up to 90 °C, and pressure in the mixing tank can be set up to 5 bar (refer to Table 2). These tests have shown that these two tests have proven that the whole parts in this mixing tank worked well.

For the Machine Test, these new RTM machines produced in this study give good results on the hinge of aircraft parts that have been produced (Fig. 3). Normally, the weight for the metallic hinge on the market is 214.4 g, while the product hinge built in this study is around 114.8 g (based on 12 construction plies made in this study). This study has shown that this machine has optimized injection parameters such as compacting pressure and resin flow rate. This will ensure to produce smooth resin penetration between the plies and avoid the formation of micro-bubbles.

Table 1. Blank mixing tank testing.

Blank mixing tank testing			
No.	Part name	Result	
1	Vacuum	0 mbar	PASSED
2	Pressure	Up to 5 bar	PASSED
3	Heater: bottom	Up to 100 °C	PASSED
4	Heater: up	Up to 100 °C	PASSED
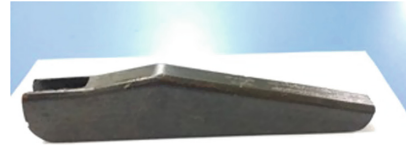
Fig. 3. Hinge product produced by newly developed RTM machine.

Table 2. Liquid testing.

Liquid testing				
No.	Functionality	Result		
1	Leak	0 mbar	PASSED	No leaking
2	Heat	Set heat to 90 °C	PASSED	No leaking during heating
3	Pressure	Up to 5 bar	PASSED	No leaking at mixing tank

4   Conclusion

High quality of NCFs carbon fibre hinge aircraft part were successfully fabricated by using the newly developed of RTM machine. Also, the NCFs carbon fibre hinge weight was reduced about 50% compared to existing metallic hinge in the market. However, further need regarding mechanical, physical as well as thermal properties on the hinge part must be studied and analyzed for future aircraft application. As a conclusion, the RTM process should be further deliberated to apply in aircraft manufacturing in line with out-of-autoclave manufacturing techniques for the cost reduction in total.

References

1. Taylor, T., Zhang, J., Yanagimoto, J.: Evaluation of a concept out-of-autoclave process for manufacturing carbon fibre reinforced polymer automotive parts. Proc. CIRP **86**, 162–166 (2020). https://doi.org/10.1016/j.procir.2020.01.030
2. Sun, Z., et al.: Preparation of high-performance carbon fiber-reinforced epoxy composites by compression resin transfer molding. Materials (Basel). **12**(1), 13 (2018). https://doi.org/10.3390/ma12010013
3. Jiang, L., Walczyk, D., McIntyre, G., Bucinell, R., Li, B.: Bioresin infused then cured mycelium-based sandwich-structure biocomposites: resin transfer molding (RTM) process, flexural properties, and simulation. J. Clean. Prod. **207**, 123–135 (2019). https://doi.org/10.1016/j.jclepro.2018.09.255
4. Vasudevan, A., Kumar, B.N., Depoures, M.V., Maridurai, T., Mohanavel, V.: Tensile and flexural behaviour of glass fibre reinforced plastic - Aluminium hybrid laminate manufactured by vacuum resin transfer moulding technique (VARTM). Mater. Today Proc. **37**(Part 2), 2132–2140 (2020). https://doi.org/10.1016/j.matpr.2020.07.573

Mixing Behaviour of Nickel and Titanium Hydride Mixture for Injection Moulding Process

Ros Atikah Abdul Kadir[1,4], Ab Aziz Mohd Yusof[2], Kamarliah Kamardin[2], Nor Shamimi Shaari[3,4], Mahfuzah Zainudin[3,4], and Muhammad Hussain Ismail[4(✉)]

[1] School of Mechanical Engineering, College of Engineering, Universiti Teknologi MARA, Cawangan Terengganu, Kampus Bukit Besi, 23200 Bukit Besi, Dungun, Terengganu, Malaysia
[2] College of Engineering (Mechanical), Universiti Teknologi MARA, Johor Branch, Kampus Pasir Gudang, 81750 Masai, Johor, Malaysia
[3] Advanced Mechanic Research Group, School of Mechanical Engineering, College of Engineering, Universiti Teknologi MARA Cawangan Pulau Pinang, Kampus Pulau Pinang, 13500 Kampus Permatang Pauh, Pulau Pinang, Malaysia
[4] Industrial Metallurgy Research Group (IMReG), School of Mechanical Engineering, College of Engineering, Universiti Teknologi MARA, 40450 Shah Alam, Malaysia
hussain305@uitm.edu.my

Abstract. Recently, porous nickel titanium (NiTi) made from nickel (Ni) and titanium hydride (TiH$_2$) has been used for biomedical implants such as staples due to its pseudo-elastic and shape memory behaviour. Many methods are available to produce porous NiTi such as casting, metal injection moulding process, and additive manufacturing process. The metal injection moulding is one of the famous methods in producing porous NiTi. To obtain a good flowability during the injection process, it is important to find the ideal powder loading before conducting the injection moulding process. In this paper, the critical powder volume percentage (CPVP) and mixing process were discussed to determine the optimum powder loading for the feedstock before conducting the metal injection moulding process. From the calculation, the critical powder loadings for 50.0 at% Ni and 50.4 at% Ni were 69.6% and 71.4%, respectively. The ideal powder loading should be 2% to 5% from the critical powder loading. Therefore, the ideal powder loadings for 50.0 at% Ni was 65.5 and 67.5% vol%, while the ideal powder loadings for 50.4 at% Ni was 67.5 and 69.5 vol% .

Keywords: Nickel titanium · Critical powder loading · Injection moulding

1 Introduction to Porous Nickel Titanium

Nickel titanium (NiTi) has many potential applications in the engineering industry. Due to its unique shape memory effect (SME) and pseudo-elasticity (PE), it can be used as an active, adaptive or a smart structure for biomedical applications [1]. It has been reported that most biomedical materials for bone implant research have been produced by powder metallurgy routes such as metal injection moulding (MIM) [2]. MIM is the best method to produce complex shapes and small parts because it can create a variety of components

from metal powders [3]. Most green parts cannot be injected well during the injection moulding process due to the lack of knowledge on powder loading value. To obtain a good flowability during the injection process, it is important to find the ideal powder loading to feed the powder into the barrel. Several methods can be used to determine the critical powder loading such as mixing torque analysis or critical powder volume percentage (CPVP), melt flow density approach, and viscosity versus composition [4]. In this study, CPVP was carried out to determine the critical powder loading before mixing the powder with binder to produce feedstock [5]. A successful injection moulding process could be achieved with a good understanding of powder mixture and the rheology behavior [6].

1.1 Methodology

In this study, the Ni atomic percent of 50 at% and 50.4 at% was used to investigate the optimum powder loading for each composition. The CPVP technique is a modification of ASTM D281-12 for the standard test of oil absorption [7]. During this process, oleic acid ($C_{18}H_{34}O_2$) was added together with Ni and TiH_2 into the Brabender mixer. The oil based oleic acid was added to the Brabender machine until the torque reading reached the highest peak. Powder loading is calculated using the optimum powder based on 2% to 5% of critical powder loading [8]. Oleic acid was dropped for 5 min alternately until the maximum torque value was reached. When the critical powder loading was achieved, the torque value started to decrease with the addition of powder The change of torque was recorded until the critical powder loading reached to a substantial decrease of torque. The CPVP then can be calculated using Eq. 1 as follows:

$$CPVP = 100 \times \frac{V_f}{V_0}$$

$$Vf = volume\ of\ oleic\ used\ at\ highest\ peak$$

$$V_0 = \frac{Weight\ of\ powder(g)}{Density\ of\ powder(g/cm^3)}$$

(1)

1.2 Results

During the CPVP technique, the torque development graph was plotted from the Brabender equipment as shown in Fig. 1:

Figure 1 shows that 12 mL of oleic was needed for 50.0 at% Ni, while 11 mL of oleic was needed for 50.4 at% Ni to achieve the maximum torque. From the calculation, the critical powder loadings for 50.0 at% Ni and 50.4 at% Ni were 69.6% and 71.4%, respectively. Then, two powder loadings were prepared from the CPCV value for each composition. As reported by German (1997), the ideal powder loading should be 2% to 5% from the critical powder loading [4]. Therefore, the ideal powder loading for 50.0 at% Ni were 65.5 vol% and 67.5% while the ideal powder loading for 50.4 at% Ni, it were 67.5 vol% and 69.5 vol%.

Next, the torque analysis was used to analyse the homogeneity of the feedstock throughout the mixing process. The analysis shows that high powder loading resulted in
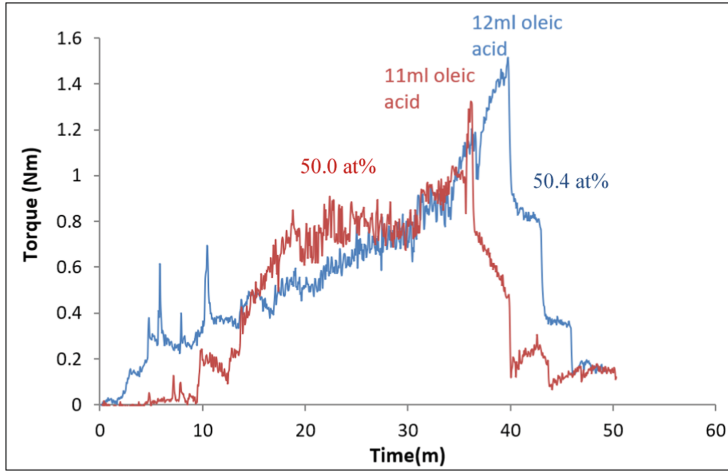
Fig. 1. Comparison of maximum torque and oleic acid used for 50.0 at% Ni and 50.4 at%Ni.

high maximum torque level. With the torque analysis, the homogeneity of the feedstock can be estimated correctly to avoid prolonged mixing process due to the deterioration of binder that produced the inhomogeneity of feedstock [10]. Figure 2 shows the three stages of mixing process: Stage 1, Stage 2, and Stage 3.
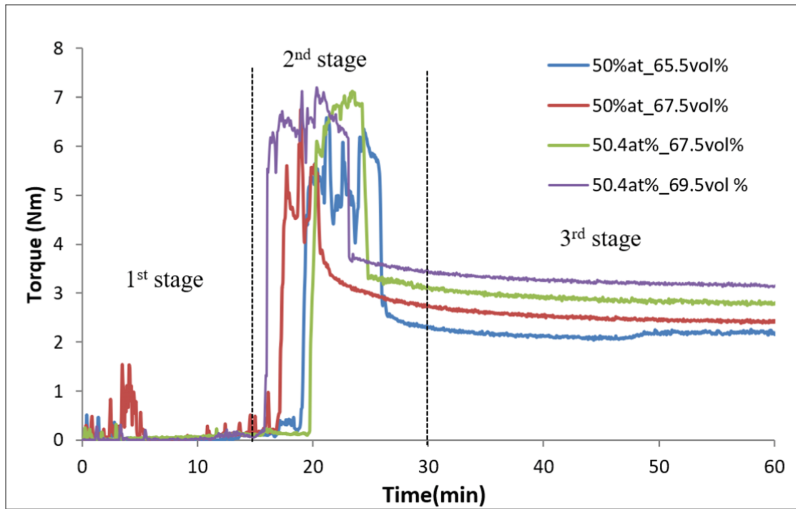
Fig. 2. Mixing behaviour at different compositions and powder loadings.

Stage 1 is the preliminary stage of mixing process that indicates the time required before achieving the maximum torque. During this stage, the powder and binder were fed into the mixer alternately until the maximum torque was achieved. It took about 15 min before it reached the critical torque value. For Stage 2, the torque peak represents

the loading of powder after the binder was fed into the mixer. Meanwhile, the stabilized torque after the peak corresponded to the friction caused only by the feedstock. The highest peak was obtained by 50.4 at% Ni (69.5 vol%), followed by 50.4 at% Ni (67.5 vol%), 50.0 at% Ni (67.5 vol%), and 50.0 at% Ni (65.5 vol%). The patterns of the torque values were consistent for all volume powder loadings.

Powder loading significantly affected the torque values where the torque value increased with the increasing of powder loadings [11]. This change was due to the greater friction as a result of greater amount of powder compared to binder; thus, extra force is needed for the blades to consistently mix a higher viscous mixture. For the powder loading of 69.5 vol%, more time was required for the mixture to achieve a steady torque variation compared to the other powder loadings. Stage 3 shows the time required for the feedstock to achieve steady torque value. Practically, the feedstock was continously mixed for 30 min to detect any torque changes during the process. No significant torque changes were detected at Stage 3, which indicates that the feedstock was homogenously mixed.

2   Conclusion

As conclusion, to obtain a good flowability during injection moulding process the preliminary observation such as critical powder loading observation, and torque analysis is important to obtain a homogenous mixture.

References

1. Bansiddhi, A., Dunand, D.C.: Shape-memory NiTi foams produced by replication of NaCl space-holders. Acta Biomater. **4**(6), 1996–2007 (2008). https://doi.org/10.1016/j.actbio.2008.06.005
2. Samarov, V., Seliverstov, D.: Fabrication of Near Net Shape Cost-Effective Titanium Components by Use of Prealloyed Powder and Hot Isostatic Pressing - Alamo Chapter (2015). http://www.asminternational.org/web/alamo-chapter/membership/join/
3. Hamidi, M.F.F.A., et al.: A review of biocompatible metal injection moulding process parameters for biomedical applications. Mater. Sci. Eng. C **78**, 1263–1276 (2017). https://doi.org/10.1016/J.MSEC.2017.05.016
4. German, A., Bose, R.M.: Injection Moulding of Metal and Ceramics (1997)
5. Zakaria, M.R.R., Yusuf, M., Ramli, M.I.: Determination of Critical Powder Loading of Titanium-Hydroxyapatite with Powder Space Holder for Powder Injection Molding Feedstocks/Mohd Yusuf Zakaria...[et al.] - UiTM Institutional Repository. https://ir.uitm.edu.my/id/eprint/38504/. Accessed 15 Sept 2021
6. Dehghan-Manshadi, A., StJohn, D., Dargusch, M., Chen, Y., Sun, J.F., Qian, M.: Metal injection moulding of non-spherical titanium powders: processing, microstructure and mechanical properties. J. Manuf. Process. **31**, 416–423 (2018). https://doi.org/10.1016/J.JMAPRO.2017.12.004
7. Stanimirovi, Z., Stanimirovi, I.: Ceramic injection molding. Some Crit. Issues Inject. Molding (2012). https://doi.org/10.5772/34660
8. Ali, M., Ahmad, F.: Influence of powder loading on rheology and injection molding of Fe-50Ni feedstocks. Mater. Manuf. Process. **35**(5), 579–589 (2020). https://doi.org/10.1080/10426914.2020.1734616

9. Randall, A.B., German, M.: Metal Powder Industries Federation (1997)
10. Supati, R., Loh, N.H., Khor, K.A., Tor, S.B.: Mixing and characterization of feedstock for powder injection molding. Mater. Lett. **46**(2–3), 109–114 (2000). https://doi.org/10.1016/S0167-577X(00)00151-8
11. Hidalgo, J., Jiménez-Morales, A., Torralba, J.M.: Torque rheology of zircon feedstocks for powder injection moulding. J. Eur. Ceram. Soc. **32**(16), 4063–4072 (2012). https://doi.org/10.1016/j.jeurceramsoc.2012.06.023

Influence of Zirconia Content to the Mechanical Behaviour of Alumina Zirconia Composite Prepared via Colloidal Method

Ananthan Soosai[(✉)], Sivakumar Sivanesan, Suresh Muniandy, and Teow Hsien Loong

Taylors University Lakeside Campus, No.1, Jalan Taylors, Selangor Darul Ehsan 47500 Subang Jaya, Malaysia

{ananthan.soosai,sivakumar.sivanesan,
suresh.muniandy}@taylors.edu.my,
teowhsienloong@sd.taylors.edu.my

Abstract. The Alumina zirconia composite was proposed in biomedical application to overcome the low temperature degradation and poor toughness experience by zirconia and Alumina, respectively. The main issue in developing zirconia-Alumina composite is the homogeneous of the microstructure in the powder mixing. In these studies, Alumina zirconia composite will be prepared by using colloidal method with different vol% of zirconia contain ranging from 5% to 20%. The specimen was tested for its hardness and fracture toughness. Hardness tested by using micro indentation method and fracture toughness by measuring the dimension of the radial crack on the sample induced by Vickers. The specimen with 10% zirconia content yielded the maximum fracture threshold value of 5.0 MPa. $m^{1/2}$.

Keywords: Alumina zirconia · Colloidal method · Mechanical properties

1 Introduction

Medical device that naturally interacts with human body without any harmful side effects is categorized as biomaterials [1]. The research and the development of the biomaterials are continuously evolving since past few decades. Since the first introduction of metal alloys in treating bone fracture by using as the plate to realign the bone, the type of material act as the biomaterial became variety such as metals (titanium alloys, stainless steel), ceramics (Alumina, zirconia, hydroxyapatite), composites made of carbon, polymers(silicone) and the list is growing [2]. The biomaterial is used to support the healing process (bone plates, screws), to improve function such as cardiac pacemaker or to align spinal rod.

Ceramics especially zirconia and Alumina have great potential in the biomedical field due to its superior compatibility to the human physiological environment. Alumina for instance, due to its excellent chemical and mechanical properties such as high melting point, low thermal expansion, high strength, high hardness, and good wear resistance [3]. These superior properties make alumina ceramics a suitable material for the manufacturing of ball valves, piston pumps or any advanced structural applications [4]. Zirconia

on the other hand, has been gaining popularity in the 1990s replacing alumina ceramics due to its brittleness [5, 6]. In addition, zirconia also possesses excellent mechanical properties among oxide ceramics mainly attributed to its special ability to transform [7–8]. Besides that, zirconia also has excellent dielectric properties and possesses stability at high temperature as its melting point is quite high at 2680 °C hence making it an important material for high temperature application such as in refractories or aerospace application [9]. Other than that, due to its chemical inertness and their aesthetic properties ceramics are very attractive to the dental implantations.

Alumina zirconia composites have been developed to constructively coupling their strength and produce a material with greater hardness, wear resistance and good strength for biomedical applications [10]. Alumina has its own weaknesses such as poor behavior against toughness and the other hand zirconia exhibits poorly in low temperature degradation. At the same time Zirconia exhibits superior mechanical properties and toughness which an important characteristic required for the material which to be used for biomedical applications [11]. In this work, the aim is to focus to the important role mainly to the processing parameters such as powder processing and forming method which determines the degree or dispersion of zirconia grains to yield the optimum mechanical properties [12–14]. To achieve this, the Alumina zirconia composite will be prepared by using colloidal method with different vol% of zirconia as the manipulated variable.

2   Methodology

Alumina powder (TM-DAR TAIMICRON) commercially available distributed by Taimei chemicals Co. Japan will be used to prepare the ZTA composite powder for investigation. At the preliminary stage, the Alumina powder will be dispersed in H_2O for a duration of 3 h by incorporating Alumina sphere (powder and sphere in the ratio of 1/6). Throughout the process, the pH value of the mixer to be maintain at 6.5. Next stage the dispersed Alumina will be added to the zirconium chloride aqueous as complexing agent with suitable volume to modify the pH without zirconium hydroxide precipitation. Then thermal treatment will be initiated to develop the desired ZTA composite. After thermal treatment, aqueous salt solution will be prepared by adding ammonium citrate as the complexing agent (A substance capable of forming a complex compound with another material in solution).

Ammonium citrate capable to maintain the pH of the salt solution without precipitation of zirconium hydroxide. After intense stirring about two hours, the formation of salt segregation will be prevented by diluting the suspension down to 4 volume percentage with spray drying. The drying process will be initiated by using drying machine with a two-fluid nozzle. After that, slip casting is done. For this process, the aqueous solution needed must be prepared with 65 volume percentage in solid phase and dispersion done by ball milling together with Alumina sphere. The optimum ratio for liquid: sphere is 1: 6. After the dispersion, polyethylene glycol (PEG 4000) will be added to yield better strength to the composite sample. High strength is needed to prevent any cracks formation during undergoing drying process. Sintering is a process of making a powder to be compact by using pressure or heat without changing the phase to liquid. The powder obtains from isostatic pressing and slip casting will be sintered at 1500 °C by using

electrical furnace by exposing to air. After natural sintering, Hot isostatic pressing (HIP) will be conducted to maintain the mechanical property and the density of the composite powder. The HIP will be done with the heating rate of 10 °C per minute. This done until the temperature reaches 1520 °C in a duration of 2 h. After that, microstructural studies will be conducted by using XRD curve to evaluate the type of phase content and followed by SEM imaging to investigate about the grain size. Image analysis was carried out on several SEM micrographs which enable to evaluate the alumina and zirconia grain size distribution. Micro indentation method to be used to analyze the hardness of the composite. The hardness measured by using the formula (1) below.

$$Hv = 1\,x\,10^3\,x\,\frac{P}{A_s} = 2\,x\,10^3 Px\,sin(\alpha/2)/d^2 = 0.0018544\,x\,p/d^2 \qquad (1)$$

where P = force in Newton, A_s = the surface area of the indentation, d = average diagonal length and the α = angle of indenter.

The Vickers indentation analysis will be conducted on the sample to evaluate the toughness of the sample against fracture due to crack growth. This is done by measuring the dimension of the radial crack on the sample induced by Vickers. The intensity crack growth (K_{10}) which measures the rate of crack growth can be determine by using the Eq. (2) as shown below.

$$K_{10} = \chi \cdot P \cdot c^{-3/2} \qquad (2)$$

where c = dimension of the crack, P = applied load and χ = constant.

Finally, the specimen will be tested for flexural strength.

3   Experimental Outcome and Discussion

3.1   Discussion

The greenbody developed by using slip casting technique reached the best high solid loading and less viscosity. The slip casting technique not only develope full densification to the composite, but high degree of homogeneity at microstructural level was achieved. This ensures the more smaller zirconia grains well dispersed and distributed without any gaps inside Alumina matrix which possess larger grain size atleast twice relative to the zirconia. The composite processing via colloidal method involves slip casting prove to be a better technique compare to normal powder processing via applying isostatic pressure in producing the composite. The Fig. 1 shows the SEM image of the four composites contains different volume percentage of zirconia from 5% to 20%.

By referring to the SEM image above, we able to evaluate the grain size and its dispersion between Alumina and zirconia of each specimen quantitatively. The mean size of Alumina and zirconia grain on each specimen was listed at the Table 1 below. According to the data below, it was concluded that the grain size of zirconia is directly correlated with amount of vol% content zirconia. But the grain size of Alumina is inversely proportional to amount of volume percentage content of zirconia. This is because of zirconia which compresses the grain growth of Alumina under beneath it. The more zirconia is available around the Alumina, the higher degree of compression will be exerted. The

a. ZTA5   b. ZTA10

c. ZTA15   d. ZTA20
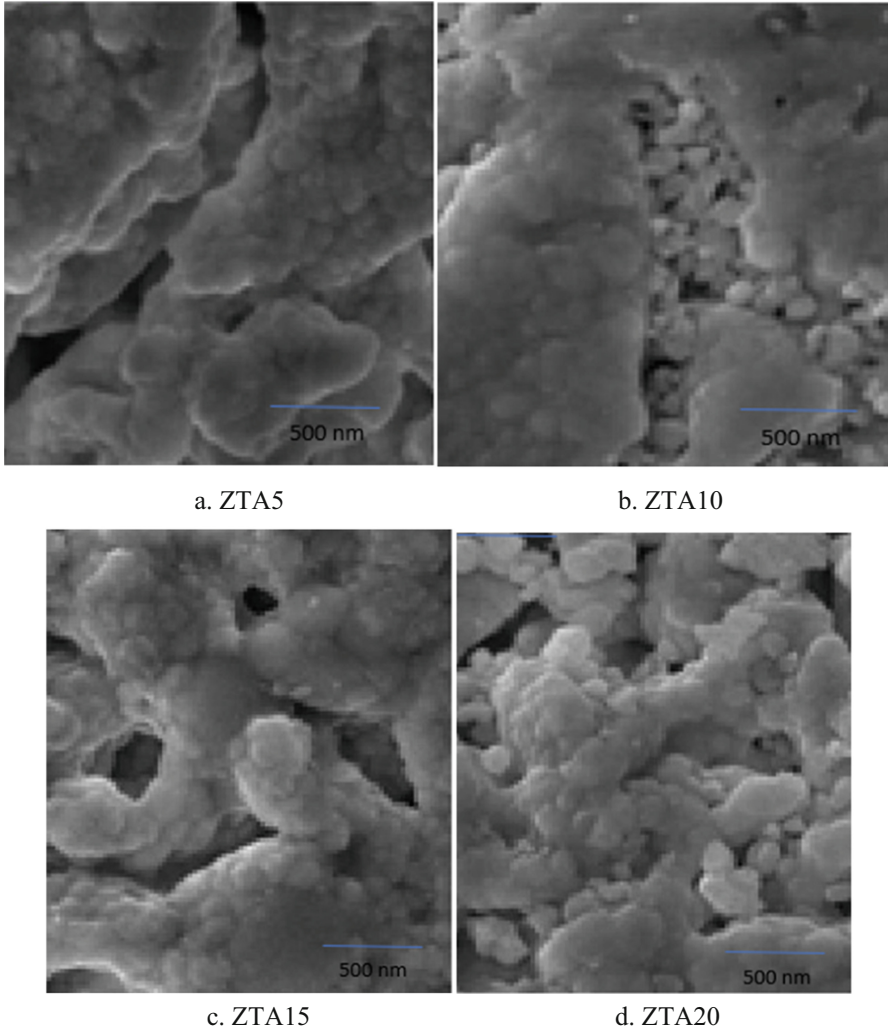
Fig. 1. SEM image of the four composites contains different volume percentage of zirconia from 5% to 20%.

opposite trend shown in the grain size of zirconia and Alumina as listed below clearly proves this pinning effect exerted by zirconia on the Alumina microstructure [15–17].

Referring to the Fig. 2, the XRD analyses was conducted to the four specimens from ZTA5 to ZTA 20 on the free surface on this composite substance after sintering. This is to evaluate the ratio between the tetragonal and monoclinic phase ratio. It's clear that the tetragonal phase is still exist in the zirconia due to its smaller grain size and the compressive stress induced by the stiffer Alumina matrix. The amount of monoclinic phase in the composite rises when the zirconia content increases. This is due to increase

a. ZTA5

b. ZTA10

c. ZTA15
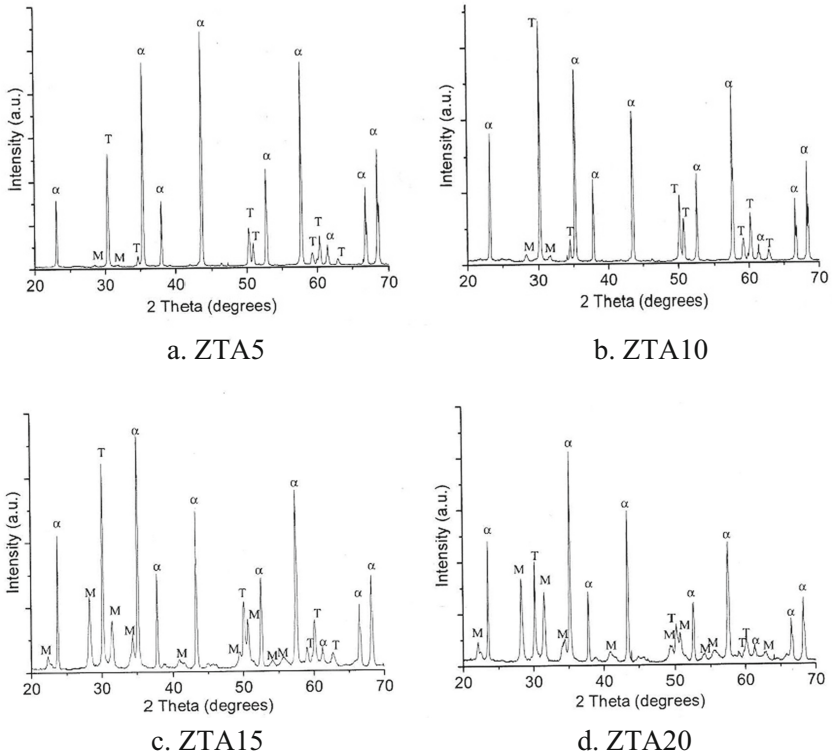
d. ZTA20

Fig. 2. XRD curve of the four composites contains different volume percentage of zirconia from 5% to 20%.

Table 1. The grain size of Alumina and Zirconia in the sample from ZTA 5 to ZTA 20.

Sample	Alumina grain size (nm)	Zirconia grain size (nm)
ZTA 5	840	240
ZTA 10	780	290
ZTA 15	710	290
ZTA 20	660	340

in the grain size of the zirconia causes higher zirconia fraction transforms its phase from tetragonal to monoclinic phase during cooling down after sintering.
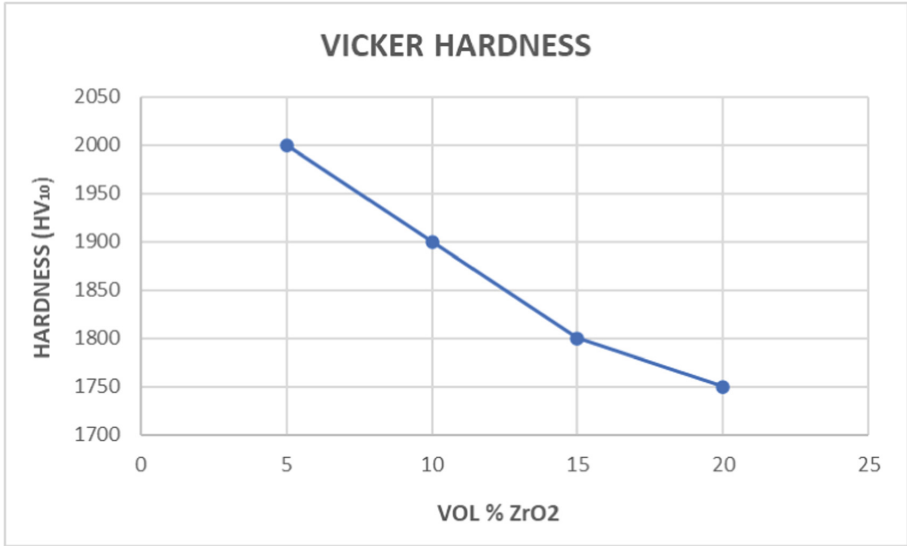
Fig. 3. Variation of Vicker hardness of ZTA vs Volume Percentage ZrO_2.

Referring to the Fig. 3, the Vicker hardness versus volume percentage content of zirconia from ZTA 5 to ZTA 20 was plotted. As the percentage content of zirconia decreases, the grain size increases which causes the hardness to decrease. This is due to hardness is solely dependent to the grain size and the interaction between the grain boundaries. Smaller the grain size, will yield greater hardness and brittleness to the composite. the indentation cracks become more significant shows reduction in the Vicker hardness. The length of the indentation cracks measured to evaluate the threshold K10 for slow crack propagation. K10 is a critical value where the crack velocity reaches the greatest drop close to zero which means no effective crack growth is detected The Fig. 4 shows how K10 value changes with volume percentage content of zirconia as the function. According to Aza et al. [18], the degree of fracture toughness of a composites is dependent to the pattern of the structure at microscopic level, the amount and the type of zirconia contain and the dimension of the grain of both Alumina and zirconia which populated the matrix. The amount of energy dissipated cause by the frictional crack is intensified with increase in grain size which contribute greater toughness. Unfortunately, when the grain size increases, the density of the microcrack increases which eventually weakens the material. According to the graph, the K10 value was minimal in ZTA5 which is 2.7 MPa. m1/2. This is due to insufficient amount of zirconia will prevent the transformation toughening at the crack tip to occur which eventually increases the stress at the tip results to poorer threshold value. The ZTA 10 achieved the maximum K10 value among all the specimen due to availability of sufficient zirconia grain able to react against the crack by transforming the phase from tetragonal to monoclinic which creates a compressive stress at the crack tip and eventually stops the crack growth velocity close to zero [19]. On the other hand. The increase in zirconia content more than 10% decreases the fracture toughness with lower K10 value. This happens due to excessive zirconia will

rise the brittleness of the composite; therefore, the rate or micro cracking formation out-weighs the transformation toughening which leads to greater crack growth velocity [20]. The composite with less than 10% volume percentage zirconia was exhibiting intergranular crack, a type of crack which progress along the grain border without piercing the grain. Meantime, composite with more than 10% volume percentage zirconia exhibited crack which was linear and trans granular. The brittle materials are normally exhibiting cracks that expands in trans granular method by piercing the grains. Overall ZTA10 exhibited the best hardness and fracture toughness among all the specimens.
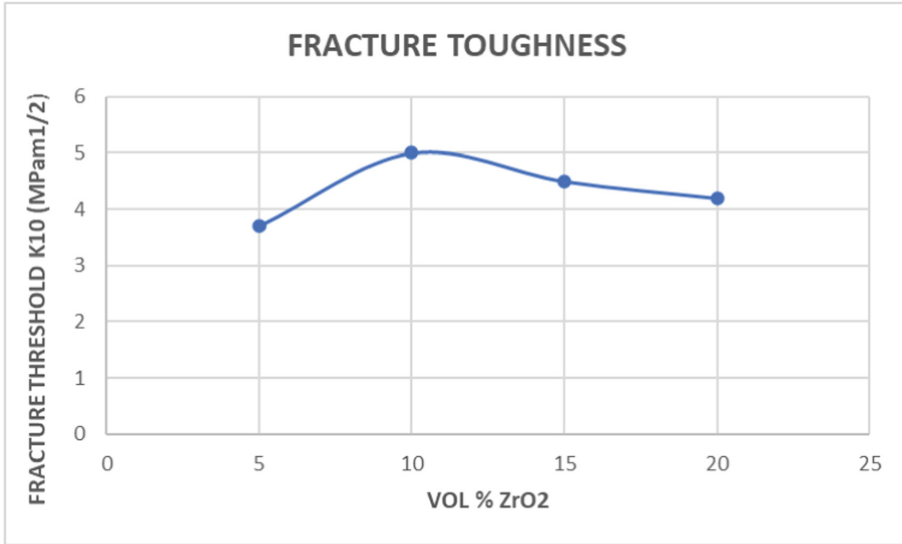
Fig. 4. Variation of fracture toughness of ZTA vs Volume Percentage ZrO_2.

Referring to the Fig. 5, Flexural strength also increases with increase in zirconia content. Zirconia is a type of ceramic which exhibits excellent mechanical properties among oxide ceramics. So, its coexistence with Alumina could overcome the weakness of Alumina which is the brittleness. The decrease in grain size of Alumina for higher zirconia content will cause the ratio of surface area to volume to be increased where greater grain boundaries to be dislocated thus strength increases. On top of this, its capability to transform the type of phase content when under stress contributes greatly to the toughness of the structure as well as flexural strength. The highest value of flexural strength exhibited by ZTA 20 reached up to 1250 MPa.
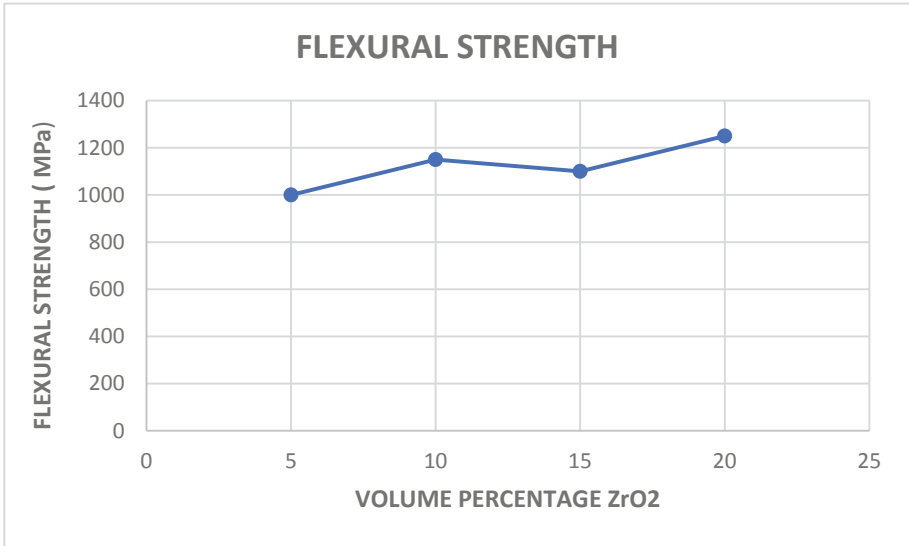
Fig. 5. Variation of flexural strength of ZTA vs Volume percentage ZrO_2.

4 Conclusion

In this work, Alumina zirconia composite was successfully developed by adapting to the colloidal method involving slip casting technique. In earlier discussion, it was predicted that to increase in the mechanical properties such as fracture toughness, flexural strength and Vicker hardness possess by the ZTA is highly dependent to the microstructure characters especially the grain size and the techniques used during the development of the composites. The coexistence of nano size zirconia on the bigger size Alumina grains results to the significant improvement in handling resistance towards slow crack growth and overall stability. The slip casting technique has improved the mechanical strength of ZTA significantly. The ZTA10 exhibited highest fracture threshold value up to 5.0 MPa. m1/2, good Vicker hardness and flexural strength, which was at 1900 Hv and 1100 MPa, respectively.

References

1. Ban, S., Sato, H., Suehiro, Y., Nakanishi, H., Nawa, M.: Biaxial flexural strength and low temperature degradation of Ceria -zirconia/alumina nanocomposite and Y-TZP as dental restorative. J Biomed. Mater. Res. B Appl. Biomater. **87**, 492–498 (2008)
2. Loong, T.S., Sivakumar, S., Namasivayam, S., Fouladi, M.H.: Effect of CeO_2 addition on slip cast Yttria tetragonal zirconia polycrystals toughened Alumina (ZTA). Scientific.net. **814**, 340–346 (2019)
3. Srdic, L.R.: Transformation toughening in sol-gel-derived alumina-zirconia composites. J. Am. Ceram. Soc. **80**(8), 2056–2060 (1997)
4. Namasivayam, S., Sivanesan, S., Loong, T.H., Fouladi, M.H.: Two stage sintering of Alumina-Y-TZP (Al2O3/Y-TZP) composites. Scientific.Net **814**, 12–18 (2019)

5. Piconi, C., Porporati, A.A.: Bioinert ceramics: zirconia and alumina. In: Antoniac, I.V. (ed.) Handbook of Bioceramics and Biocomposites, pp. 59–89. Springer, Cham (2016). https://doi.org/10.1007/978-3-319-12460-5_4

6. Ghalme, S.G., Mankar, A., Bhalerao, Y.: Biomaterials in hip joint replacement. Int. J. Mater. Sci. Eng **4**(2), 113–125 (2016)

7. Garvie, R.C., Hannink, R.H., Pascoe, R.T.: Ceramic steel. Nature **258**(5537), 703 (1975)

8. Turon-Vinas, M., Anglada, M.: Strength, and fracture toughness of zirconia dental ceramics. Dental Mater. **34**(3), 365–375 (2018)

9. Ferrage, L., Bertrand, G., Lenormand, P.: Dense yttria-stabilized zirconia obtained by direct selective laser sintering. Addit. Manuf. **21**, 472–478 (2018)

10. Sivanesan, S, Singh, R., Teow, H.L., Chuan, Y.L., Chin, J.K.: Leong effect of short time sintering on the mechanical properties of undoped zirconia ceramics. Scientific.net **629**, 420–425 (2014)

11. Azhar, A.Z.A., Mohamad, H., Ratnam, M.M., Ahmad, Z.A.: Effect of MgO particle size on the microstructure, mechanical properties, and wear performance of ZTA–MgO ceramic cutting inserts. Int. J. Refract. Metals. Hard Mater. **29**(4), 456–461 (2011)

12. Sivanesan, S., Teow, H.L., Singh, R., Niakan, A., Mase, N.: The effect of iron oxide on the mechanical and ageing properties Y-TZP ceramic. Scientific.net **701**, 250–254 (2016)

13. Tuan, R.Z., Chen, T.C., Wang, C.H., Cheng, P.S.K.: Mechanical properties of Al2O3/ZrO2 composites. J. Eur. Ceram. Soc. **22**, 2827–2833 (2002)

14. Leong, C.K., Sivanesan, S., Singh, R.: The governance of sintering regimes on the properties and ageing resistance of Y-TZP ceramic. Scientific.Net **545,** 81–87 (2012)

15. Teoh, H.L., Sivanesan, S., Eh Noum, S.Y.: Effect of Fe_2O_3 on the densification behaviour and mechanical properties of zirconia- toughened alumina (ZTA) composites prepared by two stage sintering. AIP.scitation.org. **2233**, 020–029 (2020)

16. Yoshimura, M.: Phase stability of zirconia. Am. Ceram. Soc. Bull. **67**(12), 1950–1995 (1988)

17. Sivakumar, S., Ramesh, S., Chin, K.L., Tan, C.Y., Teng, W.D.: Effect of sintering profiles on the properties and ageing resistance of Y-TZP ceramic. Int. J. Autom. Mech. Eng. **4**, 405–413 (2011)

18. Aza, C.G., Fantozzi, M., Schehl, R.T.: Crack growth resistance of alumina, zirconia and zirconia toughened alumina ceramics for joint prostheses. Biomaterials. **23**, 937–945 (2002)

19. Caravaca, C.F., Flamant, Q., Anglada, M., Gremillard, L., Chevalier, J.: Impact of sandblasting on the mechanical properties and aging resistance of alumina and zirconia based ceramics. J. Eur. Ceram. Soc. 38, 915–925 (2018)

20. Chen, H., Luo, L., Chen, J., et al.: Effects of zirconium element on the microstructure and deuterium retention of $W-Zr/Sc_2O_3$ composites. Sci. Rep. **6**, 32678 (2016)

Effect of Sintering Temperature and Low Weight Percentage of Zirconia in Hydroxyapatite-Zirconia Composite on Mechanical Properties for Biomedical Application

Suresh Muniandy[(✉)], Ananthan Soosai, Teow Hsien Loong, and Siva Kumar Sivanesan

Taylor's University, No.1, Jalan Taylors, 47500 Subang Jaya, Selangor Darul Ehsan, Malaysia
```
{suresh.muniandy,ananthan.soosai,
  sivakumar.sivanesan}@taylors.edu.my,
    teowhsienloong@sd.taylors.edu.my
```

Abstract. Zirconia (ZrO_2) powder from 1 weight percentage (wt%) to 5 wt% in comparison of wt% of Hydroxyapatite (HA) was added to form HA-ZrO_2 composites to produce HA-ZrO_2 composites that will exhibit desirable mechanical properties which can be useful in biomedical applications. Simple wet precipitation method was employed to produce HA and ZrO_2. Low wt% ZrO_2 of 1, 2, 3 and 5 wt% were used to prepare the composites which were pressureless sintered at 750 °C, 1050 °C and 1250 °C respectively for 2 h. Volume Fraction Porosity (VFP) was investigated and mechanical properties of Young's modulus and microhardness were used for evaluation. It was found that composite that consist of 1 wt% ZrO_2 sintered at 1250 °C showed the highest Young's modulus and microhardness as both corresponds to the lowest VFP. The Young's modulus and microhardness of this composite were found to be 100 GPa and 2.78 GPa respectively. This can be advantage in the field of orthopaedics in which implant materials have to withstand high stress.

Keywords: HA-ZrO_2 composites · Volume fraction porosity · Mechanical properties

1 Introduction

HA with chemical formula $Ca_{10}(PO_4)_6(OH)_2$ is a naturally occurring calcium phosphate mineral. The ratio of Ca/P in HA is 1.67 which is very comparable of that in human bones which varies from 1.3 to 2.0 [1, 2]. This makes implants and fillers that are made of HA very biocompatible and bioactive [3]. Furthermore, HA is the only apatite member that is stable when it comes to in contact with human tissues [4]. Unfortunately, owing to its inferior mechanical properties like fracture toughness and tensile strength [5], HA cannot largely and directly be used in biomedical field as transplant material in areas

where large stress is applied like in hip joints. It can be only used in areas where high stress is not needed like the auditory ossicles fine bones in the middle ear [6, 7] and as implant materials to enhance bone growth [8].

To capitalize the full potential of HA as replacement for bone related transplant materials, HA can be reinforced with a second-phase material that can help to elevate the mechanical properties. This material should not compromise the overall biocompatibility and bioactivity when made as an implant. ZrO_2 has gain interest among researchers as it possesses high fracture toughness and strength [9, 10] and furthermore ZrO_2 is also bioinert [11]. HA-ZrO_2 composites have received much attention due to their combination of the desirable mechanical properties of ZrO_2 and the excellent bioactivity of HA [12].

The major challenge in producing HA-ZrO_2 composites that is useful in orthopedic field as bone implant is that, ZrO_2 requires high sintering temperature (>1500 °C) [13] to fully densify but in such high temperature like this (>1350 °C), HA will undergo decomposition from primary to secondary phases such as α-tricalcium phosphate (α-TCP), β-tricalcium phosphate (β-TCP) and calcium phosphate (CaO) which are brittle minerals and directly decreases the mechanical properties of HA-ZrO_2 composites [14]. Samples sintered below 750 °C will show poor densification with open porosities as high as 50%, as the no reaction between HA and ZrO_2 (17). This has huge negative impact on the mechanical properties. For these reasons, sintering temperature was chosen between 750 °C and 1250 °C.

The objective of current investigation is to discover the favourable sintering temperature and wt% of ZrO_2 in HA-ZrO_2 that will reveal desirable Young's modulus and microhardness and hence will be useful in biomedical applications.

2 Experimental

2.1 Preparation of HA Powder

HA was prepared by precipitation of calcium nitrate tetrahydrate with diammonium hydrogen phosphate (Taimei Chemicals Co., Japan), taken in the molar ratio of 1.67, above pH of 10 [15]. The reaction is shown in Eq. (1):

$$10Ca(NO_3)_2.4H_2O + 6(NH4)_2HPO_4 + 8NH_4OH \rightarrow Ca_{10}(PO_4)_6(OH)_2$$
$$+20NH_4NO_3 + 20H_2O \tag{1}$$
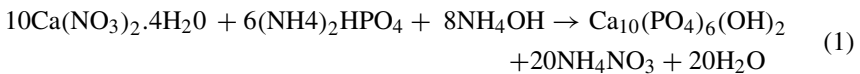
2.2 Preparation of Zirconia Powder

Zirconium oxychloride (Tosoh, Japan) was dissolved in distilled water and the transparent solution that was produced was made to react with ammonia while incorporating dropwise ammonia solution [16, 17]. Constant stirring and care was taken to maintain the pH at 8. The precipitate was then let to stand for 24 h at room temperature, and then centrifuged at 8000 rpm for 300 s. Pure zirconium dioxide was formed, and it was calcined at 600 °C for 6 h to produce monoclinic zirconia. The reactions are shown Eqs. (2) and (3).

$$ZrOCl_2 + NH_4OH \rightarrow Zr(OH)_4 + 2NH_4 \tag{2}$$

$$Zr(OH)_4 \rightarrow ZrO_2 + 2H_2O \tag{3}$$
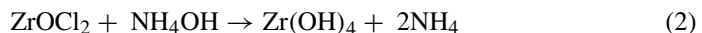
2.3 Preparation of HA-ZrO₂ Composite

ZrO_2 powder was taken as 1%, 2%, 3% and 5% by weight of HA. The two powders were then ball-milled for 3 h using zirconia balls as milling medium. The powder was then sun dried for 3 h. Eventually, the powder containing HA and ZrO_2 was compressed for 120 s at 35 MPa to form pellets [16]. The pellets were then sintered in furnace at 750 °C, 1050 °C and 1250 °C at the rate of 5 °C/min.

2.4 Determination of Volume Fraction Porosity (VFP)

Fluid displacement method was applied to determine VFP of the sample. First the dimensions of the sample were measured in order to calculate the bulk volume, V_b. Then the dry weight, W_d of the sample is measured in air. This is followed by vacuum saturation with water to ensure water fills up all the pore spaces and no air is trapped in the sample. The sample was measured again to obtain its saturated weight, W_s. Therefore, weight of water, W_w in pore spaces is given by $W_w = W_s - W_d$. To calculate the pore volume, V_p, Eq. (4) was used.

$$V_p = \frac{W_w}{\rho_w} \tag{4}$$

where ρ_w is density of water since water was used as the soaking medium.

Volume fraction porosity (VFP), was calculated by the Eq. (5).

$$\text{VFP} = \frac{V_p}{V_b} \tag{5}$$

2.5 Young's Modulus, E

Young's modulus which is measurement of stiffness of a material was determined by using ultrasonic pulse-echo technique (GrindoSonic: MK5, "Industrial", Belgium). The Eq. (6) was used to determine Young's modulus [18],

$$E = \frac{\rho(3V_l^2 - 4V_t^2)}{((V_l^2)/(V_t^{(2)}) - 1)} \tag{6}$$

where ρ = density of the sample, V_l = longitudinal sound velocity, V_t = transverse sound velocity.

V which is the velocity of ultrasound in the sample can be calculated by using Eq. (7).

$$V = \frac{2L}{t} \tag{7}$$

where L = thickness of the sample, t = time taken for ultrasound wave to travel back and forth in the sample which can be determine with the help of a calibrated cathode ray oscilloscope.

2.6   Microhardness, H_v

Hardness is the ability of the material to resist deformation when it is subjected to either mechanical indentation or abrasion. Equation (8) was used to calculate microhardness.

$$Hv = 1.85\frac{F}{d^2} \tag{8}$$

where F = applied force and d = mean diagonal length of the indenter.

The hardness of the samples was measured by a Vickers hardness tester (Shimadu, Japan). In this study, samples sintered at 1050 °C and 1250 °C were indented with a load of 120 N for 10 s and samples sintered at 750 °C were indented at 80 N for 10 s [19]. Only low loads were used to prevent cracking from the diagonal corners. After the load is removed, the impression that appears on the sample is a square of two diagonals having similar lengths. The two impression diagonals were measured with a built in filar micrometer attached to the microscope in the Vickers machine which is calibrated to the nearest 0.1 µm. These two readings were then averaged.

2.7   Surface Characteristics Studies of Samples by SEM

The surface characteristics of all the samples were investigated by using Philips XL30 scanning electron microscope (SEM). To produce clearer images, each sample was gold coated to create a thin conductive layer on the sample that obstruct charging hence reduces thermal destruction.

3   Results and Discussion

3.1   Analysis of Mechanical Properties

Figure 1, distinctly indicates sharp increase in VFP with decreasing temperature. All samples sintered at 750 °C showed the highest VFP from 0.51 for 1 wt% to 0.54 for 5 wt%. Lowest VFP was recorded for all samples sintered at 1250 °C compared to samples sintered at 750 °C and 1050 °C. 1 wt% ZrO_2 sintered at 1250 °C recorded the smallest VFP of 0.10. These results shows that sintering temperatures of 750 °C and 1050 °C are insufficient for densification [19]. These temperatures are still low for Ca^{2+} to be extracted from HA matrix by ZrO_2 which explains poor level of densification. At 1250 °C, Ca^{2+} of HA matrix diffuses well into ZrO_2 which causes VFP to be reduced. With increased amount of wt% ZrO_2, decomposition of HA to TCP can occur which enhances porosity. XRD analysis will be done in the future to verify this.

Based on Fig. 2, high sintering temperature is needed to produce higher E when the densification activity is relatively effective. 1 wt% ZrO_2 of VFP 0.10 at 1250 °C resulted value of E of 100 GPa which is the largest obtained. At 750 °C, E remains the lowest for all samples where densification did not take place. For temperatures 1050 °C and 1250 °C, E decreases with addition of wt% ZrO_2. This decrease is mainly due to well exchange of Ca^{2+} and ZrO^{2+} ions between HA and ZrO_2 that causes decomposition of HA [20]. The value of E is noticed to decline with amount of wt% ZrO_2 and with decreasing sintering temperature which corresponds with increase in VFP.
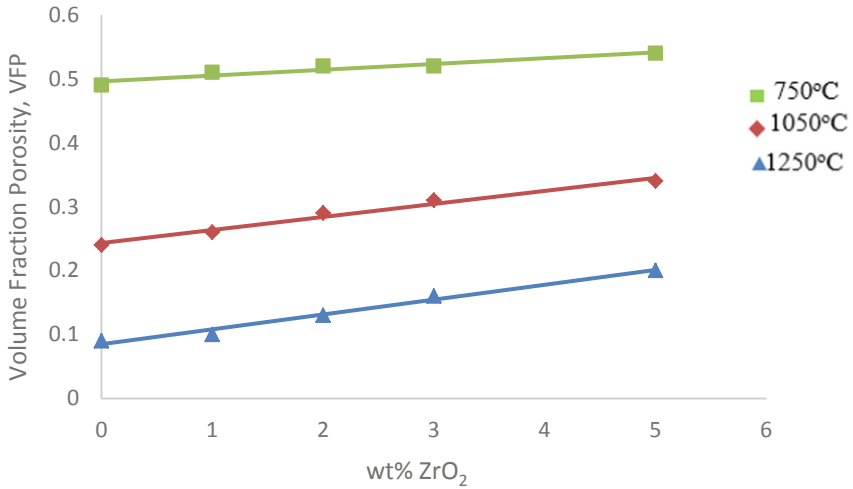
Fig. 1. Effect of different amount of wt% ZrO_2 on VFP for sintering temperatures of 750 °C, 1050 °C and 1250 °C.
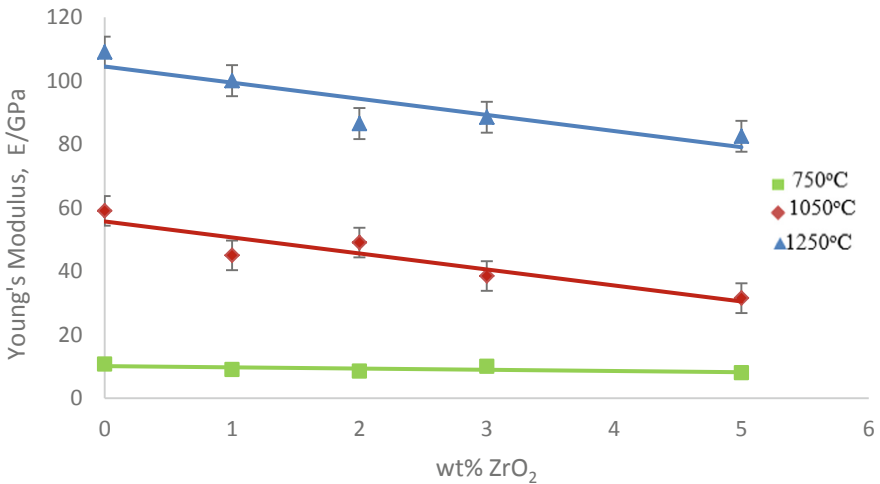
Fig. 2. Shows the relation between volume fraction porosity on Young's modulus.

From Fig. 3, the highest, H_v of 2.78 GPa is observed for sample of 1 wt% ZrO_2 sintered at 1250 °C. All samples sintered at 1250 °C recorded higher H_v compared other samples. The trends for 1050 °C and 1250 °C exhibits a downward shift in hardness with addition of wt% ZrO_2 which correlates with the increase of VFP [21].
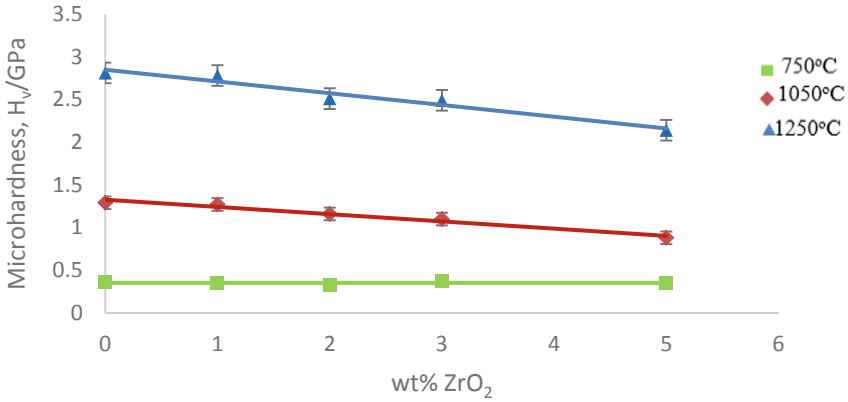
Fig. 3. Effect of microhardness with addition of wt% ZrO_2.

3.2 Distribution of Grains

Figure 4 are SEM micrographs of grain distribution in HA-ZrO_2 powder composites with different wt% ZrO_2 sintered at 1250 °C. SEM images were only done for composites sintered at this temperature because only these composites showed beneficial mechanical properties.
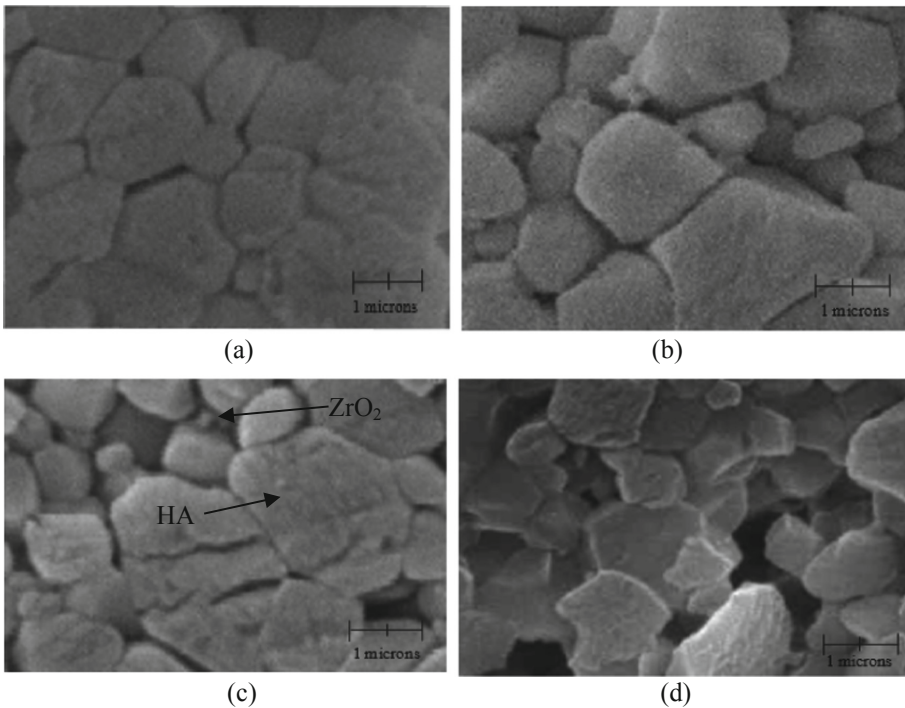
Fig. 4. SEM images of microstructure HA-ZrO_2 samples of (a) 1 wt% (b) 2 wt% (c) 3 wt% and (d) 5 wt% ZrO_2. Magnification at 10000X, EHT = 20.00 kV.

These SEM micrographs in Fig. 4 clearly shows presence of high porosity with increased amount of wt% ZrO_2. 1wt% and 2 wt% ZrO_2 shows a compact microstructure.

Presence of high amount of ZrO_2 grains in HA-ZrO_2 composite prevents the densification activity by shutting the diffusion channels along the outer limits of the HA structure and therefore hinders the exchange of ions between ZrO^{2+} and Ca^{2+} in the HA matrix [17].

4 Conclusion and Future Studies

The purpose of this study was to probe the influence of different sintering temperatures and wt% of ZrO_2 in HA-ZrO_2 that gives optimum Young's modulus and hardness. The HA-ZrO_2 composite with wt% 1 ZrO_2 sintered at 1250 °C showed desirable Young's modulus and hardness of 100 GPa and 2.78 GPa respectively. Lowest was observed for HA-ZrO_2 composite with wt% 5 ZrO_2 sintered at 750 °C with Young's modulus and hardness of 8 GPa and 0.33 GPa respectively. Sintering temperatures of 750 °C and 1050 °C are insufficient to cause densification whereas increasing amount ZrO_2 hinders the movement of ions, in which boundary migration becomes more effective compared to boundary diffusion.

Future studies will include effect of higher compressive stress (>35 MPa) and holding time (>120 s) on the formation of HA-ZrO_2 pellets together with wt% ZrO_2 less than 1% on the mechanical properties of HA-ZrO_2 samples.

References

1. Sheikh, Z., Drager, J., Zhang, Y.L., Abdallah, M.N., Tamimi, F., Barralet, J.: Controlling bone graft substitute microstructure to improve bone augmentation. Adv. Healthc. Mater. **5**, 1646–1655 (2016)
2. Maidaniuc, A., et al.: Induced wettability and surface-volume correlation of composition for bovine bone derived hydroxyapatite particles. Appl. Surf. Sci. **438**, 158–166 (2018)
3. Hench, L.L.: Bioceramics. J. Am. Ceram. Soc. **81**, 1705–1728 (1998)
4. Hench, L.L., Wilson, J.: Surface active biomaterials. Science **226**, 630 (1984)
5. Pan, Y., Chen, Y., Shen, Q.: Flexural mechanical properties of functional gradient hydroxyapatite reinforced polyetheretherketone bio composites. J. Mater. Sci. Tech. **32**, 34–40 (2016)
6. Shen, Z., Adolfason, E., Nygren, M., Gao, L., Kawaoka, H., Niihara, K.: Dense hydroxyapatite–zirconia ceramic composites with high strength for biological applications. Adv. Mater. **13**(3), 214–216 (2001)
7. Brzezinska-Miecznik, J., Haberko, K., Sitarz, M., Bucko, M.M., Macherzynska, B., Lach, R.: Natural and synthetic hydroxyapatite/zirconia composites: a comparative study. Ceram. Int. **42**, 11126–11135 (2016)
8. White, A.A., Best, S.M., Kinloch, I.A.: Hydroxyapatite-carbon nanotube composites for biomedical applications: a review. Int. J. Appl. Ceram. Technol. **4**(1), 1–13 (2007)
9. Yin, L., Nakanishi, Y., Alao, A., Song, X.: A review of engineered zirconia surfaces in biomedical applications. Proc. CIRP. **65**, 284–290 (2017)
10. Li, J., Wang, X., Lin, Y., Deng, X., Li, M., Nan, C.: In vitro cell proliferation and mechanical behaviors observed in porous zirconia ceramics. Materials **9**(4), 218 (2016)

11. Masonis, J.L., et al.: Zirconia femoral head fractures: a clinical and retrieval analysis. J. Arthroplast. **19**(7), 898–905 (2004)
12. Hannora, A.E., Ataya, S.: Structure and compression strength of hydroxyapatite/titania nanocomposites formed by high energy ball milling. J Alloys Compd. **658**, 222–233 (2016)
13. Sivanesan, S., Singh, R., Teow, H.L., Chuan, Y.L., Leong, J.K.C.: Effect of short time sintering on the mechanical properties of undoped zirconia ceramics. Scientific.Net. **629**, 420–425 (2014)
14. Pokhrel, S.: Hydroxyapatite: preparation, properties and its biomedical applications. Adv. Chem. Eng. Sci. **8**, 225–240 (2018)
15. Chevalier, J., Gremillard, L.: Zirconia as a Biomaterial, pp. 95–108. Elsevier, Amsterdam (2011)
16. Mariana, V.F., Nunes-Pereira, J., Sónia, M.P.: Microstructural, mechanical and biological properties of hydroxyapatite - CaZrO3 biocomposites. Ceram. Int. **45**, 8195–8203 (2019)
17. Curran, D.J., Fleming, T.J., Towler, M.R., Hampshire, S.: Mechanical properties of hydroxyapatite–zirconia compacts sintered by two different sintering methods. J. Mater. Sci. Mater. Med. **21**, 1109–112 (2010)
18. Ren, F., Case, E.D., Morrison, A., Tafesse, M., Baumann, M.J.: Resonant ultrasound spectroscopy measurement of Young's modulus, shear modulus and Poisson's ratio as a function of porosity for alumina and hydroxyapatite. Philos. Mazazine. **89**, 1163–1182 (2009)
19. Naga, S.M., et al.: Forsterite/nano-biogenic hydroxyapatite composites for biomedical applications. J. Asian Ceram. Soc. **8**(2), 373–386 (2020)
20. Nayak, Y., Rana, R.P., Pratihar, S.K., Bhattacharyya, S.: Pressureless sintering of dense hydroxyapatite-zirconia composites. J. Mater. Sci. Mater. Med. **19**, 2437–2444 (2008)
21. Mansour, S.F., Eldek, S.I., Ahmed, M.K.: Physico-mechanical and morphological features of zirconia substituted hydroxyapatite nano crystals. Sci. Rep. **7**, 1–21 (2017). https://doi.org/10.1038/srep43202

Fabrication and Wear Behavior of Alumina Based Cutting Tools on Machining AISI 1045

Abdul Aziz Adam[1], Hadzley Abu Bakar[2(✉)], Anis Afuza Azhar[2], Norfauzi Tamin[2], Umar Al-Amani[2], and Safarudin Gazali Herawan[3]

[1] Kolej Kemahiran Tinggi MARA Masjid Tanah, KM 1, Persiaran, Kampung Paya Lebar, 78300 Masjid Tanah, Melaka, Malaysia

[2] Fakulti Teknologi Kejuruteraan Mekanikal dan Pembuatan, Universiti Teknikal Malaysia Melaka, Hang Tuah Jaya, 76100 Durian Tunggal, Melaka, Malaysia
hadzley@utem.edu.my

[3] Industrial Engineering Department, Faculty of Engineering, Bina Nusantara University, Jakarta 11480, Indonesia

Abstract. The goal of this research was to fabricate an alumina-based cutting tool by powder metallurgy process. The process began with the compacting of spray dried alumina powders by using hydraulic hand press and Cold Isostatic Press in the form of round inserts. The alumina compacts were sintered at elevated temperature to form hard solidified structures. Machining trials were held with turning AISI 1045 cutting speeds between 200 m/min to 350 m/min with constant 0.15 mm/rev and 0.5 mm depth of cut. The results show that wear performance, the compacted alumina can machine AISI 1045 with a maximum tool life of 52 s at a cutting speed of 250 m/min. Because of the single particle packing without toughening, the sintered cutting tool exhibited brittle characteristics.

Keywords: Alumina · Powder metallurgy · Machining · Wear

1 Introduction

Machining is a manufacturing process that transforms the raw material into the desired shape. The process use cutting tools to remove unwanted materials by shearing the workpiece with engaging rotating parts in opposite direction. In the manufacturing industry, there are a lot of machines used to cut the stocks or parts through several operations such as turning, milling and drilling. Three important criteria for efficient machining process are properties of workpiece to be machine, the performance of cutting tool and the cutting parameters employed [1, 2].

Among the various collection of ready stock cutting tools in the industry, ceramic based cutting tool has been used widely for rough and finish machining. Ceramic, specifically, alumina (Al_2O_3) is used as a cutting tool as this type of material has very high strength that allows it to cut even the hardest materials. It is also reported that Al_2O_3 cutting tools are very good at producing fine surface finish quality on precision metal parts [3, 4].

In this study, Al_2O_3 based cutting tools have been fabricated with powder metallurgy processes and sintered at elevated temperature. Intention of the study focused on the wear

performance when machining with AISI 1045 with varied cutting speeds. Further, the alumina that possess highest density being machined with AISI 1045 to assess their capability in machining operation.

2   Methodology

Al_2O_3 powders were prepared in spray dried condition as shown in Fig. 1(a). The powders were ball milled for 12 h to avoid the risks of agglomeration (Fig. 1(b)). The ball milled powders then were inserted into the mold (Fig. 1(c)) and pre-pressed with the manual hydraulic press (Fig. 1(d)) and cold isostatic press (Fig. 1(e)) to form preliminary round shapes as shown in Fig. 1(f)).
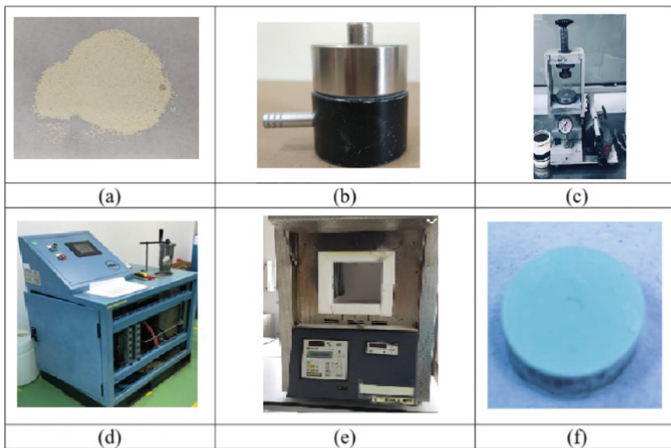
Fig. 1. The procedure to fabricate alumina based cutting tool.

Machining trials of the sintered alumina were held by using CNC turning machine as shown in Fig. 2. The evaluation of cutting tool performance were analyzed by wear progression process via optical microscopy observation.

Parameters	Unit
Cutting Speeds (m/min)	200,250, 300, 350
Feed Rate (mm/rev)	0.15
Depth of Cut	0.5 mm
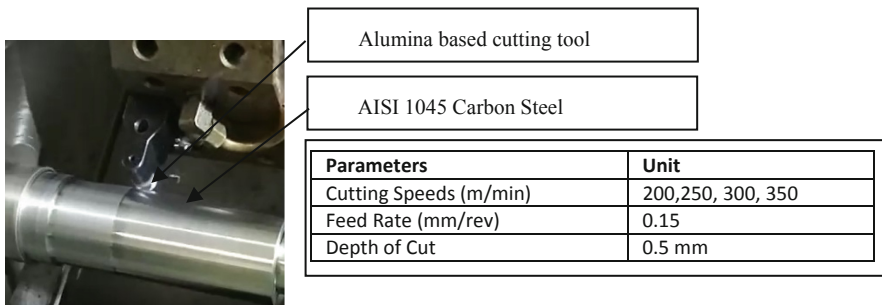
Fig. 2. Experimental setup and cutting parameters for machining trials.

3   Results and Discussion

Figure 3(a) shows effect of cutting speeds on flank wear for Al_2O_3 cutting tools at the feed rate of 0.15 mm/rev. Based on Fig. 3(a), at 200 m/min, only 30 s tool life recorded for the cutting tool to perform before it suddenly experienced breakage. When machining performed at 250 m/min, the tool life was increased to maximum 52 s. However, when the cutting speed increased to 300 m/min and 350 m/min, the tool life slightly decreased to 36 s and 48 s respectively. This shows that the fabricated cutting tool suitable to be applied at the cutting speed of 250 m/min for optimal condition machining performance.

Figure 3(b) shows the wear formation of Al_2O_3 cutting tool. The wear demonstrated that the notch wear continues to spread until it reached 0.3 mm tool life criterion within few second of machining. This shows that brittle characteristics of Al_2O_3 providing easy fracture at the contact region between cutting tool and workpiece. Inside the worn region, there are evidence of ridges formation inside the wear area. These parallel ridges prove that abrasive wear was dominant at the tool-chip interface [5, 6].
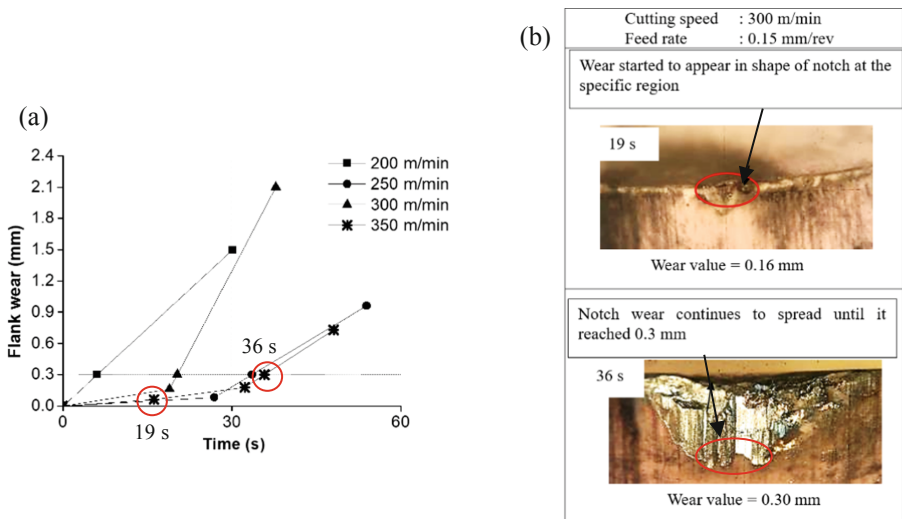
Fig. 3. (a) Development of flank wear for Al_2O_3 cutting tool at varied cutting speeds (b) Wear behavior of Al_2O_3 cutting tool at the 300 m/min cutting speed, 0.15 mm/rev and 0.5 mm depth of cut.

4   Conclusion

Fabrication of the alumina-based ceramic cutting tool via powder metallurgy processes was presented in this study. The cutting tools were machined with AISI 1045 within 200–350 m/min cutting speeds. Alumina cutting tool fabricated in this study demonstrating capability to machine AISI 1045 with maximum 52 s tool life at 250 m/min cutting speed. The cutting tool however demonstrated brittleness which capture early notch wear during materials engagement.

References

1. Kamely, M.A., Noordin, M.Y., Hashim, A.Y.B., Yahya, A.Y.: The performance of low cost cutting tools when machining hardened steel of 60 Hrc. J. Adv. Manuf. Technol. **6**(1), 1–12 (2012)
2. Xie, W., Fang, F.: Effect of tool edge radius on material removal mechanism in atomic and close-to-atomic scale cutting. Appl. Surf. Sci. **504**, 144451 (2020)
3. Liu, C., He, Y., Wang, Y., Li, Y., Wang, S., Wang, L., Wanv, Y.: Effects of process parameters on cutting temperature in dry machining of ball screw. ISA Trans. **101**, 493–502 (2020)
4. Dogra, M., Sharma, V.S., Dureja, J.: Effect of tool geometry variation on finish turning – a review. J. Eng. Sci. Technol. Rev. **4**(1), 1–13 (2011)
5. Lindvalla, R., Lenricka, F., Perssona, H., M'Saoubiab, R., EricStåhla, J., Bushlyaa, V.: Performance and wear mechanisms of PCD and PcBN cutting tools during machining titanium alloy Ti6Al4V. Wear **454–455**, 203329 (2020)
6. Mondal, B., Mandal, N., Doloi, B.: Development of Ce-PSZ-/Y-PSZ-toughened alumina inserts for high-speed machining steel. Int. J. Appl. Ceram. Technol. **11**, 228–239 (2014)

Mechanical Properties and Microstructural Properties of Zirconia Toughened Alumina Composite (ZTA) Doped with Copper Oxide Prepared via Various Sintering Profiles of Two-Stage Sintering

Teow Hsien Loong[✉], Sivakumar Sivanesan, Ananthan Soosai, and Suresh Muniandy

Taylor's University Lakeside Campus, 47500 Subang Jaya, Malaysia
teowhsienloong@sd.taylors.edu.my

Abstract. In this study, samples of Zirconia Toughened Alumina (ZTA) Composite with Y-TZP content between 0 to 20 vol% and 0.6 vol% copper oxide (CuO) were prepared and sintered via various sintering profiles of Two-Stage Sintering. The microstructural and mechanical properties such as bulk density, Vickers hardness, Young's modulus and fracture toughness of these samples were determined to investigate the efficacy of the sintering profiles employed. Based on the data obtained, ZTA containing 10 vol% Y-TZP content and 0.6 vol% CuO with a heating rate of 10 °C/min, T_1 1450 °C, T_2 1350 °C and holding time of 6 h were found to be the optimum sintering profile. The sample's grain size were reduced by >10% and mechanical properties were able to meet international standards such as ISO 6474 as the sample achieved full densification (>99%. T.D.), Vickers hardness, Young's modulus and fracture toughness of 18.5 GPa, 409 GPa and 8.1 MPam$^{1/2}$, respectively. This research could lead to development of ZTA composites with enhanced mechanical properties.

Keywords: ZTA · Zirconia · Alumina · Two-stage sintering

1 Introduction

ZTA or Zirconia Toughened Alumina Composite is an advanced ceramic material used in various industries due to its high mechanical properties and ability to resist ageing [1–4]. This composite consists of two phases which are the Alumina (Al_2O_3) as primary phase and Yttria-Tetragonal Zirconia Polycrystals (Y-TZP) as the secondary phase. This composite was developed a few decades back as a material to address the weakness of alumina and Y-TZP. One of the significant weaknesses of alumina is that it possesses low fracture toughness but has good ageing resistance as one of its' advantages. Y-TZP, on the other hand, has high fracture toughness but suffers from low-temperature degradation upon exposure to a hostile environment for a period of time [5–7]. ZTA composite, which consists of alumina and Y-TZP, exhibits excellent hardness from alumina, high

fracture toughness from Y-TZP and at the same time, possess excellent ageing resistance from alumina therefore, making this material of significant importance, especially in the biomedical field [8]. Many researchers have investigated the fracture toughness enhancement of ZTA composite compared to pure alumina. They concluded that the enhancement of fracture toughness of ZTA was due to the presence of tetragonal grains of Y-TZP in the composite matrix undergo stress-induced transformation toughening when there is an advancing crack [9–12]. Few researchers have linked the enhancement of ZTA's fracture toughness to other toughening mechanisms such as residual stresses and microcracking, in addition to stress-induced transformation toughening [13, 14]. As the grain size of the composite significantly affects its' mechanical properties, it is essential that at the final stage of sintering, the grain size of the composite should be kept small enough. Small grain size would prevent microcracks from forming, but the grain size should be large enough for the Y-TZP tetragonal grains to undergo stress-induced transformation toughening [15, 16]. Chen and Wang [17] have succeeded in producing a nanosized grain Y_2O_3 ceramic with no significant grain growth during the final stage of the sintering process. The authors employed a novel sintering method known as two-stage sintering (TSS). The material is sintered at a relatively higher temperature, rapid cooled to a lower temperature and held for a long time. Other researchers have also successfully employed this sintering technique to other ceramic materials resulting in ceramic material with improved densification. In addition, this sintering technique also resulting nanosized grains and successfully prevented significant grain growth at the final sintering stage [18–23]. In this study, the microstructural and mechanical properties of ZTA composites doped with 0.6 vol% CuO prepared two-stage sintering sintered in various sintering profile will be investigated.

2   Methodology

The as-received powders of commercially available pure alumina (Al_2O_3) by Sigma-Aldrich, USA, high purity Y-TZP powders by Kyoritsu, Japan and pure copper oxide (CuO) by Sigma-Aldrich, USA were used in this study. These powders have approximately 200 nm mean particle size, and based on the BET method, the specific surface area (SSA) determined to be 13 m^2/g. The Y-TZP content of the ZTA composite was varied between 0 to 20 vol%, and the CuO content was set at 0.6 vol%. The powders were prepared through 3 mm alumina ball milling for 24 h, then dried in an oven for 24 h to produce a filtered cake. The filtered cake is then crushed and sieved using 212 µm mesh to produce fine powders. These powders were then bench pressed into samples consist of 20 mm diameter disc and rectangular bar of 5 mm width, 5 mm height and 15 mm length. The pressed disc and bar samples were then pressed via Cold Isostatic Pressing (CIP) followed by two-stage sintering. The sintering profiles are shown in Table 1. The samples were sintered in a sintering furnace manufactured by ModuTemp, Australia using air as the sintering medium. After sintering, the sintered samples were ground on one surface using Silicon Carbide (SiC) papers graded from 120 to 1200, followed by polishing using the diamond paste of 6 µm and 1 µm to obtain a reflective surface for clear SEM images. The mechanical properties of the samples, such as bulk density, were measured using the Archimedes method (ASTM C373-00), and the hardness was

measured using the Vickers Indentation method. Young's modulus was measured using ASTM C769 standard, and its fracture toughness was determined using the equation proposed by Niihara et al. [24]. Using the scanning line intercept method on the SEM images obtained, the average grain size was determined. Ten measurements were taken at ten different random locations of the surface to improve the grain size measurement's accuracy.

Table 1. .

Sintering profiles	Heating rate (°C/min)	First stage sintering Temperature T_1 (°C)	Second stage sintering Temperature T_2 (°C)	Holding time (hours)
TSS 1	10	1400	1350	6
TSS 2	20	1400		12
TSS 3	10	1450		6
TSS 4	20	1450		12
TSS 5	10	1500		6
TSS 6	20	1500		12

3   Results and Discussions

Based on Fig. 1, only samples containing 10 vol% Y-TZP sintered via TSS 3 achieved density exceeding 99% T.D. There was lower bulk density observed for pure alumina samples as there was significant grain growth for alumina at the final stage sintering except for alumina sintered at TSS 3 and TSS 4. At TSS 3 and TSS 4, the alumina samples have better densification than the alumina sintered at other sintering profiles, and significant grain growth was observed, leading to inferior densification. The highest bulk density of 99.2% T.D. were recorded for ZTA with 10 vol% Y-TZP content sintered at sintering profile TSS 3. Other researchers have also observed similar observation which 10 vol% Y-TZP [25, 26] and 0.6 vol% Cuo [27, 28] are the optimum amounts for enhanced densification, and the CuO further aided the densification by filling the oxygen vacancies due to the existence of liquid phase at high temperature [28]. The reduction in relative bulk density observed as the Y-TZP content increases may be caused by the coefficient of thermal expansion (CTE) differences between the alumina and Y-TZP. The theoretical density of material represents its' actual density without the presence of pores. Lower relative density would indicate higher porosity in those materials, whereas higher relative density would indicate lower porosity. Relative bulk density above 99% T.D. indicates that the sintered body achieved full densification. A higher amount of porosity would cause a degradation of its mechanical properties, such as Vickers hardness and Young's modulus [29].

Figure 2 shows the Vickers hardness of the ZTA composites sintered via various sintering profiles of two-stage sintering. Similar to observation for bulk density, all
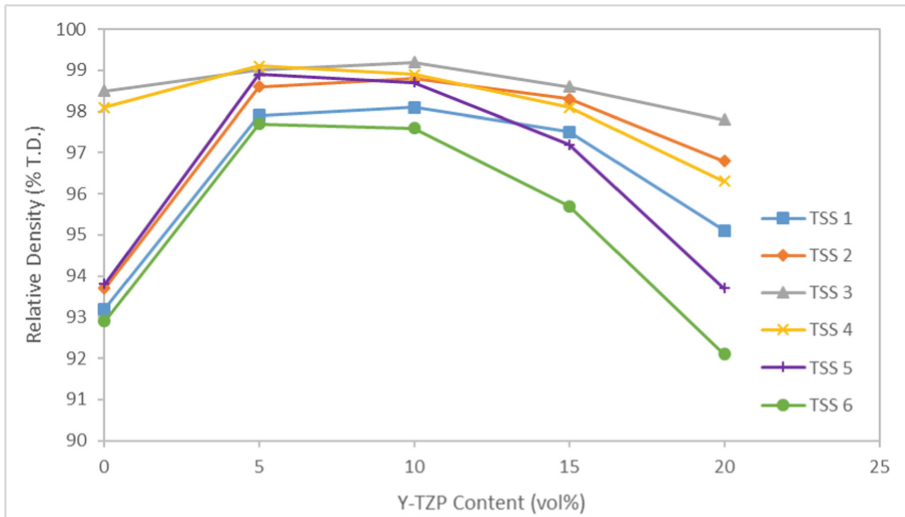
Fig. 1. Relative bulk density of ZTA composites doped with 0.6 vol% CuO sintered via various sintering profile of two-stage sintering.

samples containing 10 vol% Y-TZP and 0.6 vol% CuO content could achieve Vickers hardness up to 18.5 GPa when sintered at TSS3. As the Y-TZP content increases to 15 vol% and beyond, reduction in Vickers hardness can be observed mainly for samples sintered at TSS 1, TSS 5 and TSS 6. This observation of decreasing Vickers hardness can be observed in bulk density as well. This reduction of Vickers hardness is due to the influence of bulk density on hardness. Many researchers have also observed [18, 30] that the material bulk density heavily influences the material's Vickers hardness. Materials such as ceramic do not possess plastic deformation. Therefore, if any energy is transferred to the ceramic, the ceramic's inability to absorb any energy will advance the crack until the ceramic fractures.

Based on Fig. 3, the maximum value of Young's modulus recorded was 409 GPa which the sample contained 10 vol% Y-TZP and 0.6 vol% CuO sintered under sintering profile TSS 3. Figure 3 also shows a decreasing trend when the Y-TZP content increases to 15 vol% and above for all samples. This downward trend of Young's modulus can be attributed to the reduction of bulk modulus of the samples as porosity formed in the samples significantly reduced Young's modulus. The size and amount of pores formed may also overwhelm the amount of the CuO liquid phase, limiting the pores that the CuO liquid phase can fill, leading to higher vacancies. The presence of Y-TZP content up to 10 vol% have shown improved Young's modulus of the composite on samples sintered via TSS 1, TSS 2, TSS 3 and TSS 4 as it has successfully prevented significant grain growth of the alumina grains at the final sintering stage.
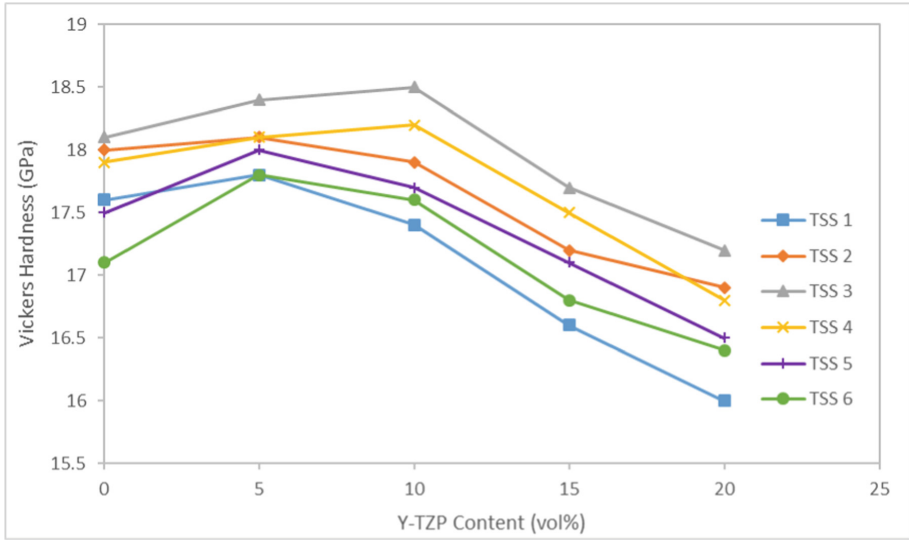
Fig. 2. Vickers hardness of ZTA composites doped with 0.6 vol% CuO sintered via various sintering profile of two-stage sintering.
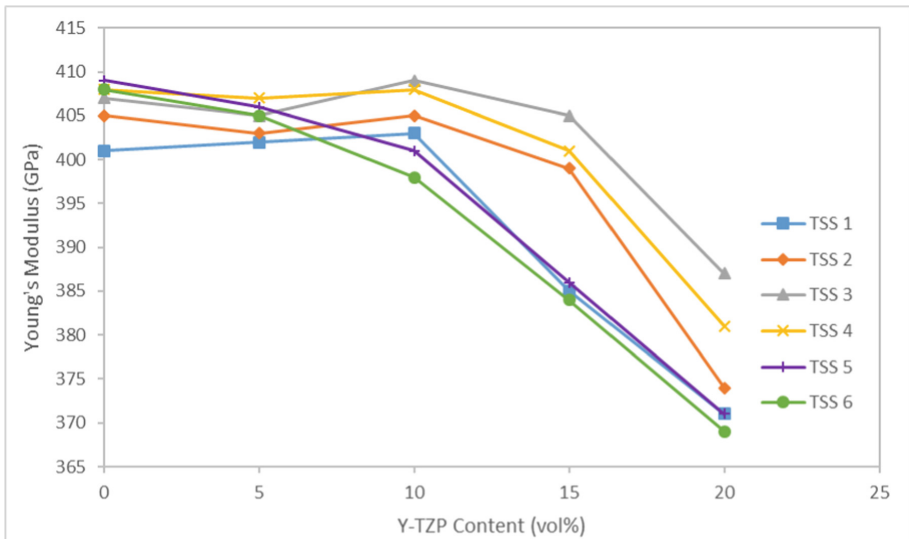
Fig. 3. Young's Modulus of ZTA composites doped with 0.6 vol% CuO sintered via various sintering profile of two-stage sintering.

Figure 4 shows the fracture toughness obtained from the samples. As shown in Fig. 4, alumina samples' fracture toughness fluctuated between 3 MPam$^{1/2}$ to 3.4 MPam$^{1/2}$. Pure alumina exhibits low fracture toughness in general. Therefore, the incorporation of Y-TZP into the alumina matrix has dramatically improved the composites' fracture toughness which after incorporation of Y-TZP content, the values were fluctuating between 3.9 MPam$^{1/2}$ to 4.8 MPam$^{1/2}$ regardless of sintering profiles. One striking observation is that at 10 vol% Y-TZP, 0.6 vol% CuO, the fracture toughness was significantly higher, which are 8.1 MPam$^{1/2}$ and 7.7 MPam$^{1/2}$ when sintering at sintering profile of TSS 3 and TSS 4, respectively. In agreement with the works of other researchers [18, 30], the authors have attributed this significant increase to the critical grain size of the composite. The critical grain size for 5 vol% Y-TZP content regardless of sintering profile and 10 vol% Y-TZP content sintered at sintering profile TSS 1 and TSS 2 are smaller than those samples containing 10 vol% Y-TZP content sintered at TSS 3 and TSS 4. On the other hand, the other samples, such as samples containing 15 vol% Y-TZP content and above, have grown, exceeding the critical grain size of 0.47 μm. This would lead to overstabilization of the tetragonal grain causing it to transform into monoclinic prematurely and unable to undergo stress-induced transformation toughening [31], resulting in lower fracture toughness. For a material such as Y-TZP, there is a critical grain size at every temperature. The closer the average grain size of Y-TZP to its critical grain size, the larger its transformation capability [32, 33].
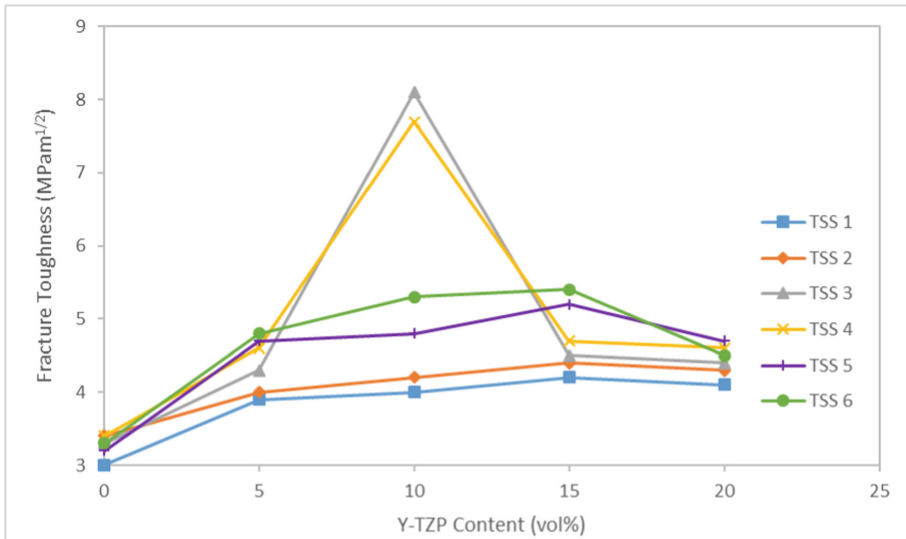
Fig. 4. Fracture toughness of ZTA composites doped with 0.6 vol% CuO sintered via various sintering profile of two-stage sintering.

The average grain sizes of the composite sintered at sintering profile TSS 3 and TSS 4 are as shown in Table 2. In a ZTA composite matrix, the Y-TZP tetragonal grain's ability to undergo stress-induced information toughening is greatly influenced by its' critical grain size. Tetragonal grains that are too large will not transform toughen as they

exceeded their critical grain size. Hence, to produce a composite with excellent fracture toughness, the tetragonal grain size must be as close as possible to its' critical grain size. Figure 5a shows the SEM images of ZTA composite containing 10 vol% Y-TZP and 0.6 vol% CuO sintered via TSS3. In contrast, Fig. 5b shows the SEM images of ZTA composite containing 20 vol% Y-TZP content sintered via TSS6, indicating a significant grain growth and pores which may be detrimental to the bulk density and mechanical properties.

Table 2. Alumina and ZTA composites' average grain size sintered via TSS 3 and TSS 4 sintering profile.

Y-TZP content (vol %)	Average grain size (μm)					
	TSS 1	TSS 2	TSS 3	TSS 4	TSS 5	TSS 6
0	0.76	0.80	0.82	0.89	0.93	0.97
5	0.36	0.39	0.40	0.45	0.51	0.54
10	0.43	0.45	0.48	0.49	0.54	0.56
15	0.51	0.52	0.53	0.55	0.58	0.61
20	0.52	0.55	0.57	0.64	0.63	0.66
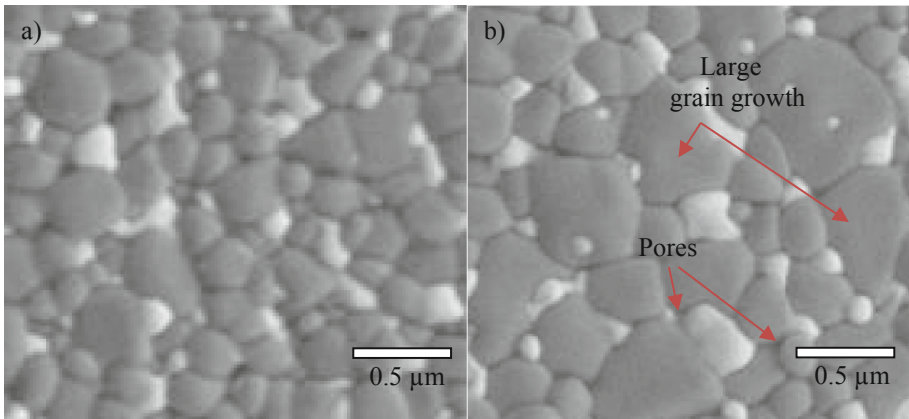
Fig. 5. SEM images of ZTA composites with 10 vol% Y-TZP and 0.6 CuO content sintered via sintering profile TSS 3 (a) And sample containing 20 vol% Y-TZP and 0.6 CuO content sintered via TSS 6 (b).

4   Conclusion

This study has shown the effect of various sintering profiles on ZTA composites consist of 0 to 20 vol% Y-TZP content and 0.6 vol% CuO sintered via two-stage sintering. Based on the results obtained, it is possible to produce ZTA composites that meet the

industry-standard such as ISO 6474, as the data obtained shows that samples sintered at shorter holding time combined with lower heating rate were able to produce ZTA composite with almost full densification, Vickers hardness 18.5 GPA, Young's modulus of 409 GPa and fracture toughness of 8.1 MPam$^{1/2}$.

References

1. Wang, Z., Li, P.: Dynamic failure and fracture mechanism in alumina ceramics: experimental observations and finite element modelling. Ceram. Int. **41**(10), 12763–12772 (2015)
2. Fan, J., et al.: Effect of sintering temperature on microstructure and mechanical properties of zirconia-toughened alumina machinable dental ceramics. Ceram. Int. **43**(4), 3647–3653 (2017)
3. Wang, J., Stevens, R.: Zirconia-toughened alumina (ZTA) ceramics. J. Mater. Sci. **24**(10), 3421–3440 (1989)
4. Ghalme, S.G., Mankar, A., Bhalerao, Y.: Biomaterials in hip joint replacement. Int. J. Mater. Sci. Eng. **4**(2), 113–125 (2016)
5. Tuan, W.H., Chen, R.Z., Wang, T.C., Cheng, C.H., Kuo, P.S.: Mechanical properties of Al2O3/ZrO2 composites. J. Eur. Ceram. Soc. **22**, 2827–2833 (2002)
6. Perrichon, A., Reynard, B., Gremillard, L., Chevalier, J., Farizon, F., Geringer, J.: A testing protocol combining shocks, hydrothermal ageing and friction, applied to Zirconia Toughened Alumina (ZTA) hip implants. J. Mech. Behav. Biomed. Mater. **65**, 600–608 (2017)
7. Aragón-Duarte, M.C., et al.: Nanomechanical properties of zirconia-yttria and alumina zirconia-yttria biomedical ceramics, subjected to low temperature aging. Ceram. Int. **43**(5), 3931–3939 (2017)
8. Aherwar, A., Patnaik, A., Bahraminasab, M., Singh, A.: Preliminary evaluations on development of new materials for hip joint femoral head. Proc. Inst. Mech. Eng. Part L. J. Mater. Des. Appl. **233**(5), 885–899 (2019)
9. Green, D.J.: Transformation Toughening of Ceramics. CRC Press, Hoboken (2018)
10. Sommer, F., Landfried, R., Kern, F., Gadow, R.: Mechanical properties of zirconia toughened alumina with 10–24 vol.% 1Y-TZP reinforcement. J. Eur. Ceram. Soc. **32**(16), 4177–4184 (2012)
11. Kern, F.: Properties of 25Y-TZP manufactured from alumina-doped yttria-coated pyrogenic zirconia nanopowder. J. Ceram. Sci. Technol. **2**(2), 89–96 (2011)
12. Azhar, A.Z.A., Mohamad, H., Ratnam, M.M., Ahmad, Z.A.: Effect of MgO particle size on the microstructure, mechanical properties, and wear performance of ZTA–MgO ceramic cutting inserts. Int. J. Refract. Metals Hard Mater. **29**(4), 456–461 (2011)
13. Zhu, T., Xie, Z., Han, Y., Li, S.: Microstructure and mechanical properties of ZTA composites fabricated by oscillatory pressure sintering. Ceram. Int. **44**(1), 505–510 (2018)
14. Lopes, A.C.O., et al.: Microstructural, mechanical, and optical characterization of an experimental aging-resistant zirconia-toughened alumina (ZTA) composite. Dent. Mater. **36**(12), 365–374 (2020)
15. Roa, J.J., TuronVinas, M., Anglada, M.: Surface grain size and texture after annealing ground zirconia. J. Eur. Ceram. Soc. **36**(6), 1519–1525 (2016)
16. Lucas, T.J., Lawson, N.C., Janowski, G.M., Burgess, J.O.: Effect of grain size on the monoclinic transformation, hardness, roughness, and modulus of aged partially stabilized zirconia. Dent. Mater. **31**(12), 1487–1492 (2015)
17. Chen, I.W., Wang, X.H.: Sintering dense nanocrystalline ceramics without final-stage grain growth. Nature **404**(6774), 168 (2000)

18. Sivanesan, S., Loong, T.H., Namasivayam, S., Fouladi, M.H.: Two-Stage Sintering of Alumina-Y-TZP (Al$_2$O$_3$/Y-TZP) Composites. Key Eng. Mater. **814**, 12–18 (2019)
19. Bodišová, K., Šajgalík, P., Galusek, D., Švančárek, P.: Two-stage sintering of alumina with submicrometer grain size. J. Am. Ceram. Soc. **90**(1), 330–332 (2007)
20. Mazaheri, M., Simchi, A., Golestani-Fard, F.: Densification and grain growth of nanocrystalline 3Y-TZP during two-step sintering. J. Eur. Ceram. Soc. **28**(15), 2933–2939 (2008)
21. Polotai, A., Breece, K., Dickey, E., Randall, C., Ragulya, A.: A novel approach to sintering nanocrystalline barium titanate ceramics. J. Am. Ceram. Soc. **88**(11), 3008–3012 (2005)
22. Lee, Y.I., Kim, Y.W., Mitomo, M., Kim, D.Y.: Fabrication of dense nanostructured silicon carbide ceramics through two-step sintering. J. Am. Ceram. Soc. **86**(10), 1803–1805 (2003)
23. Wang, X.H., et al.: Two-step sintering of ceramics with constant grain-size, II: BaTiO$_3$ and Ni–Cu–Zn Ferrite. J. Am. Ceram. Soc. **89**(2), 438–443 (2006)
24. Niihara, K.: A fracture mechanics analysis of indentation-induced Palmqvist crack in ceramics. J. Mater. Sci. Lett. **2**(5), 221–223 (1983)
25. Meunier, C., Zuo, F., Peillon, N., Saunier, S., Marinel, S., Goeuriot, D.: In situ study on microwave sintering of ZTA ceramic: Effect of ZrO$_2$ content on densification, hardness, and toughness. J. Am. Ceram. Soc. **100**(3), 929–936 (2017)
26. Hossen, M.M., Chowdhury, F.U.Z., Gafur, M.A., Hakim, A.A., Hossen, M.B.: Effect of zirconia substitution on structural and mechanical properties of ZTA composites. IOSR J. Mech. Civil Eng. **11**(2), 01–07 (2014)
27. Ran, S., Winnubst, L., Wiratha, W., Blank, D.H.: Synthesis, sintering and microstructure of 3Y-TZP/CuO nano-powder composites. J. Eur. Ceram. Soc. **26**(4–5), 391–396 (2006)
28. Ramesh, S., et al.: Effect of microwave sintering on the properties of copper oxide doped Y-TZP ceramics. Ceram. Int. **44**(16), 19639–19645 (2018)
29. Jayaseelan, D.D., Rani, D.A., Nishikawa, T., Awaji, H., Gnanam, F.D.: Powder characteristics, sintering behavior and microstructure of sol–gel derived ZTA composites. J. Eur. Ceram. Soc. **20**(3), 267–275 (2000)
30. Teow, H.L., Sivanesan, S.K., Noum, S.Y.E.: Densification behaviour and mechanical properties of CuO doped zirconia-toughened alumina (ZTA) composites prepared by two-stage sintering. AIP Conf. Proc. **2233**(1), 020028 (2020)
31. Moradkhani, A., Baharvandi, H.: Effects of additive amount, testing method, fabrication process and sintering temperature on the mechanical properties of Al$_2$O$_3$/3Y-TZP composites. Eng. Fract. Mech. **191**, 446–460 (2018)
32. Casellas, D., Cumbrera, F.L., Sánchez-Bajo, F., Forsling, W., Llanes, L., Anglada, M.: On the transformation toughening of Y-ZrO$_2$ ceramics with mixed Y–TZP/PSZ microstructures. J. Eur. Ceram. Soc. **21**(6), 765–777 (2001)
33. Eichler, J., Rödel, J., Eisele, U., Hoffman, M.: Effect of grain size on mechanical properties of submicrometer 3Y-TZP: fracture strength and hydrothermal degradation. J. Am. Ceram. Soc. **90**(9), 2830–2836 (2007)

Multi-response Optimization of Machining Simulation Approach Using Grey Relational Analysis

Mohd Amran Md Ali[1(✉)] 🄳, Sivarao[1] 🄳, Zulkeflee Abdullah[1] 🄳, Raja Izamshah[2] 🄳, Mohd Shahir Kassim[2], and Ahmad Shahir Jamaludin[3] 🄳

[1] Faculty of Manufacturing Engineering, Universiti Teknikal Malaysia Melaka, 76100 Durian Tunggal, Melaka, Malaysia
mohdamran@utem.edu.my

[2] Advanced Manufacturing Centre, Faculty of Manufacturing Engineering, Universiti Teknikal Malaysia Melaka, 76100 Durian Tunggal, Melaka, Malaysia

[3] Faculty of Manufacturing and Mechatronic Engineering Technology, Universiti Malaysia Pahang, 26600 Pekan, Pahang, Malaysia

Abstract. This study is to find the multi-response optimization of machining by finite element analysis simulation software using the grey relational analysis approach. The parameters selected are cutting speed, feed rate, and depth of cut towards the responses that are velocity, displacement, and temperature. Stainless steel was selected as workpiece and carbide material as cutting tool. L4 orthogonal array was implemented as an experimental design. In pre-processing the experimental result was normalized followed by determination optimization parameters from the highest value. It is found that optimum parameters for all responses are 150 m/min of the cutting speed at level 1, 0.5 mm of the depth of cut at level 1, and 0.3 mm/rev of the feed rate at level 1. Analysis result shows that the cutting speed is the significant factor that affects all responses followed by feed rate and depth of cut.

Keywords: Multi-response · Grey relational analysis · Machining

1 Introduction

Finite Element Analysis (FEA) is an engineering simulation program that is used to evaluate different manufacturing processes, providing an important analysis method for an industrial application study. According to Prasad et al. [1], various Computer-Aided Engineering (CAE) simulation software such as DEFORM-3D, ABAQUS, ANSYS, etc. are Finite Elements Method (FEM) approach that are used to evaluate the various formation processes employed by steel shaping sectors and similar ones. By simulating fabrication processes make designers and engineers decreasing the need for costly shop floor trials and redesign of tooling and processes [2].

The machining process parameters that most affected the machining characteristics are cutting speed, feed rate, and depth of cut. The suitable material and machining

process parameter needs to be investigated so that the optimum parameters can enhance the quality for the machining characterization [3].

In this paper, the finite element analysis of DEFORM 3D software was used. The cutting parameters are cutting speed, feed rate, and depth of cut meanwhile the selected responses are velocity, displacement, and temperature. The main objective of this paper is to find the most significant parameters and optimize the parameters by multi-response optimization using the grey relational analysis.

2   Experimental Work

Three independent variables machining parameters are selected which are cutting speed (150 m/min to 250 m/min), depth of cut (0.5 mm to 0.6 mm), and feed rate (0.3 mm/rev to 0.5 mm/rev) while the responses are velocity, displacement and temperature. Machining parameters of cutting speed, depth of cut, and feed rate were set up in the process setting in DEFORM 3D software. Next, the carbide cutting tool insert was loaded in the program then generated mesh. The selection 316 L stainless steel was chosen as a workpiece then generated mesh on the workpiece. After the command bar shows the complete process for turning simulation. Data can be analyzed by selecting types of the variable for the response. Choose types of response that are required for velocity, displacement and temperature. The determination of grey relational analysis (GRA) method was followed from the previous researcher approach [4].

3   Multi-response Optimization Result and Discussion

3.1   Grey Relational Analysis

The result from the experiment was taken for analysis by Grey Relational Analysis (GRA). Application of the GRA approach to identify optimum levels of parameters of significance. The outcome of the confirmation test indicated that the optimal combination of parameters that have been determined effectively increases the cutting speed performance of the product properties [5].

Table 1. Result of grey relational analysis (GRA).

Runs	Velocity (mm/sec)	Displacement (mm)	Temperature (°C)	GRA of velocity	GRA for displacement	GRA of temperature
1	5070	40.5	1600	0.8435	0.5526	1
2	3450	57.3	2020	1	0	0.8667
3	5680	35.0	4750	0.7850	0.7336	0
4	13800	26.9	3630	0	1	0.3556

The smaller the better characteristic was used for calculation the GRA for each run as shown in Table 1. The table shows that run number 1, 2 and 4 has a different high result from one to another with a value of 1 for each answer that is velocity, displacement, and temperature. The result shows when used the smaller the better for experiment result with value zero was run numbers 2, 3, and 4. The value for displacement was 0 value at run number 2, meanwhile run number 3 shows 0 value for temperature.

3.2   Grey Relational Coefficient (GRC)

Next, analyze using GRC where the maximum value of process parameters is evaluated using the higher GRG. Higher values of mean grade values of GRG are selected as the optimal multi-response, therefore as shown in Table 2, run number 1 is the optimal run of multi response optimization for the three responses.

Table 2. Data of GRC and GRG.

Runs	Cutting speed (m/min)	Depth of cut (mm)	Feed rate (mm/rev)	GRC of velocity	GRC of displacement	GRC of temperature	Grey Relational Grade (GRG)
1	150	0.5	0.3	0.7616	0.5278	1	0.7631
2	150	0.6	0.5	1	0.3333	0.7895	0.7076
3	250	0.5	0.5	0.6989	0.6524	0.3333	0.5615
4	250	0.6	0.3	0.3333	1	0.4369	0.5901

3.3   Ranking the Most Parameters Affected on Responses

The response factor diagram is shown in Fig. 1 which shows the parameters main effect plot of speed, depth of cut, and feed rate versus the data means.

The result indicates that the optimum level of parameters of cutting speed is 150 m/min at level 1, meanwhile for depth of cut is 0.6 mm at level 1and for the feed rate is 0.3 mm/rev at level 1. The result shows the multi-response optimization fall under run number 1. From the figure it shows that cutting speed is the most influence factor follow by feed rate and depth of cut. The result similar report by Hadzley et al. [2] that the cutting speed higher the influence of velocity, displacement and temperature very sensitive due to as the cutting speeds increases the strain rate increases at shear zone thus more heat is generated rapidly with respective to speed.
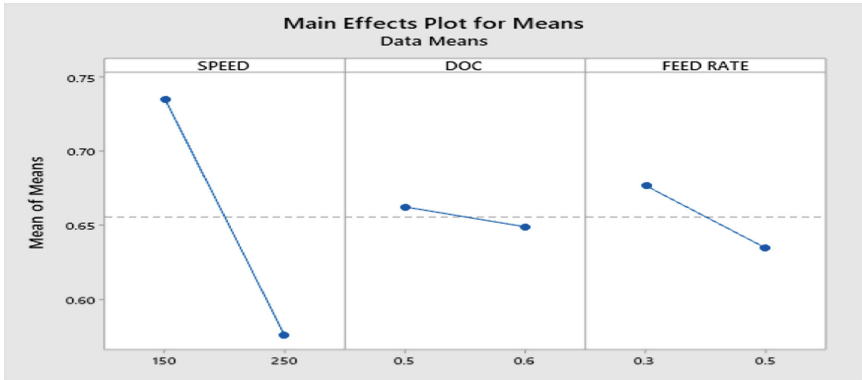
Fig. 1. Parameters main effect plot of speed, depth of cut, and feed rate.

4   Conclusion

It can be concluded that the response factor shows that the Gray Relation Analysis (GRA) was obtained. This result indicates that the optimum parameters of multi-response are 150 m/min of the cutting speed at level 1, 0.5 mm of the depth of cut at level 1, and 0.3 mm/rev of the feed rate at level 1. From this result, using multiple responses shows that cutting speed is the most parameter that affected all responses.

References

1. Prasad, K.K., Tamang, S.K., Chandrasekaran, M.: Comparative study on cutting force simulation using DEFORM 3D software during high speed machining of Ti-6Al-4V. Key Eng. Mater. **856**, 50–56 (2020)
2. Hadzley, A.M., Azahar, W.W.M., Izamshah, R., Shahir, K.M., Amran, A.M., Afuza, A.: Response surface methodology approach on effect of cutting parameter on tool wear during end milling of high thermal conductivity steel-150 (HTCS-150). IOP Conf. Ser. Mater. Sci. Eng. **114**(1), 1–7 (2016)
3. Bakar, M.H.A., et al.: Surface integrity of LM6 aluminum metal matrix composite when machined with high speed steel and uncoated carbide cutting tools. J. Mech. Eng. Sci. **6**, 854–862 (2014)
4. Md Ali, M.M., et al.: Multi-response optimization of plastic injection moulding process using grey relational analysis based in Taguchi method. J. Adv. Manuf. Technol. **12**(1), 87–98 (2018)
5. Izamshah, R., Husna, N., Hadzley, M., Amran, M., Shahir, M., Amri, M.: Effects of cutter geometrical feature on machining polyetheretherketone (PEEK) engineering plastic. J. Mech. Eng. Sci. **6**, 863–872 (2012)

Evaluation of Monotonic Tensile Properties of Napier Single Fibre

R. M. Luqman, Mohamad Zaki Hassan[(✉)] [iD], and Mohamed Azlan Suhot

Razak Faculty of Technology and Informatics, Universiti Teknologi Malaysia, Jalan Sultan Yahya Petra, 54100 Kuala Lumpur, Malaysia
`mzaki.kl@utm.my`

Abstract. Natural fibres are derived from plants and animals, and they are the most efficient replacement for synthetic fibre. However, these fibres differ widely in physicochemical characteristics, hollow of lumen, uniformity, and degree of crystallinity, resulting in inconsistent mechanical property values. In this study, the tensile properties of a single Napier fibre were investigated according to ASTMD 3822-07. The test was performed using universal testing machines at a crosshead displacement rate of 1 mm/min. It revealed that the average tensile strength and modulus of a single Napier fibre were 23.47 MPa and 0.18 GPa, respectively. The Weibull modulus was determined to be 1.4261 with a Weibull parameter estimation error of 48%.

Keywords: Natural fibres · Napier fibre · Single fibre · Weibull modulus

1 Introduction

Napier grass, a tropical fodder crop native to Africa and classed in the Poaceae family. Predominantly, the Napier fibre strands could be extracted from the grass internodes using a unique blend of mechanical and water-retting techniques. The surface of this fibre was protected by compounds such as α-cellulose (47.12%), hemicellulose (31.27%), Lignin (21.63%), wax, and other impurities (non-cellulosic elements) [1]. Nowadays, this fibre is recognized as an ecologically friendly resource due to its biodegradability and regenerative features. However, inconsistency in the mechanical characteristics of a single fibre, heterogeneity in fibre qualities with plant age, and poor adhesion to manmade polymer matrix restrict their potential applications.

Many researchers have evaluated the tensile properties of a single natural fibre by using a universal testing machine [2–4]. According to Adusumalli et al. [2], the Weibull modulus of natural fibres (from 1 to 3.4) is lower than those of synthetic fibres (from 6 to 12) due to irregularity at the nanostructural level between the cell wall and lumen of the fibre. Similarly, Hassan et al. [3] summarised that the Weibull modulus value for almost natural fibre must be lower than four resultant in the inconsistency of fibre diameter. Moreover, Ibrahim et al. [3] found that fairly linear stress-strain curves before failure were obtained. They also mentioned that the most beneficial alkaline concentration

threshold was shown to be 6%, beyond this tensile characteristic of single kenaf fibre was deteriorated.

To our knowledge, no prior research has used a Weibull statistical analysis to evaluate the tensile properties of single Napier fibres. In this study, the reliability qualities using an exponential distribution and Weibull modulus characteristics of the fibres population of single Napier fibres based on the mechanical properties are predicted.

2 Material and Method

Napier fibre was collected from the Napier grass at Port Dickson, Negeri Sembilan, Malaysia. The grass stems were shattered using fluted rollers and followed by water retting for a week. Eventually, the fibre was properly cleaned and dried in a hot air oven.

The tensile characteristics were measured using a Shimadzu Universal Testing Machine with a crosshead speed of 1mm/min and a constant gauge length of 10 mm as shown in Fig. 1.
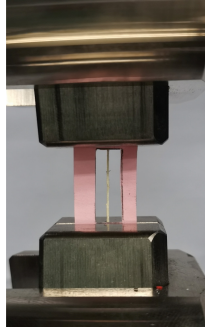
Fig. 1. Tensile test for single Napier fibre.

According to Weibull analysis, the probability distribution function of material strength is expressed as Eq. (1),

$$P(\sigma) = 1 - \exp\left[-V\left(\frac{\sigma_m}{\sigma_o}\right)^2\right] \tag{1}$$

where $P(\sigma)$ is the probability of survival, V is the fibre volume, m is the Weibull modulus, σ and σ_o are known as the applied stress and characteristic strength, respectively. The ranking of the Napier fibre strength is evaluated by using a probability index expressed by Eq. (2):

$$P(\sigma) = \frac{i - 0.3}{n + 0.4} \tag{2}$$

3   Result and Discussions

3.1   Tensile Test

The average values of the tensile strength and tensile modulus for single Napier fibres are shown in Fig. 2. A lower tensile strength of Napier was recorded as compared with jute and sisal fibres [5]. As can be observed in Fig. 2, the tensile modulus has a large standard deviation with nearly 48% inaccuracy. It agrees with the finding reported by Belaadi et al. [5] when they conducted tensile property for single sisal fibres.
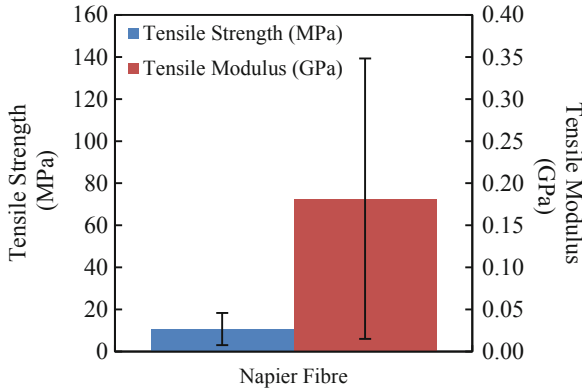
Fig. 2. Typical tensile strength and tensile modulus of a single Napier fibre.

3.2   Weibull Analysis

Table 1 presents the Weibull parameters of the single Napier fibre following the tensile strength test. The percentage difference between the experimental and absolute tensile strength value was 48.36% with its related deviation. It was found that the Weibull modulus value was 1.43, which is quite similar to the values reported by Bezazi et al. [6]. This Weibull modulus (m) is remarkably associated with the rupture of the most prominent defects at the fibre surface.

Table 1.   Weibull parameter for the tensile strength of single Napier fibres.

Weibull modulus, m	Tensile strength σ_o (MPa)	Measure, σ (MPa)	Percentage error (%)
1.43	23.47	12.12 ± 3.558	48.36

Figure 3 shows the trend of lnln(1/(1-F)) versus ln(σ) of the single Napier samples. Here, all the value in Fig. 3 is unimodal, i.e., with only one straight line corresponding to the point at each interval. It also illustrates the R^2 value of 0.9049 reveals that the regression model fits the observed data. This plot proves that the Weibull model can

predict the properties of fibre strength, and it gives a good fit to the distribution very well. A similar finding was obtained by Ibrahim et al. where they found that the prediction of Weibull analysis for consistent kenaf fibre strength increased approximately by about 12% [7].
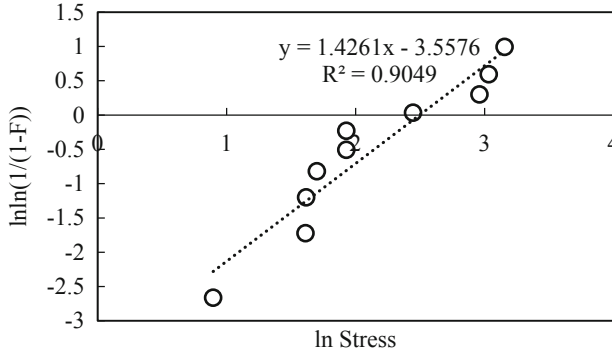
Fig. 3. The trend of lnln(1/(1-F)) versus ln(σ) of the single Napier fibre.

4   Conclusion

In this study, the stress-strain behaviour of the fibre strand of Napier grass was observed. The highest value of tensile strength and tensile modulus of Napier fibre was recorded as 23.47 MPa and 0.18 GPa, respectively. The study has proved that the Weibull probability statistic can predict the absolute values of mechanical properties of a single Napier fibre. The Weibull modulus and the parameter estimation error of the tensile strength compared to the experimental results were 1.43 and 48%, respectively.

References

1. Kommula, V., Reddy, K.O., Shukla, M., Marwala, T., Reddy, E.S., Rajulu, A.V.: Extraction, modification, and characterization of natural ligno-cellulosic fiber strands from napier grass. Int. J. Polym. Anal. Charact. **21**(1), 18–28 (2016). https://doi.org/10.1080/1023666X.2015.1089650
2. Adusumalli, R.B., Venkateshan, K.C., Kunchi, C., Vadlamani, S.R.: Tensile testing of single fibres. Proc. Struct. Integr. **14**, 150–157 (2019). https://doi.org/10.1016/j.prostr.2019.05.020
3. Ibrahim, M.I., Hassan, M.Z., Dolah, R., Yusoff, M.Z.M., Salit, M.S.: Tensile behaviour for mercerization of single kenaf fiber. Malaysian J. Fundam. Appl. Sci. **14**(4), 437–439 (2018). https://doi.org/10.11113/mjfas.v14n4.1099

4. Hassan, M.Z., Ibrahim, M.I., Sapuan, S.: Tensile properties analysis and characterizations of single fiber and biocomposites: a weibull analysis and future trend. In: Value-Added Biocomposites, pp. 87–101. CRC Press (2021)

5. Belaadi, A., Bezazi, A., Bourchak, M., Scarpa, F., Zhu, C.: Thermochemical and statistical mechanical properties of natural sisal fibres. Compos. B Eng. **67**, 481–489 (2014). https://doi.org/10.1016/j.compositesb.2014.07.029

6. Bezazi, A., Belaadi, A., Bourchak, M., Scarpa, F., Boba, K.: Novel extraction techniques, chemical and mechanical characterisation of Agave Americana L. natural fibres. Compos. B Eng. **66**, 194–203 (2014). https://doi.org/10.1016/j.compositesb.2014.05.014

7. Ibrahim, I., Sarip, S., Bani, N.A., Ibrahim, M.H., Hassan, M.Z.: The Weibull probabilities analysis on the single kenaf fiber. AIP Conf. Proc. **1958**(1), 020009 (2018). https://doi.org/10.1063/1.5034540

The Activated Carbon Adsorption of Polycyclic Aromatic Hydrocarbons: The Best Evidence Review

Nurul Afwanisa' Ab Razak, Mohd Hafidzal Mohd Hanafi[✉], Nurul Hanim Razak, Asriana Ibrahim, and Anis Ainaa Omar

Centre for Advance Research on Energy, Fakulti Kejuruteraan Mekanikal, Universiti Teknikal Malaysia Melaka, Hang Tuah Jaya, 76100 Durian Tunggal, Melaka, Malaysia
`hafidzal@utem.edu.my`

Abstract. Persistent organic contaminants having two or more fused aromatic rings are called polycyclic aromatic hydrocarbons (PAHs). PAHs were produced from incomplete combustion of organic substances and cooking food at temperatures above 200 °C. Despite the numerous studies that have highlighted the rising health danger caused by PAHs, research on activated carbon (AC) adsorption for PAH elimination has been limited. This review aims to discuss the best-recommended AC adsorption to remove PAHs. A selected number of the most prevalent AC adsorption with the highest removal efficiency of PAHs were reviewed. Summarily, this review concluded that the best method goes to AC adsorption using wheat straw pyrolyzed with limiting oxygen conditions at 800 °C for 6 h with 2 g/L dosages. The process yields 652 m^2/g BET surface area and 0.634 m^3/g total pore volume which has successfully removed 98.6% fluoranthene. It is interesting to note that the excellent removal efficiency is also due to the interaction mechanism between AC and PAHs that is hydrogen bonding, $\pi - \pi$ interaction and van der Waals attraction.

Keywords: Polycyclic aromatic hydrocarbons · Adsorption · Activated carbon · Biomass

1 Introduction

Polycyclic aromatic hydrocarbons (PAHs) are persistent organic contaminants made up of two or more fused aromatic rings that are found everywhere in the environment [1]. Incomplete combustion of organic materials such as coal, wood or petroleum in the industry as well as carbohydrates, fat and protein while cooking at temperatures above 200 °C can produce the PAHs. PAHs are known to be strong carcinogens or mutagens and the US Environmental Protection Agency and the European Commission have designated them as priority pollutants [1].

Many studies are reported to remove PAHs, however, the accessible literature has been limited to adsorption with activated carbon (AC). To fill the gap, this review purposed to offer the best-matched adsorption with AC to remove PAHs. Adsorption has

been acknowledged as a significant method for efficient removal because of the strong affinity from a variety of organic contaminants [2] It is a straightforward, flexible and effective method for removing contaminants from liquid systems [1].

During the adsorption process, contaminants in the solution are trapped on the surface of suspended particles, known as adsorbent material [2]. The most frequently utilized adsorbent for the removal of contaminants is AC [1]. AC adsorption is a more environmentally friendly and economical way to eliminate PAHs [3]. AC adsorption offers an option for converting waste material into valuable resources in the interest of environmental sustainability [2]. From the review study as shown in Table 1, three categories of PAHs adsorption by AC are carried out which are biomass material, polymer waste and raw material. This review study also presents some important parameters which influence in adsorption capacity and PAHs removal efficiency. The parameters are Brunauer, Emmett and Teller (BET) surface area and total pore volume.

A study conducted by Li et al. (2014) has the highest removal efficiency proved that 98.6% fluoranthene was successfully removed with wheat straw pyrolyzed with limiting oxygen conditions at 800 °C for 6 h with 2 g/L dosages. It is also interesting to note that, a finding follows as the second-highest removal efficiency is by using polyethylene terephthalate (PET) waste. That finding was reported to remove 92.44% pyrene through PET waste prepared at 600 °C for 1 h.

Li et al. (2014) have suggested that for the highest efficiency removal to be achieved, as the pyrolytic temperature increase, the PAHs removal also increasing at a specific AC dose. It can be seen from Table 1, although sawdust has a significantly bigger surface area than the wheat straw, they are comparative in PAHs removal efficiency. This implying that BET surface area alone may not be sufficient to control PAH adsorption. Other adsorbents structural or chemical characteristics may also have a role in PAH adsorption.

2   AC: Mechanism and Removal Efficiency

AC is extremely porous carbon materials derived from biomass, polymer waste and raw material including high carbon content in the form of starch, simple sugars, proteins, lipids, lignin, hemicellulose and cellulose. The synthesis of AC required the thermal breakdown of this material in the presence of a restricted air supply proceeded by the activation to produce extremely porous carbon material [3]. Significant contributing element for pollutant adsorption is AC surface are and pore volume distribution. The AC was analyzed by the Brunauer, Emmett and Teller (BET) surface area analyzer and the total pore volume was calculated accordingly. The BET theory helps to explain the physical adsorption of gas molecules on solid surfaces and forms the foundation for a critical analytical approach for calculating the specific surface area of materials. The theory yields a specific surface area result, that is measured in units of area per mass of sample (m^2/g).

The interaction mechanism between AC and organic contaminants including hydrogen bonding, hydrophobic and $\pi - \pi$ (pi – pi) interaction and van der Waals attraction or repulsion [9]. The adsorption of organic pollutants on the surface of AC has been explained as complicated interactions between electrostatic and dispersion interactions, primarily when weak organic electrolytes are involved. However, because PAHs are

not accounted to be electrolytic, intermediate hydrogen bonding and van der Waals attractions have been the most often suggested mechanism in the literature [10].

Table 1. PAHs adsorption with various types of AC.

Classes of material	AC/Adsorbent	BET surface area (m²/g)	Total pore volume (cm³/g)	Adsorption capacity (mg/g)	Removal efficiency	PAHs/Adsorbate	Reference
Biomass	Coconut waste	89.890	0.1081	-	81.94	Benzo[a]pyrene	[4]
	Grass waste	127.987	0.1345	-	79.81	Benzo[a]anthracene	[4]
	Green tea waste	131.80	0.065	28.08	-	Benzo[b]fluoranthene	[5]
	Guava waste	87.987	0.1034	-	76.42	Benzo[a]anthracene	[4]
	Orange waste	123.186	0.1087	-	79.97	Benzo[a]anthracene	[4]
	Rice husk waste	52.10	0.050	97.6	-	Phenanthrene	[3]
	Sawdust	1409.43	0.3180	-	80.00	Naphthalene	[6]
	Sunflower husk	440.00	0.810	-	81.00	Benzo[a]pyrene	[7]
	Wheat straw	652.00	0.6340	-	98.60	Fluoranthene	[8]
Polymer waste	Polyethylene terephthalate (PET) waste	65.35	0.009	-	92.44	Pyrene	[9]
	Polystyrene (PS) waste	50.14	0.010	-	82.3	Benzo[ghi]perylene	[9]
Raw material	Birch wood	950.00	0.860	-	77.00	Benzo[a]pyrene	[7]
	Coal	686.06	0.390	160	-	Pyrene	[10]
	Coal	1770.49	0.990	117.65	-	Pyrene	[11]

3   Conclusion

In this review study, the collection of research papers pertaining to the highest PAHs removal efficiency based on AC adsorption are presented. Based on the studies, it was suggested that the AC adsorption for PAHs removal could be enhanced by maintaining a larger BET surface area and higher total pore volume. It is important to note that the mechanism of PAHs removal efficiency is due to the interaction mechanism between AC and PAHs that is hydrogen bonding, $\pi - \pi$ interaction and van der Waals attraction.

References

1. Gupta, H., Gupta, B.: Adsorption of polycyclic aromatic hydrocarbons on banana peel activated carbon. Desalin. Water Treat. **57**(20), 9509–9898 (2016)
2. Zango, Z.U., et al.: An overview and evaluation of highly porous adsorbent materials for polycyclic aromatic hydrocarbons and phenols removal from wastewater. Water (Switzerland) **2**(10), 1–40 (2020)
3. Guo, W., et al.: Sorptive removal of phenanthrene from aqueous solutions using magnetic and non-magnetic rice husk-derived biochars. R. Soc. Open Sci. **5**, 1–11 (2018)
4. de Jesus, J.H.F., da S. Matos, T.T., da C. Cunha, G., Mangrich, A.S., Romão, L.P.C.: Adsorption of aromatic compounds by biochar: influence of the type of tropical biomass precursor. Cellulose **26**(7), 4291–4299 (2019). https://doi.org/10.1007/s10570-019-02394-0
5. Inbaraj, B.S., Sridhar, K., Chen, B.H.: Removal of polycyclic aromatic hydrocarbons from water by magnetic activated carbon nanocomposite from green tea waste. J. Hazard. Mater. **415**, 1–15 (2021)
6. Kumar, A., Gupta, H.: Activated carbon from sawdust for naphthalene removal from contaminated water. Environ. Technol. Innov. **20**, 1–11 (2020)
7. Minkina, T., et al.: Sorption of benzo[a]pyrene by Chernozem and carbonaceous sorbents: comparison of kinetics and interaction mechanisms. Environ. Geochem. Health **44**(1), 133–148 (2021). https://doi.org/10.1007/s10653-021-00945-8
8. Li, H., et al.: Selective removal of polycyclic aromatic hydrocarbons (PAHs) from soil washing effluents using biochars produced at different pyrolytic temperatures. Biores. Technol. **163**, 193–198 (2014)
9. Ilyas, M., Ahmad, W., Khan, H.: Utilization of activated carbon derived from waste plastic for decontamination of polycyclic aromatic hydrocarbons laden wastewater. Water Sci. Technol. **84**(3), 609–631 (2021)
10. Ge, X., et al.: Enhanced PAHs adsorption using iron-modified coal-based activated carbon via microwave radiation. J. Taiwan Inst. Chem. Eng. **64**, 235–243 (2016)
11. Xiao, X., et al.: Preparation of activated carbon from Xinjiang region coal by microwave activation and its application in naphthalene, phenanthrene, and pyrene adsorption. J. Taiwan Inst. Chem. Eng. **53**, 160–167 (2015)

Rubberwood-Recycled Polypropylene Composites: Effect of Water Immersion on Tensile Properties

Zaleha Mustafa[1]([✉]), Tuan Muhammad Idzzuddin Nawi[1], Vaseetha Ravichandran[1], Toibah Abd. Rahim[1], and Thanate Ratanawilai[2]

[1] Faculty of Manufacturing Engineering, Universiti Teknikal Malaysia Melaka, Hang Tuah Jaya, 76100 Durian Tunggal, Melaka, Malaysia
zaleha@utem.edu.my

[2] Department of Industrial and Manufacturing Engineering, Faculty of Engineering, Prince of Songkla University, Hat Yai, Songkhla 90110, Thailand

Abstract. Considerable interest in the natural fibre thermoplastic composite has been catalyst by their outstanding properties and as well as to reduce the environmental issue. Rubberwood polymer composite has been regarded as an excellent alternative for timber-based products. Rubberwood fibre is hydrophilic thus susceptible to moisture during application. Thus, this study aims to evaluate the effect of water immersion on the tensile properties of the rubberwood reinforced recycled polypropylene composite. The composite has good initial strength and modulus of 26.33 MPa and 1.69 GPa respectively. After 30 days of water immersion, the tensile strength and modulus of the composite decreased with moisture uptake, where their tensile strength and modulus significantly reduced to 12.19 MPa and 0.74 GPa respectively indicated the deleterious effect of the moisture onto their structural integrity. In contrast, their strain is increase after the water ageing process.

Keywords: Rubberwood composite · Water immersion · Tensile properties

1 Introduction

Wood polymer composite (WPC) has garnered an increase in interest due to its outstanding properties and is seen as a good alternative to preserve the timber. The wood flour used in manufacturing WPC is often resourced from the waste of the timber industry in form of sawdust, sawmill chips, wood flour, wood fibre, thus providing a solution to the increase of the environmental issue such as landfill and pollutions [1, 2]. However, wood fibre like any other natural fibre is hydrophilic. Therefore, these materials are often subject to changes in their properties during their operating life because of their environmental conditions. One such condition is that exposure to solvent water or humidity, in particular, can trigger major ageing phenomena and might affecting their mechanical properties [3–5] during applications. Thus, this study aims to evaluate how deleterious the effect of the moisture onto the initial properties of the rubberwood recycled polypropylene composites.

2   Materials and Methods

The materials and fabrication method for wood polymer composite (WPC) pellet was optimized and reported in the previous work [6]. The WPC pellet contains recycled PP (50.3 wt.%), rubberwood flour (37.5 wt.%) and calcium carbonate (7 wt.%) and additives (5.1 wt.%) consist of MAPP, UV and lubricant. The pellet then was compressed moulded using a hot press (Carver, USA) at 190 °C under 1000 psi and cut into a flat dumbbell shape according to ASTM D638 with thickness and length of 4 mm and 136 mm. Ten specimens were immersed in tap water at room temperature for 30 days. At the end of immersion time, the specimens were removed from the water and thoroughly dried in a drying oven at 60 °C until they achieved a constant weight. The static tests were performed at a constant cross-head speed of 5 mm/min using a 20 kN Universal Testing Machine (AGS-X Shimadzu, Japan).

3   Results and Discussion

The initial tensile strength of the WPC is 26.33 ($\pm$0.60) MPa with a percentage strain at break of 1.59% ($\pm$0.17) as shown in Fig. 1. Subsequently, upon exposure to the moisture, the composite has experienced a significant degradation of approximately 53.70% of its initial strength and reduced to 12.19 MPa. A similar observation is shown for the modulus of elasticity of the composite (Fig. 2). The tensile modulus of the aged WPC is significantly decreased from 1.69 GPa to 0.74 GPa, approximately 56.21% of their initial stiffness indicating the deleterious effect of moisture onto the rubberwood composite properties. At the same time, the tensile strain of the aged specimen is slightly higher suggesting that when the composite has become more ductile due to plasticizing effect [2] during the water immersion test.

Moisture significantly reduced the initial strength and stiffness of the composite. This is due to the presence of the hydrophilic phase (rubberwood fibre) in the composite. Upon exposure to the moisture, the water molecules infiltrate into the composite causing the wood flour to swell and subsequently caused microcrack formation in the matrix. The swelling of the fibre will also reduce the adhesion bonding between rubberwood fibre and the rPP matrix [2, 4, 5]. Consequently, the tensile properties of rubberwood/rPP composite will be decreased.
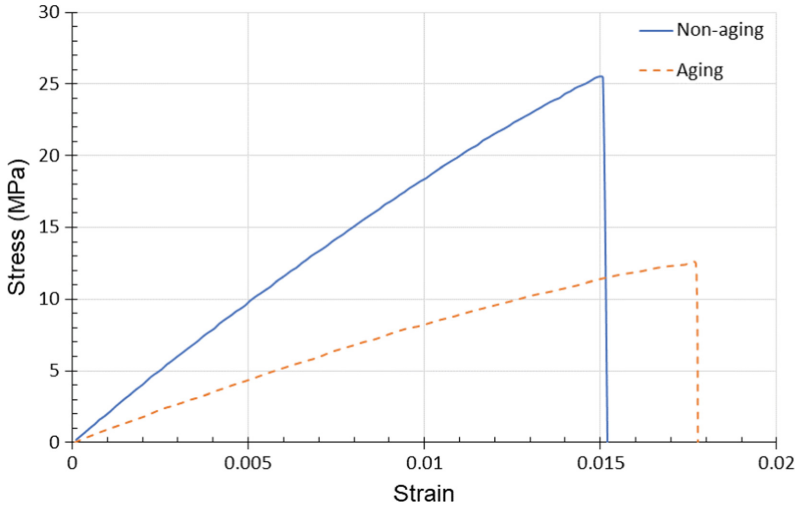
Fig. 1. Stress-strain curve for non-aged and aged rubberwood/recycled PP.
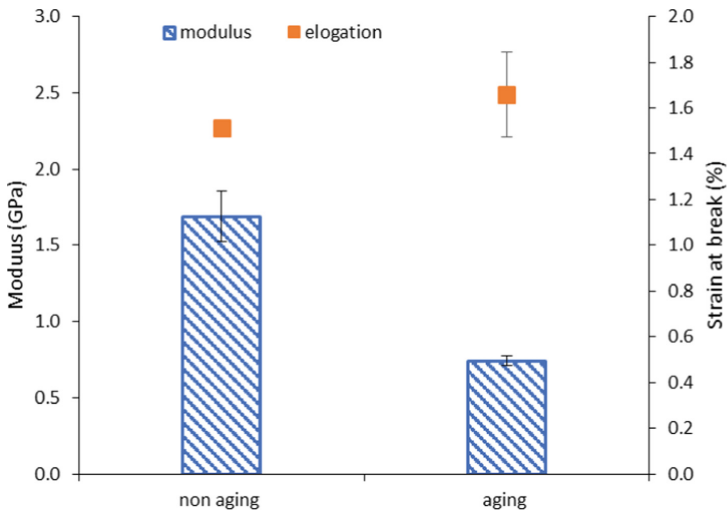
Fig. 2. Effect of water ageing on the tensile modulus and strain at break of rubberwood/recycled PP.

4   Conclusions

Rubberwood- recycled polypropylene composites provide good initial mechanical properties and can be used to provide an alternative to timber products. However, like any other natural fibre, rubberwood fibre is also sensitive to moisture. The preliminary study of the influence of the moisture shows that their mechanical properties are significantly affected by the water immersion environment where their initial strength and modulus

are significantly reduced from 26.33 MPa to 12.19 MPa and 1.69 GPa to 0.74 GPa respectively.

References

1. Fadzullah, S.S.M., Mustafa, Z.: Fabrication and processing of pineapple leaf fibre reinforced composites. In: Green Approaches to Biocomposite Materials Science and Engineering, pp. 125–147. IGI Global (2016)
2. Homkhiew, C., Ratanawilai, T., Thongruang, W.: Long-term water absorption and dimensional stability of composites from recycled polypropylene and rubberwood flour. J. Thermoplast. Compos. Mater. **29**(1), 74–91 (2016)
3. Alessi, S., Pitarresi, G., Spadaro, G.: Effect of hydrothermal ageing on the thermal and delamination fracture behaviour of CFRP composites. Compos. B Eng. **67**, 145–153 (2014)
4. Zulkafli, N., Malingam, S.D., Fadzullah, S.H.S.M., Mustafa, Z., Zakaria, K.A., Subramonian, S.: Effect of water absorption on the mechanical properties of cross-ply hybrid pseudo-stem banana/glass fibre reinforced polypropylene composite. Mater. Res. Exp. **6**(9), 095326 (2019)
5. Jumadi, M.T., Mansor, M.R., Mustafa, Z.: Influence of water absorptivity on kenaf fibre reinforced recycled-polymer composite properties. Progr. Indus. Ecol. Int. J. **12**(3), 220–233 (2018)
6. Srivabut, C., Ratanawilai, T., Hiziroglu, S.: Effect of nanoclay, talcum, and calcium carbonate as filler on properties of composites manufactured from recycled polypropylene and rubberwood fibre. Constr. Build. Mater. **162**, 450–458 (2018)

Effect of Addition Bio-Based Plasticizer on Thermal Properties of Polylactic Acid (PLA): A Review

Anis Ainaa Omar, Mohd Hafidzal Mohd Hanafi[✉], Nurul Hanim Razak, Asriana Ibrahim, and Nurul Afwanisa' Ab Razak

Centre for Advance Research on Energy, Fakulti Kejuruteraan Mekanikal, Universiti Teknikal Malaysia Melaka, Hang Tuah Jaya, 76100 Durian Tunggal, Melaka, Malaysia
`hafidzal@utem.edu.my`

Abstract. Polylactic Acid (PLA) are being utilized in various applications such as food packaging, biomaterial healthcare applications and 3D printing filament. Despite of all excellent properties of PLA, it has drawbacks which are low toughness, low in tensile elongation and high brittleness and low thermal characteristics. Hence, the aim of this paper is to review the effect of the addition bio-based plasticizer towards thermal properties of PLA. Many studies have been reported by researchers in producing a bio-based plasticizer originated from vegetable oils to replace the petroleum-based plasticizers which is harmful towards human and ecosystems. Four types of bio-based plasticizer were presented such as Epoxidized Karanja Oil (EKO), Epoxidized Rubber Seed Oil (EeRSO), Epoxidized Palm Oil (EPO) and a mixture of Epoxidized Palm Oil and Soybean Oil (EPSO). Blending ratio of bio-based plasticizer and PLA has affected the thermal properties which are glass transition temperature (T_g), crystallization temperature (T_{cc}) and melting temperature (T_m) are carried out. The findings from this review study shows that the highest reduction of T_g, T_{cc}, and T_m are at 10.13% for EKO, 12.2% for EPSO and 1.88% for EPSO. These results contribute significant improvement in flexibility and durability of PLA by mixing with bio-based plasticizer.

Keywords: Vegetable oil · Thermal properties · Bio-based plasticizer

1 Introduction

Rapid industrial development in various countries has resulted in a significant increase in plastic manufacturing such as Polylactic Acid (PLA) all over the world. The restoration of plastic waste continues to remain low due to the poor recycling of plastic, lack of awareness among society and deficiency in technological help. A lot of plastic garbage was dumped in the ocean, disposed of in landfills, or incinerated [1]. Pollution, food chain contamination, energy waste, and economic loss are all consequences of these massive amounts of plastic waste [1]. PLA is well known as a biodegradable polymer, but it has weakness which limit its usage in some applications such as low in toughness, high brittleness [2] and low thermal properties [3].

Currently, researchers are focusing more on improving properties of PLA by adding bio-based plasticizer to replace the petroleum-based plasticizer [4]. Vegetable oils were chosen as the feedstock for the bio-based plasticizer as it is low cost, environmentally safe and abundantly available [5]. By adding bio-based plasticizer towards PLA, this blend reduced T_g value where lower T_g, explained that the state of the material is in rubbery [6] state which indicates that the flexibility and durability were enhanced [7]. Hence, this paper aims to review the effect of addition bio-based plasticizer on thermal properties of Polylactic Acid (PLA).

2   Thermal Properties of Pure PLA and Plasticized PLA

Thermal properties of the samples are shown in Table 1. Several types of vegetable oil were used which are Epoxidized Karanja Oil (EKO), Epoxidized Rubber Seed Oil (EeRSO), Epoxidized Palm Oil (EPO) and a mixture of Epoxidized Palm Oil and Soybean Oil (EPSO). The thermal properties evaluated are glass transition temperature (T_g), crystallization temperature (T_{cc}) and melting temperature (T_m). The blending ratio of the bio-based plasticizer being added are 1%, 2.5%, 5% and 10%. PLA 99% indicates that the blending ratio between PLA and bio-based plasticizer is 99% of PLA while the remaining 1% is the bio-based plasticizer.

Table 1.   Thermal properties of all samples.

Authors	Vegetable oil	Blending ratio		Glass transition temperature (°C)	Crystallization temperature (°C)	Melting temperature (°C)
		Polymer	Plasticizer			
[8]	EKO	PLA (100%)	-	61.2	98.8	173
		PLA (99%)	EKO (1%)	61.1	93.1	171.8
		PLA (97.5%)	EKO (2.5%)	60.4	91.3	171.4
		PLA (95%)	EKO (5%)	58.3	90.4	171
		PLA (90%)	EKO (10%)	55	90.6	171.3
[7]	EeRSO	PLA (100%)	-	65	115.5	167.5
		PLA (95%)	EeRSO (5%)	60	112.5	165.7
[9]	EPO and a mixture of EPSO	PLA (100%)	-	62.85	124.11	149.79
		PLA (95%)	EPO (5%)	60.12	114.16	147.62
		PLA (95%)	EPSO (5%)	60.79	108.97	146.97

Epoxidized Karanja Oil (EKO), Epoxidized Rubber Seed Oil (EeRSO), Epoxidized Palm Oil (EPO) and a mixture of Epoxidized Palm Oil and Soybean Oil (EPSO)

2.1   Glass Transition Temperature (T_g)

Table 1 shows the glass transition temperature for all samples using different types of bio-based plasticizer such as epoxidized Karanja oil (EKO) [8], epoxidized palm oil (EPO), a mixture of epoxidized palm oil and soybean oil (EPSO) [9], and epoxidized rubber seed oil (EeRSO) [7]. Only EKO provides the data for all plasticizers and PLA blending meanwhile no data is provided in the articles for 1%, 2.5% and 10% of EPO, EPSO and EERSO. The highest glass transition temperature T_g was observed at pure PLA. The lowest T_g value was stated at 10% of EKO. As the content of the plasticizer increases, the T_g decreases. The reduction of T_g is due to the plasticizing effects resulting in less rigid material [10]. Low molecular weight of bio-based plasticizer will penetrate through the matrix, filling intermolecular regions between the polymer chains thus creating free volume which allowing the polymer chains to move more. The temperature above T_g, will act like rubbery material. While below T_g, the materials behave at glassy or crystalline state [6]. This shows that the PLA's flexibility is improved [8].

2.2   Crystallization Temperature (T_{cc})

In Table 1 the crystallization temperature, T_{cc} for EKO [8], EeRSO [7], EPO and EPSO [9] are carried out. PLA 99% indicates that the blending ratio between PLA and bio-based plasticizer is 99% of PLA while the remaining 1% is the bio-based plasticizer. No data is provided for 1%, 2.5% and 10% of EeRSO, EPO and EPSO same as the glass transition temperature. Pure PLA has the highest T_{cc} for all the samples meanwhile the lowest is at 5% of bio-based plasticizer. The T_{cc} of the samples reduced in parallel with the drop in [11]. When a bio-based plasticizer is diffused in PLA, the crystallization peak changes significantly towards lower temperatures.

2.3   Melting Temperature (T_m)

Melting temperature, T_m for all samples were shown in Table 1 for EKO [8], EeRSO [7], EPO and EPSO [9]. However same as glass transition and crystallization temperature where no data is provided for 1%, 2.5% and 10% of EeRSO, EPO and EPSO. Pure PLA has the highest T_m value meanwhile the lowest is at 5% of bio-based plasticizer for all the samples. The decrease in T_m of this blended samples shows that the compounds in the blends are more miscible [12]. All of the samples had a small decrease in melting temperature, showing that the addition of bio-based plasticizers exhibited less effect on PLA melting temperature [11].

3   Conclusion

The thermal characteristics of pure PLA and plasticized PLA using several types of bio-based plasticizer such as EKO, EeRSO, EPO and EPSO are discussed in this review study. The highest reduction of glass transition temperature is at 10.13%, resulting in better flexibility and durability where greater elongation at break occurred at low temperature. Meanwhile the highest reduction of crystallization and melting temperature are

12.2% and 1.88% for EPSO. PLA's characteristics are improved by adding bio-based plasticizers. 5% bio-based plasticizers mixed with PLA is the optimum blend. These finding shows that vegetable oil is a great placement to replace the petroleum-based plasticizer. Further study on using WCO as the feedstock for the bio-based plasticizer should be focused as WCO possess great benefits towards ecosystem.

References

1. Chow, C.-F., So, W.-M.W., Cheung, T.-Y., Yeung, S.-K.D.: Plastic waste problem and education for plastic waste management. In: Kong, S.C., Wong, T.L., Yang, M., Chow, C.F., Tse, K.H. (eds.) Emerging Practices in Scholarship of Learning and Teaching in a Digital Era, pp. 125–140. Springer, Singapore (2017). https://doi.org/10.1007/978-981-10-3344-5_8
2. Farah, S., Anderson, D.G., Langer, R.: Physical and mechanical properties of PLA, and their functions in widespread applications—a comprehensive review. Adv. Drug Deliv. Rev. **107**, 367–392 (2016)
3. Kamarudin, S.H., Abdullah, L.C., Aung, M.M., Ratnam, C.T.: Thermal and structural analysis of epoxidized jatropha oil and alkaline treated kenaf fibre reinforced poly (lactic acid) biocomposites. Polymers **12**(11), 2604 (2020)
4. Hosney, H., Nadiem, B., Ashour, I., Mustafa, I., ElShibiny, A.: Epoxidized vegetable oil and bio-based materials as PVC plasticizer. J. Appl. Polym. Sci. **135**(20), 1–12 (2018)
5. Jia, P., Xia, H., Tang, K., Zhou, Y.: Plasticizers derived from biomass resources: a short review. Polymers **10**(12), 1303 (2018)
6. Ebnesajjad, S.: Introduction to Plastics, vol. 45, 6th edn. Elsevier Inc., Amsterdam (1969)
7. Thuy, N.T., Duc, V.M., Liem, N.T.: Properties of poly (lactic acid) plasticized by epoxidized rubber seed oil. Vietnam J. Chem. **56**(2), 181–186 (2018)
8. Garcia-Garcia, D., Carbonell-Verdu, A., Arrieta, M.P., López-Martínez, J., Samper, M.D.: Improvement of PLA film ductility by plasticization with epoxidized karanja oil. Polym. Degrad. Stab. **179**, 0141–3910 (2020)
9. Chieng, B.W., Ibrahim, N.A., Then, Y.Y., Loo, Y.Y.: Epoxidized vegetable oils plasticized poly (lactic acid) biocomposites: mechanical, thermal and morphology properties. Molecules **19**(10), 16024–16038 (2014)
10. Suzuki, A.H., Botelho, B.G., Oliveira, L.S., Franca, A.S.: Sustainable synthesis of epoxidized waste cooking oil and its application as a plasticizer for polyvinyl chloride films. Eur. Polymer J. **99**, 142–149n (2018)
11. Thuy, N.T., Lan, P.N.: Investigation of the impact of two types of epoxidized vietnam rubber seed oils on the properties of polylactic acid. Adv. Polymer Technol. 1–9 (2021)
12. GiitaSilverajah, V.S., Ibrahim, N.A., Wan, Z., Yunus, W.M., Hassan, H.A., Woei, C.B.: A comparative study on the mechanical, thermal and morphological characterization of poly (lactic acid)/epoxidized palm oil blend. Int. J. Mol. Sci. **13**(5), 5878–5898 (2012)

The Effect of Sintering Temperature on Physical Properties of Sintered Green Glass Ceramic Composite (GCC) Using Design of Experiments (DOE) Software

Zurina Shamsudin[1(✉)], Masturah Mesri[1], and Rafidah Hassan[2]

[1] Fakulti Kejuruteraan Pembuatan, Universiti Teknikal Malaysia Melaka, Hang Tuah Jaya, 76100 Durian Tunggal, Melaka, Malaysia
`zurina.shamsudin@utem.edu.my`

[2] Fakutli Kejuruteraan Mekanikal, Universiti Teknikal Malaysia Melaka, Hang Tuah Jaya, 76100 Durian Tunggal, Melaka, Malaysia

Abstract. The influence of sintering temperature on properties of green glass ceramic composite (GCC) on various filler loadings was investigated. Experiment was conducted by using Design of Experiments (DOE) software. DOE applied was full factorial design which two factors and four levels. GCC was prepared using soda lime silicate glass (SLSG), spent bleach earth (SBE) and eggshell (ES). The results showed by increasing the sintering temperature, properties of the GCC will be improved. Sintering temperature was divided into 750, 800, 850, and, 900 °C at 2 °C/min with holding time 1 h. The GCC was formed using hydraulic dry pressing for eggshell at 0, 5, 10 and, 15 wt. % as filler loading. This study is focused on physical properties of the sintered green GCC according to ASTM C373. At highest sintering temperature 900 °C, apparent porosity was reduced from 17.95% to 12.97% and water absorption was reduced from 17.43% to 12.39%. The findings concluded that the suitable sintering temperature can be controlled for alternative materials for structural applications.

Keywords: Spent bleach earth · Soda lime silicate glass · Eggshell · Design of experiments

1 Introduction

The key technological point is the preliminary dissolution of waste into glasses, which allows the practically permanent stabilization of pollutants, whereas the main applications are in the building industry as floor and roof tiles or road surfacing panels [1]. The interest in soda lime silica glass (SLSG) waste is because of its composition and the large volume which is produced in Malaysia. Among the conventional glasses, SLSG is known as the most common commercial glass product that contributes up to 90–95% of the glass produced around the world. These types of glasses are commonly used because SLS glasses have a virtuous glass-forming nature compared to others several conventional glass system [2].

Spent bleaching earth (SBE) is one of the palm oil solid wastes that can be utilized to produce recycle product. SBE can be defined as an industrial waste that is mainly generated from the edible oil processing. SBE is commonly disposed in landfill without any pretreatment and usually contains 20–40 wt% of oil [3].

Eggshell which contains about 94 wt% calcium carbonate ($CaCO_3$) in its composition is not being considered a hazardous waste, its inappropriately landfill disposal can result in considerable environmental liabilities due to the large amount of eggs produced [4]. This element of $CaCO_3$ through process calcination to transform to CaO which is very important for structural applications since it attributed the improvement in strength in structure and thermal stability. To find the optimum solution, Response Surface Methodology (RSM) can be used. With the help of RSM modelling best values of output can be obtained for the optimum values of input variables. The main advantage of RSM is that it has predefined set of number of experiments runs for specific number of input variables and these numbers of experiment runs are very low as compared to other optimization techniques [5].

For this problematic material, this study represents an important contribution to developing new waste management option. This study reports on the effect of sintering temperature of green glass ceramic composite by analyzing the apparent porosity and water absorption via Design of Experiments (DOE) software.

2 Methodology

Glass waste in the form of soda lime silicate glass (SLSG) was collected from the household waste. The preparation of the glass waste undergone crushing, planetary ball milling and sieving below 45 μm. ES crushed using planetary ball mill and sieved to fine powders ($<45\,\mu$m). The raw SBE was cleaned for oil extraction using sonication process followed by filtrating and drying in oven to form fine powder. Particle size of SLSG, SBE and ES was determined using particle size analyzer, Mastersizer 2000 (Malvern Instrument Ltd model). The studied compositions is shown in Table 1. All samples were produced using conventional ball milling and manual hydraulic pressing prior to sintering. The square sample (18 × 18 × 4 mm) was pressed under 2.5 tons pressure and sintered at 750, 800, 850 and 900 °C using laboratory electric furnace Carbolite 1300 model at constant heating rate of 2 °C/min and 1 h holding time. The sintered samples were proceeded to physical testing according to ASTM C373. The sample was boiled in distilled water for 8 h and soaked for 24 h, the level of distilled water in the beaker was maintained. Analyses involved were water absorption, and apparent porosity. Then, all result were verified by using Analysis of Variance (ANOVA) generated from Design of Expert (DOE) software which involved two variables, apparent porosity and water absorption. Full factorial design (2k) as described by Montgomery was used [3]. Figure 1 shows a flowchart for preparation and analysis of sintered green GCC.
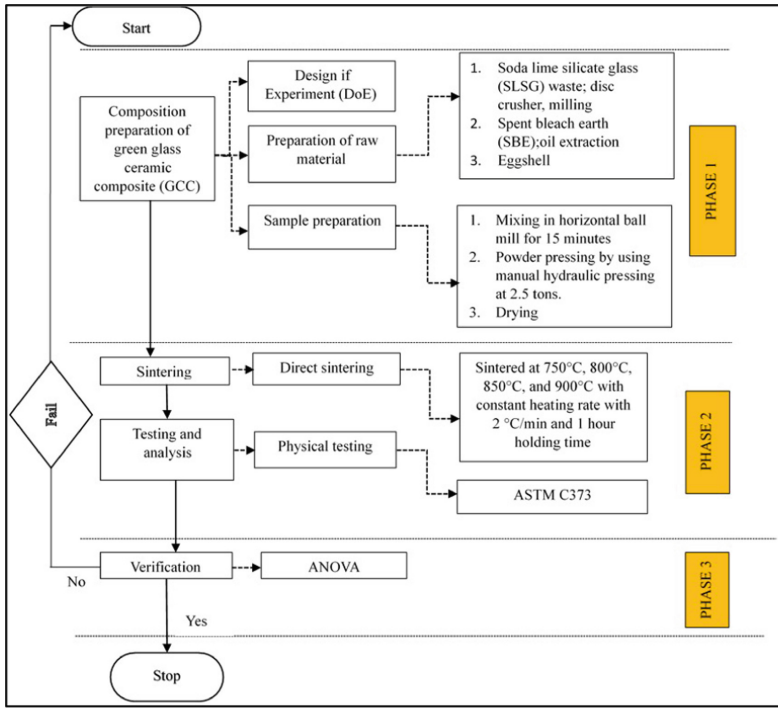
Fig. 1. Flowchart of sintered green GCC.

Table 1. Composition of sintered green GCC.

Sample	SLSG (wt. %)	SBE (wt. %)	Eggshell (wt. %)
A1	55	45	0
A2	50	45	5
A3	45	45	10
A4	40	45	15

3 Result and Discussion

Design of Experiment (DOE) software was used to conduct the experiment. For checking the adequacy of the developed model, F-test was performed. The next subsection will provide the details of the developed model and influence of sintering temperature on physical properties of sintered green GCC.

3.1 Influence of Sintering Temperature on Water Absorption and Apparent Porosity

A regression model was developed to evaluate the water absorption and apparent porosity of green GCC via direct sintering. The model of Eq. 1 and Eq. 2 were greater than F-tabulated value, which implies that the model is statistically correct and can be used for the forecasting of water absorption and apparent porosity of GCC. The probability value (p-value) of water absorption and apparent porosity were less than 0.5, which implies that model is fit within the confidence interval of 95. The model is considered significant since the F-value for water absorption was 24.08 and 21.77 for apparent porosity. The likelihood of the F-value occurring as a noise is only 0.01%. Also, the model terms are significant as the P-values are less than 0.0500. In this case, sintering temperature is significant model terms. Conversely, the model terms are not significant when the values are greater than 0.1000. The result is summarized in Table 2 below.

$$\text{Water absorption} = +51.45700 - 0.041207 \times \text{sintering temperature} \qquad (1)$$

$$\text{Apparent porosity} = +52.26700 - 0.041373 \times \text{sintering temperature} \qquad (2)$$

Table 2. ANOVA for physical properties.

Physical properties	F-value	P-value	
Water absorption	21.77	0.0001	Significant
Apparent porosity	24.08	<0.0001	Significant

Figure 2(a) illustrates the influence of sintering temperature on water absorption of green glass ceramic composite (GCC). Result showed that increased sintering temperature is accompanied by a decrease in the water absorption of GCC. Sintering temperature are vital in the enhancement of good GCC. The porosity of sintered green (GCC) was reduced due to the fine size of raw powder. Hence, there was alteration in the values of water absorption rate in accordance with the amount of available porosity. When the porosity is highly abundant, the sintering temperature increases, leading to less water absorption [6].

Figure 2(b) illustrates the influence of sintering temperature on apparent porosity of green GCC. The result showed that increased sintering temperature led to the decrease in the apparent porosity of GCC. Sintering temperature play important roles in the enhancement of good GCC. The porosity formation in glass ceramic could be influenced by several factors. [7] reported that the volume of the glass powder influenced the rate of pore formation in the glass ceramic. In conclusion, the increment of the eggshell content was associated with a decrease in the porosity of the glass ceramic as a result of lack of glassy form to assist viscous flow.
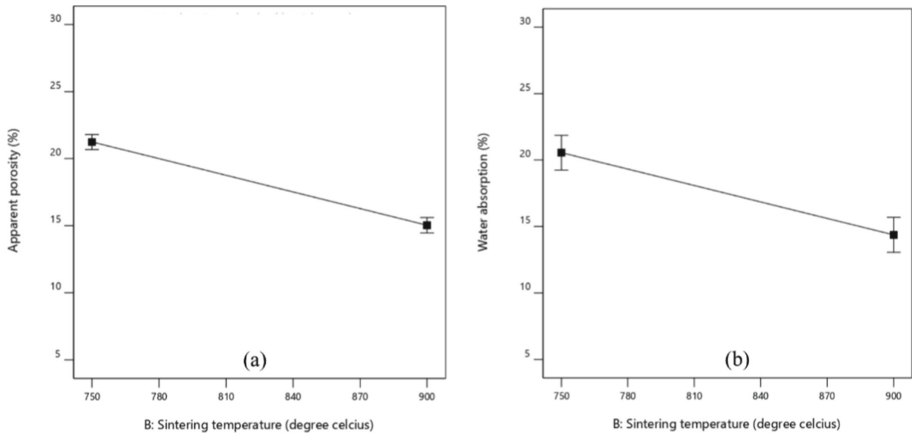
Fig. 2. Effect of sintering temperature on water absorption of sintered green GCC.

4   Conclusion

The effect of sintering temperatures on apparent porosity and water absorption of sintered green glass ceramic composite (GCC) was investigated. The sintering temperatures is important for physical properties of sintered green GCC. From this study, indicated higher sintering temperatures improved physical properties of sintered green GCC. The results showed that higher sintering temperature reduced apparent porosity and water absorption of GCC. Therefore, this study reveal the sintering temperature influence the composite.

References

1. Bernardo, E., Esposito, L., Rambaldi, E., Tucci, A., Pontikes, Y., Angelopoulos, G.N.: Sintered esseneite-wollastonite-plagioclase glass-ceramics from vitrified waste. J. Eur. Ceram. Soc. **29**(14), 2921–2927 (2009). https://doi.org/10.1016/j.jeurceramsoc.2009.05.017
2. Almasri, K.A., Sidek, H.A.A., Matori, K.A., Zaid, M.H.M.: Effect of sintering temperature on physical, structural and optical properties of wollastonite based glass-ceramic derived from waste soda lime silica glasses. Results Phys. **7**, 2242–2247 (2017). https://doi.org/10.1016/j.rinp.2017.04.022
3. Musa, M.L., Mat, R., Tuan Abdullah, T.: Optimised biofuel production via catalytic cracking of residual palm oil recovered from spent bleaching earth (SBE) over Ni/HZSM-5 Zeolite. J. Adv. Res. Fluid Mech. Therm. Sci. **51**(2), 108–123 (2018)
4. De Oliveira, K.G., Teixeira, A.H.B., De Oliveira, A.P.N.: Glass foams produced from glass bottles and eggshell wastes. Process Saf. Environ. Prot. (2017). https://doi.org/10.1016/j.psep.2017.06.011

5. Choudhary, S., Sharma, A., Gupta, S., Purohit, H., Sachan, S.: Use of RSM technology for the optimization of received signal strength for LTE signals under the influence of varying atmospheric conditions. EVERGREEN Joint J. Novel Carbon Resour. Sci. Green Asia Strategy **07**(04), 500–5009 (2020)
6. Ayoob, N.F., Juoi, J.M., Rosli, Z.M., Rosli, N.R.: Characterisation and properties of sintered glass-ceramics produced from recycling glass by using pressure-less method. Key Eng. Mater. **471–472**, 933–938 (2011). https://doi.org/10.4028/www.scientific.net/KEM.471-472.933
7. Mustafa, Z., et al.: Development and characterization of charcoal filled glass-composite materials made from SLS waste glass. In: AIP Conference Proceedings, vol. 1669 (2015). https://doi.org/10.1063/1.4919205

Observation of Graphene Oxide (GO) Nanoplatelets Stability in Water

Noor Syahadah Yussoff, Nik Roselina Nik Roseley(✉), and Nor Hayati Saad

School of Mechanical Engineering, College of Engineering, Universiti Teknologi MARA, 40450 Shah Alam, Selangor, Malaysia
`roselina.roseley@uitm.edu.my`

Abstract. Unique combination of extraordinary properties has made graphene and its derivatives as a promising filler for composite materials in a wide range of applications. However, due to its weak dispersibility and agglomeration, the design of homogeneous graphene composite is very challenging as it may influence the final properties of the composite materials. One of the most crucial preliminary steps in the fabrication of graphene composite is the preparation of a stable and well-dispersed graphene dispersion. Many studies reported the usage of surfactant or dispersing agents which are mostly highly toxic and non-biodegradable. The current study discussed the dispersion of graphene oxide (GO) in distilled and deionized water at various dispersion times. The main aim was to investigate the effect of dispersion medium and sonication time on GO dispersibility. In this work, the GO nanoplatelets were sonicated using ultrasonic bath for a duration from one (1) to four (4) hours in distilled and deionized water. Observations immediately after sonication and after 24-h were recorded respectively. Results show that the GO dispersions in deionized water was comparably more dispersed than GO in distilled water. In addition, the observation after 24 h also shows long-term stability of all GO in deionized water. The darker color of dispersion for GO in deionized water as compared to GO in distilled water indicates lesser agglomeration and more dispersibility of the nanoplatelets. The outcome of this work contributed to the facile and environmentally friendly method of the GO dispersion and worthy to be used for the preparation of homogeneous graphene composite specifically for graphene composite coating using electrodeposition method.

Keywords: Graphene oxide · Dispersion · Suspension · Distilled water · Deionized water

1 Introduction

Graphene is a legitimate starting point for new disruptive technologies across a wide range of areas due to its unique mix of exceptional features. At one atom thick (a million times thinner than a human hair), graphene is the thinnest compound known to man, the strongest compound discovered (between 100 and 300 times stronger than steel), the lightest material known (one square metre weighing around 0.77 mg), and the most flexible material known [1–3]. Graphene is also impenetrable to molecules and electrically

and thermally conductive, allowing electrons to move far quicker than silicon. It is also a transparent conductor that excels at combining electrical and optical functions [4, 5]. Graphene can be conceived of as a massive molecule that can be chemically modified and used in a wide range of applications, including electronics and composite materials. It is one of the potential materials that may solve the limitations of many applications and can be used to enhance the efficiencies of products in the scientific and technology sectors. Long-term engineering applications can benefit from the incorporation of graphene or graphene oxide (GO) into a suitable metal matrix. The poor dispersibility of graphene in water, on the other hand, can severely limit the creation of homogenous metal-graphene composite coatings on large substrates, thus reducing their performance. This could result in a financial loss as well as inefficiency in the process.

Dispersibility of graphene is one of the challenges for preparation of new matrix of graphene composite. Many researchers have reported the preparation of the graphene dispersion and its stability. A group of graphene can be dispersed in hot boiling solvents such as N-methyl-pyrrolidone or ortho-dichlorobenzene [6, 7]. In addition, it also can disperse in low-boiling solvents such as chloroform or isopropanol, neoteric solvents like supercritical fluids and ionic liquids [8]. Another research of graphene-polymer composites and graphene dispersions in organic media reported that a few hundred nanometers in size of graphene sheets were stable for the long-term in these dispersion techniques [9]. Most of the previous works have proven that stability of graphene dispersion is critical and challenging. It depends strongly on the graphene properties and the surface tension of the solvent-graphene and solubility parameters [10].

Graphene oxide (GO) has a 2D structure like graphene decorated with oxygen containing groups such as hydroxyl, epoxide and carbonyl [11]. Due to the existence of oxygen-containing functional groups, GO is hydrophilic in nature with high water dispersibility [12]. Therefore, most works have been done in aqueous environments. Many works also reported GO suspension in other solvents, particularly organic solvents which have made the actual usage considerably easier [13, 14]. There are also many works reported usage of various compounds and polymers in organic solvents by covalent operation of the graphene oxide sheets. However, for most applications, the presence of these stabilisers is not desired [15, 16].

The main aim of the work was to investigate the effect of dispersion medium and sonication time on GO dispersibility in water. Notably, the graphene oxide may be exfoliated into individual graphene oxide sheets in deionized water, resulting in dispersions with long-term stability equivalent to graphene oxide dispersions in distilled water. This finding may aid in the creation of homogeneous graphene composites specifically for graphene composite coatings using the electrodeposition method.

2   Experimental Section

Graphene oxide (GO) nanoplatelets with diameter of approximately size of 0.5–5 μm and thickness of 0.8–1.2 nm was mixed and dispersed in deionized and distilled water for one to four hours to obtain a good dispersion of graphene. A well-dispersed graphene solution is important to avoid aggregation of graphene when deposited on the surface. The GO was dispersed via ultrasonication for one (1) to six (6) hours in distilled water

and 1 to 4 h in deionized water. The sonication of GO in deionized water was not extended to more than four (4) hours as no significant changes can be observed when the duration was prolonged. GO nanoplatelets of 0.04 g was added into 1.0 L of deionized and distilled water prior to sonication via ultrasonication method. Figure 1 shows the schematic illustration of the flow for GO dispersion test.
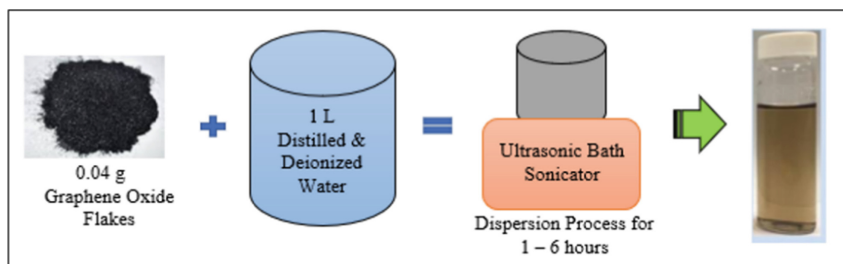
Fig. 1. Schematic illustration of graphene oxide dispersion test.

3 Results and Discussion

GO nanoplatelets were ultrasonicated for a duration from one (1) to six (6) hours in distilled and one (1) to four (4) hours in deionized water. Observations immediately after sonication and after 24 h were recorded. This test is a qualitative method to characterise the stability of graphene oxide in each solvent. Figure 2 shows the observation of GO dispersion in distilled water immediately after one (1) to six (6) hours dispersed in ultrasonic from left to right. As can be seen, even immediately after sonication, sedimentation can be seen as dark area at the bottom of the sample vial for GO dispersed for one (1) to five (5) hours in dotted red box in Fig. 2. The results reveal the settlement of some of the GO nanoplatelets after sonication and almost no sedimentation of GO in suspension of distilled water sonicated for six (6) hours.

In order to quantitatively measure the dispersion, the grayscale level of the dispersion was also measured. The interpretation of greyscale value can be seen in Fig. 3, where the lowest value of grayscale (0) represents complete black colour and vice versa. The grayscale of the three (3) positions of the suspension was measured using ImageJ analysis software along the lines at Point 1, Point 2 and Point 3 displayed in the inlet of Fig. 4. For a suspension with liquid and solid, point 1 is commonly known as supernatant, while Point 2 and 3 are the dispersion, and the sediment is the settlement of solid particles at the bottom of the suspension. Fig. 4 presents the grayscale values of GO-distilled water suspension at three (3) points sonicated for one (1) to six (6) hours. In general, the grayscale of the suspension shows a gradual increase of value as the sonication time increased from one (1) to three (3) hours, before significantly reduced. There might be lesser effect of GO sonication from one (1) to three (3) hours in distilled water. GO dispersed for six (6) hours was darker in colour with the lowest grayscale value. The values of grayscales are also almost similar in all three (3) points which reveals the good homogeneity of the GO-distilled water suspension sonicated for six (6) hours compared to others.
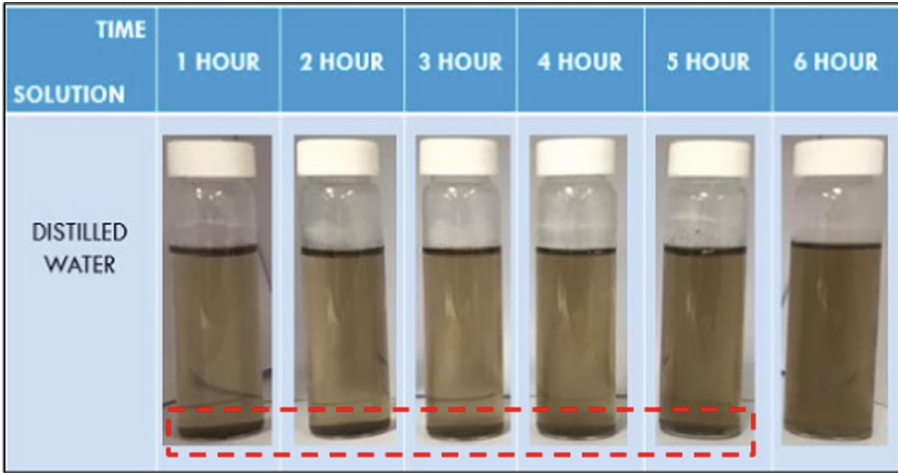
Fig. 2. Observation of GO dispersed in distilled water immediately after sonicated for one (1) to six (6) hours.

Fig. 3. Interpretation of grayscale value.
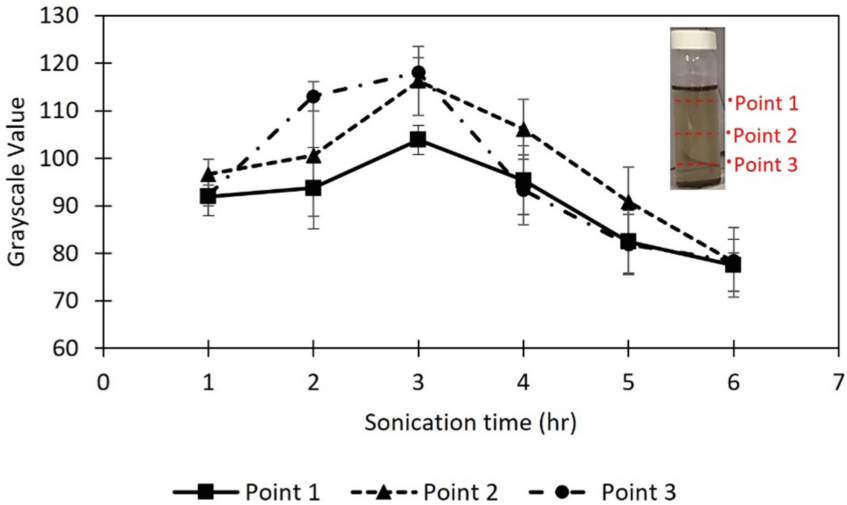
Fig. 4. Grayscale of GO dispersed in distilled water immediately after sonicated for one (1) to six (6) hours.

The observation after 24 h in Fig. 5 demonstrates that more GO nanoplatelets had settled to the bottom of the sample vials for all GO suspensions as can be seen in the red dotted line in Fig. 5. The colour of all suspensions seems to be brighter than the colour of suspensions in Fig. 2. Existence of nanoplatelets floating in the suspension become more obvious in all suspension creating uneven suspensions. The grayscale measurement at three (3) points of suspensions is shown in Fig. 6. Interestingly, the grayscale values showed inverse dispersion behaviours after being left for 24 h as compared to after sonication. GO-Distilled water suspension sonicated for once (1) hour exhibited the lowest grayscale value with nearly similar values for all positions of Point 1, 2 and 3. Contrary, suspension sonicated for six (6) hours has among the highest grayscale value. More GO nanoplatelets may have been settled down leaving brighter colour of suspension. In addition, higher standard deviation of grayscale values for suspension sonicated for six (6) hours confirmed the discrepancy of GO dispersion in the suspension as seen in Fig. 5.
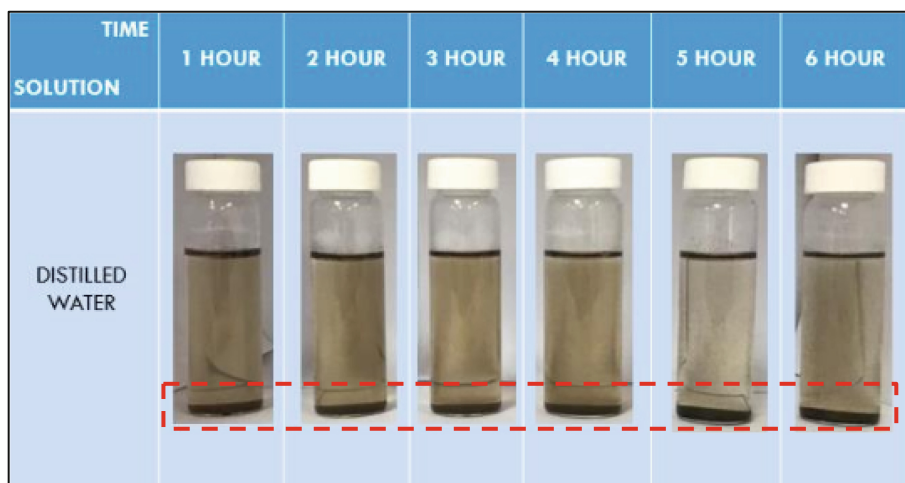
Fig. 5. Observation after 24 h of GO-distilled water suspensions sonicated for one (1) to six (6) hours.

The grayscale of suspensions has also been compared to examine the change of stability after 24 h. The comparison of grayscale at Point 1 for all suspensions, immediately after sonication and 24 h is presented in Fig. 7. As expected, the grayscale values of all suspension raised after 24 h. Although suspensions sonicated longer hour (5 and 6 h) appear to have better dispersity after sonication, it did not assist in improving the stability of suspension.

GO nanoplatelets were also dispersed in deionized water to further investigate the dispersion of GO. Similar to GO dispersed in distilled water, the GO nanoplatelets were added into deionized water and sonicated accordingly. The observations of GO dispersed in deionized water for one (1) to four (4) hours are presented in Fig. 8. Dispersion time was limited to a maximum of four (4) hours since no noticeable changes were detected after three (3) hours. Observation in Fig. 8 shows that the GO dispersed in deionized
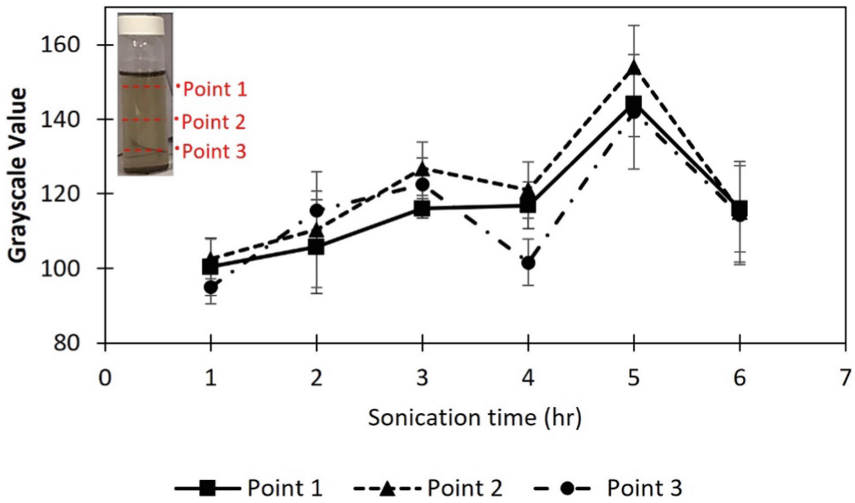
Fig. 6. Grayscale values of GO-distilled water suspensions sonicated for one (1) to six (6) hours after 24 h.
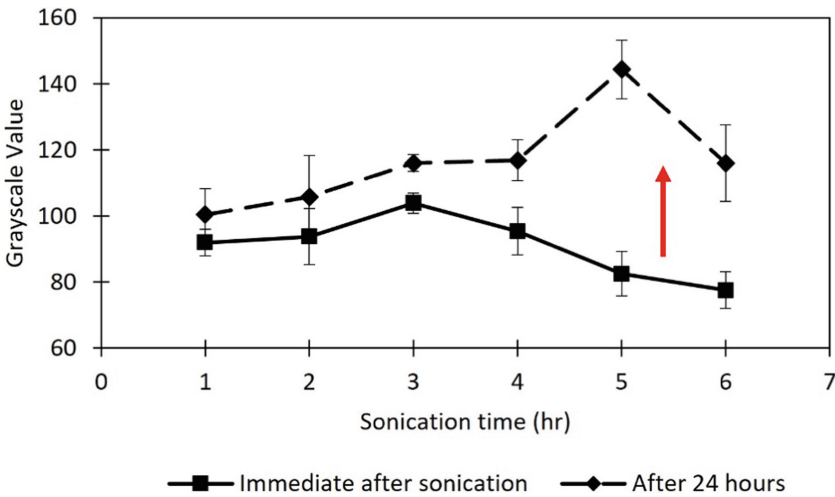
Fig. 7. Comparison of grayscale values of GO-distilled water suspensions immediately after sonication and after 24 h.

water was comparably more stable with lighter colour of suspension compared to GO dispersed in distilled water. No obvious settlement of GO nanoplatelets can be observed at the bottom of the vials of all dispersions except small amount in suspension sonicated for one (1) hour.

Quantitative analysis using grayscale of all suspensions at the three (3) points of suspension are presented in Fig. 9. The grayscale values of GO-deionized water are totally different from GO-distilled water suspensions in Fig. 4. The values for all three

(3) points are quite distinguish from each other especially at Point 1. Point 1 has the lowest grayscale values for all suspensions followed by Point 2 and 3. All four (4) suspensions have almost the same grayscale values at Point 1. This shows the black colour of suspension turned lighter from Point 1 to Point 3. The results indicate that most of GO nanoplatelets were at the top area of all the suspensions after sonication. In this work, the indirect sonication method using ultrasonication was used. It may has pushed most nanoplatelets far away from the bottom of vial and resulted more stable nanoplatelets to be at the top areas.
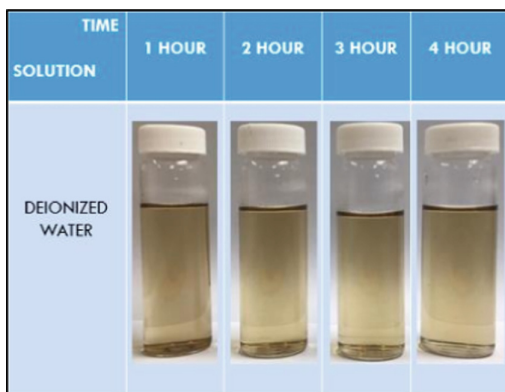
Fig. 8. Observation of GO-deionized water suspensions immediately after one (1) to four (4) hours sonication.
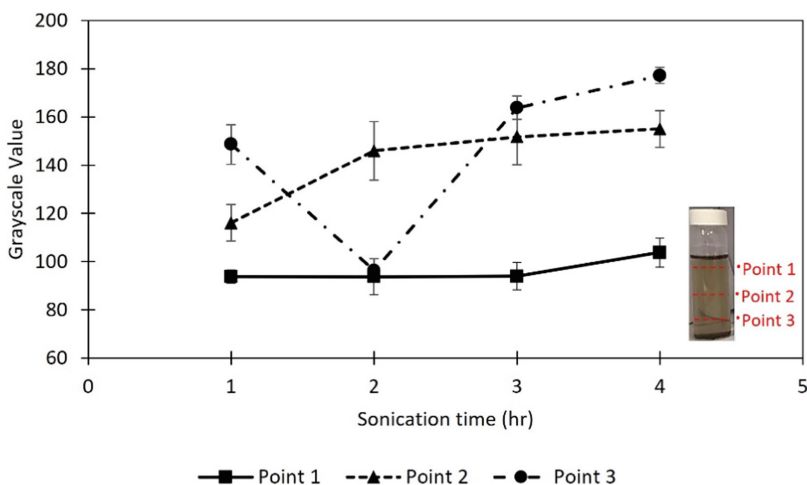
Fig. 9. Grayscale of GO-deionized water suspensions immediately after sonicated for one (1) to six (6) hours.

The observations after 24 h in Fig. 10 show that all GO dispersions in deionized water are still stable with darker colour of dispersions compared to the suspensions after

sonication in Fig. 8. More nanoplatelets can be seen in all suspensions with suspension sonicated for one (1) hour having rather more sediment compared to others. The grayscale values in Fig. 11 show that all three (3) points of Point 1, 2 and 3 still possess different grayscale values identical to the trend observed in Fig. 9. There was only insignificant increase in grayscale values from suspension sonicated for one (1) to four (4) hours at all points.
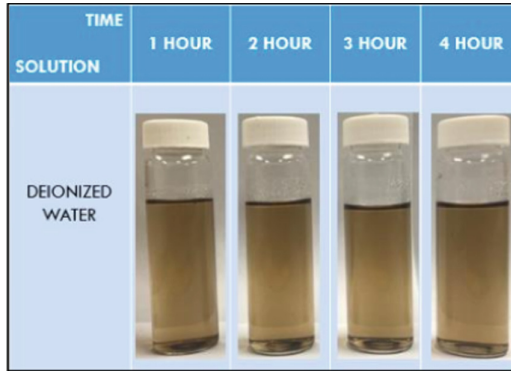
Fig. 10. Observation after 24 h of GO-deionized water suspensions sonicated for one (1) to four (4) hours.
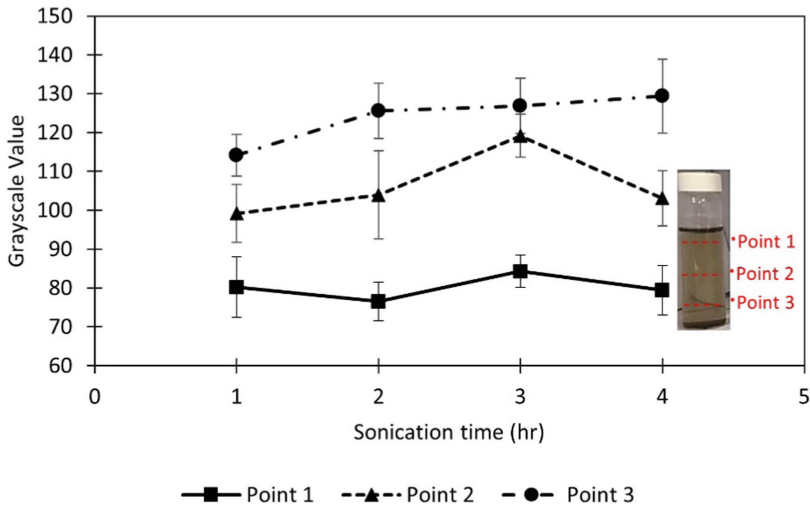
Fig. 11. Grayscale values of GO-deionized water suspensions sonicated for one (1) to four (4) hours after 24 h.

Figure 12 represents the comparison of grayscale values of suspension immediately after sonication and after 24 h. Point 1 was used as reference similar to the previous comparison for GO-distilled water suspensions. Inverse to the results seen from GO-distilled water suspensions in Fig. 7, the grayscale values went from high to low. The

colours of all suspensions after 24 h were darker than the suspension after sonication. The stability of the suspensions also seems to be almost equally stable with higher standard deviation for suspension sonicated for one (1) hour, which suggest there may perhaps be more uneven distribution of nanoplatelets in the suspension. Extending sonication time for GO-deionized water suspension may have very small effect on the stabiligy of suspension after two (2) hours of sonication.
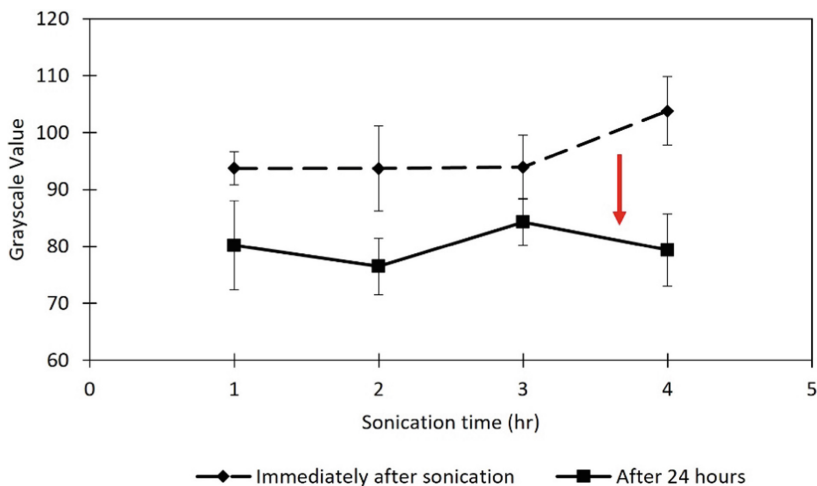
Fig. 12. Comparison of grayscale values of GO-deionized water suspensions immediately after sonication and after 24 h.

Finally, the stability of GO suspensions in both distilled and deionized water is compared in Fig. 13. It is apparent that the grayscale values of suspensions for GO-deionized water after 24 h are the lowest of all that represent the stability of black GO in deionized water. The region marked in the red dotted box in Fig. 13 is where grayscale values of all suspension after sonication mostly lies with some exception for suspension GO-distilled water sonicated for five (5) and more hours. It is evident that sonication may has enhanced the dispersion of GO in distilled water. Ultrasonication is known as one of the well-known methods that can produce stable dispersion by particles size reduction in liquid [17–19]. GO nanoplatelets may have broken into smaller size with prolonged sonication time over five (5) hours thus improve the GO nanoplatelets dispersion right after the sonication. Ye and Feng has also reported that sonication damaged and break GO sheets into smaller sizes [20]. Further work will be carried out in the next study to investigation the size of the GO nanoplatelets in all suspensions.

However, despite the substantial effect of sonication time, the GO-distilled water suspensions did not maintain its stability after 24 h. On the other hand, results also show that GO-deionized water improves its stability over time. The outcomes imply a present of Brownian motion effect of GO nanoplatelets in deionized water but not distilled water. The Brownian motion is a well-known phenomenon that keep submicron particles disperse in liquid [21, 22]. GO is hydrophilic in nature due to existence of hydroxyl, epoxy groups, carbonyl and carboxyl groups which make it easy to disperse in water [23]. Figure 14 illustrates the dispersion of GO nanoplatelets in distilled and deionized water over time. Deionized water is treated water that contain lesser number or no ions and mineral salts in it as compared to distilled water that may have impurities. The existence of impurities like mineral salts in distilled water may have hindered the Brownian motion effect GO nanoplatelets hence cannot stay stable over long time.
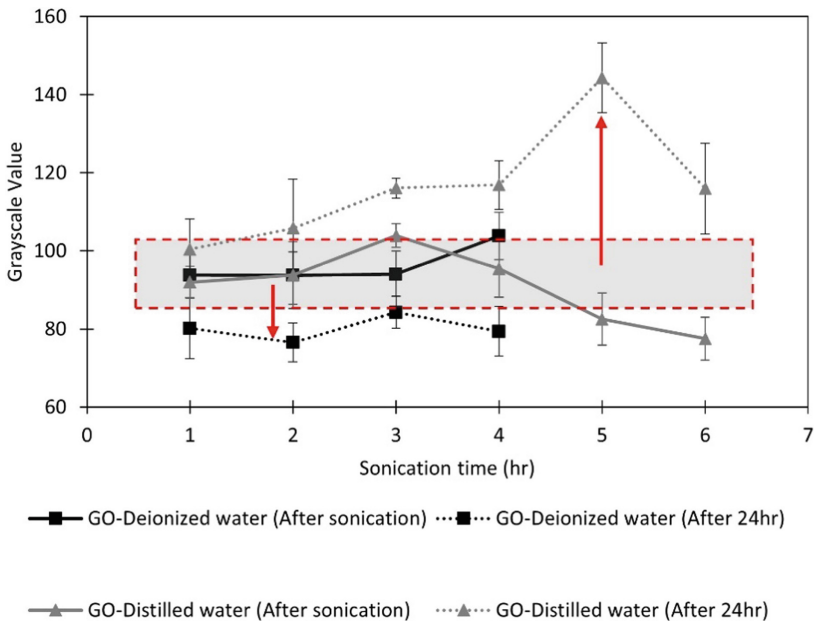
Fig. 13. The comparison of grayscale values of GO-deionized and GO-distilled water suspensions after sonication and 24 h.
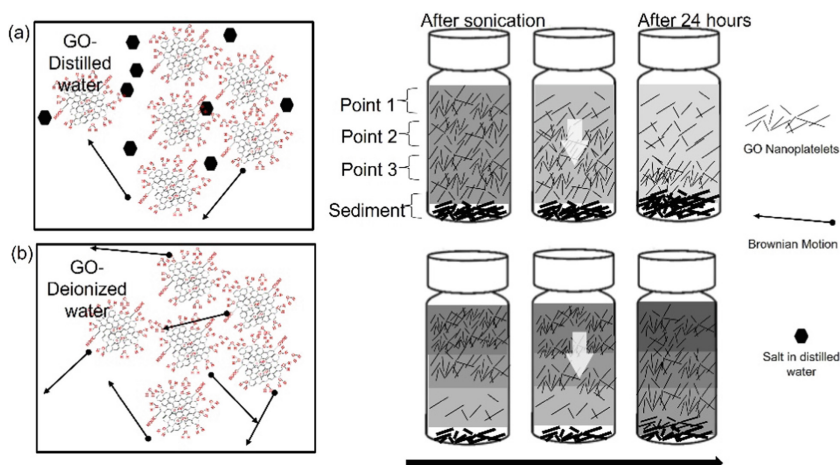
Fig. 14. Schematic illustration of GO dispersion in distilled water and deionized water.

4 Conclusion

Graphene oxide (GO) nanoplatelets were dispersed in distilled and deionized water and compared. The suspensions of GO-deionized water reveal good dispersibility compared to GO-distilled water. Prolong sonication time may improve the dispersibility of GO nanoplatelets in distilled water but not the stability over time. It is therefore understood that the selection of type of water significantly affects the GO processing for further application. The processing method of GO dispersion in deionized water carried out in this work will be extended for the preparation of homogeneous graphene composite coatings using the electrodeposition method.

References

1. Ren, W., Cheng, H.M.: The global growth of graphene. Nat. Nanotechnol. **9**(10), 726–730 (2014)
2. Barkan, T.: Graphene: the hype versus commercial reality. Nat. Nanotechnol. **14**(10), 904–906 (2019)
3. Dong, L.-X., Chen, Q.: Properties, synthesis, and characterization of graphene. Front. Mater. Sci. China **4**(1), 45–51 (2010). https://doi.org/10.1007/s11706-010-0014-3
4. Wang, S., Hossain, Z., Zhao, Y., Han, T.: Fundamental of graphene. In: Wang, S., Hossain, Z., Zhao, Y., Han, T. (eds.) Graphene Field-Effect Transistor Biosensors, pp. 1–19. Springer, Singapore (2021). https://doi.org/10.1007/978-981-16-1212-1_1

5. Khrapach, I., et al.: Novel highly conductive and transparent graphene-based conductors. Adv. Mater. **24**(21), 2844–2849 (2012)
6. Wang, W., Gai, Y., Song, N., Xiao, D., Tan, H., Zhao, Y.: Highly efficient production of graphene by an ultrasound coupled with a shear mixer in supercritical CO_2. Ind. Eng. Chem. Res. **57**, 16701–16708 (2018)
7. Zhang, B., et al.: Stable dispersions of reduced graphene oxide in ionic liquids. J. Mater. Chem. **20**, 5401–5403 (2010)
8. Bordes, E., et al.: Dispersion and stabilization of exfoliated graphene in ionic liquids. Front. Chem. **7**, 223 (2019)
9. Villar-Rodil, S., Paredes, J.I., Martínez-Alonso, A., Tascón, J.M.D.: Preparation of graphene dispersions and graphene-polymer composites in organic media. J. Mater. Chem. **19**, 3591–3593 (2009)
10. Hernandez, Y., Lotya, M., Rickard, D., Bergin, S.D., Coleman, J.N.: Measurement of multicomponent solubility parameters for graphene facilitates solvent discovery. Langmuir **26**, 3208–3213 (2010)
11. Tarcan, R., Todor-Boer, O., Petrovai, I., Leordean, C., Astilean, S., Botiz, I.: Reduced graphene oxide today. J. Mater. Chem. C **8**(4), 1198–1224 (2020)
12. Chauhan, D.S., Quraishi, M.A., Ansari, K.R., Saleh, T.A.: Graphene and graphene oxide as new class of materials for corrosion control and protection: present status and future scenario. Prog. Org. Coat. **1**(147), 105741 (2020)
13. Du, H., Pang, S.D.: Dispersion and stability of graphene nanoplatelet in water and its influence on cement composites. Constr. Build. Mater. **167**, 403–413 (2018)
14. Paredes, J.I., Villar-Rodil, S., Martínez-Alonso, A., Tascón, J.M.D.: Graphene oxide dispersions in organic solvents. Langmuir **24**(19), 10560–10564 (2008)
15. Kim, D.W., Kim, D., Min, B.H., Lee, H., Jung, H.T.: Sonication-free dispersion of large-area graphene oxide sheets using internal pressure from release of intercalated carbon dioxide. Carbon N. Y. **88**, 126–132 (2015)
16. Shojaeiarani, J., Bajwa, D., Holt, G.: Sonication amplitude and processing time influence the cellulose nanocrystals morphology and dispersion. Nanocomposites **6**, 41–46 (2020)
17. Lu, S., Pugh, R.J., Forssberg, E.: Dispersion of particles in liquids. In: Lu, S., Pugh, R.J., Forssberg, E. (eds.) Interfacial Separation of Particles, pp. 517–558. Elsevier, Amsterdam (2005)
18. Tyurnina, A.V., et al.: Ultrasonic exfoliation of graphene in water: a key parameter study. Carbon **168**, 737–747 (2020)
19. Turner, P., Hodnett, M., Dorey, R., Carey, J.D.: Controlled sonication as a route to in-situ graphene flake size control. Sci. Rep. **9**(1), 1–8 (2019)
20. Ye, S., Feng, J.: The effect of sonication treatment of graphene oxide on the mechanical properties of the assembled films. RSC Adv. **6**(46), 39681–39687 (2016)
21. Hoffman, B.D., Shaqfeh, E.S.: The effect of Brownian motion on the stability of sedimenting suspensions of polarizable rods in an electric field. J. Fluid Mech. **624**, 361–388 (2009)
22. Maragó, O.M., et al.: Brownian motion of graphene. ACS Nano **4**(12), 7515–7523 (2010)
23. Ouyang, G., Hussain, A., Li, J., Li, D.: Remarkable permeability enhancement of polyethersulfone (PES) ultrafiltration membrane by blending cobalt oxide/graphene oxide nanocomposites. RSC Adv. **5**(86), 70448–70460 (2015)

Mechanical and Morphological Properties of Pineapple Leaf Fibre/Kenaf Fibre Reinforced Vinyl Ester Hybrid Composites

M. A. F. Aznan[1], R. Nadlene[1,3(✉)], M. T. Mastura[2,3], M. Nuzaimah[2,3], M. Noryani[1,3], and M. A. Shaharuzaman[1,3]

[1] Fakulti Kejuruteraan Mekanikal, Universiti Teknikal Malaysia Melaka, Hang Tuah Jaya, 76100 Durian Tunggal, Melaka, Malaysia
nadlene@utem.edu.my

[2] Fakulti Teknologi Kejuruteraan Mekanikal & Pembuatan, Universiti Teknikal Malaysia Melaka, Hang Tuah Jaya, 76100 Durian Tunggal, Melaka, Malaysia

[3] Centre for Advanced Research on Energy, Universiti Teknikal Malaysia Melaka, Hang Tuah Jaya, 76100 Durian Tunggal, Melaka, Malaysia

Abstract. Pineapple leaf (PALF) and kenaf fibre has wide potential to be used as a reinforcement material in polymer composites for different applications. Hybrid composites of natural fibre is one of the favorable method in order to improves the mechanical properties of the composites. This research investigates the mechanical and morphological properties of PLAF/kenaf fibre reinforced vinyl ester hybrid composites. The fibre was treated with alkalization and samples were prepared using hand lay-up method. Tensile and flexural test were conducted to determine mechanical properties of the hybrid composite. From the obtained results, treated fibre successfully enhanced the mechanical properties of vinyl ester hybrid composite. The morphological examination of neat polymer, treated and untreated fibre composite-reinforced vinyl esters were carried out to anlyse the morphological properties. Treated fibre composites showed less fibre pull-out compared to untreated fibre composite. The observation indicates the improvement of interfacial bonding between fibre and polymer which improved the tensile and flexural properties of the composites. Combination of PALF and kenaf fibre gives outstanding properties to mechanical properties of the composites.

Keywords: Natural fibre composites · Vinyl ester · Hybrid composites

1 Introduction

Natural fibre possess a crucial concern in developing fibre reinforced polymer (FRP) composite to conclude the present ecological and environmental issue. Lucintel released a market report that told global natural fibre composite material market is increasing at a Compound Annual Growth Rate (CAGR) of 8.2% from 2015 to 2020 [1]. There is concern in bio-based materials especially natural fibre reinforced composites that correspond not only with legislation popularized in wide markets such as European

Union (Directive 2000/53/EC) but with the priority of many major automakers' interest in global sustainability. The industries demand a lower price for production of fibre components at the same time with an improvement in quality as there is high price in composites [2]. In order to resolve the ongoing ecological and environmental issues, natural fibres could show a meaningful part in establishing biodegradable composite [3].

Natural fibres especially sisal, jute, banana, coir and pineapple captivated the attention of materials scientists and technologists for purpose of consumer goods, reasonable structural materials and automotive parts. Natural fibre also have low density, renewable and biodegradable [4]. The natural fibre which has magnificent potential to be passed down as reinforcing materials in green composite product are pineapple leaf fibre (PALF) and kenaf fibre (KF).

Pineapple leaf fibre was chosen as natural fibre used in this research in the interest of comparatively better mechanical properties, accessible and economical than the established natural fibre such as kenaf and jute [3]. The manufactory treats pineapple leaves as agricultural wastes formed or burnt by country person after the fruits are harvested when focusing on the fruits and related foodstuffs [5]. Already well-known in Malaysia as well as South-East Asia is kenaf fibre [1] where possessing flexural strength combined with its outstanding tensile strength caused kenaf bast fibre as material of choice for a wide range of extruded, molded and non- woven products [6].

In this research, mechanical and morphological properties of PALF/kenaf fibre reinforced vinyl ester hybrid composites are analyzed. The outcomes were used to enhance the perceptive of PALF and kenaf fibre and their need as reinforcement in vinyl ester hybrid composites in the attempt to employ these outstanding fibres.

2   Materials and Method

2.1   Materials

Pineapple leaf fibre was acquired at plantation site from Kota Tinggi-Mersing, Johor, and Kenaf fibre was in the form of powder received from Lembaga Kenaf dan Tembakau Negara, Kedah. The PLAF obtained in the form of yarn was manually cut into 1cm of length. Next, the fibers were cleaned by using distilled water and dried in the sunlight before been treated.

Vinyl ester (VE) obtained from Polymer Technology Pte. Ltd. (Singapore) was used in this study. The density, heat distortion temperature (HDT), viscosity and glass transition temperature of VE are 1.6 g/cc, 120 °C, 400 cps, and 104.44–143.33 °C, respectively. Methyl ethyl ketone peroxide (MEKP) was used as a hardener.

NaOH solution for the alkalization, sodium hydroxide pellets 99% grade was obtained from QRac (Asia) Sdn. Bhd., Malaysia. The fibers were immersed into 6% of NaOH concerntration for 2 h at room temperature in a basin. After the chemical treatment of the fibers, it were thoroughly washed with running water and dried in oven at 104 °C for 48 h to eliminate the moisture effect of the fibers.

Composites samples were fabricated by hand lay-up method. Figure 1 shows the hand lay-up process.
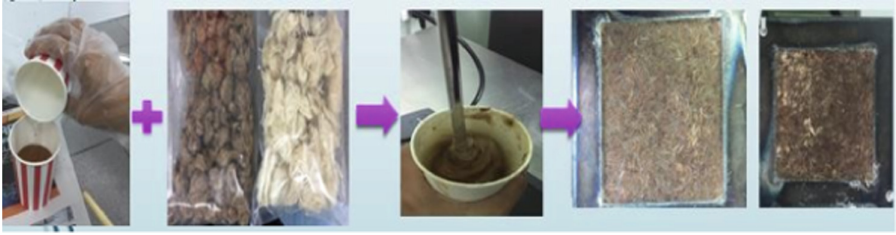
Fig. 1. Hand layup process of hybrid composites.

2.2 Methods

Tensile test is used to identify the mechanical properties of the materials which also recognized as a simple and common test. Tensile test was conducted according to ASTM D3039. The gauge length of the samples was 100 mm, and the cross-head speed was 50 mm/min with a 5 kN load cell. Five samples were prepared to perform a tensile test for each group of neat polymer, treated fibre composites and untreated fibre composites.

ASTM D790 standard was used for the flexural tests performed by using a three-point bending setup. For the flexural test, five samples at least were tested for each types of samples. 100 mm (l) × 10 mm (w) × 3 mm (t) were dimension of the samples which are tested by using Universal Testing Machine, Instron 5585.

Morphological studies were performed in detail on the fractured surface of impact test samples using a scanning electron microscope (SEM), model Joel (JSM-IT800 Field Emission Scanning Electron Microscope), at an accelerating voltage of 15 kV. The samples were platinum coated to provide electrical conductivity, which did not significantly affect the resolution, thus obtaining good quality results.

3   Results and Discussions

Tensile test were performed in this project to determine the mechanical properties of PALF/KF reinforced vinyl ester hybrid composites. The ultimate tensile strength was used to evaluate the fibre resistance towards maximum force and stress while being stretched before rupture. 20 wt% of fibre (50% PALF and 50% kenaf) was used as reinforcement material to study the effect of treatments on mechanical properties of the composite. 20% wt has been choose for this project based on the results optimization of PALF reinforced vinyl ester composites. Neat polymer (100% vinyl ester) shows the highest tensile strength at 17.54 MPa. The presence of fibre decreases the tensile strength of the fibre composite. It might be due to the incompatibility of the fibre and polymer. However, the treatment of the fibre showed an improvement in tensile properties compared to the untreated fibre. The result shows that treated fibre composite has higher tensile strength, 7.8 MPa compared to untreated fibre composite, 4.92 MPa. The result was supported by previous research that states the strength and interfacial adhesion increase by chemical treatment [7] (Fig. 2).
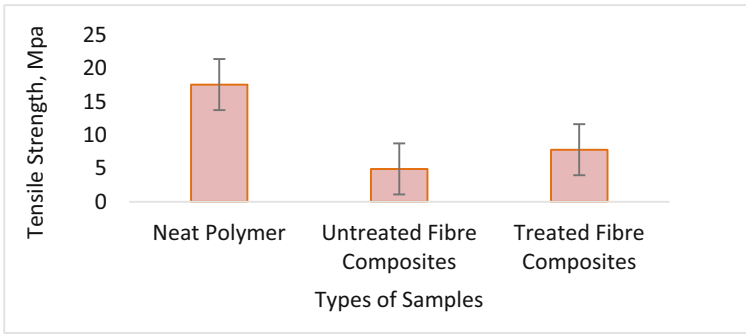
Fig. 2. Tensile strength of PALF/kenaf fibre reinforced ve hybrid composite.

Flexural test is performed to evaluate strength and ability of the resistance material to the deformation under bending loads before it failed. Figure 3 shows the results of flexural strength. The flexural strength on the treated fibre composite is the highest, 72.40 MPa compared to untreated fibre composite, 13.12 MPa and the lowest is neat polymer at 46.78 MPa. It shows that alkaline treatment improves mechanical properties. From previous studied, it was found that, the fibre in the matrix is expected to increase the flexural strength of the composites because of the presence of rigid particles in the matrix [8]. According Ibrahim et al. (2012), the relative stiffness of a material is indicated by its modulus. It is widely understood that the addition of filler will improve the stiffness of composites [9]. In this study, the addition of hybrid fibre improved the stiffness of the vinyl ester matrix, since the flexural strength of the composites increases in the presence of fibre. However untreated fibre is found to be lower due to the voids content in the composites and agglomeration of the fibre which leads to be non-uniform dispersion of fibre and the matrix [10]. Other possibility leads to this lower results is the weak adhesion between fibre and matrix. It obviously, shows treated fibre improves the adhesion between hybrid fibre and the polymer.
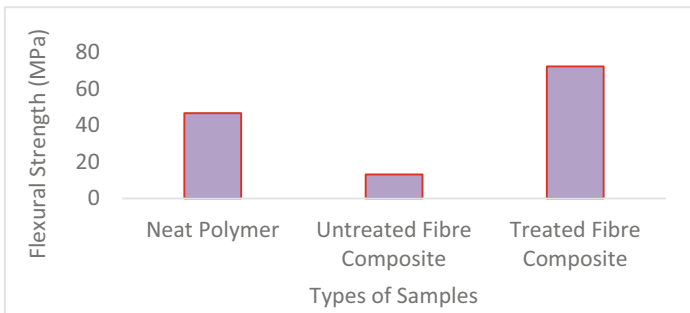
Fig. 3. Flexural strength of PALF/kenaf fibre reinforced ve hybrid composite.

Morphological analysis was conducted on the fracture surface of tensile test sample. SEM on the fracture surface of tensile test for neat polymer and hybrid composite. Neat

polymer surface fracture in Fig. 4a shows a smooth surface. Figure 4b and Fig. 4c shows untreated and treated fibre respectively. Fibre pull-out is obviously observed in untreated samples and it also showed a rough surface. It means that is a brittle manner failure [11].

From the observation, there are presence of void, air bubble, matrix and less fibre pull-out in treated PALF/KF hybrid composite. The distribution between fibre content and matrix was uniform compared to untreated fibre. Less fibre pull out and less gap seen in treated hybrid samples leads to the good mechanical properties of the hybrid composites.
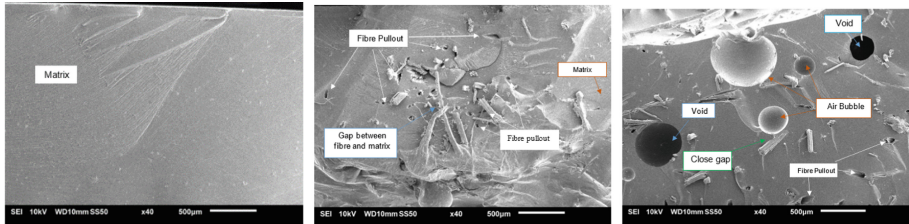
Fig. 4. Morphological analysis on; a) neat polymer, b) untreated fibres, and c) treated fibres hybrid composites.

4   Conclusions

The mechanical and morphological properties of PALF/kenaf fibre reinforced vinyl ester hybrid composites were analyzed Alkalization was performed to remove impurities of the fibre. This treatment could promote better mechanical properties such as tensile and flexural strength.

Based on the results, treated fibre composite gives higher tensile strength compared to untreated fibre composite while neat polymer shows the highest tensile strength. For flexural strength, the treated fibre composite was the highest compared to untreated fibre composite and neat polymer due to the rigidity behavour of the fibre. SEM results which shows matrix and fibre pull-out in the fracture samples. It can be conclude that alkalization improves the mechanical properties of hybrid fibres.

References

1. Asim, M., et al.: Thermal, physical properties and flammability of silane treated kenaf/pineapple leaf fibres phenolic hybrid composites. Compos. Struct. **202**, 1330–1338 (2018). https://doi.org/10.1016/j.compstruct.2018.06.068
2. Arib, R.M.N., et al.: Mechanical properties of pineapple leaf fibre reinforced polypropylene composites. Mater. Des. **27**(5), 391–396 (2006). https://doi.org/10.1016/j.matdes.2004.11.009
3. Kasim, A.N., et al.: Numerical characterization of mechanical properties of fiber network materials. Jurnal Teknologi (Sci. Eng.) **21**, 2013 (2013). https://doi.org/10.11113/jt.v77.6617
4. Udaya Kumar, P.A., et al.: Mechanical and tribological behavior of vinyl ester hybrid composites. Tribol. Ind. **40**(2), 283–299 (2018). https://doi.org/10.24874/ti.2018.40.02.12

5. Mohamed, A.R., Sapuan, S.M., Khalina, A.: Mechanical and thermal properties of josapine pineapple leaf fiber (PALF) and PALF-reinforced vinyl ester composites. Fibers Polym. **15**(5), 1035–1041 (2014). https://doi.org/10.1007/s12221-014-1035-9

6. Aji, I.S., et al.: Kenaf fibres as reinforcement for polymeric composites: a review. Int. J. Mech. Mater. Eng. (IJMME) **4**(3), 239–248 (2009)

7. Mohd Nurazzi, N., Khalina, A., Sapuan, S.M., Dayang Laila, A.H., Rahmah, M., Hanafee, Z.: A review: fibres, polymer matrices and composites. Pertanika J. Sci. Technol. **25**(4), 1085–1102 (2017)

8. Aprilia, N.A.S., et al.: Exploring material properties of vinyl ester biocomposites filled carbonized jatropha seed shell. BioResources **9**(3), 4888–4898 (2014)

9. Ibrahim, M.S., Sapuan, S.M., Faieza, A.A.: Mechanical and thermal properties of composites from unsaturated polyester filled with oil palm ash. J. Mech. Eng. Sci. (JMES) **2**, 133–147 (2012)

10. Jamadi, A.H., Nadlene, R., Petrů, M., Mastura, M.T., Noryani, M., Ilyas, R.A.: Effect of chemically treated kenaf fibre on mechanical and thermal properties of PLA composites prepared through fused deposition modeling (FDM). Polymers **13**, 3299 (2021). https://doi.org/10.3390/polym13193299

11. Nadlene, R., Sapuan, S.M., Jawaid, M., Ishak, M.R., Yusriah, L.: The effects of chemical treatment on the structural and thermal, physical, and mechanical and morphological properties of roselle fiber-reinforced vinyl ester composites. Polym. Compos. **39**(1), 274–287 (2018)

Design and Optimization

Structural Analysis of Moveable Fence Barrier Near the Exit Toll

A. E. Yusof[1], E. Mat Tokit[1,2(✉)], M. Musa[1], and N. A. Rahman[1,2]

[1] Fakulti Kejuruteraan Mekanikal, Universiti Teknikal Malaysia Melaka, Hang Tuah Jaya, 76100 Durian Tunggal, Melaka, Malaysia
ernie@utem.edu.my

[2] Centre of Advanced on Energy, Universiti Teknikal Malaysia Melaka, Hang Tuah Jaya, 76100 Durian Tunggal, Melaka, Malaysia

Abstract. The existed moveable fence barrier at toll highway exit Ayer Keroh, Melaka, Malaysia is a ground reinforced cable wire barrier, which is used to mitigate the vehicle impact at the highway area from any errant vehicles. There are few liabilities with the existed design of the barrier that needs to be improved. The analysis included for the barrier inspection were structural analysis, impact force analysis and wind force analysis. The load given considered the vehicle's weight and speed. The Finite Element Analysis, FEA was applied for this analysis. The design lies under the limit value of 10 kN impact load. Under this condition, the predicted total deformation, equivalent stress and the factor of safety were predicted at 5.176×10^{-4} m, 3.241×10^7 Pa and 2.6933. The small value of deformation was due to the material that absorb the vehicle's impact and also the small ductility of steel. The factor of safety bigger than 2 also showed the acceptance of the fence design strength for the intended load.

Keywords: Moveable fence · Highway road · Conceptual design

1 Introduction

A moveable fence as shown in Fig. 1 is used for exit toll Ayer Keroh. It is a flexible cable barrier comprises of 4 core cable wire that linked together with the end post, and bolted into tar foundation and weight supported by stainless steel base. This fence is less favors in term of movability as it is complicated to be moved and the fence design is too heavy in composition. The purposes of the constructed cable barrier are to reduce the impact of lost control vehicle, act as a barrier to prevent road users from making risky U-turn and high in durability to restrain the pressure difference caused by the nearby passing mobile. The application of fences is also described [1] where the sand fences are used to stabilize the form of dunes or initiate, and to control sand deposition. Besides, the effectiveness of mitigating crop damage by mammals can be varied by installation and maintenance of fences. Though, the drainage ditches which intersect the fences position can reduce the effectiveness of the fence [2].

Fig. 1. Current moveable fence at exit toll Ayer Keroh, Melaka.

To improve the current design of the fence, a structural analysis is applied. Noraphaiphipaksa [3] briefly explained Finite Element Analysis (FEA) which is used to analyze the root cause of the failure in a vessel. The poor design and installation work of sight port which under high stress condition might eventually leads to the failure of pressure vessel. Therefore, a new design is created and evaluated by using FEA. Guo [4] also approached the FEA to predict various condition that includes crack causes, propagation, plastic behavior and mechanical properties. Therefore, this study is conducted to improve the performance of the safety barrier system for the traffic management by enhancing the current barrier design, to create a new portable barrier system and to evaluate the performance of the design.

2   Methodology

The speed vehicle limit is set to be 60 km/h if temporary speed limits, accident and incident location is taking into account [5]. Therefore, velocity variations are investigated at 60 km/h, 45 km/h and 30 km/h. Three selected vehicles on the Malaysian's road are Myvi, Hilux 4 × 4, and Hiace Van that weigh around 1000 kg, 2000 kg, and 3000 kg respectively. The weight considered in this analysis is purposely chosen to be tested and suitable for road barrier traffic design at speed limit below 60 km/h and factor of safety 1.2 to 2 according to the load and resistance design for barrier and bridge [6]. Based on these condition, the applied load given to the fence was selected at 10 kN, 15 kN, and 20 kN as shown in Table 1.

3   Result and Discussion

The predicted structural data as shown in Fig. 2 in terms of the predicted deformation, equivalent stress and factor of safety are investigated for 10 kN load. The data obtained lies below the limit value while the safety factors is greater than 2. The predicted data in Table 2 well agrees with the fence material allowable range values. Although the barrier reaches fatigue point when reaching 15 kN and 20 kN load applied, the maximum opening setup proved to be successful in structural analysis term.

The small value of deformation was due to the material that absorb the vehicle's impact and due to the small ductility of steel. The factor of safety, *FOS* higher than 2 also showed the acceptance of the fence design strength for the intended load. In this study, fatigue to stress analysis is important in order to determine the performance level of the structural that involved in the design that has been created. This determines the estimated *FOS* of the product based not only from the design itself but also the type of material used as well as the loading condition. Generally, *FOS* is related to the durability that affect the life span of a certain product that involved with fatigue as well as loading condition (which contributed to stress-strain). In structural analysis, the fatigue value of a material upon load were influenced by stress. So the relationship of fatigue to stress is inversely proportional.

Table 1. Estimated equivalent impact load at exit toll highway Ayer Keroh, Melaka.

No	Expression	Mass (kg)	Velocity (km/h)	Equivalent impact load (kN)
1	$F = \left[\frac{0.5 \cdot m \cdot v^2}{d}\right]$ $F =$ equivalent impact load, $V =$ object velocity on impact, $d =$ collision distance or deformation distance of the object, $m =$ mass of colliding object	1000 e.g.: Myvi	30	1.736
			45	3.906
			60	6.944
2		2000 e.g.: Hilux 4 × 4	30	3.472
			45	7.813
			60	13.889
3		3000 e.g.: Hiace Van	30	5.208
			45	11.719
			60	20.833

(a)   (b)
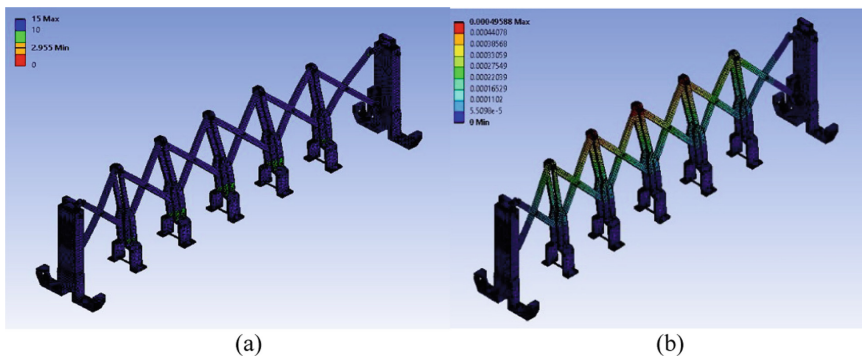
Fig. 2. (a) Safety factor and (b) total deformation at impact load of 10 kN during the fence maximum opening set up.

Table 2. Predicted data at maximum opening fence setup.

No	Items	Load (kN)			Limit value
		10	15	20	
1	Total deformation (m)	5.176×10^{-4}	7.764×10^{-4}	1.035×10^{-3}	7.764×10^{-4}
2	Equivalent stress (von-misses) (Pa)	3.241×10^{7}	4.862×10^{7}	6.482×10^{7}	2.5×10^{8}
3	Factor of safety	2.6933	1.7956	1.3467	>2

4   Conclusion

The FEA was used to analyse the structure of the moveable fence at maximum opening set up. Under 10 kN impact load, the predicted total deformation, equivalent stress and the factor of safety were $5.176e \times 10^{-4}$ m, 3.241×10^{7} Pa and 2.6933. Whereas under higher impact load of 15 kN and 20 kN, the factor of safety is less than 2 even though the total deformation and the equivalent stress were under the limit value. The small value of deformation is due to the impact absorption and ductility of the steel.

References

1. Ning, Q.L.: Fence height control on sand trapping. Aeol. Res. **46**, 100617 (2020). https://doi.org/10.1016/j.aeolia.2020.100617
2. Honda, T.: A technique for preventing wildlife intrusion via the intersection between drainage ditches and fences: deer, macaque, raccoon dog, fox, and badger damage management. Crop Prot. **113**, 29–32 (2018). https://doi.org/10.1016/j.cropro.2018.07.012
3. Noraphaiphipaksa, N.P.: Failure analysis of pressure vessel with sight ports using finite element analysis. Eng. Fail. Anal. **117**, 104791 (2020). https://doi.org/10.1016/j.engfailanal.2020.104791
4. Guo, Q.Y.: Constitutive models for the structural analysis of composite materials for the finite element analysis: a particular review of recent practices. Compos. Struct. **260**, 113267 (2020). https://doi.org/10.1016/j.compstruct.2020.113267
5. PLUSLINE: PLUS Highways/Expressways. Frequently Asked Questions, 1 (2021)
6. Michael, A., Grubb, P.K.: Load and Resistance Factor Design (LRFD) for Highway Bridge. Load and Resistance Factor Design (LRFD), 19 (2015)

Design and Analysis of Low-Cost Aircraft Landing Gear Trainer System for Aviation Maintenance Training

Nur Nadiah Azhari[2], Ridhwan Jumaidin[1(✉)], and Fudhail Abdul Munir[2]

[1] Fakulti Teknologi Kejuruteraan Mekanikal & Pembuatan, Universiti Teknikal Malaysia Melaka, 76100 Durian Tunggal, Melaka, Malaysia
ridhwan@utem.edu.my

[2] Fakutli Kejuruteraan Mekanikal, Universiti Teknikal Malaysia Melaka, 76100 Durian Tunggal, Melaka, Malaysia

Abstract. Landing gear mechanism trainer is an important and useful equipment for aircraft module training. It is essential for trainees to comprehend the theory as well as practical training related to maintenance of the landing gear system. The device can also be used in the lecture or during ground school course training. In this work, the design of low-cost aircraft landing gear system for training purpose is proposed. Market feasibility study is first conducted, and the design parameters of the proposed hydraulic landing gear trainer system is based on the survey results. The landing gear system is equipped with retractable main and nose landing gear. By using engineering methods such as House of Quality (HoQ), and Morphological Method, three conceptual designs of hydraulic landing gear trainer system were proposed. The final design was selected by using the engineering approach which is Weighted Decision Matrix (WDM). The engineering drawing of the final design was made using CATIA software. Finite Element Analysis (FEA) was performed focusing on the landing gear structure and the main body frame. The results show that the proposed design is able to meet the minimum structure required with factor of safety 1.5.

Keywords: Landing gear mechanism trainer · Landing gear system · Finite Element Analysis (FEA)

1 Introduction

As a aircraft maintenance personnel, it is crucial to practically know how the landing gear system works. Failures of landing gears in aircraft represent approximately 10% of the aerospace industry's total failures [1]. The failures associated with factors including the environmental and overload causes. These failures can be avoided with good engineering and maintenance practices, commonly conducted in the aerospace industry. One of the most crucial subsystems found in an aircraft is the landing gear of which has the biggest influence on aircraft structural configuration as it is to be said as the most significant load-carrying subsystems of an aircraft [2]. The main function of aircraft landing gear

is to provide a suspension system during take-off, landing, and taxing the aircraft. The main design requirement of an aircraft landing gear design is it should be able to absorb and dissipate the landing impact's kinetic energy that results to the decrease of the impact loads transmitted to the airframe.

In this research work, a low-cost hydraulic system of landing gear for raising and lowering an aircraft landing gear known as a side brace is proposed. This design includes complete wheel and tire assembly with a hydraulic landing gear system. Then, followed by the design analysis studies in ensuring the functionality of the landing gear trainer system. This proposed research is expected to be able to provide a complete design of a hyraulic landing gear trainer system and, eventually, a hands-on training environment for aircraft maintenance training.

2   Research Methodology

In this project, a Work Breakdown Structure (WBS) is firstly constructed to be followed. Starting from the literature review of this topic is done by citation extracted from previous research articles, journals, and internet which brings relevance with the research topic. Next, discussion is made on the market feasibility in thorough. The results from the market survey are discussed so that a design parameter can be listed to finalize the design of the hydraulic landing gear trainer system. The aspect and performance criteria to be met for this project will be determined by benchmarking against similar items. This followed by the design parameter of landing gear trainer system that consist of customer requirement, engineering characteristics and House of Quality (HOQ). This brings to next step, which is Product Design Specification (PDS) and continued with the concept generation, the product's function structure, feasible concept and weighted decision matrix have been generated as well. Data and information gained from previous methods are used to create the detailed final design of hydraulic landing gear trainer system (Fig. 1). After that, finite element analysis is run to find the analysis study of this project. The process of refining design and developing proposals, requirements and projections is discussed in this section. Besides, the complete design ensures that the final design approach fulfils the purpose of the project.
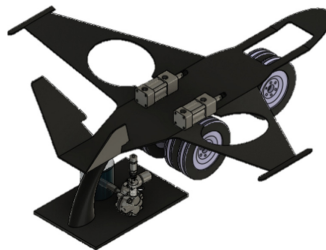
Fig. 1. Final design of hydraulic landing gear training system.

3   Results and Discussion

This section reviews the results and analysis of designing the landing gear trainer system, the theoretical calculation, and the results of Finite Element Analysis (FEA) by using ANSYS and Fusion 360 software. This computer simulation is primarily concerned with the structural design and analysis of the main landing gear for a trainer aircraft that is both cost-effective and has a high strength-to-weight ratio while being basic in design. With the aid of the finite element application ANSYS Workbench, the linear static analysis is carried out to compute the main landing gear's deflections and measure the internal stresses. Discussing on the material selection, the material used in the analysis is AISI 1030 Steel, Water quenched at 870 °C with a temper of 650 °C. It's made of high-carbon steel and has a yield power of 395 N/mm^2. In its as-rolled state, it has a soft hardness and strength, as well as good machinability. Cold practice will help it get both harder and stronger [3]. First and foremost, the analysis was carried out using a mesh rig. This configuration provides the best calculus results. Then it depicts the load applied on the desired part, which holds the major load of the landing gear trainer system based on the configuration. Meanwhile, Fig. 2 and Fig. 3 show the stress and displacement results of the static failure analysis. The stress analysis experiments show that deformation occurs regardless of the applied force: the stronger the force, the more distorted the support becomes [4]. Reshaping the geometry and employing a new material are two possibilities to consider. Furthermore, the test cannot be considered valid under stress analysis settings due to the significant deformations in relation to the applied force.
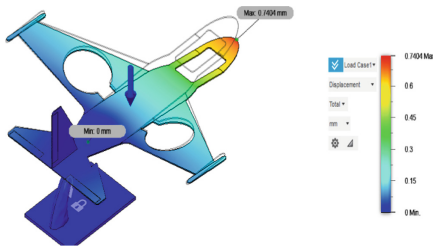
Fig. 2. Displacement analysis result.   **Fig. 3.** Stress (von mises) analysis result.
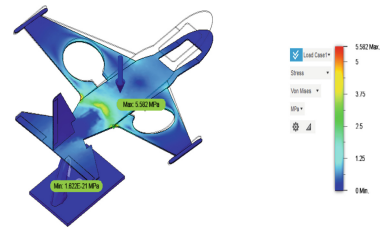
4   Conclusion

The max stress obtained in the component is 5.582 MPa which is less than ultimate tensile strength (UTS) of the component taken as 540 MPa. Thus, it states that the model is safe. There are 6 components in total. Finite Element Analysis (FEA) has been conducted on the final design CAD drawing of hydraulic landing gear trainer system to ensure the functionality of the product.

References

1. Gudmundsson, S.: The anatomy of the landing gear. In: General Aviation Aircraft Design, vol. 94 (2014)
2. Manjunath, S.V., Monisha, M.P.S.: Design and structural analysis of main landing gear for lockheed T-33 jet trainer aircraft. Int. J. Eng. Res. Adv. Technol. **9**, 2454–6135 (2018)
3. Gowda, A., Novid, S.: Linear static and fatigue analysis of nose landing gear for trainer aircraft. Trends Mech. Eng. Technol. 2347–9965 (2014)
4. Bigoni, A.: Autodesk FUSION 360: static stress analysis of a mechanical support (2017)

Natural Fiber Composite Filaments Selection for Drone Frame Structures

Muhammad Hilmi Senan[1], M. A. Shaharuzaman[1,3(✉)], M. T. Mastura[2,3], and M. Noryani[1,3]

[1] Fakulti Kejuruteraan Mekanikal, Universiti Teknikal Malaysia Melaka, Hang Tuah Jaya, 76100 Durian Tunggal, Melaka, Malaysia
adrinata@utem.edu.my

[2] Fakulti Teknologi Kejuruteraan Mekanikal & Pembuatan, Universiti Teknikal Malaysia Melaka, Hang Tuah Jaya, 76100 Durian Tunggal, Melaka, Malaysia

[3] Centre for Advanced Research On Energy, Universiti Teknikal Malaysia Melaka, Hang Tuah Jaya, 76100 Durian Tunggal, Melaka, Malaysia

Abstract. Five product criteria are being considered in this paper for the natural fiber composites selection for the drone frame structures. The weightage criteria were calculated by using the analytic hierarchy process (AHP) method. The highest weightage of the criteria is the performance with the value of 0.337 followed by environmental 0.311, cost 0.193, weight 0.086, and size 0.073. Then, by using the same method by considering the most important criteria which is the performance, three natural fiber composite filaments were chosen where poly-lactic acid (PLA) reinforced with 6.3% Jute (PLA/Jute), polypropylene (PP) reinforced with 30% Harakeke (PP/Harakeke), and PP reinforced with 30% Hemp (PP/Hemp) were compared. The highest-ranking for the natural fiber composites filament is PLA/Jute with the value of 0.417 for the tensile strength and 0.478 for the modulus followed by PP/Harakeke and PP/Hemp. Finally, the best natural fiber composite filament for the drone structures is PLA/Jute with the value of 0.449 compared to the other two filaments. This research shows that AHP can assist engineers and researchers in deciding the best natural fiber composite filaments with the structured and well-defined goal.

Keywords: FDM · Mechanical properties · NFRC filament · UAV · AHP

1 Introduction

Generally, a drone is a flying machine that can be remotely controlled or fly autonomously with the help of software-based Bluetooth controlled in their system together with the sensors and Global Positioning System (GPS) [1, 2]. UAV applications are widely used for agricultural surveillance, meteorological data acquisition, and disaster monitoring because of their flexibility and small size varying from a bird to a helicopter [3]. There are many benefits from drones technology as the drones are easy to deploy, enabling flight path programming during service [4]. Previous research on topology optimization and cellular structures has resulted in complex lightweight structures that cannot be

fabricated by using conventional manufacturing techniques [5]. The previous work to fabricate the drone frame structures use conventional manufacturing processes which have many disadvantages such as high cost, high lead time and have design constraint. Apart from that, some studies contributed to the drone frame structure fabricating process with design and material selection [1, 4, 6, 7].

During the last three decades, 3D printing technologies were developed to shorten the product development cycle and produce customized parts with defined functionality and individuality [8]. FDM technology was used for 3D printing in this study [9]. Among several AM techniques, Fused Deposition Modelling (FDM) can be performed on thermoplastic polymers or composites, to allow a filament to be printed in layers. The main benefits of FDM are its low cost, relatively high speed, and potential for reinventing the design process [10].

In this paper, for the decision making of the drone frame structures material. Analytic hierarchy process (AHP) process are being used to calculate and analyse for selecting the best natural fiber composite filament material for the drone frame structures.

Table 1. Natural fiber composite filaments.

Sample code	Tensile strength (MPa)	Tensile modulus (GPa)	Ref.
PLA + Jute 6.3 wt%	55	5.00	[11]
PP + Harakeke 30 wt%	39	2.77	[12]
PP + Hemp 30 wt%	38	2.68	[12]

2   Research Methodology

From Table 1, the previous study conducted by Wang et al. [11], the study use PLA and reinforced with Jute 6.3% with 55 MPa for tensile strength and 5 GPa for the modulus strength. Then, Stoof utilizes polypropylene (PP) to be reinforced with other materials which are Hemp and Harakeke to create fused deposition modelling (FDM) filament [12]. The highest tensile and modulus strength in the study is when 70% of PP being reinforced with Harekeke which is 39 MPa and 2.77 GPa. The second highest tensile strength is 70% PP and 30% of Hemp which is 38 MPa and 2.68 GPa.

Therefore, for this study (FDM) is being used to fabricate the parts. There are 5 design criteria as shown in Fig. 1 taken into the early stage for the drone frame structures which are performance, size, weight, cost, and environmental. The criteria (red-marked) are being analyzed by using the analytic hierarchy process (AHP) which is performance, size, weight, cost, and environmental.

In this study, the most important criteria that being considered is the performance with the sub-criteria (blue-marked) is strength tensile strength (MPa) and tensile modulus (GPa) and analyzed by using the AHP process for material selection for the drone frame structures as shown in Fig. 2 and Fig. 3.
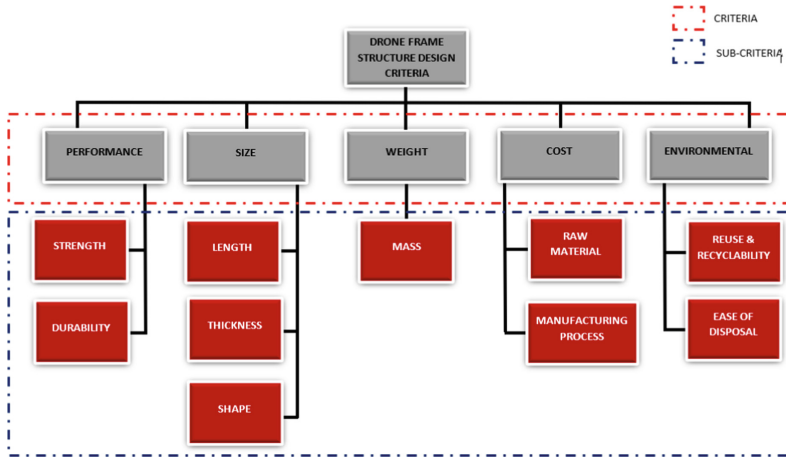
Fig. 1. Drone frame structure design criteria.

3   Results and Discussion

3.1   Goal

The results indicated excellent consistency in subjective judgments of each performance and the average value of CR less than 0.1 which is 0.088. After being analyzed by using the analytic hierarchy process (AHP). The criteria that are being heavily considered is the performance of the drone frames with a 0.337 average value which is the strength and durability of the parts. Then, followed by environmental with 0.311, cost of materials with 0.193, and the lowest average value is the size which is 0.073. Therefore, performance sub-criteria which is strength is being analyzed by using the AHP process by using tensile strength and tensile modulus value.

3.2   Sub Criteria

The performance average value for filament selection for drone frame structures is 0.500. This is because tensile strength and tensile modulus are equally important in drone frame structures design. After all, it will influence the performance of the product.
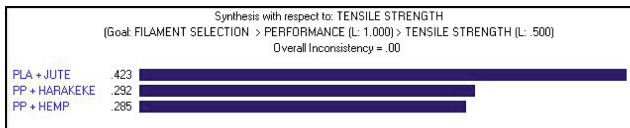
Fig. 2. Performance sub criteria (tensile strength).

Then, for the sub-criteria of the performance which is tensile strength, the highest value in terms of average value is 0.423 for PLA/Jute, followed by PP/Harakeke (0.292) and PP/Hemp (0.285) as shown in Fig. 2.

Figure 3 shows the sub-criteria of the performance which is tensile strength the highest value in terms of average value is 0.478 for PLA/Jute, followed by PP/Harakeke 0.265 average value. Meanwhile, PP/Hemp is the lowest average value with 0.256.
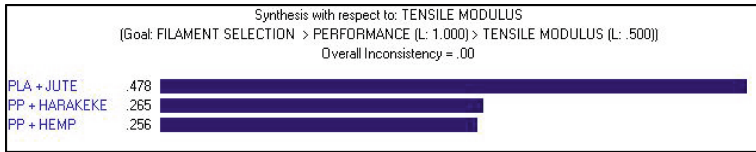
Fig. 3. Performance sub criteria (tensile strength).

3.3 Ranking

The overall weightage average value shows that PLA/Jute outperforms other composite filaments with 0.449 followed by PP/Harakeke with 0.280 and PP/Hemp with 0.271 average value (Fig. 4).
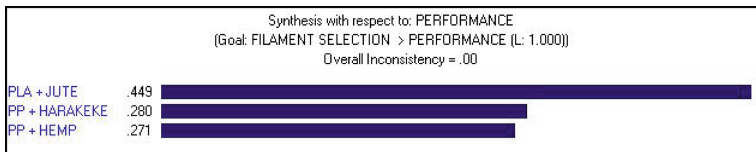
Fig. 4. Overall ranking and performance of the natural fiber filament using AHP.

4   Conclusion

The highest weightage of the criteria is the performance from AHP with the value of 0.337 followed by environmental 0.311, cost 0.193, weight 0.086, and size 0.073. Then, by using the same method and considering the most important criteria which is the performance, three natural fiber composite filaments were compared which is PLA/Jute with 55 MPa tensile strength and 5.5 GPa modulus strength, PP/Harakeke with is 39 MPa, and 2.77 GPa and PP/Hemp which is 38 MPa and 2.68 GPa. The highest weightage value by using AHP is for PLA/Jute which is 0.417 (strength) & 0.478 (modulus) followed by PP/Harakeke with 0.295 (strength) & 0.267 (modulus) and 0.288 (strength) & 0.255 (modulus) for PP/Hemp. Finally, the most suitable natural fiber composite filament with the highest ranking is PLA/Jute with a 0.449 overall average value which outperforms other natural fiber composite filaments. The structured strategy to select the best natural fiber composite filaments with the AHP method has shown that the goals can be achieved to perform multiple criteria decisions making which help engineers and researchers in making a decision.

References

1. Adams, S.M., Friedland, C.J.: A survey of unmanned aerial vehicle (UAV) usage for imagery collection in disaster research and management BT. In: 9th International Workshop on Remote Sensing for Disaster Response, vol. 8, February 2011
2. Nex, F., Remondino, F.: UAV for 3D mapping applications: a review. Appl. Geomat. **6**(1), 1–15 (2013). https://doi.org/10.1007/s12518-013-0120-x
3. Goh, G.D., Agarwala, S., Goh, G.L., Dikshit, V., Sing, S.L., Yeong, W.Y.: Additive manufacturing in unmanned aerial vehicles (UAVs): challenges and potential. Aerosp. Sci. Technol. **63**, 140–151 (2017)
4. Muralidharan, N., Pratheep, V.G., Shanmugam, A., Hariram, A., Dinesh, P., Visnu, B.: Structural analysis of mini drone developed using 3D printing technique. Mater. Today Proc. **46**(17), 8748–8752 (2021)
5. Walker, D., Liu, D., Jennings, A.: Wing design utilizing topology optimization and additive manufacturing. In: Additive Manufacturing Handbook Product Development for The Defense Industry, 1st edn. CRC Press, Boca Raton, pp. 823–840, January 2017
6. Bright, J., Suryaprakash, R., Akash, S., Giridharan, A.: Optimization of quadcopter frame using generative design and comparison with DJI F450 drone frame. In: IOP Conference Series Material Science Engineering, vol. 1012, no. 012019 (2021)
7. Lee, J., Huang, A.: Fatigue analysis of FDM materials. Rapid Prototyping J. **19**(4), 291–299 (2013)
8. Jin, M., Neuber, C., Schmidt, H.W.: Tailoring polypropylene for extrusion-based additive manufacturing. Addit. Manuf. **33**(January), 1–13 (2020)
9. Sodeifian, G., Ghaseminejad, S., Yousefi, A.A.: Preparation of polypropylene/short glass fiber composite as Fused Deposition Modeling (FDM) filament. Results Phys. **12**, 205–222 (2019)
10. Le Duigou, A., Barbé, A., Guillou, E., Castro, M.: 3D printing of continuous flax fibre reinforced biocomposites for structural applications. Mater. Des. **180**, 107884 (2019)
11. Wang, Y., Zhou, Y., Lin, L., Corker, J., Fan, M.: Overview of 3D additive manufacturing (AM) and corresponding AM composites. Compos. A Appl. Sci. Manuf. **139**, 106114 (2020)
12. Stoof, D., Pickering, K.: Sustainable composite fused deposition modelling filament using recycled pre-consumer polypropylene. Compos. Part B Eng. **135**, 110–118 (2018)

Optimization Study on Width of Cut and Cutting-Edge Radius During Side Milling of DAC 55 Steel

S. H. Tomadi[(✉)], Nor Farah Huda Abd Halim, A. N. Dahnel, Amar Syazwan Rosman, G. Umma Sankar, and Lim Joo Eng

International Islamic University Malaysia, Jalan Gombak, 53100 Kuala Lumpur, Selangor, Malaysia
sharyani@iium.edu.my

Abstract. Surface quality of machined surface such as the surface roughness play important role in determining the final part of the products. Thus, selection of the cutting parameters and cutting tool geometry during machining are crucial to determine progression of the tool wear as well as the surface quality of the machined surface. The objective of this paper is to optimize the cutting-edge radius (CER) of the cutting tools and the width of cut during machining of DAC 55 steel. In this study, side milling of DAC 55 steel was carried out with a constant cutting speed of 2800 RPM and feed rate of 350 mm/min. Width of cut of 0.1, 0.6 and 1.2 mm and CER of 10, 20 and 30 µm were implemented to observe the effect of both parameters on surface roughness and tool wear. The influence of cutting parameters combination were evaluated using Full factorial method. From the results, it was observed that the width of cut is the most significant effect on improving the surface roughness quality compared with CER. It was found that by implementing 30 µm CER and 0.1 width of cut resulting in optimum quality of surface finish. For the cutting tool wear, it found that the cutting tool edge radius 30 µm and width of cut 0.1 mm experienced less wear when they reached the 4400 mm of distance travelled.

Keywords: Cutting-edge radius · End-milling · DAC steel

1 Introduction

Optimization is the process where some variables are maximized, and some variables are minimized to fulfil the objectives of the activities. In order to perform the optimization, optimization tools are needed to accomplish it [1]. Design of Experiment (DOE) is a statistical method of studying the effects of the output (Y) with controlling the variation of the inputs (X) to the process [2]. In DOE, there are three ways to approach the optimization process namely traditional or classical methods, Taguchi's methods, and Shainin methods [3]. When a workpiece is machined, the surface performance is one of

the important factors in deciding the quality of the machining process. To produce better surface finish, the optimization of the machining parameters needs to be assessed.

The widths of cut 0.1, 0.6 and 1.2 mm, and 10, 20, and 30 µm CER of the cutting tool are the variable machining parameters used in this side milling operation. Therefore the number of experiments is 9 by using full factorial DOE. Other parameters such as cutting speed (2800 rpm), feed rate (350 mm/min), and depth of cut (6 mm) are fixed. These Machining parameters are investigated and optimized for the lower surface roughness and tool wear. Other response such as chip formation, minimum chip thickness, cutting forces, and tool life can also been further investigated [4]. The material used in this experiment is DAC 55 steel which consist of Chromium, Molybdenum, Vanadium, and Nickel with the composition of 5.2Cr-2.2Mo-V-Ni. The application of this steel is used for high performance die and squeeze die that are anti-crack with the material hardness range from 50 to 53 HRC. Cutting tools used for this study are from a manufacturing company named HPMT. The cutting tools are uncoated tungsten carbide which has 4 flutes and a diameter of 6 mm.

2 Results and Discussion

Based on experiments performed, the surface roughness observed on the DAC 55 machined surface with 30 µm CER is better (0.27 µm) compared with 20 µm (0.32 µm) and 10 µm CER (0.45 µm). While in terms of width of cut, it was observed that milling DAC 55 with lower width of cut of 0.1 mm resulted in better surface roughness as compared with 0.6 and 1.2 mm width of cut. It was also observed that milling DAC 55 with lower width of cut (0.1 mm) resulting in lower tool wear when compared with higher width of cut (0.6 and 1.2 mm) in all CER cases. For the tool wear, the cutting tool with 30 µm CER and 0.1 mm for width of cut experienced less wear (Fig. 1) compared to the other at 20 µm CER and width of cut 1.2 mm which the cutting tool was worn-out (Fig. 2) when they reached the 4400 mm of distance travelled. Result obtained by Design Expert, it was indicated that to generate optimum result of surface roughness and tool wear, the combination of 30 µm CER with 0.1 mm width of cut should be implemented. From this study, it was also observed that the width of cut plays more significant effect in the tool wear and the surface roughness of the machined material compared to the CER of the cutting tool.
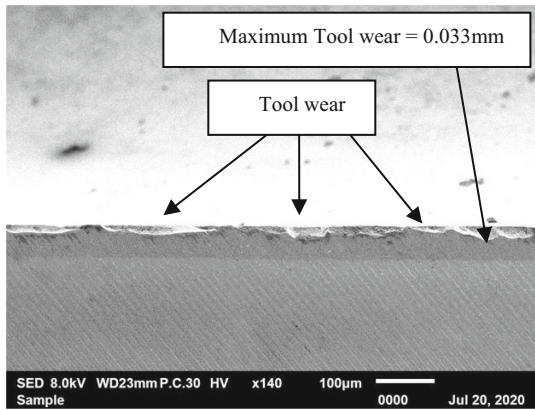
Fig. 1. SEM image of end mill tool having 30 μm CER cutting tool and milling with 0.1 width of cut after 4400 mm distance travelled.
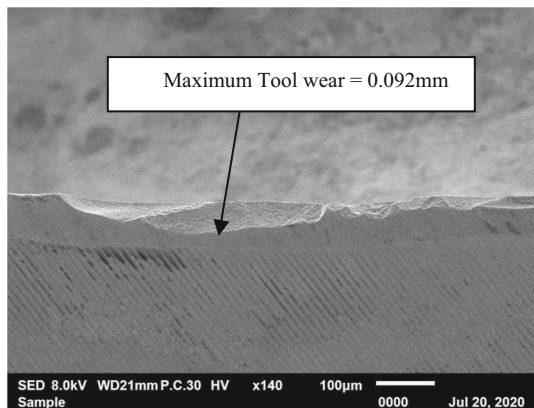
Fig. 2. SEM image of end mill tool having 20 μm CER cutting tool and milling with 1.2 width of cut after 4400 mm distance travelled.

References

1. Khan, S., Asjad, M., Ahmad, A.: Review of modern optimization techniques. Int. J. Eng. Res. **4** (2015). https://doi.org/10.17577/IJERTV4IS041129
2. Souza, J.P.E., Alves, J.M., Damiani, J.H.S., Silva, M.B.: Design of experiments: its importance in the efficient project management. In: 22nd International Conference on Production Research, ICPR 2013. International Foundation for Production Research (IFPR) (2013)
3. Konda, R., Rajurkar, K.P., Bishu, R.R., Guha, A., Parson, M.: Design of experiments to study and optimize process performance. Int. J. Qual. Reliab. Manag. **16**(1), 56–71 (1999). https://doi.org/10.1108/02656719910226914
4. Zhao, T., Zhou, J.M., Bushlya, V., Ståhl, J.E.: Effect of cutting edge radius on surface roughness and tool wear in hard turning of AISI 52100 steel. Int. J. Adv. Manuf. Technol. **91**(9–12), 3611–3618 (2017). https://doi.org/10.1007/s00170-017-0065-z

Machining Parameter Optimization for Laser Machining

Muhammad Mirza Muhamad Adlan, Alias Mohd Saman[(✉)], and Mohd Afril Hafiz Sariman

School of Mechanical Engineering, College of Engineering, Universiti Teknologi MARA (UiTM), 40450 Shah Alam, Selangor, Malaysia
aliasms@uitm.edu.my

Abstract. This study was performed at the local company where the use of fiber laser is applied in cutting sheet metal. The company faces a problem to identify the optimum laser parameters for cutting varies thickness of sheet metal. This study aims to evaluate the best combination of parameters for producing quality machining result by using statistical method via JMP software. Laser power and cutting speed were found the most influence parameters in the formation of burrs. Thus, the best combination between these parameters should be considered.

Keywords: Fiber laser · Burr thickness · Laser machining

1 Introduction

The advancement of new manufacturing materials, systematic design requirements, irregular work piece size, and complex shape has now limited the usage of traditional machining processes and approaches. As a result, some traditional machining techniques were deemed to be evolving into nonconventional machining methods known as advanced machining processes (AMPs) [1]. Laser machining for example, able to handle various materials with complicated sizes and forms, as well as hard-to-reach surfaces, with greater precision than traditional machining [2]. Laser beam can also be used for milling and turning, though it is most commonly used for cutting metallic and non-metallic sheets [3].

Using the correct combination of parameters throughout the laser machining process is critical for achieving good cutting quality, which is crucial in product planning. Using high power and low cutting speed, for example, will result in the production of material defects such as dimension inaccuracy or burn. Formation of burr after laser machining is another key deciding factor that impacts laser cutting efficiency due to the additional workload required for burr removal [4].

This study was done at a local automotive company to evaluate the laser machining parameters combination for producing quality metal sheet cutting via JMP software. The company limits the burr size of maximum 0.5 mm for each cutting. The company is afflicted by not having optimal laser parameters. Furthermore, laser power and cutting speed parameters combination used were poor due to lacking experimental analysis capability and scheduling restriction.

2   Methodology

2.1   Experimental Setup

Material used in this study was cold rolled mild steel JIS G3141. A 6-axis robot with a fiber laser cutting unit was used for experimental study. The machine was capable of 2D laser cutting works and employs 1000 W laser power. The nozzle diameter (1.5 mm) and gas pressure (14 bar) were kept constant throughout the experimentation.

The parameter variable for cutting process is shown in Table 1. Robot master software was used to control the laser cutting process. Laser power and cutting speed were changed and controlled using the software programming. The material sheets were loaded manually based on its thickness, while nozzle distances were set manually at the machine. The experiments were proceeded with full factorial design method, where 360 specimens were produced for the evaluation.

Table 1.   Variable parameter of the experiments.

Variable Parameter	Factor of Variable	Total number of Variable
Material thickness (mm)	1.4, 2.0, 2.3, 3.0	4
Nozzle Distance (mm)	0.3, 0.5, 0.9	3
Laser Power (%)	50, 60, 70, 80, 90, 100	6
Cutting Speed (mm/s)	v10, v50, v80, v100, v150	5

The thickness of cut specimens were measured using vernier caliper. Burr thickness value was gained by subtracted with original sheet metal thickness. JMP Statistical Software was used to analyze the data gained from the experiments.

3   Results and Discussion

Figure 1 shows the measured burr plotted over the expected burr derived using linear regression. The 45-degree line is the best match, while the dotted ones is 95 percent confidence intervals.

Formation of burr as a function of material thickness, nozzle distance, cutting speed and laser power are represent in Fig. 2. The black line represents the burr over various parameters and the blue line show the confidence intervals between them. The predicted burr in Fig. 1 serves as the foundation for this function.

The increasing gradient of the dependency demonstrates the varying importance of different factors in the burr formation. However, because all four elements affect response, the following response surface graphs explains their correlation.
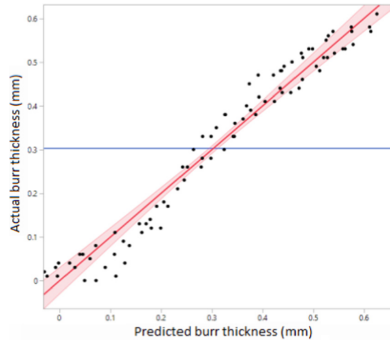
Fig. 1. Actual burr vs predicted burr (JMP).

The most important interaction parameters in determining surface quality for laser cutting were found to be cutting speed and laser power [5]. Figure 3 shows the contour surface of burr thickness versus cutting speed and laser power for nozzle distance at 0.5 mm. In overall, it shown that in order to limit the burr thickness forming, the cutting speed should be lower, but the laser power must be higher.
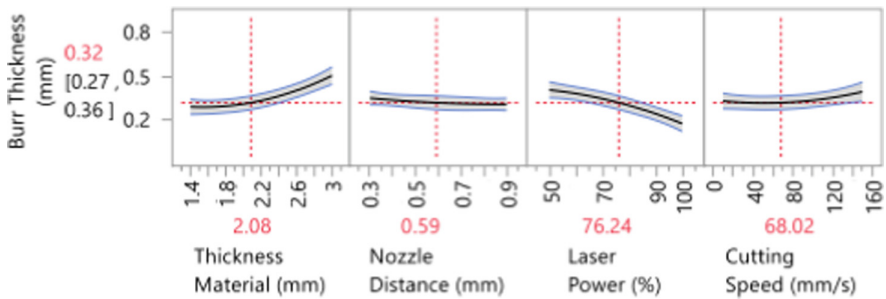
Fig. 2. Influence response of burr over the parameters.

Figure 3(d) clearly shows that burr thickness can be reduced with higher laser power and lower cutting speed. Burr from the laser cutting process affected the quality of machining surface. If laser power used is too high, the burr formation will be too thick. However, if the laser power is too low, cutting is not possible. Therefore, the optimum combination between laser cutting parameters should be benefited.
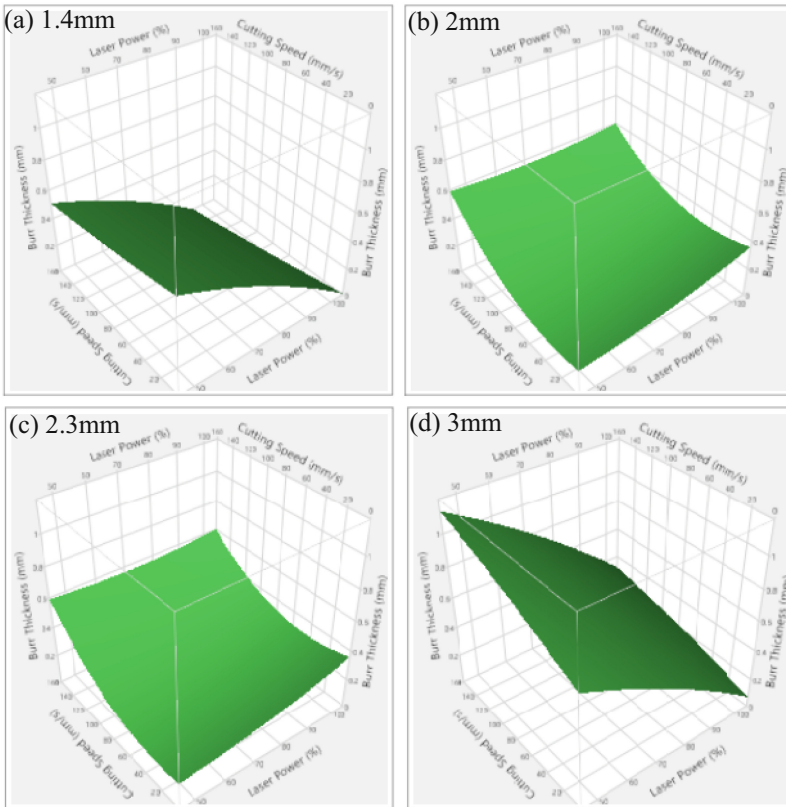
Fig. 3. Interaction effect on burr thickness response.

4 Conclusion

This study evaluates the combination of laser cutting parameters to produce good machining result by using statistical method via JMP software. 4 variable parameters were considered including material thickness, laser nozzle distance, laser power and laser cutting speed. By using linear regression approach, the correlation between predicted and actual experimental burr thickness was established. Consequently, the formation of burr as a function of different variables are able to be anticipated. Thus, the best combination of the parameters for each sheet metal thickness can be selected. Cutting speed and laser power shown as the most important interaction parameters in burr formation. Therefore, the outcome of the study should be utilized in selecting appropriate laser cutting parameters in future operation.

References

1. Dubey, A.K., Yadava, V.: Laser beam machining-a review. Int. J. Mach. Tools Manuf. **48**(6), 609–628 (2008)

2. Machining, E.D., et al.: Laser beam machining machining processes utilizing thermal energy. Mod. Mach. Technol. **1**(3), 161–363 (2020)
3. Adelmann, B., Hellmann, R.: Fast laser cutting optimization algorithm. Phys. Procedia **12**(1), 591–598 (2011)
4. Himeno, K.: Basics and features of high-power fiber laser. Fujikura Tehnical Review (2015)
5. Kotadiya, D.J., Kapopara, J.M., Patel, A.R., Dalwadi, C.G., Pandya, D.H.: Parametric analysis of process parameter for laser cutting process on SS-304. Mater. Today Proc. **5**(2), 5384–5390 (2018)

Energy Efficiency, Energy Engineering and Management

Thermodynamic Analysis of a Gamma - Type Stirling Engine for mCHP Application

Jufrizal[1,2] , Farel H. Napitupulu[1(✉)], Ilmi[1] , Himsar Ambarita[1] ,
and Mahadi Meliala[2]

[1] Mechanical Engineering, Universitas Sumatera Utara, Medan, Indonesia
farel@usu.ac.id

[2] Mechanical Engineering, Institut Teknologi Medan, Medan, Indonesia

Abstract. Stirling engine as the prime mover is again the focus of development because it has many advantages, including being able to operate with various types of heat sources. Because of these advantages, it can be used for applications in micro-scale combined heat and power systems (mCHP) for household applications. The heat source for the Stirling engine is obtained from the combustion of LPG gas. This study aims to analyze the performance of the 2nd generation Stirling engine with an ideal cycle thermodynamic analysis approach. This research uses a gamma-type Stirling engine with air as the working fluid and the preload pressure of the working gas is the atmospheric pressure. This engine has a maximum volume of 0.000201 m^3. The results showed that the average thermal efficiency was 24.6%. The average engine speed and power produced are 415 rpm and 37.9 W. The average maximum pressure produced during the testing process is 2.446 bar.

Keywords: Gamma-type Stirling engine · Performance · Thermodynamic

1 Introduction

The development of the Stirling engine has again become the focus of researchers in the world due to the issue of saving and using environmentally friendly energy. This issue arises because of the increase in world energy consumption and environmental damage that continues to increase every day. In Indonesia, energy demand until 2050 is predicted to continue to increase with a total energy demand rate of 5.3% per year. Energy demand increases from 795 million barrels of oil equivalent (BOE) in 2016 and is predicted to be 4,569 million BOE in 2050 [1]. Based on these facts, it is necessary to consider efforts to save energy in various sectors of life. Among the methods used is by utilizing waste heat from a Diesel engine using a heat exchanger system to dry agricultural products [2]. Another method is the development of an engine that can work with one fuel, but produces heat and electricity simultaneously or known as a combined heat and power (CHP) system. The engine used in a micro-scale CHP system is usually a Stirling engine.

The Stirling engine was chosen to be developed because it can be operated with heat sources from various types of fuels, waste heat, and solar energy. Stirling engines also

have the advantages of controlled combustion, long life, long maintenance time, high efficiency, low noise, and low emissions [3–7]. Stirling engine based on configuration is divided into three types, namely alpha, beta, and gamma. Where each configuration has its advantages and disadvantages. In this study, the authors are more interested in developing a gamma-type Stirling engine because of the same thermodynamic advantages as the design beta, but its construction is simpler and can move at low-temperature differences [8]. The model of the low-temperature difference (LTD) Stirling engine according to the gamma configuration is run with a temperature difference below 100 °C [9]. The design of the Stirling engine for all configurations is usually adapted to the available heat source. This study aims to analyze the prototype of the 2nd generation gamma type Stirling engine with an ideal cycle thermodynamic analysis approach.

2 Methodology

This research was carried out experiments and thermodynamic analysis using the equation proposed by Thombare and Wagner [8, 10]. An overview of the tests carried out in the study is shown in Fig. 1.
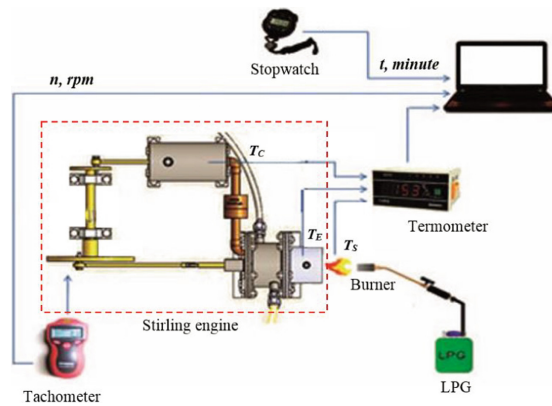
Fig. 1. Test scheme of the gamma-type Stirling engine. T_S, T_E, T_C are the temperature of the heat source, the temperature on the hot side, and the temperature on the cold side, respectively. n is the engine speed at the flywheel.

The temperature of each point is measured using a digital thermometer and a thermocouple sensor. For measuring engine rotational speed, a non-contact digital tachometer is used. The test was carried out using liquefied petroleum gas (LPG). The calorific value and density of LPG are 48.8 MJ/kg and 1.71 kg/m^3, respectively [11]. The working fluid used is air under ambient conditions.

3 Results and Discussion

The 2nd generation gamma-type Stirling engine that has been manufactured is named mCHPSE-012019. The diameters of the displacer and piston are 0.056 m and 0.048 m,

respectively. The stroke length of the displacer and the pistons are 0.04 m and 0.05 m, respectively. This engine has a maximum volume of 0.000201 m³. The results of the mCHPSE-012019 test, including temperature profile and the engine speed are presented in graphical form in Fig. 2 and Fig. 3.
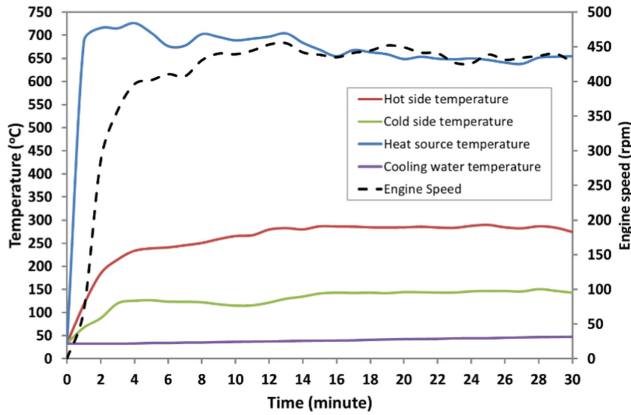
Fig. 2. The average temperature profile and an engine speed of the Stirling engine.
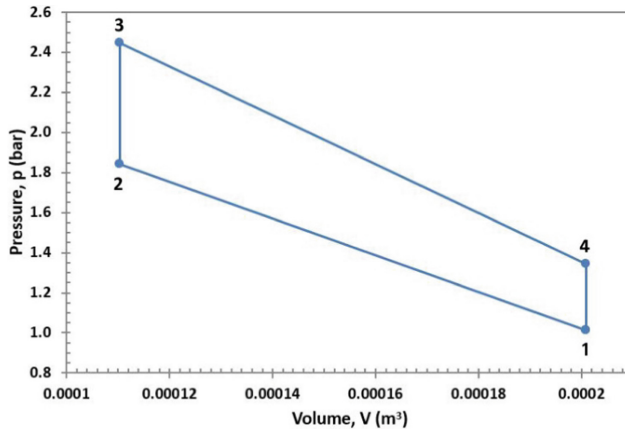
Fig. 3. p-V diagram for the ideal process of the Stirling engine.

Figure 2 shows that the heat source temperature (T_S) has an average value of 674 °C. Hot side temperature (T_E) and cold side temperature (T_C) also change with average values of 264 °C and 131 °C, respectively, so that the temperature difference (ΔT) is around 133 °C. Based on the values of T_E and T_C, the thermal efficiency of the ideal Stirling cycle is 24.6%. Figure 2 also shows that engine speed is strongly influenced by ΔT, where the higher ΔT, the higher the engine speed, and vice versa. The rotational speed and the average power generated from the ideal Stirling cycle are 415 rpm and 37.9 W, respectively.

Figure 3 shows that the resulting pressure is strongly influenced by the total volume and temperature at each state. The initial pressure (p_1) is considered equal to atmospheric pressure because, during the test process, there is no additional pressure from outside the system. The pressure on state 2 (p_2) is obtained under isothermal conditions of 1.843 bar. The pressure on state 3 which is the maximum pressure (p_3) produced by the Stirling engine during the testing process is 2.446 bar and the pressure at state 4 (p_4) is 1.345 bar.

4   Conclusion

After testing and analyzing the 2nd generation Stirling engine, it is concluded that the thermal efficiency, engine rotational speed, ideal power, and Stirling engine pressure are highly dependent on the temperature difference between the hot and cold sides (ΔT). The higher ΔT, the higher the value of the three performance parameters.

References

1. BPPT: Indonesia Energy Outlook 2018. Agency for the Assessment and Application of Technology, Jakarta (2018)
2. Zainuddin, Z., Nurdin, J., Is, E.: The heat exchanger performance of shell and multi tube helical coil as a heater through the utilization of a diesel machine's exhaust gas. Aceh Int. J. Sci. Technol. **5**(1), 21–29 (2016)
3. Kaarsberg, T., Deppe, A., Kumar, S., Rosenfeld, A., Romm, J., Gielen, L.: Combined heat and power for saving energy and carbon in residential buildings. Build. Ind. Trends **10**, 149–159 (2000)
4. Kirillov, N.G.: Power units based on Stirling engines: New technologies based on alternative fuels. Russ. Eng. Res. **28**, 104–110 (2008). https://doi.org/10.1007/s11980-008-2002-z
5. Scarpete, D., Uzuneanu, K., Badea, N.: Stirling engine in residential systems based on renewable energy. In: 4th WSEAS International Conference on Energy Planning, Energy Saving, Environmental Education and the 4th WSEAS International Conference on Renewable Energy Sources, pp. 124–129. WSEAS Press, Tunisia (2010)
6. Harrison, J., On, E.: Stirling engine systems for small and micro combined heat and power (CHP) applications. In: Small and Micro Combined Heat and Power (CHP) Systems: Advanced Design, Performance, Materials and Applications, pp. 179–205. Woodhead Publishing Limited (2011)
7. Jufrizal, Napitupulu, F.H., Ilmi, Ambarita, H.: Manufacturing and testing prototype of a gamma type Stirling engine for micro-CHP application. In: 3rd Nommensen International Conference on Technology and Engineering, pp. 1–9. IOP Publishing (2020)
8. Thombare, D.G., Verma, S.K.: Technological development in the Stirling cycle engines. Renew. Sustain. Energy Rev. **12**(1), 1–38 (2008)
9. Romanelli, A.: Stirling engine operating at low temperature difference. Am. J. Phys. **88**(4), 319–324 (2020)
10. Wagner, A.: Calculations and experiments on γ-type Stirling engines. Ph.D. thesis, Cardiff University. ProQuest LLC, UK (2008)

11. Ambarita, H., Setyawan, E.Y., Ginting, S., Naibaho, W.: Performance of a small compression ignition engine fuelled by liquified petroleum gas. In: 1st Nommensen International Conference on Technology and Engineering, pp. 1–8. IOP Publishing (2017)

A Study of Spectral Match and Spatial Non-uniformity for Indoor Solar Simulator

Mohd Afzanizam Mohd Rosli[1,2(✉)], Muhammad Aiman Danial Hamizan[1], Muhammad Zaid Nawam[1], Muhamad Fakhrul Akmar Fazli[1], Siti Nur Dini Noordin Saleem[1], Noriffah Md Noh[1], and Faridah Hussain[3]

[1] Fakulti Kejuruteraan Mekanikal, Universiti Teknikal Malaysia Melaka, Hang Tuah Jaya, 76100 Durian Tunggal, Melaka, Malaysia
`afzanizam@utem.edu.my`
[2] Centre for Advance Research on Energy, Universiti Teknikal Malaysia Melaka, Hang Tuah Jaya, 76100 Durian Tunggal, Melaka, Malaysia
[3] SIRIM Standards Technology Sdn. Bhd., Seksyen 15, 40200 Shah Alam, Selangor, Malaysia
`faridahh@sirim.my`

Abstract. This paper presents a study on the characteristics of indoor solar simulator which include the spectral match and spatial non-uniformity assessment. A halogen based solar simulator from Universiti Teknikal Malaysia Melaka (UTeM) had been setup at one of its laboratories named as Applied Solar Energy Laboratory (ASEL). Like other solar simulator, several tests need to be done towards this ASEL's solar simulator to ensure its compliance to the standard set for solar simulator. The performance of the solar simulator was evaluated based on International Standard of IEC 60904-9, which involve the spectral match, spatial non-uniformity and temporal instability of the irradiance. The objective of this research was set to identify the characteristics of spectral match and spatial non-uniformity. The results show that ASEL's solar simulator managed to produce spectral match value of 0.40 and 1.46 at a wavelength range of 400–500 nm and 500–600 nm respectively. Meanwhile, through the mapping method, it reveals that this solar simulator able to produce a good percentage of spatial non-uniformity which is up to 8.42% across the tested area of 104 cm × 80 cm.

Keywords: Halogen lamp · Indoor solar simulator · Spatial non-uniformity · Spectral match

1 Introduction

1.1 Indoor Solar Simulator

The solar simulation technology was being referred to as a technology that purposely formed to mimic the light energy emit by the sun. In parallel with that, solar simulator is the device known to produce the light energy which has the intensity and spectral composition that was closed to the standard sunlight spectrum, AM1.5G. There are 3

basic components were usually used for a set-up of solar simulator; these includes the power supply, optical filters and light source.

In order to produce a good light emission, the light source which was considered as the most important part through its function of emitting light were usually formed from several types of lamps such as the light emitting diode (LED), xenon arc lamp, quartz tungsten halogen (QTH) and metal halide. In a several studies conducted before, the combination of different type of lamps were also being applied by the researcher as an approach to obtain a good light emission. Figure 1 below shows the comparison of standard sunlight spectrum (AM1.5G) to the light spectrum of different type of lamps [1].
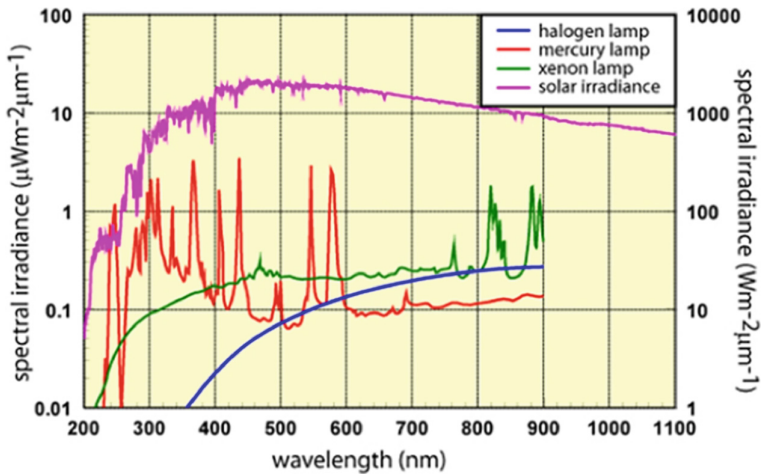
Fig. 1. Comparison of standard sunlight spectrum (AM1.5G) to the light spectrum from different type of lamps.

Even though the output produced from different light source would be varied, the performance of the solar simulator will still be evaluated by using 3 common characteristics. In accordance to the international compliance standard of IEC 60904-9 and ASTM E927-10, these 3 characteristics include the spectral match, spatial non-uniformity and temporal instability. As the test for each characteristic were completed, it will then be classed to either class A, B or C which for every class will indicate its performance. Table 1 below shows the classification of solar simulator based on its characteristics as referred to IEC 60904-9 [2] and ASTM E 927-10 [3] standards.

2   Methodology

For this study, there were two types of experiment that been done separately to achieve each of the objective set. Application of mathematical modelling was used for the first experiment regarding the spectral match; this method was stated by Pavithran *et al.* where among the data required for this experiments were the intensity of light in illuminance

Table 1. Classification of solar simulator based on its characteristics as referred to IEC 60904-9 and ASTM E 927-10 standard.

Parameter	IEC-60904-9	ASTM E927-10
Spectral match		
Class A	0.75–1.25	0.75–1.25
Class B	0.6–1.4	0.6–1.4
Class C	0.4–2.0	0.4–2.0
Spatial non-uniformity		
Class A	$\leq$2%	$\leq$3%
Class B	$\leq$5%	$\leq$5%
Class C	$\leq$10%	$\leq$10%
Temporal stability		
Class A	$\leq$2%	$\leq$2%
Class B	$\leq$5%	$\leq$5%
Class C	$\leq$10%	$\leq$10%

and spectral power distribution to form the conversion factor [4]. Meanwhile, for the spatial non-uniformity test, the method used was the irradiance intensity mapping method where an irradiance map with a labelled coordinated was formed.

2.1 Spectral Match Measurement

Mathematical modelling method involved the conversion of illuminance with the unit of lux to irradiance in W/m^2. This conversion named as the photometric to radiometric conversion was carried out by using the formula shown in (1); the CF stated below was known as the conversion factor. As for this experiment, the data of illuminance was measured by using lux meter at 5 different voltages supply of 192 V, 204 V, 216 V, 228 V and 240 V where it all were varied by using the voltage regulator.

$$\text{Irradiance} = \text{CF} \times \text{Illuminance} \tag{1}$$

For the calculation of conversion factor, it can be formed by using the equation stated in (2). As shown in the equation, parameters involved in the calculation are the photopic luminosity function, $P(\lambda_i)$ and the spectral distribution function, $\sum_i f(\lambda_i, \lambda_p, \Delta\lambda)$; in order to obtain this function, the spectral intensity distribution of the light source need to be measured.

$$\text{CF} = \frac{\sum_i f(\lambda_i, \lambda_p, \Delta\lambda)}{683 \times \sum_i f(\lambda_i, \lambda_p, \Delta\lambda) P(\lambda_i)} \tag{2}$$

As for this study, the intensity distribution which also indicates the light concentration or energy as function of wavelength was being determined by using a device known as

SM442 CCD Spectrometer. This device will work with SMProMX_5.6.0 software to form a graph that was referred as spectral power distribution. After the conversion of illuminance to irradiance was being done, it was proceeded with the calculation of spectral irradiance and followed by the determination of spectral match by using the formula stated in (3) and (4). The spectral match value obtained will then be classified to either class A, B or C by referring to Table 1 stated before.

$$SM = \frac{\text{Actual Percentage of Irradiance}}{\text{Required Percentage of Irradiance (AM1.5G)}} \tag{3}$$

$$\text{Actual Percentage of Irradiance} = \frac{\int_{\lambda_n}^{\lambda_{n+1}} S(\lambda)d\lambda}{\int_{400}^{1100} S(\lambda)d\lambda} \tag{4}$$

2.2 Spatial Non-uniformity Measurement

For the spatial non-uniformity test, it was being conducted by using irradiance intensity mapping method where maps with size area that was within the light source illumination area was drawn. As for this study, 4 type of maps with size area of 156 cm $\times$ 120 cm, 130 cm $\times$ 100 cm, 104 cm $\times$ 80 cm and 78 cm $\times$ 60 were used. With the difference size of maps drawn, the number of coordinates for each map would also be differ; these were between 49 to 169 coordinates. Figure 2 below shows the example for 130 cm $\times$ 100 cm map's size.
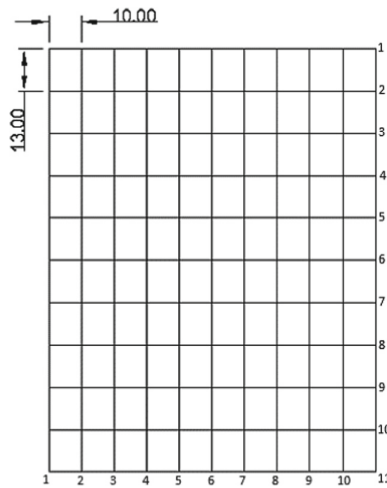
Fig. 2. 130 cm $\times$ 100 cm map's size.

This map will then be placed under the ASEL's solar simulator illumination for the testing purpose. A device named solar power meter was used to take the irradiance intensity reading at every coordinates. From the results obtained, the percentage of

spatial non-uniformity will be calculated by using formula (5) where the E_{max} and the E_{min} stated was the maximum and minimum irradiance respectively.

$$\text{Spatial Non-uniformity}(\%) = \frac{E_{max} - E_{min}}{E_{max} + E_{min}} \tag{5}$$

3   Results and Discussion

For the spectral match results that were being measure at 3 wavelength range of 400–500 nm, 500–600 nm and 600–700 nm; the results obtained were as tabulated in Table 2 below. As shown in table below, the spectral match for every supplied voltage was classified to either class A, B or C according to its value. For the spectral match value that was beyond the standard range set, the class column will be specified with '$\sim$' sign.

Table 2. Results of spectral match and class obtained.

Voltage (V)	Spectral match					
	400–500 nm		500–600 nm		600–700 nm	
192	0.32	~	1.25	A	3.97	~
204	0.31	~	1.26	B	4.01	~
216	0.31	~	1.26	B	4.01	~
228	0.33	~	1.36	B	3.90	~
240	0.40	C	1.46	C	3.75	~

According to Table 2, the spectral match value obtained at 600–700 nm was beyond the standard range set, whereas at 400–500 nm wavelength range only supplied voltage of 240 V able to achieve the minimum requirement set with class C. Light emit by the solar simulator with a supplied voltage of 240 V was considered as the best result obtained with 2 wavelength range of 400 nm–500 nm and 500 nm–600 nm managed to be placed within the standard range set. From the tabulated data, it can be seen that the spectral match value recorded at the 600–700 nm region was far beyond the minimum standard range set at this region which is 0.4–2.0. This gap could be explained by the characteristics of the halogen lamp where its emission is high at the near infrared region. Meanwhile, at the 400–500 nm region, there's a deficiency of the irradiance emission compare to the standard spectrum AM1.5G; this was due to the lack of blue colour spectrum in this region [5].

On the other hand, for the spatial non-uniformity test, the results gained was as tabulated in Table 3 below. Out of the 4 maps tested, 3 maps with size area of 130 cm × 100 cm, 104 cm × 80 nm and 78 cm × 60 cm were able to record a spatial non-uniformity percentage of lower than 10%. With the spatial non-uniformity percentage of 9.02%, 8.42% and 8.49; all these results were classed in class C according to the standard set by IEC 60904-9. Among these 3 maps, the suggested test size area that should be applied at

Table 3. Results of spatial non-uniformity.

Size of intensity map (cm^2)	Average irradiance intensity (W/m^2)	Spatial non-uniformity (%)
156 × 120	990.10	10.15
130 × 100	991.41	9.02
104 × 80	981.98	8.42
78 × 60	981.93	8.49

ASEL's solar simulator was 104 cm × 80 cm as the spatial non-uniformity percentage was the lowest compare to the other 3.

Summary

In summary, both approaches use in this study are able to identify the characteristics of ASEL's solar simulator in term of spectral match and spatial non-uniformity. Out of 3 wavelength range involved in the spectral match test, 2 of it managed to be placed within the standard range set by IEC 60904-9. These are the 400–500 nm and 500–600 nm wavelength range with spectral match value of 0.4 and 1.46 respectively. Meanwhile, the spatial non-uniformity test also reveals that ASEL's solar simulator able to produce a good irradiance uniformity with non-uniformity percentage of as low as 8.42%.

References

1. Standard Solar Spectra. https://www.pveducation.org/pvcdrom/appendices/standard-solar-spectra. Accessed 24 June 2021
2. ISO 527-2: International Standard International Standard. 61010-1 © Iec2001 (2003)
3. ASTM E927-10: Standard Specification for Solar Simulation for Photovoltaic Testing (2015)
4. Mohan, M.V.A., Pavithran, J., Osten, K.L., Jinumon, A., Mrinalini, C.P.: Simulation of spectral match and spatial non-uniformity for LED solar simulator. In: 2014 IEEE Global Humanitarian Technology Conference-South Asia Satellite, GHTC-SAS 2014, pp. 111–117 (2014)
5. Namin, A., Jivacate, C., Chenvidhya, D., Kirtikara, K., Thongpron, J.: Construction of tungsten halogen, pulsed LED, and combined tungsten halogen-LED solar simulators for solar cell I–V characterization and electrical parameters determination. Int. J. Photoenergy (2012)

Life Cycle Analysis (LCA) Using CES-Edupack Software of New Wood Dust Reinforced Recycled Polypropylene Composite Filament for Fused Deposition Modelling (FDM)

Wong Chun Yip, Yusliza Yusuf[(✉)], and M. T. Mastura

Fakulti Teknologi Kejuruteraan Mekanikal dan Pembuatan, Universiti Teknikal Malaysia Melaka, Hang Tuah Jaya, 76100 Durian Tunggal, Melaka, Malaysia
yusliza@utem.edu.my

Abstract. FDM filament is mainly made of polymers, specifically PP, ABS, and PLA. Humans leave many 3D printed objects utilising FDM filament despite their good state. So recycling FDM filament, especially polypropylene waste, helps reduce landfill dumping. Using the CES-Edupack Software, this study will show a simple approach for material selection and life cycle analysis of recycling polypropylene with wood dust as reinforcement. This method assesses a product's environmental impact throughout its life cycle, from raw material extraction through final disposal. The project collects data on energy use, carbon dioxide emissions, toxicity, recycling, and sustainability. As a result, suggesting recycling polypropylene with bio-composite as reinforced materials allowed a user to form conclusions regarding a sustainable recycling method for plastic waste and it may become an alternative strategy for managing plastic waste.

Keywords: Life Cycle Analysis (LCA) · CES-Edu pack · Polypropylene · Bio-composite

1 Introduction

1.1 Life Cycle Analysis (LCA)

Life Cycle Analysis (LCA) is a methodological framework for assessing the environmental impact of a product, service, or process throughout its life. It is also a technique for estimating the environmental aspects and potential impacts of a process, service, or product by compiling a list of relevant energy and material inputs, assessing the potential environmental impact, and clarifying the result in order to make a more informed decision about the product's final disposal [1, 2]. LCA will be conducted in this study utilising the CES-Edupack software in conjunction with the Eco Audit Tool application. The eco audit tool identified the life stages of a product (Material, Manufacture, Transportation, Use, and End of life) that consume the most energy and produce the most CO_2. This is the starting point for eco product design because it identifies which attributes

should be targeted to reduce the product's eco footprint [3]. Additionally, the Eco Audit Tool included in CES-EduPack can analyse and summarise energy consumption and CO_2 emissions by tracing the stages of a product's life cycle using an environmental factor design approach (Fig. 1). The Eco Audit's purpose is to calculate the embodied energy produced, the carbon footprint, the water consumption, the proportion of CO_2 released into the atmosphere, the toxicity factor, and the sustainability factor.
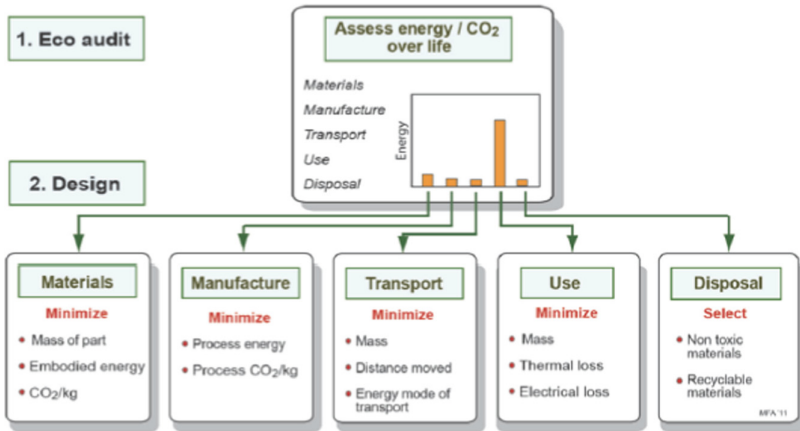
Fig. 1. Software CES Edupack integrating the life cycle assessment tool.

1.2 Recycles PP and Wood Dust Bio-composites

Polypropylene (PP) is a thermoplastic polymer made up of propylene monomers in various combinations [4]. It is used in a wide variety of application and field. For FDM filament made by PP is one of among the most mass distributed plastic in every country. Employment of the recycled materials for fabrication using FDM would give significant contribution in managing plastic waste and solve environmental issues in manufacturing industry.

Bio-composite materials such as wood dust are frequently seen in industrial or manufacturing settings or in carpentry. Each type of wood dust varies in size according to the size of the teeth on the instrument employed. Kapur was used in this study as an example of wood dust. Kapur, also known as 'Borneo Camphorwood,' originates in Asia or Oceania. Its colour ranges from red brown to pink brown and has a camphor scent. It had a density of 0.74 g/cm^3 at 12% moisture content. This wood is commonly used in the manufacture of furniture, veneer, flooring, joinery, and formwork.

2   Methodology

The methodology used in this study was divided into three phases [5]:
Phase 1: Searching information and data collection:

– Identification of various components, their materials, and manufacturing methods.
– If you do have an identifying number on the product, search for information materials on the manufacturer's website products.
– Research on the recycling of various materials in order to populate the programme with data.

Phase 2: Placing data in the software:

– Entering the amount and material of each component, the recycling percentage (0–100%), the component's weight, the main process, and the component's final destination (landfill, incineration, down cycle, reuse, remanufacturing, recycling). It was initially utilised to ascertain the student's viewpoint and subsequently to do study on the probable final component of our context.
– Display of numerous modes of travel and their proximity to each phase of the life cycle that requires transportation.
– Calculation of the energy expenses associated with the product's usage phase. When it comes to pushing the wasted Cooling is a predictor of use.
– In this step, we utilised the CES EduPack software in conjunction with the Eco Audit tool to conduct a life cycle assessment.

Phase 3: Analysis of the data:

– A cost-benefit analysis of each phase's energy consumption.
– CO_2 emissions analysis at each stage.
– A comparison of the various product samples.
– A comparative investigation of life spans in order to squeeze out further life estimates.

3   Result and Discussion

The Eco Audit Tool, which is available, displays expanded eco property data and estimates the cost of products [6]. Additionally, the analysis aided in the improvement of material processing and end-of-life concerns. It is the means of minimising environmental effect. At the same time, it facilitated the quick identification of domain life phases [6]. This study defines three (3) different categories of material. These include Acrylonitrile Butadiene Styrene (ABS), Polypropylene (PP), and Kapur wood dust. For the purposes of analysis, the data input for each material was kept consistent in terms of presumed value and statistics. The data obtained and the outcome of the Eco Audit for PP filament are depicted in Fig. 2. Meanwhile, Fig. 3 illustrates the output of Energy (kcal), Energy (percent), Mass of CO_2 (lb), and CO_2 (percent that may be used to determine which parameters can be optimised to lower the product's eco-footprint.

Product definition | Report

Product name: PP Filament

Compare with... ▼ | Clear | Open | Save

⌄ 1. Material, manufacture and end of life ❓

	Qty.	Component name	Material	Recycled content	Mass (lb)	Primary process	End of life
	100	PP Filament	■ PP (homopolymer, low	Virgin (0%)	0.002	Polymer molding	Landfill
	1		📅		0		

⌄ 2. Transport ❓

	Name	Transport type	Distance (miles)
	Johor to Melaka	14 tonne truck	121.8

⌄ 3. Use ❓

Product life: 1   Years

Country electricity mix: Asia (excl.China) ▼

Static mode
☑ Product uses the following energy:

Mobile mode
☐ Product is part of or carried in a vehicle

Energy input and output: Electric to mechanical (electric moto ▼   Fuel and mobility type: Diesel – ocean shipping ▼

Power rating: 0.12   kW ▼   Usage: 0   days per year

Usage: 2   days per year   Distance: 0   miles per day

Usage: 24   hours per day

⌄ 4. Report ❓

Fig. 2. Eco Audit Tool product definition.

Phase	Energy (kcal)	Energy (%)	CO2 (lb)	CO2 (%)
Material	2.06e+03	13.6	0.766	8.8
Manufacture	132	0.9	0.0912	1.0
Transport	3.61	0.0	0.00237	0.0
Use	1.3e+04	85.5	7.86	90.1
Disposal	4.33	0.0	0.0028	0.0
Total (for first life)	1.52e+04	100	8.73	100
End of life potential	0		0	

(a)

Phase	Energy (kcal)	Energy (%)	CO2 (lb)	CO2 (%)
Material	1.62e+03	9.7	0.397	4.1
Manufacture	474	2.8	0.328	3.4
Transport	3.61	0.0	0.00237	0.0
Use	1.46e+04	87.4	8.83	92.4
Disposal	4.33	0.0	0.0028	0.0
Total (for first life)	1.67e+04	100	9.56	100
End of life potential	0		0	

(b)

Phase	Energy (kcal)	Energy (%)	CO2 (lb)	CO2 (%)
Material	224	1.7	0.177	2.2
Manufacture	0	0.0	0	0.0
Transport	3.61	0.0	0.00237	0.0
Use	1.3e+04	98.2	7.86	97.7
Disposal	4.33	0.0	0.0028	0.0
Total (for first life)	1.32e+04	100	8.05	100
End of life potential	0		0	

(c)

Fig. 3. The output of energy and CO_2 for (a) ABS (b) PP and (c) Kapur wood dust.

The Eco Audit Tool calculates the amount of emissions and the percentage of energy and CO_2 produced by a product once it has been analysed. The interpretation process is used to determine which material properties exist and how they interact with the environment. According to the target and scope definitions, the analysis produced a thorough and ready-to-use LCA result. In this finding, even though the ABS shows lower energy than PP, both are thermoplastic types of filaments widely used in 3D filament manufacturing. PP is lightweight and very practical to use to print out parts with precise dimensions. Besides ABS is also unsuitable for high-temperature applications and medical implants due to its low melting point. It also has low solvent and fatigue resistance, and unless adequately covered, it is susceptible to UV exposure and weathering.

4   Conclusion

Generally, recycling PP waste is a recovering process of the materials that are melted in high temperature and turn into something that useful through particular process such as Fused Deposition Modeling (FDM). PP and new wood dust have the potential to be utilised as FDM filament materials. LCA is performed by comparing the significant impact of wood dust reinforced recycled polypropylene (r-WoPPC) filament for FDM with the others related materials such as ABS on environment, human and economy.

References

1. Silvestri, L., Fornina, A., Silvestri, C., Loppolo, G.: Life cucle assessment of sanitaryware production: a case study in Italy. J. Clean. Prod. **251**, 119708 (2020). https://doi.org/10.1016/j.jclepro.2019.119708
2. Carneiro, O.S., Silva, A.F., Gomes, R.: Fused deposition modeling with polypropylene. Mater. Des. **83**, 768–776 (2015). https://doi.org/10.1016/j.matdes.2015.06.053
3. Cebon, D., Ashby, M.F., Bream, C., Lee-Shothaman, L.: CES EduPack User's Manual, Release 4 (2009). http://www.grantadesign.com/download/pdf/EduPack-2009-Manual.pdf
4. Spiryn, J.: What's The Difference Between PLA And ABS? Zmorph S.A. ZMORPH, 29 October 2019. https://zmorph3d.com/blog/difference-between-pla-abs/
5. Marques, A.C.: Sustainability in design education: introduction of life cycle assessment. In: MDPI the 3rd World Sustainability forum session Environemntal Sustainability Forum, November 2013. https://doi.org/10.3390/wsf3-a009
6. Doicin, C.V., Ionescu, N., Savu, T., Nitu, E.: Eco-audit environmental impacts of products. Appl. Mech. Mater. **834**, 34–39 (2016). https://doi.org/10.4028/www.scientific.net/AMM.834.34

Biodiesel Storage Stability: Evaluation and Monitoring Advancements

N. Satishwara Rao[1], N. H. M. Zini[1,3(✉)], M. N. A. Saadun[1,3], and F. Shikh Anuar[2,3]

[1] Fakulti Kejuruteraan Mekanikal, Universiti Teknikal Malaysia Melaka, Hang Tuah Jaya, 76100 Durian Tunggal, Melaka, Malaysia
nurulhilwa@utem.edu.my
[2] Fakulti Teknologi Kejuruteraan Mekanikal dan Pembuatan, Universiti Teknikal Malaysia Melaka, Hang Tuah Jaya, 76100 Durian Tunggal, Melaka, Malaysia
[3] Centre for Advanced Research on Energy, Universiti Teknikal Malaysia Melaka, Hang Tuah Jaya, 76100 Durian Tunggal, Melaka, Malaysia

Abstract. Due to the challenges of the IR 4.0 era and the Covid-19 pandemic at the same time, this paper provides a brief review of the published studies predominantly on biodiesel storage tank materials and followed by the Internet of Things (IoT) system as an alternative monitoring method in biodiesel industries. The suitability of storage material for a longer storage duration due to lower oil demands amidst this pandemic becomes a major concern. In this paper, two important parameters: kinematic viscosity and flashpoint in consideration of storage tank materials relating to surrounding conditions and biofuel blends were discussed. It was found that the degradation of fuel in plastic and glass storage tanks is significant for outdoor storage. Over time, the kinematic viscosity of biodiesel shows an increasing trend meanwhile the flashpoint is in decreasing trend or almost constant. However, these physical properties show very limited changes when stored at an ambient temperature. On another note, IoT systems to date are mostly used to detect fuel theft, fuel consumption, fuel impurities, and fuel tank level but are yet to be used to observe the fuel quality under a longer storage period, more than 6 months. IoT solution with suitable embedded sensors has potential to become the advance solution for remote biodiesel quality monitoring, reducing the need for manpower and interaction. This review paper provides necessary information for further investigations on biodiesel stability, storage material, and monitoring advancement systems.

Keywords: Biodiesel storage stability · Storage tank material · IoT system

1 Introduction

Bio-oil can be divided into two categories: (1) bioethanol and (2) biodiesel. This fuel is often referred to as monoalkyl esters with long-chain fatty acids. It is cheaper, environment-friendly, renewable, and obtained from organic materials such as palm, rapeseed, and soybean. Biodiesel has superior properties compared to petrodiesel in

many aspects: low ash content, low nitrogen content, low sulfur content, higher lubricity, low carbon residue, and non-toxic [1]. However, the stability of biodiesel deteriorates with a longer storage period and environmental conditions.

2   Evaluation of Storage Stability: Environmental and Material Effects

The storage stability of biodiesel can be evaluated by measuring its physical properties such as kinematic viscosity and flashpoint, where the values should be in the range of 1.9–6.0 mm^2/s and 130 °C, respectively, according to ASTM standard D6751 [2]. However, depending on the environmental condition and storage material, these values can be affected as shown by the results of various past research presented in Fig. 1 [3–6]. The low biodiesel fuel, e.g., B5 blend degrades faster than B15 in outdoor exposure as shown in Fig. 1(a). The oxidation process is further expedited by storing B5 in the plastic tank. For indoor storage, the viscosity managed to be kept at the lowest viscosity increment or almost constant as the storage duration increase, as shown in Fig. 1(b); this is true for higher biodiesel blends stored in glass and HDPE [4]. However, most of them used glass as their storage material. It is also stated that metal storage tends to increase the rate of kinematic viscosity due to the higher rate of oxygen solubilization at a lower temperature [2]. Meanwhile, the flashpoint can be significantly affected by the number of double bonds and carbon atoms [5]. The formation of bio-lipids with more free fatty acids and higher water content leads to a lower flashpoint value. Observation with other materials apart from glass is very less for flashpoints due to most of the experimental works were concentrated on biodiesel blend quality.

In general, the formation of peroxides indicates the beginning of the oxidation process of methyl esters, which increases the kinematic viscosity of biodiesel when the peroxide reaches a certain level. The oxidation process increases the formation of double bond isomerization, free fatty acids, and higher molecular weight production which increases the viscosity along the storage period. The polar formation, oxygen-containing molecules, and oxidized polymeric compounds increase the viscosity of methyl esters during storage which leads to the formation of sediments that clogs the filter. To be noted, pure biodiesel viscosity is high due to higher fatty acid compositions. A higher ratio of diesel in the fuel blends is more stable because the content of oxygen in diesel is lower which prevents the oxidation process from occurring [4, 5].
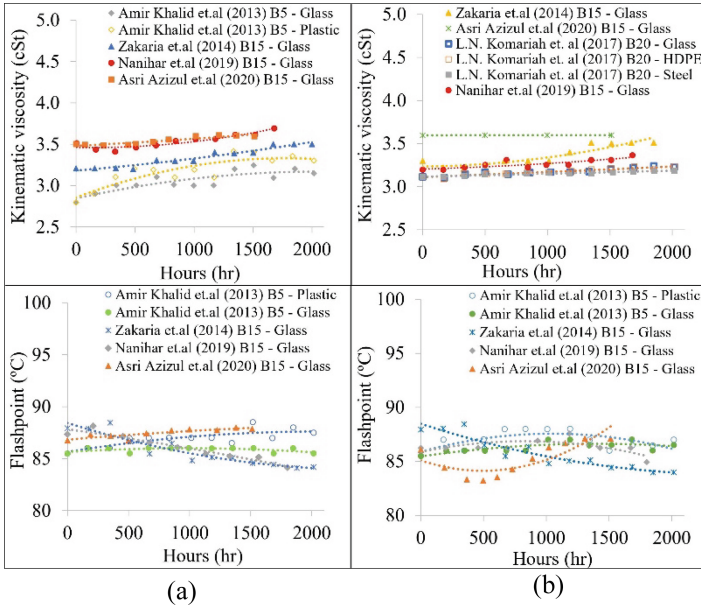
Fig. 1. Comparison of kinematic viscosity and flashpoint versus hours for various biodiesel blends and storage tank materials: (a) outdoor and (b) indoor.

3 Sensor and Technologies of IoT in Biodiesel Storage Tank

Internet of Things (IoT) system has been used in various potential applications [8]. Current IoT systems for biodiesel application have many integration sensors, e.g., ultrasonic sensors, pH level sensors, and temperature sensors. The embedded IoT system allows real-time data collection practices. However, biodiesel storage tanks monitored with IoT systems have limited published literature [9]. Most of the IoT systems developed are used either to detect theft or to locate fuel retailers for the user via GPRS. In addition, an ultrasonic sensor or flow sensor can be installed as a fuel level indicator in the storage tank; temperature and humidity sensors can be used to capture the inside and outside environmental conditions of the storage tank. To observe oxygen concentration and acid value in the fuel, oxygen sensor and pH sensor can be used, respectively. All the references for these sensors are tabulated in Table 1. By introducing these sensors into biodiesel storage systems, manpower and interaction can be reduced.

Table 1. IoT sensors frequently used in fuel tank monitoring system.

Sensor type	Sensor	Detection/Measurement	Ref
Non-contact	Ultrasonic; Hall effect	Fuel level	[10]
Mechanical	Flow	Fuel consumption	[11]
Resistive-based	Float	Fuel level	[12]
Strain-gauge	Pressure	Tank pressure	[13]

4   Conclusion

Glass is commonly used as a storage material, yet it also causes high degradation effects on the fuel. In outdoor storage conditions, the value of biodiesel viscosity increases with the storage period; meanwhile, the flashpoint showed the opposite reaction. On another note, IoT sensors has the capability to obtain real-time data from the storage tank for a short and storage period but it is mostly used to detect theft and fuel level detection. Thus, IoT based smart monitoring system can serve as a potential research area for the biodiesel storage tank.

References

1. Adipah, S.: Introduction of biodiesel as a sustainable resource. J. Environ. Sci. Public Heal. **03**(01), 99–103 (2018)
2. Mahmudul, H.M., Hagos, F.Y., Mamat, R., Adam, A.A., Ishak, W.F.W., Alenezi, R.: Production, characterization and performance of biodiesel as an alternative fuel in diesel engines – a review. Renew. Sustain. Energy Rev. **72**(2), 497–509 (2017)
3. Azizul, M.A., Khalid, A., Nanihar, N., Manshoor, B., Ngadiron, Z.: Effects of storage characteristics on flash point and water content of biodiesel derived from crude palm oil, Jatropha, and waste cooking Oil. J. Adv. Res. Fluid Mech. Therm. Sci. **76**(2), 154–162 (2020)
4. Nanihar, M.N., Khalid, A., Zulkifli, A.F.H., Sunar, N.M., Manshoor, B., Zaman, I.: Effects of storage duration and ambient condtion on jathropha derived biodiesel properties and characteristic. J. Phys. Conf. Ser. **1150**(1) (2019)
5. Zakaria, H., Khalid, A., Sies, M.F., Mustaffa, N., Manshoor, B.: Effect of storage temperature and storage duration on biodiesel properties and characteristics. Appl. Mech. Mater. **465–466**(December), 316–321 (2014)
6. Komariah, N., Marwani, L., Aprisah, S., Rosa, Y.S.L.: Storage tank materials for biodiesel blends; the analysis of fuel property changes. In: MATEC Web of Conference, vol. 101 (2017)
7. Berrios, M., Martín, M.A., Chica, A.F., Martín, A.: Storage effect in the quality of different methyl esters and blends with diesel. Fuel **91**(1), 119–125 (2012)
8. Shkurti, L., Bajrami, X., Canhasi, E., Limani, B., Krrabaj, S., Hulaj, A.: Development of ambient environmental monitoring system through wireless sensor network (WSN) using NodeMCU and 'WSN monitoring. In: 2017 6th Mediterranean Conference on Embedded Computing (MECO): including ECYPS 2017. June, pp. 11–15 (2017)

9. Xiong, H., Guo, X., Xie, W.: Biodiesel remote monitoring system design based on IOT. In: Zu, Q., Hu, B., Gu, N., Seng, S. (eds.) HCC 2014. LNCS, vol. 8944, pp. 750–756. Springer, Cham (2015). https://doi.org/10.1007/978-3-319-15554-8_65
10. Gijre, M.M., Mane, A., Gadade, R.: Smart fuel level indication system. Glob. Res. Dev. J. Eng. **2**(6), 205–209 (2017)
11. Ali, A.S., Hasan, A.H., Lafta, H.A.: Antitheft vehicle tracking and control system based IoT. J. Crit. Rev. **7**(9), 88–92 (2020)
12. Krishnasamy, R., Jayapalan, B., Karthikeyen, K., Nowfal, M.: Automatic fuel monitoring system. Int. J. Recent Technol. Eng. **8**(4S2), 348–352 (2019)
13. Kavitha, M., Atchaya, D., Pavithra, S.: Intelligent vehicle technology and combustion fuel alert using IOT. Int. J. Recent Technol. Eng. **8**(1), Special Issue 4, 614–618 (2019)

Utilization of Alternative Renewable Heat Sources to Produce Electrical Energy

Ai Nurhayati^(✉) (ID)

Sekolah Tinggi Teknologi Bandung, West Java 40235, Indonesia
`ai.nurhayati@sttbandung.ac.id`

Abstract. Energy sources from oil and gas will eventually run out and run out, so it is necessary to look for other energy sources. The purpose of this research is to obtain a source of energy obtained from solar heat which is trapped in a prototype device. The method used is to use a Peltier device that functions as a tool to convert solar heat into electrical energy. The result of this research is a prototype that is connected in series to generate electricity.

Keywords: Electricity · Energy · Heat

1 Introduction

Energy sources that cannot be renewed from nature, such as coal, which has been used to generate electrical energy, really need to be conserved in their use because over time they will decrease and will soon run out. The use of coal as an energy source in the international world in 1990 amounted to 750 million tons. Coal consumption continues to experience a very significant increase until in 2020 by 2500 million tons [1]. Coal commodity reserves are estimated to be depleted in the next 20 years if coal production continues to increase annually [2]. The question to be solved in this research is how to find alternative sources of renewable energy. The purpose of this study is to obtain a source of energy obtained from heat trapped in a prototype device to generate electricity. The method used is to use a Peltier device which functions as a tool to convert heat into electrical energy.

2 Literature Review

Peltier is a slab-shaped component that is often used to create cold or hot effects on certain tools [3]. Electronic components that can produce the Peltier effect are Thermo Electric Coolers or commonly abbreviated as TEC [4]. The simplest Peltier thermoelectric device is a thermocouple consisting of connected semiconductor wires of n-type and p-type conductivity [5]. With a certain circuit, the electric voltage applied to this component can produce a hot effect on one side and cold on the other side at the same time [5]. This condition is caused because the TEC functions as a heat pump from the 2 cold side to the side where the heat exits [6]. The way TEC works is by flowing electricity

from the positive semiconductor type, to the negative type through a metal that conducts electricity [7]. This electric current process causes one side that is potentially exposed to a negative voltage to cool down [8]. On the other hand, the other side, which is exposed to a positive voltage, will be a place for heat to escape [9]. Previous researchers only used Peltier as a tool to cool or freeze it. The difference in this new study is that it uses a Peltier to generate electricity as a light source.

3   Methodology

In this research, the process of searching for alternative energy sources that can replace fuel energy sources such as coal is carried out which has been used as lighting for electricity. The search for alternative energy sources that are renewable and readily available in nature, such as solar energy sources. The flow chart of this process can be seen in Fig. 1.
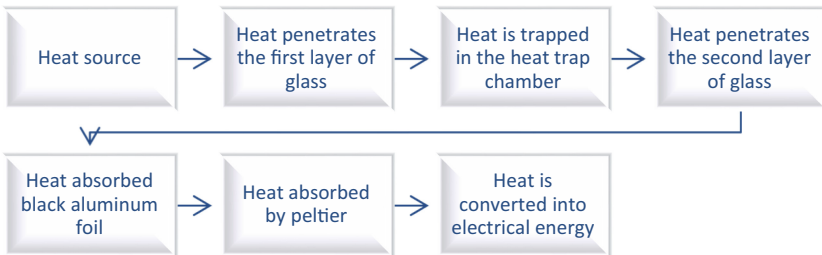
Fig. 1. Process flow chart.

The source of energy from the shining sunlight can be captured by a heat trap. Heat can be absorbed by the Peltier device, then converted into electrical energy.

4   Results

Figure 2 shows a prototype that is made using styrofoam and only uses 2 peltiers. The glass used is ordinary glass and coated glass for car windows.

The test was carried out by exposing the prototype under the hot sun. Solar heating was obtained from 6 am to 6 pm (Western Indonesia Time) on a very sunny day and the air temperature happened to be very hot when the experiment was carried out. The sun's heat received by the prototype is valid for 12 h, although with different levels of heat intensity depending on the hour. At 6 a.m., the sun just rose so that the level of light and heat intensity received by the prototype was only slightly, and similarly in the afternoon before 6 o'clock, the prototype received a dim light intensity so that the heat intensity was reduced because it was approaching sunset. The high level of solar heat intensity was received by the prototype at noon. Thus, for a total of 12 h, the prototype was left outside to be exposed to the sun, although the intensity of the heat received was different during those 12 h. To increase the cold temperature difference from one side

Styrofoam

Black aluminium foil

Peltier on the inside

Radiator coolant water
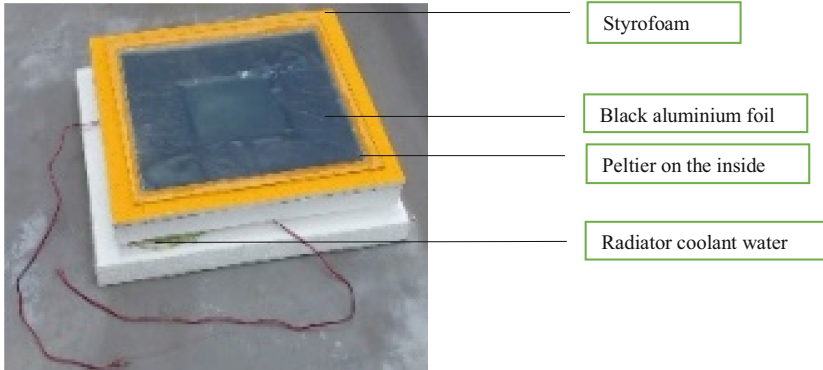
Fig. 2. Prototype.

of the Peltier plate, it is done by connecting one side of the Peltier plate to the radiator coolant water stored on the inside of the prototype which can be used as a cooler for one side of the Peltier. Thus there is a significant temperature difference between the side of the Peltier and the side of the Peltier in the opposite direction. The result is that the highest current and voltage achieved is a short circuit current of 480 μA and an open-circuit voltage of 24 mV. The following Table 1 gives a summary of all heading levels.

Table 1. Effect of temperature difference on current and voltage.

Heating time (hour)	Current (μA)	Voltage (mV)	Temperature inside heat trap (°C)	Temperature environment (°C)
3	60	3	60	30
6	120	6	65	40
9	240	12	70	41
12	480	24	82	42

If the temperature difference between the inside of the heat trap and the ambient temperature is greater, the current and voltage generated will be greater. The use of styrofoam insulation on the inside of the prototype can reduce the heat that comes out of the tool. The prototype part is covered by black aluminum foil to increase the heat by radiation. This tool will be used to charge a dry accumulator battery which has a voltage of 12 V. To be used it is necessary to increase the current and voltage. This is done by making several products and connecting them in series and parallel.

5   Conclusions

Based on the results of the research, the prototype can only produce an electric current of 480 μA with an electric voltage of 24 mV because the heat source comes from the sun,

so it is very dependent on sunlight for a maximum of 12 h a day. For the development of prototypes in the future, prototypes can be made with conductor material to absorb heat faster so that heating the prototype does not take a long time. For the development of prototypes in the future is to look for heat sources other than the sun.

References

1. Martins, F., Felgueiras, C., Smitkova, M., Caetano, N.: Analysis of fossil fuel energy consumption and environmental impacts in European countries. Energies **12**(6), 1–11 (2019)
2. Pulgarin, D., Montoya, G., Restrepo, J., Leiva, F.: Fossil or bio-energy? Global fuel market trends. Renew. Sustain. Energy Rev. **143**(1), 1–11 (2021)
3. Kuzichkin, O., Konstantinov, I., Vasilyev, G., Surzhik, D.: Control of operability of Peltier modules in cooling systems based on the analysis of transient operating modes. Thermodynamics **42**(2), 31–42 (2021)
4. Chu, W., Jiahe, H.N.: Finite element analysis of Peltier effect based thermoelectric energy conservation cooling system for microprocessors. In: 6th International Conference on Energy Science and Applied Technology, vol. 804, pp. 1–6. IOP Publishing (2021)
5. Poklonski, N., Vyrko, S., Kovalev, A., Anikeev, I., Gorbachuk, N.: Design of Peltier element based on semiconductors with hopping electron transfer via defects. Dev. Methods Measur. **12**(1), 13–22 (2021)
6. Parashchuk, T., Sidorenko, N., Ivantsov, L., Sorokin, A., Maksymuk, M., Dzundza, B.: Development of a solid-state multi-stage thermoelectric cooler. J. Power Sour. **496**(1), 1–8 (2021)
7. Kwan, T., et al.: Integration of radiative sky cooling to the photovoltaic and thermoelectric system for improved space cooling. Appl. Therm. Eng. **196**(1), 1–13 (2021)
8. Casallas, I., Pérez, M., Fajardo, A., Paez-Rueda, C.: Experimental parameter tuning of a portable water generator system based on a thermoelectric cooler. Electronics **10**(141), 1–14 (2021)
9. Xie, Y., Li, X., Dong, S., Zhang, H., Wu, H.: Experimental investigation on operating behaviors of loop heat pipe with thermoelectric cooler under acceleration conditions. Energies **33**(3), 852–860 (2020)

Airfoil Performance of an Active Car Spoiler

Muhammad Safwan Asyraf Ramli[1], Shamsul Anuar Shamsudin[1(✉)],
Zairulazha Zainal[1], Norasra A. Rahman[1], and Zulkhairi Zainol Abidin[2]

[1] Fakulti Kejuruteraan Mekanikal, Universiti Teknikal Malaysia Melaka, Hang Tuah Jaya,
76100 Durian Tunggal, Melaka, Malaysia
`shamanuar@utem.edu.my`

[2] Jabatan Kejuruteraan Mekanik dan Pembuatan, Fakulti Kejuruteraan dan Alam Bina,
Universiti Kebangsaan Malaysia, UKM, 43600 Bangi, Selangor, Malaysia

Abstract. A car spoiler can alter the aerodynamic forces acting on the car while driving. The benefits of it include manipulating the drag force and lift force. The fuel consumption can decrease and the car becomes more stable after attaching the spoiler. Here, a spoiler that could actively assume three configurations was studied. This could be an automatic spoiler that can morph into three shapes based on situations such as to decrease the fuel consumption for economic driving and to increase car stability while cornering or in high-performance handling of the car. The basic shapes of the spoiler were drawn using the SolidWorks package. The spoiler comprises of a 290 mm main plane and a 120 mm flap. The target design has no gap between main plane and the trailing-edge flap. Next, the spoiler design from SolidWorks is imported to ANSYS Fluent package, where simulations and analysis on the spoiler were executed to get the coefficients of drag and lift. In the end, the simulation shows that the active spoiler without the gap can achieve higher down force when fully deployed at 40° and it shows, at least, a slightly higher drag force as well.

Keywords: Car · Spoiler · Dynamics

1 Introduction

1.1 Problem Statement

A car spoiler's main role is to improve their grip on the road when usually, the car's own weight is the only force acting downwards. The only way to increase the grip by increasing the weight, without using spoiler. Spoiler works like the wing of the aircraft except upside down. The spoiler creates its own downward force on the car's frame.

Low drag imposed by the car body is desired to reduce the fuel consumption when driving along straight line. The car will increase downward force when taking cornering to keep the car stable and increase the friction between the tires and the ground.

On the other hand, the spoiler is also an important component to help reduce drag friction and decrease the downward force. However, not many spoilers can change shape based on different conditions. This initial study looks at spoiler that can morph in different situations that could possibly use some rigid body mechanism to achieve those shapes.

1.2 State-of-the-Art for Car Spoilers

Aerodynamic drag starts to become resistance once the vehicle reaches the speed 80 km/h or more, while the fact is almost 65% of the engine power is required to overcome aerodynamic. Using rear spoiler can decrease the drag coefficient and improve the fuel consumption by decreasing the lift coefficient drag [1]. A rear spoiler is mostly not for stylish look but it has serious performance advantages that depend on different designs.

Car performance, handling, safety and comfort are affected by aerodynamic properties such as drag force and lift force. Even for a new car, the need for increased performance like speed may require extra parts such as a spoiler to improve the stability and maintain economic fuel consumption. Consequently, passenger cars could benefit from rear spoilers for decreasing the drag [2].

Drag is the resistance force that is a product of motion when the vehicle is travelling through fluid. It is a force that is in opposite direction of the thrust. Figure 1 shows the direction for thrust, weight, lift, and drag forces. When a low drag is applied to the car at a straight path, it can decrease the fuel consumption [1–3].

2 Analysis Procedure

The spoiler was drawn by using SolidWorks software that consists of main plane and flap wing. The chord length for main static plane is 290 mm while the flap wing distance is 120 mm. This follows the NACA 2412 wing and flap in [4]. However, there is no gap between main plane and flap wing in this work. There are three angles of attack between main plane and flap wing which are 0°, 20° and 40° (see Fig. 1).
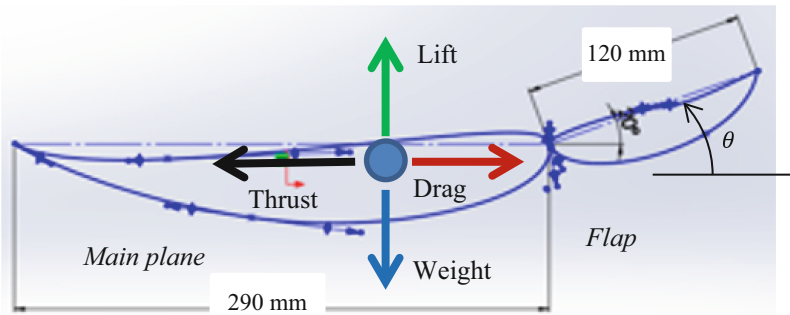
Fig. 1. Design of spoiler with different angles of attack $\theta = 0°$, 20° and 40°.

ANSYS Fluent is a Computational Fluid Dynamics (CFD) analysis package that can analyze the pressure field, velocity vector fields and simulated aerodynamic forces. Spoiler models that are created in a Computer Aided Design (CAD) package such as SolidWorks are then imported into ANSYS to simulate lift and drag coefficients. Firstly, analyze the spoiler with a 10 mm vertical gap between main plane and flap and get the amount of drag and lift coefficients. Next, compare the amount of drag coefficient with the reported data from [4] for validation. After the results are acceptable, the spoiler

with and without gap will undergo the same simulation procedure to get drag and lift coefficients. All six design which are the spoiler with gap and the spoiler without gap with three different angles of attack will go through the simulation. Some data are assumed to be constant such air density, $\rho = 1.2754$ kg/m^3 (data for 0 °C and 100 kPa of dry air), vehicle velocity, $V = 80$ km/h@22.22 m/s and spoiler mass, $W = 10$ kg. The aerodynamic drag coefficient C_D or lift coefficient C_L can be calculated as

$$C_i = \frac{F_i}{\frac{1}{2}\rho V^2 A} \tag{1}$$

Here, F_i is either the drag force or lift force, A is the frontal area of the spoiler, ρ is the air density, and V the car velocity.

3   Results

An output of the CFD is shown in Fig. 2. For the spoiler without gap, the lowest lift coefficient and the lowest drag coefficient were recorded while at 0° angle of attack has. Moreover, for spoiler without gap between spoiler and wing, when at 40° angle of attack, also has the lowest lift coefficient and highest drag coefficient. To achieve these profiles, similar solutions shown by Shamsudin and Ismail as well as Myszka can be followed [5, 6]. Additionally, Table 1 shows that the downward force is larger without the gap by the C_L values. Consequently, the drag can be noticeably higher in the proposed no-gap design as well as evident in the C_D values.

(a) $\theta = 0°$

(b) $\theta = 20°$

(c) $\theta = 40°$

(d) Linkage Mechanism
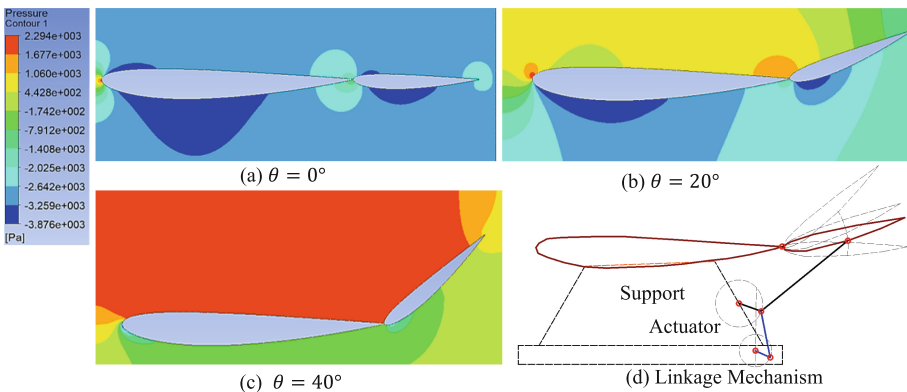
Fig. 2. A CFD of the spoiler at three angles of attack and its mechanism.

Table 1. Data summary of drag and lift coefficients.

Attack Angles	Spoiler without gap		NACA 2412 short with 10 mm gap [4]	
(°)	C_L	C_D	C_L	C_D
0	−0.025	0.01	-	-
20	−0.027	0.025	-	-
40	−1.2	0.18	−0.7133	0.1436

4 Conclusion and Suggestion

In conclusion, the spoiler without gap with 40° angle of attack achieved the highest downward force and is suitable when taking corners. Meanwhile, the spoiler without gap with 0° angle of attack have the lowest drag and it is suitable to use when in economic mode driving and also in high-performance driving. Spoiler with gap will have higher drag coefficient compared to the spoiler without gap for each angle of attack except for spoiler with 40° angle of attack. In the future, more angles of attack should be tested. The physical model of the shape-changing spoiler should be fabricated to test the reliability of its operation.

References

1. Hamut, H., El-Emam, R., Aydin, M., Dincer, I.: Effects of rear spoilers on ground vehicle aerodynamic drag. Int. J. Numer. Meth. Heat Fluid Flow **24**(3), 627–642 (2014)
2. Kumar, V., Narayan, K., Rao, L., Ram, Y.: Investigation of drag and lift forces over the profile of car with rear spoiler using CFD. Int. J. Adv. Sci. Res. **1**(8), 331–339 (2015)
3. Kurec, K., Remer, M., Meyer, T., Tudruj, S., Piechna, J.: Flow control for a car-mounted rear wing. Int. J. Mech. Sci. **152**, 384–399 (2019)
4. Azmi, A., Sapit, A., Mohammed, A., Razali, M., Sadikin, A., Nordin, N.: Study on airflow characteristics of rear wing of F1 car. IOP Conf. Ser. Mater. Sci. Eng. **243**, 012030 (2017)
5. Shamsudin, S., Ismail, M.: The applications of shape-changing rigid body mechanisms in arts and engineering. J. Adv. Manuf. Technol. **12**(2), 301–311 (2018)
6. Myszka, D.: Machines & Mechanisms: Applied Kinematic Analysis. 4th edn. Pearson, Upper Saddle River (2012)

Performance of Solar Assisted Dual Condenser Heat Pump Drying System

K. Sopian[✉], G. Y. Abusaibaa, R. Abdullah, H. Jarimi, A. Ibrahim, A. F. Abdullah, and A. B. Al-Aasam

Solar Energy Research Institute, Universiti Kebangsaan Malaysia, 43600 Selangor, Malaysia
ksopian@ukm.edu.my

Abstract. The solar-assisted heat pump system consists of an evacuated tube solar collector, compressor, dual condensers, fan coil, expansion valve, and evaporator. Two basic functions of the heat pump are to heat the dryer and dehumidify the air as well as recirculate it and the solar drying assisted by the heat pump will achieve high efficiencies. The effectiveness of the heat pump is denoted through its COP, described as the ratio of whole heat delivered by using the heat pump to the quantity of electrical energy needed in order to run the heat pump. With the addition of the dual condensers, the temperature of the dryer was 60 °C with a relative humidity of 70% and the COP of the system was 5.546 under the Malaysia climate conditions.

Keywords: Heat pump · Dryer · Dual condensers · Evacuated tubes · TRNSYS simulation

1 Introduction

The high consumption of natural fuel sources and the effect on environmental pollution has drawn the attention of energy researchers to the applications of solar-assisted heat pump systems (SA-HPS). Solar energy is one of the most significant renewable energy resources with high economic efficiency. The food products that were produced by agricultural and marine based products are the most consumer of green energy. Heat pump dryer systems have been reported as being economical, reducing energy consumption, and their ability to produce dried food with high quality and efficiency [1]. The SA-HPS systems are among the most important applications that reduce energy consumption while maintaining the high efficiency of the system, which enhances their widespread use. Table 1 summarizes and reviews the research that used SAHP dryers.

Research investigations were limited in SA-HPS dryers as more empirical research and simulations are required to improve system efficiency. This study presents a new design of a smart heat pump dryer with a dual condenser and assisted with solar evacuated tube collector system. It has the ability to increases the coefficient of performance (COP) of the SA-HPS with a high solar fraction.

Table 1. SAHP system uses for drying.

Ref	Work	COP
[2]	Investigated the outputs of an SPV-THP dryer for saffron processing	-
[3]	Used a hybrid photovoltaic thermal collector (PVT) to improve the heat pump air heating functionality. It also uses an environment-friendly refrigerant (R134a)	1.96 to 2.28
[4]	Examined The efficiency of a novel solar-powered dryer for drying mint leaves	5.0
[5]	Investigated The effectiveness of SA-HPS for industrial heating	3.54
[6]	Used A SA-HPS dryer to dry mushrooms	2.1 to 3.1
[7]	Used A SA-HPS dryer to dry radishes. In this configuration, heat pump coils are connected with a drying chamber	3.21 to 3.49
[8, 9]	The performance of the SA-HPS was examined experimentally. They claim that as compared to other existing systems, SA-HPS produces much greater product quality with an energy-efficient heat pump	5.19 to 6.25
[10, 11]	The performance of the SAHP dryer using R22 refrigerant was tested to dry coconut	2.31 to 2.77

2   Theoretical Model and Modelling

In this study, a Smart Heat Pump Dryer (SHPD) with a dual condenser and assisted solar Evacuated tube collector (ETC) system were analyzed. The SHPD system was modeled and simulated using TRNSYS and EES programs as shown in Figs. 1 and 2. The SHPD device in the present research work as seen in Fig. 1. In the SHPD system, a heat exchanger was attached to the ETC and the storage tank to the heat pump unit. The heat pump device consists of a Freon compressor, an evaporator coil, a double coil condenser, a fan for each coil, and an expansion valve. In the SHPD system, the solar collector supplies heat to the heat pump by means of the intermediate fluid (water) by exchanging heat
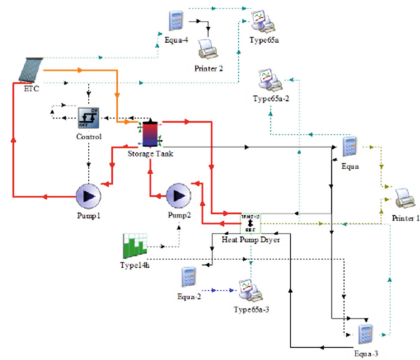
Fig. 1. TRNSYS model for Smart Heat Pump Dryer with a dual condenser and as-sisted solar Evacuated tube collector system.

between the water and the R-32 refrigerant through the heat exchanger. The R-32 refrigerant absorbs the added heat from the solar collector and then rejects this heat inside the first and second condensing coil. This heat, which was rejected by the condenser coil fan, heats the space within the dryer to the desired temperature. Then the R-32 refrigerant goes to the expansion valve and from there to the evaporator to complete its cycle.

The ETC had a south-facing orientation with a 15° inclination, and a 3.2 m² area. The maximum flow rate for ETC and SHPD was taken as 120 kg/h and 200 kg/h respectively. The storage tank capacity was taken as 0.3 m³.

A solar system was used to assist the heat pump. The useful energy gain Qu, and the efficiency η of the ETC portion of the solar system can be calculated [12, 13] as follows:
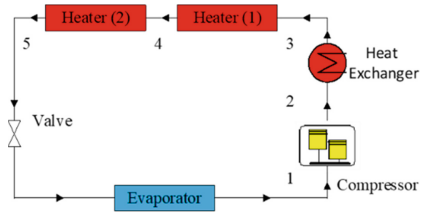
Fig. 2. EES The Thermodynamic system.

$$\eta = a_0 - a_1 \frac{(\Delta T)}{I_T} - a_2 \frac{(\Delta T)^2}{I_T} \tag{1}$$

$$Q_u = m_{dot} * C_p * (T_{out} - T_{in}) \tag{2}$$

a_o intercept (maximum) of the collector efficiency, a_1 Negative of the first-order coefficient in collector efficiency equation, a_2 Negative of the second-order coefficient in collector efficiency equation, I_T Global radiation incident on the solar collector on a tilted surface. The Coefficient of Performance COP and Solar fraction SF for space of dryer heating SHPD is defined as follows:

$$COP_{HP} = Q_{con}/W_{comp} \tag{3}$$

$$Q_{con} = m_{dot} * C_p * \Delta T \tag{4}$$

$$SF = Q_u/W_{comp} \tag{5}$$

3   Results and Observations

This system consists of SHPD and ETC, where ETC was used primarily to obtain hot water to provide the heat energy needed to operate the dryer and reducing the electrical consumption of the heat pump. In this system, the heat pump placed in the dryer will be activated at low solar radiation or at night.
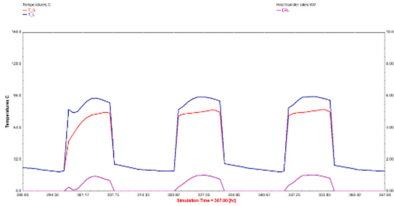
Fig. 3. Storage tank simulation.
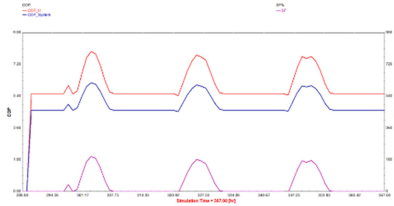
Fig. 4. Simulation CO_{PH}, COP_{system} and SF with Time.

The simulation is performed for three days (13, 14, 15) in the months of January, with a simulation time step of 1 h. Figure 3 shows the highest energy value provided by the storage tank from ETC to the SHPD, which is around 1.7 kW at 2.00 pm.

The highest value of SF is approximately 200% at 2 pm. Also, the highest and lowest values of COP_{hp} were around 7.9 at 2 pm and 5.5 at sunset, respectively, as well the highest and lowest values of COP_{system} were 6.18 at 2 pm and 4.62 at sunset, as shown in Fig. 4. Also, Fig. 5 shows the P-H diagram for the SHPD cycle in the absence of solar energy and Fig. 6 shows the P-H diagram for the SHPD cycle in case of solar energy availability. Furthermore, Fig. 7 shows the EES model for Smart-Heat Pump Dryer with a dual condenser and explains the air cycle in the dryer room with temperature and humidity throughout the drying process.
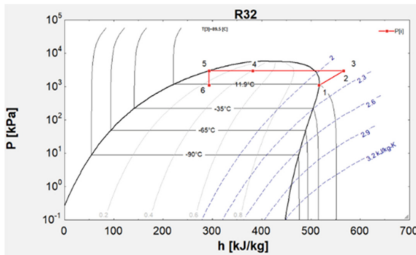
Fig. 5. P-h diagram without solar energy.
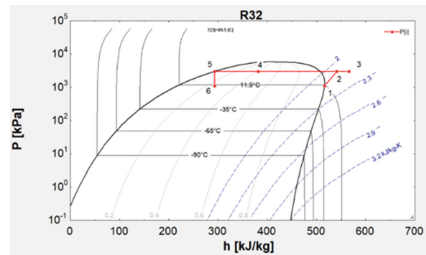
Fig. 6. P-h diagram with solar energy.
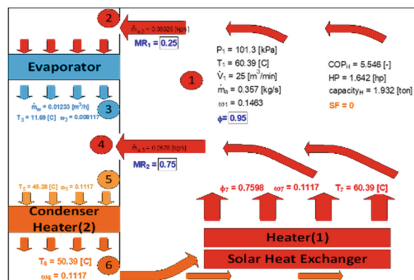
Fig. 7. EES model.

4 Conclusions

TRNSYS was used to simulate the solar SHPD system. The final optimal system consisted of a 3.2 m^2 ETC area and number ETC in series 22 tilted at 15° for Kuala Lumpur from the horizontal and a 0.5 m^3 of Hot water storage tank (HWST). Where the highest energy value provided by the storage tank from ETC to the SHPD, around 1.7 KW at 2.00 pm. The highest value of SF is approximately 200% at 2 pm. Also, the highest and lowest values of COP$_{hp}$ were around 7.9 at 2 pm and 5.5 at sunset, respectively, as well the highest and lowest values of the COP$_{system}$ were 6.18 at 2 pm and 4.62 at sunset respectively. It is certain that the reduction of electricity consumption that resulted from this system reduces the dependence on energy sources that increase global warming due to the harmful emissions that result from the environment. The results obtained from this research confirm the possibility of using SHPD in the Malaysian climate conditions, as well as providing an incentive for further research within the framework of SHPD.

References

1. Colak, N., Hepbasli, A.: A review of heat pump drying: Part 1–systems, models and studies. Energy Conv. Manag. **50**(9), 2180–2186 (2009)
2. Mortezapour, H., et al.: Saffron drying with a heat pump–assisted hybrid photovoltaic–thermal solar dryer. Drying Technol. **30**(6), 560–566 (2012)
3. Şevik, S.J.S.E.: Experimental investigation of a new design solar-heat pump dryer under the different climatic conditions and drying behavior of selected products. Sol. Energy **105**, 190–205 (2014)
4. Ceylan, İ., Gürel, A.E.: Solar-assisted fluidized bed dryer integrated with a heat pump for mint leaves. Appl. Thermal Eng. **106,** 899–905 (2016)
5. Suleman, F., Dincer, I., Agelin-Chaab, M.: Energy and exergy analyses of an integrated solar heat pump system. Appl. Thermal Eng. **73**(1), 559–566 (2014)
6. Şevik, S., et al.: Mushroom drying with solar assisted heat pump system. Energy Convers. Manage. **72**, 171–178 (2013)
7. Qiu, Y., et al.: Performance and operation mode analysis of a heat recovery and thermal storage solar-assisted heat pump drying system. Sol. Energy **137**, 225–235 (2016)
8. Li, Y., et al.: Experimental investigation on a solar assisted heat pump in-store drying system. Appl. Therm. Eng. **31**(10), 1718–1724 (2011)
9. Li, H., Dai, Y., Dai, J. et al.: A solar assisted heat pump drying system for grain in-store drying. Front. Energy Power Eng. China **4**, 386–391 (2010). https://doi.org/10.1007/s11708-010-0003-3
10. Mohanraj, M.: Performance of a solar-ambient hybrid source heat pump drier for copra drying under hot-humid weather conditions. Energy Sustain. Dev. **23**, 165–169 (2014)
11. Mohanraj, M., et al., Performance of a heat pump drier for copra drying. Proc. Inst. Mech. Eng. Part A J. Power Energy **222**(3), 283–287 (2008)
12. McIntire, W.R.: Factored approximations for biaxial incident angle modifiers. Solor Energy **29**(4), 315–322 (1982)
13. Theunissen, P.-H., Beckman, W.A.: Solar transmittance characteristics of evacuated tubular collectors with diffuse back reflectors. Solor Energy **35**(4), 311–320 (1985)

The Performance of Small-Scale Generator Set Using Alcohol Fuel

Ridwan, Suyitno[(⊠)], Albert Xaverius Ilyas, and Afif Faishal

Sebelas Maret University, Jl. Ir. Sutami 36A, 57563 Surakarta, Indonesia
suyitno@uns.ac.id

Abstract. Alcohol is a renewable energy source that may be used to power an internal combustion engine and generate electricity via a generator set. As a result, the goal of this research is to investigate at the performance of small-scale generator sets powered by alcohol. The fuel utilized was an alcohol combination of 86.52% methanol and 9.97% ethanol. The test findings revealed that the higher the engine rotation, the greater the engine power. The resultant power rose from 733 W to 2000 W, or by 2.7 times, when the motor rotated at 2100–2800 rpm. Specific fuel consumption drops dramatically and hits a minimum at around 2800 rpm.

Keywords: Biogas · Electric generation · Pressure · Specific fuel consumption

1 Introduction

Alternative fuels such as ethanol and methanol can be generated as a replacement for fossil fuels by the fermentation of sugar and water solutions. In reality, the price of ethanol is significantly higher than the price of methanol and slightly higher than the price of gasoline. The price of ethanol, methanol, gasoline, and diesel in the international market is 2.48 USD/gal, 0.107 USD/gal, 2.38 USD/gal, and 2.15 USD/gal, respectively. Because the price of ethanol is substantially greater than the price of methanol, a mixture of methanol and ethanol is employed to provide a competitive fuel price. However, fuel derived from this sort of methanol-ethanol combination is still understudied in terms of generator set performance.

Ethanol has a fairly high research octane number (RON), which is 106 to 110. Ethanol has a small cetane number (5–8), so it cannot be used as diesel motor fuel [1]. According to other studies [2], the motor octane number (MON) of ethanol, methanol, and gasoline is 90, 89, and 82–89, respectively. As a result, ethanol and methanol are appropriate for use as gasoline motor fuel or to enhance the octane and anti-knocking index (AKI) number of gasoline fuel. However, ethanol and methanol have half the calorific value of gasoline heat. The calorific value of ethanol is 27.2 MJ/kg, methanol is 19.9 MJ/kg, and gasoline is 42.5 MJ/kg. As a result, 1.6 times more alcohol fuel is required to produce the same energy production [3]. Meanwhile, as compared to ethanol, the use of methanol in the internal combustion system requires extra caution due to its aggressive behavior toward specific components in the combustion system, such as plastic and even metals [3]. As a result, the usage of alcohol fuel with a high methanol concentration should be investigated on a generator set.

2   Methods

The alcohol was obtained from a local market. The ethanol and methanol concentration in alcohol were determined using gas chromatography (GC). The alcohol was then delivered into the internal combustion engine (ICE) with spark ignition (SI), which was linked to the generator.

The SI-ICE has a 4 stroke, 1 cylinder, and a capacity of 160 cc. The compression ratio is approximately 8.5:1. The engine is outfitted with an automated voltage regulator (AVR), which ensures that the alternating current voltage (AC voltage) is 220 V at a frequency of 50 Hz. The generator's loads were acquired from electric lights. The quantity of alcohol entering the ICE was monitored with a fuel meter. The generated electric energy was then measured using a DL69-2047 digital multimeter.

The performance of an ICE is measured in terms of power and efficiency. The ICE generator system's efficiency is measured as the ratio of output power to fuel flow rate multiplied by the lower heating value of the fuel utilized as written in Eq. 1.

$$\eta = P/(\dot{m} \times LHV) \tag{1}$$

Specific fuel consumption (sfc) is the ratio of the amount of fuel consumed (kg) to the amount' of energy generated (kWh), or the ratio of the actual fuel flow rate to the power produced[4] as follows.

$$sfc = m/(P \times t) \tag{2}$$

3   Results and Discussion

Figure 1 shows a voltage (V) curve graph against retention time (minutes) while testing chemical levels with Gas Chromatography. Each peak in the graph represents the presence of one chemical in the sample. The compound's peak area must then be calculated in order to determine its v/v content. The peak area is then compared to the compound's external standard area, and a percentage represents the compound's v/v content relative to the sample. The monogram in Fig. 1 has two peaks at 5.469 and 6.317 min. Figure 1 depicts two peaks, indicating the presence of two chemicals in the sample. The first peak corresponds to methanol, whereas the second corresponds to ethanol. The magnitude of methanol content is 86.52% based on the size of the two peaks, ethanol content is 9.97%, and the remaining is water. The calorific value of alcohol may be estimated using this content to be 18.85 MJ/kg.

Figures 2 and 3 depict the connection between power, SFC, and efficiency with generator motor rotation. The higher the motor rotation, it looks, the greater the motor power. The resultant power rose from 733 W to 2000 W, or by 2.7 times, when the motor was rotated at 2100–2800 rpm. Power rises up at revolutions faster than 2800 rpm. This phenomena differs significantly from earlier research' findings of power increasing practically linearly with speed. The power boost is still noticeable at rotations above 2500 rpm.

The behavior shown with SFC differs from that seen with power. SFC reduces significantly when engine rotation increases from 2200 to 2800 rpm, peaking at 2800 rpm. The

SFC increases as the engine revolutions approach 3000 rpm. The gasoline motor with the lowest SFC has the lowest power-to-fuel ratio. At low speeds, the amount of alcohol fuel required is modest. The quicker the motor rotates, the more alcohol that enters the combustion chamber. Meanwhile, at 2100 rpm, the motor power output is substantially reduced, resulting in a high SFC. Similarly, with rotation speeds larger than 2800 rpm, the resultant motor power increases with ramps, as shown in Fig. 2, but the required SFC steadily increases, leading the SFC to climb as well.
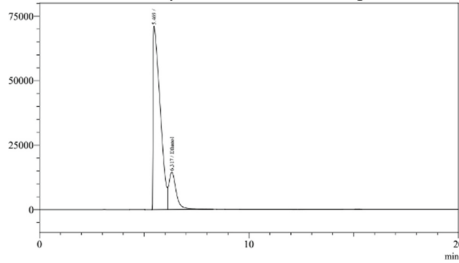
Fig. 1. Voltage curve (μV) against retention time (minutes) of alcohol sample.
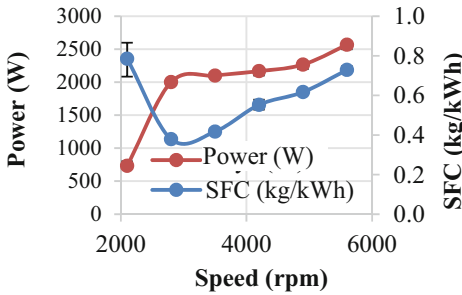
Fig. 2. The relationship between power and SFC with the speed of an alcohol-fueled generator set motor.
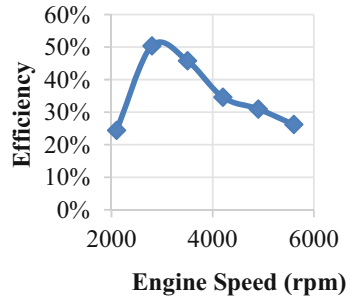
Fig. 3. The relationship between efficiency and the rotation of alcohol-fueled generator sets.

It is also worth mentioning that the best particular fuel economy occurs at 2800 rpm, with a gain of 0.379 kg/kWh at a load of 2000 W. The lowest SFC value in this test is 0.40 kg/kWh, which is somewhat higher than in previous study [5] when runs on ethanol fuel. The lowest SFC in this investigation was also better than the lowest SFC methanol-fueled engine with a compression ratio of 10 of 0.5912 kg/kWh [6].

Specific fuel consumption is inversely related to efficiency, with the value increasing with increasing load but decreasing at a particular point of load, and this also applies to increasing engine rotation. In the event of an unstable motor flame or engine rotation variations, the generator's motor cannot accomplish engine rotation below 2000 rpm. This occurs because at low rotation, the quality of the fuel-air combination is weak, resulting in inefficient combustion [5].

According to Fig. 3, the greatest efficiency of an alcohol-fueled generator set is 50.40% at 2800 rpm. This maximal efficiency number is greater than the 43% and 42%

values for methanol and ethanol-fueled engines, respectively. Methanol's flame speed is well known to be significantly faster than that of hydrocarbon fuels. This increased flame speed results in more perfect combustion, leading in a low SFC and a high efficiency [6]. Furthermore, because methanol has a high evaporation heat, it may absorb heat in the cylinder during the compression stage, increasing the machine's overall efficiency [6]. Because alcohol has a high evaporation heat, the efficiency of this alcohol-fueled generator set is likewise higher than that of gasoline.

4 Conclusions

Alcohol fuel, a combination of methanol and ethanol, has been successfully tested for power generation on a generator set. When utilizing alcohol, the maximum efficiency of generator sets was 50.40%. When alcohol is used, the specific fuel consumption is 0.38 kg/kWh. When utilizing alcohol, the maximum power is 2567 W.

References

1. Xing-cai, L., Jian-guang, Y., Wu-gao, Z., Zhen, H.: Effect of Cetane number improver on heat release rate and emissions of high-speed diesel engine fueled with ethanol–diesel blend fuel. Fuel **83**, 2013–2020 (2004). https://doi.org/10.1016/j.fuel.2004.05.003
2. Anderson, J.E., Kramer, U., Mueller, S.A., Wallington, T.J.: Octane numbers of ethanol− and methanol−gasoline blends estimated from molar concentrations. Energy Fuels. **24**, 6576–6585 (2010). https://doi.org/10.1021/ef101125c
3. Iliev, S.: A comparison of ethanol and methanol blending with gasoline using a 1-D engine model. Procedia Eng. **100**, 1013–1022 (2015)
4. Fagundez, J., Sari, R., Mayer, F., Martins, M., Salau, N.: Determination of optimal wet ethanol composition as a fuel in spark ignition engine. Appl. Therm. Eng. **112**, 317–325 (2017)
5. Duy, V.N., Duc, K.N., Cong, D.N., Xa, H.N., Le Anh, T.: Experimental study on improving performance and emission characteristics of used motorcycle fueled with ethanol by exhaust gas heating transfer system. Energy Sustain. Dev. **51**, 56–62 (2019). https://doi.org/10.1016/j.esd.2019.05.006
6. Çelik, M.B., Özdalyan, B., Alkan, F.: The use of pure methanol as fuel at high compression ratio in a single cylinder gasoline engine. Fuel **90**, 1591–1598 (2011). https://doi.org/10.1016/j.fuel.2010.10.035

Return of Investment for Small Scale Hydroponic System Powered by Off-Grid Photovoltaic

Mohd Afzanizam Mohd Rosli[1,2(✉)], Muhamad Fakhrul Akmar Fazli[1],
Suhaimi Misha[1,2], Muhammad Zaid Nawam[1], Noriffah Md Noh[1],
Siti Nur Dini Noordin Saleem[1], and NurFarhana Salimen[1]

[1] Fakulti Kejuruteraan Mekanikal, Universiti Teknikal Malaysia Melaka, Hang Tuah Jaya,
76100 Durian Tunggal, Melaka, Malaysia
{afzanizam,suhaimimisha}@utem.edu.my

[2] Centre for Advance Research on Energy, Universiti Teknikal Malaysia Melaka, Hang Tuah
Jaya, 76100 Durian Tunggal, Melaka, Malaysia

Abstract. Hydroponics is a recent method of agricultural production in which plants are grown in a soilless media. Various issues have been widely discussed in the hydroponic system, one of which is the hydroponic system's power supply. Typically, it is powered by conventional electrical energy and should be operated at all times. The objective of this project is to integrate a sustainable energy source into a small-scale hydroponic system and also evaluate the return on investment (ROI) from the installation of the Off-Grid Photovoltaic (OGPV) system. This system is comprised of a 25 W photovoltaic panel and 9 Ah batteries to provide energy storage for the DC water pump and monitoring system, which utilize around 53.64 Wh/day. The investment into the OGPV system can achieve the return in 2 years and 9 months via utility bill cost reduction.

Keywords: Hydroponic · Off-grid photovoltaic · Return on investment

1 Introduction

1.1 Hydroponic Farming

Hydroponic farming is the method of growing plants using a nutrient-enriched water source without soil [1]. Unlike the conventional farming technique that uses soil as a medium to grow the plant, hydroponic farming uses other materials such as rock wool, coconut fibre, and perlite as the growing medium. These media do not provide the plants with any nutrients, but they provide the plants with a place to anchor, much like soil. Most hydroponic systems use pumps to deliver the nutrient solution and oxygen to the root of plants. These systems need electricity to be run and a few of them need to be run 24 h a day which needs a lot of energy.

The main sources of electricity generation, such as oil, gas, and nuclear power, are now costlier than ever. In addition to the price, as the world's demands continue to

increase, the quantity of non-renewable resources is declining and beginning to run out. In addition, greenhouse gas emissions will increase due to the combustion of fossil fuels, and these gases can make global warming faster. Malaysia is ideal for solar renewable energy since it is located near the equator, receive a monthly solar irradiance of approximately 400 to 600 MJ/m^2 [2]. Thus, solar energy is the perfect renewable energy to power the pumps in order to supply the nutrient solution for a hydroponic system. The high initial costs and the return on investment (ROI) of the system are some of the main challenges in building the hydroponic system. The initial expenses to build the proper hydroponic system are very costly due to the components involved in the system such as water pump, oxygen pump, growing tray, nutrient container, and irrigation system. Moreover, the cost of this system will increase with the addition of the operational cost which is the electricity and maintaining cost. In the future, the cost of electricity will increase gradually due to the increase of the electricity tariff.

2 Methodology

2.1 Geographical and Irradiance

The development of the solar-powered hydroponic system was conducted at Applied Solar Energy Laboratory (ASEL) located at Technology Campus, Universiti Teknikal Malaysia Melaka (UTeM), (2°16′45″N 102°16′27″E), Ayer Keroh Melaka. Solar radiation is very important to design and develop the OGPV system. Figure 1 illustrates the solar irradiance data for 12 months in Melaka. Based on the measurement, Melaka receives an average daily solar irradiance of about 4.947 kWh/m^2/day. Based on the data, the configuration of the OGPV system can be determined and by that means the return on investment (ROI) can be calculated using Eq. 1.

$$\text{Return on Investment} = \frac{\text{Initial Investment of OGPV system}}{\text{Saving from the reduction of electrical utility cost}} \quad (1)$$

2.2 Solar Powered Hydroponic System

The classification of the design can be seen in the block diagram illustrated in Fig. 2. It includes three main blocks, the solar photovoltaic (PV) system, the hydroponic system, and the monitoring system. The PV solar system consists of PV solar panel, a solar charger, a battery, and a timer. The PV solar system functions as the main power supply to the hydroponic system while the battery acts as a backup when the PV solar is unable to supply electricity to the DC water pump and monitoring system. On the other hand, the hydroponic system consists of a DC water pump and an irrigation system. The third block is the monitoring system used to monitor the pH and electrical conductivity (EC) of the nutrient solution. The monitoring system is important in the hydroponic system to constantly monitor the fluctuation of pH and EC level which if the level is out of optimum range, can cause the unhealthy growth of plants [4].
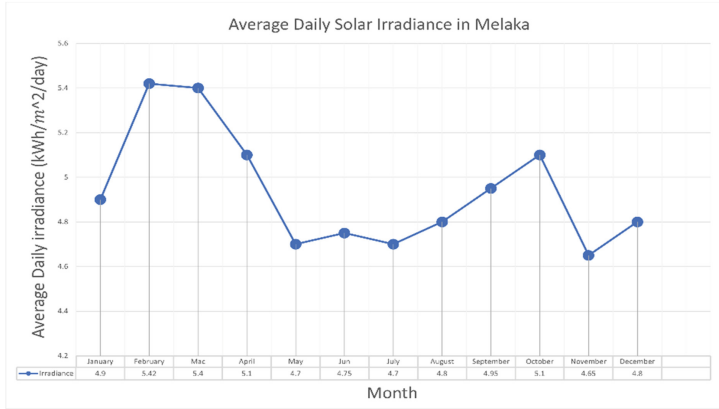
Fig. 1. Average daily solar irradiance at Melaka [3].
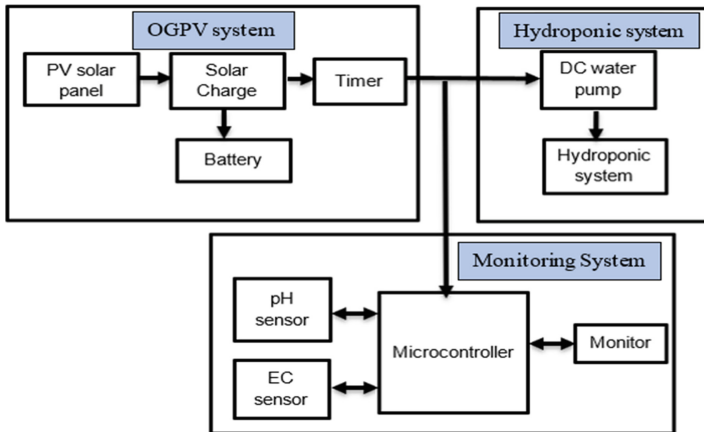
Fig. 2. Block diagram for hydroponic system.

2.3 Off-Grid PV (OGPV) Configuration

This off-grid photovoltaic (OGPV) system consists of PV solar panel, solar charge controller, lead-acid battery, timer and DC load which is a DC water pump and monitoring system. The schematic diagram of the system design is illustrated in Fig. 3. The power source was connected to the solar charge controller to regulate the current from the PV solar panel to the lead-acid battery. This is very important to prevent overcharging the battery that can cause harm to the battery. The lead-acid battery played an important role in this system since it stores and supplied the energy to the DC water pump and monitoring system. The DC water pump will operate for 9 hours per day and the monitoring system will operate for 24 hours per day as shown in Table 1.

The total power consumption of the hydroponic system is 53.64 Wh/day. The sizing of the PV solar system had been carried out and specification for all the component of the PV solar system is shown in Table 2. As a result of the sizing analysis, the 25W

PV solar panel will be utilized to deliver power to the load during daylight hours while simultaneously charging the batteries to their full capacity. Based on the load, the battery needs to produce about 8.94 Ah with the consideration of 2 days of autonomy to support the DC water pump and monitoring system. The day of autonomy is required to support the system while the battery needs to meet the load demand without any solar energy input. The OGPV system estimated can be generated about 448.16 Wh/day based on the solar irradiance at Melaka.
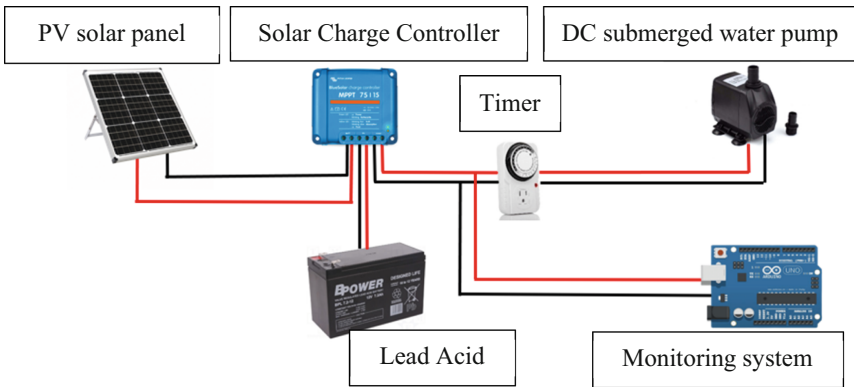
Fig. 3. The schematic diagram of the PV solar system.

Table 1. The total system loads.

Load	Rating	Operating time	Consumption
Submerged water pump	5 W	9 h	45 Wh/day
Monitoring system	0.36 W	24 h	8.64 Wh/day
Total daily power consumption			53.64 Wh/day

Table 2. OGPV component specification.

No	Components	Specification	Value/Type
1	Photovoltaic module	Max power (Pmax) Max power voltage (Vmp) Max power current (Imp) Open-circuit voltage (Voc) Short-circuit current (Isc)	25 Wp 18 V 1.37 A 22.2 V 1.45 A
2	Battery	Type Nominal voltage Capacity	Lead Acid 12 V 4.5 Ah
3	Solar charge controller	Charging current Float charge	10 A 13.7 V

3   Result and Discussion

3.1   Development of OGPV Hydroponic System

For the hydroponic system, the flood and drain irrigation types was be implemented to the system. The hydroponic system operates 9 hours per day which submerged water pump will pump the nutrient solution to the hydroponic system. The monitoring system is located beside the nutrient solution tank and will operate for 24 h to monitor the pH and EC value of the solution over time. Those systems are powered by the 25 W OGPV system that is integrated into a single module with a hydroponic system and monitoring system as illustrated in Fig. 4. The battery and solar charge controller for the OGPV system is placed in the electrical box to ensure that those items are protected from water ingress by rain or water leaking.

3.2   Return on Investment (ROI)

The installation cost of a system is important while designing and developing a system. Table 3 shows the list of prices for each component of the PV solar system. The total for the installation of the off-grid PV system is RM 98. The total cost includes the maintenance cost for the system that is required 2 times every year.

Utilizing the OGPV system as a power source to the hydroponic system besides the use of grid connection can help reduce the utility bill cost. The return on investment (ROI) is the time required to recoup the cost of the installation system. According to the Malaysian Electricity Tariff, the first 200 kW of power will be charged at a rate of 21.8 cents/kWh. The return on investment will be 2 years 9 months for the installation of an off-grid solar-powered system. After that period, RM35.65 per year can be saved in the electrical bill and the user will receive a return on their investment and will continue to receive free electrical power generated by the OGPV system.
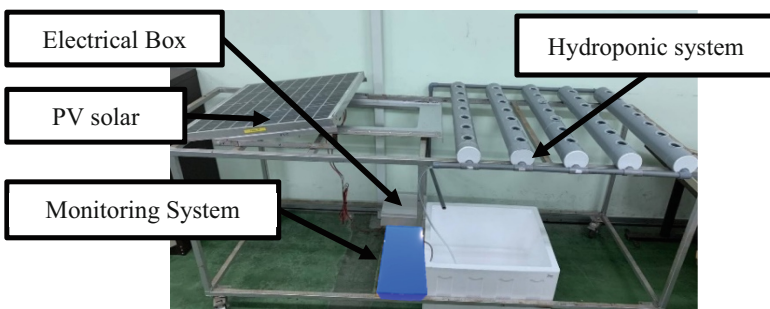
Fig. 4. The OGPV hydroponic system.

Table 3. Off-grid PV system items cost.

No	Items	Quantity	Prices (RM)
1	50 W PV solar panel	1	40.00
2	Solar charge controller	1	13.00
3	Lead acid battery	2	30.00
4	Maintenance (½ years)		15.00
Total			98.00

4   Conclusion

The development of an off-grid PV system for the hydroponic is to supply the energy to the DC water pump and the monitoring system of the hydroponic. The total cost for the development of the OGPV system is RM 98. Also, the installation of the OGPV system can generate an annual saving of RM35.65 by reduction of utility bills and the return on investment can be achieved in 2 years and 9 months.

References

1. Bumgarner, N.: An Introduction to small-scale soilless and hydroponic vegetable production. An introduction to small-scale soilless and hydroponic vegetable production, pp. 1–2 (2019)
2. Shivashankar, S., Mekhilef, S., Mokhlis, H., Karimi, M.: Mitigating methods of power fluctuation of photovoltaic (PV) sources – a review. Renew. Sustain. Energy Rev. **59**, 1170–1184 (2016)
3. Ranjit, S.S.S., Tan, C.F., Subramaniam, S.K.: Implementation off-grid solar-powered technology to electrify existing bus stops. In: 2011 Second International Conference on Intelligent Systems, Modelling and Simulation, pp. 231–234. IEEE, January 2011
4. Kulkarni, B.P., Sambhaji, M.A., Venkatesh, P.S., Rajiv, Y.P.: Automation of hydroponic system. Int. J. Sci. Technol. Eng. (IJSTE) **3**, 600–602 (2017)

Performance Evaluation of Vehicle Braking System Employing an Electronic Wedge Brake Mechanism

Sharil Izwan Haris[1,2]([✉]), Mohd Hanif Che Hassan[3], Fauzi Ahmad[1], and Ahmad Kamal Mat Yamin[1]

[1] Fakulti Kejuruteraan Mekanikal, Universiti Teknikal Malaysia Melaka, Hang Tuah Jaya, 76100 Melaka, Malaysia
sharil_izwan@yahoo.com

[2] MARA High Skills College of Masjid Tanah, Km 1, Persiaran Paya Lebar, Ramuan China Besar, 78 300 Masjid Tanah, Melaka, Malaysia

[3] Fakulti Teknologi Kejuruteraan Elektrik & Elektronik, Universiti Teknikal Malaysia Melaka, Hang Tuah Jaya, 76100 Melaka, Malaysia

Abstract. This article describes the performance evaluation of an electronic wedge brake (EWB) in a vehicle braking system. Simulation and experimental research were utilized as assessment methodologies. The vehicle braking system was simulated utilizing a verified quarter vehicle traction model with a validated EWB model as the brake actuator. To investigate the efficacy of the EWB, a dynamic test, meaning sudden braking at constant speeds of 40 and 60 km/h, was employed, and the results of simulation and experiment were compared and evaluated. Several aspects of the vehicle's performance are examined, including its vehicle speed, wheel speed, longitudinal slide, and stopping distance. The study's findings indicate that the proposed EWB braking system may provide excellent performance and be recommended for usage in actual automobile brake systems.

Keywords: Electronic wedge brake · Vehicle braking · Dynamic test

1 Introduction

Brake by wire (BBW) is a revolution in braking systems that changes from mechanical to electrical control in order to enhance the active safety system of the vehicle such as EHB, EPB, and EMB. Later, the BBW system was enhanced by using a 12 V power supply to offer high torque brakes and faster response which resulted in the expansion of the latest braking system known as EWB [1]. This study uncovered the basic design of a contemporary EWB brake system as a possible braking solution. The new floating caliper brake type, called the EWB, is basically a redesigned version of the traditional hydraulic brake. The EWB model with the PI torque tracking controller was correlated to the validated quarter car vehicle traction model for the assessment of braking performance, and the output of the vehicle braking system was tested both in simulation and experimentally. The vehicle's dynamic performance is evaluated by tyre longitudinal slip, vehicle speed, wheel speed, and stopping distance.

2   The Electronic Wedge Brake

Figure 1 depicts the EWB system's actuator and heart brake. A DC motor drives EWB, which is connected to the heart braking mechanism via a lead screw. The lead screw converts angular motion of the DC motor to axial motion of the braking wedge.
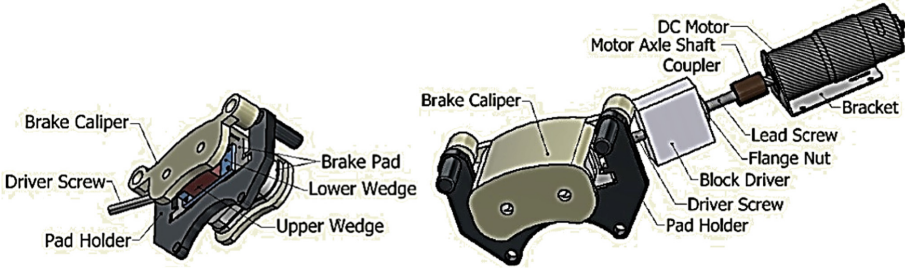
Fig. 1. EWB design.

The entire EWB architecture structure can be modelled mathematically using a fifth-order linear state space form, as shown below, where X_w as the wedge movement, V_w as the wedge velocity, θ_m as the motor angle, ω_m as the angular velocity and the I_m as motor current and F_c is the clamping force. Noted that of the EWB model can be depicted in [2].

$$\begin{cases} \dot{X} = Ax + Bu \\ y = Cx + Du \end{cases}$$

$$x = [X_w, V_w, \theta_m, \omega_m, I_m]^T, y = F_c$$

$$A = \begin{bmatrix} 0 & 1 & 0 & 0 & 0 \\ \frac{-K_a-a_1a_4^2}{a_2a_4^2} & \frac{-D_a}{a_2a_4^2} & \frac{K_aa_3}{a_2a_4} & \frac{D_aa_3}{a_2a_4} & 0 \\ 0 & 0 & 0 & 1 & 0 \\ \frac{K_aa_3}{\eta J_m a_4} & \frac{D_aa_3}{\eta J_m a_4} & \frac{-K_aa_3^2}{\eta J_m} & \frac{-D_m}{J_m} - \frac{D_aa_3^2}{\eta J_m} & \frac{K_t}{J_m} \\ 0 & 0 & 0 & \frac{-K_e}{L_m} & \frac{-R_m}{L_m} \end{bmatrix}, B = \begin{bmatrix} 0 \\ 0 \\ 0 \\ 0 \\ \frac{1}{L_m} \end{bmatrix} \quad (1)$$

$$\text{and } C = \begin{bmatrix} K_{cal}\tan(\alpha) \\ 0 \\ 0 \\ 0 \\ 0 \end{bmatrix}^T$$

where;

$$a_1 = K_{cal} tan\alpha (tan\alpha - \mu)$$

$$a_2 = M_w \left(tan^2 \alpha + 1 \right)$$

$$a_3 = \frac{N_a L_a}{2\pi}$$

$$a_4 = cos \beta,$$

$$\beta = \begin{cases} 0, & \textit{for normal actuation EWB} \\ \alpha, & \textit{for optimized acuation EWB} \end{cases}$$

Figure 2 depicts a PI-based brake torque control scheme for the EWB. The control parameters are $P = 1.3333 \times 10^3$ and $I = 55.77$.
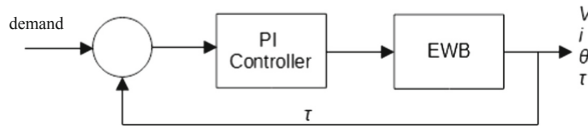
Info: V = voltage; i = current; θ = motor shaft position; τ = torque

Fig. 2. Brake torque tracking controller.

3 The Vehicle Model

Figure 3 show the vehicle model utilized in this research which is the two-DOF quarter vehicle traction model. In this figure, m is the quarter vehicle mass, v is the vehicle velocity, F_x is the tyre longitudinal force, τ_w is the wheel torque, τ_B is the braking torque, F_z is the normal force, and ω is the wheel angular velocity. The mathematical model derivation and modelling assumption is depicted in [3].
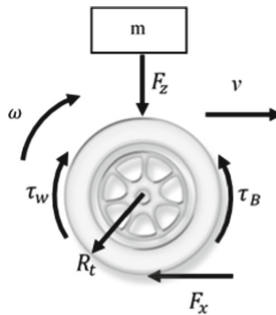
Fig. 3. Quarter vehicle traction model.

4   EWB Performance Results

Figure 4(a) and (b) illustrate the EWB model's braking performance at 40 and 60 km/h, respectively, which includes the vehicle's speed, wheel speeds, slip, and stopping distance. The experimental and simulated results show a similar trend. However, the findings showed some discrepancies, with the experiment responses being slower than the simulation data. This slow response is caused by internal frictions inside the hardware system, most notably between wedge contact surfaces and the inertia of the DC motor's internal component. According to [4], the most critical property of a control-oriented model is its trend. As long as the model responses follow a pattern that is nearly comparable to the measured responses with an acceptable degree of variances and errors, the findings may be agreed upon. As a result, the EWB's performance may be described as satisfactory.
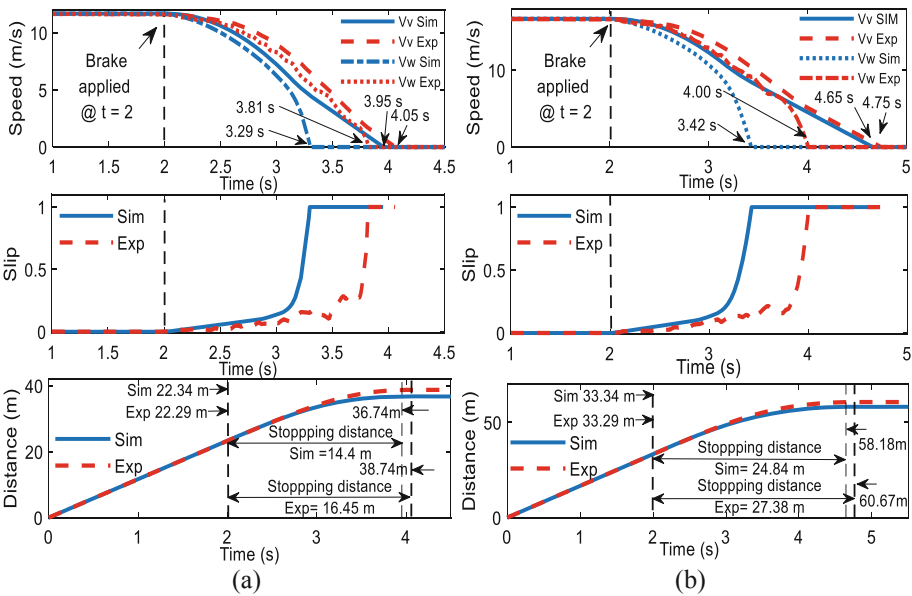
Fig. 4. Braking performance of EWB.

5   Conclusion

This study evaluated the performance of EWB in vehicle braking system. A dynamic test, particularly the abrupt brake test, was performed at constant speeds of 40 and 60 km/h. The evaluation was on the vehicle and wheel speed, tire longitudinal slip, and vehicle travel distance. The EWB actuator offers a system with outstanding responsiveness, performance, and stability. Besides that, the experimental results matched the modelling results with slight time differences. The delay in time reactions is caused by the mechanical system's friction, which was disregarded in the simulation. Overall, the proposed EWB is reliable enough to be used as the vehicle's braking system.

References

1. Che Hasan, M.H., Hassan, M.K., Ahmad, F., Marhaban, M.H.: Modelling and design of optimized electronic wedge brake. In: 2019 IEEE International Conference on Automatic Control and Intelligent Systems, I2CACIS 2019, pp. 189–193, June 2019
2. Che Hasan, M.H., Hassan, M.K., Ahmad, F., Marhaban, M.H., Haris, S.I.: A dynamic model of electronic wedge brake: experimental, control and optimization. Indones. J. Electr. Eng. Comput. Sci. **23**(2), 740–751 (2021)
3. Haris, S.I.: Modelling and validation of quarter vehicle traction model. NSA Conf. Ser. Indust. Revol. 4.0 **1**(01), 65–73 (2020)
4. Hudha, K.: Non-parametric modelling and modified hybrid skyhook Groundhook control of magnetorheological dampers for automotive suspension system. Universiti Teknologi Malaysia (2005)

Development of UTeM United Future Fuel Design Training Center Under Erasmus+ United Program

Noreffendy Tamaldin[1(✉)] , Muhd Ridzuan Mansor[1], Ahmad Kamal Mat Yamin[1],
Mohd Fadzli Bin Abdollah[1] , Thomas Esch[2], Andrea Tonoli[3],
Karl Heinz Reisinger[4], Hanna Sprenger[4], and Hisham Razuli[5]

[1] Automotive Department, Fakulti Kejuruteraan Mekanikal, Universiti Teknikal Malaysia
Melaka, Hang Tuah Jaya, 76100 Durian Tunggal, Melaka, Malaysia
noreffendy@utem.edu.my

[2] Faculty of Aerospace Engineering, FH Aachen, Hohenstaufenallee 6, 52064 Aachen, Germany

[3] Department of Mechanics and Aerospace Engineering, Turin Polytechnic University,
Corso Duca degli Abruzzi, 24-10129 Turin, Italy

[4] Institute of Automotive Engineering, FH Joanneum Gesellschaft mbH, Alte Poststraße 149,
8020 Graz, Austria

[5] Research & Development Centre (HQ), Dreamedge Sdn Bhd, C-16-01, Level 16, iTech Tower,
Jalan Impact, Cyber 6, 63000 Cyberjaya, Selangor, Malaysia

Abstract. The industrial revolution IR4.0 era have driven many states of the art technologies to be introduced especially in the automotive industry. The rapid development of automotive industries in Europe have created wide industry gap between European Union (EU) and developing countries such as in South-East Asia (SEA). Indulging this situation, FH Joanneum, Austria together with European partners from FH Aachen, Germany and Politecnico Di Torino, Italy is taking initiative to close the gap utilizing the Erasmus+ United grant from EU. A consortium was founded to engage with automotive technology transfer using the European framework to Malaysian, Indonesian and Thailand Higher Education Institutions (HEI) as well as automotive industries. This could be achieved by establishing Engineering Knowledge Transfer Unit (EKTU) in respective SEA institutions guided by the industry partners in their respective countries. This EKTU could offer updated, innovative, and high-quality training courses to increase graduate's employability in higher education institutions and strengthen relations between HEI and the wider economic and social environment by addressing University-industry cooperation which is the regional priority for Asia. It is expected that, the Capacity Building Initiative would improve the quality of higher education and enhancing its relevance for the labor market and society in the SEA partners. The outcome of this project would greatly benefit the partners in strong and complementary partnership targeting the automotive industry and enhanced larger scale international cooperation between the European and SEA partners. It would also prepare the SEA HEI in sustainable partnership with Automotive industry in the region as a mean of income generation in the future.

Keywords: Malaysian automotive industry · UTeM Engineering Knowledge Transfer Unit · Technology transfer · Erasmus+ United

1 Introduction

The industrial revolution IR4.0 era have triggered many states of the art technologies to be integrated in the manufacturing sector and various industries. The higher education sector also been hugely impacted by these aggressive moves to meet the demand for futuristic workforce market. As the main players of training for future graduates to fulfill the industrial requirements, the Universities have work with their global network to ensure the graduates produce remains relevant and workforce ready urgently. As part of the continuous effort by the European (EU) Countries to share their expertise to the Southeast Asian (SEA) partners, the Erasmus+ Capacity building in Higher Education grant was introduced with the aim to enhance business cooperation between the Universities in the EU and SEA together with their respective industries in the region.

1.1 Erasmus+ Automotive United Program Background

The Erasmus+ Automotive United have been approved among the top 10% of the proposal received for funding from all over the world. This project was initiated by FH Joanneum, in Graz Austria together with the top automotive institutions in the European Countries such as FH Aachen, in Germany and PT Di Torino in Italy. The SEA partners identified are Malaysia, Indonesia, and Thailand. The selection of these SEA partners is because they represent the largest automotive industries (considering the rise in number of units produced) in the Southeast Asian region and are highly important for global car production. However, little is being done to ensure technical advancement through research and development (R&D). Considering the outlook and current industry figures, more engineers are needed.

The initial funding of this project takes 3 years from Jan 2019 to Jan 2022, however subject to project extension. The approved budget was approximately EU980 000 distributed to all 9 universities (3 in EU and 6 in SEA) as well as 2 automotive industries from each SEA country. Currently, most OEMs with subsidiaries in Malaysia, Indonesia, and Thailand employ engineering staff from overseas to fill existing knowledge gaps, which is further evidence of the lack of qualified human capacities at a local level. All partners from Malaysia, Indonesia, and Thailand face a challenge which inhibits them from further growth in the automotive industry: the lack of highly educated engineers focusing on automotive development. Table 1 gives a summary of all participating partners in the project.

2 Objectives

The aim of this Erasmus+ United Automotive project, addresses the current lack of skilled labor in automotive engineering while drive towards increasing the positive impact of the automotive industry on regional development and internationalization.

3 Methodology

The methodology deployed to achieve the objectives of this project aligned with the EU framework for internalization and business cooperation as stated in the EACEA

Table 1. List of all 11 participating partners from EU and SEA.

Countries	Institutions	Categories
Austria	FH Joanneum	EU/coordinator
Germany	FH Aachen	EU partner
Italy	Politecnico Di Torino	EU partner
Malaysia	University Putra Malaysia, UPM	Research University
Malaysia	Universiti Teknikal Malaysia Melaka, UTeM	Technical University
Malaysia	Dreamedge Sdn Bhd	Malaysian Automotive partner
Indonesia	Universitas Sumatera Utara, USU	Research University
Indonesia	Udayana University, UNUD	Comprehensive University
Thailand	Chulalongkorn University, CKU	Research University
Thailand	Mahasarakham University, MSU	Comprehensive University
Thailand	Atipong Motors	Thailand Automotive Partner

guidelines. To addresses the lack of skilled labor in automotive engineering and making impact to the regional development of automotive industry, various strategic initiatives in three stages. Stage one involved Capacity building by means of expert training at the partner HEIs in Indonesia, Malaysia and Thailand for academic staff, students and companies interested in automotive engineering. The stage two involved setting up and operation of Engineering Knowledge Transfer Units (EKTUs) at the partner HEIs in Indonesia, Malaysia, and Thailand to increase awareness of and expertise in mechanical and automotive engineering (AE) by offering workshops to the target groups. Finally, stage three fostering university-business cooperation via the EKTUs, focusing on current trends in automotive engineering and building up the UNITED network for international exchange on the topic of AE. This will lead to increased knowledge on AE, higher standards in teaching and higher employability of graduates in the partner countries.

4   Results and Discussion

Based on the SEA gap analysis performed, it was observed that, Malaysia needs for expert in hybrid automotive and fuel management system while Indonesia focusses on Electric, Hybrid and Fuel cell vehicle. Thailand, on the other hand will focus on Hybrid power train and simulation. Therefore, the EKTU develop in all SEA countries will be focus on the key focus area identified in the gap analysis and prevent duplications. UTeM EKTU established have been focusing on fuel management trainers which is the key for hybrid fuel saving strategies. The UTeM EKTU is named as UTeM Future Fuel Training Center and as shown in Fig. 2.

Fig. 2. UTeM future fuel training center equipped with fuel management system.

5   Conclusion

The UTeM EKTU have been successfully established and the official launching have taken place in May 2021 despite of the constraint with Covid19 situation in Malaysia. The operation of UTeM EKTU continue using asynchronous and synchronous mode.

Disclaimer. This project has been funded with support from the European Commission. This publication reflects the views only of the author, and the Commission cannot be held responsible for any use which may be made of the information contained therein.

References

1. Abidin, S.Z., et al.: The challenges of developing a validation protocol for the new curriculum of making 4.0: between Malaysian and European education systems. Int. J. Innov. Creat. Change **14**(5), 767–786 (2020)
2. Mansouri, S., Ouzizi, L., Aoura, Y., Douimi, M.: Production planning and its impact on quality in the automotive industry. In: Advances in Integrated Design and Production. CPI 2019. LNME. Springer, Cham (2021). https://doi.org/10.1007/978-3-030-62199-5_23
3. Jusufi, G., Ajdarpasic, S.: The impact of EU programmes on financing higher education Institutions in Western Balkans-Evidence from Kosovo. LeXonomica **12**(1), 107–128 (2020)
4. Kilic-Bebek, E., et al.: Discussing modernizing engineering education through the erasmus+ Project Titled. In: International Instructional Technologies in Engineering Education Symposium, Location: Ege University, Izmir, Turkey (2020)

5. Macher, G., Veledar, O.: Balancing exploration and exploitation through open innovation in the automotive domain – focus on SMEs. In: Yilmaz, M., Clarke, P., Messnarz, R., Reiner, M. (eds.) EuroSPI 2021. CCIS, vol. 1442, pp. 336–348. Springer, Cham (2021). https://doi.org/10.1007/978-3-030-85521-5_22

6. Mathiyazhagan, K., Mani, V., Mathivathanan, D., Rajak, S.: Evaluation of antecedents to social sustainability practices in multi-tier Indian automotive manufacturing firms. Int. J. Prod. Res.1–22 (2021)

7. Matt, D.T., Rauch, E., Riedl, M.: Knowledge transfer and introduction of industry 4.0 in SMEs: a five-step methodology to introduce industry 4.0. In: Research Anthology on Cross-Industry Challenges of Industry 4.0, pp. 275–302. IGI Global (2021)

8. Rauch, E., De Marchi, M., Jitngernmadan, P., Martin, F.M.: A descriptive analysis for education and training on automation 4.0 in Thailand. In: Proceedings of the 11th Annual International Conference on Industrial Engineering and Operations Management Singapore, 7–11 March 2021

Experimental Study Influences End Length of Blades with Additional Deflector on Savonius Water Turbine Performance

Ilham Bagus Pratama, Syamsul Hadi[✉],
and Dominicus Danardono Dwi Prija Tjahjana

Mechanical Engineering Department, Faculty of Engineering, Universitas Sebelas Maret,
Jl. Ir. Sutami 36A, Surakarta 57126, Indonesia
syamsulhadi@ft.uns.ac.id

Abstract. Savonius turbine is a type of drag turbine which has a simple construction design and good starting torque. However, this turbine still has low efficiency. This research was conducted to determine the effect of adding end-length of blades on the performance of the Savonius water turbine. The research uses the vertical fall fluid method with 3 discharge conditions at each addition of a deflector variation that is used to direct the focus of the fluid flow, so as to increase the torque working moment. Savonius water turbine performance is analyzed through Power Output. There are 4 variations of the Savonius turbine which were tested experimentally, namely the ratio value of l and r = 0; 0.2; 0.3; and 0.4. The maximum electric power is achieved with a variation of l/r 0.2 at a 20° deflector with a value of 11.51 W on water discharge of 1621.62 lpm.

Keywords: Savonius water turbine · End length of blade · Electric power

1 Introduction

Energy is an important factor in human life. In Indonesia, the use of electrical energy in 2018 sourced from fossils (non-renewable) still dominate [1]. One of the efforts made by the government to increase renewable energy is the Green Building (GB) program. The purpose of this program is reuse existing resources in a building construction as provider of the building's energy needs [2]. One of the resources that can be reused is building waste water discharged through a pipe system can be used as a hydroelectric power plant which is included in the pico/nano category. Hydrokinetic turbines is proper generator system that use water as a source of kinetic energy at low speeds are considered appropriate to be applied [3]. The Savonius turbine is a type of hydrokinetic turbine. The fundamental shape of this turbine is the S-type, which has two blades and a half circle and having a small overlap [4]. Savonius turbine has a low manufacturing cost, simple construction and can receive fluid from all directions and has a good starting torque but still have a poor efficiency [5].

Research on savonius turbine has been carried out using simulation and experimen methods. Sharma [6], had compared between Savonius turbines using wind and water fluids, the results obtained show that the performance of water fluid increases by 61.32%.

Prasetyo [8], had added deflectors with variations in angles of 0°, 20°, 30°, 40°, and 50° with a deflector ratio of 50%, the result is deflector of 30° has the best performance and can increase the power output of around 85%. Hindasageri [9], had researched on the effect of the number of blades,The results obtained from the study stated that at a depth of 50 mm with 5 Savonius turbine blades experience a higher rotational speed of the blades 3 and 4 blade.

Soo [10], had improved performance with the addition endplate turbines, the results using circular endplate (ER = 1) has the best performance. Sanditya [11], had compared the angle of curvature of the blade of 110°, 120°, 130°, and 140° where the results the angle of curvature of the blade 120° had the best performance. Altan [12], had modified turbine Savonius conventionally by adding end-length of blade and the results stated that with such modifications can increase coefficient maximum power of 20% of the conventional Savonius turbine.

Referring to the literature that has been studied, it is interesting to modify the Savonius water turbine in this study to obtain the most optimal performance and utilizing the use of a deflector which also has a significant effect on the Savonius turbine, so this study aims to determine the effect of end-length of blade with the addition of a deflector on the performance of the Savonius water turbine.

2   Methodology

The method used in this research is the experimental method. This research was conducted using 3 variations of water flow discharge at each variation of the deflector in the test of each variation of the turbine. With discharges ranging from 611.2 lpm, 1025.6 lpm, and 1643.8 lpm at 20° deflector and 460 lpm; 710,05 lpm; and 1299.63 lpm at 30° deflector which is regulated by varying the valve opening on the output pipe and at a constant head of 2.5 m.

The Savonius water turbine in this study has a semi-circular blade shape and using variation of l/r on the turbine, turbine design plan by comparing the ratio l/r with r = 23.67 mm to get 4 value of end length of blade with each value of 0; 4.73; 6.75; and 9.47 mm. The comparison can be seen in Fig. 1.
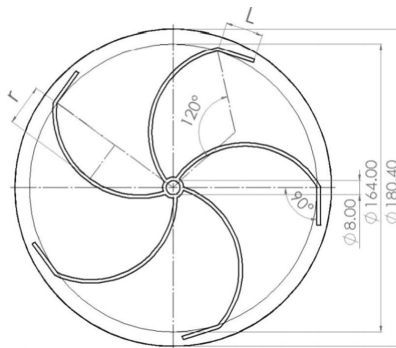
Fig. 1. Savonius turbine modified l/r design schematic.

3   Result and Discussion

The electrical power is the electrical power generated from the rotation of the generator which is connected to the turbine shaft. The electrical power is strongly influenced by the flow of incoming fluid in the form of water based on two variations of the deflector used, namely 20° and 30°. In the use of a 20° deflector the highest electrical power that can be measured is the Savonius turbine with a variation of l/r 0.2 with a value obtained of 11.51 W at a discharge of 1621.62 lpm as shown in Fig. 2. While the use of a 30° deflector the electrical power that is measured is the 0.3 l/r variation turbine with a value of 10.685 W at a discharge of 1299.63 lpm as shown in Fig. 3.
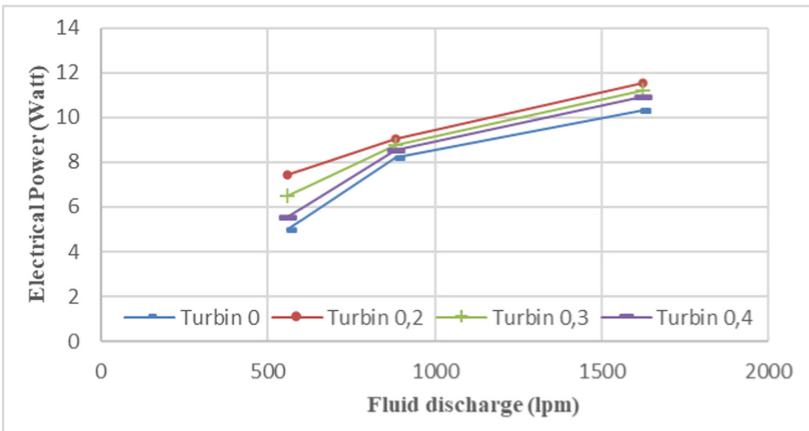
Fig. 2. Graph of the relation electrical power and fluid discharge at 20° deflector.
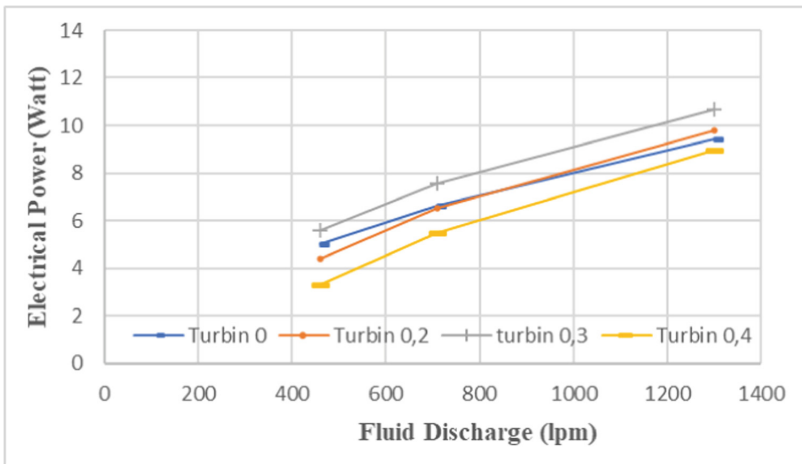
Fig. 3. Graph of the relation electrical power and fluid discharge at 30° deflector.

4 Conclusion

Based on the research data and data analysis that has been carried out, can be conclude that in the use of a 20° deflector, the Savonius turbine with an additional variation of end length l/r 0.2 produces a maximum turbine power of 21.969 W at a discharge of 1621.62 lpm. While the maximum electric power obtained by the Savonius turbine with a variation of 0.2 is 11.51 W at the same discharge.

References

1. Tim Sekretaris Jenderal Dewan Energi Nasional: Indonesia energy out look 2019. J. Chem. Inf. Model. **53**, (9) (2019)
2. Nguyen, H.T., Skitmore, M., Gray, M., Zhang, X., Olanipekun, A.O.: Will green building development take off? An exploratory study of barriers to green building in Vietnam. Resour. Conserv. Recycl. **127**(May), 8–20 (2017)
3. Vanzwieten, J., et al.: In-stream hydrokinetic power : review and appraisal. J. Energy Eng. **141**(3), 04014024, 1–16 (2014)
4. Savonius, S.J.: The S-Rotor and its applications. Mech. Eng. **53**(5), 333–338 (1931)
5. Kumar, A., Saini, R.P.: Performance parameters of Savonius type hydrokinetic turbine – a review. Renew. Sustain. Energy Rev. **64**, 289–310 (2016)
6. Sarma, N.K., Biswas, A., Misra, R.D.: Experimental and computational evaluation of Savonius hydrokinetic turbine for low velocity condition with comparison to Savonius wind turbine at the same input power. ENERGY Convers. Manag. **83**, 88–98 (2014)
7. Kamoji, M.A., Kedare, S.B., Prabhu, S.V.: Experimental investigations on single stage modified Savonius rotor. Appl. Energy **86,** 1064–1073 (2009)
8. Prasetyo, A., Kristiawan, B., Danardono, D., Hadi, S.: The effect of deflector angle in Savonius water turbine with horizontal axis on the power output of water flow in pipe. J. Phys.: Conf. Ser. **979** (2018)
9. Hindasageri, V., Ramesh, H., Kattimani, S.C.: Performance of Savonious rotors for utilizing the orbital motion of ocean waves in shallow waters. **2014**(October) (2011)
10. Soo, K., Ik, J., Pan, J., Ryu, K.: Effects of end plates with various shapes and sizes on helical Savonius wind turbines. Renew. Energy **79**, 167–176 (2014)
11. Sanditya, T.A., Prasetyo, A., Kristiawan, B., Hadi, S.: Effect of blade curvature angle of Savonius horizontal axis water turbine to the power generation. J. Phys.: Conf. Ser. **979**, 012044 (2018)
12. Deda, B., Altan, G., Kovan, V.: Investigation of 3D printed Savonius rotor performance. Renew. Energy **99**, 584–591 (2016)

The Effect of Blade Arc Angle on the Performance of Gravitational Water Vortex Turbine: Case Study on Type-L Blade Runner

Rieky Handoko[1], Syamsul Hadi[2(✉)], D. Danardono Dwi P. T.[2], and Ari Prasetyo[2]

[1] Graduate Program of Mechanical Engineering Department, Universitas Sebelas Maret, Surakarta, Indonesia
[2] Mechanical Engineering Department, Universitas Sebelas Maret, Surakarta, Indonesia
syamsulhadi@ft.uns.ac.id

Abstract. The flow of rivers and lakes that flow throughout the year has the potential for developing water energy in the world. Dams to make heads are needed as a hydroelectric power plant that can cause environmental and ecological changes, disrupt river flow and even local population migration. The application of micro-hydro power plants is one of the efforts to overcome this problem. Gravitational Water Vortex Turbine (GWVT) is a relatively new technology in the field of micro-hydro power generation and is still in the process of being developed to obtain maximum turbine power values. The blade shape research has been carried out using the experimental method in this study. The research was conducted using a water tunnel with a cone type basin to create a water vortex with three variations of water discharge. Design and testing of prototype L-type runners with variations of three blade angles; 75°, 90°, 105°, the inclination of the blade to the vertical axis of 60°, and the number of blades 5 have been completed in this study. The results showed that the L runner with an blade arc angle of 90° produced the highest turbine power followed by a blade angle of 75° and 105°.

Keywords: Microhydro · GWVT · Blade arc angle

1 Introduction

Rivers and lakes that flow throughout the year have the potential to develop water energy in the world [1]. The dam to make the head is needed as a hydroelectric power plant. However, it can cause environmental and ecological changes, disruption of river flow and even local population migration. Therefore, small-scale hydropower without dams is one of the environmentally friendly and cost-effective technologies in recent years [2].

Gravitational Water Vortex Turbine (GWVT) is a relatively new technology in the field of micro hydro power generation and is still in the process of being developed to obtain maximum turbine power values. In principle, the water flow in the GWVT flows

tangentially into the basin and forms a strong eddies with water outlet holes made at the bottom of the basin as the outlet [3]. The effect of low pressure in the orifice causes the water to restructure its flow into a vortex-like pattern. Unlike most other types of water turbines where only one part of the blades is exposed to water, in this GWVT water hits all the blades at the same time, so the active blade area is relatively larger [4]. The water vortex that is formed will rotate a turbine which is connected to a generator [3].

Sritram and Suntivarakorn [5] investigated the effect of the number of blades and the addition of baffle plates on the blades. The results showed that the number of blades and the addition of baffle plates on the blades affected the turbine performance. Dhakal and Khanal [6] conducted experimental research by varying the radius of curvature of the blade with the hub between 15°–25° with 1° intervals. The 19° angle between the blade and the hub was found to be the best result with a maximum efficiency of 80%. Saleem et al. [7] examined the effect of blade orientation with a 90° configuration on eddies and 68.5° tilting flows. The basic principle of this development is to optimize the turbine in capturing the existing power from the axial velocity of the whirlpool so as to improve turbine performance. Nadhief et al. [8] conducted research on the design and testing of the prototype L type Savonius water turbine blade with variations in the blade arc angle; 120°, 135°, and 150°. The results showed that the variation of the L-type blade with a blade arc angle of 135° produced the highest power coefficient of 27% at a TSR of 1.32 compared to other turbines. This study aims to determine the effect of vortex turbine runners with variations of L type turbine blades with blade arc angles of 75°, 90°, 105°.

2   Methodology

This study was conducted using a water tunnel with a cone type basin to create a water vortex with three variations of inlet water discharge 1, 2, 3; 7.5×10^{-3} m^3/s, 8.5×10^{-3} m^3/s, and 9.5×10^{-3} m^3/s. Turbine power is obtained from the measurement of turbine rotation speed multiplied by turbine torque. Turbine rotational speed measurement is carried out using a digital tachometer while the turbine torque measurement uses a prony brake system which is used to measure the shaft force by involving a rope pulley system that is loaded and balanced with a loadcell. The loadcell readings are recorded as braking force. The schematic of the prony brake system can be seen in the Fig. 1.

2.1   Vortex Turbine Design

The Vortex turbine design is based on the literature that has been studied (Fig. 2). Vortex turbines are made based on several references to vortex turbines so that the following designs are obtained [6]:

1. Blade Width: 80 mm
2. Blade Height: 160 mm
3. Hub Diameter: 100 mm
4. Number of Blade: 5
5. Shaft Diameter: 12 mm
6. Blade Inclination: 60°

Fig. 1. Prony brake system schematic.
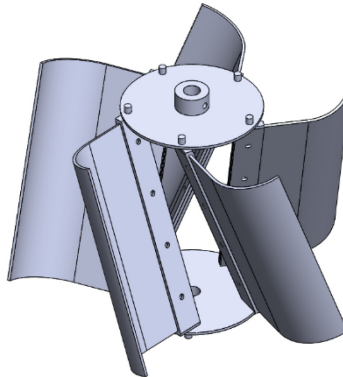
Fig. 2. Vortex turbine.

7. Blade Arc Angle: 75°, 90°, 105°
8. Turbine Material: 2 mm thick aluminum plate

2.2 Variation of Arc Angle Blade

The variation that will be used in this study is the Blade Arc Angle variation shown in Fig. 3.
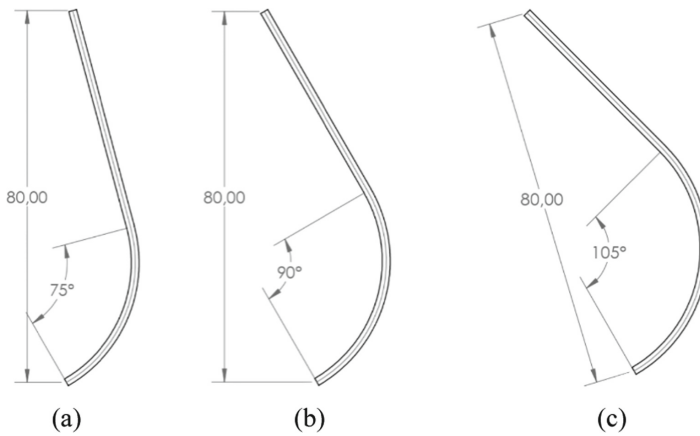
Fig. 3. Vortex turbine blades; (a) with blade arc 75°, (b) with blade arc 90°, and (c) with blade arc 105°.

3   Result

Figure 4 shows a graph of the comparison of turbine variations to mechanical power and turbine rotational speed at three variations of inlet water discharge. The turbine with a variation of the 90° blade arc angle produces turbine power and turbine speed of 18.64 W and 217.7 RPM followed by a 75° arc angle turbine variation with a power output of
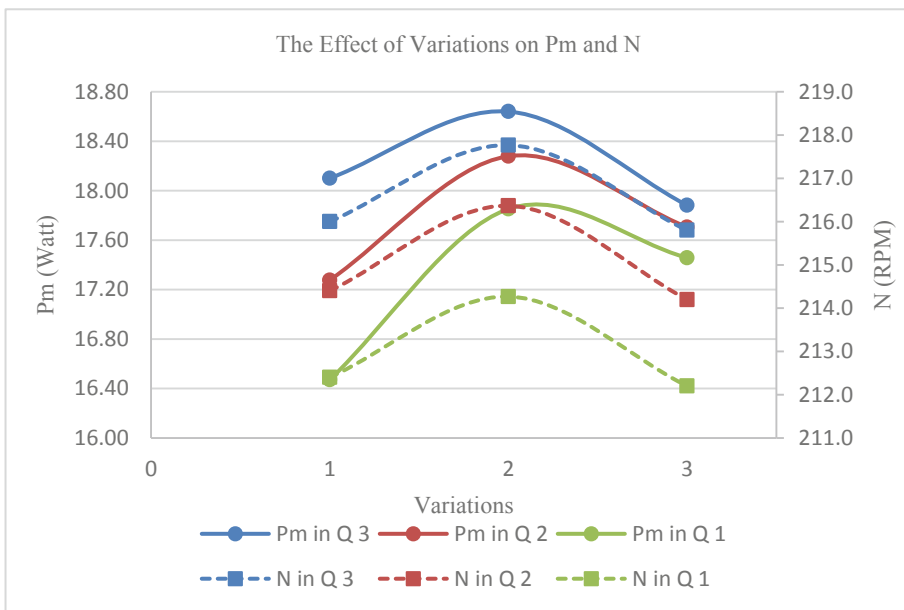
Fig. 4. Effect of Variation blade angles; 75°, 90°, 105° on Pm and N.

18.10 W and a rotational speed of 216 RPM, then the turbine arc angle variation of 105° with a power 17.88 W and a rotational speed of 215.8 RPM at discharge 3. Turbine with a variation of 90° still produces the largest turbine power than turbines with variations in arc angle of 75° and 105° at discharge 2. Likewise at discharge 1 turbine with variations in arc angle of 90° produces a value of highest than other variation turbines.

4   Conclusion

Based on this research, it can be concluded that the arc angle of the blades 75°, 90°, 105° on the vortex turbine affects the value of the mechanical power and rotational speed of the resulting turbine. The largest value of power and turbine rotational speed is produced by a vortex turbine with a variation of 90° followed by a variation of 75° and 105° at discharge 3 (9.5×10^{-3} m³/s). At discharge 2 (8.5×10^{-3} m³/s), the largest turbine power is produced by a turbine with an arc angle variation of 90° followed by 105° and 75°. While the largest rotational speed value at discharge 2 is produced by a turbine with an arc angle variation of 90° followed by a variation of 75° and 105°. At discharge 1 (7.5×10^{-3} m³/s) the largest turbine power is produced by a turbine with an arc angle variation of 90° followed by 105° and 75°. While the largest rotational speed value at discharge 1 is produced by a turbine with an arc angle variation of 90° followed by variations of 75° and 105°. Based on the variations used, the turbine with an arc angle variation of 90° produces the largest power and turbine rotational speed for each variation of discharge in this study.

References

1. Hidayat, M.N., Ronilaya, F., Eryk, I.H., et al.: Design and analysis of a portable spiral vortex hydro turbine for a Pico Hydro Power Plant. In: IOP Conference Series: Materials Science and Engineering, vol. 732, p. 012051, 27 January 2020
2. Pamuji, D., Effendi, N., Sugati, D.: Numerical study on the performance and flow field of varied conical basin for efficient gravitational water vortex power plant. Innov. Sci. Technol. Mech. Eng. Ind. 4.0 **2187**, 020001 (2019)
3. Dhakal, S., Timilsina, A.B., Dhakal, R., et al.: Comparison of cylindrical and conical basins with optimum position of runner: gravitational water vortex power plant. Renew. Sustain. Energy Rev. **48**, 662–669 (2015)
4. Chattha, J.A., Cheema, T.A., Khan, N. H.: Numerical investigation of basin geometries for vortex generation in a gravitational water vortex power plant. In: 2017 8th International Renewable Energy Congress (IREC), pp. 1–5 (2017)
5. Sritram, P., Suntivarakorn, R.: The effects of blade number and turbine baffle plates on the efficiency of free-vortex water turbines. In: IOP Conference Series: Earth and Environmental Science, vol. 257, p. 012040, 10 May 2019
6. Dhakal, R., Khanal, K.: Computational and experimental investigation of runner for gravitational water vortex power plant. In: 6th International Conference on Renewable Energy Research and Applications 2017, San Diego, CA, USA (2017)
7. Saleem, A.S., Cheema, T.A., Ullah, R., et al.: Parametric study of single-stage gravitational water vortex turbine with cylindrical basin. Energy **200**, 117464 (2020)
8. Nadhief, M., Prabowoputra, D., Hadi, S., et al.: Experimental study on the effect of variation of blade arc angle to the performance of Savonius water turbine flow in pipe. Int. J. Robot. Res. **9**, 779–783 (2020)

The Effect of the Number of Blades on Performance of Savonius Water Turbine in Vertical Pipe with Additional Deflector

Ilham Malia Widiyasa, Syamsul Hadi[✉],
and Dominicus Danardono Dwi Prija Tjahjana

Mechanical Engineering Department, Faculty of Engineering, Universitas Sebelas Maret, Jl. Ir. Sutami 36A, Surakarta 57126, Indonesia
syamsulhadi@ft.uns.ac.id

Abstract. Indonesia is a tropical country that has high rainfall. The potential of water is used to drive the Savonius water turbine in high-rise buildings with low head. Turbine can rotate at low fluid flow velocity but still low efficiency. This study aims to determine the effect of the number of blades on the output power produced by using a deflector. Experimental research using 20° and 30° deflectors with variations in the number of blades 5, 7, 9, 11. To determine the performance of the turbine analyzed using data Power Output, Coefficient Of Power and Tip Speed Ratio. The 20° deflector produces the best performance on a 7 blades turbine at discharge of 27.03 L/s with an electrical power of 13.29 W, while the Coefficient of Power is 0.079 with a TSR value of 0.694 at a discharge of 9.29 L/s. The 30° deflector produces the best performance on a 7 blades turbine at discharge of 21.66 L/s with an electric power of 10.55 W, while the Coefficient of Power is 0.087 with a TSR value of 1,600 at a discharge of 7.67 L/s. The 7 blades turbine produce the best performance in both variations deflector 20° and 30°.

Keywords: Savonius water turbine · Number of blades · Deflector · Coefficient of power · Tip speed ratio

1 Introduction

Energy is an important aspect in the running of life in a country. In 2018, electricity generation was mostly sourced from fossil energy, especially coal (50%), followed by natural gas (29%), fuel (7%), and renewable energy (14%) [1]. Indonesia is a tropical country that has high rainfall with rainfall intensity of 20, 50, and 100 mm/day [2]. It is used as a source of energy for power plants, namely rainwater and household waste that flows in high-rise buildings [3]. In multi-storey buildings, hydrokinetic turbines are optimally used because they operate by converting water flow into kinetic energy by utilizing water flow velocity and low head height [4]. There are two types of savonius turbines based on the axis of rotation, namely turbines with a horizontal axis and turbines with a vertical axis [5].

The characteristics of the blades affect the performance of the turbine and have advantages according to the application [6]. By modifying the number of blades can improve turbine performance. Sule et al. with the number of blades 8 obtain the best performance with an efficiency of 17.06% [7]. In an effort to reduce negative torque using a deflector to direct the water flow [8].

According to the literature that has been studied, the parameter of the number of blades is interesting to do in this study because the effect of the number of blades affects the surface area of the concave blade when it receives water collisions. This study observes the effect of the number of blades on the work performance of the savonius horizontal axis water turbine with the use of a deflector because there are differences in results for each number of blades.

2 Methodology

Research using Savonius turbine blade-shaped semi-circullar. The parameters of the turbine use aspect ratio (H/D) 0.5, End-plate parameter (D0/D) 1.1, Overlap ratio (β) 0 [9, 10]. The diameter (D) is 164 mm, the shaft diameter (d) is 8 mm, and the height (H) is 82 mm. Turbine made using aluminum material with the curvature of the blade 120° [11]. Turbine blade thickness of 2 mm [9]. The parameters to be studied using variations in the number of blades are 5, 7, 9, and 11, blades. Selection of the number of the blade because the more the number the greater the efficiency of the turbine blade Savonius water [7]. The deflector angles are 30° and 20° [8]. Research carried out by the experimental method. The design of the savonius water turbine, deflector and schematic of the test equipment is shown in Fig. 1.
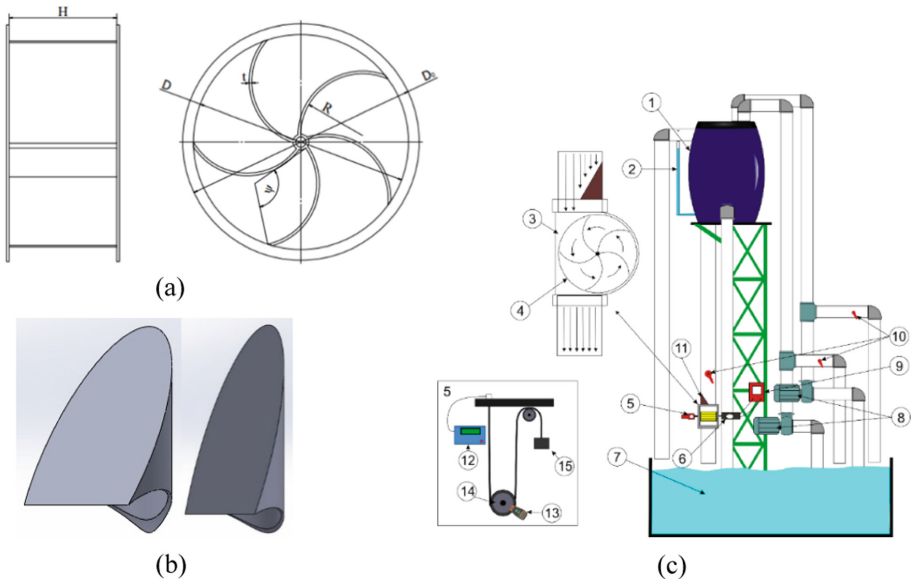
Fig. 1. (a) Design of the savonius water turbine, (b) Design deflector 20° and 30°, (c) Testing equipment schematic.

3   Result and Discussion

Based on Fig. 2, the value of the maximum generator output power generated by a 7 blade turbine at a discharge of 27.03 L/s is 13.29 W. While the value of the minimum generator output power generated by the 11 blade turbine at a discharge of 9.29 L/s is 6.51 W.
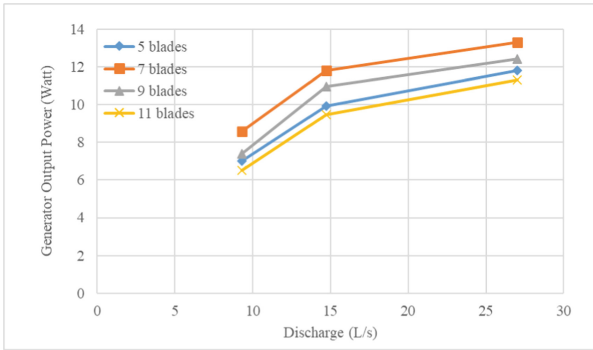
Fig. 2. The relationship between electrical output power and water discharge at a deflector angle of 20°.

Based on Fig. 3, the value of the maximum generator output power generated by a 7 blades turbine at a discharge of 21.66 L/s of 10.55 W. While the value of the minimum generator output power generated by an 11 blade turbine at a discharge of 7.67 L/s of 5.66 W.
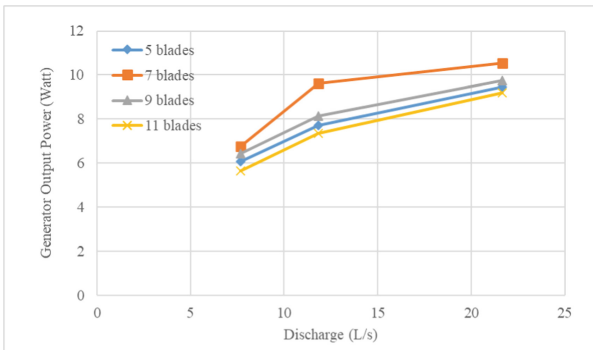
Fig. 3. The relationship between electrical output power and water discharge at a deflector angle of 30°.

In this experiment, the maximum generator output power value is always obtained on a 7-blades turbine in both the 20° and 30° deflectors. In both variations of the deflector the minimum generator output power value is obtained at a 11 blades turbine. The

addition of too many blades causes the distance between the blades to be smaller and the impact of the water current is reduced so that the water current causes resistance to the movement of the blade rotation and produces negative torque [12]. The use of a 20° deflector generated a higher output power than a 30° deflector, because the flow pattern on a 20° deflector is able to reduce negative torque due to the flow of water coming out of the pipe directly hitting the concave blades of the turbine and the flow of water from the blades being wasted directly into the bottom reservoir.

4 Conclusion

Based on the results of a study on the performance of the Savonius water turbine on the effect of the number of blades on the output power produced by the use of a deflector. That the use of a 20° deflector generated a higher power value than a 30° deflector. The 7 blade turbine generated the best performance on both deflectors with an electrical power of 13.29 W at a discharge of 27.03 L/s at a 20° deflector and 10.55 W at a discharge of 21.66 L/s at a 30° deflector.

References

1. Tim Sekretaris Jenderal Dewan Energi Nasional: Indonesia Energy Out Look 2019. (2019)
2. Tren Curah Hujan | BMKG. https://www.bmkg.go.id/iklim/?p=tren-curah-hujan
3. Sarma, N.K., Biswas, A., Misra, R.D.: Experimental and computational evaluation of Savonius hydrokinetic turbine for low velocity condition with comparison to Savonius wind turbine at the same input power. Energy Convers. Manag. **83**, 88–98 (2014). https://doi.org/10.1016/j.enconman.2014.03.070
4. VanZwieten, J., et al.: In-stream hydrokinetic power: review and appraisal. J. Energy Eng. **141**, 04014024 (2015)
5. Latif, M.: Efisiensi Prototipe Turbin Savonius pada Kecepatan Angin Rendah. J. Rekayasa Elektr. **10**, 147–152 (2013). https://doi.org/10.17529/jre.v10i3.1030
6. Chen, L., Chen, J., Zhang, Z.: Review of the Savonius rotor's blade profile and its performance. J. Renew. Sustain. Energy. **10**, 13306–13304 (2018)
7. Sule, L., Rompas, P.T.D.: Performance of Savonius blade waterwheel with variation of blade number. IOP Conf. Ser. Mater. Sci. Eng. **306** (2018)
8. Prasetyo, A., Kristiawan, B., Danardono, D., Hadi, S.: The effect of deflector angle in Savonius water turbine with horizontal axis on the power output of water flow in pipe. J. Phys. Conf. Ser. **979**, 1–6 (2018). https://doi.org/10.1088/1742-6596/979/1/012043
9. Kamoji, M.A., Kedare, S.B., Prabhu, S.V.: Experimental investigations on single stage modified Savonius rotor. Appl. Energy. **86**, 1064–1073 (2009). https://doi.org/10.1016/j.apenergy.2008.09.019
10. Mahmoud, N.H., El-Haroun, A.A., Wahba, E., Nasef, M.H.: An experimental study on improvement of Savonius rotor performance. Alexandria Eng. J. **51**, 19–25 (2012). https://doi.org/10.1016/j.aej.2012.07.003
11. Sanditya, T.A., Prasetyo, A., Kristiawan, B., Hadi, S.: Effect of blade curvature angle of savonius horizontal axis water turbine to the power generation. J. Phys. Conf. Ser. **49**, 115–120 (2018). https://doi.org/10.1088/1742-6596/979/1/012044
12. Sritram, P., Suntivarakorn, R.: The effects of blade number and turbine baffle plates on the efficiency of free-vortex water turbines. IOP Conf. Ser. Earth Environ. Sci. **257** (2019)

Effects of Reaction Temperature and Inlet Velocity of a Bubble Column Reactor on the Bubble Size for Biodiesel Production

Muhammad Nur Amirulhaq Mohd Yusof and Nurul Fitriah Nasir$^{(\boxtimes)}$

Faculty of Mechanical and Manufacturing Engineering, Universiti Tun Hussein Onn Malaysia, 86400 Parit Raja, Batu Pahat, Johor, Malaysia
fitriah@uthm.edu.my

Abstract. Bubble column reactors (BCR) are multiphase reactors used in the production of biodiesel. A bubble column reactor can withstand a higher temperature and provide higher efficiency in the process. During the transesterification process in the bubble column reactor, the bubble will be produced and will affect the bubble column reactor performance in biodiesel production. This study aimed to determine the effects of various reaction temperature and inlet velocity in a bubble column reactor on the sizes of the bubble for the transesterification reaction in the production of biodiesel. Different design of perforated plate is also used to find the effects of bubble size. The temperature used are 523 K, 543 K and 563 K and the inlet velocity are 2 m/s, 4 m/s and 6 m/s, respectively. Design and simulation of BCR were performed using SOLIDWORK 2018 ANSYS Fluent. The results obtained show that a drastic changing of gas holdup was found for design *A* at 563 K and 6 m/s inlet velocity. On the other hand, high circulation pattern occurred on the inlet, outlet, holes of perforated plate, and wall of reactor.

Keywords: Bubble column reactor · Biodiesel · Computational fluid dynamics · Gas holdup

1 Introduction

Nowadays, the production of biodiesel occurs in the gas-liquid reactor to produce biodiesel. To define a correct choice of reactors to be used, optimum pressure, temperature of reaction and production size are the factors that need to be considered. In general, any reactor types should provide appropriate residence time, heat exchange, and mass transfer for efficient product formation [1].

Bubble column reactors are preferred as it can be used for conducting a variety of two phase and three phase reactions. Some advantages of bubble column reactors are they have excellent heat and mass transfer characteristics, require little maintenance, and have low operating cost. For bubble columns to work efficiently, several conditions must be complied. These working conditions include temperature, pressure, superficial gas velocity, velocity magnitude and fluid flow pattern. To analyze and solve problems that involves fluid flows, computational fluid dynamics (CFD) can be used to achieve

this objective. CFD analysis uses numerical analysis and data structures to perform calculations required to fabricate the simulation of the flow of the fluid, along with its interactions and constraints. The simulation of CFD acts as a convenient tool for predicting process characteristics and their dependence on design and operating variables [2]. This study aimed to determine the effects of different reaction temperature and inlet velocity on the bubble size of transesterification reaction mixture in bubble column reactor. For simulation, it focuses on different perforated plate column design.

2 Methodology

Two different designs of the bubble column reactor were suggested based on previous work [3]. The perforated plate inside the bubble column reactor for Design *A* is circular shaped, while for Design *B*, the perforated plate is hexagonal shaped. Figure 1 shows the cross-sectional view and the top view of the plate for both designs.
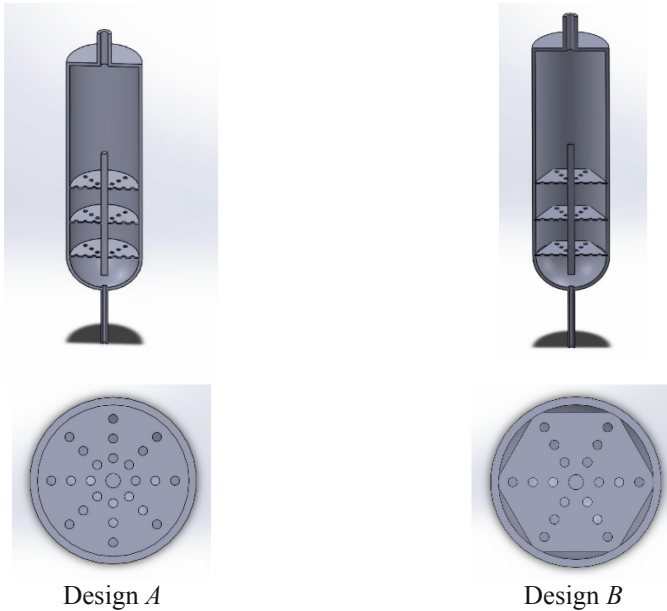
Design *A*   Design *B*

Fig. 1. Cross sectional view of design *A* and *B*.

2.1 CFD Simulation

Boundary conditions are compulsory constraints for the solution of a boundary value problem. The inlet boundary condition was set up as the mixture of methanol vapor and triglyceride, with a set of inlet velocity of 2 m/s, 4 m/s, and 6 m/s while the outlet boundary condition as pressure boundary condition, was set at 100 kPa (atmospheric pressure). The backflow oil volume fraction value at outlet was set to one. Wall boundary condition

for vapor wall and liquid wall was set as stationary wall and no slip wall. The properties of materials and boundary conditions used in the flow analysis were summarized in Table 1 and 2, respectively.

Table 1. Properties of materials.

Properties	Air	Methyl alcohol vapour	Palm oil
Density (kg/m^3)	1.225	1.43	909
C_p (Specific Heat) (J/kg-K)	1006.43	' – '	281.0665
Thermal conductivity (W/m-K)	0.0242	0.0163	0.1041
Viscosity (kg/m-s)	1.7894e − 05	1.35e − 05	0.069
Molecular weight (kg/kmol)	28.966	32.04	885.4321
Standard state enthalpy (J/kgmol)	' – '	−2.01097e + 08	−2.056e + 09
Reference temperature (K)	298.15	298.15	298.15

Table 2. Boundary condition used in fluid domain.

Boundary condition	Value
Inlet Velocity (m/s)	2, 4, 6
Pressure (kPa)	100
Temperature (K)	523–563 in 20 K interval
Multiphase	Volume of Fluid
Turbulence	k-epsilon
Wall	No-slip

3   Results and Discussions

3.1   Results on Gas Holdup

Gas holdup is an important characteristic to determine the effect of velocity and temperature on reaction rate. The value of gas holdup was defined as the volume fraction of methanol gas in the total volume mixture of triglyceride and methanol vapor in the reactor which is obtained from this simulation. Gas holdup is related to the bubble sizes and velocity. Therefore, the increase of the velocity and temperature will give an increase in the value of gas holdup, which could affect the bubble sizes in the bubble column reactor. The results of the gas holdup at 523 K for Design *A* are shown in Fig. 2.
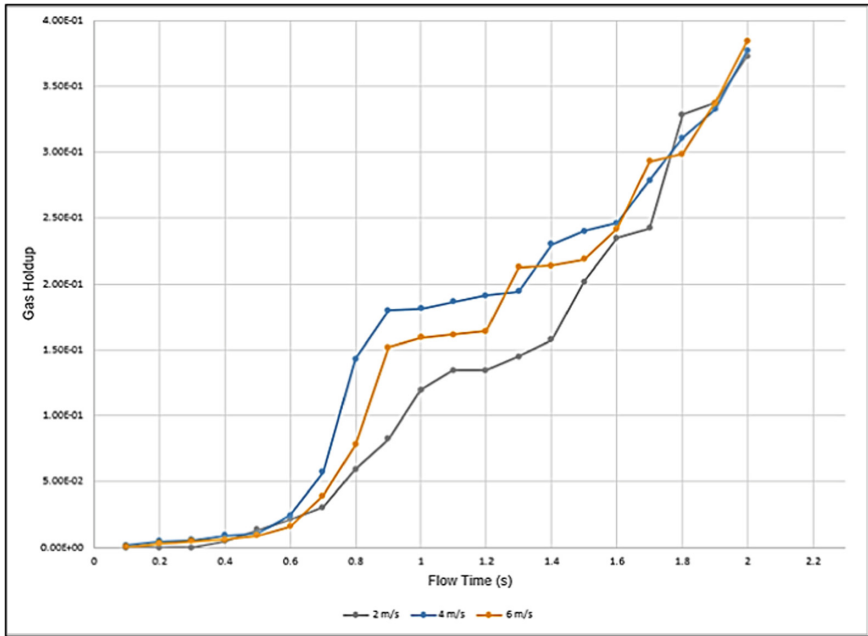
Fig. 2. Gas holdup versus flow time for 523 K for Design *A*.

4 Conclusion

In conclusion, the bubble sizes were obtained based on the value of gas holdup which referring the vapor volume fraction in volume mixture in the bubble column reactor. The increase of the inlet velocity in the simulation produced the increasing value of gas holdup. The higher value of gas holdup produced the small bubble size in the reactor while the large bubble sizes occur when the decreases value gas holdup. The value of gas holdup shown for Design *A* was increasing when temperature and inlet velocity increase. The value of gas holdup obtained from Design *B* shows constant value for the whole flow time and this suggest that the design of perforated plate need modification with other parameters.

References

1. Tabatabaei, M., et al.: Reactor technologies for biodiesel production and processing: a review. Prog. Energy Combust. Sci. **74**, 239–303 (2019)
2. Joelianingsih, H., et al.: A continuous-flow bubble column reactor for biodiesel production by non-catalytic transesterification. Fuel **96**, 595–599 (2012)
3. Suhaimi, A.A., Nasir, N.F.: Study of the fluid flow pattern in a bubble column reactor for biodiesel production. IOP Conf. Ser. Mater. Sci. Eng. **243**, 012035 (2017)

Automated Control System Strategies to Ensure Safety of PEM Fuel Cells Using Kalman Filters

Yadu Krishna Morassery Veettil[1], Shantam Rakshit[1], Oliver Schopen[1], Hans Kemper[1], Thomas Esch[1(✉)], and Bahman Shabani[2]

[1] FH Aachen University of Applied Sciences, Aachen, Germany
esch@fh-aachen.de
[2] RMIT University, Melbourne, Australia

Abstract. Having well-defined control strategies for fuel cells, that can efficiently detect errors and take corrective action is critically important for safety in all applications, and especially so in aviation. The algorithms not only ensure operator safety by monitoring the fuel cell and connected components, but also contribute to extending the health of the fuel cell, its durability and safe operation over its lifetime. While sensors are used to provide peripheral data surrounding the fuel cell, the internal states of the fuel cell cannot be directly measured. To overcome this restriction, Kalman Filter has been implemented as an internal state observer. Other safety conditions are evaluated using real-time data from every connected sensor and corrective actions automatically take place to ensure safety. The algorithms discussed in this paper have been validated thorough Model-in-the-Loop (MiL) tests as well as practical validation at a dedicated test bench.

Keywords: Control system · PEM fuel cells · Kalman filter

1 Introduction

In a world of advancing discussions around carbon footprint reduction and carbon neutrality, it is imperative that the transport sector responds with rapid changes. From an aviation point of view, one major step to minimize impacts could be using fuel cells instead of conventional energy conversion devices [1, 2]. The innovations that fuel cells have undergone in recent decades have transformed them from laboratory experiments to a possible successor to the internal combustion engine. Mass-produced vehicles, as well as the sheer number of research projects worldwide do currently demonstrate this.

A control system in such a setting needs to prioritize safety, by reading data from the connected sensors, interpreting them and passing them through control algorithms that then monitor the assembly and regulate valves to take corrective action in the occurrence of errors. Control engineering approaches using dynamic modelling of the fuel cell, both via distributed parameter modelling [3] and lumped parameter modelling [4] have been reviewed in papers before [5]. This paper aims to bring these methods into real time operation at a dedicated test bench, and scale such a control system so that it is suited for

aerial applications. To this end, PID Controllers [6] as well as Stateflow in MATLAB Simulink [7] have been adapted for system specific applications.

Dynamic operation of the fuel cell for extended periods, especially in a mobility perspective, would lead to fluctuations in internal states, which cannot be directly measured. Therefore, internal state observers are necessary in this context. Variations of the Kalman Filter has been proven to be well suited for the requirements [8, 9], and preferred over Luenberger observers or high-order sliding mode (HOSM) state observers due to convergence and computational effort, respectively. Kalman Filter is used in this paper to estimate the internal mass flow, pressures and temperature at the anode and cathode, based on the current demanded from the fuel cell and stoichiometry at the anode and cathode. The overall control system then becomes an integral part in the internal health monitoring of the fuel cell.

2 System Description

The dedicated test bench set up, for the purposes of the control system, has been summarized in Fig. 1. The most important component in the test bench assembly is the Proton Exchange Membrane fuel cell with 48 cells and a rated power output of less than 10 KW. The different operating limits and safety boundaries are as specified by the manufacturer, and are the most important conditions the control system has to observe and ensure during operation. This includes physical limits to operating temperatures, pressures, relative humidity, conductivity of the cooling loop, current drawn from the fuel cell, presence of negative current and minimum cell voltages. The system is able to provide a maximum current of around 230 A, and individual cell voltages as low as 0.4 V safely.
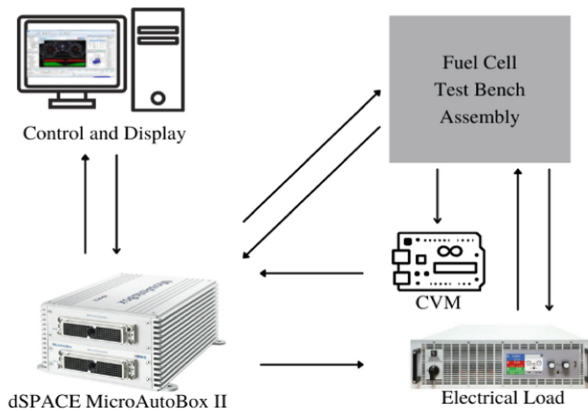

Fig. 1. System data acquisition module.

The prototyping unit used at the assembly is a dSPACE MicroAutoBox II, with voltage interface at input (0–5 V) and output (0–4.5 V). The different electrical connections at the test bench are designed to facilitate easy interfacing and data transfer between the

connected components and the prototyping unit, and through it, to the user. Model based software development through MATLAB Simulink is used for realizing the underlying algorithms and dSPACE ControlDesk for designing a User Interface. C-Code is built in Simulink and then exported into ControlDesk. The Cell Voltage Monitoring (CVM) System is built specifically to interact with the fuel cell and output fuel cell voltages and current into the prototyping unit.

The first iteration of the control system is designed to allow the user to manually control all the valves and read all the sensor values within one screen. Subsequent versions automate the system in steps, starting with implementing automatic monitoring and state correction, based on different safety limits and precautions. Inbuilt functions, PID Controllers and Stateflow on MATLAB Simulink are used for control automation.

3   Overview of Safety Functionalities

This section aims to give an overview of the project specific safety functionalities programmed for test bench applications, most of which can be scaled for use in aerial applications. Continuous safety checks for observing and maintaining physical safety limits for the fuel cell and components in the assembly are realized through Stateflow on MATLAB Simulink. Functions such as signal filtering and safety check debouncing are programmed specifically for the components used. Since a failure in components can lead to wrong readings and incorrect actions, algorithms for checking sensor health and actuator health are programmed according to their operating ranges and physical effects, including detection of conditions where the user would have to recalibrate the sensor. The Open Circuit Voltage (OCV) of the fuel cell is recorded and can be compared over time for analysing degradation and changes in performance.

Due to the dynamic nature of operation at the test bench, it can be expected that the fuel cell system can enter undesired states. To counter this, an algorithm specifically designed for exiting to a safe state, much like the limp-home mode in automobiles, and an emergency exit strategy algorithm for crucially critical operating points, have been programmed. The overall control system has been designed by integrating all of these into one module. The Stateflow charts are used as the main control element in deciding the operating point of the fuel cell, which then controls the connected actuators to realise the required conditions.

4   Kalman Filter Implementation

The connected sensors relay information surrounding the fuel cell, i.e., about the supply conditions in each loop – air, hydrogen and cooling water. The information about internal states of the fuel cell cannot be directly measured from these measurements, and thus, need to be estimated. A mathematical model of the fuel cell system is formed by combining the Eqs. (1) and (2) with the Kalman Filter, with their expansions to estimate the internal states. Mass flows on the cathode and anode side are respectively denoted as *mcathode* and *manode*. Temperature of the stack is *Tstack,* and pressure on either sides are denoted as *pcathode* and *panode*. Current drawn from the fuel cell stack is denoted

as *IFC*. The stoichiometry on the cathode and anode side are represented as $\lambda cathode$ and $\lambda anode$ respectively. The system dynamic equations are:

$$x = \begin{bmatrix} m_{cathode}, & m_{anode}, & T_{stack}, & p_{cathode}, & p_{anode} \end{bmatrix}^T \tag{1}$$

$$u = [I_{FC}, \ \lambda_{cathode}, \ \lambda_{anode}]^T \tag{2}$$

To assure higher levels of safety, more accurate internal fault detection and increased mean operation time between failures, other Kalman Filter techniques will be integrated into the overall control system in the next step. One such adaptation will be to perform online Electrochemical Impedance Spectroscopy (EIS) using experimental impedance data from the test bench. At further stages, an unscented Kalman Filter may be implemented for fault detection in valve positions, which are also not directly measurable.

References

1. Kadyk, T., Winnefeld, C., Hanke-Rauschenbach, R., Krewer, U.: Analysis and design of fuel cell systems for aviation. Energies **11**(2) (2018)
2. Baroutaji, A., Wilberforce, T., Ramadan, M., Olabi, A.: Comprehensive investigation on hydrogen and fuel cell technology in the aviation and aerospace sectors. Renew. Sustain. Energy Rev. **106** (2019)
3. Luna, J., Usai, E., Husar, A., Serra, M.: Nonlinear observation in fuel cell systems: a comparison between disturbance estimation and High-Order Sliding-Mode techniques. Int. J. Hydrogen Energy **41**(43), 19737–19748 (2016)
4. Pukrushpan, J.T., Peng, H., Stefanopoulou, A.G.: Control-oriented modeling and analysis for automotive fuel cell systems. J. Dyn. Syst. Measure. Control Trans. ASME **126**(1), 14–25 (2004)
5. Jahnke, T., Futter, G., Latz, A., et al.: Performance and degradation of Proton Exchange Membrane Fuel Cells: State of the art in modeling from atomistic to system scale. J. Power Sources **304**(1–2), 207–233 (2016)
6. Daud, W., Rosli, R., Majlan, E., Hamid, S., Mohamed, R., Husaini, T.: PEM fuel cell system control: a review. Renew. Energy **113**, 620–638 (2017)
7. Li, X., Xu, L., Hua, J., Lin, X., Li, J., Ouyang, M.: Power management strategy for vehicular-applied hybrid fuel cell/battery power system. J. Power Sources **191**(2), 542–549 (2009)
8. Yuan, H., Dai, H., Wei, X., & Ming, P.: Model-based observers for internal states estimation and control of proton exchange membrane fuel cell system: a review. J. Power Sources **468** (2020)
9. Headley, A.J., Gross, M., Chen, D.: Membrane electrolyte assembly health estimation method for proton exchange membrane fuel cells. J. Electrochem. Energy Conv. Storage **14**(4) (2017)

Modeling and Simulation

Study of Lubrication Fluid Pressure in Artificial Hip Joint During Bowing (Ruku')

Taufiq Hidayat[1(✉)], J. Jamari[2], A. P. Bayuseno[2], Rifky Ismail[2], Mohammad Tauviqirrahman[2], and Prayudha Naufal Wijaya[2]

[1] Program Studi Teknik Mesin, Universitas Muria Kudus, Kudus, Indonesia
`taufiq.hidayat@umk.ac.id`
[2] Program Studi Teknik Mesin, Universitas Diponegoro, Semarang, Indonesia

Abstract. Synovial fluid (SF) represents a clear and sticky fluid, which could be released by the synovial membrane and acts as a lubricant for joints and tendons. The purpose of this study was to analyze the hydrodynamic pressure of this lubricant in the artificial hip joint during bowing, in that the Moslem acts prayer positions. Computational Fluid Dynamics (CFD) coupled with Fluid-Structure Interaction (FSI) methods-based simulation was employed in the study for examining the lubrication fluid performance. In this case, the SF fluid was modeled as non-Newtonian fluids, whereas Newtonian fluids are modeled as water. The non-Newtonian fluid model was used as cross modeling. The material from the acetabular cup, outer liner, femoral head, and stem is Stainless Steel. While the inner liner is Polyethylene. Lubrication occurs in the elastohydrodynamic regime. The result is the hydrodynamic pressure in non-Newtonian fluids (SF) is higher than in Newtonian fluids significantly.

Keywords: Artificial hip joint · Synovial Fluid · Elastohydrodynamic

1 Introduction

The hip joint is a sphere-shaped joint that connects the acetabulum part and the femoral head part in the human pelvic area. This hip joint is wrapped by a kind of lubrication fluid called Synovial Fluid (SF). This lubrication fluid serves to reduce friction at the hip joint. The hip joint is surrounded by ligaments and tendons that make it flexible and strong [1]. Artificial Hip Joints (AHJ) have been used for many years as a replacement for damaged hip joints by permanently implanted in the human body. Here the implementation of AHJ may include hard on hard, soft on soft, and hard on soft pairs.

Concerning the lubricating performance of the hip joint, Chaturvedi et al. [2] analyzed the elastohydrodynamic performance of Metal-on-Metal hip joint implants for Newtonian lubrication fluids. They used the modified Reynolds equation combined with restrictor flow equations to obtain numerical solutions for pressure, film thickness, and displacement. The maximum pressure of the film was shown to be significantly reduced in the acetabular cup.

Recently, Jamari et al. [3] used Computational Fluid Dynamics (CFD) coupled with Fluid-Structure Interaction (FSI) methods to simulate the AHJ under praying conditions. Here, the effect of micro-dimples on the surface of the liner and femoral head with different materials between metal and ceramic on prayer movements, lubrication performance was analyzed. Necas et al. [4, 5] said that the form of the lubricating film differs between hard-on-soft and hard-on-hard pairs. In the hard-on-hard pair, the lubricant film decreases faster than the hard-on-soft pair. The film thickness increases with time, but the rate of increase is determined by the type of movements, such as constant speed or sinusoidal velocity. The use of the classical EHL model to describe AHJ lubrication is too simplistic and imprecise [6]. Ruggiero developed a new mathematical formula to describe contacts in AHJ lubrication [7].

This paper analyses the lubrication fluid performance in AHJ using a Computational Fluid Dynamics (CFD) coupled with Fluid-Structure Interaction (FSI) in one of the Moslem prayer movements, namely bowing. The Newtonian and non-Newtonian lubricant types representing the synovial fluid in AHJ are compared.

2   Materials and Methods

The modeling of the unipolar AHJ is shown in Fig. 1. Synovial fluid is located between the inner liner cup and the femoral head. These SF are modeled as non-Newtonian fluids, while Newtonian fluids are modeled as water. Cross modeling is used to describe the non-Newtonian fluid model. CFD coupled with FSI methods-based simulation was employed in the study for examining the lubrication fluid performance. The simulation was performed on one of the movements in Moslem prayer, namely bowing. Bowing is bending the body so that the spine is flat with the head and placing both palms on both knees and then stretching them. The position of the bowing can be seen in Fig. 2.

The material for the acetabular cup, outer liner, femoral head, and stem is Stainless Steel. As for the inner liner, the material is Polyethylene. From the normal position of the hip joint or also called the anatomical position (standing position), the angle is applied by rotating the position of the femoral head [8]:

– Flexion (x-axis) = 87°
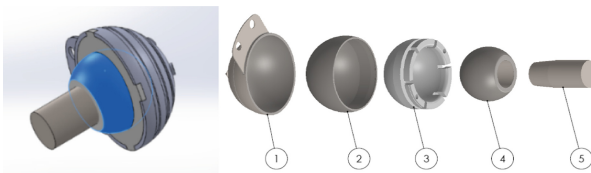– Abduction (y-axis) = 0°
– Rotation (z-axis) = 0°

Fig. 1. Unipolar artificial hip joint models (Notes: 1. Acetabular Cup, 2. Outer Liner, 3. Inner Liner, 4. Femoral Head, 5. Stem).

Fig. 2. Bowing position.

3 Results and Discussion

Synovial fluid is a lubricant that keeps load-bearing joints like hip joints lubricated and operating properly. It has different rheology than Newtonian fluids because protein molecules are seen to aggregate at low shear rates, generating a three-dimensional network that breaks down at high shear rates [9].

Figures 3 and 4 show the hydrodynamic pressure either in contour or distribution profiles, respectively for non-Newtonian and Newtonian fluids. From these figures, the maximum pressure is 4581 Pa which occurs at an angle of 140°, marked by a red contour. For a Newtonian fluid, the maximum pressure as indicated in Fig. 4 is 15.42 Pa. Based on Figs. 3 and 4, the non-Newtonian lubricant has a higher value of pressure compared to the Newtonian one. From the physical point of view, it indicates modeling synovial fluids with non-Newtonian matches well with the real condition. At a low shear rate as occurs during the Bowing situation, the pressure value tends to become higher as a response to the external load. As a consequence, the load-carrying support due to synovial fluid is higher and it makes the AHJ is more stable.
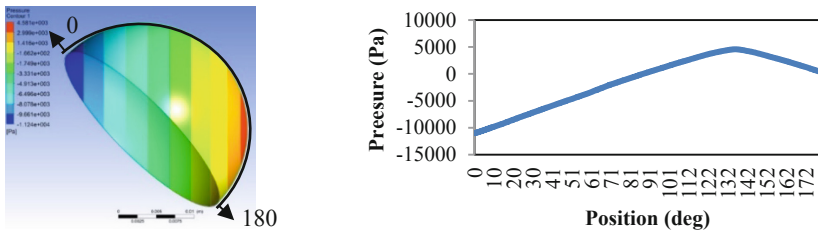

Fig. 3. Hydrodynamic pressure distribution in SF under bowing position.

To reduce wear and tribo-corrosion, good lubrication in the elastohydrodynamic regime is required. At low shear stress, the thickness of the lubricant film becomes large. The higher viscosity of the lubricant, the thicker the lubricant film will be [10].
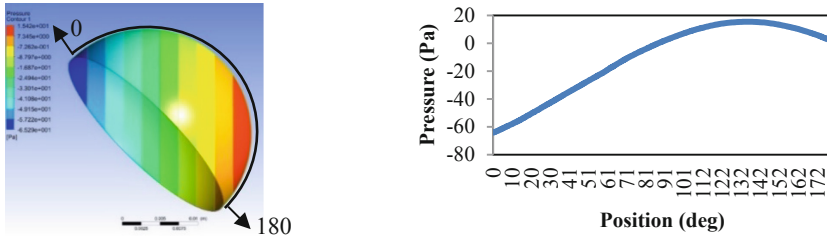
Fig. 4. Hydrodynamic pressure distribution in Newtonian fluid under bowing position.

4 Conclusion

The investigation of a lubricated prosthetic hip joint is undertaken in this study utilizing the computational fluid dynamics (CFD) method, with a particular emphasis on the behavior of the synovial fluid. The numerical results indicated that the difference in hydrodynamic pressure between non-Newtonian fluids (SF) and Newtonian fluids is quite significant. Thus, a well-chosen lubricant type for modeling the synovial fluid must be of particular care when the lubricated AHJ is studied.

References

1. Hamill, J., Knutzen, K.M., Derrick, T.: Biomechanical basis of human movement (2014)
2. Chaturvedi, S., Kumar Bharti, P., Nadeem Akhtar, S.: Metal-on-Metal hip prostheses lubrication analysis for Newtonian elastohydrodynamic fluid. Mater. Today Proc. **46**, 6859–6866 (2021)
3. Tauviqirrahman, J.M., Muchammad, H.R.H.: Effect of surface texturing on the performance of artificial hip joint for Muslim prayer (Salat) activity. Biotribology **26**, 100177 (2021)
4. Nečas, D., Vrbka, M., Galandáková, A., Křupka, I., Hartl, M.: On the observation of lubrication mechanisms within hip joint replacements. Part I: Hard-on-soft bearing pairs. J. Mech. Behav. Biomed. Mater. **89**(2018), 237–248 (2019)
5. Nečas, D., Vrbka, M., Gallo, J., Křupka, I., Hartl, M.: On the observation of lubrication mechanisms within hip joint replacements. Part II: Hard-on-hard bearing pairs. J. Mech. Behav. Biomed. Mater. **89**(2018), 249–259 (2019)
6. Myant, C., Cann, P.: On the matter of synovial fluid lubrication: implications for Metal-on-Metal hip tribology. J. Mech. Behav. Biomed. Mater. **34**, 338–348 (2014)
7. Ruggiero, A., Sicilia, A.: Lubrication modeling and wear calculation in artificial hip joint during the gait. Tribol. Int. **142**(2019), 105993 (2020)
8. Jamari, J., Anwar, I.B., Saputra, E., van der Heide, E.: Range of motion simulation of hip joint movement during salat activity. J. Arthroplasty **32**(9), 2898–2904 (2017)
9. Oates, K.M.N., Krause, W.E., Jones, R.L., Colby, R.H.: Rheopexy of synovial fluid and protein aggregation. J. R. Soc. Interface **3**(6), 167–174 (2006)
10. Gao, L., Dowson, D., Hewson, R.W.: A numerical study of non-Newtonian transient elastohydrodynamic lubrication of metal-on-metal hip prostheses. Tribol. Int. **93**, 486–494 (2016)

Finite Element Analysis of a Walkable Chair Design for Surgeon

Syahibudil Ikhwan Abdul Kudus[1]([✉]), Ng Zhen Xiong[1], Masjuri Musa Othman[2], Mohd Khairi Mohamed Nor[3], and Yudhi Ariadi[4]

[1] Fakulti Teknologi Kejuruteraan Mekanikal & Pembuatan, Universiti Teknikal Malaysia Melaka, Hang Tuah Jaya, 76100 Durian Tunggal, Melaka, Malaysia
syahibudil@utem.edu.my

[2] Fakulti Kejuruteraan Mekanikal, Universiti Teknikal Malaysia Melaka, Hang Tuah Jaya, 76100 Durian Tunggal, Melaka, Malaysia

[3] Fakulti Kejuruteraan Mekanikal, Universiti Teknikal Malaysia Melaka, Hang Tuah Jaya, 76100 Durian Tunggal, Melaka, Malaysia

[4] School of Mechanical, Aerospace and Automotive Engineering, Coventry University, 3 Gulson Road, Coventry CV1 2JH, UK

Abstract. Muscular strain and fatigue are always associated with prolonged standing and causing an increased risk of musculoskeletal disorders among surgeons. Lack of ergonomic awareness and aging in the population also further increases the risk of musculoskeletal disorders. This paper analysed the design of a walkable chair that straps to surgeons' lower extremities to support their weight while performing surgical operations in a half-sitting posture through finite element analysis. Nonlinear static analysis is carried out to analyse the design by using Solidworks. Design optimisation is also implemented to ensure the walkable chair is functional under a desired applied load. In this analysis, the 6061-T6 aluminium alloy was selected as the main material due to its high strength-to-weight ratio and excellent corrosion resistance. The result showed 61.54 MPa of maximum von Mises stress located at the joint support component after the walkable chair is subjected to 50 kg of applied load per extremity. While other components bear lesser von Mises stress compared to joint support. Based on the result, a 4.47 value factor of safety is calculated, and this indicated the structural design can sustain four times the maximum von Mises stress without fail.

Keywords: Finite element analysis · Walkable chair · Surgeon

1 Introduction

A surgeon is a medical practitioner who is qualified to perform surgery activities such as transplant surgery, cardiac surgery and neurological surgery. Surgeons and their assistants such as nurses and surgical technologists need to diagnose and treat a wide range of diseases and they are required to work under prolonged hours with significant pressure dealing with various subspecialties. The average operating hours of surgeons in Malaysia was 4.78 hours a day, and a significant variation of operating hours ranged

from 2.21 to 13.60 hours per surgeon in a week [1]. Standing in prolonged hours could cause muscle fatigue [2]. Therefore, surgeons will experience work burnout and suffer muscular fatigue and pain, especially in their lower extremities. Although the prevalence of musculoskeletal disorders among surgeons is well-recognized, the majority of surgeons did not practice good working posture and had a low rate of ergonomic awareness that leads to an increase in the risk level of musculoskeletal disorders [3]. Sometimes, surgeons are extremely attentive during lengthy surgery and do not notice their uncomfortable standing posture. Prolonged standing does cause muscular fatigue and decreases surgical accuracy [4].

To solve the aforementioned problems, a walkable chair can be designed to help surgeons by supporting their lower extremities during surgical operations. Although there are walkable chairs or other similar exo-chair products that are commercially available, it was not designed to meet a specific requirement for surgeons and medical staff. A walkable chair for surgeons is a passive exoskeleton that is designed to strap to surgeons' lower body limbs to support them in a half-sitting position and allow them to actively switch between sitting, standing and walking at any time in their daily working conditions. Several studies found that the exoskeleton that assists or supports human lower body limbs can reduce muscle strain and fatigue [5]. Therefore, attention is needed to reduce these effects among medical professionals [6]. Hence, this paper aims to analyse the design of a walkable chair that allows a surgeon to sit on while performing surgeries. Finite element analysis is used to determine the stress distribution of a model at every meshed element through simulation. The structural deformation behaviour can be evaluated also to identify possible failures after the design model is subjected to an applied load.

2   Methodology

The following steps were taken to design a walkable chair for surgeons and to evaluate the design.

i.   Product design research - Gather information and secondary data related to the walkable chair and also the limitations to satisfy the design outcome. Design criteria are determined in this phase.
ii. Embodiment design - Preliminary design is illustrated in this phase. This phase includes design parameters, function and material selection to design a walkable chair that meets the requirements in this study.
iii. Detail design - This phase includes detailed drawings, product specifications and a bill of material (BOM). The final design is generated as the result of this phase by using Solidworks software.
iv. Product design analysis - Nonlinear static analysis is conducted by using Solidworks software to analyse the walkable chair design to ensure it is functional under desired applied loads without fail. The shape of deformation, von Mises stress and factor of safety are evaluated in this phase.
v.   Design optimisation - Detail design and product design analysis are repeated in this phase to modify the design to make further improvements.

The main aspects of this paper are product design analysis and design optimisation. Finite element analysis has been highlighted in this study to analyse and verify the final design of a walkable chair that can sustain the maximum applied weight without fail. In the analysis stage, all contact surface areas between each component are selected as no penetration contact which means the model is not bonded as one component and allows stress to transfer from one to another through the contact area to simulate real-world behaviour. Pins with retaining rings are also added to allow rotational movement but the axial movement is restricted. Through simulation and illustration of von Mises stress, design optimisation can be applied to achieve the expected result. Improve the geometry of structural components such as chamfering the holes, eliminating sharp corners and increasing cross-section area to reduce the stress concentration.

3   Result and Discussion

Several design criteria have been identified to design the walkable chair that is suitable to use in an operating room. Such as ergonomic, lightweight, 150° body-thigh sitting posture, able to support 100 kg human weight and adjustable sitting pad. 6061-T6 aluminium alloy is selected as the main material to develop the walkable chair because of its high strength-to-weight ratio which minimizes the burden on surgeons while wearing it. It has 310 MPa tensile strength, 275 MPa yield strength and 2700 kg/m^3 mass density. It also has an excellent corrosion resistance that satisfies daily disinfection and sterilization whereby corrosive cleaning agent is generally used to maintain a clean and hygienic operating room environment.

3.1   Walkable Chair Design

A walkable chair is a passive exoskeleton that does not require electronic devices or power to operate. This eliminates the potential risk of electronic devices affecting other medical devices in an operating room. Surgeons can wear the walkable chair with the use of thigh straps and the thigh pad is designed to be adjustable according to the surgeon's comfort. The walkable chair uses a simple mechanical design. When surgeons want to sit down, the end of the lower leg will be in contact with the ground. Then, the upper leg moves backward and downward until the joint support touches the top surface of the lower leg. This will restrict the movement and the walkable chair will support the applied weight. Surgeons will adopt a 150° body-thigh sitting angle with a half-sitting posture and the sitting height is approximately 770 mm. The mass of the walkable chair is estimated to be 2.43 kg per extremity. This design gives a lesser weight to the walkable chair, thereby reducing the burden on surgeons. Table 1 shows components of the walkable chair, while Fig. 1 shows the final design of the walkable chair.

As for the design, the length of the upper leg is 344.6 mm with 50.8 mm width and 52.5 mm height. While the length of the lower leg is 427.37 mm with 50.8 mm width and 49.71 mm height. Both upper leg and lower leg are connected by a linkage and joint support. The linkage is an L-shaped design structure that helps to limit the forward movement of the lower leg and avoid hitting surgeons' legs. The length of linkage is 72 mm with 50 mm width and 75 mm height. While the joint support is designed to

Table 1. Components of the walkable chair.

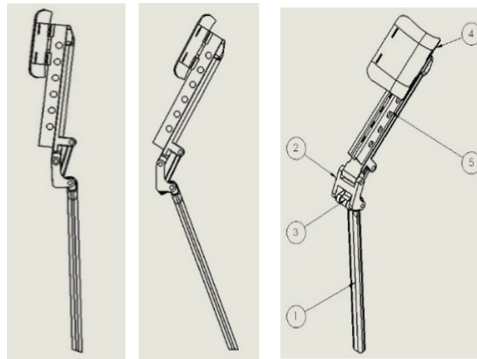| No.	Part name
1	Lower leg
2	Linkage
3	Joint support
4	Thigh pad
5	Upper leg

Fig. 1. The final design of the walkable chair.

support and provide a 150° body-thigh sitting angle. This helps surgeons to smoothly sit at the half-sitting position without using their hands to adjust it. The length of joint support is 119 mm with 25.4 mm width and 18 mm height. Each of the components is assembled by 10 mm diameter of the pin. Furthermore, the length of the thigh pad is 160 mm with 140 mm width and 74.5 mm height. The thigh pad is mounted on the upper leg with a 15 mm diameter of the pin and it is adjustable. The upper leg consists of 6 holes with a 40 mm gap between each hole. This allows surgeons to move the thigh pad according to their comfort when strapping to their thighs. The final design of the walkable chair is designed and illustrated by using Solidworks software.

3.2 Finite Element Analysis

With 100 kg human weight, the weight is divided equally to 50 kg per extremity and the applied force is 490.5 N.

$$Applied\ force = \frac{100\ kg}{2} \times \frac{9.81\ N}{1\ kg}$$

$$= 490.5\ N$$

Nonlinear static analysis is an analysis where a nonlinear relation holds between applied forces and displacement. It is used while large deformation is considered or

changes in physical contact and allows stress transfer between structural components. Therefore, nonlinear static analysis is more accurate to select to simulate the design model in this study by using Solidworks software. The thigh pad is mounted to the hole at the highest height in the simulation analysis and this will produce the largest force in the structure when a total of 490.5 N force is applied on the surface of the thigh pad. This is because the longer the moment arm, the greater the force acting on the joint axis through leverage. Furthermore, the final state of sitting weight is acting vertically downward, the same as the direction of gravity. Hence, the direction of applied force in the analysis is vertically downward on the surface of the thigh pad. Due to material selection, von Mises stress is the criterion for yielding and it is valid to determine the yielding of 6061-T6 aluminium alloy while subjected to a given load condition for this analysis. Figure 2 shows the change of displacement and stress accumulated at the critical component. Table 2 shows the maximum von Mises stress and displacement for each component.
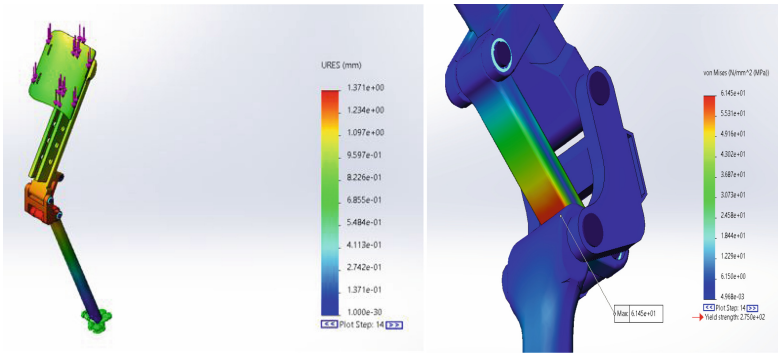
Fig. 2. Result change of displacement and stress accumulated at the critical component.

Table 2. Maximum von Mises stress and displacement for each component.

Part name	Maximum von mises (MPa)	Maximum displacement (mm)
Lower leg	27.55	1.360
Linkage	4.860	1.329
Joint support	61.54	1.371
Thigh pad	22.85	1.043
Upper leg	14.05	1.285

Based on the result shown in Fig. 2, the maximum von Mises stress is 61.54 MPa and it is located at the joint support component. This indicates the joint support is the main member of the structure and needs to bear the major distribution of forces whereby

greater stresses are located at the contact area between joint support and the lower leg. By increasing the cross-section area and fillet radius, stress concentration can be further reduced. However, it does not exceed the yield strength of 6061-T6 aluminium alloy which is 275 MPa. Moreover, the maximum change of displacement is 1.371 mm which is also located at the joint support component after the load is applied in the analysis. The factor of safety for the design is 4.47 and the joint support is the only critical component that needs to pay more attention to during designing the walkable chair and design optimisation. While other components sustained much lesser von Mises stress compared to the joint support. This indicates the design structure can withstand 50 kg of load per extremity without fail. The factor of safety is acceptable because the aluminium alloy is a ductile material and the maximum von Mises stress did not exceed the yield strength of the material.

$$Factor\ of\ safety = \frac{275\,\text{MPa}}{61.54\,\text{MPa}}$$
$$= 4.47$$

4   Conclusion

In this study, the design of the walkable chair can bear major human weight and could withstand 100 kg of applied load without fail. The calculated value of the factor of safety is 4.47 and this indicates the design model will fail under four times the design load. Hence, the design model is safe to sit on and it also meets the desired result whereby the structural components will not undergo plastic deformation after being subjected to the desired load. Furthermore, the adjustable sitting thigh pad allows surgeons to strap on their thighs according to their comfort, making the walkable chair more ergonomic. The simple mechanism design also minimizes the burden on the surgeons. Due to daily disinfection and sterilization in an operating room, 6061-T6 aluminium alloy can be anodized to increase the surface protection to resist corrosive cleaning agents, thereby enhancing corrosion resistance. It is easy to manufacture and less expensive in fabricating a prototype. This study allows researchers and designers to develop a better and safer walkable chair design for surgeons to use to reduce the risk of musculoskeletal disorders. The operating room environment, rules and regulations and safety guidelines need to be considered and evaluated before developing a walkable chair for surgeons. Thus, a prototype can be developed and tested to make continuous improvements.

References

1. Harjit, S., et al.: Surgical services in Malaysian hospitals. National Healthcare Establishment and Workforce Statistics 2011, pp. 59–72 (2011)

2. Halim, I., Omar, A.R., Saman, A.M., Othman, I.: Assessment of muscle fatigue associated with prolonged standing in the workplace. Saf. Health Work **3**(1), 31–42 (2012)
3. Aaron, K.A., et al.: The risk of ergonomic injury across surgical specialties. PLoS ONE **16**(2), 1–13 (2021)
4. Dorion, D., Darveau, S.: Do micropauses prevent surgeon's fatigue and loss of accuracy associated with prolonged surgery? An experimental prospective study. J. Vasc. Surg. **57**(4), 1173 (2013)
5. Yan, Z., Han, B., Du, Z., Huang, T., Bai, O., Peng, A.: Development and testing of a wearable passive lower-limb support exoskeleton to support industrial workers. Biocybern. Biomed. Eng. **41**(1), 221–238 (2021)
6. Permarupan, Y.Y., Al Mamun, A., Samy, N.K., Saufi, R.A., Hayat, N.: Predicting nurses burnout through quality of work life and psychological empowerment: a study towards sustainable healthcare services in Malaysia. Sustainability **12**(1), 388 (2020)

The Effect of Half-Circle Slot Depth on Eddy Current Brake Performance Using the Finite Element Method

Sulthan Gumay[1] , Dominicus Danardono Dwi Prija Tjahjana[1,2(✉)],
Muhammad Nizam[2,3,4] , and Mufti Reza Aulia Putra[1]

[1] Mechanical Engineering Department, Universitas Sebelas Maret, Jl. Ir. Sutami 36A, Surakarta 57126, Indonesia
danar1405@gmail.com

[2] National Center for Sustainable Transportation Technology (NCSTT) ITB, Bandung 40132, Indonesia

[3] Electrical Engineering Department, Universitas Sebelas Maret, Jl. Ir. Sutami 36A, Surakarta 57126, Indonesia

[4] Lithium Battery Research and Technology Centre, Universitas Sebelas Maret, Jl. Slamet Riyadi 435, Surakarta 57146, Indonesia

Abstract. This study discusses the Eddy Current Brake (ECB) system with the application of electromagnets. Half-circle slots will be applied on the surface of the ECB conductor to further investigate its effect on the resulting torque value. This study uses the Finite Element Method (FEM) in the simulation process of the ECB system with variations in the depth of the half circle slots of 0.5, 0.6, 0.7, 0.8, and 0.9 mm. The results of the study showed that the highest braking torque value was 15.139 Nm produced by slot depth variations of 0.7 mm at a rotary speed of 450 rpm and the smallest torque was 8.557 Nm, produced by a variation of 0.5 mm in slot depth at 150 rpm. The results also indicate that there is an effect of the depth of the half circle slot on the braking torque value produced by the ECB system, although it is not significant.

Keywords: Eddy Current Brake · Half-circle slotted · Finite Element Method (FEM) · Electromagnet

1 Introduction

Eddy Current Braking is a type of electric braking that generates braking forces using eddy currents [1]. Eddy currents are induced currents caused by changes in a conductor's magnetic field. Because the ECB braking system does not require friction, these brakes are much easier to maintain than traditional brakes. This is due to the fact that the ECB brake has no wear rate, makes no noise, and responds quickly [2]. Putra et al. studied single disk axial ECB utilizing semi-permanent magnets and varying the number of coils and air gaps, finding that braking torque is directly proportional to the number of coils, while it is inversely proportional to the air gap [3]. Sattarov et al. experimented with

ECB by comparing solid conductors and slotted conductors and concluded that slotted conductors have a 10–20% higher braking torque than solid conductors [4]. Prayoga et al. conducted research on the influence of some slot shapes on the aluminum conductor disk, resulting in the half-circle slotted conductor disk having the highest torque compared to other slot shapes [5].

Many researches in the field of ECB have been carried out, including variations in air gaps, conductor materials, and the shape of the contour disk of the conductor. In this study, a magnetic field simulation of an electromagnet as a stator and a disk conductor as a rotor was carried out by varying the depth of half-circle slots which had never been developed before. This research is expected to improve the performance of the ECB.

2 Methodology

The ECB's performance was modeled using the Finite Element Method (FEM) in this study. The data obtained throughout the simulation process took the shape of a trend curve, which described the relationship between the parameters and the ECB's performance. The variation used in this simulation is the depth half-circle type slots in a certain rotational speed to see how they affected the ECB's performance. The depth of the slots that were tested in this research was 0.5, 0.6, 0.7, 0.8, and 0.9 mm, with slot width and the number of slots used being constant in each variation. The design that will be used in the research can be seen in Fig. 1.

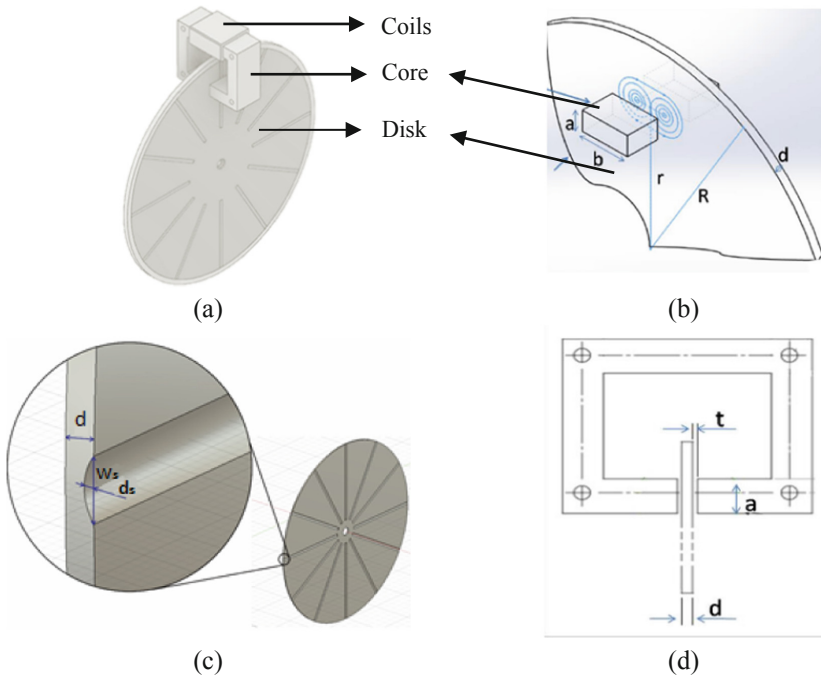(a)   (b)

(c)   (d)

Fig. 1. (a) 3D model ECB; (b) Eddy current and design variable [6]; (c) Half-circle slot dimension; (d) Air gap in cross section area [6].

3   Result and Discussion

The relationship between braking torque and rotational speed is shown in Fig. 2. The simulation results are plotted as a parabolic curve, with the peak of the curve at 450 rpm. This is due to the ECB's use of an aluminum or non-ferrous metal conductor disk with a braking torque characteristic that causes a critical speed and tends to decrease the braking torque when the rotary speed passes the critical speed [7]. The appearance of the skin effect causes a decrease in braking torque at high speeds. The skin effect is the accumulation of electrons in the conductor's skin, which is focused in the conductor's skin [6]. Figure 2 shows that the variation of half-circle slot depth has a slight effect on the braking performance of the ECB (less than 1 Nm or about 3–7%). The highest braking torque is 15.139 Nm that is generated by 0.7 mm slot depth at 450 rpm and the smallest braking torque is 8.557 Nm, which is generated by 0.5 mm slot depth at 150 rpm.
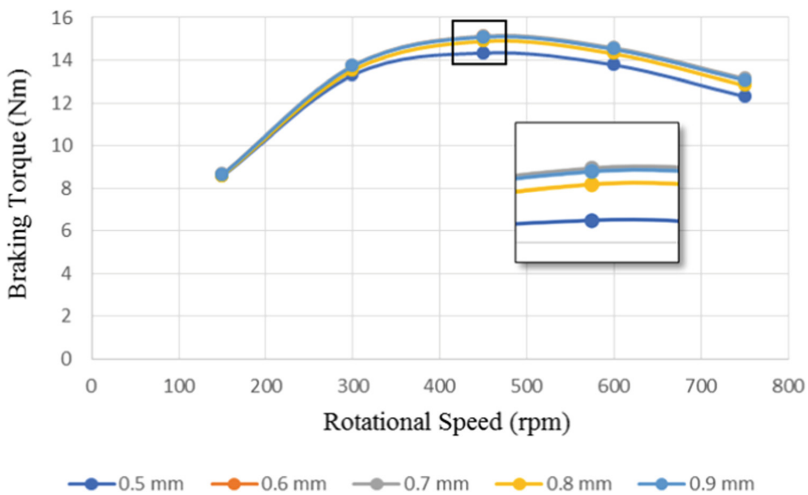
Fig. 2. The relationship between braking torque and rotational speed.

4   Conclusion
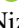
From the research conducted, the braking torque value on the ECB is affected by the depth of the half-circle type slot variation of 0.5, 0.6, 0.7, 0.8, and 0.9 mm, but the difference is not too significant. The greatest braking torque value is produced in the variation of the depth of the half circle type slot with a depth of 0.7 mm at a rotational speed of 450 rpm, which is 15.139 Nm. The smallest torque value is 8.557 Nm, which is obtained by varying the depth of a half circle type slot with a depth of 0.5 mm at a speed of 150 rpm. For each variation of the rotational speed used in this research, the slot with a depth of 0.7 mm produces the highest braking torque value.

References

1. Lequesne, B.: Eddy-current machines with permanent magnets and solid rotors. IEEE Trans. Ind. Appl. **33**(5), 1289–1294 (1997). https://doi.org/10.1109/28.633808
2. Karakoc, K., Suleman, A., Park, E.J.: Analytical modeling of eddy current brakes with the application of time varying magnetic fields. Appl. Math. Model. **40**(2), 1168–1179 (2016). https://doi.org/10.1016/j.apm.2015.07.006
3. Putra, M., Nizam, M., Tjahjana, D.D.D.P., Ubaidillah, A.M., Choirunisa, I.: Design study in single disk axial eddy current brake. In: Proceeding - 2018 5th International Conference on Electric Vehicular Technology, ICEVT 2018, pp. 158–160 (2019). https://doi.org/10.1109/ICEVT.2018.8628358
4. Sattarov, R.R., Fedosov, E.M., Tumanov, A.A., Ismagilov, R.R.: Experimental studies of torque-speed characteristics of eddy current brakes with slotted disk rotor. In: 2019 International Conference on Industrial Engineering, Applications and Manufacturing, ICIEAM 2019, pp. 1–5 (2019). https://doi.org/10.1109/ICIEAM.2019.8743071
5. Prayoga, A.R., Nizam, U.M., Waloyo, H.T.: The influence of aluminum conductor shape modification on eddy-current brake using finite element method. In: ICEVT 2019 - Proceeding International Conference on Electric Vehicular Technology, pp. 146–150 (2019). https://doi.org/10.1109/ICEVT48285.2019.8994005
6. Waloyo, H.T., Ubaidillah, U., Tjahjana, D.D.D.P., Nizam, M., Aziz, M.: A novel approach on the unipolar axial type eddy current brake model considering the skin effect. Energies **13**(7), 1–15 (2020). https://doi.org/10.3390/en13071561
7. Putra, M.R.A., Nizam, M., Tjahjana, D.D.D.P., Aziz, M., Prabowo, A.R.: Application of multiple unipolar axial eddy current brakes for lightweight electric vehicle braking. Appl. Sci. **10**(13) (2020). https://doi.org/10.3390/app10134659

Analysis of Addition the Number of Half Circle Type Slot on Performance Characteristics of Disc Conductor Eddy Current Brake

Alfian Jihan Saputra[1] , Dominicus Danardono Dwi Prija Tjahjana[1,2(✉)],
Muhammad Nizam[2,3,4] , and Mufti Reza Aulia Putra[1]

[1] Mechanical Engineering Department, Faculty of Engineering, Universitas Sebelas Maret, Jl.
Ir. Sutami 36A, Surakarta 57126, Indonesia
danar1405@gmail.com

[2] National Center for Sustainable Transportation Technology (NCSTT) ITB, Bandung 40132,
Indonesia

[3] Electrical Engineering Department, Faculty of Engineering, Universitas Sebelas Maret, Jl. Ir.
Sutami 36A, Surakarta 57126, Indonesia

[4] Lithium Battery Research and Technology Centre, Universitas Sebelas Maret, Jl. Slamet
Riyadi 435, Surakarta 57146, Indonesia

Abstract. Brake is a vital component of a vehicle, particularly for motor vehicles.
One of the braking used the principle of Eddy Current Brake (ECB) by utilizing
electromagnetic. ECB is a braking technology without direct contact by utilizing
eddy currents. ECB performance can be influenced by several factors, one of them
is the surface shape of the disc conductor. Using finite element simulation, this
research examines the impact of increasing the number of slot half-circles on the
performance of the ECB with the number of slot changes. Variations number of
slots that used are 6, 8, 10, and 12 slots. The result of this study obtained the best
braking torque value in the variation with the number of 10 slots at a rotational
speed of 450 rpm with a 15,930 Nm torque value. The addition slots of the number
of half-circle types have a less significant effect on the torque from the simulation.

Keywords: Eddy Current Brake (ECB) · Finite Element Method (FEM) ·
Half-circle slotted

1 Introduction

Vehicles currently use a lot of conventional brakes to slow down the speed and the most
common types of brakes are drum brakes and disc brakes. The working principle of the
two types of brakes is to use the friction principle. The friction will reduce the speed until
the vehicle stops. However, the friction between the two objects will almost definitely
produce an increase in temperature surrounding the brakes [1].

To solve the problem of friction-based braking systems, contactless braking systems
have been developed. One of them is the ECB [2]. ECB does not produce wear, makes
little noise, and responds quickly [3]. Cho, et al. in his research about the design of eddy

current brakes to replace conventional brakes with ECB [4]. Robert, et al. analyze the surface design of disc conductors by adding slots. The addition of the number of slots in this research affects the resulting braking torque. The results showed that the torque of the brakes with slotted disk rotor is more the torque of the brake with plain rotor in 1.1–1.2 times [5]. Prayoga et al. investigate the form of the conductor's slot surface. In comparison to other shapes, the conductor disc with a half-circle shape has the maximum torque value [6]. In this research, research will be carried out with variations in the number of slots on the half-circle type conductor disc. The problem to be solved in this research is how the number of slots on a half-circle type conductor disc affects the braking torque of an Eddy Current Brake with a single magnet.

2   Methodology

The simulation methodology in this work employs the finite element method (FEM). Fusion 360 software is used for modeling, and Ansys Electronics 2018 is used for simulation. The simulation data is shown in the form of a curve representing the rotational speed and braking torque generated for each modification. Variations in the number of half-circle slots employed in this study included 6, 8, 10, and 12 slots. Another difference is the disc rotation speed, which can range from 150 to 750 rpm. Figure 1 shows the design that will be used in the simulation.
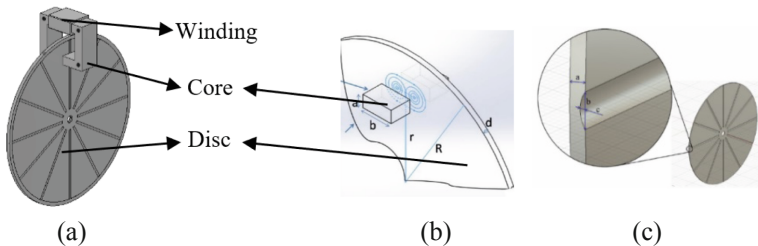
Fig. 1. (a) 3D Design ECB, (b) Eddy Current Design Variable [7], (c) Aluminium disc slot dimension.

3   Result and Discussion

The highest braking torque value for each modification in the number of slots is shown in Table 1 at a speed of 450 rpm. The highest braking torque value produced is 10 slots at a speed of 450 rpm, which is 15.93 Nm. As the rotational speed increases beyond 450 rpm, the resulting data tends to decrease. This is due to the nature and features of the non-ferrous disc conductor, specifically aluminum, which causes a critical speed point to appear during the braking process [8].

Figure 2 depicts the relationship between braking torque and rotational speed. The graph shows that each variation in the number of slots has a nearly same graph pattern. Figure 2 demonstrates that when the number of slots increases from 6 to 8 to 10, the

Table 1. The results of ECB simulation.

No	Rotating speed (rpm)	Braking torque (Nm)			
		6 Slots	8 Slots	10 Slots	12 Slots
1	150	8,86	8,99	9,18	9,02
2	300	14,09	14,27	14,51	14,26
3	450	15,52	15,71	15,93	15,72
4	600	14,93	15,12	15,30	15,07
5	750	13,66	13,70	3,80	13,63

brake torque value increases. However, when 12 slots are added to the conductor disc, the resulting brake torque value in 12 slots falls short of the value in 10 slots. The graph tends to indicate a diminishing trend after passing the 450 rpm mark. This occurs as a result of the skin effect [7]. The braking torque on the rotational speed will be affected by the skin effect. The addition of half-circle type conductor disc slots to the ECB braking system has only a little impact on the ECB's braking performance.
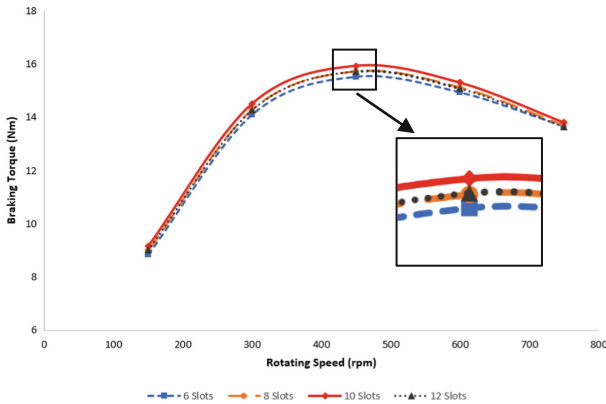
Fig. 2. The relationship between braking torque and rotational speed.

Calculation of braking is done by braking force when the vehicle slows down from a certain speed. The calculation is only to prove the characteristics of the modeling process used, namely regarding the effect of adding a conductor disk slot. At the next stage the braking process can be analyzed with several additional parameters such as rolling resistance, etc.

4   Conclusion

From this research, it can be concluded that the addition of a half-circle type slot with a slot variation of 6, 8, 10, and 12 slots does not have a significant effect on the torque generated from the simulation. The highest braking torque value is produced by a variation

of 10 slots at a rotational speed of 450 rpm with a torque of 15.93 Nm. The lowest torque value is produced by a variation of 6 slots at a rotational speed of 150 rpm with a torque of 8.86 Nm. The higher the rotational speed, the resulting area will also widen because the magnetic field strength will spread further and is influenced by the skin effect that appears at high speeds which can reduce the amount of braking torque.

References

1. Gerdes, J.C., Hedrick, J.K.: Brake system modeling for simulation and control. J. Dyn. Syst. Meas. Control. Trans. ASME **121**(3), 296–503 (1999). https://doi.org/10.1115/1.2802501
2. Putra, M.R.A., Nizam, M., Tjahjana, D.D.D.P., Aziz, M., Prabowo, A.R.: Application of multiple unipolar axial eddy current brakes for lightweight electric vehicle braking. Appl. Sci. **10**(13) (2020). https://doi.org/10.3390/app10134659
3. Cho, S., Liu, H.C., Ahn, H., Lee, J., Lee, H.W.: Eddy current brake with a two-layer structure: calculation and characterization of braking performance. IEEE Trans. Magn. **53**(11) (2017). https://doi.org/10.1109/TMAG.2017.2707555
4. Cho, S., et al.: Design and analysis of the eddy current brake with the winding change. J. Magn. **22**(1), 23–28 (2017). https://doi.org/10.4283/JMAG.2017.22.1.023
5. Robert, R.S.: 2D model of axial-flux eddy current brakes with slotted conductive disk rotor. In: 2017 International Siberian Conference on Control and Communications SIBCON 2017 - Proceedings, pp. 0–5 (2017). https://doi.org/10.1109/SIBCON.2017.7998501
6. Prayoga, A.R., Nizam, U.M., Waloyo, H.T.: The influence of aluminum conductor shape modification on eddy-current brake using finite element method. In: ICEVT 2019 - Proceeding 6th International Conference on Vehicle Technology 2019, pp. 146–150 (2019). https://doi.org/10.1109/ICEVT48285.2019.8994005
7. Waloyo, H.T., Ubaidillah, U., Tjahjana, D.D.D.P., Nizam, M., Aziz, M.: A novel approach on the unipolar axial type eddy current brake model considering the skin effect. Energies **13**(7), 1–15 (2020). https://doi.org/10.3390/en13071561
8. Kou, B., Jin, Y., Zhang, H., Zhang, L., Zhang, H.: Modeling and analysis of force characteristics for hybrid excitation linear eddy current brake. IEEE Trans. Magn. **50**(11) (2014). https://doi.org/10.1109/TMAG.2014.2323334

The Effect of Changes in Half Circle Type of Slot Width on Unipolar Axial Eddy Current Brake Conductor

Muhammad Satria Yudha Mahendra[1],
Dominicus Danardono Dwi Prija Tjahjana[1,2(✉)], Muhammad Nizam[2,3,4],
and Mufti Reza Aulia Putra[1]

[1] Mechanical Engineering Department, Faculty of Engineering, Universitas Sebelas Maret, Jl. Ir. Sutami 36A, Surakarta 57126, Indonesia
danar1405@gmail.com

[2] National Center for Sustainable Transportation Technology (NCSTT) ITB, Bandung 40132, Indonesia

[3] Electrical Engineering Department, Faculty of Engineering, Universitas Sebelas Maret, Jl. Ir. Sutami 36A, Surakarta 57126, Indonesia

[4] Lithium Battery Research and Technology Centre, Universitas Sebelas Maret, Jl. Slamet Riyadi 435, Surakarta 57146, Indonesia

Abstract. Eddy Current Brake (ECB) is an innovation in the braking system by utilizing the eddy current generated by induction when the rotor rotates due to the magnetic field generated by the stator. The development of the ECB braking system is needed to provide a better design overview from existing research. This study discusses the effect resulting from the use of half circle type slots on the surface of the disc conductor on the braking torque generated in light vehicles. This research uses Finite Element Method (FEM) in the ECB modeling process. The variations used are the width of the half circle type slots of 2, 3, 4, 5, 6, 8 and 10 mm. The results obtained from this study are the greatest braking torque value occurs in the 5 mm slot width in each rotational speed variation. The results of the study show that there is an effect of changing the width of the half circle type slot on the braking torque produced by the ECB braking system but the resulting value is not significant.

Keywords: Eddy Current Brake · Half-circle slotted · Finite Element Method (FEM) · Electromagnet

1 Introduction

Vehicle accidents often occur due to failure of the braking system. Braking system failure usually occurs because the brake lining wears out which causes a loss of pressure to apply braking [1]. Eddy Current Brake (ECB) is one of the technology developments used in vehicle braking systems. The ECB utilizes electrical energy to perform braking. The use of ECB can improve braking performance compared to friction braking such as, fast

response time, braking without direct contact, not causing wear due to friction, and does not make noise [2].

Research on ECB has been carried out using both simulation and experimental methods. Sattarov [3], conducted experimental research on ECB by varying the conductors using slots or grooves. Slotted conductors shows that the braking torque on slotted conductors is 10–20% greater than that of solid conductors. Prayoga [4], conducted research by varying the surface shape of the conductor with aluminum and mid iron materials and three variations of slot shape, sawtooth, square and half circle. The results of this study showed that variations in the shape of the half circle surface produce the largest torque. Putra [5], conducted both simulation and experimental research on the use of Multiple Unipolar Axial Eddy Current Brakes on light vehicles using semi-permanent magnets. It was found that with the compact design of the ECB that was made, it could reduce 93.66% of the braking torque.

Previous studies have investigated the ECB with variations in conductor material, variations in slot shapes and comparisons with solid conductors. The problem to be solved in this study is to determine the effect of changing the width of the half circle slot width on the braking torque of the unipolar axial eddy current brake.

2   Methodology

This research will be carried out by simulation using the finite element method (FEM). Variations used in this research are slot width and rotational speed. The width variations used are 2 mm, 3 mm, 4 mm, 5 mm, 6 mm, 8 mm and 10 mm. The rotational speed variations used are 150, 300, 450, 600 and 750 RPM. The slot depth and the number of slots used are constant in each variation is 0.5 mm and 12 slots respectively. The design that will be used in the research can be seen in Fig. 1.
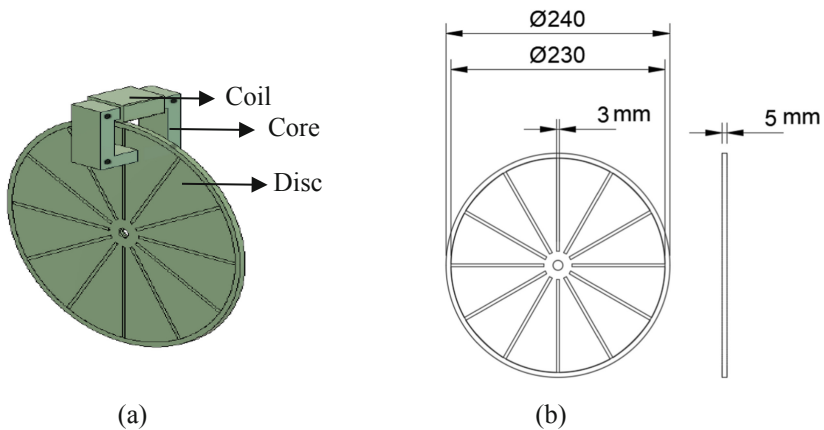

(a)   (b)

Fig. 1. (a) 3D Design ECB, (b) Conductor disc design with slots.

3   Result and Discussion

Figure 2 shows a graph of the comparison between braking torque and rotational speed for each variation used. The graph of the simulation results produces a parabolic graph, where braking torque increases from low rotational speed to 450 RPM and decreases after passing 450 RPM. This is because the use of a conductor disk material with aluminum or non-ferrous material on the ECB has a braking torque characteristic that produces a critical speed [6]. The decrease in braking torque at high speeds occurs due to the appearance of the skin effect. The skin effect is the phenomenon of the accumulation of electrons in the conductor which is concentrated in the skin of the conductor [7].
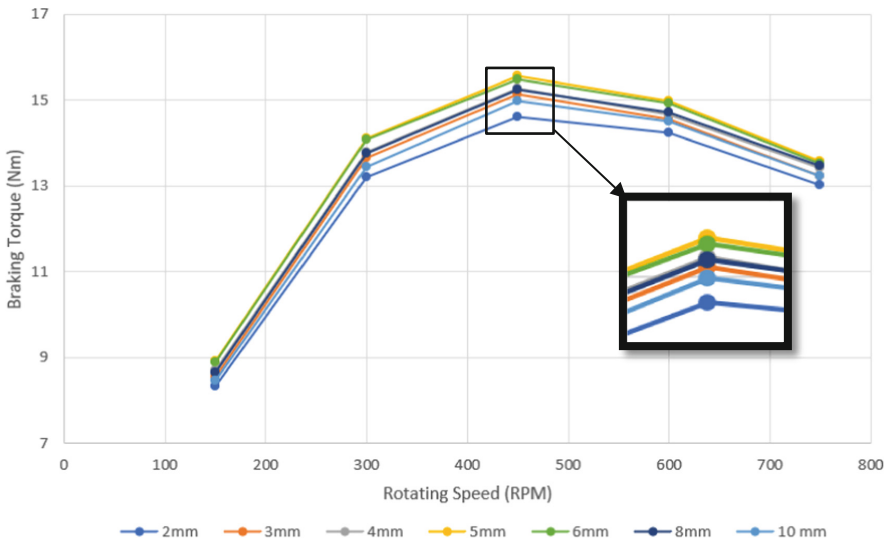
Fig. 2. The relationship between braking torque and rotational speed.

Table 1 describes the data from the simulations that have been carried out. In Table 1 the largest braking torque occurs at the 5 mm half circle slot width, which is 15.573 Nm at a rotational speed of 450 RPM. The lowest braking torque occurs at the width of the 2 mm half circle slot, which is 8.333 Nm at a rotating speed of 150 RPM. Half circle slots with a width of 5 mm have the largest trend of braking torque values in all variations of rotational speed compared to other simulated slot width variations, although the differences between variations are not too large.

Table 1. The results of ECB simulation.

Rotating speed (RPM)	Braking torque (Nm)						
	2 mm	3 mm	4 mm	5 mm	6 mm	8 mm	10 mm
150	8.333	8.555	8.695	8.919	8.881	8.657	8.455
300	13.195	13.645	13.794	14.114	14.089	13.755	13.444
450	14.613	15.137	15.280	15.573	15.490	15.246	14.974
600	14.248	14.566	14.657	14.981	14.932	14.714	14.496
750	13.012	13.241	13.425	13.587	13.514	13.477	13.238

4   Conclusion

From the research conducted, it can be concluded that the width of the half circle type slot with sizes of 2, 3, 4, 5, 6, 8 and 10 mm affects the braking torque value on the ECB although the difference is not too significant. The greatest braking torque value is produced in the variation of the width of the half circle type slot with a width of 5 mm at a rotational speed of 450 RPM, which is 15.573 Nm. The smallest torque value is produced in the variation of the width of the half circle type slot with a width of 2 mm at a speed of 150 RPM, which is 8.333 Nm. Of all the variations in width used, the slot width with a width of 5 mm produces the largest torque value for each variation of the rotational speed in this study.

References

1. Deepa, N., Dasmunshi, S., Verma, S., Shukla, A., Nanda, S.: Brake failure detection and electronic auxiliary braking system. Int. J. Eng. Technol. **7**(2.8), 350 (2018). https://doi.org/10.14419/ijet.v7i2.8.10439
2. Karakoc, K., Suleman, A., Park, E.J.: Analytical modeling of eddy current brakes with the application of time varying magnetic fields. Appl. Math. Model. **40**(2), 1168–1179 (2016). https://doi.org/10.1016/j.apm.2015.07.006
3. Sattarov, R.R., Fedosov, E.M., Tumanov, A.A., Ismagilov, R.R.: Experimental studies of torque-speed characteristics of eddy current brakes with slotted disk rotor. In: 2019 International Conference on Industrial Engineering, Applications and Manufacturing, ICIEAM 2019, pp. 1–5 (2019). https://doi.org/10.1109/ICIEAM.2019.8743071
4. Prayoga, A.R., Nizam, U.M., Waloyo, H.T.: The influence of aluminum conductor shape modification on eddy-current brake using finite element method. In: ICEVT 2019 - Proceeding 6th International Conference on Vehicle Technology 2019, pp. 146–150 (2019). https://doi.org/10.1109/ICEVT48285.2019.8994005
5. Putra, M.R.A., Nizam, M., Tjahjana, D.D.D.P., Aziz, M., Prabowo, A.R.: Application of multiple unipolar axial eddy current brakes for lightweight electric vehicle braking. Appl. Sci. **10**(13) (2020). https://doi.org/10.3390/app10134659

6. Waloyo, H.T., Ubaidillah, U., Tjahjana, D.D.D.P., Nizam, M., Koga, T.: Mini review on the design of axial type eddy current braking technology. Int. J. Power Electron. Drive Syst.**10**(4), 2198–2205 (2019). https://doi.org/10.11591/ijpeds.v10.i4.2198-2205
7. Waloyo, H.T., Ubaidillah, U., Tjahjana, D.D.D.P., Nizam, M., Aziz, M.: A novel approach on the unipolar axial type eddy current brake model considering the skin effect. Energies **13**(7) (2020). https://doi.org/10.3390/en13071561

Effect of Damping and Stiffness Constants on the Vibration Properties of Seismic Building: Simulation Approach

Aji Masa'id[1], Bhre Wangsa Lenggana[1], Ubaidillah[1(✉)], Fitrian Imaduddin[1], Yusep Muslih[2], Harjana[3], Gigih Priyandoko[4], and Fajri Sri Ardion[1]

[1] Department of Mechanical Engineering, Engineering Faculty, Universitas Sebelas Maret, Surakarta 57126, Indonesia
ajimasaidd@student.uns.ac.id, ubaidillah_ft@staff.uns.ac.id

[2] Department of Civil Engineering, Engineering Faculty, Universitas Sebelas Maret, Surakarta 57126, Indonesia

[3] Department of Physics, Mathematics and Natural Science Faculty, Universitas Sebelas Maret, Surakarta 57126, Indonesia

[4] Departement of Electrical Engineering, Universitas Widyagama Malang, Malang, Indonesia

Abstract. By utilizing additional smart dampening devices, semi-active vibration control is considered a powerful way of lowering the dynamic reactions of structures. The task is carried out by making diagrams in Simulink and the Matlab program. This is used to determine the natural frequency of a building and the vibration response that occurs in the building. In addition, the shape mode of a building model that will be tested with the application of damping devices can also be known. In this paper, simulation by Simulink will be elaborate to observe the effect of damping and stiffness constants on the vibration properties of a seismic building to evaluate shape mode and vibration response of structure model. The building simulation is a model of a four-story building. The response from the fourth floor achieved the highest peak displacement at 3.7 cm and reached stability with the longest time of 550 ms.

Keywords: Natural frequency · Shape mode · Vibration response

1 Introduction

Earthquakes are one of the natural disasters that often occur in several countries. This results in losses in the form of material, physical and mental [1]. These losses can be minimized by using several methods, one of which is the application of damping technology to building structures, such as residential buildings, office buildings, and bridges [2]. Viscous damping technology is quite popularly used to anticipate earthquakes [3].

However, before fabricating the prototype of the MR damper as a device that can be applied and tested, it is better to use a numerical approach to avoid fatal errors [4]. One approach that can be done is to use software such as Matlab [5]. This approach is carried out by making diagrams in Simulink and the Matlab program [6]. This is used

to determine the natural frequency of a building and the vibration response that occurs in the building [7].

This paper contributes a simulation approach to a model of a four-story building to observe the effect of damping and stiffness constants on the vibration properties of a seismic building to evaluate the shape mode and vibration response of the structure model.

2   Methodology

The design of the building structure model and the MR damper that have been determined both in terms of material and performance is an important part of the accuracy of the approach. The parameters that need to be considered, as shown in Table 1, greatly affect the results of the approach taken with Matlab.

Table 1. MR damper building structure parameters.

Parameter	Value	Unit
F_1	11.6	N
F_2	46.6	N
F_3	105	N
F_4	186.6	N
c	6.64	Ns/cm
$m_1 = m_2 = m_3 = m_4$	10	kg
$k_1 = k_2 = k_3 = k_4$	276.4	kg/s^2

Furthermore, the model of the building structure is changed in the form of a Simulink diagram. It aims to determine the vibration response and the value of the natural frequency of the building structure. Then the shape mode is known through a simple Matlab program with the specified parameters (Fig. 1).
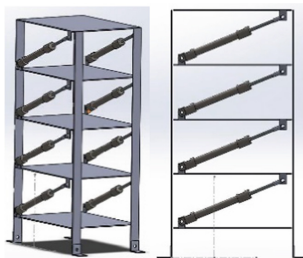

Fig. 1. Design of a four-story building.

The design of a four-story building is equipped with a damper on each floor. The dampers are installed diagonally and two dampers are installed on each floor.

3   Result and Discussion

After all of the parameters are entered into the MATLAB Simulink program, the simulation process is then carried out. One example of the results of the simulation approach is shown in the figure below (Fig. 2).
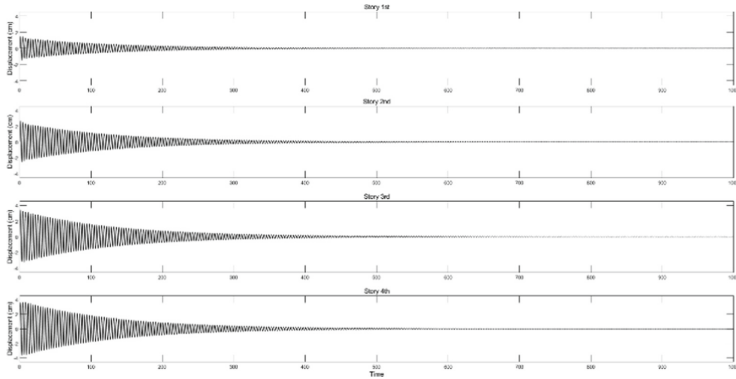

Fig. 2. Vibration response.

From the Figure, it can be seen the results of the Vibration Response from the first story to the fourth story. The results of the first Vibration Response Story obtained a peak displacement of 1,75 cm and reached stability at 400 ms. The second story has a peak displacement of 2,8 cm and reaches stability after 500 ms. The third and fourth stories obtained almost the same peak displacement at 3.5 cm and 3.7 cm, respectively, and reached stability after 550 ms for the third story and 570 ms for the fourth story, respectively (Fig. 3).
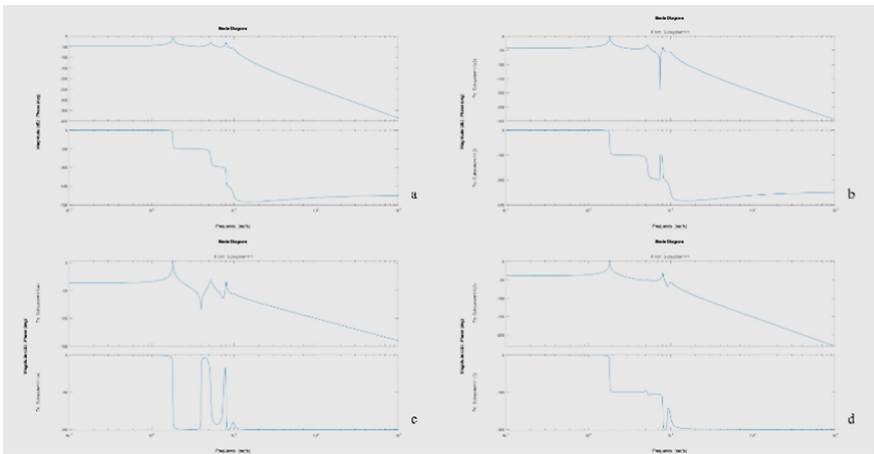

Fig. 3. Simulink Bode Plot Result (a) 1st Story (b) 2nd Story (c) 3rd Story (d) 4th Story.

Next is shown in the Figure Bode Plot of each floor which is represent the actual behaviour of the building for a given condition, Figures (a) through (d) showing the first through fourth floors, respectively. The Bode Plot is a combination of magnitude, expressing the magnitude of the frequency response, and a phase plot, expressing the phase shift. Both quantities are plotted about the horizontal axis proportional to the logarithm of the frequency (Fig. 4).
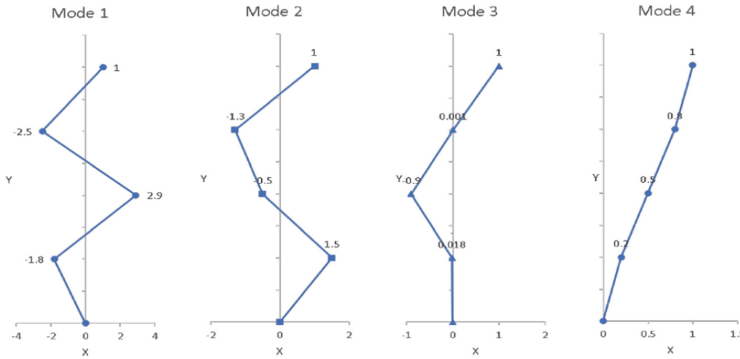

Fig. 4. Structure shape mode.

The Figure above shows several forms of vibration mode, obtained from the equation of motion that affects the stiffness of the building structure k, mass m, and natural frequency ωn. The structural mode shape is an important step in the research because with it we can predict the response of the building when it receives a certain load.

4 Conclusion

Vibration mode was obtained from the equation of motion that affects the stiffness of the building structure k, mass m, and natural frequency ωn. Natural frequency, shape mode, and modeling vibration response to a model of a four-story building with the installation of an MR damper have been discussed in this paper. Diagrams in Simulink and the Matlab program have been carried out. The vibration response from the fourth floor achieved the highest peak displacement at 3.7 cm and reached stability with the longest time of 550 ms.

References

1. Irjaya, N., Pamungkas, A.: Penentuan Zona Kerentanan Bencana Gempa Bumi Tektonik di Kabupaten Malang Wilayah Selatan. J. Tek. POMITS **3**(2, 3), 107–112 (2014)
2. De Roeck, G., Degrande, G., Lombaert, G., Müller, G.: Active and semi- active control of structures: a review of recent advances. In: Proceedings of the 8th International Conference on Structural Dynamics EYRODYN pp. 62–69 (2011)
3. Heysami, A.: Types of dampers and their seismic performance during an earthquake. Curr. World Environ. **10**, 1002–1015 (2015). https://doi.org/10.12944/cwe.10.special-issue1.119
4. Zapateiro, A.M., Pozo, F., Karimi, H.R., Luo, N.: Semiactive control methodologies for suspension control with magnetorheological dampers. IEEE/ASME Trans. Mechatron. **17**(2), 370–380 (2012). https://doi.org/10.1109/TMECH.2011.2107331
5. Imaduddin, F., Mazlan, S.A., Zamzuri, H.U., Fatah, A.Y.A.: Testing and parametric modeling of magnetorheological valve with meandering flow path. Nonlinear Dyn. **85**(1), 287–302 (2016).https://doi.org/10.1007/s11071-016-2684-6
6. Pokaad, A.Z.B., Hudha, K., Nasir, M.Z.B.M., Ubaidillah, N.A.: Simulation and experimental studies on the behaviour of a magnetorheological damper under impact loading. Int. J. Struct. Eng. **2**(2), 164 (2011). https://doi.org/10.1504/IJSTRUCTE.2011.039422
7. Utami, D., et al.: Material characterization of a magnetorheological fluid subjected to long-term operation in damper. Materials **11**(11), 2195 (2018). https://doi.org/10.3390/ma11112195

CFD Analysis of Water Content and Minimum Droplet Temperature of Spray Drying Product with Inlet Temperature and Air Flow Direction Variation

Eflita Yohana[1(✉)], Mohammad Tauviqirrahman[1], Eka Dharmawan[1], Mohamad Endy Julianto[2], Kwang- Hwan Choi[3], and Luhung Damarran Achmad[1]

[1] Departement of Mechanical Engineering, Diponegoro University, Jl. Prof. Soedarto, S.H., Semarang 50275, Indonesia
eflitayohana@live.undip.ac.id

[2] Departement of Chemical Engineering, Vocational School, Diponegoro University, Jl. Prof. Soedarto, S.H., Semarang 50275, Indonesia

[3] College of Engineering, Pukyong National University, 365 Sinseon-ro, Nam-gu, Busan 608739, Korea

Abstract. This study aimed to analyze the effect of inlet temperature and airflow direction variation of a spray dryer on the product's water content and minimum droplet temperature using the means of computational fluid dynamics (CFD). The airflow direction types were mixed and co-current. The k-ω SST and standard k-ε models were used to simulate the flow, and the Eulerian-Lagrangian approach was used to predict the motion of particles. The simulation results showed that water content decreased as temperature increased for both airflow directions and vice versa for the minimum droplet temperature. A mixed flow spray dryer produced the lowest water content (0%) product with droplets diameter of 10 μm and 30 μm and an inlet temperature of 180 °C. The lowest minimum droplet temperature (32.73 °C) occurred in the mixed flow spray dryer with an inlet temperature of 100 °C.

Keywords: Spray dryer · Water content · Droplet temperature

1 Introduction

Spray drying is a widely used commercial drying process for products such as tea, powdered milk, instant coffee, and vitamins [1, 2]. The low product temperature and short drying time allow the spray-drying method to be used to dry products that are highly sensitive to heat and maintain product qualities such as color, taste, and nutrition [3]. For example, the process of drying tea into powder products generally involves spray drying technology.

A study by Anandharamakrishnan *et al.* [4] and Habtegebriel *et al.* [5] showed that CFD analyses yielded reasonably good predictions of the temperature and velocity

distributions in the spray dryer compared with the experimental approach. In addition, drying air temperature has been shown to influence the water content of the dried product of the spray dryer—higher drying air temperature results in a product with lower water content [6, 7].

Based on previous descriptions, it has been shown that the inlet temperature of a spray dryer influences the water content of the dried product. Therefore, this study aimed to gain a deeper understanding of inlet temperature and airflow direction variations of a spray dryer on the product's water content and minimum droplet temperature using Computational Fluid Dynamics (CFD) method.

2   Method

2.1   Basic Theory

This study used a three-phase flow solution with the Eulerian-Lagrangian approach to predict particle tracking in a spray dryer. The continuous phase is air, while the discrete phase is particles [5]. The particle movement was analyzed using the Eulerian approach by solving the Navier-Stokes equation. The forces acting on particles include drag and gravity. For incompressible fluid flows, the continuity, momentum, and energy equation were used. Finally, the particle trajectory in a stream was calculated using the discrete phase model (DPM) to track individual particles [8].

2.2   CFD Model

The present work used the k-ω SST turbulence model and standard k-ε turbulence model for mixed flow and co-current flow spray dryer to produce more accurate fluid flow characteristics [4, 5, 9, 10]. Figure 1 shows the shape and geometric dimensions of the spray dryer created with SOLIDWORKS. The co-current flow spray dryer design is based on the research of Anandharamakrishnan *et al.* [4]. The dimensions of mixed flow (co-current flow) spray dryer are: body diameter D1 = 600(600), cylinder diameter D2 = 50(50), nozzle diameter Dn1 = 40(81), nozzle diameter 2 Dn2 = 20(55), nozzle diameter 3 Dn3 = (20), inlet dimension a $\times$ b = 147 $\times$ 125, spray dryer length L = 1275(1275). All dimensions are in millimeters.

Mesh generation of the spray dryer geometry was performed based on the element size using ANSYS Mesh. The body sizing feature with the curvature size function was added to the meshing of the geometry, with tetrahedral cells being the shape of the element. Grid independence analysis was conducted in grid size varied from 0.015 m (coarse mesh) to 0.013 m (fine mesh), shown in Table 1. Gride size of 0.0145 m (medium mesh) was adopted for all following simulations because it gives an acceptable level of grid independence with feasible computational time.

The boundary conditions for the inlet and outlet were the inlet velocity and the outlet pressure. Meanwhile, the boundary condition specified at the spray dryer surface is wall pressure with the following settings: "DPM escape" condition for the spray dryer surface and "reflect" for pipe wall. Drying air intake speed was 8 m/s, the hydraulic diameter is 0.1351 m, the turbulence intensity is 3.94, the initial temperature is 100 °C, 120 °C,
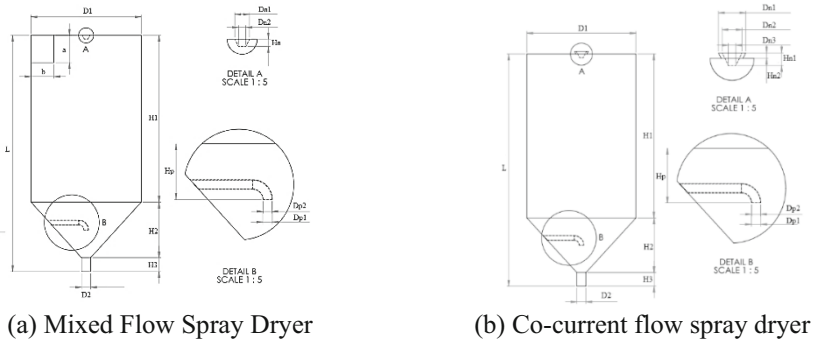
(a) Mixed Flow Spray Dryer   (b) Co-current flow spray dryer

Fig. 1. Spray dryer shape and geometric dimensions.

Table 1. Grid independence test results.

Grid	Outlet temperature (°C)
0.0130	32.39
0.0135	33.09
0.0140	32.89
0.0145	32.73
0.0150	34.56

140 °C, 160 °C, and 180 °C, the mass loading value of 0.0015 kg/s, the particle density is 816.4 kg/m^3, and the gas density is 1.225 kg/m^3. Rosin-Rammler distribution was used for the analysis of Particle Size Distribution (PSD), with particle diameter ranging from 10 µm to 130 µm and average diameter $\bar{d}$ of 50 µm [11].

The governing equations were solved numerically using ANSYS Fluent, and SIMPLE scheme was used for pressure-velocity coupling to achieve convergence. The second-order scheme was chosen for pressure discretization to precisely predict velocity and temperature distribution under actual conditions. The first-order upwind scheme was used for the momentum, dissipation rate, and kinetic energy. For discretization of the energy equation, the first-order upwind scheme was adopted to avoid numerical instability and achieve better convergence. The convergence criteria of 1×10^{-4} were applied to all solution variables, and the convergence criteria of 1×10^{-6} was used for the energy equation.

The simulation results in this study were compared with the results of experimental research done by Habtegebriel *et al.*, which showed good agreement with the reference; therefore, the present methodology was adopted for all following simulations [5].

3   Results and Discussion

In this study, the water content in the final product is examined by plotting the simulation results into a graph. Product with lower water content is preferred as it is less likely to

be contaminated by microbes, thus increasing the quality of the product [6]. In general, a mixed flow spray dryer resulted in droplets with lower water content than a co-current flow spray dryer. The higher inlet temperature of a mixed flow dryer results in a higher probability of mass flow changes; thus, the water content in the droplets decreases [5].

Figure 2 shows the comparison of the water content in the final dried product between the spray dryer with the mixed and co-current flow. The droplet diameter of 50 μm is given the emphasize as it is the average droplet diameter in this study. It can be seen that in a mixed flow spray dryer, droplets with diameters of 10 μm and 30 μm and inlet temperature of 180 °C have the lowest water content (0%) compared with other droplets diameters. Droplets with the highest water content (58.15%) are 130 μm in diameter and have an inlet temperature of 100 °C. For the spray dryer with the co-current flow, droplets with diameters of 10 μm and 30 μm and an inlet temperature of 180 °C have the lowest water content (0%) compared with other droplet diameters. A droplet with 130 μm has the greatest water content (59.32%) with an inlet temperature of 100 °C.
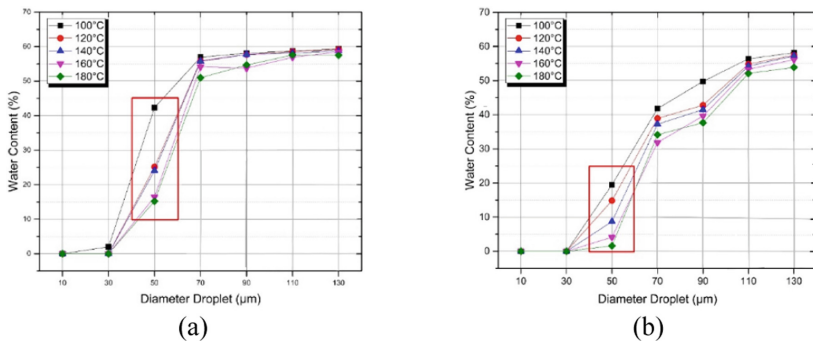

Fig. 2. Comparison of water content in droplets in the drying chamber of (a) Mixed Flow Spray Dryer and (b) Co-Current Flow Spray Dryer.

The minimum temperature of particles that exit the spray dryer influences the product quality and post-drying processes. Increasing the inlet temperature can increase the minimum droplet temperature that exits the spray dryer [12]. Figure 3 shows the comparison of the minimum droplet temperature produced by each spray dryer. The lowest minimum droplet temperature (32.73 °C) occurred in the spray dryer with the mixed flow with an inlet temperature of 100 °C, and the highest (62.85 °C) occurred in the spray dryer with the co-current flow with an inlet temperature of 180 °C.

Co-current flow spray dryer had a higher average minimum droplet temperature compared to the mixed flow spray dryer. This is due to the high-temperature airflow in the co-current flow spray dryer that is concentrated in the center of the drying chamber, which pushes the droplets directly to the outlet [5]. Figure 4 shows the difference in temperature contour and the temperature distribution along the radial direction at several elevations for the mixed flow and co-current flow spray dryer at an inlet temperature of 180 °C.

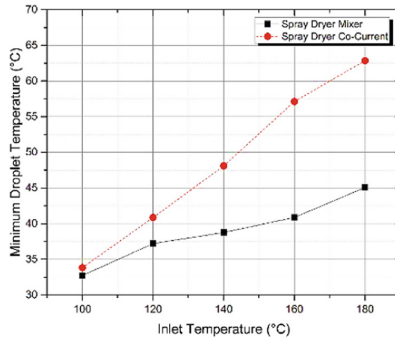**Fig. 3.** Minimum droplet temperature in the drying chamber.

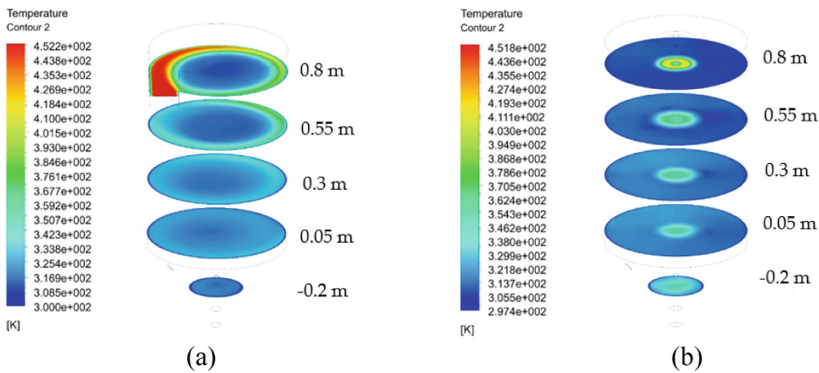(a)   (b)

Fig. 4. Temperature contour and temperature distribution of (a) Mixed Flow Spray Dryer and (b) Co-Current Flow Spray Dryer at an Inlet Temperature of 180 °C.

4   Conclusion

This paper presents a study of water content and minimum droplet temperature analysis of spray drying products with inlet temperature and airflow direction variation. It can be concluded that inlet temperature plays a significant role in water content and minimum droplet temperature of spray drying products. Therefore, a mixed flow spray dryer produces a product with lower water content and minimum droplet temperature than a co-current flow spray dryer.

References

1. Schmitz-Schug, I., Kulozik, U., Foerst, P.: Modeling spray drying of dairy products - impact of drying kinetics, reaction kinetics and spray drying conditions on lysine loss. Chem Eng Sci. Elsevier **141**, 315–329 (2016). https://doi.org/10.1016/j.ces.2015.11.008
2. O'Sullivan, J.J., Norwood, E.A., O'Mahony, J.A., Kelly, A.L.: Atomization technologies used in spray drying in the dairy industry: a review. J. Food Eng. Elsevier B.V. **243**, 57–69 (2019)

3. Ruano Uscategui, D.C., Ciro Velásquez, H.J., Sepúlveda Valencia, J.U.: Concentrates of sugarcane juice and whey protein: study of a new powder product obtained by spray drying of their combinations. Powder Technol. Elsevier B.V **333**, 429–438 (2018). https://doi.org/10.1016/j.powtec.2018.04.025

4. Anandharamakrishnan, C., Gimbun, J., Stapley, A.G.F., Rielly, C.D.: A study of particle histories during spray drying using computational fluid dynamic simulations. Dry Technol. **28**, 566–576 (2010)

5. Habtegebriel, H., Edward, D., Motsamai, O., Wawire, M., Seifu, E., Daniel, S.: The potential of computational fluid dynamics simulation to investigate the relation between quality parameters and outlet temperature during spray drying of camel milk. Dry Technol. Taylor & Francis, 1–15 (2019). https://doi.org/10.1080/07373937.2019.1684317

6. Arepally, D., Goswami, T.K.: Effect of inlet air temperature and gum Arabic concentration on encapsulation of probiotics by spray drying. Lwt. Elsevier **99**, 583–593 (2019). https://doi.org/10.1016/j.lwt.2018.10.022

7. Aguirre-Alonso, R.O., Morales-Guillermo, M., Salgado-Cervantes, M.A., Robles-Olvera, V.J., García-Alvarado, M.A., Rodríguez-Jimenes, G.C.: Effect of process variables of spray drying employing heat pump and nitrogen on aromatic compound yield in powders obtained from vanilla (Vanilla planifolia Andrews) ethanolic extract. Dry Technol. Taylor & Francis **37**, 1806–1820 (2019). https://doi.org/10.1080/07373937.2018.1540011

8. Jayaraju, S., Lacor, C., Verbanck, S.: Study of the air flow and aerosol transport in the human upper airway using LES and DES methodologies [Ph.D]. Vrije Universiteit Brussel (2019)

9. Liu, Y., Rao, Y., Weigand, B.: Heat transfer and pressure loss characteristics in a swirl cooling tube with dimples on the tube inner surface. Int. J. Heat Mass Transf. Elsevier Ltd **128**, 54–65 (2019). https://doi.org/10.1016/j.ijheatmasstransfer.2018.08.097

10. Jubaer, H., et al.: The impact of self-sustained oscillations on particle residence time in a commercial scale spray dryer. Powder Technol. Elsevier B.V **360**, 1177–1191 (2020). https://doi.org/10.1016/j.powtec.2019.11.023

11. Ansys, I.: Ansys Fluent 12.0 Theory Guide. Published online 2009

12. Langrish, T.A.G., Premarajah, R.: Antioxidant capacity of spray-dried plant extracts: experiments and simulations. Adv. Powder Technol. The Society of Powder Technology Japan **24**, 771–779 (2013). https://doi.org/10.1016/j.apt.2013.03.020

The Impact of Stress Distribution on the Electrical Performance of Different Silver Stretchable Conductive Ink Pattern Using FEA Simulation

Daniel Azlan Mohd Azli[1] , Mizah Ramli[1,2(✉)], Mohamad Shukri Zakaria[1] ,
Mohd Nur Azmi Nordin[1,2] , Abdul Halim Lim Abdullah[3], and Ghazali Omar[1,2]

[1] Fakulti Kejuruteraan Mekanikal, Universiti Teknikal Malaysia Melaka, Hang Tuah Jaya,
76100 Durian Tunggal, Melaka, Malaysia
{mizah,mohamad.shukri,ghazali}@utem.edu.my

[2] Advanced Material and Characterization Laboratory, Universiti Teknikal Malaysia Melaka,
Hang Tuah Jaya, 76100 Durian Tunggal, Melaka, Malaysia

[3] Top Empire Sdn. Bhd., Lot 16037, jalan Teknologi 6, Kawasan Perindustrian Tangkak, 84900
Tangkak, Johor, Malaysia
halim@topempire.com.my

Abstract. Stretchable conductive ink has been widely investigated to be used in the fabrication of stretchable electrical devices. Experimentation methods to test the mechanical and electrical behaviors of the stretchable conductive ink composite are widely applied, however, not much of computational method has been used to further validate the results. In this paper, finite element analysis method has been employed to investigate the relationship between the stress distribution of the stretchable conductive ink with the highest strain obtained. This research validates the past experimentation works of different patterns of stretchable conductive ink for its stretchability and electrical performance. The average stress distribution of the stretchable conductive ink played a significant role in the determination of its electrical performance, rather than the localization of high Von Mises stress (VMS) at certain locations within the stretchable conductive ink pattern. The lower average stress distribution contributed to a better stretchability which is indicated by a higher strain rate prior to electrical conductivity.

Keywords: Stress distribution analysis · FEA · SCI · Stretchability

1 Introduction

The electronics industry has experienced a paradigm change in recent years toward the development of both flexible and stretchable devices [1]. Flexible and printable electronics have received considerable interest and are generally regarded as the electronic industry's future [2]. Stretchable electronic circuit (SEC) is a technique that has been developed to boost the flexibility, twistability and stretchability of a rigid printed circuit board (PCB) [3], while conductive circuit is a critical component of PCB. Stretchable

conductive ink (SCI), as it goes by the name is a type of ink that can be stretched while maintaining its electrical conductivity. SCI is the primary component of SEC [4].

The SCI composite must include some kind of conductive filler as the dispersed phase in order to be conductive. SCI is used to assess the composite's electrical or thermal conductivity, as well as its ability to stretch or flex, which varies based on the type of conductive filler used. Numerous kinds of conductive fillers have been shown in the laboratory [5–7] as well for commercial usage [8, 9]. Silver (Ag), gold (Au), and copper (Cu) nanoparticles are presently the most often used conductive fillers. Silver nanoparticle is often used as a conductive ink filler to increase the ink's conductivity, since it has the greatest electrical conductivity of all metal-based fillers [10]. Experiments using printed SCIs on flexible substrates have shown remarkable electrical, thermal, and mechanical properties. However, the technique of experimentation may be expensive owing to the need to repeat each experiment to get normalized or averaged data. However, the performance of a SCI-based composite may be assessed computationally as well as experimentally. The primary goal of computer analysis is to validate experimental research rather than totally replace it, since the experimental findings may be the input parameters for the computational approach. In this study, a stress distribution analysis of Ag SCI will be conducted to validate the experimental result [1] obtained through finite element analysis (FEA) method. From the experiment conducted, in terms of maximum elongation percentage before the ink started to lose conductivity, zig-zag line pattern showed the best result, following sinusoidal, square and lastly straight pattern as shown in Table 1.

Table 1. Maximum elongation rate before each pattern starts losing its conductivity [1].

Pattern	Maximum strain (%)
Straight	1.11
Square	3.33
Sinusoidal	6.67
Zig-zag	7.78

2   Methodology

Von Mises Stress (VMS) of each of different patterns used is obtained. For the preliminary testing, a few patterns for screen-printing were identified and developed within the simulation software. The patterns are adapted from the past experimentation works conducted to further examine the effect of stress distribution towards the electrical performance of SCI [1]. Here, Abaqus software was employed to run the finite element analysis (FEA) simulation upon the patterns. The stretchability of the patterns was evaluated by observing the Von Mises stresses of the patterns at different locations. In this research activity, there were a few patterns outlined: (1) straight, (2) sinusoidal, (3) zig-zag and (4) square-line patterns. The straight-line was made as the baseline patterns for

the comparison purpose. Separate study shows that the grid test of the model is less than 10% with the mesh seed density of the model is set to be 1.8 and 8 for ink and substrate respectively. For the respective mesh seed density, the number of nodes and elements used in the modeling is 411 and 136 consecutively.

2.1 Model of SCI

As afore-mentioned, there were four different patterns were chosen, modelled and simulated by FEA software to further analyze the behavior of the stress-strain of each pattern. The length of each pattern was set to be 90 mm. The width and the thickness of the ink was 3 mm and 0.005 mm respectively. For the substrate, the length, width and thickness were set to be 92 mm, 25 mm and 0.1 mm respectively, proving 1 mm clearance for both ends of the pattern. Figure 1 shows the general dimension for the model of the patterns for straight line pattern, and the same dimension is applied to other patterns. Figure 2 shows the model for other patterns employed in this research viewed from the top.
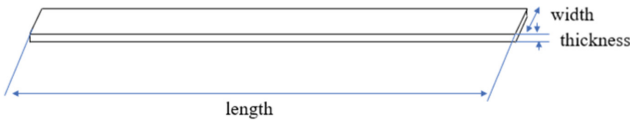

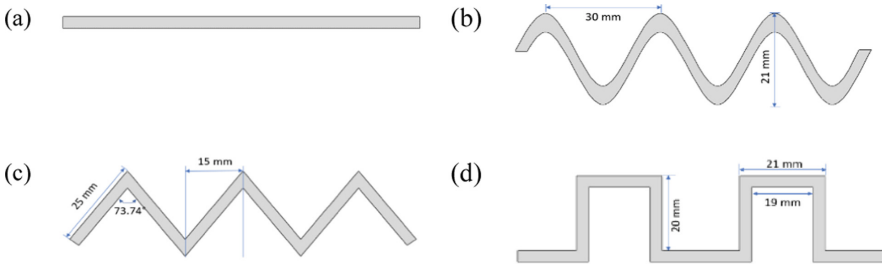**Fig. 1.** General dimension for the model of pattern.

Fig. 2. Modelled patterns of (a) Straight, (b) Sinusoidal, (c) Zig-zag and (d) Square.

2.2 Material Properties

The material used as the SCI is silver ink which is a metal nanoparticles filler and Thermoplastic urethane (TPU) substrate. Mechanical data such as Young's Modulus and Poisson's ratio for the silver ink was obtained from other research employing similar type of ink and substrate [11]. Table 2 describe the properties of silver ink and TPU substrate employed in the simulation. The mechanical behavior of the SCI was set to be elastically behaving to observe the elasticity of the SCI when subjected to uniaxial stretching of 10%.

Table 2. Properties of ink and filler used in the simulation.

Materials	Properties		
	Young's modulus (MPa)	Poisson's ratio	Density (ton/mm^3)
Silver	1034.21	0.25	2.2×10^9
TPU	11.55	0.45	1.2×10^9

2.3 Boundary Conditions (BC)

Boundary conditions (BC) are limitations that must be met in order to solve a boundary value issues. All the models made of different patterns used in the simulation were subjected to uniaxial tensile test. One end of the model was subjected to fixed end, while another end was subjected to mechanical loading as shown in Fig. 3. In this case, the mechanical loading was elongation stress. For the simulation purpose, there were three boundary conditions employed for the model of the patterns, namely BC1, BC2 and BC3 respectively. Figure 3 shows the schematic diagram of the model subjected to the loadings from boundary conditions.

BC1 is the fixed end. One end of the SCI model is fixed, where the displacements and reaction forces in all axes (x, y and z) were constrained. BC1 was applied at the cross-sectional area region of the end (substrate), causing the whole surface area to be constrained in terms of displacement and reaction force.

BC2 covered the whole body of the model, where the whole body in general is subjected to be stationary in all directions except for the direction parallel to the stretching mode (in this case: x-axis). All displacements and reaction forces in all directions are constrained except for the displacement in x-axis. This is done to allow the elongation stress that will be applied to deform the model only in x-axis.

For the BC3 established in the model, a reference point is constructed at the center point of the cross-sectional area of another end. A coupling system is established for the whole cell coupling the cross-sectional area to the reference point, where the elongation stress is applied. Since the best elongation rate obtained experimentally is 7.78% according to Table 1, the point that is representing the whole end was subjected to stretching that caused the model to elongate with 10% strain.
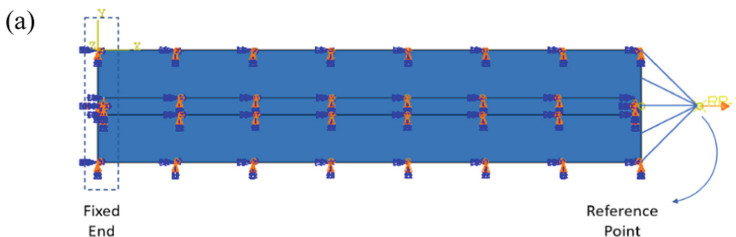
(a)

Fixed End   Reference Point

Fig. 3. Schematic diagram of the model at application of BC1, BC2 and BC3. The location of fixed end and loading point is denoted by the dotted line and arrow respectively.

3   Results and Discussion

During the simulation, surface of both ink and substrate are tied to each other through master and slave tie method while the silver ink is modelled as isotropic material possessing a linear elastic behavior. Table 3 shows the Von Mises Stress (VMS) obtained for all the patterns when subjected to uniaxial tensile loading of 10%. The average stress is given by the following equation:

$$\sigma_{avg} = (\sigma_{max} + \sigma_{min})/2 \qquad (1)$$

where σ_{avg}, σ_{max} and σ_{min} representing average stress, maximum stress and minimum stress respectively.

3.1   Maximum VMS Distribution on Patterns

From the tabulated data obtained through simulation process, the highest VMS occurred in zig-zag pattern, with the maximum stress captured at 114.188 MPa, followed by straight, square and sinusoidal patterns with 107.729, 105.617 and 99.190 MPa correspondingly. For zig-zag and sinusoidal line, the high concentration of stresses is located at various locations within the ink near to the longitudinal centerline of the substrate (line of half width of substrate) as shown in Fig. 4(b) and 4(d). For straight ink, it is observed that the highest stress is located at the edge of ink nearest to the tensile loading point with the stress value of 107.729 MPa. As for the square ink pattern, higher stress accumulated at line parallel to tensile load. The FEA finding shows agreement with the experimental research conducted [1], approving that the presence of a parallel-stretching zone in the intended structure is likely to contribute to the pattern's inability to tolerate a greater strain [1].

3.2   Average VMS Distribution on Patterns

The average stress distribution depicted different perspective on the analysis of the maximum strain rate before failure of SCI to conduct electricity as portrayed in Table 1. Although zig-zag line had the highest point of stress concentration compared to the rest, it actually possessed the lowest average stress with ~68 MPa, followed by sinusoidal, square and straight pattern each with 68.661, 70.457 and 93.771 MPa respectively. High average stress distributed within the pattern contributed to the electrical conductivity's failure more than the localization of high stress at certain location within the conductive patterns. The results of average stress within each pattern shows a good agreement with the results tabulated in Table 1. The high average stress could incite the formation of more cracks within the silver ink's pattern, causing more defects, thus the electron transfers are unable to move smoothly due to scattering mechanism.

Table 3. Tabulation of VMS for all the patterns.

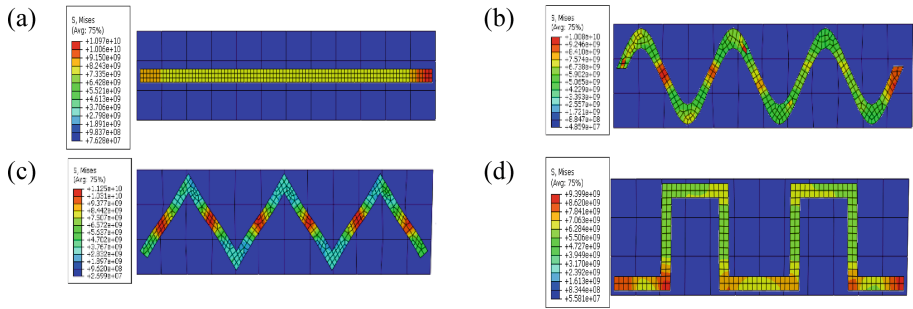| Pattern	Von Mises Stress (VMS) (MPa)		
	Maximum	Minimum	Average
Straight	107.729	79.8128	93.7709
Sinusoidal	99.1902	38.130	68.660
Zig-zag	114.188	21.829	68.009
Square	105.617	35.296	70.457

Fig. 4. The stress distributions when subjected to uniaxial tensile loading for (a) straight, (b) sinusoidal, (c) zig-zag and (4) square pattern respectively.

4 Conclusion

In summary, a study incorporating FEA method by Abaqus has been conducted to validate the effect of stress distribution on the electrical performance of the silver-filled SCI. From the study, it can be concluded that the average stress distribution played a significant role in the determination of the electrical performance of silver SCI subjected to uniaxial tensile loading with 10% strain rate incorporated for the simulation process. From the simulation, the lowest stress distribution level contributed to a better electrical performance of SCI and better stretchability, and this might be due to appearance of lesser cracks within the SCI allowing the electron transfers to be efficiently conducted. From both experiment and simulation conducted, it can be summarized that the electrical performance of different patterns of silver ink subjected to straining can be indicated as: zig-zag > sinusoidal > square > straight line.

References

1. Yunos, A.M., Omar, G., Hamid, H.A., Salim, M.A., Masripan, N.A.: The influence of geometrical dimensions on electromechanical performance in stretchable circuit. J. Phys. Sci. **31**(2), 75–89 (2020)
2. Gupta, S., Heidari, H., Vilouras, A., Lorenzelli, L., Dahiya, R.: Device modelling for bendable piezoelectric FET-based touch sensing system. IEEE Trans. Circuits Syst. I Regul. Pap. **63**(12), 2200–2208 (2016)
3. Bossuyt, F., Vervust, T., Vanfleteren, J.: Stretchable electronics technology for large area applications: fabrication and mechanical characterization. MRS Online Proc. Lib. **3**(2), 229–235, (2013)
4. Mou, Y., Zhang, Y., Cheng, H., Peng, Y., Chen, M.: Fabrication of highly conductive and flexible printed electronics by low temperature sintering reactive silver ink. Appl. Surf. Sci. **43**(May), 249–256 (2018)
5. Mohammed, A., Pecht, M.: A stretchable and screen-printable conductive ink for stretchable electronics. Appl. Phys. Lett. **109**(18) (2016)
6. Kim, D.S., Jeong, J.-M., Park, H.J., Kim, Y.K., Lee, K.G., Choi, B.G.: Highly concentrated, conductive, defect-free graphene ink for screen-printed sensor application. Nano-Micro Lett. **13**(1), 1–14 (2021). https://doi.org/10.1007/s40820-021-00617-3
7. Xu, L.Y., Yang, G.Y., Jing, H.Y., Wei, J., Han, Y.D.: Ag-graphene hybrid conductive ink for writing electronics. Nanotechnology **25**(5) (2014)
8. Ashikin, A.A., Omar, G., Tamaldin, N., Nordin, M.A., and Akop, M.Z.: Electrothermal Effects of Stretchable Conductive Ink (SCI), pp. 18–19 (2017)
9. Rozali, N.S., et al.: Effect type of conductive inks to stretchable printed circuit under thermal performance. (May), pp. 279–280 (2018)
10. Kosmala, A., Wright, R., Zhang, Q., Kirby, P.: Synthesis of silver nano particles and fabrication of aqueous Ag inks for inkjet printing. Mater. Chem. Phys. **129**(3), 1075–1080 (2011)
11. Anwar, M., Michael, P.: A stretchable and screen-printable conductive ink for stretchable electronics. Appl. Phys. Lett. **109**. 184101 (2016). https://doi.org/10.1063/1.4965706

Mechanical Behavior Analysis
of Hydroxyapatite Bone Scaffold as Bone
Implant Candidate

Fikan Mubarok Rohimsyah, Gusti Umindya Nur Tajalla$^{(\boxtimes)}$, and Ananda Yudistira

Department of Materials Science and Engineering, Institut Teknologi Kalimantan, Balikpapan, Indonesia
`gusti.unt@lecturer.itk.ac.id`

Abstract. During the years 2011–2012, WHO recorded that the mortality of senior citizens caused by bone fractures globally reached 5.6 million, which lowers the quality of life. Bone grafting is a known method that is used for solving bone defects, but it is costly. Furthermore, the disease transmission and the immune response increase the significant danger to the elderly's health. One of the renowned tissue engineering products is the bone scaffold. Hydroxyapatite (HAp) with the molecular formula $Ca_{10}(PO_4)_6(OH)_2$ is frequently used for this application. It has properties similar to bone tissue in humans, however the mechanical stiffness and strength are too high. To modify mechanical properties, biomaterials Hydroxyapatite should lower its stiffness to match the mechanical strength of the surrounding bone to prevent stress shielding and it should support bone tissue regeneration. Pore distribution and size in hydroxyapatite coincide with the function of the porous scaffold. The effects of porous media with variations in model of dense (HAp), centralized porosity, and homogeneous porosity were studied using simulation. In response to compressive stress (MPa) and displacement (mm) of the femur bone, the percentages of porosity in each porous model were 30%, 40%, 50%, 60%, 70%, 80%, and 90%, and pore size was 300 m. The model that results is close to and suitable for the application as a bone implant is the homogeneous porosity bone scaffold model with variations of pore size of 300 µm and percentage of 90% porosity. The compressive stress value and displacement value of the model are, respectively, 32.163 MPa and 0.000831mm.

Keywords: Bone · Bone scaffolds · Hydroxyapatite · Porosity

1 Introduction

An estimated 2.2 million bone grafts are performed annually worldwide, but limited supplies and donor locations are significant problems. Bone grafts are an alternative used for this problem. Commonly, bone grafts are utilized in various fracture conditions, such as fractures in joints, fractures due to accidental injury or infection, and fractures that remain unhealed after undergoing orthopedic treatment [1].

Therefore, tissue engineering is used to induce new functional tissues that have been integrated with the host without causing any reaction [2]. One application of tissue

engineering is bone scaffolds. Bone scaffolds have been used widely to improve various clinical conditions in orthopedic surgery, maxillofacial surgery, and dentistry. Bone scaffolds play a significant role in the successfulness of bone grafting in host tissues and provide mechanical support to the skeleton [3]. One of the materials often used for bone scaffolds is hydroxyapatite (HAp), with the molecular formula $Ca_{10}(PO_4)_6(OH)_2$. Hydroxyapatite has similarities with human bone tissue [4]. Because of its biocompatibility and bioactive properties, hydroxyapatite is a promising candidate for use as a filler in bone repair and replacement [5].

A wide range of unit cell structure designs and methodologies have been presented in the literature in recent years. The problem remains that the mechanical properties of solid hydroxyapatite are much different from the mechanical properties of human bone. So, a porous design is adapted to reduce the difference that occurred [6]. However, porous biomaterials have a much-reduced modulus of elasticity compared to solid ones. Thus, it is possible to fit the modulus of elasticity of a porous implant with the modulus elasticity of bone. The fitness in the modulus of elasticity with respect to porosity serves to minimize the problem of stress shielding [7]. The goal of this project is to use a finite element approach to develop, analyze, and optimize initial bone scaffolds design for application in femur bone. Therefore, a simulation method is used to reduce the stress shielding by controlling the distribution and arrangement of the porosity in a bone scaffold model made of hydroxyapatite as a bone implant.

2 Materials and Simulation Step

In this study, the material used is hydroxyapatite data collected from literature. Solid-Works software is utilized to create a geometric design also for compression test simulation.

Materials Data Collection
To obtain mechanical properties of hydroxyapatite, percentage of total porosity, pore size, and bone scaffold design, a literature review and data collection were conducted. Elastic modulus of 40 MPa, Poisson's Ratio of 0.27, Mass Density 3.16 kg/m^3, Tensile Strength 147 MPa, Compressive Strength 294 MPa, and Yield Strength 1.35 MPa are the mechanical properties of hydroxyapatite used [8]. The percentages of porosity used are 30% and 40% [4].The dimensional data used is per the dimensions used by I. Sabree et al. [9]. The material dimensions used are 6mm x 6mm x 6mm.

Bone Scaffold Design
The specimen is a cube with a size of 6 mm × 6 mm × 6 mm. Then the shape of the specimen used is shown below (Fig. 1):

Simulation
Simulations were carried out to determine the load that could be applied to the bone scaffold model. Where the sample using 3 variations of design with variations in the percentage of porosity and pore size and arrangement were simulated with a compressive load of 3000 N or 85 N/mm^2 (Fig. 2).

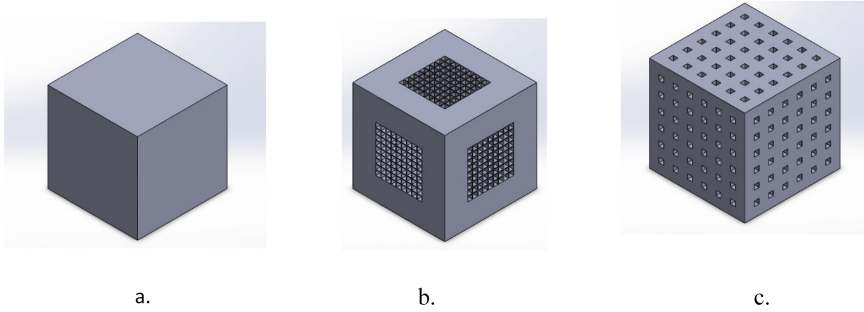a.   b.   c.

Fig. 1. a.) Variation of Solid (Dense) on Bone Scaffold Model, b.) Variation of Centralized Porosity on Bone Scaffold Model, c.) Variation of Homogeneous Porosity on Bone Scaffold Model.
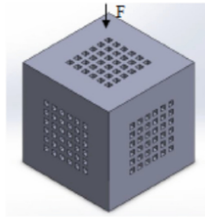

Fig. 2. Illustration compression load applied in simulation.

3   Results and Discussion

According to Karuppudaiyan in 2018, the maximum acceptable stress on the femur is around 36.3 MPa, while the acceptable displacement is around 0.002 mm. In this work mechanical behaviour of 3 variations of porous bone scaffold proposed model was designed and analyzed. We observed that maximun stress and displacement depends on distribution and arangement of porous hydroxyapatite bone scaffold which shows in Fig. 3. It can be seen that the bone scaffold with a homogeneous porosity design has a more even distribution of normal stresses because the structural form of homogeneous porosity has the same cross-sectional area, while the centralized porosity design has a different cross-sectional area so that the stress distribution is uneven and will has a greater stress at the center of the bone scaffold.
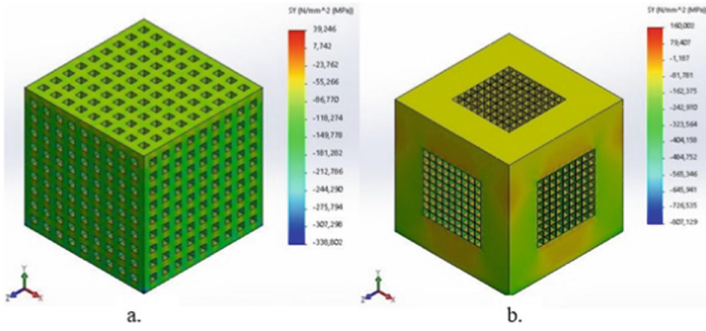
Fig. 3. Stress in Bone Scaffold At (a.) 40% Homogeneous Porosity (b.) 40% Centralized Porosity.
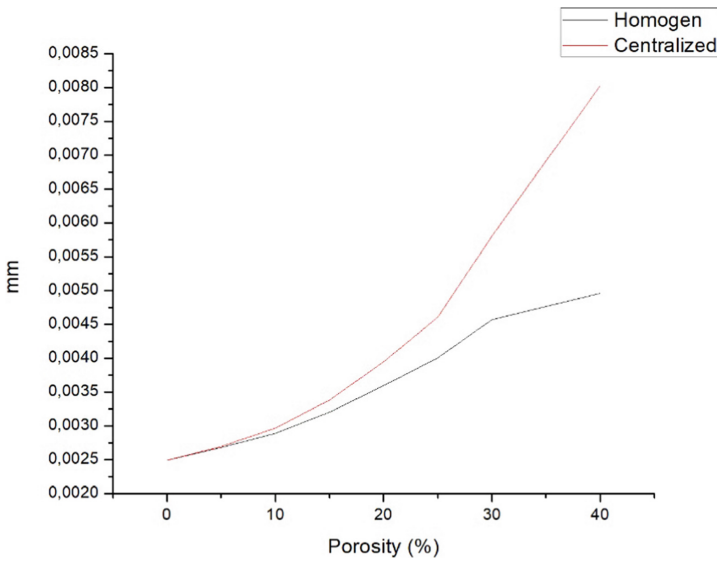

Fig. 4. Displacement of porosity variation bone scaffold design.

As Fig. 4 Shows increasing porosity of bone scaffold resulted in increasing displacement during loading. This is in accordance with the results of the stress distribution in the variation of the centralized porosity there will be a concentration of stress in the central structure of the bone scaffold thus increasing the displacement of material. Meanwhile the principal stress (Sy) decreased as porosity increase. This was because porosity of the scaffold reduced the elastic modulus so that the stress induced in bone scaffold decrease as porosity increase (Fig. 5).
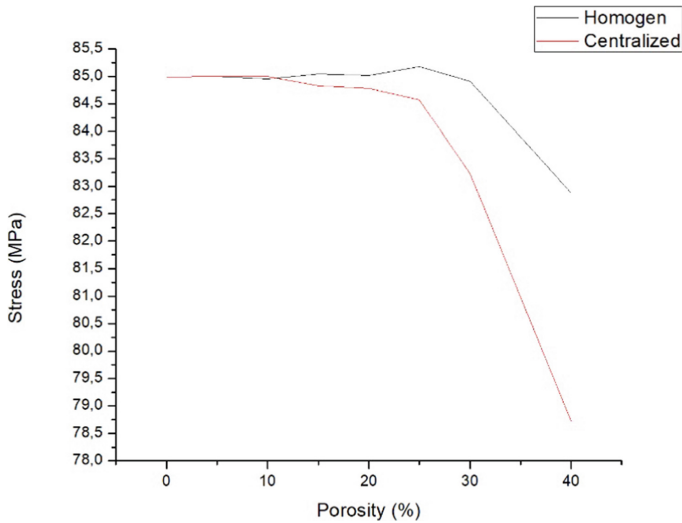
Fig. 5. Stress resulted from porosity variation bone scaffold design.

4   Conclusion

Based on the criteria, the displacement value of the bone scaffold is 0.002 mm. The results that are close to these criteria are obtained in the 5% homogeneous porosity bone scaffold model with a displacement value of 0.0028 mm, this result indicates that the bone scaffold model is suitable to minimize the effect of stress shielding however, the stress showed from the simulation higher than in bone femur so that the initial model need to be optimized by using multiple biomaterial and optimized geometry model.

References

1. Fu, Q., Saiz, E., Rahaman, M., Tomsia, A.: Bioactive glass scaffolds for bone tissue engineering: state of the art and future perspective. Mater. Sci. Eng. **31**(7), 1245–1256 (2011)
2. Akter, F., Ibanez, J.: Bone and Cartilage Tissue Engineering. Tissue Engineering Made Easy, pp. 77–97 (2016)
3. Barralet, J.E., Wang, L., Lawsom, M., Triffit, J.T., Cooper, P.R., Shelton, R.M.: On the effect of X-Ray irradiation on the deformation and fracture behavour of human cortical bone. J. Mater. Sci. Mater. Med. **16**(6), 515–519 (2005)
4. Wang, P., Zhao, L., Liu, J., Weir, M., Zhou, X., H.H.K.: bone tissue engineering via nanostructural calcium phospate biomaterials and stem cells. Bone Res. **2**, 14017 (2014)
5. Ren, F.: Characterzation and structural analysis of zinc-substitued hydroxiapatite (5(8) ed.). Acta Biomaterialia (2009)
6. Wang, L.K.: Mapping porous microstructure to yield desired mechanical properties for application in 3D printed bone scaffolds and orthopaedic implants. Mater. Des. **133**, 62–68 (2017)
7. Huiskes, R., Weinans, H., Rietbergen, B.: The relationship between stress shielding and bone resorption around total hip stems and the effects of flexible materials. Clin. Orthop. Relat. Res. **274**, 124–134 (1992)

8. Karuppudaiyan, S., Singh, D.K.J., Santosh, V.M.: Finite element analysis of scaffold for large defect in femur. In: 2nd International Conference on Advances in Mechanical Engineering (ICAME 2018), vol. 402 (2018)
9. I. Sabree, I., Gough, J.E., Derby, B.: Mechanical properties of porous ceramic scaffold: influence of internal dimensions. ELSEVIER. Ceramic Int. **41**, pp. 8425–8432 (2015)

Simulation Analysis on Palm Oil Mill Effluent (POME) Recycling System into Bioethanol

Ardian Rahmat Irawan Sinaga[1], Taufiq Bin Nur[1,2(✉)], and Indra Surya[2,3]

[1] Department of Mechanical Engineering, Faculty of Engineering, Universitas Sumatera Utara, Padang Bulan, Medan 20155, Indonesia
`taufiq.bin_nur@usu.ac.id`
[2] Sustainable Energy and Biomaterial Center of Excellence, Universitas Sumatera Utara, Padang Bulan, 20155 Medan, Indonesia
[3] Department of Chemical Engineering, Faculty of Engineering, Universitas Sumatera Utara, Padang Bulan, Medan 20155, Indonesia

Abstract. Indonesia is one of the largest exporting countries for palm oil production globally. In 2018, the country had a plantation area of 14.3 Million Ha, with palm Oil Production (Crude Palm Oil) of 40.5 million tons. It generates large amounts of waste as Palm Oil Mill Effluent (POME), empty fluid bunch (EFB), fiber, and shells. POME has an organic content and contains carbohydrates, lipids, and proteins. Generally, the POME by-products from palm oil mills in North Sumatra Province are processed using an Anaerobic treatment before release to the environment. This method still disposes of pond waste. It produces CH_4 and bad smells into the environment. This research uses Aspen plus software to simulate POME becoming bioethanol renewable energy and reduce environmental pollution caused by POME. Bioethanol production is processed biologically by fermentation. Based on the analysis of simulation, 10 L tons/day POME can produce main products 0.187 L Ton/day bioethanol with the content of up to 41.95% C_2H_5OH, 9.29% H_2O, and 48.76% CO_2, and by-products 9.823 L Ton/day with the content 99.7% H_2O.

**Keywords:** POME · Palm oil · Bioethanol · Simulation · Environment

1 Introduction

Indonesia is one of the largest palm oil-producing and exporting countries in the world. In 2018, the palm oil plantations area was 14.3 million Ha, and it has produced about 40.5 million tons [1]. The products exported of crude palm oil (CPO) and others get value 16.53 billion US$ from 27.89 million tons. Then, palm kernel oil (PKO) and others get a value of 1.7 billion US$ from 1.77 million tons [2].

The part of waste products is palm oil mill effluent (POME), Decenter Cake, Fiber, and Shells [3]. The result of the fresh fruit bunch gets 10% only [4]. POME has three sources of wastewater such as hydro cyclone wastewater (approximately 4%), sterilizing condensate (approximately 36%), and separator sludge (approximately 60%) [5]. POME

is the liquid waste that can not be reprocessed easily in a short time to extract valuable products to the factory's internal area system [6]. Seventy million tons of fresh fruit bunches will produce about 50 million tons of POME [8].

The composition and characteristics of POME depends on the quality of palm fruit, processing techniques, quality control of individual mills, harvest season, and others. In general, Composition and parameters which contained in POME such as Temperature: 80–90 °C, pH: 3.4–5.5, BOD: 10,000–44,000 mg/L, COD: 15,000–100,000 mg/L, TS: 11,500–79,000 mg/L, SS: 5,000–54,000 mg/L, TVS: 9,000–72,000 mg/L, TN: 80–1,400 mg/L, NH3-N: 4–80 mg/L, oil and grease: 4,000–8,000 mg/L, P: 180 mg/L, K: 2,270 mg/L, Mg: 615 mg/L, Ca: 439 mg/L, B: 7.6 mg/L, Fe:46.5 mg/L, Mn: 2 mg/L, Cu: 0.89 mg/L, Zn: 2.3 mg/L, [8, 9], containing 0.5–2% oil, 2–4% suspended solids, 93–96% water, and 4–5% total solid [6, 7]. POME is non-toxic waste, has a high organic content and contains of carbohydrates, lipids, and proteins [10], from the results of testing 1-L POME samples taken from local Palm Oil Mills in Galang sub-district, Deli Serdang district, North Sumatra province, Indone-sia. Water content: 92.17%, Carbohydrate content: 1.75%. Carbohydrates ($C_6H_{12}O_6$) can be converted to ethanol (C_2H_5OH), with reaction equation as shown in Eq. (1).

$$C_6H_{12}O_6 \rightarrow 2C_2H_5OH + 2CO_2 \tag{1}$$
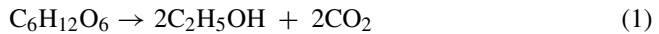
2   POME Treatment

POME could be treated by biological process, physicochemical process, thermochemical process, and integrated treatment. The above processes mentioned above have advantages and disadvantages [9, 10]. The POME processes generally use an anaerobic ponding system or mix with EFB for composting, as shown in Fig. 1.
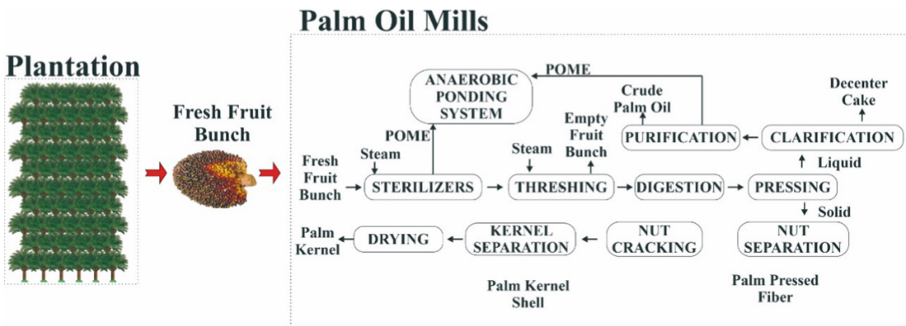

Fig. 1. Process flow of palm oil mill.

The treatment of one ton of POME by an anaerobic process will generate methane gas around 12.36 kg, leading to thinning the ozone layers. Therefore, it needs to establish a POME recycling system that does not need a large area takes a long time but still produces bioethanol.

3   Methodology

For saving costs and avoid failures in the manufacture of digester systems, simulations can be carried out with Aspen plus. Aspen simulation package has many databanks for some models like mixers, pressure changers, phase separators, splitters, distillation columns, reactors, heat exchangers, and solve the thermodynamic problem that occurs in real-time industrial implementation [11]. Specifications properties and components of POME that will be processed in the simulation are adjusted to the actual components. This simulation will convert carbohydrate content into bioethanol from the above reaction equation. Ten-liter tonnes of POME per day in the pound will be used as input data in this simulation, as shown in Fig. 2. The POME has a temperature range of 80–90 °C.
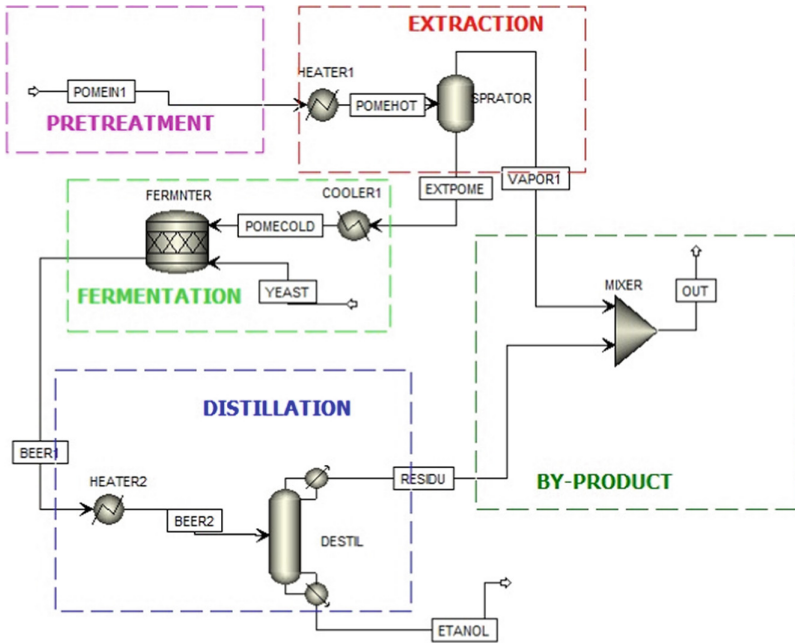

Fig. 2. Design simulation.

4   Result

The outputs simulation will generate two main products, namely ETHANOL and by-products (OUT). It can be seen from Fig. 3, 10 L tonnes/day of POME can produce main products of 0.187 L tonnes/day. main products be composed of 0.017 L Tons/day H_2O, of 0.079 L Tons/day C_2H_5OH, 0.090 L Ton/day CO_2, and 0.002 Tons/day contents others. By-products of 9.823 L Ton/day are composed of 9.797 L Ton/day H_2O, 0.0169 L Ton/day C_2H_5OH, and 0.0097 L Ton/day contents others.
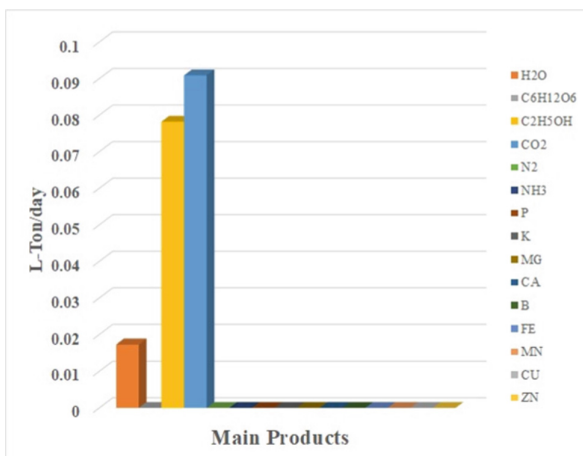
Fig. 3. Main products composition.

5   Conclusion

The recycling of POME into bioethanol as a renewable energy fuel has been done in the simulation environment to reduce environmental pollution caused by POME. Ten L Ton/day of POME can generate bioethanol 0.186 L Ton/day with the composition of 41.95% C_2H_5OH, 9.29% H_2O, and 48.76% CO_2. However, more research is needed to make that bioethanol usable as vehicle fuel. The by-products of 9.823 Ton/day with 99.7% H_2O can be utilized as water sources in industry or watering the plantation. The water and carbohydrates content also influence the result of the bioethanol content.

References

1. Perkebunan, D.: Statistik Perkebunan Indonesia (Tree Crop Estate Statistics Of Indonesia 2017–2019) Kelapa Sawit (Palm Oil), Directorate General of Estate Crops at Ministry of Agriculture Indonesia, pp. 1–81 (2019). http://ditjenbun.pertanian.go.id
2. BPS-Statistics Indonesia, Indonesian oil palm statistics 2018 (2019)
3. Foong, S.Z.Y., Andiappan, V., Foo, D.C.Y., Ng, D.K.S.: Flowsheet Synthesis and Optimisation of Palm Oil Milling Processes with Maximum Oil Recovery. Green Technologies for the Oil Palm Industry (2019). https://doi.org/10.1007/978-981-13-2236-5_1
4. Awalludin, M.F., Sulaiman, O., Hashim, R., Nadhari, W.N.A.W.: An overview of the oil palm industry in Malaysia and its waste utilization through thermochemical conversion, specifically via liquefaction. Renew. Sustain. Energy Rev. **50**, 1469–1484 (2015). https://doi.org/10.1016/j.rser.2015.05.085
5. Poh, P.E., Wu, T.Y., Lam, W.H., Poon, W.C., Lim, C.S.: Waste management in the palm oil industry: plantation and milling processes (2020)
6. Igwe, J.C., Onyegbado, C.C.: A Review of palm oil mill effluent (POME) Water Treatment **1**(2), 54–62 (2007)
7. Hassan, M.A., Abd-Aziz, S.: Waste and Environmental Management in the Malaysian Palm Oil Industry. AOCS Press (2011)

8. Lee, Z.S., Chin, S.Y., Lim, J.W., Witoon, T., Cheng, C.K.: Treatment technologies of palm oil mill effluent (POME) and olive mill wastewater (OMW): a brief review. Environ. Technol. Innov. 100377 (2019). https://doi.org/10.1016/j.eti.2019.100377

9. Poh, P.E., Yong, W.J., Chong, M.F.: Palm oil mill effluent (POME) characteristic in high crop season and the applicability of high-rate anaerobic bioreactors for the treatment of pome. Ind. Eng. Chem. Res. **49**(22), 11732–11740 (2010). https://doi.org/10.1021/ie101486w

10. Garritano, A.N., de O. Faber, M., De Sà, L.R.V., Ferreira-Leitão, V.S.: Palm oil mill effluent (POME) as raw material for biohydrogen and methane production via dark fermentation. Renew. Sustain. Energy Rev. **92**(2017), 676–684 (2018). https://doi.org/10.1016/j.rser.2018.04.031

11. Yadav, E.S., Indiran, T., Nayak, D., Aditya Kumar, C., Selvakumar, M.: Simulation study of distillation column using Aspen plus Mater. Today Proc. (2020) https://doi.org/10.1016/j.matpr.2020.07.609

An Enhancement of Crack Formulation for Vibration Analysis of Thin Plate with Three Parallel Cracks

Muhamad Syafwan Azmi[1] , Rainah Ismail[1,2]([✉]) , Tiew Yong Leek[1],
Mohd Hafizil Izuan Mohmad Nasir[3], and Maimunah Ismail[3]

[1] Fakulti Kejuruteraan Mekanikal, Universiti Teknikal Malaysia Melaka, Hang Tuah Jaya,
76100 Durian Tunggal, Melaka, Malaysia
rainah@utem.edu.my
[2] Centre for Advanced Research on Energy, Universiti Teknikal Malaysia Melaka, Hang Tuah
Jaya, 76100 Durian Tunggal, Melaka, Malaysia
[3] Kolej Komuniti Kuantan, B24, Jalan Im3/13, Bandar Indera Mahkota, 25200 Kuantan,
Pahang, Malaysia

Abstract. The natural frequency of a structure can be highly affected by the condition of damage presented in the structure. This study aims to diversify the past studies by conducting a theoretical analysis of a thin plate with three parallel horizontal cracks. First, Kirchoff's classical plate theory was used to obtain the governing equation of a thin plate. Next, Galerkin's method was employed on the governing equation and Berger formulation for transverse deflection. The governing equation was then finalized for the CCSS boundary condition to obtain the fundamental natural frequency. Results from the comparison show that a good agreement can be obtained with a maximum percentage error of 0.60%. Later, the fundamental natural frequency for a single crack at upper, middle and lower and all three cracks was computed. A decreasing trend can be observed with the lowest natural frequency exhibited when all three cracks are presented due to stiffness loss. This study supplements the existing theoretical analysis on a thin plate for three parallel horizontal cracks.

Keywords: Theoretical analysis · Vibration · Thin plate · Multiple cracks

1 Introduction

Plate-like structures have been used widely in many engineering applications, typically as shells or faces for enclosed structures, such as automobiles or aeroplanes. The use of a thin plate structure also helps in reducing the overall weight. Unfortunately, thin plate structures are susceptible to high vibration. Prolonged exposure to vibration can lead to extensive damage such as cracks due to fatigue, potentially leading to catastrophic failure.

From the literature, many theoretical studies have been conducted on thin-plate structures with cracks. Israr et al. (2009) studied a single centre partially cracked thin isotropic plate [1]. Bose et al. (2013) investigated part through single centre cracked plate structure with random crack's orientation [2]. One of the authors' previous studies in Ismail (2012) investigated thin plate with variable single surface crack angles [3]. The work was then extended by Joshi (2014) which studied a single and two perpendicular internal cracks located at the centre of the plate [4]. Similar work has been done by Ramtekkar et al. (2015), which investigated single and multiple perpendicular cracks at the centre of the thin plate [5]. Jain et al. (2018) further investigated for multiple part through cracks at the centre of a plate [6].

This study aims to extend the study by adding a theoretical analysis of a thin plate with three parallel horizontal cracks. The developed model was first compared to the previous study by Jain et al. (2018) to validate the derived mathematical model [6]. The results for a single crack at each location and three parallel cracks were computed upon good agreement.

2 Methodology

The plate under consideration in this study with three parallel horizontal cracks is illustrated in Fig. 1.
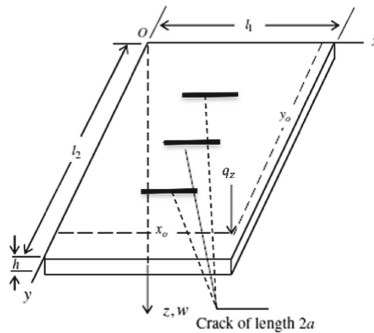

Fig. 1. Isotropic plate with three parallel horizontal cracks.

The derivation began with the formulation of governing equation of the plate from the well-accepted Kirchhoff's plate theory, also known as classical plate theory. Then, the formulation of the crack term with three parallel cracks was carried out using the line spring model (LSM). From the past literature, a sequence of equations with the different behaviour of crack of a thin plate for the relationship between bending stress and nominal tensile at the crack location had been obtained by using the LSM formulation. Similarly, the governing equation was then modified to obtain new relations between the plate's nominal tensile and bending stresses with three parallel cracks (one-third, centre, and

two-thirds along the y-axis of a plate). Finally, the substitution and derivation produced the final simplified form in Eq. (1) when considering the crack length 2a in three parallel arrangements.

$$D\left(\frac{\partial^4 w}{\partial x^4} + 2\frac{\partial^4 w}{\partial x^2 \partial y^2} + \frac{\partial^4 w}{\partial y^4}\right) = -\rho h \frac{\partial^2 w}{\partial t^2} + n_x \frac{\partial^2 w}{\partial x^2} + q_z - \frac{6a}{(6a_{tb} + a_{tt})(1 - v^2)h + 2a} n_o \frac{\partial^2 w}{\partial y^2}$$

$$+ \frac{6aD\left(\frac{\partial^4 w}{\partial y^4} + v\frac{\partial^4 w}{\partial x^2 \partial y^2}\right)}{3\left(\frac{a_{bt}}{6} + a_{bb}\right)(3 + v)(1 - v)h + 2a} \tag{1}$$

The symbol D is defined as flexural rigidity with the formula applied $D = (Eh^3)/12(1-v^2)$, where E is the Young modulus of an aluminium plate, h is the thickness of the plate, v is the Poisson's ratio. The other symbol w is transverse deflection, n_x and n_o are the in-plane forces per unit length, ρ is the density of the aluminium plate and q_z is the lateral load. The elements $a_{tb} = a_{bt}$ are non-dimensional stretching-bending compliance or non-dimensional bending-stretching compliance, a_{tt} is non-dimensional stretching compliance, a_{bb} is non-dimensional bending compliances. By applying the Galerkin's method for boundary condition and Berger formulation for transverse deflection, the equation for natural frequency can be obtained.

3 Results and Discussion

The fundamental natural frequency was computed using the derived equation for intact and cracked plates with half crack length of $a = 0.01$ m. The boundary condition considered was clamp-clamp-simply supported-simply supported (CCSS). The properties of the material used were the Young modulus of aluminium plate with 5083-grade $E = 70.3$ GPa, the density of aluminium plate $\rho = 2660$ kg/m^3 and the thickness of the plate $h = 10$ mm, the Poisson's ratio $v = 0.33$ and crack depth = 6 mm. The results were validated by comparing to study by Jain et al., (2018) for intact plate and middle cracked plate at the centre [6]. The results are tabulated in Table 1. A good agreement can be observed from the comparison with a minimal percentage error at a maximum of 0.60%. Hence, using the validated derived equation, the results for upper and lower crack as well as all three cracks were computed. The results are tabulated in Table 2. From the results presented in Table 2, it can be observed that the fundamental natural frequency show decreasing trend with all three cracks exhibited the lowest values due to decreasing stiffness of the plate.

Table 1. Comparison of the fundamental natural frequency of intact and cracked plate with Jain et al. 2018 [6].

			Natural frequency (first mode), w(rad/s)					
	Length of the plate (m)		Intact plate			Cracked plate, a=0.01m		
Boundary conditions	L1	L2	Present	Jain et al., 2018 [6]	Error (%)	Present	Jain et al., 2018 [6]	Error (%)
CCSS	1	1	444.03	445.73	0.38	432.00	430.79	0.28
	0.5	1	1161.37	1161.80	0.04	1153.88	1153.30	0.05
	1	0.5	1161.37	1161.80	0.04	1086.94	1080.45	0.60

Table 2. Results of fundamental natural frequency for intact, single and multiple cracked plate.

			Natural frequency (first mode), w(rad/s)				
	Length of the plate (m)		Intact plate	Cracked plate, a=0.01m			
Boundary conditions	L1	L2		Upper	Middle	Lower	3Cracks
CCSS	1	1	444.03	434.27	432.00	430.17	416.86
	0.5	1	1161.37	1156.08	1153.88	1151.91	1144.55
	1	0.5	1161.37	1108.90	1086.94	1067.23	992.70

4   Conclusions

This study presents the mathematical modelling for three parallel horizontal cracks in a thin plate as an addition to existing studies in the literature. The derived governing equation was validated through comparison to the previous study where good agreement can be obtained. The fundamental natural frequency for each horizontal crack in a thin plate shows a decreasing trend from upper, middle, and lower crack locations. The lowest value of fundamental natural frequency was obtained when all three cracks were presented. The developed mathematical modelling can be used with great confidence for multiple horizontal cracks in a thin plate.

References

1. Israr, A., Atepor, L.: Investigation of the nonlinear dynamics of a partially cracked plate. J. Phys. Conf. Ser. **181**(1), 1–8 (2009)
2. Bose, T., Mohanty, A.R.: Vibration analysis of a rectangular thin isotropic plate with a part-through surface crack of arbitrary orientation and position. J. Sound Vib. **332**(26), 7123–7141 (2013)
3. Ismail, R., Vibration analysis of a plate with an arbitrarily orientated surface crack. PhD's thesis, University of Glasgow (2012)
4. Joshi, P.V., Jain, N.K., Ramtekkar, G.D.: Analytical modeling and vibration analysis of internally cracked rectangular plates. J. Sound Vib. **333**(22), 5851–5864 (2014)
5. Ramtekkar, G.S., Jain, N.K., Joshi, P.V.: Vibration Analysis of Isotropic Plate with Perpendicular Surface Cracks. Advances in Structural Engineering. Springer, New Delhi (2015)
6. Jain, N.K., et al.: An extension of line spring model for vibration analysis of thin isotropic plate containing multiple part-through cracks: an analytical approach. Vib. Phys. Syst. **29**, 1–25 (2018)

Modelling Salt Film During Localized Corrosion of Steel in Aqueous Chloride Solution

Suhaila Salleh[1(✉)], Alzakri Ekhwan[2], and Noor Mirza Syamimi Mortadha[1]

[1] Fakulti Kejuruteraan Mekanikal, Universiti Teknikal Malaysia Melaka, Hang Tuah Jaya, 76100 Durian Tunggal, Melaka, Malaysia
suhaila@utem.edu.my

[2] Mechanical Section, Engineering Department, Group Technical Solutions Project Delivery & Technology (PD&T), Petroliam Nasional Berhad (PETRONAS), 50088 Kuala Lumpur, Malaysia

Abstract. Salt film formation is an occurrence that happens during pit growth. A new perspective on pitting corrosion has been proposed which involves salt film formation as a consequence to pitting corrosion, rather than a requirement for stable pit growth. This paper presents a two-dimensional axial symmetry corrosion model representing a microscale pit in steel. The corrosion activities are studied using a commercial finite element program, COMSOL Multiphysics 5.6. The mass transport is considered and solved using Nernst-Planck resolutions. The model allows the prediction of pit propagation after the initiation state by applying thermodynamics formulas based on Pourbaix diagram of iron and is able to incorporate the salt film formation on the metal surface and produce polarization curve as in published literature. The results show that the salt film forms on the metal surface is in agreement to a newly proposed model, which stated that salt film is as a consequent formation to stable pit growth.

Keywords: Corrosion · Model · Steel

1 Introduction

A wide range of engineered materials receives an impact in the chloride induced corrosion of metals. In the presence of chloride ions, corrosion is highly accelerated and propagates aggressively [1–3]. This destruction of materials due to its reaction with its surroundings results in measurable changes [1]. Through literature, it has been established that there are three stages of pitting, namely pit induction/initiation, pit propagation and stable pitting [1–4]. These stages of pitting are controlled by the ability of metal to be in active to passive condition, and vice-versa. Pitting, a form of aqueous corrosion, is a common localized corrosion and most destructive, due to its perforating nature. It has also been known that the presence of halides induced pitting corrosion. This phenomenon whereby an active corroding metal suddenly turns passive and remain passive, is called the repassivation of metal, a condition significant to illustrate pitting propagation.

In this research, steel immersed in aqueous chloride solution of pH7 is studied. In the presence of chloride ions, Cl^-, in the electrochemical reaction with its surrounding produces a layer covering the metal surface, known as salt film. The film formed on iron is predominantly the solid iron (II) chloride, $FeCl_2$ [5], which forms due to the build-up of a highly concentrated and acidic metal chloride solution at the near-metal surface. A newly proposed model by Li [6, 7] suggests that the salt film precipitating on the metal surface is just a consequence of the saturated ionic species which allows the pit to achieve diffusion-controlled pit growth, rather than charge transfer control. This concludes that the salt film is not a prerequisite for stable pit growth. The aim of this study is to affirm that a two-dimensional axial symmetry model representing a micropit in aqueous sodium chloride solution with pH7 with the framework similar to the model done by Salleh [5], is in lieu with the findings in Li's proposed model. COMSOL Multiphysics 5.6 is used as a tool to run the results.

2   Method

The model applies the framework using Nernst-Planck formulation on the electrochemistry of ionic species and a unique incorporation of mathematical equations to formulate salt film formation during stable corroding activities [5]. It uses the stated framework but taking into account eleven neutral aqueous chemical species to illustrate the corrosion model with salt film formation (Fe^{2+}, OH^-, H^+, $FeOH^+$, Na^+, Cl^-, $FeCl^+$, H_2, Fe^{3+}, FeO_2^- and $FeCl_2^+$). The manner of these ionic species is being governed by the Nernst-Planck law for the case where electroneutrality is enforced.

The model incorporates the respective currents for metal dissolution and reduction of hydrogen ions, H^+, to counter for the active state of metal. These reactions applied Tafel expression. The metal dissolution rate and the hydrogen ions reduction rate follow Fick's First Law of Diffusion. This, in turn, stated that the kinetics produce their respective ionic fluxes. The calculation of saturated ion concentration, C_{sat}, is shown by Salleh [5]. A critical passivation current density inside the pit environment is then incorporated in the model, which increases the total metal ion concentration, C_m. This is actually the pit solution chemistry. By using a function that relates the total metal ion concentration, C_m, and the saturation concentration of metal ions inside the pit, the critical passivation current density can be calculated. If the local chemistry has high C_m values (for example >70% saturation) in corrosion products, passivation can be prevented. Saturation is calculated using the formula below:

$$\frac{C_m}{C_{sat}} \times 100\% \tag{1}$$

3   Results and Discussion

The model has provided sophisticated corrosion predictions that account for the ionic species being considered. Figure 1 shows the polarization curve of five points inside and at the mouth of the pit. The five points of referral being Point 1 at the bottom of the pit

with Point 5, 6, and 7 inside the pit, and point 8 is at the mouth of the pit. Points 1, 5 and 6 are corroding stably. The current density in Point 7 is reducing and soon results in passivity, whilst the sudden drop in the current density of Point 8 suggests immediate passivity at time 1150 s, indicating the occurrence of pitting corrosion.
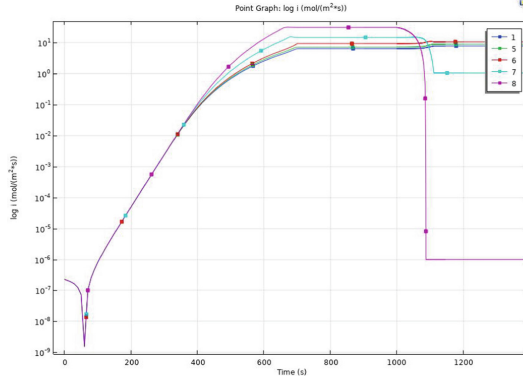

Fig. 1. Polarization curve plotted against time.

The total concentration of metal ion, C_m, and the saturation concentration of metal ion, C_{sat}, are plotted in Fig. 2(a) and (b), respectively. For the stated points, the graphs reach a plateau level due to the saturatedness being implemented in the model.

(a)   (b)
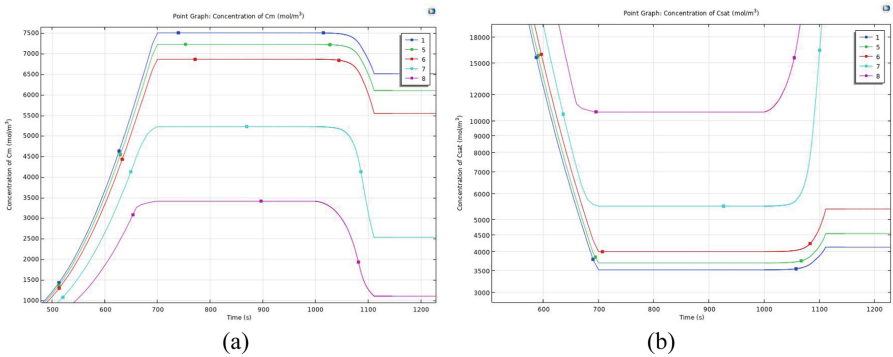
Fig. 2. (a) C_m against time and (b) C_{sat} against time.

Through the formation of salt film, saturation of iron is calculated and shown in Table 1. As stated by Li, when $C_m < C_{sat}$, salt film will not form on the pit surface [6]. Satisfying this condition, Points 1, 5 and 6 are the points where salt film occurs, indicating stable corrosion. This relates to the polarization curve in Fig. 1, which suggests salt film forms at actively corroding points, as stated by Li.

Table 1. Saturation percentage at active points.

Point in geometry	C_m (in mol/m^3)	C_{sat} (in mol/m^3)	Saturation (%)
1	7500	3500	214
5	7200	3700	194
6	6850	4000	171
7	5300	5500	96
8	3400	10600	32

4   Conclusion

This work was devoted to show the capability of the two-dimensional axial symmetry model to show that salt film precipitating on the metal surface is a consequence of saturated ionic species. The model showed evidence of more than 100% saturation that active corroding points, indicated by high level of current densities, results in high concentration of total metal ion and saturated ion concentration ratio.

References

1. Guo, P., et al.: Direct observation of pitting corrosion evolutions on carbon steel surfaces at the nano-to-micro-scales. Sci. Rep. **8**(7990), 1–12 (2018)
2. Boraei, N.F.E., Rehim, S.S.A.E.: Electrochemical behavior of tin anode in ascorbic acid solutions. Mater. Chem. Phys. **215**, 332–338 (2018)
3. Yu, Q., Pan, T.: Microstructural modeling of pitting corrosion in steels using an arbitrary Lagrangian-Eulerian Method. Metall. and Mater. Trans. A. **48**(5), 2618–2632 (2017)
4. Ahmad, Z.: Principles of Corrosion Engineering and Corrosion Control. Butterworth-Heinemann, Burlington, MA (2006)
5. Salleh, S.: Modelling pitting corrosion in carbon steel materials. Ph.D. dissertation, School of Materials, University of Manchester, Manchester, UK (2013)
6. Li, T., Scully, J.R., Frankel, G.S.: Lozalized corrosion: passive film breakdown vs. pit growth stability: part III. a unifying set of principal parameters and criteria for pit stabilization and salt film formation. J. Electrochem. Soc. **165**(11), C762–C770 (2018)
7. Li, T., Scully, J.R., Frankel, G.S.: Lozalized corrosion: passive film breakdown vs. pit growth stability: part IV. the role of salt film in pit growth: a mathematical framework. J. Electrochem. Soc. **166**(6), C115–C124 (2019)

Effects of Winglet on the Aerodynamic Characteristics of Airfoil Wing NACA 4415

Rofi Juliatma[1,2], Farel H. Napitupulu[2], and Himsar Ambarita[1,2(✉)]

[1] Sustainable Energy Research Centre, Universitas Sumatera Utara, Kampus Padang Bulan, Medan 20222, Indonesia
himsar@usu.ac.id

[2] Mechanical Engineering Department, Faculty of Engineering, Universitas Sumatera Utara, Kampus Padang Bulan, Medan 20222, Indonesia

Abstract. The objective of this work is to explore numerically the effect of the winglet on the aerodynamics performance of the aircraft wing NACA 4415. Three-dimensional governing equation on the wing have been developed. The turbulence was modeled using standard k-epsilon model. The numerical method was carried out using commercial CFD code. The flow fields were plotted and drag and lift coefficients were calculated. The results show that the fluid flow over the wing with winglet was more streamline in comparison with original wing. This makes the drag coefficient is lower, but the lift coefficient is higher. Thus, the performance of the wing with winglet is better.

Keywords: Winglet · NACA 2415 · CFD

1 Introduction

Study on the fluid flow characteristics over airfoil can be used to predict the performance of an aircraft wing. There are two performance parameters typically used to predict the performance, they are lift and drag forces. The lift force depend on the shape of the airfoil, the area of the wing and the speed. During takeoff and landing, the aircraft's speed is relatively low, here the lift force should be kept maximum to improve the performance of the aircraft. Thus, there performance of the wing should be optimized. Studies on the optimum design of an aircraft wing have come under scrutiny [1]. The studies can be numerically and experimentally. The focus is to get a design that can increase the lift force of the aircraft, and reduce the drag force.

There are several studies on how to optimize the performance of aircraft airfoils have been reported. Koreanschi et al. [2] employed genetic algorithm to carried out an optimization problem for improving the aerodynamics performances of an aircraft wing tip through upper surface morphing. The work was carried out on airfoil NACA 4412 for 16 flight cases expressed in terms of various combinations of speeds, angles of attack and aileron directions. Another issues on the air craft study is the vortices that occur in the wings of the aircraft, especially in the wingtip area of the aircraft [3]. This is due to the high air flow rate which causes negative effects such as increasing drag and

ultimately lowering the aircraft's lift [3]. One of the potential solution to this problem is employing winglet to the wing. It was demonstrated that the aircraft wing performance is increasing by modifying and varying the main geometry of the airfoils and winglets. The winglet serves to reduce drag in the wing top area which can ultimately reduce drag on the aircraft wing, which has an effect on the efficiency of fuel use [4]. The winglet has been widely applied to modern aircraft today. However, studies on the winglet design is still an interesting topics to be carried out [5, 6]. In order to explore the effect of winglet, experimental and numerical methods can be employed. Considering the cost and time, numerical method using commercial Computational Fluid Dynamics (CFD) is known as a popular tool to solve the fluid flow characteristics over aircraft wing [7, 8]. Study on winglets by using CFD has been reported by several literature. Effects of semicircular winglets and elliptical winglets on an airfoil NACA 65321 have been explored using a turbulent model [9, 10]. The results showed that semicircular winglets choosing higher performance with an angle of 450. The simulation method was also used to evaluate the effect of using winglets on the mileage of an aircraft, and it was seen that there was an increase in mileage of 10%. The most recent work by Seshaiah et al. [10] carried out a CFD simulation to explore air craft winglet at different angles. The emphasis was on the modeling of various winglet (blended winglet and rated winglet).

It was shown that study on the winglet effect on the aircraft wing by using CFD need to be explore more. Many of airfoil types that installed with winglet have not been reported. One of them is NACA 4415 that is used in an aircraft TBM 700 produced by Socata. In this study, CFD is employed to study the fluid flow characteristics of aircraft wing of NACA 4415. The objective is to explore the effect of winglet to the performance of the wing. The results are expected to supply necessary information for optimizing the wing design of the aircraft.

2 Methods

The original wing model without winglet and the modified wing model with winglet are shown in Fig. 1. Here a three-dimensional computational domain is employed and shown in the figure. The governing equations that solved here are mass conservation and momentum equations given below.

$$\frac{\partial \rho}{\partial t} + \frac{\partial}{\partial x_i}(\rho u_i) = 0 \tag{1}$$

$$\rho \frac{Du_i}{Dt} = -\frac{\partial p}{\partial x_i} + \frac{\partial}{\partial x_j}\left[\mu\left(\frac{\partial u_i}{\partial x_j} + \frac{\partial u_j}{\partial x_i} - \frac{2}{3}\delta_{ij}\frac{\partial u_i}{\partial x_i}\right)\right] + \frac{\partial}{\partial x_j}\left(-\overline{\rho u_i' u_j'}\right) \tag{2}$$

The turbulent in the above equations closed by using the standard $k - \varepsilon$ turbulence model proposed by Lauder and Spalding. The $k - \varepsilon$ equations are as follows.

$$\rho \frac{Dk}{Dt} = \frac{\partial}{\partial x_i}\left[\left(\mu + \frac{\mu_t}{\sigma_k}\right)\frac{\partial k}{\partial x_i}\right] + G_k + G_b - \rho\varepsilon - Y_M \tag{3}$$

$$\rho \frac{D\varepsilon}{Dt} = \frac{\partial}{\partial x_i}\left[\left(\mu + \frac{\mu_t}{\sigma_\varepsilon}\right)\frac{\partial \varepsilon}{\partial x_i}\right] + C_{1\varepsilon}\frac{\varepsilon}{k}(G_k + C_{3\varepsilon}G_b) - C_{2\varepsilon}\rho\frac{\varepsilon^2}{k} \tag{4}$$

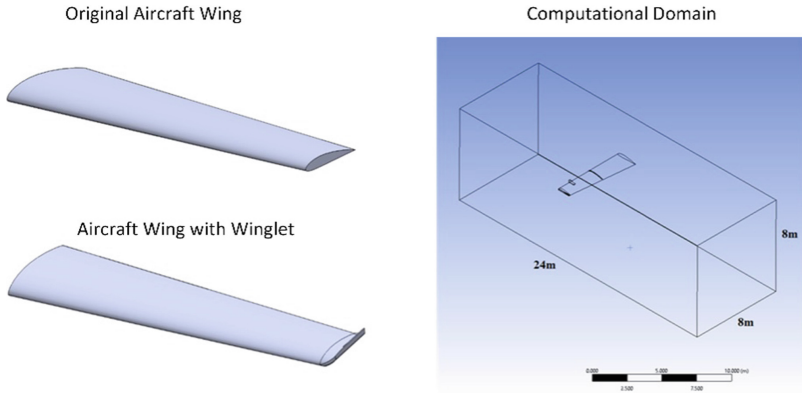The above equations solved iteratively by using commercial CFD code ANSYS Fluent.

Fig. 1. Wing models and computational domain.

3   Results

3.1   Fluid Flow Characteristics

The fluid flow characteristics are analyzed by plotting streamlines, vector velocity and vortex flow. Figure 2 shows the vector velocity and vortex flows over the original wing and wing with winglet.
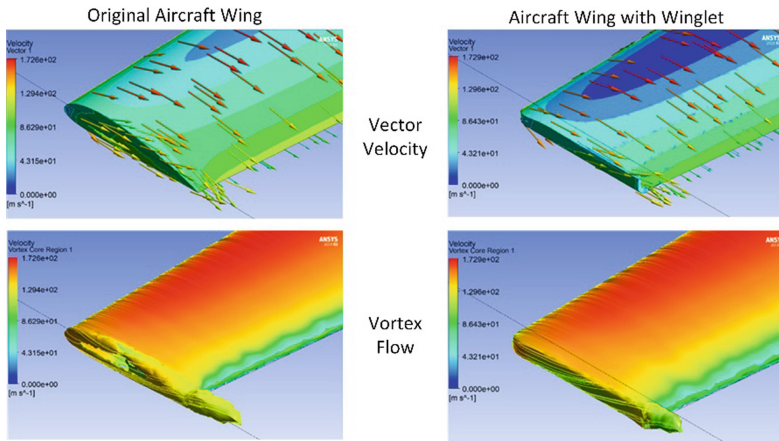

Fig. 2. Vector velocity and vortex flow over the aircraft wing.

The vector velocity shows that on the edge of the original wing some vectors leaving the wing edge with a relatively bigger than the wing with winglet. On the other hand, for wing with winglet, the gradient of vector velocity on the edge is relatively lower. This leads to a better performance of the wing with winglet. A more clear comparison shown by vortex flow. It can be seen that the flow around the wing with winglet more

streamline in comparison with original wing. This fact suggest that the presence of the winglet makes the fluid flow more streamlines.

3.2 Lift and Drag Coefficients

In order to explore effects of the winglet to the performance of the wing, the lift coefficient and drag coefficient have been calculated and shown in Table 1. The comparison is made at the same Max Chamber of 4%. As expected the drag coefficient of the wing with winglet is lower than wing with winglet. This agree with the vector velocity and vortex shown before. On the other hand, the lift coefficient of wing with winglet is higher that original wing. The effect of the winglet shows improvement of the wing.

Table 1. The performance of the original wing and wing with winglet.

Type	MAX chamber	Cd	C_p	Pressure (Pa)	CL
Original wing	4%	0.008565	0.005335	499.38	0.17909
Wing with winglet	4%	0.008548	0.005314	510.15	0.18053

4 Conclusion

A numerical simulation using commercial code CFD has been carried out to explore effect of the winglet to the wing performance of NACA 4415 profile. Vector velocity and vortex have been plotted. The lift and drag coefficients have been calculated. The conclusions are as follows. The presence of the winglet makes the flow field more streamline around the edge. This makes the drag coefficient is lower, but the lift coefficient is higher. Thus, the performance of the wing with winglet is better.

References

1. Bartl, J., Sagmo, K.F., Bracchi, T., Sætran, L.: Performance of the NREL S826 airfoil at low to moderate Reynolds numbers—a reference experiment for CFD models. Eur. J. Mech.-B/Fluids **75**, 180–192 (2019)
2. Koreanschi, A., et al.: Optimization and design of an aircraft's morphing wing-tip demonstrator for drag reduction at low speed, Part I - Aerodynamic optimization using genetic, bee colony and gradient descent algorithms. Chin. J. Aeronaut. **30**(1), 149–163 (2017)
3. Whitcomb, R.: A design approach and selected wind tunnel results at high sub-sonic (1976)

4. Johansen, J., Sørensen, N.N.: Numerical analysis of winglets on wind turbine blades using CFD. In: Proceeding of European Wind Energy Conference and Exhibition, Milan, Italy (2007)
5. Takenaka, K., Hatanaka, K.: Multidisciplinary design exploration for a winglet. J. Aircr. **45**, 1601–1611 (2012)
6. Verstraeten, J.G., Slingerland, R.: Drag characteristics for optimally span-loaded planar, wingletted and C wings. J. Aircr. **46**(3), 962–971 (2009)
7. Guerrero, J., Sanguineti, M., Wittkowski, K.: CFD study of the impact of variable cant angle. Aerospace **5**, 126 (2018)
8. Zhang, T., Elsakka, M., Huang, W., Wang, Z.: Winglet design for vertical axis wind turbines based on a design of experiment and CFD approach. Energy Convers. Manag. **195**, 712–726 (2019)
9. Azlin, M.A., Mat Taib, C.F.: CFD analysis of winglets at subsonic flow. In: Proceedings of the World Congress on Engineering, London, UK (2011)
10. Panagiotou, P., Kaparos, P., Yakinthos, K.: Winglet design and optimization for a MALE UAV using CFD. Aerosp. Sci. Technol. **39**, 190–205 (2014)
11. Seshaiah, T., Vasu, B., Reddy, K.V.K., Bridjesh, P.: Analysis on air craft winglet at different angles by using CFD simulation. Mater. Today: Proc. (2021). https://doi.org/10.1016/j.matpr.2021.02.073

Surface Engineering and Tribology

Study on Lubrication Performance of Journal Bearing with Heterogeneous Rough/Smooth Pattern

Mohammad Tauviqirrahman[1(✉)] , Jamari[1], Eflita Yohana[1],
Arjuno Aryo Wicaksono[1], and Muchammad[1,2]

[1] Laboratory for Engineering Design and Tribology, Diponegoro University, Semarang,
Indonesia
mohammad.tauviqirrahman@ft.undip.ac.id

[2] Laboratory for Surface Technology and Tribology, Enschede, The Netherlands

Abstract. The main goal of this research is to evaluate the surface roughness level on the performance of journal bearing using the computational fluid dynamics (CFD) method. Aiming to further enhance the acoustic and tribological lubrication performance, a novel heterogeneous rough/smooth pattern is introduced. The results reveal that increasing the roughness level can improve the load support and reduce the bearing noise. However, an undesirable scenario is observed, namely increased friction force of the heterogeneous rough/smooth bearing.

Keywords: Acoustic · Computational fluid dynamics (CFD) · Roughness

1 Introduction

As is well known, no surface is smooth due to natural irregularities. Incorrect surface finishing during journal bearing production might also result in unexpected surface roughness. Recent studies [1–4] have explored the impact of surface roughness on hydrodynamically lubricated journal bearings. In many studies, surface roughness models, such as the Christensen stochastic model [1], the Greenwood-Williamson (GW) contact model, the sinusoidal waviness model [3], and the sand-grain model [4], have been employed, and it has been demonstrated that surface roughness has a significant impact on lubrication performance. Furthermore, by constructing an engineered heterogeneous bearing surface, on which the roughness is imparted to a given area and is absent in others, the lubrication performance can be increased [4]. Based on extensive literature survey, few research works have been conducted to determine the influence of bearing surface roughness on noise.

Considering the increased interest in improving bearing performance with enhanced computer technology, this research focuses on investigating the effect of artificial surface roughness on acoustic and tribological bearing performance using the computational fluid dynamics (CFD) approach. To more accurately represent the cavitation phenomena that may occur in the bearing, the multi-phase cavitation approach is used in this research, as addressed by several authors [5, 6].

2   Method

A journal bearing requires two sliding surfaces in order to properly lubricate itself. The problem is solved using the Navier-Stokes and continuity equations based on a finite volume technique. The commercial CFD software ANSYS FLUENT® is utilized [7].

The momentum equation can be described as [7]:

$$\rho \frac{Du_i}{Dt} = -\frac{\partial p}{\partial x_i} + \rho G_i + \frac{\partial}{\partial x_j}\left[2\eta e_{ij} - \frac{2}{3}\eta(\nabla.u_i)\delta ij\right] \tag{1}$$

The continuity equation can be written as follows

$$\frac{\partial}{\partial x_i}(\rho u_i) = 0 \tag{2}$$

The flow is considered turbulent in order to represent the bearing characteristic more accurately. Standard wall functions are utilized to implement the turbulent model of realizable k-ε. To model cavitation phenomena, the Zwart-Gelber-Belamri multi-phase cavitation model is adopted [7]. Moreover, the sand-grain model is used to characterize the roughness profile of the sleeve surface in this work. The modified law-of-the-wall for mean velocity is used to represent the surface roughness.
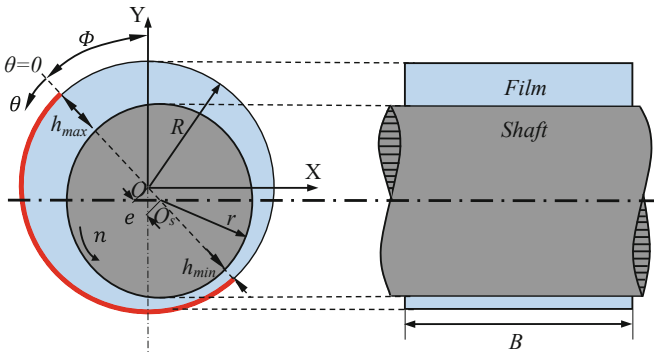

Fig. 1. Representation of heterogeneous rough/smooth bearing.

The bearing noise indicated by the acoustic power level is of particular interest in this acoustic analysis. Due to the turbulence in the lubricant, noise typically occurs during bearing operation. The broadband noise source model is used in this work to solve the noise generated by the lubricant [7].

The CFD model of a journal bearing with artificial roughness is shown in Fig. 1. Here, the roughness is applied to a specific area of the bearing, i.e. from θ 0° to 180° in a circumferential direction. The R_a (the arithmetic average of the roughness profile) is adopted to represent the level of surface roughness. In this work, R_a is categorized to precision ($R_a = 0.1$ µm), fine ($R_a = 0.8$ µm), medium ($R_a = 6.3$ µm), and rough ($R_a = 25$ µm). The SIMPLE algorithm is used in the velocity-pressure coupling for all

subsequent computations. The momentum equations are discretized using a first-order upwind technique, whilst the volume fraction equations are discretized using the QUICK scheme.

3   Results and Discussion

Figure 2 illustrates the load-carrying capacity, friction force, and average acoustic power level at various levels of surface roughness. Numerous observations can be made in light of Fig. 2. To begin, all load-carrying capacity values are greater than zero, indicating that the application of surface roughness affects load-carrying capacity. As is well known, ordinary journal bearings (smooth) do not have load carrying capacity in this concentric scenario ($\varepsilon = 0$). Second, load-carrying capacity increases with increasing the R_a level. The increase in load-carrying capacity varies by case; for example, the "fine" case increases by 12.7% in comparison to the "precision" surface. This result is consistent with [8], which evaluated the influence of surface roughness on hybrid journal bearings using the transverse and longitudinal direction of texturing. They claimed that by employing a transverse model of surface roughness, the load-carrying capacity of the journal bearing might be increased.
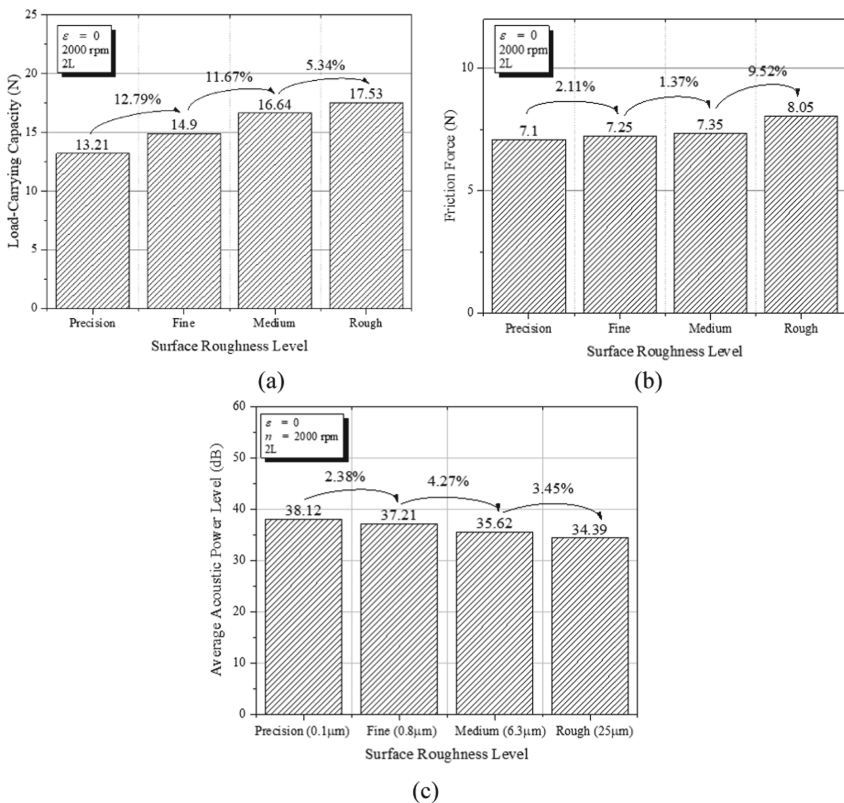

(a)   (b)

(c)

Fig. 2. Lubrication performance: (a) load-carrying capacity, (b) friction force, and (c) average acoustic power levels of journal bearings with varying levels of surface roughness.

In terms of friction force, Fig. 2(b) illustrates the friction force value for each value of surface roughness variation. As observed in Fig. 2(b), the frictional force does not exhibit a substantial rise in magnitude as the surface roughness increases. When comparing the "fine" and "medium" surfaces, the friction force decreases by 2% in the "fine" case and rises by 2.1% in the "medium" one. The friction force increases by 11% in the "rough" instance. In contrast to load-carrying capability, heterogeneous rough/smooth bearings result in increased friction force as the roughness rises. For this issue, future research will focus on how to minimize friction force through the optimization of artificial roughness parameters.

Regarding the noise indices of the bearing, Fig. 2(c) depicts the correlation between the average acoustic power level and the surface roughness level. It is found that the average acoustic strength level reduces as the surface roughness increases. According to the numerical results, it appears that adding surface roughness to the journal bearing can improve its acoustic and tribological performance, particularly by lowering the average acoustic power level and increasing load-carrying capacity. As can be observed from the data shown above, the rough surface roughness level provides the greatest improvement in tribological and acoustic performance when compared to other models.

4   Conclusion

The influence of surface roughness on finite length journal bearing was investigated using CFD. The multi-phase cavitation model was used to produce realistic results. The numerical results indicate that the journal bearings with a higher level of surface roughness have a positive effect on increasing the load support and reducing the noise. However, at the same time, the negative effect of heterogeneous rough/smooth bearing is highlighted, i.e. the increased friction force.

References

1. Kalavathi, G.K., Dinesh, P.A., Gururajan, K.: Influence of roughness on porous finite journal bearing with heterogeneous slip/no-slip surface. Tribol. Int. **102**, 174–181 (2016)
2. Cui, S., Gu, L., Fillon, M., Wang, L., Zhang, C.: The effects of surface roughness on the transient characteristics of hydrodynamic cylindrical bearings during startup. Tribol. Int. **128**, 421–428 (2018)
3. Al-Samieh, M.F.A.: Surface roughness effects for newtonian and non-newtonian lubricants. Tribol. Ind. **41**(1), 56–63 (2019)
4. Tauviqirrahman, M., et al.: CFD analysis of journal bearing with a heterogeneous rough/smooth surface. Lubricants **9**(9), 88 (2021)
5. Sun, D., Li, S., Fei, C., Ai, Y., Liem, R.P.: Investigation of the effect of cavitation and journal whirl on static and dynamic characteristics of journal bearing. J. Mech. Sci. Technol. **33**(1), 77–86 (2019). https://doi.org/10.1007/s12206-018-1208-3
6. Tauviqirrahman, M., Afif, M.F., Paryanto, P., Jamari, J., Caesarendra, W.: Investigation of the tribological performance of heterogeneous slip/no-slip journal bearing considering thermo-hydrodynamic effects. Fluids **6**(2), 48 (2021)
7. ANSYS, ANSYS Fluent, version 16.0: user manual. ANSYS, Inc., Canonsburg, USA (2017)
8. Tala-Ighil, N., Fillon, M., Maspeyrot, P.: Effect of textured area on the performances of a hydrodynamic journal bearing. Tribol. Int. **44**(3), 211–219 (2011)

CFD Analysis of Hydrodynamically Lubricated Textured Slider Bearings

Imam Syafaat[1(✉)] , Navis Rizqi[1], Muchammad[2] ,
Mohammad Tauviqirrahman[2] , and Budi Setiyana[3]

[1] Mechanical Engineering Department, Universitas Wahid Hasyim, Semarang, Indonesia
imamsyafaat@unwahas.ac.id
[2] Mechanical Engineering Department, University of Diponegoro, Semarang, Indonesia
[3] Laboratory for Surface Technology and Tribology, University of Twente,
Enschede, The Netherlands

Abstract. This study aims to analyze the effect of both a single rectangular and a semicircular shape to determine the distribution of pressures on the slider bearings. The results show the rectangular pocket with no slip conditions, the general pressure distribution on the inlet side, the pressure decreases when it enters the pocket. There is no effect of pressure in applying the slip boundary in rectangular pocket. The effect of giving a slip boundary makes a pressure drop of about 6%. The highest pressure increases in the highest Reynolds number, and vice versa. The rectangular pocket is more advantageous than the semicircular shape on the bearing surface.

Keywords: Hydrodynamics · Slider bearings · CFD

1 Introduction

Over the last several years, considerable research has been conducted with the goal of increasing machine efficiency by minimizing power losses caused by bearings. Due to their efficiency, cheap cost, and simplicity, bearings are critical components that are widely utilized in propulsion and industrial applications.

Many studies have been conducted to improve the performance of slider bearings on machines. Bearing surfaces are simplified into specific geometries. The experiment conducted by Henry et al. [1] examined the impact of hydrodynamic lubrication on textured thrust bearings. Song et al. [2] investigated the influence of slip conditions on the turbulence that occurs during thrust bearing lubrication. Nanbu et al. [3] investigated the effects of texture bottom shape and surface relative motion on the surface. They performed simulations on various pocket shapes but disregarded cavitation. Tauviqirrahman et al. [4] recently published a research on lubricated bearings with two pockets and a slip boundary.

On the basis of prior research, it has been shown that the influence of surface roughness, slip or no slip circumstances, and the usage of cavitation in lubricating performance has a significant effect on slider bearings. The purpose of this study is to examine

the influence of various forms on the pressure distributions while taking the Reynolds number and slippage into account.

2   Method

2.1   Basic Theory

For the lubricant film flow, the steady two-dimensional turbulent Navier-Stokes equations are computed, taking into account the impacts of the body force and inertial force components. The analysis of fluid dynamics relies on the solution of momentum conservation (Eq. (1)) and mass conservation (Eq. (2)) equations.

$$\frac{\partial}{\partial x_i}\left(\rho u_i u_j\right) = -\frac{\partial p}{\partial x_i} + \frac{\partial}{\partial x_j}\left[\mu \frac{\partial x_i}{\partial x_j} - \overline{\rho u_i' u_j'}\right] \tag{1}$$

$$\frac{\partial}{\partial x_i}(\rho u_i) = 0. \tag{2}$$

In Eqs. (1) and (2), ρ is the density of the fluid; u_i and u_j are the average velocity components for x, y; p is the static hydrodynamic pressure; μ is the viscosity; u'_i and u'_j are the fluctuation velocities; $-\overline{\rho u_i' u_j'}$ is the Reynolds stress; and $i, j = 1, 2$ (x, y). In the present work, the Reynolds stress is solved by the standards k and ε [5].

2.2   CFD Modelling

In the present work, two pocket shapes are developed to analyses the pressure behavior as shown Fig. 1. Ansys software uses in this simulation. The length of bearing (B) is 2 mm, length of inlet (a) is 0.75 mm, length of texture shapes (b) is 0.75 mm, length of outlet (c) is 0.5 mm, maximum height (h_p)is 0.006 mm, minimum height (h_o) is 0.004 mm, and depth of texture (h_d) is 0.002 mm (Muchammad et al. [6]). In order to identify the boundary between the liquid and gas phases where cavitation occurs, vaporization pressure is taking into account.
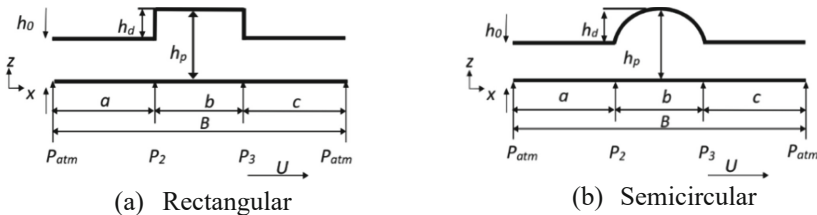

(a) Rectangular   (b) Semicircular

Fig. 1. Varied pocket shapes.

In the geometry modelling, top wall is a stationary situation and bottom wall is moving condition. The Reynolds number (R_e) in the present study are 0.028, 0.28, and 2,8 to maintained the laminar flow. These value parameters in the term of velocity are applied in the moving wall. Before simulation is performed, the model has been verified from the previous model [7] which shows good result. The deviation of present model in the pressure distributions is about 0.9%.

3   Results and Discussion

Figure 2 shows the pressure distributions in rectangular shape at three varied of Reynolds numbers. In general view the highest Reynolds number makes the high pressure distribution in the end of pocket texture. Due to the cross-sectional enlargement in the area along of texture, cavitation occurs which indicates the pressure of 0.05 MPa. This happens because at high speeds, there will be great pressure when meeting the location of the narrowing area. The highest Reynolds number R_e 2.8 made the pressure increase by 0.349 MPa in the no slip case and 0.342 MPa in the slip case. There is no effect of pressure in applying the slip limit here. However, for the pressure at the inlet, in the case of slip, it directly cavitates due to the high velocity.
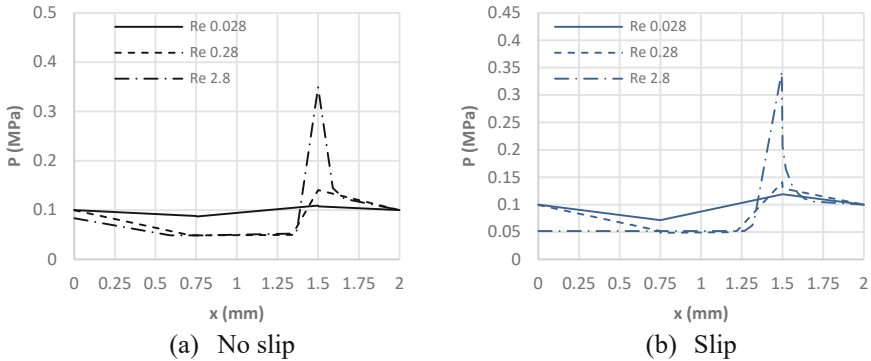
Fig. 2. Pressure distributions in rectangular shape.

Figure 3 describes the pressure distributions for semicircular shape. Similar to the rectangular shape, simulation results the highest Reynolds number affects the highest pressure. The effect of giving a slip boundary makes a pressure drop of about 6% at 0.186 MPa. As in the rectangular shape, in the slip condition, the instantaneous inlet pressure also cavitates for the case of R_e 2.8. The highest pressure increases in the highest Reynolds number, and vice versa. Compare to the rectangular shape, the semicircular shape has low pressure. This behavior occurs because the geometry of the fillet in the design can reduce the concentration of pressure that develops slowly according to the sloping shape. All models experience cavitation with different lengths of cavitation region. In application, the rectangular pocket is more advantageous than the semicircular shape on the bearing surface because the pressure generated is greater so that the bearing strength improves.
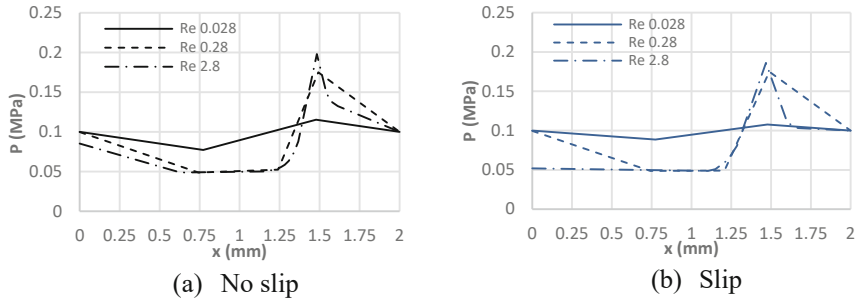
(a) No slip   (b) Slip

Fig. 3. Pressure distributions in semicircular shape.

4   Conclusion

The paper presents a study of hydrodynamic lubrication on textured slider bearings with Reynolds number variations considering the slippage. It can be concluded the texture of rectangular produces the higher pressure than semicircular shape. The highest Reynolds number makes the high pressure distribution.

References

1. Henry, Y., Bouyer, J., Fillon, M.: An experimental analysis of the hydrodynamic contribution of textured thrust bearings during steady-state operation - a comparison with the untextured parallel surface configuration. Proc. Inst. Mech. Eng. Part J: J. Eng. Tribol. **229**(4), 362–375 (2015)
2. Song, Z., Guo, F., Liu, Y., Hu, S., Liu, X., Wang, Y.: Investigation of slip/no-slip surface for two-dimensional large tilting pad thrust bearing. Ind. Lubr. Tribol. **69**(6), 995–1004 (2017)
3. Nanbu, T., Ren, N., Yasuda, Y., Zhu, D., Wang, Q.J.: Micro-textures in concentrated conformal-contact lubrication - effects of texture bottom shape and surface relative motion. Tribol. Lett. **29**(3), 241–252 (2008)
4. Tauviqirrahman, M., et al.: An optimization study on texture depth for bearing sliders with slip. In: Sabino, U., Imaduddin, F., Prabowo, A. (eds.) Proceedings of the 6th International Conference and Exhibition on Sustainable Energy and Advanced Materials. LNME, pp. 563–571. Springer, Singapore (2020). https://doi.org/10.1007/978-981-15-4481-1_52
5. ANSYS. ANSYS Fluent user's guide - Release 16.0 ANSYS, Inc., Canonsburg (2017)
6. Muchammad, M., Hilmy, F., Tauviqirrahman, M., Jamari, J., Schipper, D.J.: CFD analysis of texture depth effect on the performance of hydrodynamic lubricated bearing. J. Phys: Conf. Ser. **1090**(012067), 1–6 (2018)
7. Muchammad, M., Tauviqirrahman, M., Jamari, J., Schipper, D.J.: Analysis of the effect of the slip-pocket in single and double parallel bearing considering cavitation - a theoretical approach. Lubricants **9**(1), 3, 1–20 (2021)

Experimental Study and Analysis on Surface Integrity by Hardened Steel End Milling

S. Nallusamy[1(✉)], S. Sundar[2], and S. Saravanan[2]

[1] Department of Adult Continuing Education and Extension, Jadavpur University, kolkata 700032, India
ksnallu@gmail.com

[2] Department of Mechanical Engineering, Dr. M.G.R. Educational and Research Institute, Chennai 600095, Tamil Nadu, India

Abstract. The aim of this research work is to analyze the Surface Integrity (SI) of Custom-465 hardened steel over end milling process. End milling process with high cutting speeds becomes an economical practice for manufacturing the parts with high quality and accuracy. High speed end milling is now used for machining of hardened steels for making aerospace and automotive components at higher production rate. The effect of operating parameters such as Cutting Speed (CS), Feed (F) and Depth of Cut (DoC) on SI is more important to control the quality of work piece. In this paper the SI studies includes the measurement of surface roughness (Ra), cutting forces and deformation measurement using coordinate measuring machines was discussed. Then the results were made based on the observations and the surface integrities are studied. From the final results it was found that, the percentage of feed contributes more on Material Removal Rate (MRR) with 61.73% and also the MRR increased with enriched feed.

Keywords: End milling · Surface integrity · Hardened steel · Operating parameters

1 Introduction

High speed end milling is employed for production of parts, dies made of hardened steels and landing gears in aircrafts which are made of C-465 steel [1]. More investigations were carried out for milling to describe the SI with different settings of milling [2]. The SI studies in face milling are conducted. The experimental analysis is done by simulating face milling using 3D-FEM. This shows good agreement with tool wear measurements [3]. The SI is studied based on the different positions of cutting tool, measurements of residual stresses, micro-hardness, roughness and texture are studied. Both residual stress and roughness has the larger impact on the tilt angle than the lead angle [4]. The cryogenic machining was significantly enhanced the Ra with coated solid carbide cutters in end milling processes. The flood type machining achieves good roughness than the dry machining as 18% and 21%. 0.58 µm is achieved as the lowest roughness value [5]. Ra depends on the collective result of feed and radial DoC. The fatigue life occurs after

1million cycles, so that the influence of the roughness in minor [6]. Two different surface conditions were analyzed by milling and EDM using SEM techniques the Ra is studied [7]. The surface irregularities were studied by SEM image with the magnification of $100\times-1000\times$. By varying the MRR the detailed SI is studied [8]. The SI studies in dry milling are studied by measuring both the maximum and minimum roughness values. The speed and DoC with minimum and higher feed studies the beneficial results in these studies [9].

1.1 Cutting Force Analysis

Cutting forces of machining processes are to be measured by dynamometers. When the importance of dynamometers as concern, it is used to design a mechanical structure which can with stand based on the cutting force, power intake fortitude, tool life expectation and productivity improvement. The stationary type of KISTLER dynamometer was used for experimentation as shown in Fig. 1.
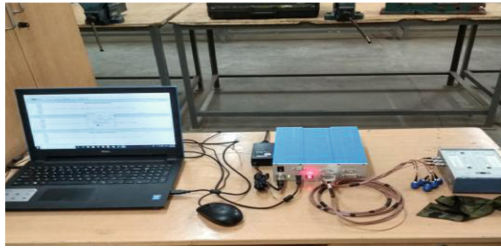
Fig. 1. KISTLER dynamometer experimental setup.

2 Experimental Setup and Methods

The work material is custom 465 steel which is corrosion resistant due to the composition of nickel and chromium which is shown in energy-dispersive spectroscopy. The 12 mm diameter cutting tool with TiAlN coated was used for machining purpose. The operating parameters are shown in the Table 1. Three levels of cutting speed, feed and depth of cut were selected then with the help of Grey Relational Analysis (GRA) analysis the optimization parameters were found. The milling is done for each level of parameters then the SI studies are measured such as roughness, cutting force and deformation measurements were carried out. After machining the roughness were measured with Kosaka SE-3500 surface roughness tester as shown in Fig. 2. The measured roughness values are shown in Table 2. And based on that roughness values the min Ra values are taken for further analysis. GRA is done to find the relation between the parameters and measurements. Using GRA the best optimum conditions for further entire milling were analyzed. Figure 3 shows the end milling experimental setup in which the fixture is placed above the dynamometer, the component was placed above the fixture then milling is done. Based on constrains the Cutting Force (N) was measured and MRR was calculated. Table 2 shows the force values, MRR values and Ra values for each and every condition measured with 0.8 mm cut-off length.

Fig. 2. Measurement of Ra.

Fig. 3. Experimental setup.

Table 1. Milling parameters.

Cutting constraints	Speed (m/min)	Feed (m/min)	DoC (mm)
1	150	0.0751	0.1
2	150	0.052	0.2
3	150	0.12	0.3
4	200	0.052	0.1
5	200	0.0751	0.2
6	200	0.12	0.3
7	250	0.052	0.1
8	250	0.0751	0.2
9	250	0.12	0.3

Table 2. Results of Ra, N and MRR.

Cutting constraints	Ra (μm)	Cutting force (N)	MRR (mm^3/min)
1	0.181	132.65	238.76
2	0.101	110.96	716.32
3	0.22	488.45	1432.65
4	0.171	303.96	636.72
5	0.362	496.98	1432.65
6	0.781	139.32	636.72
7	0.222	621.33	1193.87
8	0.441	169.38	596.93
9	0.162	521.80	1591.84

3 Results and Discussion

3.1 General Linear Model (GLA) ANOVA

The contribution percentage every end milling constraints had been concluded by adjusted Sum of Squares (SoS) technique and GLM ANOVA such as cutting force, MRR and roughness [10]. The ANOVA results for these parameters were calculated and based on the calculated ANOVA values the percentage contribution was obtained to find the variation between the parameters are given in Table 3 and also discussed in detail. Percentage contribution of different parameters was determined with the Eq. 1. It has been found that the DoC has a major impact on cutting force and roughness, whereas the feed has the major impact on MRR.

$$Percentage\ Contribution = \frac{Sum\ of\ Squares}{Total\ Sum\ of\ Squares} \times 100 \tag{1}$$

Table 3. Impact % of the parameters.

Constraints	N (%)	MRR (%)	Ra (%)
S	17.770	9.464	11.273
F	7.730	61.729	21.696
DoC	70.303	23.401	63.257
Error	4.191	5.399	3.771

3.2 Grey Relational Analysis

The GRA was carried out to find out the appropriate coefficient for different parameters with different normalized values. Similarly, the response ranking of Grey Relational Grade (GRG) was computed for each level of machining process is given in Table 4 and it was found that, A1, B2 and C2 with DoC being the most significant factor as evident from the rank. Then based on the optimized parameters the milling was done and again the measurements were taken. After the machining is completed the straightness values are measured for the each and every level of parameters and made to compare with the roughness values are given in Table 5.

Table 4. GRG ranking response.

Process constraints	GRG			Max-Min	Rank
	Level 1	Level 2	Level 1		
CS (A)	0.8023	0.8020	0.5121	0.2903	2
F (B)	0.5129	0.7927	0.6125	0.2799	3
DoC (C)	0.5269	0.8290	0.5212	0.3079	1

Table 5. Results of Ra.

Trial no.	Time taken (Sec)	Wear (vb)	Ra (μm)
1	11	0.191	0.077
2	12	0.222	0.072
3	12	0.31	0.051
4	12	0.382	0.049
5	11	0.411	0.050
6	12	0.452	0.058
7	12	0.491	0.069
8	11	0.513	0.088

4   Conclusion

The selections of parameters were analyzed by GRA. The SI studies such as Ra, N analysis and deformation studies were done. From the results it was concluded that, the DoC parameter contributes more with N and roughness as 70.303% and 63.257% hence, the depth of cut value was used as 0.2mm. The percentage of feed contributes more with respect to the MRR with 61.729% and also the material removal rate increased with enhanced feed. The straightness value becomes minimum when the operating parameters are used as per the GRA analysis than the other.

References

1. Wojciechowski, S., Maruda, R.W., Nieslony, P., Krolczyk, G.M.: Investigation on the edge forces in ball end milling of inclined surfaces. Int. J. Mech. Science **119**, 360–369 (2016)
2. Mikó, B., Zentay, P.: A geometric approach of working tool diameter in 3-axis ball-end milling. Int. J. Adv. Manuf. Technol. **104**(1–4), 1497–1507 (2019). https://doi.org/10.1007/s00170-019-03968-9
3. Liang, X., Liu, Z.: Experimental investigations on effects of tool flank wear on surface integrity during orthogonal dry cutting of Ti-6Al-4V. Int. J. Adv. Manuf. Technol. **93**(5–8), 1617–1626 (2017). https://doi.org/10.1007/s00170-017-0654-x
4. Ferreira, R., et al.: Analysis of the hard turning of AISI H13 steel with ceramic tools based on tool geometry: surface roughness, tool wear and their relation. J. Braz. Soc. Mech. Sci. Eng. **38**, 2413–2420 (2016)
5. Johny, A., Thiagarajan. C.: Investigation of surface integrity and it's optimization on pure titanium using molybdenum wire by reciprocated travelling WEDM-A review. Mater. Today Proc. **33**, 2581–2584 (2020)
6. Zheng, G., et al.: Surface integrity evaluation of high-strength steel with a TiCN-NbC composite coated tool by dry milling. Measurement **166**, 108204 (2020)
7. Yamamoto, A., et al.: Effects of surface grinding on hardness distribution and residual stress in low carbon austenitic stainless steel 316L. ISIJ Int. **44**, 1780–1782 (2004)
8. Prabu, M., et al.: Influence of boron nitride nano additives in cutting fluid for improving surface roughness with MRR. Int. J. Nanomanuf. **16**(1), 61–67 (2020)
9. Klocke, F., Welling, D., Dieckmann, J.: Comparison of grinding and wire EDM concerning fatigue strength and surface integrity of machined Ti6Al4V components. Procedia Eng. **19**, 184–189 (2011)
10. Jeevanantham, S., et al.: Effect of machining parameters on MRR and surface roughness in internal grinding using EN8, EN31 steel. Int. J. Appl. Eng. Res. **12**(11), 2963–2968 (2017)

Tribology's Effect on Turning Performance with Jatropha Oil and Activated Carbon Nanoparticle

Norfazillah Talib[1(✉)] , Ariff Azizi Zolkefli[1], Ainaa Mardhiah Sabri[1],
Haslina Abdullah[1] , and Amiril Sahab Abdul Sani[2]

[1] Faculty of Mechanical Engineering and Manufacturing, Universiti Tun Hussein Onn Malaysia,
86400 Parit Raja, Johor, Malaysia
`fazillah@uthm.edu.my`

[2] Faculty of Manufacturing and Mechatronic Engineering Technology, Universiti Malaysia
Pahang, 26600 Pekan, Pahang, Malaysia

Abstract. Bio-based oil has been developed as a replacement for conventional lubricants derived from mineral-based and synthetic-based oils, which are harmful to individuals and the environment. The purpose of this study was to develop a nanofluid metalworking fluid using modified jatropha oil (MJO) and 0.025 wt.% of activated carbon (AC) as a nanoparticle. Throughout the turning operation, the tool life of the nanofluid was compared to synthetic ester (SE). As a result, MJO + 0.025wt.% AC has better tribological qualities and has a longer tool life (7000 mm cutting length at 49 min machining time) and suited as environmentally benign metalworking fluid.

Keywords: Nanofluid · Modified jatropha oil · Activated carbon

1 Introduction

Due to its ecologically friendly lubricant, metalworking fluid (MWF) made from vegetable-based oil is becoming increasingly crucial in the industry to replace existing conventional oils (mineral-based and synthetic-based). Vegetable-based oil has similar qualities as MWF, such as a higher flash point, higher viscosity, and larger molecular weight [1]. However, crude vegetable-based oil lacks thermal oxidative stability, necessitating modification to address this issue [2]. The usage of MWF as a modified vegetable-based oil with additional particles (known as nanofluids) has the potential to greatly reduce friction and wear. According to Jamaluddin et al. [3] combining non-edible modified jatropha oil with nanoparticle additions results in exceptional tribological behaviors. The unique formation of molecular chain in the modified jatropha oil generated a sufficient lubricating film that reduced friction at the contact zone. Furthermore, the presence of nanoparticles in nanofluids facilitates particle mobility between the two contact surfaces, resulting in improved tribology behavior.

Previous study by Li and Radhiyah [4] initiated that the use of activated carbon (AC) as a lubricant additive exhibits remarkable improvement toward the base oil by

improving the adsorptive properties. This is because the well-structured porous structure and surface chemical capabilities of AC strengthen the relationship between polar and non-polar adhesion. In addition, the porous carbon element of AC can react to chemical and gaseous substances, enhancing adsorption abilities [5]. The main purpose of this research is to carry out the turning process to investigate the tribological behaviour of newly formulated nanofluids made from modified jatropha oil with activated carbon nanoparticle in terms of tool wear and tool life.

2   Methodology

2.1   Nanofluids Preparation

The nanofluid is the combination of the modified jatropha oil (MJO) with activated carbon nanoparticles. CJO is first transesterified into jatropha methyl ester (JME) using a two-step acid-based catalyst. MJO is formed when the JME generated reacts with trimethy-lolpropane (TMP) via transesterification with 1% sodium methoxide ($NaOCH_3$). Later, MJO was mixed with nanoparticles of 0.025 wt.% AC via magnetic stirrer at 700 rpm and 60 °C in the oil bath condition for 30 min. A synthetic ester (SE, Unicut Jinen MQL) was compared to the nanofluid.

2.2   Turning Process

The experiment was carried out on NC Harrison Alpha 400 utilizing AISI 1045 steel with a 150'mm diameter and an uncoated cermet cutting tool. The turning was done at a constant cutting speed of 300 m/min, a feed rate of 0.2 mm/rev, and a cut depth of 1 mm. The minimum quantity lubrication (MQL) approach was used to supply the metalworking fluid which is the nanofluid. Nikon MM-60 tool maker microscope was used to examine the wear progression at the flank face for average flank wear (V_{BB}), maximum flank wear (V_{BBmax}), and notch wear (V_{BN}) at 500 mm cutting length intervals. Figure 1 shows the unused cutting tool image at the flank face before tool wear occurred. Tool life was measured when the tool failed and exceeded the tool wear criteria. The tool life was determined through the total machining time (min) and total cutting length (mm). The tool life criteria that have been selected based on ISO 3685 standard are as follows:

- Average flank wear, $V_{BB} \geq 0.3$ mm
- Maximum flank wear, $V_{BBmax} \geq 0.6$ mm
- Maximum notch wear, $V_{BN} \geq 0.6$ mm
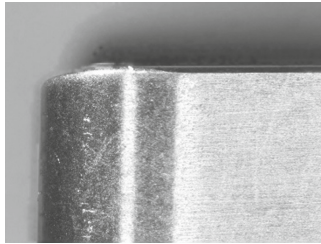
Fig. 1. Unused cutting tool image at the flank face.

3   Result and Discussion

From the results, the tool lubricate by SE failed when notch wear (V_{BN}) exceeded 0.6 mm at 6000 mm cutting length and 42 min machining time. Instead, the tool lubricated by MJO + 0.025wt.% AC, failed when its average flank wear (V_{BB}) exceeded tool wear criterion of 0.3 mm at 7000 mm cutting length and 49 min machining time.
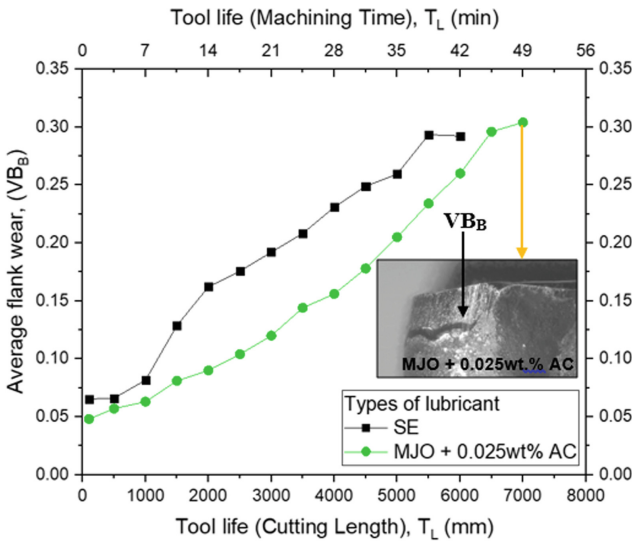
Fig. 2. Graph of average flank wear (V_{BB}) of SE and MJO + 0.025wt.% AC.

Figure 2 and Fig. 3 show the progression of average flank wear (V_{BB}) and notch wear (V_{BN}) for MJO + 0.025wt% AC and SE. When compared to SE, the nanofluid (MJO + 0.025% AC) provides a 17% of improvement in tool life. Adding 0.025wt% AC nanoparticle to the MJO can significantly extend the tool life of the cutting tool because it is highly porous and has good adsorption properties [4]. As a result, it functions as a spacer to prevent the asperities between two metals from colliding.
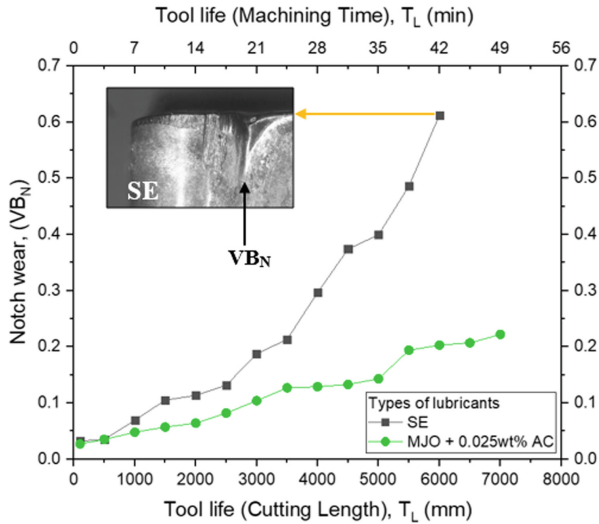
Fig. 3. Graph of notch wear (V_{BN}) of SE and MJO + 0.025wt.% AC.

4 Conclusion

The addition of AC nanoparticle to the MJO equates to good lubricating and tribological qualities. The results demonstrated that MJO + 0.025wt.% AC has a longer tool life, making it the ideal candidate as an ecologically friendly MWF for machining process.

References

1. Kuram, E., Ozcelik, B., Simsek, B.T.: The effect of extreme pressure added vegetable based cutting fluids on cutting performance in milling. Ind. Lubricat. Tribol. **3**, 181–193 (2013)
2. Syahir, A. Z., et al.: A review on bio-based lubricants and their applications. J. Clean. Prod. **168**, 997–1016 (2017)
3. Jamaluddin, N.A., Talib, N., Abdul Sani, A.S.: Tribological analyses of modified jatropha oil with hBN and graphene nanoparticles as an alternative lubricant for machining process. J. Adv. Res. Fluid Mech. Thermal Sci. **76**(2), 1–10 (2020)
4. Radhiyah, A.A., Jun Li, K.: Mini review of carbon based additive in machining lubricant. J. Modern Manuf. Syst. Technol. **4**(2), 61–65 (2020)
5. Oginni, O., Singh, K., Oporto, G., Dawson-Andoh, B., McDonald, L., Sabolsky, E.: Influence of one-step and two-step KOH activation on activated carbon characteristics. Bioresour. Technol. Rep. **7**, 100266 (2019)

Friction Behaviour of Palm Bio-Grease Formulation

Izatul Hamimi Abdul Razak[1,2] , Mohamad Ali Ahmad[2(✉)] ,
and Muhamad Azeri Rahim[2]

[1] Mechanical and Fabrication Section, Universiti Kuala Lumpur Malaysia France Institute,
Section 14, Jalan Teras Jernang, 43650 Bandar Baru Bangi, Selangor, Malaysia
[2] School of Mechanical Engineering, College of Engineering, Universiti Teknologi MARA,
40450 Shah Alam, Selangor, Malaysia
mohama9383@uitm.edu.my

Abstract. Palm ester is a sustainable bio-lubricant derived from plant-based resources. The utilization as base oil for grease formulation is attractive. In this work, the palm bio-grease was formulated with different proportion with calcium complex thickener ranges from 15–19 wt%. The consistency and frictional behaviour were assessed through NLGI grade and wear preventive tests respectively. Results obtained shows the comparable friction behaviour of the palm bio-grease with 19 wt% composition of thickener with commercial grease, indicated the good potential of the formulated palm bio-grease.

Keywords: Palm grease · Calcium complex soap · Consistency · Friction

1 Introduction

Green tribology is the concept that have been introduced recently as key strategy to overcome energy, environment and resources problems related to lubrication activities [1]. Biodegradable lubrication is stated as one of the 12 principles of the green tribology, which vegetable oils and animal fats are suggested to be used as natural sources. These type of lubricants were basically demanded for applications in which the oils or greases are lost to the environment and in services that may contain leaking risks such as agricultural, railway, and marine applications. Besides the environmental benefits, bio-lubricants and bio-greases also have huge potential for encouraging national economy by utilizing their own plants for the renewable source of base oils.

Bio-greases are mainly indicating from the base oil as the main composition. Due to that, development of the bio-grease from vegetable oil-based have been extensively being studied recently [2, 3]. Not only offers significant environmental benefits and is highly biodegradable, the vegetable oil also gives sustainable benefit since it derived from renewable raw materials. Palm oil is one of the notable bio-lubricant which demonstrates

good friction reduction and anti-wear [4, 5]. It contributed from the high composition of fatty acids which generate strong interaction with the lubricated surfaces [4]. Since Indonesia and Malaysia are the largest producer of palm oil that responsible for over 90% of the global vegetable oil production in 2019/2020 [6], the potential as alternative lubricant was explored mainly by researchers in this region. This study thus extending the efforts, which a palm-based ester was utilized for the synthesis of bio-grease. The consistency and frictional behaviour of the formulated palm-ester bio-grease were evaluated and the potential is explored.

2 Materials and Method

2.1 Materials

The Palmester 2090 trimethylolpropane trioleate (viscosity of 76.6 mm^2/s at 40 °C and density of 0.921 g/cm^3 at 15 °C) as the base oil was supplied by KLK OLEO (Petaling Jaya Malaysia). The oil is C18-unsaturated, mixed esters with oleic acid and trimethylolpropane (TMP). Calcium hydroxide (Ca(OH)$_2$) by R&M Chemicals, and stearic acid (C$_{18}$H$_{36}$O$_2$) and benzoic acid (C$_6$H$_5$COOH) by HmbG Chemicals were used to form the calcium complex thickener. Two commercial greases were used as reference grease in the study; identified as C1 (NLGI 00) and C2 (NLGI 1). Both greases are synthetic ester-based with solid lubricant content, particularly MoS2 and/or graphite.

2.2 Palm Grease Formulation

The palm bio-grease was formulated in a glass beaker with hot-plate and overhead rotary paddle apparatus. The calcium complex grease was obtained by reacting the calcium hydroxide with stearic and benzoic acid (composition ratio 0.8:1:1) into the palm ester at 80°C with uniform stirring. The saponification reaction takes about 40 min before the temperature is increased gradually up to 170 °C for 4–5 h. The thickened grease was formed after cooled down. Samples containing calcium complex thickener in proportions from 15 to 19 wt% were manufactured, which the range was estimated based on the NLGI grade of the reference greases used in this study, to produce the comparable consistency grease.

2.3 Grease Characterization

The consistency or the stiffness of the grease samples were checked using SKF Grease Test Kit TKGT 1, according to a scale developed by the standard National Lubricating Grease Institute (NLGI). The larger scale determining the harder grease structure.

The friction behaviour of the formulated palm bio-greases was evaluated using four-ball wear tester (Koehler Instrument Company, Inc.), under wear preventive test according to ASTM D2266. In the test operation, the three steel balls in a pot containing the grease sample was pressed upward with 40 kg force against the top ball rotated at 1200 rpm speed for 60 min. The friction coefficient due to the friction between the steel balls were recorded.

3   Results and Discussion

The palm grease in this study were formulated with a 0.8:1:1 ratio of metallic base (calcium hydroxide) to fatty acid (stearic acid) and complexing agent (benzoic acid) as the optimum calcium complex soap composition. An excess of the stearic acid in the formulation contributing to the good consistency yield [7], due to the long carbon chain length (C18) that created stronger interlocking fibre in the metal soap which results in a stable grease matrix [8]. Three samples of the palm greases have been formulated with thickener compositions between 15–19 wt%. The NLGI grade of the greases were depicted in Table 1, which the calcium complex thickener proportions yielded the palm grease consistency between NLGI 00 (semi-fluid) to NLGI 1 (soft).

The lubricating ability of the formulated palm bio-greases was assessed through the friction properties by a series of four-ball tests, under the rotating and sliding actions. Figure 1 illustrates the friction coefficient trends over time for the palm bio-grease samples at a constant load. The palm bio-greases with thickener compositions of 15 wt% and 17 wt% producing quite similar friction trends with friction coefficient values of 0.092 and 0.0890 (Fig. 2) respectively. Whereas, the 19 wt% of thickener composition shows the lowest and stable friction trend, indicating the ability of the palm grease sample to maintain the tribo-layer with low friction with minimum fluctuations. The average friction coefficient value of 0.0851 (Fig. 2) was also comparable with the reference grease C2 that having the equal NLGI grade. Reference greases C1 and C2 however are the commercial greases that contains additional performance additives [9]. This might have attributed to the high fatty acid content, particularly oleic acid (C18) of the palm ester that creates strong bonding with the lubricated surfaces [4]. This therefore supports the good potential of the formulated palm bio-grease, even with no presence of performance additives to be recognized as reliable bio-grease.

Table 1. The NLGI grade for the palm bio-grease samples.

	Thickener concentration	NLGI
Sample I	15%	00
Sample II	17%	0
Sample III	19%	1
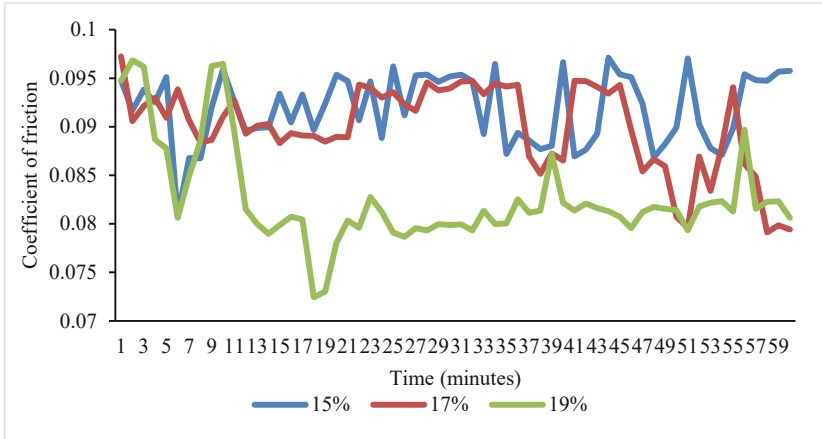
Fig. 1. The friction coefficient curves over time.
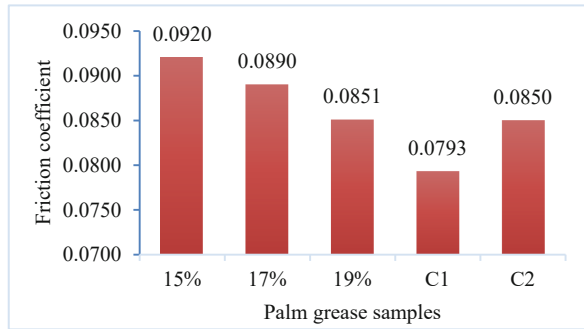
Fig. 2. The average friction coefficient of the grease samples.

4   Conclusion

Palm ester bio-grease have been synthesized in this study with different proportion of calcium complex soap thickener. The compositions of 15–19 wt% thickener produced NLGI 00 to 1 grade, representing semi-fluid to soft grease structure. The friction results demonstrating good lubricating potential of the palm ester-based grease for future bio-grease product. Further tribological and rheological analyses need to be carried out in the further development of the palm bio-grease.

References

1. Van Minh, N., Kuzharov, A., Ninh, L.., Huynh, N., Kuzharov A.: Chapter 3: Green Tribology in Tribology in Materials and Manufacturing - Wear, Friction and Lubrication, pp. 45–64. IntechOpen, Londom (2021)

2. Martín-Alfonso, J.E., Martín-Alfonso, M.J., Valencia, C., Cuberes, M.T.: Rheological and tribological approaches as a tool for the development of sustainable lubricating greases based on nano-montmorillonite and castor oil. Friction **9**(2), 415–428 (2020). https://doi.org/10.1007/s40544-020-0407-y

3. Xie, M., Cheng, J., Huo, C., Zhao, G.: Improving the lubricity of a bio-lubricating grease with the multilayer graphene additive. Tribol. Int. **150**, 1–9 (2020)

4. Dandan, A., Samion, S.: Palm oil as an alternative lubricant oil: a brief review. The Colloquium **11**, 17–19 (2017)

5. Razak, I.H.A., Ahmad, M.A., Fuad, N.N.N.A., Shahrudin, K.S.: Tribological properties of palm oil bio-lubricant with modified carbon nanotubes. Int. J. Eng. Technol. **7**(4.18), 133–137 (2018)

6. Oosterveer, P.: Sustainability of palm oil and its acceptance in the EU. J. Oil Palm Res. **32**(3), 365–376 (2020)

7. Doi, S., Yamamoto, A., Maeda, J.: US_2021_0040413_A1 - Grease composition. US Patent (2021)

8. Sharma, B.K., Adhvaryu, A., Perez, J.M., Erhan, S.Z.: Biobased grease with improved oxidation performance for industrial application. J. Agric. Food Chem. **54**(20), 7594–7599 (2006)

9. Razak, I.H.A., Ahmad, M.A., Puasa, S.W.: Tribological and physiochemical properties of greases for rail lubrication. Tribol. Online **14**(5), 293–300 (2019)

The Effect of Tensile Load on Prestressed 1 + 6 Wire Strand

N. H. M. Zini[1,2(✉)], Z. F. C. Zamri[1], and N. Ismail[1,2]

[1] Fakulti Kejuruteraan Mekanikal, Universiti Teknikal Malaysia Melaka, Hang Tuah Jaya, 76100 Durian Tunggal, Melacca, Malaysia
nurulhilwa@utem.edu.my

[2] Centre for Advanced Research On Energy, Universiti Teknikal Malaysia Melaka, Hang Tuah Jaya, 76100 Durian Tunggal, Melacca, Malaysia

Abstract. Wire strand is a simple machine to use, though it can be complex to analyse. Due to wire strand complex spatial structure, which is constructed from several multi-level components, the experimental setup for stress analysis can be complicated and costly. This paper aimed to determine tensile stress of core wire and helical wire from a prestressed 1 + 6 wire strand subjected to tensile load using ANSYS Finite Element Analysis (FEA). Tensile loads were applied on both core wire and helical wire; bonded contact was considered between core wire and helical wire while contacts between helical wires were not considered. Results indicate that core wire has more significant tensile stress values than the helical wire due to it being subjected to purely tensile load unlike the helical wire. Data trend also conforms to Costello's model and previously published experimental data. This shows the reliability of FEA as a tool to analyse complex wire strand construction.

Keywords: Wire strand · Prestressed · Tensile load

1 Introduction

Prestressed wire strands are used in various practical applications, including prestressed concrete construction and suspension bridge hangers which these applications are subjected to tensile load. Even though strands appear as a simple tool, in reality it is actually a somewhat complex machine. A wire strand is constructed from two or more wires, wound concentrically in a helix.

Wire strands are subjected to repetitive bending, load fluctuations and cyclic deformation that result in degradation mechanisms that may occur alone or together, such as fatigue, wear and corrosion. These degradation mechanisms can reduce the strength of prestressed wire strands and accelerate failure. To gain a better understanding of wire strand degradation, it is important to analyze the stress behaviour of the components that construct a prestressed wire strand under tensile load: core wire and helical wire.

Due to wire strand complex spatial construction, normal stress analysis cannot determine the mechanical properties of strands accurately [1]. It requires a series of experiments and tools, which can be costly. FEA simulation can be used to understand and

quantify the contact conditions that occur within the wire strand construction to reduce experimental trials.

2   Methodology

2.1   ANSYS Finite Element Analysis (FEA)

Table 1 lists the properties for the prestressed $1 + 6$ wire strand, based on the ASTM A416 standards for the ANSYS FEA. The nominal diameter of the prestressed steel used was 15.24 mm.

Table 1. Properties of prestressed wire strand.

Properties	Values
Modulus of elasticity	196500 MPa
Strand grade	1860 MPa
Minimum breaking load	261 kN
Poisson's ratio	0.3
Steel area of strand	140.319 mm^2

Figure 1 (a) and Fig. 1 (b) show the solid model of the prestressed wire and the contact pair of core wire and helical wire, respectively. Bonded contacts were considered for the contact conditions between core wire and helical wire; contacts between the helical wires were not taken into account. Loads up to 90 kN were applied separately on core wire and helical wire (see Fig. 1 (c)). The finite element model of the whole wire strand had 5128 nodes and 843 elements. Fixed support was placed at the end of the wire strand, opposite the surface of the wire strand where the loads were set. Displacement was only allowed in the z-direction; any rotational movement by prestressed strands was prevented.
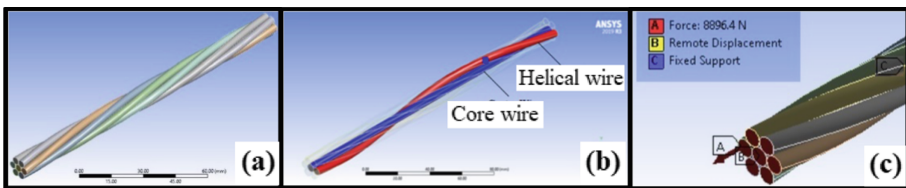
Fig. 1. (a) Solid model of prestressed wire strand, (b) Contact pairs of core wire and helical wire, (c) Loads applied to core wire and helical wire.

2.2 Simulation Validation

Tensile stress results from ANSYS FEA for both core wire and helical wire were validated by comparing to a theoretical model by Costello and a previously published experimental data of similar wire strand dimension and load condition [2, 3].

Using the Costello's model, as derived in [2], tensile stress on core wire, F^{σ_1} was found by dividing the tensile force acting on core wire, F_1 over radius of core wire, R_1 as described in Eq. (1).

$$F^{\sigma_1} = \frac{F_1}{\pi R_1{}^2} \tag{1}$$

The maximum normal tensile stress acting on a helical wire, σ is given in Eq. (2). σ is the sum of the axial stress caused by the load, T^{σ_2} and maximum normal stress due to the bending moment on an outside wire in y-direction, G^{σ_2}, described in Eqs. (3) and (4), respectively:

$$\sigma = T^{\sigma_2} + G^{\sigma_2} \tag{2}$$

$$T^{\sigma_2} = \frac{T_2}{\pi R_2{}^2} \tag{3}$$

$$G^{\sigma_2} = \frac{4G_2}{\pi R_2{}^3} \tag{4}$$

where T_2 is the axial tension in the helical wire and G_2 is the bending moments on a helical wire in y-direction. R_1 is the radius of the helical wire.

3 Result and Discussion

Figure 2 shows the results of the 1 + 6 prestressed wire strand subjected to tensile load; Fig. 2 (a) shows an example of the stress distribution of the prestressed wire strand when subjected to a tensile load while Fig. 2 (b) shows the tensile stress comparison between core wire and helical wire. It can be observed that core wire has higher tensile stress compared to helical wire. Core wire is subjected to purely tensile load, unlike helical wire that are subjected to other loads such as bending, torsional loads and shearing loads. However, these loads on helical wire are in general small and some loads, such as shearing, can be neglected. When tensile load is applied on core wire, the change in length is very minimal due to high internal resistance, resulting in high tensile stress. As for bending, the change in length of the helical wire is more because of less internal resistance, thus less tensile stress.

In addition, Fig. 2 (c) and Fig. 2 (d) present the comparison between the ANSYS FEA results with Costello's model and published experimental results. Compared to the theory, the average percentage error values for the simulation and experimental approaches are less than 8.2% and 0.4%, respectively.
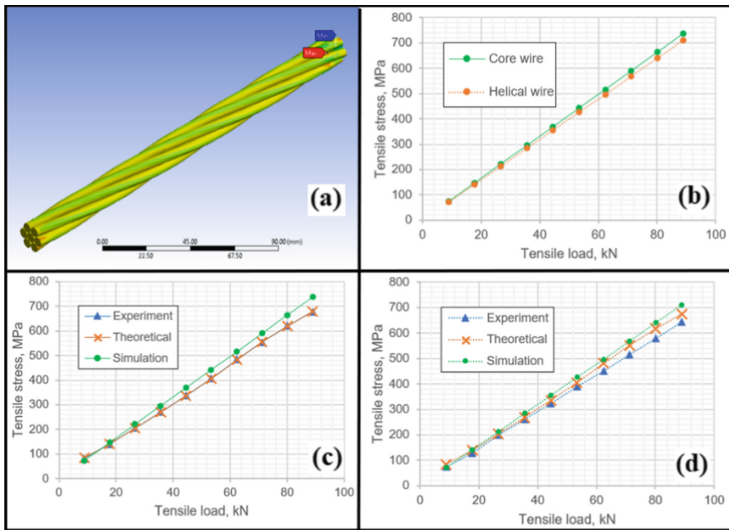
Fig. 2. (a) Example of stress distribution of the prestressed wire strand, (b Tensile stress versus tensile load: Comparison between core wire and helical wire, (c) Tensile stress versus tensile load for core wire, (d) Tensile stress versus tensile load for helical wire.

4   Conclusion

Prestressed $1 + 6$ wire strand under tensile load has been successfully simulated and analyzed whose behaviour shows good agreement with Costello's model and previously published experimental results. The effect of tensile load is more substantial on core wire due to it being subjected to purely tensile load as opposed to helical wire. As a whole, FEA has been demonstrated to be a reliable tool to determine mechanical properties of complex wire strand construction.

References

1. Wenzheng, D., Baozhu, M., Zheng, X., Dazhi, C., Peng, W.: Finite element analysis on the wire breaking rule of 1x7IWS steel wire rope. In: 2017 International Conference on Mechanical, Aeronautical and Automotive Engineering, p. 01002. MATEC Web of Conferences, Malacca (2017)
2. Onur, Y.A.: Experimental and theoretical investigation of prestressing steel strand subjected to tensile load. Int. J. Mech. Sci. **118**, 91–100 (2016)
3. Costello, G.A.: Theory of Wire Rope, 2nd edn. Springer, New York (1997)

Investigation of the Thermal Behavior of Glass Powder in Brake Block Composites Using TGA and DSC

Martinus Heru Palmiyanto[1,2(✉)], Eko Surojo[1], Dody Ariawan[1],
and Fitrian Imaduddin[1]

[1] Mechanical Engineering Department, Faculty of Engineering, Universitas Sebelas Maret, Surakarta 57126, Indonesia
martinus76palmiyanto@gmail.com

[2] Mechanical Engineering Department, Sekolah Tinggi Teknologi Warga Surakarta, Sukoharjo 57552, Indonesia

Abstract. In this study, the abrasive effect of glass powder on the thermal properties of the friction material is investigated. The thermal behaviour of the brake block composite was studied to obtain an optimal composition by adding glass powder fractions with a volume of 2%, 4% and 6% as an abrasive. Thermal properties of composite brake blocks, including decomposition rate, glass transition and heat capacity, were evaluated using Thermogravimetric Analysis (TGA) and Differential Scanning Calorimetry (DSC). The test is carried out in an atmospheric environment according to actual braking conditions. The results showed that the addition of 2% and 4% glass powder abrasives increased the decomposition temperature of the composite specimen. Meanwhile, the addition of glass powder up to 6% showed the decomposition's highest weight loss. The addition of glass powder to the composite brake block increased the average glass transition temperature (ΔTg) and average heat capacity (ΔCp). The highest mean glass transition temperature and heat capacity were found in composites with 6% glass powder.

Keywords: Abrasive · Glass powder · Decomposition · Glass transition · Heat capacity

1 Introduction

Composite brake blocks are introduced to replace cast-iron brake blocks. Composite brake blocks consist of matrix, reinforcement and filler, which are mixed and pressed together. Composite brake blocks in their application require a stable coefficient of friction, thermal resistance, and mechanical strength [1]. Train braking in emergency conditions results in a braking temperature of up to 700 °C [2]. Meanwhile, braking to reduce the speed of the train results in a braking temperature of up to 300 °C [3]. Therefore, composite brake blocks require thermal resistance according to their application.

The properties of the constituent materials influence the thermal behaviour of composite brakes. Phenolic resin has been widely used as a binder in the manufacture of

brake linings [4]. However, phenolic resins have a transition temperature of about 200–300 °C [5]. The use of phenolic resins above the transition temperature can weaken the polymer chain bonds, thereby reducing the strength of the matrix to bind the constituent materials [6]. Several researchers have investigated the increase in the thermal resistance of composites. Most of the literature mentions that modification of the matrix and filler material can increase the thermal resistance of composite brakes. However, the selection of fasteners and their modifications need to consider their cost and frictional performance.

Friction performance is closely related to abrasive materials. Abrasives improve frictional properties by increasing the surface roughness of composite brake blocks [7]. Abrasives are generally hard and play a role in supporting pressure on the contact surface [8]. Commonly used abrasives include zircon ($ZrSiO_4$), alumina (Al_2O_3), silicon dioxide (SiO_2), silicon carbide (SiC), zirconia (ZrO_2) [9, 10] and [11]. The use of silica in large quantities and long term impacts the availability of pure silica in nature. The development of composite brake blocks required an abrasive substitute for pure silica from nature. Galvao et al. stated that soda-lime glass powder waste has the main content of silica (SiO2) up to 65% [12]. Soda-lime glass is heat resistant with a melting point of 1200–1400 °C [13]. On the other hand, soda-lime glass waste is very abundant and takes millions of years to decompose in the soil [14].

The availability of soda-lime glass waste and its thermal properties have become an alternative to pure silica from nature. However, there is no information about the thermal behaviour of composite brake blocks with soda-lime glass waste as an abrasive. This investigation was conducted to determine the effect of adding soda-lime glass powder on the thermal properties of composite brake blocks. Thermal properties of composite brake blocks include decomposition rate, glass transition and heat capacity, evaluated using Thermogravimetric Analysis (TGA) and Differential Scanning Calorimetry (DSC). The test is carried out in an atmospheric environment according to the actual braking conditions.

2   Experimental

2.1   Preparation and Composition

The glass waste was crushed and purified to obtain refined grains of 200 mesh and heated at 500 °C for 3 h. The composition of the composite brake block consisting of 25% by volume fraction of phenolic resin modified with NBR (5%), cashew powder (10%), MoS_2 (5%), Graphite (10%) and $CaCO_3$ was chosen as the compensator. Table 1 shows the composition of the composite brake block.

2.2   Thermal Analysis

Thermogravimetric analysis (TGA) and Differential Scanning Calorimetry (DSC) of composite brake block specimens according to the settings in Table 1 were performed using TGA Linseis sta pt 1600. Composite specimens were weighing 8–10 mg from a temperature of 30 – 1000 ˚C at atmospheric conditions. The heating and cooling rates are set at 10 ˚C/min.

Table 1. Composition of composite brake blocks.

Abarasive code	Glass powder	Basic	CaCO$_3$
GP 0	0	67	33
GP 2	2	67	31
GP 4	4	67	29
GP 6	6	67	27

3   Results and Discussion

3.1   Thermogravimetric Analysis (TGA) of Brake Block Composite

The thermal resistance of composites refers to the ability of composites to maintain physical and mechanical properties under various temperature conditions [15]. The matrix as a binder has a consistent ability to bind composite constituents because it has intense binding energy at room temperature. Cross-linking, free energy is below the free radical diffusion formation threshold [16]. The heat that occurs in heat absorption causes an increase and an increase in free vibration energy above the threshold for free radical formation. Free radicals that trigger chain breaking, thereby triggering material degradation [17].
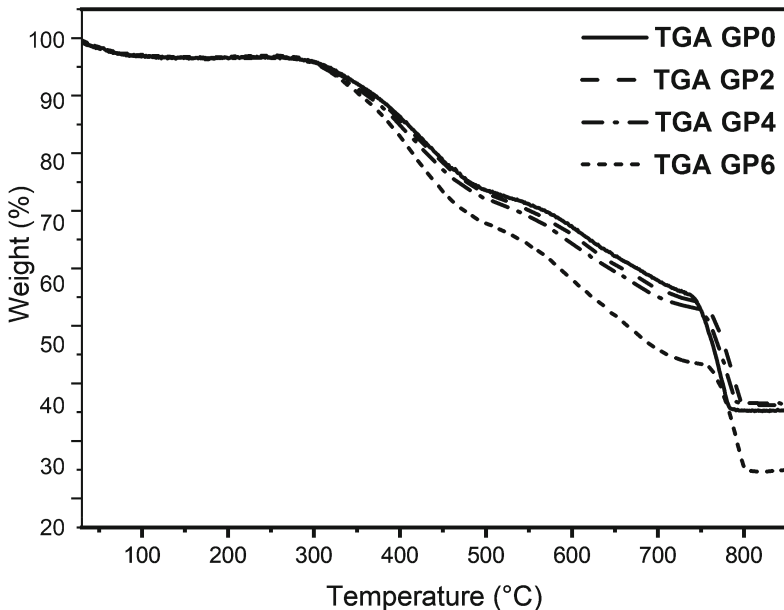
Fig. 1. TGA thermogram of glass powder friction composites.

The thermal decomposition behaviour of composite brake blocks with variations of glass powder as an abrasive is shown in Fig. 1. Specimens with 6% glass powder showed the most significant decrease in weight and decomposition temperature. On the other hand, specimens with 0% glass powder showed the lowest weight loss and decomposition temperature. Figure 2 shows that the decomposition takes place in two stages, following the literature results [18]. The initial decomposition temperature of T3% (°C) as a percentage of initial weight loss was 3%, indicating that the 2% abrasive in the composite decreased from 93.4 °C to 87.25 °C. The initial mass reduction was identified as the release of a small amount of gas consisting of H2O and unreacted monomers trapped during treatment [13]. The mass of the specimen after initial decomposition was successfully maintained up to a temperature of 300 °C. The decomposition rate showed that the addition of 2% abrasive to the composite specimen increased the temperature and mass of decomposition (wt %). The addition of 4% glass powder, although there was a decrease in temperature and decomposition mass (wt %), but did not show a significant difference compared to the specimen without glass powder. While the addition of glass powder up to 6%, it is seen that the decomposition of the first stage shows the highest weight loss.

3.2 Differential Scanning Calorimetry (DSC) of Brake Block Composite

Observing the DSC thermogram showed a significant change in the specific heat capacity of all composite brake block specimens. The specific heat capacity change is initiated by the glass transition to rubber, followed by a peak of endothermic relaxation.
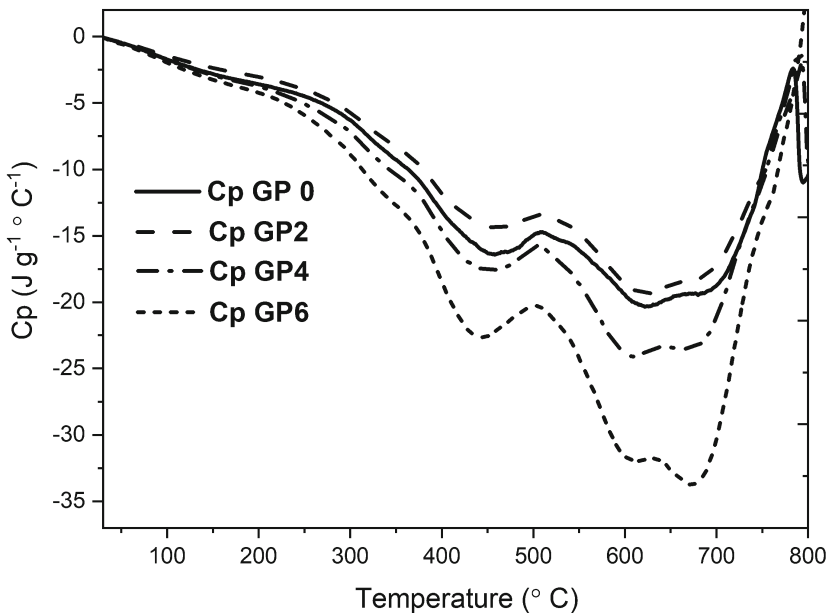
Fig. 2. DSC thermograms of composite brake block specimens.

Figure 2 shows the curve of the relationship between heat capacity and temperature of DSC. The endothermic process occurs when the composite brake block specimen melts, where the specimen absorbs the energy released by the furnace contained in the DSC machine. When a material begins to melt, the intermolecular bonds absorb energy and begin to loosen, breaking the intermolecular bonds. Since melting involves energy absorption, the DSC curve represents a significant and transient decrease in heat flow. The melted material, with the flow of heat, will return to its initial value. The shape of this curve depends on how big and how long the material takes energy to break the bonds between molecules.

Table 2. Glass transition temperature (T_g) and melting temperature (T_m) of composite brake block specimens.

Abrasive code	Glass transition		Melting	
	ΔT_g (°C)	ΔC_p (J/g.°C)	T_m (°C)	C_p (J/g.°C)
GP 0	205,13	11,90	622,74	20,34
GP 2	207,76	10,53	622,58	19,34
GP 4	201,52	12,58	608,74	24,09
GP 6	215,79	16,14	674,35	33,75

Table 2 shows the heat capacity at the glass transition temperature and the melting temperature. Composite brake block specimens without glass powder as the primary reference have the lowest average glass transition temperature and heat capacity values. The composite of brake block with glass powder showed an increase in the average value of the composite's glass transition temperature and heat capacity. The glass transition temperature is affected by the natural characteristics of the composite brake block material, such as structure, bonding, and molecular weight [20]. The high melting point indicates that the constituents have higher crystal growth [21]. The addition of glass powder showed an increase in the crystallization of the composite brake block. The growth of crystals in a material affects the amount of heat energy and the time required to break the bonds between molecules. Materials that have less strong intermolecular bonds are more easily released when heat energy enters.

Table 2 shows that the melting temperature (Tm) of the GP6 composite brake block shows the highest Tm value, while the GP4 composite brake block shows the lowest Tm value. The Tm value of the GP2 composite brake block has a curve relevant to that of the powder-free composite brake block.

4   Conclusion

The results showed that the addition glass powder abrasives in-creased the decomposition temperature of the composite specimen. Meanwhile, the addition of glass powder up to 6% showed the decomposition's highest weight loss. The addition of glass powder to

the composite brake block increased the average glass transition temperature (ΔTg) and average heat capacity (ΔCp). The highest mean glass transition temperature and heat capacity were found in composites with 6% glass powder.

References

1. Sharma, N, Nasimul, S., Chandra, B., Yadav, S., Biswas, K.: Wear behavior of silica and alumina-based nanocomposites reinforced with multi walled carbon nanotubes and graphene nanoplatelets, July 2018
2. Cai, P., Wang, Y., Wang, T., Wang, Q.: Tribology International Improving tribological behaviors of friction material by mullite. Tribol. Int. **93**, 282–288 (2016). https://doi.org/10.1016/j.triboint.2015.09.039
3. Österle, W., Urban, I.: Friction layers and friction films on PMC brake pads. Wear **257**(1–2), 215–226 (2004). https://doi.org/10.1016/j.wear.2003.12.017
4. Ramadan, M.A.: Friction and wear of sand-contaminated lubricated sliding. Friction **6**(4), 457–463 (2018). https://doi.org/10.1007/s40544-017-0192-4
5. Jang, G.H., Cho, K.H., Park, S.B., Lee, W.G., Hong, U.S., Jang, H.: Tribological properties of C/C-SiC composites for brake discs. Met. Mater. Int. **16**(1), 61–66 (2010). https://doi.org/10.1007/s12540-010-0061-4
6. Kazmi, D., Serati, M., Williams, D.J., Qasim, S., Cheng, Y.P.: The potential use of crushed waste glass as a sustainable alternative to natural and manufactured sand in geotechnical applications. J. Clean. Prod. **284**, 124762 (2021). https://doi.org/10.1016/j.jclepro.2020.124762
7. Galvão, A.C.P., Farias, A.C.M., Mendes, J.U.L.: Characterization of waste of soda-lime glass generated from lapping process to reuse as filler in composite materials as thermal insulation. Ceramica **67**, 367–373 (2015). https://doi.org/10.1590/0366-69132015613591987
8. Aktas, B., Albaskara, M., Yalcin, S., Dogru, K.: Mechanical properties of soda-lime-silica glasses with variable peanut shell contents. Acta Phys. Pol. A **131**(3), 511–513 (2017). https://doi.org/10.12693/APhysPolA.131.511
9. Kim, S.H., Jang, H.: Friction and vibration of brake friction materials reinforced with chopped glass fibers. Tribol. Lett. **52**(2), 341–349 (2013). https://doi.org/10.1007/s11249-013-0221-z
10. Park, B., Kadla, J.F.: Thermal curing behavior and tensile properties of resole phenol-formaldehyde resin/clay/cellulose. J. Wood Sci. Technol. **40**(2), 110–122 (2012)
11. Hancox, N.L.: Thermal effects on polymer matrix composites 2.pdf, pp. 93–97 (1998)
12. Shin, M.W., Cho, K.H., Lee, W.K., Jang, H.: Tribological characteristics of binder resins for brake friction materials at elevated temperatures. Tribol. Lett. **38**(2), 161–168 (2010). https://doi.org/10.1007/s11249-010-9586-4
13. Knop, A., Pilato, L.A.: Degradation of phenolic resins by heat, oxygen and high-energy radiation. Phenol. Res. 140–146 (1985). https://doi.org/10.1007/978-3-662-02429-4_8
14. Alneamah, M., Almaamori, M.: Study of thermal stability of nitrile rubber/polyimide compounds. Int. J. Mater. Chem. **5**(1), 1–3 (2015). https://doi.org/10.5923/j.ijmc.201505 01.01
15. Ramousse, S., Høj, J.W., Sørensen, O.T.: Thermal characterisation of brake pads. J. Therm. Anal. Calorim. **64**(3), 933–943 (2001). https://doi.org/10.1023/A:1011575013779
16. Noryani, M., Sapuan, S.M., Mastura, M.T., Zuhri, M.Y.M., Zainudin, E.S.: Material selection of natural fibre using a stepwise regression model with error analysis. J. Mater. Res. Technol. **8**(3), 2865–2879 (2019). https://doi.org/10.1016/j.jmrt.2019.02.019

17. Poletto, M., Júnior, H.L.O., Zattera, A.J.: Thermal Decomposition of Natural Fibers: Kinetics and Degradation Mechanisms, pp. 515–545 (2015)
18. Erickson, K.L., Oelfke, J.: Effect of ambient oxygen concentration on thermal decomposition of polyurethanes based on MDI and PMDI. ACS Symp. Ser. **1013**, 387–407 (2009). https://doi.org/10.1021/bk-2009-1013.ch023

Spectroscopy Analysis of Diesel Injector Hole Deposits Using Palm Methyl Ester-Diesel Blends in a Constant Speed Diesel Engine

Afiqah Hamzah[1,2(✉)], Ghazali Omar[1,3], and Mohd Zaid Akop[1]

[1] Fakulti Kejuruteraan Mekanikal, Universiti Teknikal Malaysia Melaka, Hang Tuah, Jaya, 76100 Durian Tunggal, Melacca, Malaysia
afiqah@utem.edu.my

[2] Centre of Advanced Research On Energy, Universiti Teknikal Malaysia Melaka, Hang Tuah Jaya, 76100 Durian Tunggal, Melacca, Malaysia

[3] Advanced Manufacturing Centre, Universiti Teknikal Malaysia Melaka, Hang Tuah Jaya, 76100 Durian Tunggal, Melacca, Malaysia

Abstract. Diesel injection nozzles are precisely machined in the order of micrometre to produce a fine fuel spray that is crucial for the engine's combustion and emission efficiency. The injector's spray quality is dependent on the generation of deposits. This paper studies the deposition in a single-cylinder 4-stroke diesel engine nozzle hole when using higher blended biodiesel blends. Using B10 and B30 palm biodiesel blends in two separate engine runs, two sets of injectors are collected. The injectors are cross-sectioned to reveal the nozzle hole of the injectors. Scanning electron microscope (SEM) analysis of the injector hole surface is presented. The analysis revealed that less deposit formation had been observed for B30 injection nozzles. From this observation, the injectors expected spray performance using a higher percentage of biodiesel blend may be predicted.

Keywords: Palm biodiesel blend · Injector hole deposit · Material compatibility

1 Introduction

The fuel delivery system is a significant vehicle system component since it determines its fuel efficiency and emissions. As technology advances to cater to a more efficient system, injector nozzle holes diameter reduces magnitude to produce better fuel spray. A common dilemma in a fuel injection system is internal injector deposit formation. Careful design of the fuel injector ensures the proper formation of fuel spray, which is usually characterised by the spray length and droplets size, which is essential for complete combustion and cleaner emission. However, deposit formation in the fuel injector is likely to cause larger fuel droplet size, causing inefficient burning, increasing pollutant emission and reducing fuel efficiency. In addition, injector internal deposit formation can cause failure in the injector charging mechanism, resulting in high maintenance costs and frequent replacement [1, 2]. As more stringent emission regulations are implemented

globally, there is an urgent need to research the formation of internal injector deposits [3, 4].

Most of the previous studies on injector hole deposition from biodiesel use are limited to analysis of deposition outside the injector surface [5]–[7]. The small injector hole geometry, usually at $100\,\mu$m magnitude, provided a challenge to analyse the internal hole deposition. Although several studies have successfully done an exact analysed internal hole deposition from the use of x-ray spectroscopy, none has focused on deposition from the use of biodiesel [8, 9]. However, as previous studies indicated, the severity of injector deposition is influenced by operating conditions and fuel quality. Therefore, it is essential to know how deposit formation occurs when using a higher percentage of biodiesel in the fuel blend.

Based on these previous investigations, the current investigation compared the deposits generated in the injector hole when a higher percentage of palm biodiesel is mixed in the fuel blend were used. The injectors were sectioned and analysed microscopically to determine the morphological characteristics of deposits along the injector holes. This study also compares deposits formed in an injector when a higher percentage of biodiesel is used as fuel. The chemistries and morphologies determined are beneficial for advancing our understanding of deposit formation and growth mechanism theories impacted by fuel qualities.

2   Methodology

In this study, palm biodiesel blended with fossil diesel fuel at 10% and 30% volume percentage. Therefore, both samples are referred to as B10 and B30, respectively, depending on the blended palm biodiesel percentage volume. Samples are stored in a sealed container at room temperature, with as little exposure to light as possible.

The study involves four stages. In the first stage, the biodiesel-blend properties were measured using ASTM standards. Then, an engine run experiment was conducted for each fuel type. Next, injector samples are collected from the engine run experiment and cross-sectioned to analyse the deposition in the injector nozzle holes' surface. Microscopic analysis was conducted by spectroscopic analysis of the injector hole using Scanning Electron Microscope (SEM).

3   Results and Discussions

Machining of fuel injector nozzle requires high precision due to the requirement to create multiple small diameter holes <300 um with thick walls. Some injector holes are designed with tapered diameter to create hydraulic situation that encourage cavitation to produce finer spray droplets [10]. The shape of injector hole used in this study is for a single cylinder CI diesel engine which measures about $200\,\mu$m, with no taper. The usual method for machining of such small holes are by using laser method, which produce stripes from recast layers. Cross sectioning of the B10 injector has exposed the nozzle hole along its entire length. Figure 1 shows the cross-sectioned nozzle hole of the B10 injector, the tapered shape of the injector is due to slight misalignment during the wire cutting process. From the Secondary-Electron (SE) image, it can be observed

that the injector wall surface is covered with precipitate deposition with diameter of around 1 um. This deposition is uniform throughout the injector hole surface from the inlet to the outlet. At the outlet of the B10 injector hole, larger diameter precipitate is found, with diameter in the order of 10 um. The Back-Scattered-Emission (BSE) image of the injector wall surface at the inlet and outlet shows a uniform brightness across the surface, with slight shadow from the injector hole curvature, indicating an overall uniform precipitate deposition throughout the injector hole.
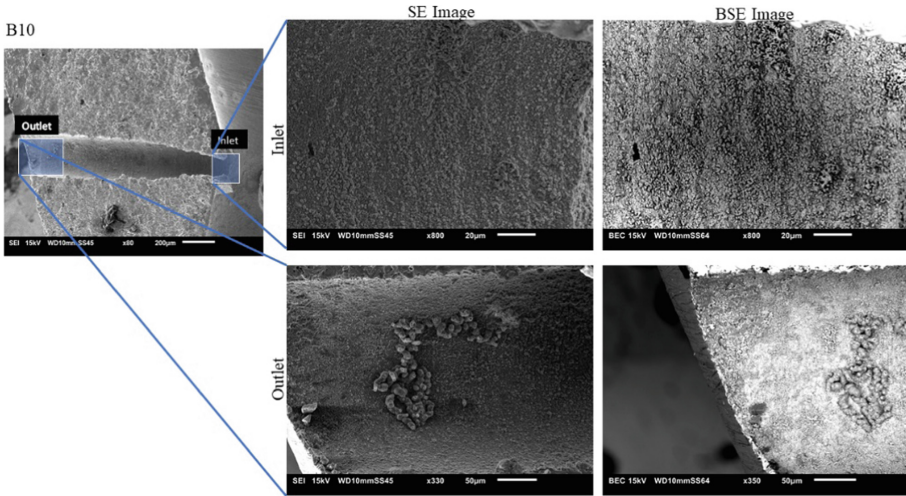
Fig. 1. Surface characteristics of the injector's hole when using B10 blend.

Figure 2 shows the cross-section nozzle hole of the B30 injector. The precipitate deposition on B30 injector hole surface appears to be two times larger in diameter compared to the ones in the B10 injector. The deposition is also more discrete and are concentrated at the machining burr lines on the injector hole wall surface. A cluster of larger sized depositions are also detected in both injector holes, however in the B10 injector, these depositions are located near the outlet while in B30 injector hole, they are located more towards the centre of the injector hole. The B30 inlet BSE image indicates a uniform precipitate composition.
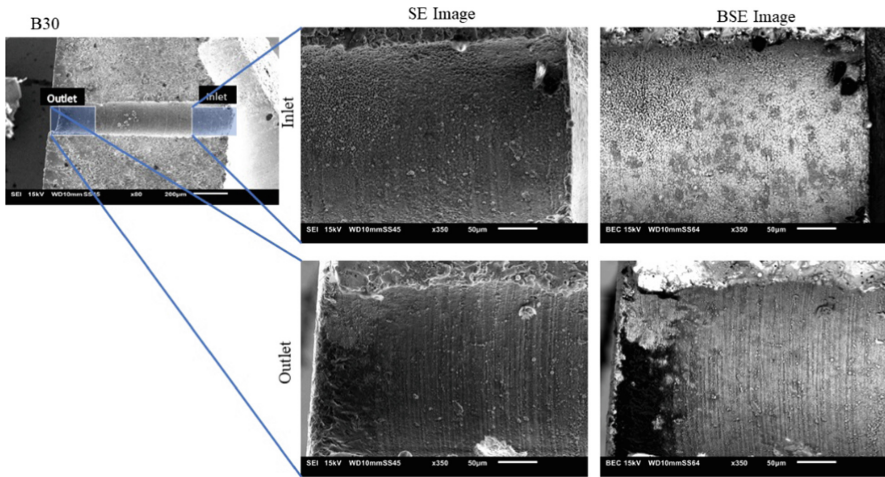
Fig. 2. Surface characteristics of the injector's hole when using B30 blend.

4   Conclusion

The deposit formation inside the fuel injector's hole has been examined in this paper using SEM. The characteristics of the deposition's changes in term of grain size when higher amount of palm methyl ester is used in the fuel blend. Further investigation to characterize the injector hole deposit is needed.

References

1. Proc, K., et al.: 100,000-mile evaluation of transit buses operated on biodiesel blends (B20). SAE Tech. Pap. **724**, 776–790 (2006). https://doi.org/10.4271/2006-01-3253
2. Ueda, D., Tanada, H., Utsunomiya, A., Kawamura, J., Weber, J.: 4th Generation Diesel Piezo Injector (Realizing Enhanced High Response Injector). SAE Technical Paper, vol. 2016, April 2016. https://doi.org/10.4271/2016-01-0846
3. Hoang, A.T., Le, A.-T.T.: A review on deposit formation in the injector of diesel engines running on biodiesel. Energy Sour. Part A Recover. Util. Environ. Eff. **41**(5), 584–599 (2019). https://doi.org/10.1080/15567036.2018.1520342
4. Höök, M., Tang, X.: Depletion of fossil fuels and anthropogenic climate change-a review. Energy Policy **52**, 797–809 (2013). https://doi.org/10.1016/j.enpol.2012.10.046
5. Birgel, A., Ladommatos, N., Aleiferis, P., Milovanović, N., Lacey, P., Richards, P.: Investigations on deposit formation in the holes of diesel injector nozzles. SAE Int. J. Fuels Lubr. **5**, 123–131 (2011). https://doi.org/10.4271/2011-01-1924

6. Liaquat, A.M., Masjuki, H.H., Kalam, M.A., Rizwanul Fattah, I.M.: Impact of biodiesel blend on injector deposit formation. Energy. **72**, 813–823 (2014). https://doi.org/10.1016/j.energy.2014.06.006

7. Reddy, S.M., Sharma, N., Gupta, N., Agarwal, A.K.: Effect of non-edible oil and its biodiesel on wear of fuel injection equipment components of a genset engine. Fuel **222**(March), 841–851 (2018). https://doi.org/10.1016/j.fuel.2018.02.132

8. Rounthwaite, N.J., et al.: A Chemical and Morphological Study of Diesel Injector Nozzle Deposits - Insights into their Formation and Growth Mechanisms (2017). https://doi.org/10.4271/2017-01-0798

9. McGilvery, C.M., Jiang, J., Rounthwaite, N.J., Williams, R., Giuliani, F., Ben Britton, T.: Characterisation of carbonaceous deposits on diesel injector nozzles. Fuel. **274**(March), 117629 (2020). https://doi.org/10.1016/j.fuel.2020.117629

10. Tong, H., Li, Y., Zhang, L., Li, B.: Mechanism design and process control of micro EDM for drilling spray holes of diesel injector nozzles. Precis. Eng. **37**(1), 213–221 (2013). https://doi.org/10.1016/j.precisioneng.2012.09.004

Determination of Surface Energy of Aramid Fibre

N. Ismail[1,2,3(✉)], M. B. deRooij[3], D. J. Shipper[3], and N. H. M. Zini[1,2,3]

[1] Fakulti Kejuruteraan Mekanikal, Universiti Teknikal Malaysia Melaka, Hang Tuah Jaya, 76100 Durian Tunggal, Melaka, Malaysia
nurhidayah.ismail@utem.edu.my
[2] Centre for Advanced Research on Energy, Universiti Teknikal Malaysia Melaka, Hang Tuah Jaya, 76100 Durian Tunggal, Melaka, Malaysia
[3] Surface Technology and Tribology Laboratory, Departments of Mechanics of Solids, Surfaces and Systems (MS3), Faculty of Engineering Technology, University of Twente, Drienerlolaan 5, 7522 NB Enschede, The Netherlands

Abstract. The physical properties of the fibre surface have a significant impact on the adhesion and frictional behaviour between fibres at the nano and microscale especially in composite materials. This paper focuses on determining the surface energy of an aramid fibre utilising the contact angle measurements with a series of test liquids. Twaron® aramid fibres, both treated and untreated are tested in three different liquids. The results show that treating the surface of the fibre increased the surface energy by approximately 36.7%. It was also discovered that the surface energy of the Twaron® aramid fibre is mostly of polar character, exhibiting a hydrophilic behaviour.

Keywords: Contact angle · Surface energy · Aramid fibre

1 Introduction

Understanding the physical properties of polymeric fibres, including the mechanism involved and the consequences, is vital in diverse array of fibre application fields. In composite materials, the physical properties of the fibre surface play an important role influencing the function of adhesive bonding between fibres in tow bundle, fibre to matrix and fibre coating [1].

Surface energy is one of the important surface properties. In general, the surface energy can be determined by measuring the contact angle between the solid surface and a series of test liquids. A sessile drop method is the most commonly used method for measuring contact angle. A proper amount of a liquid is dropped onto the solid surface using this method. However, for polymeric fibre materials the Wilhelmy method is preferable. According to the literature this method has been used on carbon [2, 3] and basalt [4] fibres, but not on more flexible material such as aramid fibres. Thus, the aim of this paper is to determine the surface energy of a single aramid fibre utilizing the contact angle measurements using the Wilhelmy method.

2 Method

2.1 Contact Angle Measurement

The contact angle of an aramid fibre with its polar and dispersive components is measured with a series of test liquids and evaluated using the Owens-Wendt method to determine its surface energy. Table 1 lists the properties of the test liquids. Twaron® aramid fibres of the similar type, but with treated and untreated surfaces, are tested. The diameter of the fibre is 12 μm, and its length is approximately 10 mm.

Table 1. Properties of the test liquids.

Test liquid	γ_L (mN/m)	γ_L^d (mN/m)	γ_L^p (mN/m)	ρ (g/cm^3)	η (mPas)
n-hexane	18.43	18.43	0	0.6603	0.3080
Distilled water	72.80	29.10	43.70	0.9982	1.002
Ethylene glycol	48.00	29.00	19.00	1.1088	21.80

The dynamic wetting force principle is used to calculate the contact angle of the fibre. The fibre is oriented perpendicular to the liquid interface, and the force exerted on it during immersion and withdrawn as a result of wetting is measured using a tensiometer, as shown in Fig. 1.
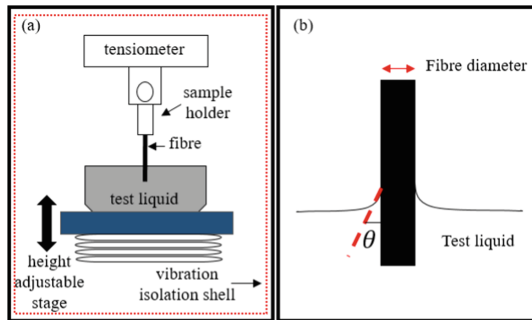
Fig. 1. (a) DCAT 11 experimental setup and (b) Contact angle.

For each sample in a test liquid, the measurement is repeated five times. The immersion depth is set to 5 mm, and each sample is treated with a fresh liquid to avoid contamination effects. The force measured during the measurement is a combination of the wetting force buoyancy and a mass. The mass contribution is zero because the tensiometer is zeroed before each measurement. This means that the relationship between the force measured, F and the contact angle θ is;

$$F = \pi D \gamma_l cos\theta \tag{1}$$

where γ_l is the surface tension of the test liquid, D is the diameter of the fibre and θ is the contact angle.

2.2 Determination of Surface Energy

According to Young's equation [4], there is a relationship between the contact angle θ, the surface tension of the liquid γ_L, the interfacial tension γ_{SL} between liquid as well as solid and the surface free energy γ_S of the solid:

$$\gamma_S = \gamma_L \cdot cos\theta + \gamma_{SL} \tag{2}$$

The second unknown variable γ_{SL} must be determined in order to calculate the surface energy of a single aramid fibre from the contact angle. The interfacial tension γ_{SL} is calculated using the Fowkes method [5], based on the two surface tensions γ_S and γ_L and the similar interactions between the phases. These interactions are interpreted as the geometric mean of a dispersive part γ^d and a polar part γ^p of the surface tension or surface free energy, resulting in:

$$\boldsymbol{\gamma_{SL} = \gamma_S + \gamma_L - 2\left(\sqrt{\gamma_S^d \cdot \gamma_L^d} + \sqrt{\gamma_S^p \cdot \gamma_L^p}\right)} \tag{3}$$

The combination of Eq. (2) and Eq. (3) leads to:

$$\boldsymbol{\gamma_L(1 + cos\theta)/2\sqrt{\gamma_L^d} = \sqrt{\gamma_s^p}\sqrt{\frac{\gamma_l^p}{\gamma_l^d}} + \sqrt{\gamma_s^d}} \tag{4}$$

The contact angle value is calculated from the capillary force using Eq. (2) and inserted in the Owens-Wendt, resulting in Eq. (4) [6].

3 Results and Discussion

Table 2 shows the contact angle measurements for both treated and untreated fibres. The untreated fibre had a slightly higher average contact angle than the treated fibre. This could be due to the effect of surface roughness on contact angle measurement. Besides, the mean contact angle for untreated fibre is slightly higher when compared to the results obtained by Hao using the sessile drop method [7].

Table 2. The mean contact angle for treated and untreated aramid fibre.

Fibre type	Contact angle $\pm$ sd
Untreated	65.1° $\pm$ 1.4°
Treated	61.3° $\pm$ 1.5°

[*]sd = standard deviation

Table 3 shows the values of surface energy and its dispersive and polar components obtained with utilizing the values of contact angles using Owens-Wendt method. All of the results show a reasonable agreement with the Owens-Wendt equation as in Eq. (4). Overall, the polar component has a higher value than the dispersive component. It is also discovered that the treated fibre has 12 mN/m more total surface energy than the untreated fibre.

Table 3. The values of surface energy and its component (dispersive and polar).

Fibre type	γ [mN/m]	γ^d [mN/m]	γ^p [mN/m]
Untreated	32.69	15.01	17.68
Treated	44.69	12.83	31.95

4   Conclusion

The surface energy was determined by utilizing the dynamic contact angle measurements using the Wilhelmy method. In a series of test liquids, the contact angle of two different Twaron® aramid fibres, treated and untreated, is measured. The Twaron® aramid fibre's surface energy is mostly polar, with a hydrophilic behaviour. The surface energy of the treated fibre surface is found to be higher than that of the untreated fibre of the similar type.

References

1. de Lange, P.J., Akker, P.G., Mader, E., Gao, S.L., Prasithphol, W., Young, R.J.: Controlled interfacial adhesion of Twaron® aramid fibres in composites by the finish formulation. J. Compos. Sci. Tech. **67**, 2027–2035 (2007)
2. Barraza, H.J., Hwa, M.J., Blakley, K., O'Rear, E.A., Grady, B.P.: Wetting behaviour of elastomer modified glass fiber. Langmuir **17**(17), 5288–5296 (2001)
3. Young, T.: An essay on cohesion of fluids. Phil. Trans. Roy. Soc. **5**, 65 (1805)
4. Yuehua Yuan, T., Lee, R.: Contact angle and wetting properties. In: Bracco, G., Holst, B. (eds.) Surface Science Techniques, vol. 51, pp. 3–34. Springer, Heidelberg (2013). https://doi.org/10.1007/978-3-642-34243-1_1
5. Fowkes, F.M.: Contact Angle, Wettability and Adhesion, p. 99. American Chemical Society, Washington DC (1964)
6. Owens, D.K., Wendt, R.C.: Estimation of the free surface energy of polymers. J. App. Polym. Sci. **13**, 1741–1747 (1969)
7. Hao, W., Yao, X., Ke, Y., Ma, Y., Li, F.: Experimental characterization of contact angle and surface energy on aramid fibers. J. Adhes. Sci. Tech. **27**(9), 1012–1022 (2013)

Thermal and Fluids

Uncertainty Analysis of Thermal Fluid Measurements for Bi-directional Flow Condition Across Tube Banks

Nurjannah Hasbullah[1,2], Fatimah Al Zahrah Mohd Saat[1,2,3(✉)],
Fadhilah Shikh Anuar[4], Mohamad Firdaus Sukri[1,2], Mohd Zaid Akop[1,2],
and Zainuddin Abdul Manan[5]

[1] Fakulti Kejuruteraan Mekanikal (FKM), Universiti Teknikal Malaysia Melaka (UTeM), Hang Tuah Jaya, 76100 Durian Tunggal, Melaka, Malaysia
fatimah@utem.edu.my
[2] Centre for Advanced Research on Energy (CARe), Universiti Teknikal Malaysia Melaka (UTeM), Hang Tuah Jaya, 76100 Durian Tunggal, Melaka, Malaysia
[3] Green Design & Manufacture Research Group, Centre of Excellence Geopolymer & Green Technology, Universiti Malaysia Perlis (UniMAP), Arau, Perlis, Malaysia
[4] Fakulti Teknologi Kejuruteraan Mekanikal dan Pembuatan (FTKMP), Universiti Teknikal Malaysia Melaka (UTeM), Hang Tuah Jaya, 76100 Durian Tunggal, Melaka, Malaysia
[5] Process Systems Engineering Centre (PROSPECT), School of Chemical and Energy Engineering, Faculty of Engineering, Universiti Teknologi Malaysia (UTM), 81310 Johor Bahru, Johor, Malaysia

Abstract. The uncertainty analysis for experimental investigation of bi-directional flow conditions of thermoacoustics is presented. The experimental rig used for loudspeaker as a flow inducer to provide acoustical flow across tube banks that is placed inside a standing wave resonator. The measured velocity and temperature changes within the vicinity of the tube banks are presented along with the uncertainty values. The standard deviation for velocity and temperature data shows that data varies with maximum deviation of 0.14 m/s and 5.78 °C, respectively. The results show that a good repeatability was obtained during the experiments which indicates that a reliable thermal-fluid measurement of bi-directional flow condition was achieved.

Keywords: Tube banks · Bi-directional flow · Uncertainty analysis

1 Introduction

Bi-directional flow represents a condition of fluid that flows back and forth in cyclic condition. The flow, which can be found in thermoacoustics or blood flow system, is also known as an oscillatory flow [1, 2]. The transient nature of flow with cyclic conditions impose certain challenges for experimental study. Precision mistakes are minimal in most experiments since sophisticated electronic apparatus, data collection systems, and computers are used to manage and process data. When large precision mistakes are

present, it is typically clear that there may be decreased by investing more time and/or money in improved equipment [3]. One way of minimizing errors in physical measurements is through repeatability and uncertainty analysis [4]. Realizing the importance of reliable data, this paper reports the uncertainty analysis for the thermal-fluids measurements of bi-directional flow experimentations as reference for better predictions of results for future study of bi-directional flow condition especially that is related to thermoacoustic energy system.

2   Methodology

2.1   Experimental Setup

The experimental study for bi-directional flow condition consists of a loudspeaker as a flow inducer and a mild steel tube as a resonator, as shown in Fig. 1.
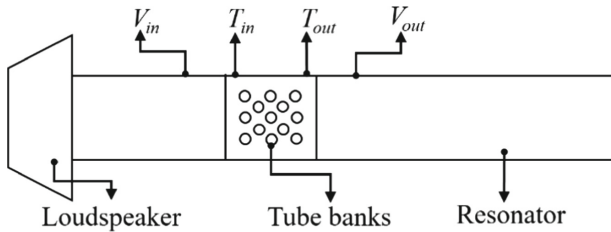
Fig. 1.   Schematic diagram of experimental setup.

Loudspeaker is connected to the function generator (AFG 21005) and an amplifier (FLP-MT1201). A tube banks heat exchanger is placed inside the resonator. The total length of resonator is 6.6 m long and the cross-sectional area is 142 mm × 142 mm. The configuration of the experimental setup is shown in Table 1. The tube banks is in staggered arrangement and the arrangement is the same as describe by Hasbullah et al. [5].

Table 1.   Configuration of experimental setup.

Parameter	Configuration
Number of tube banks	13
Diameter of tube banks (m)	0.003
Resonance frequency (Hz)	14.2

In this experiment, value of velocity and temperature are measured to obtain the difference between the values at inlet and outlet locations of the heat exchanger. The temperature of the tube banks is set at a constant temperature of $T = 80\ °C$. Hotwire

anemometer (ST-732) is used to measure the value of velocity at both locations; V_{in} and V_{out}. The hotwire is placed 120 mm to the left and right sides of the tube banks heat exchanger. For measuring temperature, type-K thermocouples are placed at the inlet and outlet, as shown in Fig. 1 as T_{in} and T_{out}. Peak-to-peak voltage amplitude, V_{pp} is the input variable for the loudspeaker and it was set using the function generator. V_{pp} is set to range between 0.02 V to 0.23 V. The variation of input voltage leads to variation of bi-directional flow amplitude inside the test rig.

2.2   Uncertainty Calculations

The experimental procedure is repeated for five times. The uncertainty calculations are calculated based on Eq. (1) and Eq. (2). Equation (1) shows the general formula that was used for calculating the mean value of data, $\bar{x}$ (also known as average value). The term n is the number of repeated measurements. The experimental error is calculated using the standard deviation, s_x, as defined in Eq. (2).

$$\bar{x} = \frac{1}{n}(x_1 + x_2 + x_3 + \cdots + x_n) \tag{1}$$

$$s_x = \sqrt{\frac{1}{n-1}\left[(x_1 - \bar{x})^2 + \cdots + (x_n - \bar{x})^2\right]}. \tag{2}$$

3   Results

Figure 2 shows the result of velocity changes with flow amplitudes of bi-directional flow condition. The locations of velocity measurements of V_{in} and V_{out} were shown in Fig. 1. The values of V_{in} and V_{out}, for both locations varies from 0.47 m/s to approximately 2.1 m/s. The error bars are observable along with the increasing values of velocity. The reason is that when the V_{pp} is increasing, the velocity of the fluid becomes bigger and the impact of oscillation of bi-directional flow becomes significant. As the fluid oscillates over the heated tubes, the cyclic flow never truly exits the system and is therefore heated by the heater. Natural convection is stronger at outlet location and hence the V_{out} is lower. Uncertainty analysis shows that maximum values at inlet and outlet locations are $V_{in} = 2.10 \pm 0.14$ m/s and $V_{out} = 1.89 \pm 0.13$ m/s.
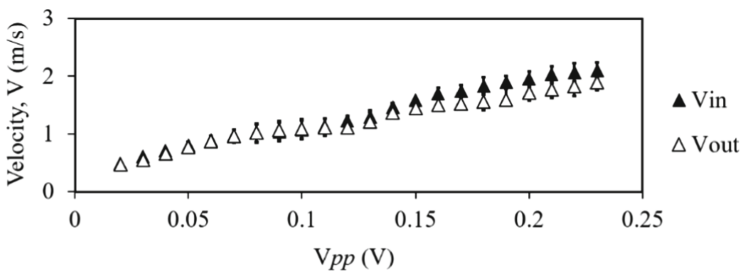
Fig. 2. Velocity changes with flow amplitudes.

Figure 3 shows the result of temperature changes with velocity for bi-directional flow condition. Temperature of tube banks was set to 80 °C. However, results showed that the fluid temperature of T_{in} and T_{out} reached more than 100 °C. Results also show a greater difference between T_{in} and T_{out} at velocity lower than 1 m/s. After 1 m/s, the value of T_{in} and T_{out} are somewhat consistently constant as the velocity increases. In addition to the natural convection effect, the feature of developing flow regime seems to be the reason for the changes of pattern between flow before and after the 1 m/s velocity. The error bars of the T_{in} and T_{out} are noticeable when the velocity is 0.11 m/s.
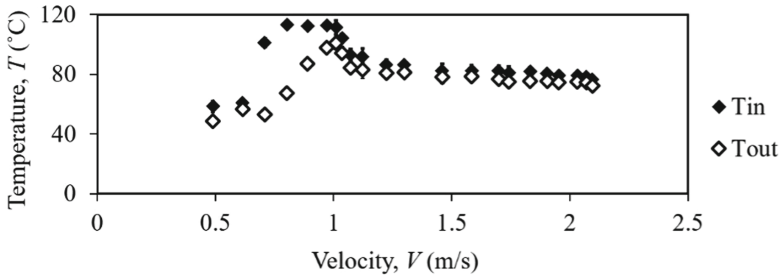
Fig. 3. Temperature changes with velocity.

The standard deviation shows that the maximum values of temperature at inlet and outlet locations can be written as $T_{in} = 91.6 \pm 5.78$ °C and $T_{out} = 83.0 \pm 5.06$ °C. From the uncertainty equation at 0.11 m/s, the difference between the values of temperature at inlet and outlet are found fluctuated by 9.38%. The plotted Fig. 3 also shows that the value of T_{in} is higher compared to the value of T_{out} as the velocity is rising.

4   Conclusion

The results disclosed that the velocity and temperature at inlet location are higher compared to the outlet location. This study reports that the error that occurs in the thermal fluid measurements of bi-directional flow conditions are related to the cyclic nature of flow across tube banks. Uncertainty values become slightly bigger as velocity of flow increases. The impact of natural flow and developing flow were also observed.

References

1. Allafi, W.A., Saat, F.A.Z.M., Mao, X.: Fluid dynamics of oscillatory flow across parallel-plates in standing-wave thermoacoustic system with two different operation frequencies. Eng. Sci. Technol. Int. J. **24**(1), 41–49 (2021)

2. Kedarasetti, R.T., Drew, P.J., Costanzo, F.: Arterial pulsations drive oscillatory flow of CSF but not directional pumping. Sci. Rep. **10**(1), 1–12 (2020)
3. Mills, A.F., Chang, B.H.: Error Analysis of Experiments. UCLA, Los Angeles (2004)
4. Taylor, J.: Introduction to Error Analysis, the Study of Uncertainties in Physical Measurements. University Science Books, New York (1997)
5. Hasbullah, N., Saat, F.A.Z.M., Anuar, F.S., Johari, D., Sukri, M.F.: Temperature and velocity changes across tube banks in one-directional and bi-directional flow conditions. Evergreen **8**(2), 428–437 (2021)

Heat Transfer Calculation for Oscillatory Flow of Thermoacoustics

Aw Lin Chou[1,2], Fatimah Al-Zahrah Mohd Saat[1,2,3(✉)], Fadhilah Shikh Anuar[2,4], and Noryani Muhammad[1,2]

[1] Fakulti Kejuruteraan Mekanikal (FKM), Universiti Teknikal Malaysia Melaka (UTeM), Hang Tuah Jaya, 76100 Durian Tunggal, Melaka, Malaysia
`fatimah@utem.edu.my`
[2] Centre for Advanced Research on Energy (CARe), Universiti Teknikal Malaysia Melaka (UTeM), Hang Tuah Jaya, 76100 Durian Tunggal, Melaka, Malaysia
[3] Center of Excellence Geopolymer and Green Technology, Universiti Malaysia Perlis, 01000 Kangar, Perlis, Malaysia
[4] Fakulti Teknologi Kejuruteraan Mekanikal dan Pembuatan (FTKMP), Universiti Teknikal Malaysia Melaka (UTeM), Hang Tuah Jaya, 76100 Durian Tunggal, Melaka, Malaysia

Abstract. This study presents a heat transfer analysis for the oscillatory flow of thermoacoustics. Experimental works and numerical simulation using the Computational Fluid Dynamics (CFD) method were done, and the heat transfer values were calculated and discussed. Results showed that a slight modification in the heat transfer calculation leads to a better representative of heat transfer for oscillatory flow. The results indicate that the direct use of heat transfer correlation that was meant for steady one-directional flow on the calculation of heat transfer for oscillatory flow may not be sufficient in providing the actual insight into the thermal performance in the oscillatory flow model.

Keywords: Thermoacoustics · Oscillatory flow · Heat transfer

1 Introduction

Thermoacoustic technology was introduced as an alternative technology for refrigerators and power generators. It uses inert gases as a working medium and it involves very minimum moving mechanisms [1]. Thermoacoustic technology mainly works by converting acoustic effects into thermal energy. The fluid in a thermoacoustic system flows back and forth in an oscillatory motion, making the fluid flow structure more complicated compared to the conventional one-directional steady flow condition found in many systems. The unique feature of the oscillatory flow also leads to complex nonlinear feature that may give influence to system's performance [2]. Heat exchanger is one of the important components in thermoacoustic system. Fluid flows across heat exchanger that is placed inside the oscillatory flow of thermoacoustics were reported to be different compared to the situation of the normal one-directional flow [3, 4]. Parameters, such as velocity and temperature, that were usually used for the calculation of heat transfer correlation were reported to exhibit a different trend of changes inside the oscillatory flow

when compared to the case of one-directional steady flow [3]. Hence, the heat transfer correlation developed for steady one-directional flow might not be valid in predicting the heat transfer performance of heat exchanger with oscillatory flow [3, 4]. In this paper, an improved way of calculating the heat transfer equation is proposed to suit the nature of the oscillatory flow across the investigated tube banks heat exchanger based on thermoacoustic flow settings.

2 Methodology

Experimental works are conducted using the available experimental rig that resembles thermoacoustic environment as shown in Fig. 1 [1, 3]. The experimental rig consists of a subwoofer connected at one end of the resonator tube to produce acoustic waves while the other end of the resonator tube is closed and this end is known as the pressure antinode. Thermocouple, hot-wired anemometer, and pressure transducer are inserted into the experimental rig to obtain temperature data, velocity and pressure, for the calculation of heat transfer. Pressure values are obtained at the location of pressure antinode to calculate the drive ratios ($P_{antinode}/P_{mean}$). Velocity and temperature values are taken at locations near the outlet and inlet of the heat exchanger test section. Surface temperature of the tube is also measured when conducting the experimental works.
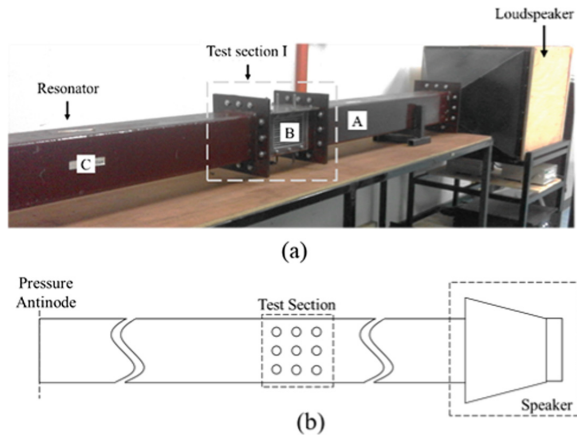
Fig. 1. (a) Experimental set up. (b) Schematic diagram of experimental set up.

Values obtained from experimental works are used to set up the boundary condition in solving the model for Computational Fluid Dynamics (CFD) method. All boundary conditions in the solver settings are set according to the actual situation of the experimental works. Detail descriptions of the experiments and CFD simulation settings can be found in the published works [3, 4]. Experimental works and numerical simulations are done for three different drive ratios with in-line tube configuration for the heat exchanger that was set with constant surface temperature of 40 °C.

3 Results and Discussion

The results are shown as a parameter known as the Colburn-j factor calculated using Eq. (1) [4]. Colburn-j factor is represented by dimensionless parameters of Nusselt number, *Nu*, Reynolds number, *Re*, and Prandtl number, *Pr*. Nusselt number and Reynolds number are obtained from Eq. (2) and Eq. (3), respectively, while Prandtl number for air was set as a constant value of 0.7323. The heat transfer coefficient, *h*, is defined by Eq. (4). Equation (5) is used to calculate the log mean temperature difference, ΔT_{ln}. Maximum velocity, V_{max} for Eq. (3) was calculated using Eq. (6) where velocity, *u*, is the velocity value obtained at location $x = 4.23$ m from the pressure antinode location.

$$j = \frac{Nu}{Re\left(Pr^{1/3}\right)} \tag{1}$$

$$Nu = \frac{hD}{k} \tag{2}$$

$$Re = \frac{\vec{V}_{max}D}{\nu} \tag{3}$$

$$h = \frac{\dot{m}c_p(\Delta T)}{A_s \Delta T_{ln}} \tag{4}$$

$$\Delta T_{ln} = \frac{(T_{tube} - T_{in}) - (T_{tube} - T_{out})}{\ln\left[\frac{T_{tube} - T_{in}}{T_{tube} - T_{out}}\right]} \tag{5}$$

$$\vec{V}_{max} = \frac{S_T}{S_T - D}u \tag{6}$$

Two methods were used to calculate ΔT in Eq. (4). The first method is the conventional method labelled as *'Conv'* in Fig. 2 where ΔT is represented by the temperature difference before and after the tube banks ($\Delta T = T_{in} - T_{out}$). The second method is the proposed method labelled as *'Prop'* in Fig. 2 where ΔT is represented by the temperature difference between the tube surface temperature and the fluid temperature ($\Delta T = T_s - T_{fluid}$). The fluid temperature are the average values recorded at $x_1 = 4.338$ m and $x_2 = 4.662$ m. Both the experiment and CFD results in Fig. 2 show that a better representation of heat transfer can be obtained by using the new proposed definition of temperature difference in the calculation of heat transfer coefficient. The values calculated with conventional method give a Colburn-j factor near to zero which describes a heat transfer of almost none in the system. This happens because temperature is almost the same at both the locations defined in conventional method. In contrary, the Colburn-j factor calculated using the proposed temperature difference shows a better trend with respect to the change of Reynolds number. Hence, the proposed definition of temperature difference is shown to offer a better prediction of heat transfer that describes the real heat transfer phenomena in the thermoacoustic flow condition. A good agreement was also found between the experimental and numerical approaches where the Colburn-j factor decreases as the Reynolds number increases when the heat transfer correlation is calculated using the proposed method.
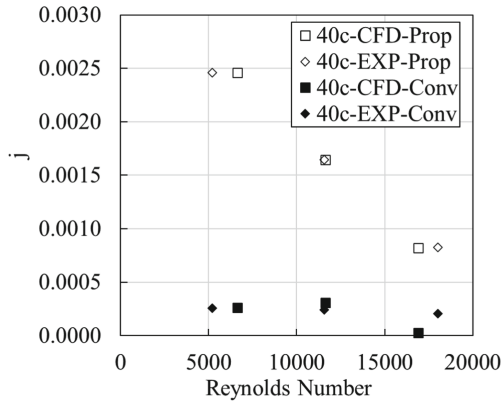
Fig. 2. Colburn-j factor values for oscillatory flow.

4 Conclusion

The temperature difference calculation as defined in the conventional way is not suitable for oscillatory flow as the temperature at inlet and outlet locations of the test section are almost similar due to the cyclic nature of the flow. The result in this paper shows that conventional way of calculating heat transfer will lead to misleading value of almost zero which does not describe the heat transfer between oscillatory fluid flow of thermoacoustics and the tube banks heat exchanger.

References

1. Saat, F.A.Z.M., Johari, D., Mattokit, E.: DeltaE modelling and experimental study of a standing wave thermoacoustic test rig. J. Adv. Res. Fluid Mech. Therm. Sci. **60**(2), 155–165 (2019)
2. Saat, F.A.Z.M., Jaworski, A.J.: The effect of temperature field on low amplitude oscillatory flow within a parallel-plate heat exchanger in a standing wave thermoacoustic system. Appl. Sci. **7**(4), 417 (2017)
3. Hasbullah, N., Al, F., Mohd, Z., Anuar, F.S., Johari, D., Sukri, M.F.: Temperature and velocity changes across tube banks in one- directional and bi-directional flow conditions. Evergreen **8**(2), 428–437 (2021)
4. Lin, C.A., Sa'at, F.A.Z.M., Anuar, F.S., Sukri, M.F., Akop, M.Z., Manan, Z.A.: Heat transfer across tube banks with a passive control vortex generator in steady one-directional and oscillatory flows. CFD Lett. **13**(1), 1–18 (2021)

Temperature Drop for Thermoacoustic Cooler with Different Stack Materials Using DeltaEC Model

Nur Damia Asma Rosle[1,2], Fatimah Al Zahrah Mohd Saat[1,2,3(✉)],
Raja Nor Firdaus Kashfi Raja Othman[4], Fadhilah Shikh Anuar[2,5],
Noryani Muhammad[1,2], and Irfan Abd. Rahim[3,6]

[1] Fakulti Kejuruteraan Mekanikal (FKM), Universiti Teknikal Malaysia Melaka (UTeM), Hang Tuah Jaya, Durian Tunggal, 76100 Melaka, Malaysia
fatimah@utem.edu.my
[2] Centre for Advanced Research on Energy, Universiti Teknikal Malaysia Melaka, Hang Tuah Jaya, Durian Tunggal, 76100 Melaka, Malaysia
[3] Green Design & Manufacture Research Group, Centre of Excellence Geopolymer and Green Technology, Universiti Malaysia Perlis (UniMAP), 02600 Perlis, Malaysia
[4] Fakulti Kejuruteraan Elektrik (FKE), Universiti Teknikal Malaysia Melaka (UTeM), Hang Tuah Jaya, Durian Tunggal, 76100 Melaka, Malaysia
[5] Fakulti Teknologi Kejuruteraan Mekanikal Dan Pembuatan (FTKMP), Universiti Teknikal Malaysia Melaka (UTeM), Hang Tuah Jaya, Durian Tunggal, 76100 Melaka, Malaysia
[6] Fakulti Teknologi Kejuruteraan Mekanikal (FTKM), Universiti Malaysia Perlis (UniMAP), 02600 Perlis, Malaysia

Abstract. Thermoacoustics offer alternative green options for technologies related to cooling and energy generation. This study presents the standing wave models of thermoacoustic refrigerating system with different used of materials for the structure known as stack. The DeltaEC results showed a temperature drop predicted of 264.14 K can be achieved by considering a non-metal material for stack that is placed inside a standing wave thermoacoustic cooler model with resonance frequency of 123 Hz.

Keywords: Thermoacoustic cooler · DeltaEC · Stack material

1 Introduction

DeltaEC software is a computer program that can calculate the performance of thermoacoustic equipment or can help user to design equipment for the desired performance [1]. The program numerically integrates the respective 1-D linear acoustic wave equation using the Runge-Kutta integration method to solve for the fundamental acoustic variables. The DeltaEC model relies on Rott's linear theory and uses a quasi-one-dimensional analysis of the dynamic equations [2]. DeltaEC can be used as verification method for design and optimization procedures of thermoacoustic system [3]. Many research groups

had carried out geometrical optimization based on either experimental work or numerical solution of linear thermoacoustic theory using software such as DeltaEC [4]. Tijani et al. [5] successfully optimized the stack unit using manual calculation of linear thermoacoustic theory as well as the numerical prediction from DeltaEC model in order to meet the requirement of cooling power at various discrete values of stack parameters including the normalized stack length and stack center position. In this paper, a numerical study is conducted by using DeltaEC to investigate the effect of temperature drop on stack with different materials and lengths. The results will be useful for the future design and fabrication of the working system.

2   Methodology

Figure 1 shows the simple design of the thermoacoustic refrigerator system that was developed for the current study. DeltaEC is based on a shooting method, thus, careful selections of initial values are necessary to maintain numerical stability and convergence. There are five segments that have been used in the DeltaEC which are 'begin', 'speaker', 'duct', 'stack', 'surface' and 'hardend'. In the model, the temperature at the left end of segment 3 of Fig. 1 was set with 296 K as a shooting initial value and DeltaE will predict the temperature at the other end based on the design that is shown in Fig. 1. The initial values for the dynamic pressure, p and volume velocity, U are defined at the BEGIN segment where the input values were set to be within the range of 1635.1911 Pa to 2470.7558 Pa and 0.2891 m^3/s 0.4369 m^3/s, respectively. Then, the corresponding phase angles were initialized at 0° and 90° for the volume velocity and pressure, respectively, in consistency with the standing mode operation. Values for the frequency and temperature will also be included in the BEGIN segment as initial value and operating conditions of the tested models.
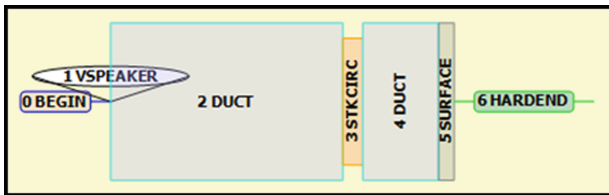
Fig. 1. The schematic diagram of the design of thermoacoustic cooler in the DeltaEC software.

The parameters that are required for VSPEAKER in DeltaEC are entered based on speaker's specification for D5 5 in.-2 way coaxial speaker model. The DUCT segment was located adjacent to the right side of VSPEAKER segment as shown in Fig. 1. The DUCT represents the resonator that will be used in the future experimental work. The length of the resonator was defined at 0.65 m with a diameter of 0.031 m. For this length, the frequency was calculated to be 123 Hz when air at atmospheric pressure is used as the working fluid. A structure known as stack is located as Segment 3 that was labelled in Fig. 1 as STKCIRC. The stack is a porous media that is usually involving a hexagon honeycomb arrangement. The model was solved for two different stack materials; metal

(Stainless steel) and non-metal (Celcor ceramic). In this thermoacoustic system, it is assumed that the thermoacoustic refrigerator system is operating in quarter wavelength environment where HARDEND is applied at the end of the quarter wavelength resonator. The HARDEND segment that was shown in Fig. 1 represents the solid end wall in the DeltaEC models. All parameters used in DeltaEC models are briefly summarized in Table 1. The models were run until convergence is successfully achieved.

Table 1. The initial parameters that were defined in the segments of the thermoacoustic model.

Parameters	Values
Initial	
Frequency, Hz	123
Mean Pressure, kPa	101325
Temperature, K	296
Resonator	
Length of resonator, m	0.65
Material	Ideal
Cross sectional area, m^2	0.07548
Stack	
Arrangement	Hexagon honeycomb
Cross sectional area, m^2	0.07548
Material	Metal and non-metal
Length, cm	0.04 and 0.08

3   Result and Discussion

The heat transfer performance of the modelled system is represented using temperature drop that can be achieved between the two ends of the stack. The results, as shown in Fig. 2 are shown for stack with two different materials and two different lengths. The results for metallic and non-metallic stack materials were collected as well as the length of stack that was tested with two values; 4 cm and 8 cm long. The results in Fig. 2 show that stack with 8 cm long, either metal or non-metal, provides better temperature drop between two ends of the stack compared to that of the 4 cm long. This can be seen by the differences in maximum temperature between the two ends. The 8 cm stack length for metal and non-metal materials produced temperature that is 114.44 K and 264.14 K higher than that of the 4 cm stack length. Figure 2 also shows that non-metal material offers better heat transfer effect based on temperature drop compared to the metal material. This is probably due to the specific heat value which is higher for non-metal material compared to the metal material. Therefore, different performance of thermoacoustic system will be achieved if materials with different specific heat value is used.
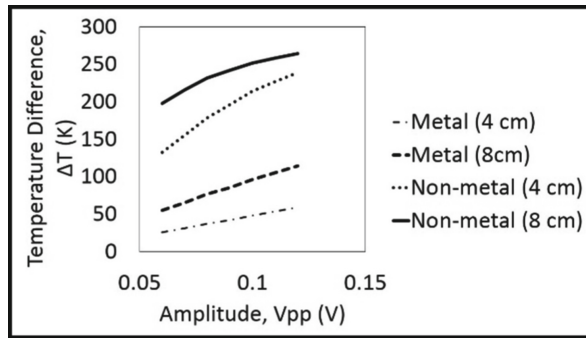
Fig. 2. Effects of temperature drop, ΔT, across stack at various peak-to-peak input voltage, Vpp, in the thermoacoustic refrigeration system.

4   Conclusions

The study shows that the temperature drop for metal materials with lengths of 4 cm and 8 cm are 59.08 K and 114.44 K, respectively. Whereas the temperature drop for a non-metal material is 238.74 K and 264.14 K when stack is 4 cm and 8 cm long, respectively. Therefore, non-metal material with 8 cm long offer the best impact of temperature drop for the standing wave thermoacoustic system when air at atmospheric pressure is used as the working fluid.

References

1. Alamir, M.A., Sidik, N.A.C.: Thermoacoustic refrigerators and heat pumps: New insights for a high performance. J. Adv. Res. Fluid Mech. Thermal Sci. **78**(1), 146–156 (2021)
2. Abd El-Rahman, A.I., Abdelfattah, W.A., Abdelwahed, K.S., Salama, A., Rabie, A., Hamdy, A.: A compact standing-wave thermoacoustic refrigerator driven by a rotary drive mechanism. Case Stud. Thermal Eng. **21**, 100708 (2020). https://doi.org/10.1016/j.csite.2020.100708
3. Babaei, H., Siddiqui, K.: Design and optimization of thermoacoustic devices. Energy Convers. Manage. **49**(12), 3585–3598 (2008)
4. Johari, D., Mattokit, E., Saat, F.A.Z.M.: Parametric study of thermoacoustic system using DeltaE. J. Adv. Res. Fluid Mech. Thermal Sci. **46**(1), 161–168 (2018)
5. Tijani, M.E.H., Zeegers, J.C.H., De Waele, A.T.A.M.: Design of thermoacoustic refrigerators. Cryogenics **42**(1), 49–57 (2002)

Effect of Diaelectric Barrier Discharge (DBD) Plasma Actuator on Aerodynamics Performance of Vehicle Spoiler

Nurfarah Diana Mohd Ridzuan Tan[1], Fudhail Abdul Munir[1(✉)], Musthafah Mohd Tahir[1], Nurfarah Nabila Saad Azam[1], and Herman Saputro[2]

[1] Fakulti Kejuruteraan Mekankila, Universiti Teknikal Malaysia Melaka, Durian Tunggal, 76100 Melaka, Malaysia
fudhail@utem.edu.my

[2] Department of Mechanical Engineering Education, Universitas Sabelas Maret, 57169 Surakarta, Pabelan, Indonesia

Abstract. Dielectric Barrier Discharge (DBD) plasma actuator has become the well-known tools in the aerodynamics flow control applications. DBD plasma actuator have no moving parts as it only involves in ionization of flow stream, fast reaction, flexible and amazingly low in mass making it good alternative to hydraulic based control system. In this study, numerical simulations of airflow on vehicle spoiler with plasma actuator were performed. The results in terms of aerodynamic performance such as coefficient of drag (C_D) and lift coefficient (C_L) are presented in this paper. The vehicle spoiler is designed based on NACA 4418 airfoil while the DBD plasma is modeled as the source term in ANSYS-Fluent software. The results suggest that, by having plasma actuator on the top part of the spoiler, there is approximately 3.4% decrease in the value coefficient of drag. As such, DBD plasma actuator can be considered as the flow controller that can be installed in automotive spoiler for better performance.

Keywords: DBD plasma actuator · Aerodynamics flow control

1 Introduction

Nowadays, aerodynamics plays significant role in vehicle design considerations. A car spoiler known as wing is an accessory that attached at the rear end of cars, which is positioned under the front bumper or mounted on the top of car's trunk. The intended of attached the spoiler at the rear is to spoil unfavourable air movement across a vehicle body of some kind in motion [1]. It is customary for racing and any other high-performance car to be fitted with spoilers. The main role of spoiler is to diffuse or spoil the airflow over and around the moving vehicle or body [2–4]. The shape of spoiler used for the vehicle spoiler are same as for aircraft but in an inverted position. Meanwhile, plasma can be defined as collection of positive and negative charged particles of partially ionized neutral gas [5]. The flow that is controlled by Dielectric Barrier Discharge is one of the active flow methods that have attracted interest among researchers. This DBD plasma

actuator has been shown to be utilized as strategies in controlling noise, increasing lift and controlling transition. DBD plasma actuator was first used as a streamlined extension by Roth et al. [6]. DBD plasma actuator involving dielectric barrier material which is Kapton film between two copper electrodes that marginally layered to one another. Each of the electrodes is covered totally by dielectric material and exposed to the air, where it is connected to a high voltage and high recurrence AC power are provided to produce capacity to these electrodes. With adequate and sufficient high voltage power is given between electrodes, the plasma is created. Dielectric Barrier Discharge (DBD) plasma actuator on the vehicle spoiler is used to substitute the current conventional flow control devices due to economical, safety and environmental concerns. In this research, the effects of DBD plasma on the aerodynamic performance of a vehicle spoiler is numerically examined. The DBD plasma is placed on top of the spoiler. Computational Fluid Dynamics (CFD) method is employed of which the coefficient of drag and lift is determined.

2 Research Methodology

Computational Fluid Dynamics (CFD) method is utilized in this research where two dimensional (2-D) numerical simulation of airflow around the vehicle spoiler with and without effect of plasma actuator were performed. The design of spoiler is based on NACA 4418. Firstly, the 2-D geometry of spoiler model was developed using Design Modeler (DM), which is a built in Computer Aided Drafting (CAD) software available in ANSYS Release 19.2. Once the geometry is ready, the meshing or better known as the grid generation is performed. Next, the governing equations were then solved using Fluent 6.3 software. In order to simulate the effect of DBD plasma actuator, User Define Function (UDF) is utilized where part of the code (C programming) is modified from Bouchmal [7]. The DBD plasma is modelled at the top of spoiler as shown in Fig. 1(a). The angle of attack is fixed to 0° while inlet velocity is set to 1.0 m/s for all cases. The results in terms of aerodynamic performance such as velocity and pressure contours, coefficient of drag and lift (C_D, C_L) were analysed and presented.
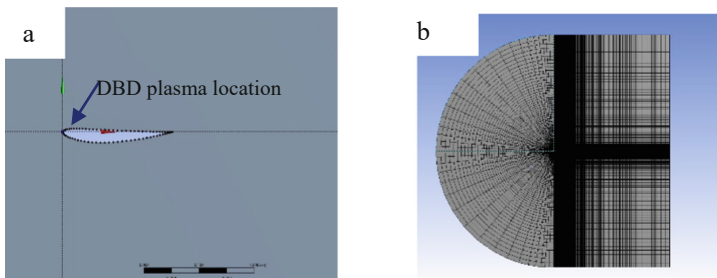
Fig. 1. (a) 2-D drawing of the vehicle spoiler (b) Grid generation.

3   Results and Discussion

The results in terms of pressure and velocity contours with and without DBD plasma effect is depicted in Fig. 2. The results suggest that there are changes of both velocity and pressure contours at the top of the spoiler when DBD plasma was activated. Apart from that, when DBD plasma was activated, the coefficient of drag (C_D) is reduced from 0.02937 to 0.028371. However, the downward force is shown to be reduced with DBD plasma activated. The coefficient of lift is reduced from 0.3699 to 0.3338. This is probably due to higher velocity is obtained around the DBD plasma location that contributes to lower pressure at the top of spoiler.

a.   Without DBD plasma

b.   With DBD plasma activated
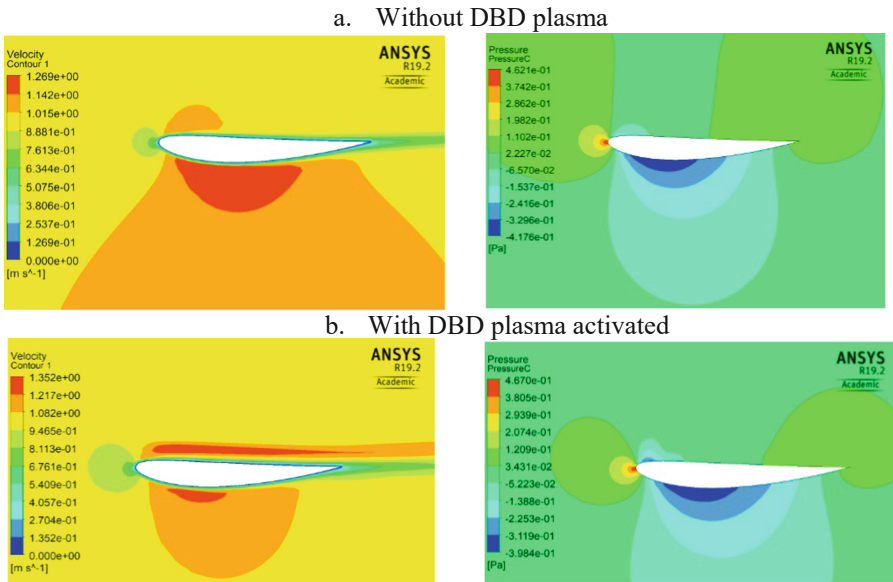
Fig. 2.   (a) Pressure and velocity contours without DBD plasma (b) Pressure and velocity contours with DBD plasma activated.

4   Conclusions

The effects of DBD plasma actuator on the aerodynamics performance of a vehicle spoiler is successfully employed. It is shown that the coefficient of drag can be reduced up to 3.4% with the activation of DBD plasma. Nevertheless, the downward force is also reduced up to 9.7%. As such, further study need to be done to investigate the effect of the DBD location on the vehicle spoiler.

References

1. Shadmani, S., Mousavi Nainiyan, S.M., Mirzaei, M., Ghasemiasl, R., Pouryoussefi, S.G.: Experimental investigation of flow control over an Ahmed body using DBD plasma actuator. J. Appl. Fluid Mech. **22**, 239–252 (2018)
2. Cheng, S.Y., Kwang, Y.C., Shuhaimi, M., Abd Basid, A.R.: Experimental study of yaw angle effect on the aerodynamic characteristics of a road vehicle fitted with a rear spoiler. J. Wind Eng. Ind. Aerodyn. **184**, 305–312 (2019)
3. Lou, B., Huang, Z., Ye, S., Wang, G.: Experimental and numerical studies on aerodynamic control of NACA 4418 airfoil with a rotating cylinder. J. Vib. Eng. Tech. **8**(1), 141–148 (2019). https://doi.org/10.1007/s42417-019-00085-5
4. Tan, N.D.M.R., Munir, F.A., Tahir, M.M., Herman, S., Mikami, M.: Preliminary investigation of using DBD plasma for application in micro combustors. J. Adv. Res. Fluid Mech. Thermal Sci. **82**(1), 105–112 (2021)
5. Shengcheng, J., Bei Z., Jiang, Li., Guangqiu, W.: Numerical study for active flow control using dielectric barrier discharge actuators. J. Aerosp. Eng. **30**(5), 04017050–1–04017050–9 (2017)
6. Roth, J.R., Sherman, D.M., Wilkinson, S.P.: Electrohydrodynamic flow control with a glow-discharge surface plasma. AIAA J. **38**(7), 1166–1172 (2000)
7. Bouchmal, A.: Modeling of dielectric-barrier discharge actuator, Master Thesis TU Delft (2011)

Temperature Measurement of Microwave and Diaelectric Barrier Discharge (DBD) Plasma

Nurfarah Diana Mohd Ridzuan Tan[1], Fadhli Syahrial[1], Fudhail Abdul Munir[1(✉)], Musthafah Mohd Tahir[1], and Herman Saputro[2]

[1] Fakulti Kejuruteraan Mekanikal, Universiti Teknikal Malaysia Melaka, Durian Tunggal, 76100 Melaka, Malaysia
fudhail@utem.edu.my

[2] Department of Mechanical Engineering Education, Universitas Sabelas Maret, 57169 Surakarta, Pabelan, Indonesia

Abstract. Plasma can be generated by corona discharge, diaelectric barrier discharge (DBD), arc discharge and microwave power. Microwave plasma has been shown to be utilized to produce hydrogen under atmospheric pressure. Meanwhile, Dielectric Barrier Discharge (DBD) plasma actuator has become the well-known tools in the aerodynamics flow control applications. In this research, two types of plasma were generated by using two different methods. The types of plasma generated are microwave and DBD plasma. The temperature distribution on the plasma surface was measured using infra-red thermal camera. The results suggest that surface temperature of microwave plasma is higher than DBD plasma.

Keywords: DBD plasma actuator · Aerodynamics flow control

1 Introduction

Plasma can be a combination of electrons, atoms, ions and free radicals (Zamri et al. 2021). Example of methods to generate plasma are corona discharge plasma, dielectric barrier discharge (DBD) plasma, arc discharge plasma, radiofrequency plasma and microwave plasma [1, 2].

Microwave plasmas can be utilized to produce hydrogen under atmospheric pressure. Apart from that, plasmas produced by microwave are also used in making carbon film, generating methane and methanol and also syngas formation [3, 4].

Meanwhile, DBD plasma is consist of two electrodes that are separated by a dielectric material [5]. One of the electrodes is exposed to air while the other electrode is completely encapsulated by a dielectric material. The electrodes are arranged in an asymmetrical way. The electrodes are connected to a high AC voltage power source. Typically, a high AC voltage of 5–20 kV is applied to the electrodes at frequencies ranging from 3–15 kHz. As a result, a cold plasma discharge appears on the dielectric material above the encapsulated. DBD plasma has been shown to be utilized to control airflow on automotive spoilers [6].

2 Research Methodology

2.1 Microwave Plasma Generation

Copper sheet and copper electrodes were used for the microwave plasma research to create an electrode microwave discharge (EMD). EMD happens when plasma is generated at the tips of the electrodes by creating a magnetic field between two or more electrode's tip points. Copper sheet acting as the electrode base was first being cut into a round shape and a hole was poked in the middle of the copper sheet. Figure 1 shows the experimental layout for microwave plasma generation.
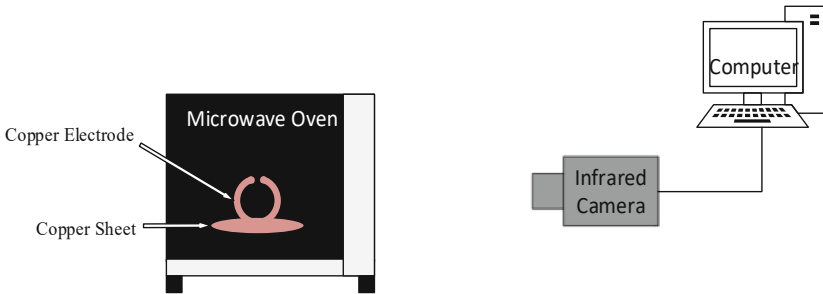
Fig. 1. Experimental layout of microwave plasma generation.

2.2 DBD Plasma Generation

Meanwhile, Fig. 2 shows the experimental layout of DBD plasma generation.
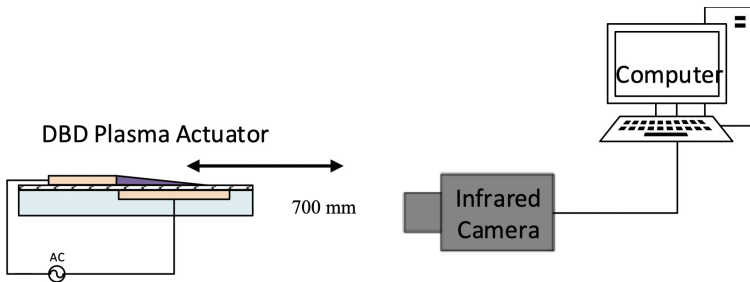
Fig. 2. DBD plasma generation experimental layout.

3 Results and Discussion

The temperature distribution for microwave plasma is shown in Fig. 3. The maximum temperature achieved for microwave plasma is 192.3 °C.
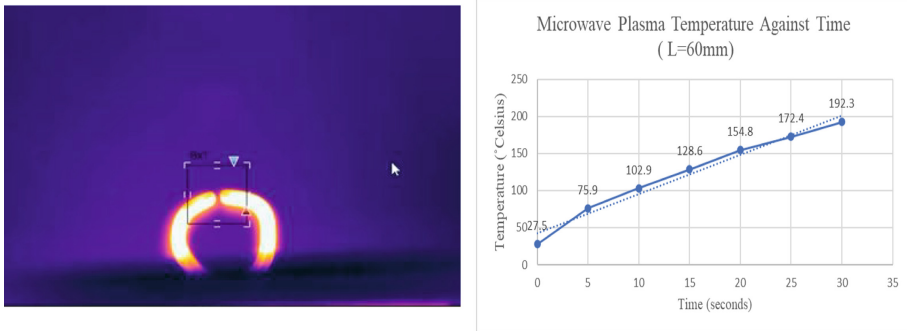
Fig. 3. Temperature distribution of microwave plasma.

Meanwhile, the maximum temperature achieved for DBD plasma is up to 90.2 °C as indicated in Figure 4. It is shown that microwave plasma causes higher temperature on the surface of the electrode. On the other hand, the DBD plasma temperature is moderately lower than microwave plasma.
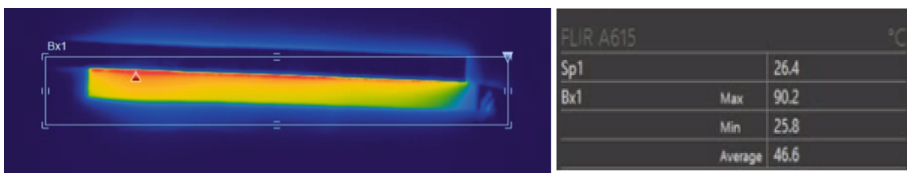
Fig. 4. (a) DBD plasma temperature distribution.

4   Conclusions

The surface temperature measurement on two types of plasma has been investigated. Microwave plasma causes the surface temperature to be significantly higher than the DBD plasma. As such, the use of DBD plasma is more appropriate to be used on plastic surfaces.

References

1. Wijittra, W., et al.: Highly effective microwave plasma application for catalyst-free and low temperature hydrogenation of biodiesel. Fuel **305**, 121254 (2021)

2. Hojoong, S., Jungwen, L., Moon, S.B.: Experiments and modeling of atmospheric pressure microwave plasma reforming of a methane-carbon dioxide mixture. J. CO2 Utilization **46**, 101464 (2021)
3. Alif, A.Z., Mei, Y.O., Saifuddin, N., Show, P.L.: Microwave plasma technology for sustainable energy production and the electromagnetic interaction within the plasma system: A review. Environ. Res. **197**, 111204 (2021)
4. Wnukowski, M., Jamroz, P., Niedzwiecki, L.: The role of hydrogen in microwave plasma valorization of producer gas. Int. J. Hyd. Energy (in-press) (2021)
5. Bouchmal, A.: Modeling of dielectric-barrier discharge actuator, Master Thesis TU Delft (2011)
6. Tan, N.D.M.R., Munir, F.A., Tahir, M.M., Herman, S., Mikami, M.: Preliminary investigation of using DBD plasma for application in micro combustors. J. Adv. Res. Fluid Mech. Thermal Sci. **82**(1), 105–112 (2021)

Exploratory Temperature Comparison on Different Profiles of Polycarbonate Corrugated Sheet for Mobile Solar Dehydrator

Siti Nur Amalina Mohd Halidi[1]([✉]), Azmeer Dahlan[1], Izwan Hakim Jini[1], and Nurul Wirdah Mafazi[2]

[1] School of Mechanical Engineering, College of Engineering, Universiti Teknologi MARA, Cawangan Pulau Pinang, Kampus Permatang Pauh, 13500 Permatang Pauh, Pulau Pinang, Malaysia
sitinur6182@uitm.edu.my

[2] Fakulti Kejuruteraan Pembuatan, Universiti Teknikal Malaysia Melaka, Hang Tuah Jaya, 76100 Durian Tunggal, Melaka, Malaysia

Abstract. Food drying has been one of the oldest methods for preserving food. The method utilizes the sun as a way of drying any ingredients needed. Over the years, developments have been made to improve drying time to which the invention for an electric powered dehydrator. However, using the simplest method of solar drying is much preferable in countries where consuming electric is costly. Two types of mobile solar dehydrator are presented in this paper, with one used the circular profiled polycarbonate sheet, and the other angular profiled polycarbonate sheet. Experiments were conducted on both dehydrators to seek its preliminary performances. The presented mobile solar dehydrator can also contain heat up to a temperature of 53.5 °C, given a sunny day weather. Based on the data obtained, the weather plays a huge role on the drying efficiency of the dehydrator. All in all, mobile solar dehydrators do provide a promising alternative to the normal open solar drying method.

Keywords: Solar dehydrator · Polycarbonate · Food preservation · World hunger

1 Background

1.1 Introduction

Long before the COVID-19 struck everyone abruptly in 2020, chronic and acute hunger were on the rise due to known factors including conflicts, socio-economic conditions, natural hazards, climate change, and pests. The pandemic has caused severe widespread increase in global food insecurity, affecting all households in almost every country [1, 2]. With the spreading fluctuates with new variants coming in occasionally, there is a high possibility that this problem may continue to increase over the next few years. However, due to the scarcity of obtaining food, many homeowners decide to homegrown their food to fulfil their own food demand [3]. Not only that, growing fresh food year-round

became a necessity for self-sufficiency. It has also helped to reduce mental and physical strains one goes through during the current situation. Having said that, one can harvest too many crops, proving a more supply than demand due to the anticipation on home farming.

With increasing number of harvests, solar dehydrator can be an alternative to preserve these agricultural products. Solar dehydrator or more commonly known as solar drying, is a method that has been applied since the olden days. A forced convection solar dryer does provide better control on required drying air conditions in compared to natural convection solar dryer which does not require any other energy during operation [4]. Solar dryers work in such a way that heat is absorbed into the chamber until a constant temperature of solar energy is reached, which then facilitates extraction of humidity from the crops inside the chamber. By drying these crops, food can be kept longer and can prevent food waste in the long run. Not only that, using a solar dryer does not contaminate the food while in exposure to the sun which may cause a decrease in food quality and flavor [5]. Direct sun drying is usually exposed to the weather, rodents, birds, insects, and other effects to which a solar dryer is not.

1.2 Methodology

To successfully take advantage of the solar radiation and to apply it into a solar dehydrator, heat absorber needs to be prepared. Selecting the right heat absorber can determine the efficiency of the solar dehydrator. The warm ambient air which is heated by the solar radiation is absorbed by the heat collector which is then passed over to the drying chamber to dehumidify the produce [6]. The most popular type of heat absorber among previous researchers is corrugated sheet. Corrugated sheet creates unique shape that offers reliable utility and enhanced strength. Heat insulators are also applied in the solar dehydrator to provide a higher specific heat capacity and to lessen thermal losses via conduction.

Circular profiled and angular profiled polycarbonate corrugated sheet is chosen as the heat absorber material. Polycarbonate is lightweight which fits the specification of having a mobile solar dehydrator and it allows more heat and light penetration through the corrugated sheet. This will improve the amount of heat energy contained inside the chamber. Since two types of corrugated sheet is used, two mobile solar dehydrators with dimensions of 26 cm × 48 cm × 77 cm are constructed. The mobile solar dehydrator is placed in an area with full sunlight exposure for 8 h from 8 AM until 5 PM. An LCD thermometer is placed on the top and middle section of the drying chamber to obtain an average temperature. The ambient temperature and relative humidity are also recorded. It must be noted that the circular profiled solar dehydrator is in Penang while the angular profiled is in Sarawak (Fig. 1).
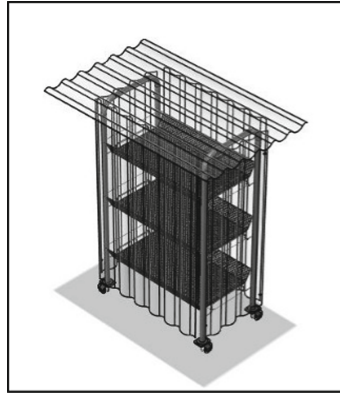
Fig. 1. A mobile solar dehydrator.

2 Results and Discussion

2.1 Results

Table 1 and 2 provide the maximum temperature, mean temperature, and standard deviation from each of the solar dehydrator, both circular and angular respectively, for consecutive 7 days. As stated earlier in the methodology section, both circular and angular profiled solar dehydrators are located at two different places. The mean temperature values are obtained based on the hourly temperature data from the solar dehydrators. Figure 2 shows a graphical representation of the mean temperature for one week.

Table 1. Mean temperature, in degrees Celsius and standard deviation for circular profiled solar dehydrator.

Day	Maximum temperature (°C)	Mean temperature (°C)	Standard deviation
1	47.7	40.0	7.277
2	49.5	42.3	7.103
3	46.4	37.3	7.700
4	45.5	38.0	4.283
5	46.6	35.1	5.642
6	47.0	39.6	7.881
7	39.0	31.0	4.561

Table 2. Mean temperature, in degrees Celsius and standard deviation for angular profiled solar dehydrator.

Day	Maximum temperature (°C)	Mean temperature (°C)	Standard deviation
1	31.5	27.5	3.079
2	53.0	39.5	9.963
3	51.5	36.9	10.131
4	33.5	29.0	3.431
5	53.0	38.1	10.672
6	53.5	42.7	10.333
7	52.0	41.4	10.043
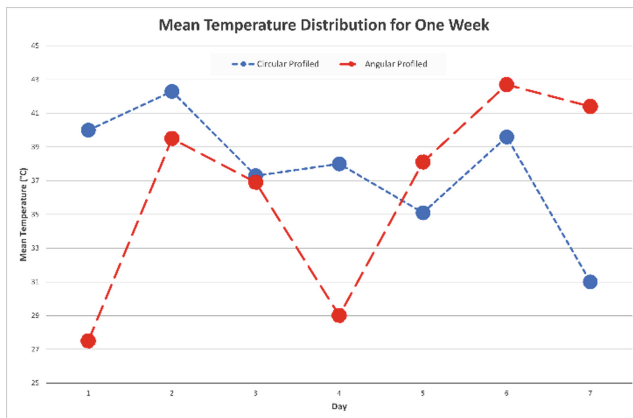
Fig. 2. Mean temperature distribution for one week for circular profiled and angular profiled solar dehydrator.

2.2 Discussion

Observing the tables presented above, a larger standard deviation value meant that the temperature is much more spread out from the mean temperature. A smaller standard deviation value meant that the temperature is less spread out from the mean temperature. This makes sense as the solar dehydrator is exposed to the sunlight, which moves accordingly throughout the day. Early mornings would indicate lower temperatures just as late evenings. Cloudy and drizzly days would have a lower mean temperature and smaller standard deviation values. Maximum temperature of the solar dehydrators is 49.5 °C and 53.5 °C for circular and angular profiled solar dehydrators, respectively. Maximum temperatures are usually obtained during mid-day, where sun rays are at its most peak, between 11 AM up until 4 PM when the sky is cloudless and the sun rays directly onto the solar dehydrators. However, placing the solar dehydrators near buildings or huge trees

can also affect the maximum temperature values, even when the weather is sunny. As the solar dehydrator is mobile, flooring effects on the temperatures may not be significant. It is also understandable that both circular and angular profiled solar dehydrators would display different values as they are in two different locations where the weather differs daily. Although the weather plays a role in the temperatures within the drying chamber of the solar dehydrator, both dehydrators used the same sheet thickness and has the same dimension.

3   Conclusion

Based on all obtained data, it can be concluded that the maximum temperature, mean temperature, and standard deviation depends on the current weather the experiment is conducted. An in-depth explanation on the heat transferred within the drying chamber of the solar dehydrator and its relation to relative humidity can be discussed further in an extensive full paper later. The effects on thickness and material used for the drying chamber is currently being studied by the researchers.

References

1. The World Bank Brief: Food Security and COVID-19. Accessed 10 Sep 2021
2. Aday, S., Aday, M.S.: Impact of COVID-19 on the food supply chain. Food Qual. Saf. **4**(4), 167–180 (2020)
3. Manning, P.: Growing your own food during the coronavirus pandemic? Plan for pests! The Conversation. Accessed 10 Sep 2021
4. Pangavhane, D.R., Sawhney, R.L., Sarsavadia, P.N.: Design, development, and performance testing of a new natural convection solar dryer. Energy **27**(6), 579–590 (2002)
5. Abideen, Z., Aziz, S., Aisha, E., Hafiz, K., Rehman, A.: Drying of tomato using indirect solar dryer. ESTIRJ **3**(1), 9–13 (2019)
6. Tripathi, A., Sinha, A.K., Powar, S.b., Patane, P.: Design, analysis, and studies on performance of the solar food dehydrator. J. Eng. Sci. Tech. **11**(9), 1263–1282 (2016)

The Effect of Cerium Oxide Addition into Algae-Biodiesel Blended Fuel on Its Dynamic Viscosity and Calorific Value Properties

Hazim Sharudin[1(✉)], N. I. Ismail[2], Sharzali Che Mat[2], Nik Rosli Abdullah[3], Nurul Nabilah Khairul Salleh[2], and A. H. Abdol Rahim[1]

[1] School of Mechanical Engineering, College of Engineering, Universiti Teknologi MARA, Cawangan Johor, Kampus Pasir Gudang, Johor, Malaysia
`hazim@uitm.edu.my`

[2] School of Mechanical Engineering, College of Engineering, Universiti Teknologi MARA, Cawangan Pulau Pinang, Kampus Permatang Pauh, Pulau Pinang, Malaysia

[3] School of Mechanical Engineering, College of Engineering, Universiti Teknologi MARA, Shah Alam, Malaysia

Abstract. In this research, cerium oxide will be used as a fuel additive as it plays a major role in increasing biodiesel performance and improve the properties of the algae-biodiesel blends upon reducing the nitrogen emission and improving the engine performance characteristics. The main phases involved in this research are the extraction of algae oil, blending process of algae biodiesel with cerium oxide and data collection of dynamic viscosity with calorific value. The data collected were used as inputs to Design Expert (DOE) software for identifying the best formula to be blended in terms of dynamic viscosity and calorific value properties. The results obtained from the analysis shows that the final optimum blend obtained by the software showed that the viscosity obtained through this research was significant and the calorific value was conformed to the biodiesel standard. Thus, it proves that cerium oxide as fuel additive assists in improving fuel characteristics in algae biodiesel.

Keywords: Algae-biodiesel · Cerium-oxide additive · Calorific value · Dynamic viscosity · Design of Expert (DOE)

1 Introduction

Recognizing the reach of energy and related pollution problems through the combustion of fossil fuels and their products has prompted many researchers to explore the possibility and prospect of using renewable energy sources as a replacement for conventional fuels [1]. One of the most promising renewable energy sources is biodiesel. It has become an alternative source of fuel to reduce the use of petroleum oil [2]. Biodiesel serves many benefits such as high performance in engine and combustion [3]. In terms of its

production, biodiesel is commonly produced from a great variety feed stocks comprising vegetables oils such as palm, sunflower, soybean, cottonseed, peanut and rapeseed, animal fats, as well as waste oils such as used frying oils [2]. Among the promising feedstock options that could offer feasible option for biodiesel are algae which also known to be the third-generation biofuel feedstock due to high yields and relatively low land demands for growth [2]. Due to the relatively high oil content of algae and rapid biomass production, algae have long been known as a potential source of biofuel production, as well as being one of the best alternative fuels for future use in transportation sector. However, the production of nitrogen oxide (NOx) is higher in biodiesel compared to diesel, thus resulting adverse impact towards environment. This problem is due to the high oxygen contents in the biodiesel [3]. To overcome this disadvantages, previous study has reported that the inclusion of fuel additives, such as cerium oxide, in the biodiesel helps to alter the fuel properties including density, sulphur content and volatility which will improve the emissions and combustion of the biodiesel [3]. However, very limited research is being done on the physicochemical properties of the algae biodiesel blends by inclusion of cerium oxides which also including in determining the optimum blend formulation for algae biodiesel blends with addition of cerium oxide. Therefore, this study directly focuses on improving algae biodiesel by adding cerium oxide as the fuel additive. Analysis was carried out by investigating the fuel properties, namely viscosity and calorific value of the algae diesel blends based on the experimental design suggested by the Design of Expert (DOE) software.

2   Methodology

2.1   Algae Oil Extraction

In this research, algae were collected from water pond located at the Sekolah Menengah Tun Syed Shah Shahabudin (SOKSEK). The extraction of algae oil was carried out at Faculty of Chemical Engineering UiTM Penang using the Soxhlet extractor. Soxhlet extraction method was employed to extract oil from the algae plant as it is the most efficient methods used to extract oil from plant-based material. The solvent used for this extraction method was ethanol with 99.9% purity. After extracting oil from the algae, residual solvent contained in the oil was removed using rotary evaporator and the algae oil was obtained.

2.2   Formulation and Blending Process of Algae Biodiesel with Cerium Oxide Using Design of Expert (DOE) Software

The Design of Expert (DOE) software was used for this research to formulate and obtain the optimum algae biodiesel with cerium addition. Generally, this software offers valuable resources to optimize the experiment based on method, mixture or combination of factors and components, besides visualizing the results and analysis on the graph. From the experimental run by the Design Expert (DOE) software, the data obtained shows in Table 1 is the suggested of the blending percentage for algae biodiesel and cerium oxide with its nomenclature. The mixing process was then carried out according to fuel blends to the experimental design by the Design Expert (DOE) software.

Table 1. Percentage blends of algae biodiesel and cerium oxide with its Nomenclature.

Fuel blends			Percentage of cerium oxide	Nomenclature
Diesel	Algae	Cerium oxide		
100	0	0	0%	B100
80	20	0	2.5%	B97.5C2.5
80	19.5	0.5	7.5%	B92.5C7.5
80	18.5	1.5	5%	B95C5
80	19	1	10%	B90C10

2.3 Fuel Properties Characterization

The fuel properties of B100, B97.5C2.5, B92.5C7.5, B95C5, and B90C10 were determined according to American Society for Testing Material (ASTM) standard which are ASTM D6751 and ASTM D7467. All the experiments were conducted in the lab facilities of Faculty of Chemical Engineering UiTM Shah Alam and similar equipment were also used by other researcher to determine the fuel properties [18]. The calorific value was determined using the IKA bomb calorimeter C200 which manufactured by IKA, UK, and dynamic viscosity was determined by Physica MCR 301 Rheometer (Anton Paar, UK).

3 Results and Discussions

3.1 Physicochemical Properties of Algae Biodiesel with Cerium Oxide Blend

Table 2. Blend ratios of algae biodiesel fuel with cerium.

Parameter	B100	B100	B97.5C2.5	B95C5	B95C5	B92.5C7.5	B90C10	B90C10
Dynamic viscosity (Pa.s)	0.122	0.124	0.141	0.126	0.127	0.134	0.143	0.140
Calorific value (J/g)	42061	42060	43594	40832	40829	40720	38950	38594

Table 2 shows the data on dynamic viscosity and calorific value obtained from eight different blending ratios of algae biodiesel and algae biodiesel with cerium. The blend ratios generated by the Design of Expert (DOE) software v11 were B100, B97.5C2.5, B95C5, B92.5C7.5, and B90C10 as listed in Table 2; B represents algae biodiesel, while C represents cerium oxide. From the experimental run, it was found that the dynamic viscosity of fuel blend increased after adding cerium oxide into the algae biodiesel. This proved that the addition of nanoparticles into biodiesel increases the resistance of the fluid

layer, hence increases the dynamic viscosity. The fuel viscosity affects the hydrocarbon emissions because of insufficient lubrication of fuel injection pumps, thereby reducing the combustion performance of the fuel [2]. The calorific value affects the conversion of thermal energy in the fuel, where good conversion of thermal energy delivers excellent brake thermal efficiency, hence leading to a better combustion system of the fuel within the engine.
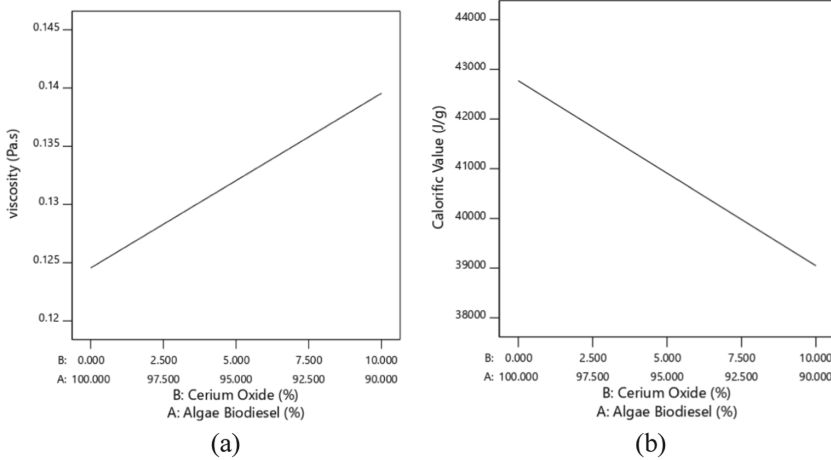
Fig. 1. The model graph of percentage blends correlates to (a) Dynamic Viscosity and (b) Calorific Value.

Figure 1 show the correlation of percentage blends with dynamic viscosity and calorific value respectively in graph form generated by the software. Based on Fig. 1(a), the statistical analysis showed that the addition of cerium oxide into the algae biodiesel increased the dynamic viscosity. Meanwhile in Fig. 1(b), the addition of cerium oxide reduced the calorific value of the algae biodiesel.

4   Conclusion

The results obtained through the Design of Expert (DOE) software on the analysis on calorific value and dynamic viscosity showed that the addition of cerium oxide as fuel additive has improved the fuel properties of the algae biodiesel blends. A minimum value of 35 MJ/kg for calorific value has been recommended by EN 14213 shows that it conformed to the biodiesel standard. The suitability of cerium oxide as fuel additive in algae biodiesel to be used as alternative fuel is able to compensate high diesel consumption.

References

1. Soudagar, M.E.M., et al.: The effect of nano-additives in diesel-biodiesel fuel blends: A comprehensive review on stability, engine performance and emission characteristics. Energy Conv. Manage. 178, 146–177 (2018)

2. Sharudin, H., et al.: Improvement of emissions characteristics and exhaust temperature in single cylinder diesel engine fuelled with algae oil additive. J. Phys. Conf. Ser. **1349**(1) (2019)
3. Sanjid, A., et al.: Performance and emission of multi-cylinder diesel engine using biodiesel blends obtained from mixed inedible feedstocks. J. Clean. Product. **112**, 4114–4122 (2016)

Combustion Phases of Evaporating Fuel Droplet

Ahmad Fuad Bin Abdul Rasid[1(✉)] and Yang Zhang[2]

[1] Fakulti Teknologi Kejuruteraan Mekanikal Dan Pembuatan, Universiti Teknikal Malaysia Melaka, 76100 Durian Tunggal, Melaka, Malaysia
a.fuad@utem.edu.my

[2] Faculty of Engineering, The University of Sheffield, Sheffield S1 3JD, UK

Abstract. The combustion characteristics of fuel spray can be examined at a basic level by fuel droplet study. Evaporation processes of a fuel droplet involves few combustion phases mainly transient heating phase, steady boiling phase and transient fuel vapour accumulation effect. The combustion phase duration is found to be consistent for a particular type of fuel with fuel vapour accumulation has the shortest duration followed by transient droplet heating and steady boiling phase. With precise quantitative measurement method conducted in the present work, high measurement repeatability is assured thus enabling the determination of droplet combustion stability categorization with clear definition through the duration of combustion phases.

Keywords: Fuel droplet · Combustion phases · Combustion stability

1 Introduction

Study on the combustion of isolated droplets provide insights on the evaporation processes of the dispersed droplets during liquid spray combustion. There are two transient processes involved throughout the lifetime of an evaporating droplet. The transient processes are droplet heating and vapour accumulation effect which are profound in a fuel with a low volatility and high boiling point [1].

Transient heating period is clearly observable in a quantitative measurement made on evaporating fuel droplet with a non-linear regression of squared droplet diameter [2]. During this period, the internal heat conduction rate is higher than the surface regression rate resulting the burning rate to increase with time [3]. Natural convection causes several temperature spots to exist within the droplet thus initiates homogeneous nucleation and forms several vapour bubble within the droplet [4]. The expansion and release of the vapour through the surface mildly distorts the surface as well as expanding the diameter of the droplet.

On the other hand, the accumulation of evaporated fuel implies that the fuel consumption is slower than the rate of evaporation [5]. During this phase, fuel starts to decompose thus making the surface of the droplet to be more viscous. Furthermore, Rasid & Zhang [6] observed that the droplet is self-contaminating its own surface with the soot produced during the vapour consumption. The presence of particles mainly on the surface of the droplet initiates a heterogeneous nucleation that forms multiple bubble

of vapour to be form within the droplet. Over time, the expanding bubble ruptures the surface of the droplet as they try to escape. The sudden loss of liquid mass via sub-droplet ejection deviates the surface regression from D^2-law causing unreliable burning rate measurement on the regression of the squared droplet diameter [7].

The aim of this study is to determine all combustion phases involved during the combustion of a single and isolated fuel droplet. The experimental work focuses on the repeatability of acquired results thus ensuring a reliable conclusion to be made on the transition of combustion phases and a more precise burning rate measurement method for a burning fuel droplet.

2 Methodology

The fuel used in this experiment was commercial Shell diesel as base fuel. The experimental setup is shown in Fig. 1. For tracking droplet lifetime and droplet dynamics at high speed, a Photron-SA4 high speed colour camera was used. A backlighting imaging was conducted by placing an IDT 19-LED high intensity illuminator with a diffuser behind the droplet; opposite to the camera lens. For droplet liquid-phase imaging, 10,000 frames per second with x40 magnification was set. Droplets initial diameters were kept constant at 1 ± 0.05 mm for each test and were suspended on 100 µm silicon carbide fibre. The recording of images was between the ignition to the flame extinction of the droplet combustion. The droplet was ignited by a thermal heating Kanthal wire positioned 1 mm away from the droplet. The codes used to process all the result obtained are segmentations and feature extractions coding developed in MATLAB scripts, which is able to evaluate the dimensions of threshold images via digital image processing tools. Regressions of droplet evolution presented in this paper are based on normalised squared diameter $(D^2/Do)^2$ against normalised time $t/(Do)^2$ throughout the droplet combustion; termed D^2 –law [8].
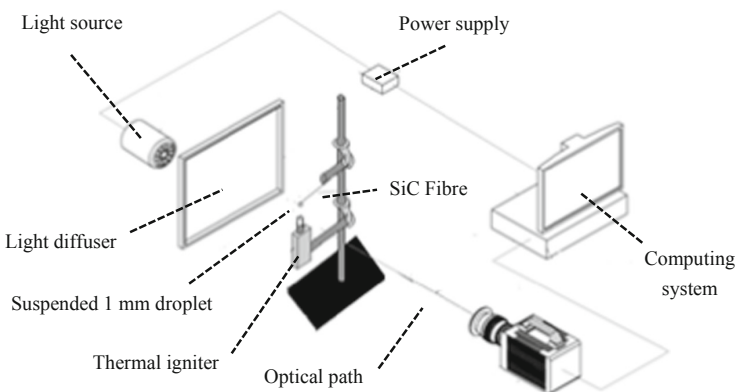
Fig. 1. Experimental setup.

3   Results and Discussions

Figure 2 (a) shows an example of three repetitive measurements of droplet surface regression for diesel. High repetitive measurements were achieved with a slight discrepancy during initiation (evaporation) and ignition (burning) process due to the insertion processes. Prior to ignition, the squared droplet diameter regressed non-linearly for a duration of 0.525 s and occupies $24.53 \pm 0.03\%$ of the droplet lifetime as shown in Fig. 2 (b). It was observed that the droplet undergoes slight expansion before transitioned to a linear reduction. The expansion is mainly caused by the thermal expansion of the liquid fuel with additional expansion of the vapour bubble inside the droplet [9].
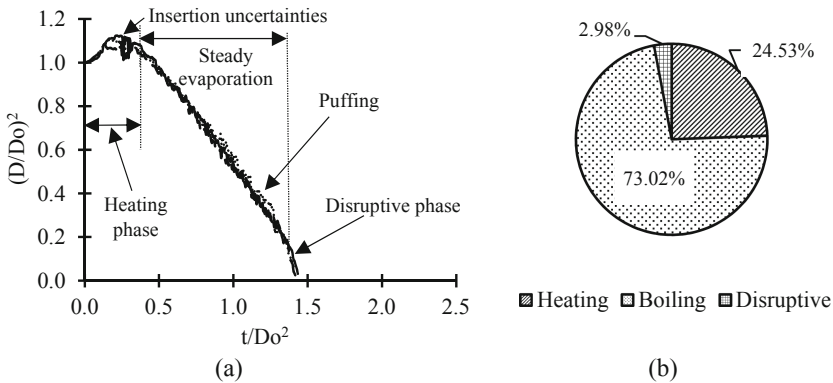
Fig. 2. Evaporation process of a burning diesel droplet on (a) D^2 Regression and (b) lifetime of combustion phases.

Once the expansion period has ended, the droplet D^2 continues to reduce linearly for 1.56 s before transitioned to a sudden increase in burning rate. This period occupies $73.02 \pm 0.02\%$ of the droplet lifetime and determined to be a reliable regression utilised in burning rate measurement on the slope. During this period, the droplet temperature was elevated near its boiling point thus maintaining the liquid-gas diffusion rate near constant. Hence, the droplet squared diameter of the droplet reduced linearly with time which conforms with the D^2-law [8].

As the combustion progresses towards the end of the droplet lifetime, the regression is observed to be abruptly increased with a period of 0.064 s. During this phase, it is observed that multiple sub-droplets are being ejected outwards contributing to a higher loss of fuel mass. During this phase, the burning rate measurement is inconsistent due to a non-uniform size and frequency of sub-droplets being ejected [10]. The disruptive period was fairly short, which occupies only $2.98 + 0.01\%$ of the droplet lifetime.

4   Conclusions

Few conclusions can be made based on the results acquired in the present work.

a) Quantitative imaging done on isolated diesel droplet ensures high repeatability which in turn enables the identification of combustion phases.
b) The lifetime of combustion phases is consistent for each repetition thus can be isolated and categorized.
c) Regression of D^2 during transient heating and vapour accumulation period provides unreliable slope for burning rate measurement.

References

1. Ma, X., Zhang, F., Han, K., Yang, B., Song, G.: Evaporation characteristics of acetone-butanol-ethanol and diesel blends droplets at high ambient temperatures. Fuel **160**, 43–49 (2015)
2. Law, C.K., Sirignano, W.A.: Unsteady droplet combustion with droplet heating-II: Conduction limit. Combust. Flame **28**(C), 175–186 (1977)
3. Avedisian, C.T., Callahan, B.J.: Experimental study of nonane/hexanol mixture droplet combustion without natural or forced convection. Proc. Combust. Inst. **28**(1), 991–997 (2000)
4. Avedisian, C.T.: Recent advances in soot formation from spherical droplet flames at atmospheric pressure. J. Propul. Power **16**(4), 628–635 (2000)
5. Aggarwal, S.K., Mawid, M.: Fuel vapor accumulation effect on the combustion characteristics of multicomponent fuel droplets. Chem. Eng. Commun. **157**, 35–51 (1997)
6. Abdul Rasid, A.F., Zhang, Y.: Comparison of the burning of a single diesel droplet with volume and surface contamination of soot particles. Proc. Combust. Inst. **38**(2), 3159–3166 (2020)
7. Ghamari, M., Ratner, A.: Combustion characteristics of colloidal droplets of jet fuel and carbon based nanoparticles. Fuel **188**, 182–189 (2017)
8. Langmuir, I.: The Evaporation of small spheres. Phys. Rev. **12**(5), 368–370 (1918)
9. Faik, A.: 12th International Conference on Heat Transfer. Fluid Mechanics and Thermodynamic **12**(1), 8–10 (2016)
10. Oyagi, H., Shigeno, H., Mikami, M., Kojima, N.: Flame-spread probability and local interactive effects in randomly arranged fuel-droplet arrays in microgravity. Combust. Flame **156**(4), 763–770 (2009)

Modification Drying Flow Direction for Reduction of Particle Residence Time in Spray Drying Using CFD

Henry Carles[1]([envelope]) [ORCID], Eflita Yohana[1], Mohammad Tauviqirrahman[1], Eka Dharmawan[1], Mohamad Djaeni[2], and Kwang-Hwan Choi[3]

[1] Departement of Mechanical Engineering, Diponegoro University, Jl. Prof. Soedarto, S.H., Semarang 50275, Indonesia
carlesup98@gmail.com

[2] Departement of Chemical Engineering, Faculty of Engineering, Diponegoro University, Jl. Prof. Soedarto, S.H., 50275 Semarang, Indonesia

[3] College of Engineering, Pukyong National University, 365 Sinseon-ro, Nam-gu, Busan 608739, Korea

Abstract. Spray drying is ideal for quickly drying food goods. This research aims to evaluate the influence of incoming airflow direction on the residence duration of particle with varying droplet sizes. The computational fluid dynamics method uses the k-ω SST and the standard k-ε model for flow simulation and particle prediction. The simulation results show that the residence time of the mixed flow is longer than the co-current flow for droplet 50 mm < and faster for droplet > 50 mm. Furthermore, the residence time of the particle changes with increasing droplet diameter; in mixed flow spray dryers, residence time tends to decrease; otherwise, it will increase in the co-current flow model.

Keywords: Mixed flow · Co-current flow · Droplet size

1 Introduction

Spray drying is frequently utilized in the food and pharmaceutical sectors[1, 2]. The liquid is converted into particles, which are then dried with hot air[3, 4]. Percentage of particles hitting the wall more than coming out through the channel[5]. Small diameter particles come out earlier than the large-diameter [6, 7], with fixed droplet size in each configuration. The co-current flow of air is in the direction of the particle flow, the countercurrent flow is in the opposite direction, and the mixed flow is a combination of the two [8]. This study aimed to compare the residence times of particles in co-current and mixed flow spray dryers regarding variations in inlet temperature and particle diameter as boundary conditions. Conclusions from experimental comparison studies [3] and fluid dynamics calculations [1] the spray dryer is relatively the same; CFD analysis produces a pretty good prediction on the spray dryer compared to the experimental approach. The use of turbulence models affects the accuracy of airflow characteristics in the drying

chamber [8]. Because the moisture content drops fast as the drying air temperature rises, drying time is reduced [7]. Modification of inlet dry airflow direction can reduce particle residence time.

2 Method

2.1 Basic Theory

Predict the tracking of individual particles in the spray dryer using the three-phase flow equation with the Eulerian-Lagrangian approach, calculated using the discrete phase model (DPM). Equations 1 and 2 are used to write the particles' equations of motion [9].

$$\frac{dx_p}{dt} = \vec{u}_p \tag{1}$$

$$\frac{d\vec{u}_p}{dt} = F_d\left(\vec{u} - \vec{u}_p\right) + \vec{g}_x \frac{(\rho_p - \rho)}{\rho_p} \tag{2}$$

Fluid velocity is $\left(\vec{u}\right)$, particle velocity is $\left(\vec{u}_p\right)$, x_p denotes particle position, $\vec{g}_x$ is gravitational force, ρ is fluid density, and τ_p denotes particle density. In Eq. (2), $F_d\left(\vec{u} - \vec{u}_p\right)$ denotes drag per unit mass of particles. F_d is calculated based on energy equation:

$$F_d = \frac{1}{\tau_p} \frac{(C_d - Re_p)}{24} \tag{3}$$

where (τ_P) is particle relaxation time, given by Eq. 4.

$$\tau_p = \frac{\rho_p d_p^2}{18\mu} \tag{4}$$

2.2 CFD Modelling

Figure 1 geometric shape of a spray dryer with a co-current flow design, used based on research of Anandharamakrishnan et al.[3].

Dimensions of mixed flow (co-current flow) are: D1 = 600(600), D2 = 50(50), Dn1 = 40(81), Dn2 = 20(55), Dn3 = (20), Dp1 = 26(26), Dp2 = 24(24), a × b = 147 × 125, H1 = 900(900), H2 = 300(300), H3 = 480(480), Nozzle height 1 Hn1 = (35), Hn2 = (15), Hn = 20, Hp = 150(150), L = 1275(1275). This study simulates two geometries, and the governing equations are solved numerically using ANSYS FLUENT with a SIMPLE scheme for velocity-pressure coupling. The turbulent model of mixed flow causes rotating flow, which is more accurate using the k-SST method [10, 11], than the standard k-ε for wall co-current flow [1, 3, 6, 12]. The drying air velocity is eight m/s, the initial temperature is 100, 120, 140, 160, and 180 °C, the particle density is 816.4 kg/m3, and the gas density is 1,225 kg/m3, DPM spry dryer escape wall surface, and reflect pipe surface.

(a)   mixed flow   (b)   co-current flow
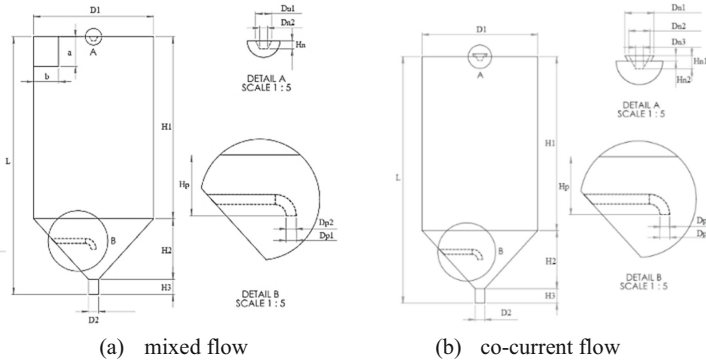
Fig. 1. The geometric of spray dryer.

3   Results and Discussion

The residence time of the particle is the length of time the particle is in the drying chamber [3]. In a mixed flow spray dryer, the residence time of the particles decreases with in-creasing droplet diameter because droplets with a smaller diameter (10.30 mm) have small momentum. The particles follow the airflow around the drying chamber to the outlet so that the particle residence time is longer. Droplets with larger diameters (50, 70, 90, 110, and 130 m) have shorter residence times. In co-current flow, droplets with a larger diameter tend to last longer than droplets with a smaller diameter. Particles of larger diameter are recirculated to the walls of the drying chamber, the same as in the study of Anandharamakrishnan et al. [3], Sadripour et al. [6], and Roustapour et al. [7], giving the particles a longer residence time. Figure 2 shows the configuration conditions of the spray dryer flow model at (a) outlet temperature and (b) particle diameter concerning time.

(a)   Outlet Temperature   (b)   Dwelling Time of Particles
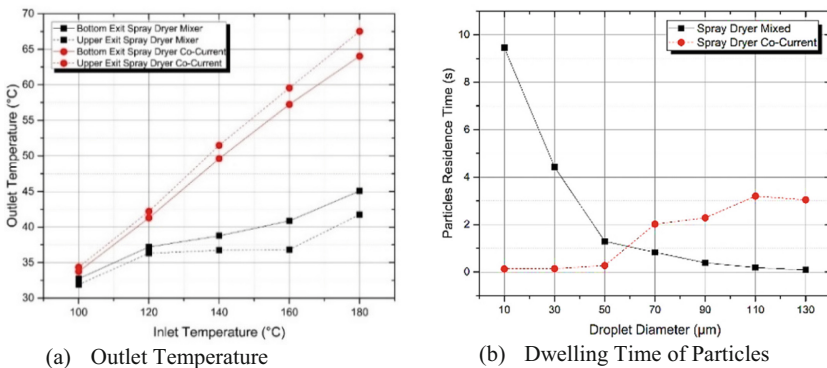
Fig. 2. Characteristics spry dryer in drying chamber.

4 Conclusion

This paper describes the results of multiphase modeling tracking residence time and particle inflow movement in a spray dryer. The residence time of particles changes with the change in droplet diameter; in mixed flow, the residence time of particles decreases with increased droplet diameter, whereas in the co-current flow tends to increase.

References

1. Habtegebriel, H., Edward, D., Motsamai, O., Wawire, M., Seifu, E., Daniel, S.: The potential of computational fluid dynamics simulation to investigate the relation between quality parameters and outlet temperature during spray drying of camel milk. Dry Technol. **0**, 1–15 (2019). Taylor & Francis https://doi.org/10.1080/07373937.2019.1684317
2. Chegini, G., Taheri, M.: Whey powder: Process technology and physical properties: A review. Middle East J. Sci. Res. **13**, 1377–1387 (2013)
3. Anandharamakrishnan, C., Gimbun, J., Stapley, A.G.F., Rielly, C.D.: A study of particle histories during spray drying using computational fluid dynamic simulations. Dry Technol. **28**, 566–576 (2010)
4. Wang, Y., Selomulya, C.: Spray drying strategy for encapsulation of bioactive peptide powders for food applications. Adv. Powder Technol. **31**, 409–415 (2020). The Society of Powder Technology, Japan https://doi.org/10.1016/j.apt.2019.10.034
5. Benavides-Morán, A., Cubillos, A., Gómez, A.: Spray drying experiments and CFD simulation of guava juice formulation. Dry Technol. **39**, 450–465 (2021). Taylor & Francis https://doi.org/10.1080/07373937.2019.1708382
6. Sadripour, M., Rahimi, A., Hatamipour, M.S.: Experimental study and CFD modeling of wall deposition in a spray dryer. Dry Technol. **30**, 574–582 (2012)
7. Roustapour, O.R., Hosseinalipour, M., Ghobadian, B., Mohaghegh, F., Azad, N.M.: A proposed numerical-experimental method for drying kinetics in a spray dryer. J. Food Eng. **90**, 20–26 (2009)
8. Jubaer, H., Afshar, S., Xiao, J., Chen, X.D., Selomulya, C., Woo, M.W.: On the effect of turbulence models on CFD simulations of a counter-current spray drying process. Chem. Eng. Res. Des. **141**, 592–607 (2019). Institution of Chemical Engineers https://doi.org/10.1016/j.cherd.2018.11.024
9. Jayaraju, S.: Study of the air flow and aerosol transport in the human upper airway using LES and DES methodologies. Vrije Univ. Brussel (2009).
10. Liu, Y., Rao, Y., Weigand, B.: Heat transfer and pressure loss characteristics in a swirl cooling tube with dimples on the tube inner surface. Int. J. Heat Mass Transf. **128**, 54–65 (2019). Elsevier Ltd. https://doi.org/10.1016/j.ijheatmasstransfer.2018.08.097
11. Jubaer, H., Afshar, S., Le Maout, G., Mejean, S., Selomulya, C., Xiao, J., et al.: The impact of self-sustained oscillations on particle residence time in a commercial scale spray dryer. Powder Technol. **360**, 1177–1191 (2020). Elsevier B.V https://doi.org/10.1016/j.powtec.2019.11.023
12. Mezhericher, M., Levy, A., Borde, I.: Droplet-droplet interactions in spray drying by using 2D computational fluid dynamic. Dry Technol. **26**, 265–282 (2008)

DeltaEC Modelling of Thermoacoustics Oscillatory Flow Condition

Dahlia Johari[1,2(✉)], Fatimah Al-Zahrah Mohd Sa'at[1,2],
and Mohamad Firdaus Shukri[1,2]

[1] Fakulti Kejuruteraan Mekanikal, Universiti Teknikal Malaysia Melaka, Hang Tuah Jaya,
76100 Durian Tunggal, Melaka, Malaysia
dahliajohari93@gmail.com

[2] Centre for Advanced Research On Energy, Universiti Teknikal Malaysia Melaka, Hang Tuah
Jaya, 76100 Durian Tunggal, Melaka, Malaysia

Abstract. The paper reports the prediction of oscillatory flow conditions inside a standing wave thermoacoustic resonator by using the Design Environment for Low-amplitude Thermoacoustic Engines (DeltaEC) software. A 6.6 m long resonator is designed with an oscillating frequency of 14.2 Hz. A design of fourteen blocks is tested and velocity changes across the rig are reported. Flow is varied with drive ratios starting from 0.65% to 3%. The results confirmed that the design follows the standing wave criteria as predicted by the theory. Due to simplification utilized by DeltaEC, it is found that the software is unable to provide detail information of temperature change across all parts inside the resonator. Different method will be needed to confirm the temperature variations within the system, but in general DeltaEC does provide sufficient information for designing purpose of the thermoacoustic system.

Keywords: Thermoacoustics · DeltaEC

1 Introduction

Thermoacoustic is a combination of two interesting fields of study that are equally important in modern technology: thermodynamics and acoustics. It comprises the effect of the thermoacoustic phenomenon where the interaction between the compressible fluids and a solid surface will cause thermodynamics processes of power or refrigeration cycles to take place. In thermoacoustics, the imposed temperature gradient can induce oscillations of the compressible fluids in the fluid solids interfaces that lead to power production [1]. On the other hand, the acoustic waves can contribute to the heat pumping effects that allow establishment of temperature gradient within the solid materials to create thermoacoustic refrigerator [2]. Since the 18th century, when Byron Higgins discovered the thermoacoustic effects based on oscillations produced by hydrogens flames, researchers started to investigate the practical application of the thermoacoustic effects in heat engines and heat pumps [4–6]. A significant breakthrough in thermoacoustic was the Carter's invention of 'stack' in 1962 [4] and a 'regenerator' by Ceperly in 1979

[5]. This porous material has significantly increased the effectiveness of fluid-solid contact, thus increasing the acoustic intensity [6]. Although the thermoacoustic study was developed centuries ago, the fundamentals of fluid dynamics and heat transfers in the thermoacoustic flows are less developed. Most of the published research focuses on the one-directional flow rather than the bi-directional (oscillatory) flow used in the thermoacoustic study. Investigating the thermal fluids fundamental aspects of thermoacoustics requires development of a test rig with correct thermoacoustic representation. In order to help designing a thermoacoustic system, Los Alamos National Laboratory developed a Design Environment for Low-amplitude Thermoacoustic Engines (DeltaEC) software that uses linear thermoacoustic equation to predict performance of the designated system [7]. In this paper, the use of DeltaEC for designing an experimental rig for the purpose of fundamental study of heat transfer within the less known oscillatory flow of thermoacoustics will be reported.

2   DeltaEC Modelling

Figure 1 shows the standing wave test rig that was designed using DeltaEC. The rig was designed with several segments so that it has the ability to be used for investigations of various experimental parameters for thermoacoustics. The total length of the resonator is 6.6 m and was represented by fourteen blocks: 8 ducts with different length, 2 instructions of 'begin' and 'minor', 1 'speaker' and 1 'hardend' to close the resonator. Initial values are defined in 'begin'. The 'DUCT" represents the segments that form the resonator. 'Minor' was used to represent potential losses due to changes of cross-sectional areas between parts. A heat exchanger is placed at a segment labelled as '7' in Fig. 1. In this design, a resonator for 14.2 Hz resonance frequency was tested. The tested drive ratio of the flow varies from 0.65% until 3.0%. The model was set to operate at atmospheric pressure. The initial temperature and pressure were set as 296.15 K and 210.89 Pa, respectively. The volume flow rate is set to change to cover various flow conditions (drive ratio).
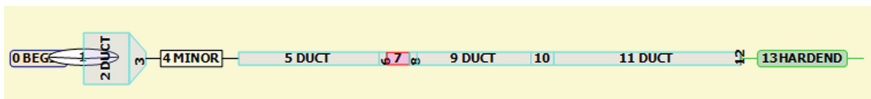
Fig. 1. DeltaEC's schematic diagram of designated standing wave thermoacoustic system.

3   Results and Discussions

Figure 2 shows the prediction of velocity across the designated rig. The pressure antinode is at the right end of the test rig, at a segment called 'Hardend'. The acoustic power is supplied by the speaker (labelled as '1' in Fig. 1). For a quarter wavelength standing wave resonator, the velocity is higher near the speaker [8]. The internal structure like stacks or heat exchangers should be placed where the product of oscillating pressure and velocity are not zero. In this design, the heat exchanger (i.e. tube banks) is placed at segment

number 7 or 4.35 m from the antinode, where the velocity is approaching the highest values, as shown in the result of Fig. 2. Figure 2 shows velocity distribution along the resonator as drive ratio (i.e. flow amplitude) changes. The black lines represent the result predicted by DeltaEC and the red lines represent the velocity calculated from theory [4]. Drive ratio is the ratio of pressure at antinode over atmospheric pressure. Differences between DeltaEC and theoretical predictions are small at low drive ratio but becomes bigger as drive ratio increases. This is expected to be due to the inclusion of the impact of losses and obstruction of flow that was included in DeltaEC calculation. Theoretical equation assumes that there was no losses or obstruction in the flow [4]. Even though the difference is quite high for the highest drive ratio, the trend is basically the same. Therefore, it can be concluded that the designated rig is able to offer thermoacoustic flow condition that is required for the future experimental works.
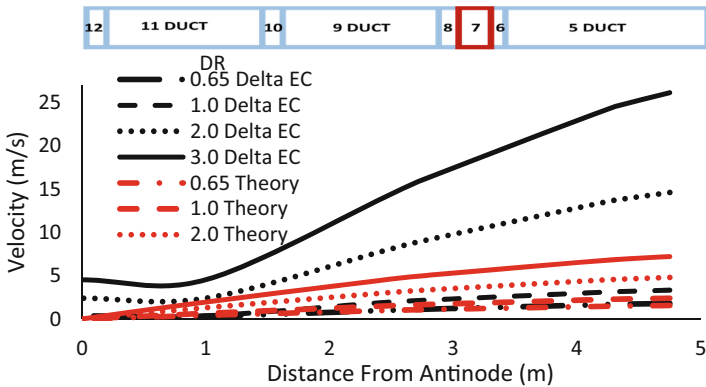
Fig. 2. The predicted velocity from the antinode.

Unfortunately, as shown in the data of Table 1, DeltaEC is unable to provide detail prediction of temperature change in the fluid inside the resonator. This happens because DeltaEC assumes that temperature effect is only happening near the stack/regenerator [4]. This indicates that fundamental understanding of change of fluid temperature across the resonator with respect to the change in heating power cannot be predicted by using DeltaEC. Therefore, in order to investigate the dynamic of change of the fluid temperature within the system, the use of other methods will be required. The results also show that the change of the drive ratio did not lead to a significant change in the temperature of the solid and the fluid. This also highlights the limitation of the current model of DeltaEC in predicting the actual results.

Table 1. Temperature of fluid and solid with changes of drive ratio and heater power.

Heater power (W)	Drive ratio (DR)	T solid (°C)	T fluid (°C)
500	1.5	221.57	210.89
	3.0	221.57	
1500	1.5	242.92	210.89
	3.0	242.92	
2500	1.5	266.27	210.89
	3.0	266.27	

4 Conclusion and Future Work

A quarter wavelength standing wave thermoacoustic rig was designed using DeltaEC software. Results showed that the standing wave criteria was met. Comparison between the results from the software and the theory indicates that DeltaEC offers better prediction compared to theory as it has the ability to model additional losses that can be expected in real operation. However, the limitation of the investigations based on DeltaEC prediction, especially related to temperature field, should be thoroughly considered especially if detail investigation of thermal behavior of flow is needed. Additional effects such as the limited range of amplitude of acoustic driver and the external factors such as the vibration of the long test rig, just to name a few, should also be considered when comparing data from DeltaEC and the real system.

References

1. Normah, M.G., Irfan, A.R., Koh, K.S., Manet, A., Zaki, A.M.: Investigation of a portable standing wave thermoacoustic heat engine. Procedia Eng. **56**, 829–834 (2013)
2. Tasnim, S.H.: An experimental study on heterogeneous porous stacks in a thermoacoustic heat pump. J. Energy Resour. Technol. **139**(4), 042005 (2017)
3. Higgins, B.: On the sound produced by a current of hydrogen gas passing through a tube. J. Nat. Philos. Chem. Arts **1**(129–131), 2 (1802)
4. Swift, G.W.: Thermoacoustics: A unifying perspective for some engines and refrigerators, 5th ed. (2003)
5. Ceperley, P.H.: A pistonless Stirling engine-The traveling wave heat engine. J. Acoust. Soc. Am. **66**(5), 1508–1513 (1979)
6. Chen, G., Tang, L., Mace, B., Yu, Z.: Multi-physics coupling in thermoacoustic devices: A review. Renew. Sustain. Energy Rev. **146**, 111170 (2021)
7. Clark, J.P., Ward, W.C., Swift, G.W.: Design environment for low-amplitude thermoacoustic energy conversion (DeltaEC). J. Acoust. Soc. Am. **122**(5), 3014–3014 (2007)
8. Marx, D., Mao, X., Jaworski, A.J.: Acoustic coupling between the loudspeaker and the resonator in a standing-wave thermoacoustic device. Appl. Acoust. **67**(5), 402–419 (2006)

Residence Times Representation of Turbulence Measurements by a Novel Laser Doppler System

M. Rusdy Yaacob[1(✉)], Rasmus K. Schlander[2], Preben Buchhave[3], and Clara M. Velte[4]

[1] Faculty of Electrical Engineering, Universiti Teknikal Malaysia Melaka, Hang Tuah Jaya, 76100 Durian Tunggal, Melaka, Malaysia
rusdy@utem.edu.my
[2] Department of Aeronautics, Imperial College, London SW7 2AZ, UK
[3] Intarsia Optics, Sønderskovvej 3, 3460 Birkerød, Denmark
[4] Department of Mechanical Engineering, Technical University of Denmark, Nils Koppels All´e, Bldg. 403, 2800 Kgs. Lyngby, Denmark

Abstract. High accuracy and dynamic range have been some of the most prominent challenges when it comes to non-equilibrium turbulence measurements. LDA is one of the most preferred measurements techniques in these challenging turbulent flow measurements for its unique favorable properties in various experimental investigations. The current commercial hardware-driven LDA systems however suffer from practical limitations in accurately representing long and short residence times. A novel software-driven LDA, has therefore been developed to enhance the measurement quality and the dynamic range. A round turbulent jet has been used as the test bed that is similar to the one used for previous measurements with a typical commercial LDA. Both data are diagnosed for dynamic range in residence times and compared to each other. Much longer residence times is captured at the lowest (near zero) velocities by the novel LDA compared to that of the commercial one, which maximum value is abruptly limited at the outermost off-axis positions (52 mm).

Keywords: Laser doppler anemometer · Residence time · Turbulent round jet

1 Introduction

Turbulence has long been an area of classical physics that is yet to be completely defined and discovered [1], despite its ubiquity in various applications, e.g., combustion engines and weather forecast. Moreover, the non-equilibrium aspects of stationary turbulence are still largely underexplored, as compared to the equilibrium counterpart that has been thoroughly investigated and understood [2]. The non-equilibrium flows are particularly hard to measure accurately due to high level of turbulence intensity and big variations in dynamic range.

The laser Doppler anemometer (LDA in the following) appears to be the most accurate and preferred existing instrument to measure these difficult flows since it intrinsically comes with a wide dynamic range, unlike e.g., correlation-based Particle Image

Velocimetry, and is able to unambiguously distinguish between and discern the velocity components (Hussein, Capp, and George 1994)), unlike e.g., hotwires. LDA has also been significantly recognized for its unique favorable properties in various experimental investigations [3][4].

However, existing commercial hardware-driven LDA systems have been restricted with some practical limitations, e.g., for turbulence measurements that require high dynamic range and signal-to-noise ratio [5]. Due to the hardware limitations in the burst sampling, both the long and short residence times are not well-represented in the data set acquired by the commercial LDA systems. It is highly necessary to accurately represent these residence times in order to obtain unbiased statistics, especially for high intensity and high shear flows [6]. It is therefore of great interest to develop a novel, software-driven LDA system that is highly flexible in this regard in order to measure turbulence more accurately, without having to deal with the misrepresentation of the residence times.

2   Methodology

2.1   Flow Generation Facility

The axisymmetric turbulent round jet used for the measurement is a replica of the one used by [6], fitted with an outer nozzle at the end, having an exit diameter, $D = 10$ mm and contraction ratio of 3.2:1. Pressurized air is fed to the jet with the glycerin particles (~1–5 µm) at regulated pressure values. The jet is mounted on a two-axis traversing system so that the jet centerline can be simply traversed to various desired coordinates within the flow for turbulence measurement at high spatial resolution.

2.2   Laser Doppler Anemometer

The burst mode LDA consists of a continuous wave laser beam (wavelength, $\lambda = 532$ nm) split into two coherent and parallel beams, which are directed through a dual Bragg cell that gives a 3 MHz frequency shift to the beams. This helps to distinguish the moving direction of the particles along the measured component axis [7]. The beams then pass through a converging lens with a focal point of 200 mm, at which the beams and creates a measurement volume (MV in the following) where the local velocity of the flow is measured. A photodetector coupled to a photomultiplier receives the light scattered by each seeding particle and generate an amplified photocurrent. A high-end oscilloscope (embedded with a A/D converter) visualizes the analog frequency modulated signal.

The experimental setup is enclosed in a large black canvas tent. The LDA system is operated in a forward-scattering detection mode by mounting the detector at 45° from the MV in order to minimize the light extinction and produce a smaller and nearly spherical MV. This allows the obtainment of unbiased measurement especially in a highly turbulent flow and realization of the highest possible spatial resolution [8].

2.3   LDA Measurement

A thorough and rigid alignment on the optical parts was done prior to the measurement to assure good quality of the Doppler signals out of it. A series of measurements were carried out, between $x/D = 5$ up to $x/D = 30$ downstream while for each downstream position, measurements were acquired at several points in the radial, r direction, as depicted in Fig. 1. The output measured and stored into the oscilloscope were processed using an in-house processor specifically developed for the novel LDA system.
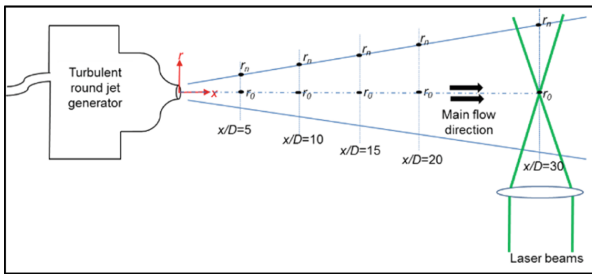
Fig. 1. Schematic of the measurement points (MP).

3   Results and Discussions

The instantaneous velocities obtained from the processor are scatter plotted against their respective residence times and compared to the commercial counterpart in the same turbulent round jet at 30 jet exit diameters downstream and two different radial positions; $r = 26$ mm and 52 mm obtained in [6]. As observed in Fig. 2, the novel processor captures much longer residence times at the lowest velocities compared to that of the commercial one, which maximum value is abruptly limited at the outermost off-axis positions (52 mm). The length of the longest measurable bursts as defined in the commercial hardware has effectively limited the maximum burst length and consequently the quality of low mean velocity (high intensity) result.
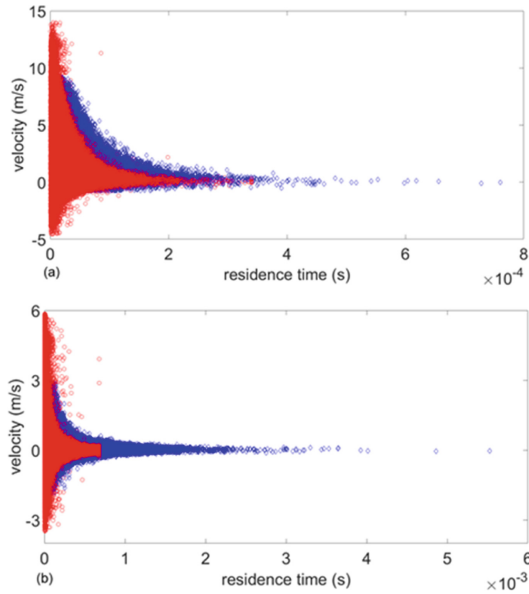
Fig. 2. Velocity vs. residence time scatter plots for **a** $r = 26$ and 27 mm, **b** $r = 52$ and 51 mm. *Red circle*: hardware driven LDA processor, *Blue diamond*: software driven LDA processor.

4   Conclusions

In conclusion, the novel LDA system has successfully represented the long and short residence times in the data set acquired by the commercial LDA systems. This proven functionality opens up an opportunity to further investigate the dynamics of non-equilibrium flows to properly test the well-known local equilibrium hypothesis for the structure of the small scale turbulence, in the full version of this manuscript.

References

1. L'vov, V., Procaccia, I.: Hydrodynamic turbulence: A 19th century problem with a challenge for the 21st century. In: Proceedings of the Turbulence Modeling and Vortex Dynamics, pp. 1–16 (2008)
2. Batchelor, G.K.: The theory of homogeneous turbulence. Cambridge University Press (1953)
3. Barker, S.J.: Laser-Doppler measurements on a round turbulent jet in dilute polymer solutions. J. Fluid Mech. **60**, 721–731 (1973)
4. Buchhave, P., George, W.K., Lumley, J.L.: The measurement of turbulence with the laser-doppler anemometer. Annu. Rev. Fluid Mech. **11**, 443–503 (1979)
5. Buchhave, P., Velte, C.M., George, W.K.: The effect of dead time on randomly sampled power spectral estimates. Exp. Fluids **55**(2), 1–8 (2014). https://doi.org/10.1007/s00348-014-1680-1
6. Velte, C.M., George, W.K., Buchhave, P.: Estimation of burst-mode LDA power spectra. Exp. Fluids **55**(3), 1–20 (2014). https://doi.org/10.1007/s00348-014-1674-z
7. Buchhave, P.: Three-component LDA measurements. Disa. Inf. (29), 3–9 (1984)
8. Buchhave, P., Velte, C.M.: Measurement of turbulent spatial structure and kinetic energy spectrum by exact temporal-to-spatial mapping. Phys. Fluids **29**(8), 085109 (2017)

Effect of Temperature on the Mechanical Performance of Joints Bonded with Electrically Conductive Adhesive

Zuraimi Ramle[1,3], Mizah Ramli[1,2,3(✉)], Siti Hajar Sheikh Md Fadzullah[1,2,3], Mohd Nur Azmi Nordin[1,2,3], Ghazali Omar[1,2,3], and Mohammad Zharfan Zaidi[1,3]

[1] Fakulti Kejuruteraan Mekanikal, Universiti Teknikal Malaysia Melaka, Hang Tuah Jaya, 76100 Durian Tunggal, Melaka, Malaysia
mizah@utem.edu.my

[2] Centre for Advanced Research on Energy, Universiti Teknikal Malaysia Melaka, Hang Tuah Jaya, 76100 Durian Tunggal, Melaka, Malaysia

[3] Advanced Manufacturing Center, Universiti Teknikal Malaysia Melaka, Hang Tuah Jaya, 76100 Durian Tunggal, Melaka, Malaysia

Abstract. Adhesively bonded connections are now commonly employed in products that may be subjected to a variety of environmental conditions. Temperature fluctuations are an element that may inflict damage on adhesive joints and lead to interconnection failure. The objective of this work is to investigate the effect of temperature on the joints bonded with electrically conductive adhesive. Adhesive joints were exposed to high and low temperatures at 85 °C and 6 °C respectively for 10, 30, and 50 h. The shear strength of the joints, which were represented by single lap joints was obtained from tensile tests. The effect of temperature was also observed on the fracture surfaces of the adhesive joints measured by a 3D profilometer. Results indicated that exposure to high temperatures increased the performance of adhesive joints significantly. The strength of adhesive joints increased as the hours of exposure to high temperatures increased. It can be concluded that at low temperature, the surface of the electrically conductive adhesive becomes more ductile due to the number and frequency of lower peak, while at high temperature, the surface of electrically conductive adhesive becomes more brittle due to the number and frequency of the higher peak.

Keywords: Adhesive joints · Electrically conductive adhesive · Low and high temperature exposure

1 Introduction

An electrically conductive adhesive is glue that is widely used in the electronic industry. An electrically conductive adhesive will act as a medium for electric current to pass through them. There are a lot of advantages to why conductive adhesive is widely used in the industry instead of soldering processes. Based on the research, some of the electronic parts cannot be soldered due to the sensitivity of temperature. Therefore, the conductive

adhesive is the best problem solving for electronic parts that are sensitive to temperature because it proves that the temperature of the soldering process is higher than conductive adhesive [1]. In addition, the ability of the conductive adhesive to with-stand vibrations is better compared to the solder. Besides, the conductive adhesive is more flexible and easier to use compared to the solder. Electrically conductive adhesive is divided into two types which are isotropic and anisotropic. Isotropic conductive adhesive (ICA) is defined as electrically conductive in all directions. For example, isotropic is used for a chip contacting and bonding electrically conductive surface mounting device (SMD). Anisotropic conductive adhesive (ACA) is electrically conductive only in one direction and it is containing special conductive particles in the μm range. For example, liquid crystal display (LCD) connection, contacting flexible printed circuit board (PCB) and bonding antenna structures on radio-frequency identification (RFID) used ACA because they contain sensitive structures on circuit boards [2].

Adhesion tends to suffer from the degradation of the joint at elevated temperature and in water compared to the other joining method, such as welding, brazing, soldering, and fastening. There are a lot of factors that must be considered to design the adhesive joints. One of them is the effects of temperature on the strength of adhesive joints. Therefore, in order to improve the temperature of adhesive joints, a lot of work has been made. Cure shrinkage, the coefficient of thermal expansion (CTE), and different adhesive mechanical properties are the most important factors to measure the strength of the adhesive joint when it is applied under the extreme temperature range. However, due to the polymeric nature of adhesives, generally, the most significant factor must be considered to design the bonded joint because of the variation of the mechanical properties of the adhesives with temperature. At low temperatures, the high thermal stresses and the brittleness of the adhesive are the origins of such behavior, while at high temperatures the adhesive strength is low [3–5].

2 Methodology

The materials used as the electrically conductive adhesive was Bare Conductive Electric Paint mixed with Araldite®Rapid (mix ratio1:1). The adherents to fabricate single lap joints were made of aluminium dimensioned 101.6 mm (L) × 25.4 mm (W) × 1.6 mm (H) each and were roughened by sandpaper to provide constant roughness to the bonding surfaces. In the bonding process to join two adherents to form a single lap joint, a jig was used to ensure the determined thickness of 0.1 mm. The purpose of the jig was also to match both top and bottom adherents in parallel. If the single lap joint is not aligned, it will affect the accuracy of the result. In this work, the jig as shown in Fig. 1 was manufactured by a 3D printer unlike the conventional jig, which was made of metal by machining process. The dimension of single lap joints is depicted in Fig. 2.

The preparation of the single lap joints was according to the ASTM D1002. The completion of bonding process was followed by a curing process at room temperature for 24 h and later at 100 °C for 30 min. The specimens were cooled down at room temperature for 24 h prior to high and low temperature exposure. The specimens were exposed to 85 °C and 6 °C for 10, 30 and 50 h. All the specimens were cured in the curing oven UF55 Memmert. Tensile tests as shown in Fig. 3 were conducted on all
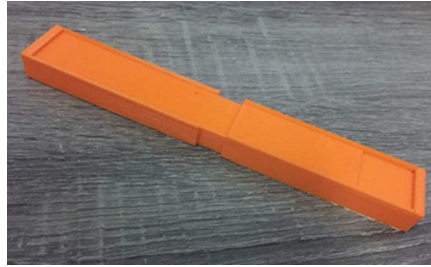
Fig. 1. The jig fabricated by a 3D printer to bond single lap joints with thickness of 0.1 mm.
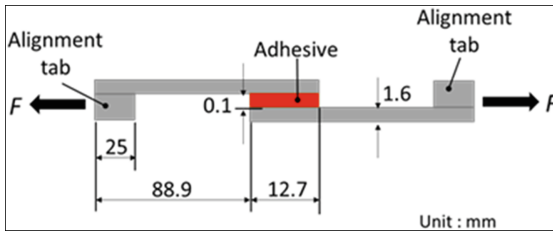
Fig. 2. The dimension of single lap joints with 0.1 mm thickness of adhesive.

specimens to measure their strength performance after the exposure to high and low heat environmental conditions. The speed of 1.30 mm/min was applied during the tensile test to determine the maximum force (N) and elongation (mm) of the single lap joints until fracture occurred. After the tensile test, the process of examining the fracture on the surface of the specimen will be carried out. A 3D profilometer was employed to determine the fracture on the surface of the specimen and surface roughness.

Fig. 3. The strengths of the single lap joints were determined from tensile testing machine.

3   Results and Discussion

3.1   Joints Without Temperature Exposure

Before scrutinizing the performance of adhesive joints affected by high and low temperature exposure, the strength of adhesive joints was first determined at room temperature. Figure 4 expresses the result of the tensile test for three specimens for room temperature condition without surface treatment on the adherents. The surface roughness measured by a 3D profilometer is shown in Table 1. The average of the maximum shear strength for all three specimens is 0.61 MPa. It is noted that the adhesive did not adhered well to the adherents, thus results in interfacial failure.

Table 1. The value of surface roughness, Ra of the adherends without surface treatment.

Sample	Unit	1	2	3
Ra1	µm	0.9010	0.7183	0.4875
Ra2	µm	0.6825	0.7279	0.2299
Ra3	µm	0.5928	0.4748	0.5587
Ra4	µm	0.3837	0.5341	0.5155
Ra5	µm	0.6673	0.7157	0.4977
Average Ra	µm	0.6455	0.6342	0.4579
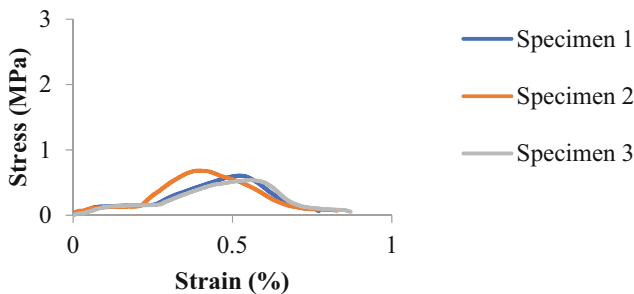
Fig. 4. The shear strength specimens for room temperature condition before the process of surface treatment.

In improving the adhesion of the adhesive joints, the bonded areas of the single lap joints were rubbed with sandpaper to produce a higher value of surface roughness. The surface roughness functioned as an interlocking medium and by increasing the surface contact areas, the adhesion became stronger. Table 2 depicts the surface roughness measurement of each specimen with surface treatment, while Fig. 5 indicated the improvement of strength due to the increase of surface roughness. The strength improved twice the value of the strength before surface treatment. For the temperature exposure testing, all specimens with surface treatment were used.

Table 2. The value of surface roughness, Ra of the adherends with surface treatment.

Sample	Unit	1	2	3
Ra1	μm	1.1357	1.1665	0.8303
Ra2	μm	1.0064	0.9876	0.6578
Ra3	μm	0.6776	0.7275	0.9765
Ra4	μm	0.7989	0.5630	0.8192
Ra5	μm	1.0166	1.0255	0.7661
Average Ra	μm	0.9270	0.8940	0.8099
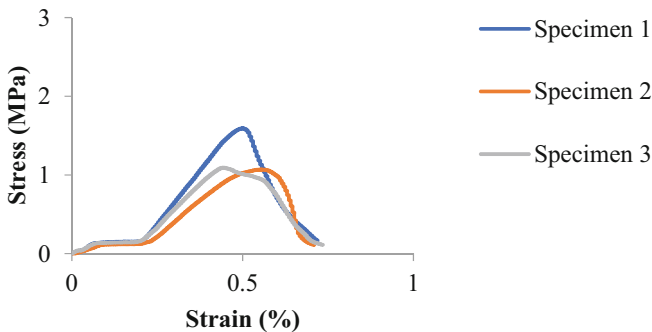
Fig. 5. The shear strength specimens for room temperature condition with surface treatment.

3.2 Low Temperature Exposure

Figure 6 showed that the average data of lap shear strength for RT, 10, 30 and 50 h of specimen at 6 ˚C. The specimens were exposed to 6 ˚C for 10, 30 and 50 h. and it showed that there are drastically decrease in the lap shear strength of the joints compared to the room temperature. It can be explained that, when the specimens were exposed to the temperature at 6 ˚C, it increased the moisture content in adhesive layer which degraded the lap shear strength. Furthermore, the number of lower peak and the frequency of lower peak occur has an important role in this section. The higher the number of lower peak and the higher the frequency of lower peak will degrade the mechanical interlocking between the surfaces [7]. Thus, it also contributed to the low of shear strength. Furthermore, the higher the number of lower peak and the higher the frequency of lower peak occur will result in ductility of the surface [6].

3.3 High Temperature Exposure

Figure 7 showed that the average data of lap shear strength for RT, 10, 30 and 50 h of specimen at 85 ˚C. The specimen was exposed at the temperature of 85 ˚C for 10, 30 and 50 h and it showed that there are drastically increase in the lap shear strength of the joints compared to the room temperature. When the specimens were tested for 10 to
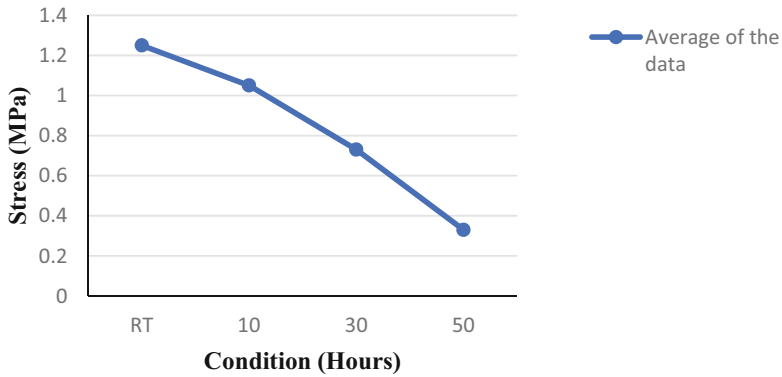
Fig. 6. Average data of lap shear strength for RT, 10, 30 and 50 h of specimen at 6 ˚C.

the 30 h, it showed that there are increases in the lap shear strength. However, there are decreases in the temperature when the specimens were tested for 30 to the 50 h. It can be explained that the adhesive becomes more ductile and the overlap contributes more to the strength as the adhesive yields when the specimens were exposed at 85 ˚C for 50 h. Furthermore, it also can be explained by, if the specimen was exposed to the heat for a long duration, it will degrade the characteristic of ECA [8]. Based on topography of the lap joint, it shows that the higher the number of high peak and the higher the frequency of high peak occur will contribute to the high in mechanical interlocking. Thus, it will increase the shear strength of lap joint.
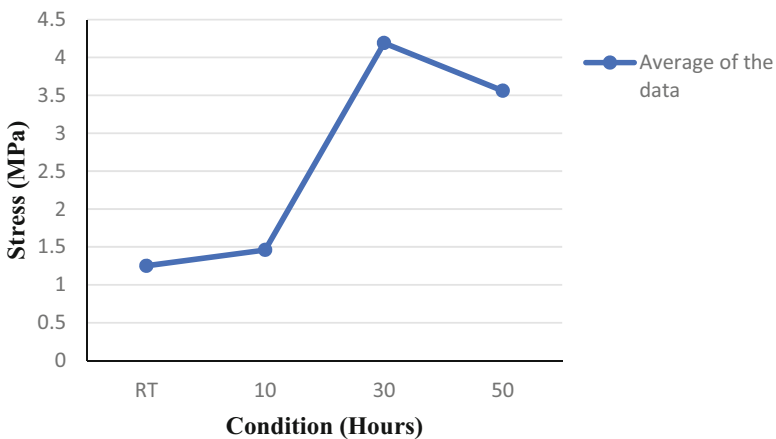
Fig. 7. Average data of lap shear strength for RT, 10, 30 and 50 h of specimen at 85 ˚C.

4   Conclusions

An electrically conductive adhesive is an advance technology used in electronic industry. Electronic parts are known due to sensitivity to the temperature. Therefore, an ECA is a problem solving to the electronic industry because the temperature of ECA is a much lower than soldering process. As a conclusion, the lap of shear strength for single lap joints tested at low temperature application of 6 ˚C for 10 h decreased approximately 16% than RT. Furthermore, approximately 41.6% of lap shear strength was decreased at 30 h application while approximately 73.6% at 50 h application. Besides that, at high temperature application of 85 ˚C for 10 h, approximately 16.8% was increased than at RT. Moreover, approximately 235.2% of lap shear strength was increased at 30 h application while approximately 184.8% for 50 h application. It can be concluded that at low temperature, the surface of the ECA becomes more ductile due to the number and frequency of lower peak, while at high temperature, the surface of ECA becomes more brittle due to the number and frequency of higher peak. ECA is advised to extend the life of electronic parts due to their ability to endure vibration. It can also be used in other industries, such as the automobile and aerospace industries. However, further research into their temperature fluctuation characteristics is required. The reaction of the adhesive to high temperatures must be carefully studied in order to guarantee that the strength of adhesive does not deteriorate. The presence of moisture content must be prevented at low temperatures from degrading the strength of adhesive.

References

1. Hummel, D.: The second international vortex flow experiment (VFE-2): Objectives and first results. Proc. Inst. Mech. Eng. Part G J. Aerosp. Eng. **220**, 559–568 (2006)
2. Luckring, J., Hummel, D.: What was learned from the new VFE-2 experiments. Aerosp. Sci. Technol. **24**, 77–88 (2013)
3. Mat, S., Green, R., Galbraith, R., Coton, F.: The effect of edge profile on delta wing flow. Proc. Inst. Mech. Eng. Part G: J. Aerosp. Eng. **230**, 1252–1262 (2015)
4. Madan, I., Tajudin, N., Said, M., Mat, S., Othman, N., Wahid, M., Mohamed Radzi, N., Miau, J., Chen, Y., Chen, L.: Influence of active flow control on blunt-edged VFE-2 delta wing model. Int. J. Automot. Mech. Eng. **18**, 8411–8422 (2021)
5. Luckring, J.: Initial experiments and analysis of blunt-edge vortex flows for VFE-2 configurations at NASA Langley, USA. Aerosp. Sci. Technol. **24**, 10–21 (2013)
6. Konrath, R., Klein, C., Schröder, A.: PSP and PIV investigations on the VFE-2 configuration in sub- and transonic flow. Aerosp. Sci. Technol. **24**, 22–31 (2013)
7. Fritz, W.: Numerical simulation of the peculiar subsonic flow-field about the VFE-2 delta wing with rounded leading edge. Aerosp. Sci. Technol. **24**, 45–55 (2013)
8. Niu, H., Yi, S., Liu, X., Lu, X., Gang, D.: Experimental investigation of boundary layer transition over a delta wing at mach number 6. Chin. J. Aeronaut. **33**, 1889–1902 (2020)

Author Index